Preface

This book contains articles presented at the Second International Symposium on Solid Mechanics, held in Rio de Janeiro, Brazil, 28-30 April 2009. The International Symposium on Solid Mechanics – MecSol – is the first Brazilian conference fully dedicated to this branch of the engineering science. It had its first edition in 2007 and takes place every two years in a Brazilian city. The MecSol Symposium is organized under the aegis of the Solid Mechanics Committee of the Brazilian Society of Mechanical Sciences and Engineering.

The Brazilian technical community working in the field of Solid Mechanics has longed for a specialized conference. Hence, the Technical Committee on Solid Mechanics, from the Brazilian Society of Mechanical Sciences and Engineering, ABCM, set as its main task to organize this conference, with the present book reflecting the effort of the committee to maintain the scientific standards attained in the first conference.

The Symposium aimed at gathering specialists in the field of Solid Mechanics for an in depth discussion of the many aspects covered by this large branch of science and technology. The book features articles with focus on fundamental and applied issues, including computational, theoretical and experimental contributions, drawing upon the various branches of engineering science and the allied areas within applied mathematics, materials science, structural engineering and applied physics.

The editors would like to take the opportunity of thanking all the contributors to this volume for their effort in meeting all the tight deadlines and in writing such fine works. We also thank Renato Yamassaki for the hard work in formatting the whole book. Ana Lucia Froés de Souza, secretary to ABCM, was most helpful in many issues related to the organization of the conference. Finally, we would like to acknowledge the support of the Brazilian Society of Mechanical Sciences and Engineering to this event.

Heraldo da Costa Mattos
Marcílio Alves
Rio de Janeiro, March 2009

Mechanics of Solids in Brazil 2009, H.S. da Costa Mattos & Marcílio Alves (Editors)
Brazilian Society of Mechanical Sciences and Engineering, ISBN 978-85-85769-43-7

Contents

Mechanics of Solids in Brazil 2009, H.S. da Costa Mattos & Marcílio Alves (Editors)
Brazilian Society of Mechanical Sciences and Engineering, ISBN 978-85-85769-43-7

Mechanics of Solids in Brazil 2009, H.S. da Costa Mattos & Marcílio Alves (Editors)
Brazilian Society of Mechanical Sciences and Engineering, ISBN 978-85-85769-43-7

Mechanics of Solids in Brazil 2009, H.S. da Costa Mattos & Marcílio Alves (Editors)
Brazilian Society of Mechanical Sciences and Engineering, ISBN 978-85-85769-43-7

A numerical procedure for the determination of elastic parameters in an incompressible solid

Adair R. Aguiar, Edmar B. T. Prado
Department of Structural Engineering - SET/EESC/USP,
São Carlos/SP – Brazil

Abstract

A class of plane problems related to the determination of the shear elastic modulus μ of biological tissues is presented. A non-iterative numerical procedure to obtain approximate solutions to these problems from known displacement fields is employed. The displacement fields are obtained from quasi-static experiments that are possible to reproduce in laboratory and are simulated numerically using the Finite Element Method. Results for the distribution of μ in a long cylinder of rectangular cross-section containing either an eccentric circular inclusion or an inclusion with a complex geometry are presented. This work is of great interest in the detection of cancerous tumors and in the differential diagnosis of biological tissues.

Keywords: Biomechanics, incompressibility, elasticity, Finite Element Method.

1 Introduction

It is known from experimental observations that abnormal biological tissues have different mechanical behavior than normal biological tissues [1]. In particular, Krouskop *et al.* [2] observe that abnormal tissues are stiffer than normal tissues. To quantify these observations, we consider biological tissues undergoing small deformations during quasi-static experiments and model these tissues isotropic, incompressible, and linearly elastic materials [3]. We are then interested on the determination of the shear elastic modulus μ everywhere inside the elastic body.

The determination of elastic properties of biological tissues from experimental data has been the subject of intense investigation in recent years. See, for instance, Park and Maniatty [4] and references cited therein. Recently, Barbone and Gokhale [5] have considered plane problems in linear elastostatics and have shown that, except for four arbitrary constants, the general expression for the shear elastic modulus of an isotropic and incompressible material can be determined from two compatible and linearly independent displacement fields, which can be obtained from two distinct experiments. The arbitrary constants can be determined from the knowledge of the shear elastic modulus in four distinct points inside the body. The authors assume that both displacement fields are differentiable.

Mechanics of Solids in Brazil 2009, H.S. da Costa Mattos & Marcílio Alves (Editors)
Brazilian Society of Mechanical Sciences and Engineering, ISBN 978-85-85769-43-7

In this work, we propose a methodology to determine μ from two linearly independent displacement fields with less restrictive assumptions. Our methodology does not require both any *a priori* knowledge of μ inside the body and differentiability of the displacement fields. The methodology uses a Finite Element Method (FEM) to construct a numerical approximation for μ inside an isotropic, incompressible, and linearly elastic body in equilibrium that is also in a state of plane strain.

2 The problem statement

Consider a long cylinder in a state of plane strain parallel to its bases and let $\mathcal{B}$ be the undistorted natural reference configuration of a cross section of the cylinder. Points $\boldsymbol{x} \in \mathcal{B}$ are mapped to points $\boldsymbol{y}(x) = \boldsymbol{x} + \boldsymbol{u}(x)$, where $\boldsymbol{u}$ is the displacement field, which is assumed to be known in $\mathcal{B}$ together with its boundary $\partial\mathcal{B}$. Park and Maniatty [4] present a brief discussion about different experimental techniques that can be used to measure the displacement of a point inside the body.

The cylinder undergoes a small deformation and is in equilibrium in the absence of body force, so that

$$div\, \boldsymbol{T}\,(\boldsymbol{x}) = 0, \quad \forall\ \boldsymbol{x} \in \mathcal{B}, \tag{1}$$

where $\boldsymbol{T}$ is the stress tensor. We assume that the body is incompressible, isotropic, and linearly elastic, so that

$$\boldsymbol{T} = -\,\pi\,\mathbf{1} + 2\mu\boldsymbol{E}, \tag{2}$$

where π is a constraint reaction field, μ is the shear elastic modulus, which may depend on $\boldsymbol{x} \in \mathcal{B}$, and

$$\boldsymbol{E} = \nabla_s \boldsymbol{u} \equiv \frac{1}{2}\left[\nabla\boldsymbol{u} + (\nabla\boldsymbol{u})^T\right] \tag{3}$$

is the infinitesimal strain tensor. Observe from (2) that $\boldsymbol{T}$ is determined from both the strain tensor $\boldsymbol{E}$ and an arbitrary tensor $-\,\pi\,\mathbf{1}$, which represents the reaction of the body to local changes of volume. For incompressible materials, any infinitesimal deformation of $\mathcal{B}$ must satisfy

$$tr\,\boldsymbol{E} = div\,\boldsymbol{u} = 0. \tag{4}$$

Substituting both (2) and (3) into (1), we obtain

$$-\nabla\pi\,(\boldsymbol{x}) + 2\,div\,(\mu\boldsymbol{E})\,(\boldsymbol{x}) = 0, \quad \forall\ \boldsymbol{x} \in \mathcal{B}. \tag{5}$$

We then consider the *inverse problem* of determining both the shear elastic modulus $\mu : \mathcal{B} \to \mathbb{R}^2$ and the pressure field $\pi : \mathcal{B} \to \mathbb{R}^2$ that satisfy the partial differential equation (5), where the displacement field $\boldsymbol{u} : \mathcal{B} \to \mathbb{R}^2$ is known everywhere in $\overline{\mathcal{B}} \equiv \mathcal{B} \cup \partial\mathcal{B}$ and satisfies the kinematical constraint (4).

Barbone and Gokhale [5] and McLaughlin and Yoon [6] show that, in general, the inverse problem stated above does not have a unique solution. Barbone and Gokhale [5] show, however, that by knowing

Mechanics of Solids in Brazil 2009, H.S. da Costa Mattos & Marcílio Alves (Editors)
Brazilian Society of Mechanical Sciences and Engineering, ISBN 978-85-85769-43-7

two compatible, linearly independent, and differentiable displacement fields from two experiments performed on the same body in a state of plane strain, the general expression of μ contains at most four arbitrary constants. We review these results below with an example and propose a procedure to compute the arbitrary constants that can be extended to the more general case of μ not being continuous.

2.1 Considerations about Uniqueness

Let $(\boldsymbol{e_1}, \boldsymbol{e_2}, \boldsymbol{e_3})$ be an orthonormal basis in $\mathbb{R}^3$ associated to a system of rectangular cartesian coordinates with the origin in O. The vectors $\boldsymbol{e_1}$, $\boldsymbol{e_2}$ are parallel to the plane that contains $\mathcal{B}$ and $\boldsymbol{e_3}$ is parallel to the axis of the straight cylinder. In this coordinate system, a point is represented by $\boldsymbol{x} + \xi_3 \boldsymbol{e_3}$, where $\boldsymbol{x} = \xi_1 \boldsymbol{e_1} + \xi_2 \boldsymbol{e_2} \in \mathcal{B}$ and $\xi_i \in \mathbb{R}$, $i = 1,\ 2,\ 3$. In addition, $\boldsymbol{u} = \upsilon_1 \boldsymbol{e_1} + \upsilon_2 \boldsymbol{e_2}$, where $\upsilon_i \in \mathbb{R}$, $i = 1, 2$. It follows from (3) that $\boldsymbol{E} = \sum_{i,j=1}^{2} \varepsilon_{ij} \boldsymbol{e_i} \otimes \boldsymbol{e_j}$, where $\boldsymbol{e_i} \otimes \boldsymbol{e_j}$ is the tensorial product between $\boldsymbol{e_1}$ and $\boldsymbol{e_2}$, which is defined by $(\boldsymbol{e_i} \otimes \boldsymbol{e_j})\, \boldsymbol{e_k} = \delta_{jk} \boldsymbol{e_i}$, and $\varepsilon_{ij} \equiv \frac{1}{2}\left(\frac{\partial \upsilon_i}{\partial \xi_j} + \frac{\partial \upsilon_j}{\partial \xi_i}\right)$. Since the cylinder is under plane strain, it follows from (4) that $\varepsilon_{22} = -\varepsilon_{11}$.

Taking the curl of (5) and assuming that $\boldsymbol{u}$ is known everywhere in $\mathcal{B}$, we eliminate π and obtain the second-order differential equation

$$L[\mu] \equiv \left(\frac{\partial^2}{\partial \xi_1^2} - \frac{\partial^2}{\partial \xi_2^2}\right)(\mu \varepsilon_{12}) - 2\frac{\partial^2}{\partial \xi_1 \partial \xi_2}(\mu \varepsilon_{11}) = 0 \tag{6}$$

where $L[\mu]$ is a linear operator on μ. Since $(\varepsilon_{11})^2 + (\varepsilon_{12})^2 > 0$, it is a standard procedure to show that L is hyperbolic [7] and that the characteristics of L are parallel and perpendicular to the principal directions of $\boldsymbol{E}$.

To illustrate the fact that μ can not be determined from Eq. (6) alone and to motivate the introduction of a weak formulation of the inverse problem in Eq. (5) that leads to the determination of μ, consider an isotopic, incompressible, and linearly elastic cylinder with square cross section in a state of plane strain perpendicular to its axis. The length of a side of the square section is $\bar{\xi}$. The cylinder is subjected to two experiments that yield the homogeneous deformation fields

$$\varepsilon_{11}^1(\xi_1, \xi_2) = -\varepsilon_{22}^1(\xi_1, \xi_2) = \varepsilon_1, \quad \varepsilon_{12}^1(\xi_1, \xi_2) = 0, \quad \text{(Bi-axial experiment)}, \tag{7}$$

$$\varepsilon_{11}^2(\xi_1, \xi_2) = \varepsilon_{22}^2(\xi_1, \xi_2) = 0, \quad \varepsilon_{12}^2(\xi_1, \xi_2) = \varepsilon_2, \quad \text{(Shearing experiment)}. \tag{8}$$

In the bi-axial experiment, the cylinder is being pulled in one direction while being compressed in the other direction. The resultant forces on both sides have normal components of intensity τ_1. In the shearing experiment, the same cylinder is subjected to tangential forces of intensity τ_2 on its lateral sides. Clearly, the deformation fields (7) and (8) satisfy the constraint (4) identically and, if $\varepsilon_1 = \varepsilon_2$, refer to the same state of simple shear. In this case, the principal directions, and hence the characteristics of L in (6), are inclined with respect to each other by an angle of 45 degrees.

Substituting the deformation fields (7) into (6) and solving for μ, we obtain

$$\mu\left(\xi_1, \xi_2\right) = \phi_1\left(\xi_1\right) + \phi_2\left(\xi_2\right) \tag{9}$$

where ϕ_i, $i = 1, 2$, are arbitrary functions of its arguments, which can not be determined from the biaxial experiment alone. To determine these functions, we substitute (5) together with the deformation fields (8) into (6). We then get

$$\mu\left(\xi_1, \xi_2\right) = \mu_0 + \mu_1\xi_1 + \mu_2\xi_2 + \mu_3\left(\xi_1^2 + \xi_2^2\right) \tag{10}$$

where $\mu_i \in \mathbb{R}$, $i = 0, ..., 3$, are arbitrary constants. The expression (10) is presented by Barbone and Gokhale [5] to illustrate the fact that, except for four arbitrary constants, μ can be determined from two compatible and linearly independent displacement fields, which yield the deformation fields given by (7) and (8).

Corresponding to the deformation fields in both (7) and (8), there exist pressure fields π^1 and π^2 that can be determined from the substitution of (10) together with either (7) or (8) into (5), yielding

$$\pi^1\left(\xi_1, \xi_2\right) = 2\varepsilon_1\left[\mu_1\xi_1 - \mu_2\xi_2 + \mu_3\left(\xi_1^2 - \xi_2^2\right) + \hat{\pi}^1\right] \tag{11}$$

$$\pi^2\left(\xi_1, \xi_2\right) = 2\varepsilon_2\left[\mu_2\xi_1 + \mu_1\xi_2 + 2\mu_3\xi_1\xi_2 + \hat{\pi}^2\right] \tag{12}$$

where $\hat{\pi}^i \in \mathbb{R}$, $i = 1, 2$, are arbitrary constants of integration.

To determine the constants $\mu_i \in \mathbb{R}$, $i = 0, ..., 3$, in (10) and $\hat{\pi}^i \in \mathbb{R}$, $i = 1, 2$, in (11) and (12), we assume that the resultant forces τ_i, $i = 1, 2$, are known from experimental measurements. Since the traction field on the boundary is given by $\boldsymbol{t}(\boldsymbol{x}, \boldsymbol{n}) = \boldsymbol{T}(\boldsymbol{x})\boldsymbol{n}$, where $\boldsymbol{n}$ is the outward normal to the boundary at $\boldsymbol{x} \in \partial\mathcal{B}$ and $\boldsymbol{T}$ is given by (2), we obtain a system of equations for the determination of the constants above. Even though this system is over-determined, we obtain the solution

$$2\mu_0\bar{\xi} = \frac{\tau_2}{\varepsilon_2} = \frac{\tau_1}{\varepsilon_1}, \quad \mu_1 = \mu_2 = \mu_3 = 0, \quad \hat{\pi}^1 = \hat{\pi}^2 = 0. \tag{13}$$

It then follows from (10) - (12) that μ is constant, which means that the cylinder is homogeneous, and that $\pi^i = 0$, $i = 1, 2$.

The procedure outlined above for the determination of μ from both known deformation fields (7) and (8) and known resultant forces acting on complementary parts of the boundary of the cylinder can be extended to the general case of a non-homogeneous cylinder for which μ may not even be continuous. In this case, the determination of the fields μ e π^i, $i = 1, 2$, is not trivial and requires the use of numerical methods that allow the construction of approximations to these fields. Below, we present a weak formulation of the inverse problem for the determination of μ and π^i, $i = 1, 2$, which together with a Finite Element Method allow the construction of these approximations.

2.2 The weak formulation of the inverse problem

Let $\boldsymbol{u}^1$ and $\boldsymbol{u}^2$ be two compatible and linearly independent displacement fields (see [5]), which are not necessarily differentiable and are obtained from two distinct experiments performed on the same body, and let

$$\boldsymbol{R}_i^j = \int\limits_{\partial_i \mathcal{B}} \left(-\pi^j \mathbf{1} + 2\mu \nabla_s \boldsymbol{u}^j \right) \boldsymbol{n}_i dL \tag{14}$$

be resultant forces that are known on r complementary parts $\partial_i \mathcal{B}$, $i = 1, ..., r$, of $\partial \mathcal{B}$, so that $\partial \mathcal{B} \equiv \bigcup\limits_{i=1}^{r} \partial_i \mathcal{B}$ and $\partial_i \mathcal{B} \bigcap \partial_j \mathcal{B} \neq \emptyset$, $i \neq j$. In (6), π^j, j = 1, 2, is the pressure field associated with the displacement field $\boldsymbol{u}^j$ and $\boldsymbol{n}_i$ is a unit normal to $\partial_i \mathcal{B}$. To satisfy the global equilibrium condition, we must have $\sum\limits_{i=1}^{r} \boldsymbol{R}_i^j = 0$, j = 1, 2.

We want to determine the shear elastic modulus $\mu : \mathcal{B} \to \mathbb{R}^2$ and the pressure field $\pi^j : \mathcal{B} \to \mathbb{R}^2$, j = 1, 2, that satisfy both

$$-\nabla \pi^j (\boldsymbol{x}) + 2\, div \left(\mu \nabla_s \boldsymbol{u}^j \right) (\boldsymbol{x}) = 0, \quad \forall\, \boldsymbol{x} \in \mathcal{B} \tag{15}$$

and the expression (14) for known resultants $\boldsymbol{R}_i^j$, where the displacement field $\boldsymbol{u}^j : \mathcal{B} \to \mathbb{R}^2$, j = 1, 2, is known everywhere in $\overline{\mathcal{B}}$ and satisfy the kinematical constraint $div\, \boldsymbol{u}^j = 0$.

Now, let $\mathcal{L}^2(\mathcal{B})$ be the set of all square-integrable functions given by

$$\mathcal{L}^{\,2}(\mathcal{B}) = \{ \varphi : \mathcal{B} \to \mathbb{R};\ |\varphi|_0 < \infty \} \tag{16}$$

where the norm $|\bullet|_0$ is given by $|\varphi|_0 \equiv \left(\int\limits_{\mathcal{B}} |\varphi|^2 dA \right)^{1/2}$, and let $\left(\mathcal{H}^1(\mathcal{B}) \right)^2$ be a Hilbert space defined by

$$\left(\mathcal{H}^1(\mathcal{B}) \right)^2 = \left\{ \boldsymbol{v} : \mathcal{B} \to \mathbb{R}^2; \|\boldsymbol{v}\|_1 < \infty \right\} \tag{17}$$

where the norm $\|\bullet\|_1$ is given by $\|\boldsymbol{v}\|_1 \equiv \left(\int\limits_{\mathcal{B}} (\boldsymbol{v} \cdot \boldsymbol{v} + \nabla \boldsymbol{v} \cdot \nabla \boldsymbol{v})\, dA \right)^{1/2}$. Here, a displacement field $\boldsymbol{u} \in \left(\mathcal{H}^1(\mathcal{B}) \right)^2$ is kinematically admissible if it satisfies $\boldsymbol{u} = \bar{\boldsymbol{u}}$ on $\partial \mathcal{B}$, where $\bar{\boldsymbol{u}}$ is known on the boundary $\partial \mathcal{B}$, and $\boldsymbol{v} \in \left(\mathcal{H}^1(\mathcal{B}) \right)^2$ is an admissible variation if it satisfies $\boldsymbol{v} = \mathbf{0}$ on $\partial \mathcal{B}$. We then introduce $\mathcal{S}$ as the set of all admissible displacements and $\mathcal{V}$ as the set of all admissible variations.

The weak form of the inverse problem that we shall consider in this work consists of finding $\mu \in \mathcal{L}^2(\mathcal{B})$ and $\pi^j \in \mathcal{L}^2(\mathcal{B})$, j = 1, 2, that satisfy

$$-\int\limits_{\mathcal{B}} \pi^j \, \mathrm{tr} \nabla_s \boldsymbol{v} dA + 2 \int\limits_{\mathcal{B}} \mu \nabla_s \boldsymbol{u}^j \cdot \nabla_s \boldsymbol{v} dA = 0, \quad \boldsymbol{u}^j \in \mathcal{S},\ j = 1, 2, \quad \forall \boldsymbol{v} \in \mathcal{V}, \tag{18}$$

together with (14) for $i = 1, ..., r$.

The weak form stated above together with a finite element methodology discussed in Aguiar and Prado [8] allow an approximate reconstruction of μ from the given data $\boldsymbol{u}^j$ and $\boldsymbol{R}_i^j$, $j = 1, 2$, $i = 1, ..., r$. Observe that this formulation does not require differentiability of $\boldsymbol{u}^j$. In the next section, we review briefly the main results of the finite element methodology.

2.3 The discrete formulation of the inverse problem

We want to construct finite element approximations for the solution $(\mu, \pi^1, \pi^2) \in \left(\mathcal{L}^2(\mathcal{B})\right)^3$ of the inverse problem given by (18) together with (14) for $i = 1, ..., r$. For this, we consider a finite element formulation based on the introduction of discrete problems over finite-dimensional subsets of $\mathcal{L}^2(\mathcal{B})$ and $\mathcal{V}$. The corresponding discrete problems can be solved using direct solvers, as opposed to iterative solvers used in the literature, such as in Park and Maniatty [4].

We begin by assuming that $\mathcal{B} \in \mathbb{R}^2$ is a polygonal domain composed of m non-overlapping quadrilaterals $\mathcal{K}_k \in \mathbb{R}^2$, $k = 1, 2, ..., m$, so that

$$\mathcal{B} = \bigcup_{k=1}^{m} \mathcal{K}_k \tag{19}$$

and such that the intersection of any two of these quadrilaterals is either empty, a point, or, a straight line. For each $\mathcal{K}_k \subset \mathcal{B}$, the interior of the quadrilateral $\mathcal{K}_k$ is non-empty.

Let $\mathcal{K}_k \in \mathbb{R}^2$, $k = 1, 2, ..., m$, be endowed with the set of nodes $\boldsymbol{x}_{ki} \in \mathcal{K}_k$, $i = 1, ..., 4$, which are the vertices of $\mathcal{K}_k$. We shall consider Lagrange finite elements $(\mathcal{K}_k, \mathcal{P}_k, \Sigma_k), k = 1, ..., m$, where $\mathcal{P}_k$ is a set of smooth functions $\varphi : \mathcal{K}_k \to \mathbb{R}$ and Σ_k is a set of degrees of freedom corresponding to the coefficients $\varphi(\boldsymbol{x}_{ki})$. The functions φ are linear combinations of normalized basis functions $\varphi_{k\,i}$, $i = 1, ..., 4$, so that $\varphi_{ki}(\boldsymbol{x}_{kj}) = \delta_{ij}$. The functions $\varphi_{k\,i}$, $i = 1, ..., 4$, are continuous over $\mathcal{K}_k$. In this way, a finite element mesh is the union of all the finite elements $(\mathcal{K}_k, \mathcal{P}_k, \Sigma_k)$, $k = 1, ..., m$.

Let us denote as $\mathcal{N} \equiv \{\boldsymbol{x}_1, \boldsymbol{x}_2, ..., \boldsymbol{x}_n\} \in \mathcal{B}$ the complete set of n nodes in $\mathcal{B}$. Then, for each i = 1, ..., m, and each k = 1, ..., 4, $\boldsymbol{x}_{ki} \in \mathcal{K}_k$ corresponds to a unique element from $\mathcal{N}$. We define the set of functions $\varphi_j : \mathcal{B} \to \mathbb{R}$, $j = 1, ..., n$, such that $\varphi_j(\boldsymbol{x}) = \varphi_{ki}(\boldsymbol{x})$ for $\boldsymbol{x} \in \mathcal{K}_k$. Thus, φ_j is continuous on $\mathcal{B}$ and satisfies $\varphi_j(\boldsymbol{x}_i) = \delta_{ij}$, $i, j = 1, ..., n$. In fact, the set of functions φ_j is a finite-dimensional basis for the set of continuous functions defined by

$$\mathcal{P} = \left\{ \varphi : \mathcal{B} \to \mathbb{R} | \varphi(\boldsymbol{x}) = \sum_{j=1}^{n} \alpha_j \varphi_j(\boldsymbol{x}), \forall (\alpha_1, \alpha_2, ..., \alpha_n) \in \mathbb{R}^n \right\} \tag{20}$$

We now define the finite-dimensional space $\mathcal{V}_h$ as follows

$$\mathcal{V}_h = \left\{ \boldsymbol{v} \in \left(\mathcal{C}^0(\mathcal{B}_h)\right)^2 : \boldsymbol{v} \in (\mathcal{P}(\mathcal{B}))^2, \boldsymbol{v} = \boldsymbol{0} \text{ on } \partial\mathcal{B} \right\} \tag{21}$$

where h stands for the characteristic length of the finite element mesh. Observe from (21) that $\mathcal{V}_h \subset \mathcal{V}$. A function $\boldsymbol{v}_h \in \mathcal{V}_h$ has the representation

$$\boldsymbol{v}_h(\boldsymbol{x}) = \sum_{i=1}^{2n} \vartheta_i \boldsymbol{w}_i(\boldsymbol{x}), \quad \boldsymbol{x} \in \bar{\mathcal{B}}, \tag{22}$$

where $\vartheta_i \in \mathbb{R}$ and $\boldsymbol{w}_i$ is a vector in $\mathbb{R}^2$ of the form

$$\boldsymbol{w}_{2i-1} = (\varphi_i, 0)\,, \quad \boldsymbol{w}_{2i} = (0, \varphi_i)\,, \quad i = 1, 2, \ldots, n, \tag{23}$$

relative to a fixed orthonormal base, with φ_i being a scalar basis function defined for the ith node in the set $\mathcal{N}$ introduced above. In particular, notice that $\boldsymbol{v}_h(\boldsymbol{X}_i) = (\vartheta_{2i-1}, \vartheta_{2i})$ for $i = 1, 2, ..., n$. Each $\vartheta_i,\ i = 1, 2, ..., 2n$, is a degree of freedom associated with $\mathcal{V}_h$. Thus, considering the fact that each node in $\mathcal{N}$ has two degrees of freedom and that $\boldsymbol{v}_h \in \mathcal{V}_h$, it is convenient to decompose the complete set of 2 n degrees of freedom into two complementary integer sets $\mathcal{Z}^*$ e $\mathcal{Z}$, such that $\vartheta_i = 0$, $\forall i \in \mathcal{Z}^*$, and $\mathcal{Z} \equiv \{1, 2, ..., n\} \setminus \mathcal{Z}^*$.

Let us also define the space

$$\mathcal{L}_h^2 = \{\mu_h : \mathcal{B}_h \to \mathbb{R} : \mu_h \text{ is piecewise continuous on } \mathcal{B}_h\} \tag{24}$$

An element $\mu_h \in \mathcal{L}_h^2$ has the representation

$$\mu_h(\boldsymbol{x}) = \sum_{k=1}^{m} \mu_k \tau_k(\boldsymbol{x})\,, \quad \boldsymbol{x} \in \bar{\mathcal{B}}, \tag{25}$$

where $\mu_k \in \mathbb{R}$ and τ_k is a scalar basis function, which is piecewise constant, has support in $\mathcal{K}_k$, and is normalized so that $\varphi_j(\boldsymbol{x}) = \delta_{ij}$ for $x \in \mathcal{K}_i$, $i, j = 1, ..., m$.

Next, we assume that both fields $\boldsymbol{u}^1$ and $\boldsymbol{u}^2$ are known and use the representation given by Eq. (22) to approximate μ and $\pi^j, j = 1, 2$, in the form

$$\mu_h = \sum_{k=1}^{m} \mu_k \tau_k \quad \text{and} \quad \pi_h^i = \sum_{k=1}^{m} \pi_k^i \tau_k, \quad \boldsymbol{x} \in \bar{\mathcal{B}}, \tag{26}$$

where $\mu_k \in \mathbb{R}$ and $\pi_k^i \in \mathbb{R}$, i = 1,2, $k = 1, 2, ..., m$. We also assume that $\partial_j \mathcal{B} \subset \partial\mathcal{B}$ is given by

$$\partial_j \mathcal{B} = \bigcup_{p \in \mathcal{Z}_j} \mathcal{D}_p \tag{27}$$

where $\mathcal{D}_p$ is a side of $\mathcal{K}_p$ that also belongs to $\partial\mathcal{B}$ and $\mathcal{Z}_j$ is the set of integer numbers that identify the finite elements with sides contained in $\partial_j \mathcal{B}$.

Substituting the Eq. (26) and v_h, given by Eq. (22), into both Eq. (14) and Eq. (18), and using the fact that the coefficients $\vartheta_i,\ i \in \mathcal{Z}$, are arbitrary, these equations can be rewritten as

$$\sum_{q=1}^{2m} \alpha_{pq}^j \omega_q^j = 0, \qquad p \in \mathcal{Z}, \tag{28}$$

$$\sum_{q \in Z_i} \beta_q^j \omega_q^j = \boldsymbol{R}_i^j, \qquad i = 1, 2, \ldots, r, \tag{29}$$

where j = 1, 2, and

$$\alpha_{p(2q-1)}^j = 2 \int_{\mathcal{K}_q} \nabla_s \boldsymbol{u}^j \cdot \nabla_s \boldsymbol{w}_p dA, \qquad \alpha_{p(2q)}^j = -\int \mathcal{K}_q \mathrm{tr}\, \nabla_s \boldsymbol{w}_p dA, \tag{30}$$

$$\beta_{2q-1}^j = 2 \int_{\mathcal{D}_q} \left(\nabla_s \boldsymbol{u}^j \right) \boldsymbol{n}_q dA, \qquad \beta_{2q}^j = - \int_{\mathcal{D}_q} \boldsymbol{n}_q dA, \tag{31}$$

$$\omega_{2q-1}^j = \mu_q, \qquad \omega_{2q}^j = \pi_q^j. \tag{32}$$

Then, the discrete inverse problem associated to the problem given by Eq. (14) and Eq. (18) consists of finding the coefficients $\omega_q^j, j = 1, 2, q = 1, \ldots, m$, defined by (32) that satisfy the linear system given by (28) - (31).

In general, the linear system given by (28) - (31) is over-determined. To solve this system, we use the Singular Value Decomposition algorithm presented by Golub and van Loan (1996). The main input data are the coefficients on the right side of both Eq. (28) and Eq. (29), the matrix $\boldsymbol{W}$ formed by the coefficients that multiply ω_q^j on the left side of these equations, the dimensions of $\boldsymbol{W}$, and a tolerance that yields the largest non-singular, square matrix of $\boldsymbol{W}$. Here, the tolerance is a non-negative number below which a singular value of $\boldsymbol{W}$ is considered to be zero. A preliminary study of the influence of the tolerance on the values of the coefficients $\mu_k, k = 1, \ldots, m$ in Eq. (26) allows to conclude that, for tolerances below 10^{-8}, all the values obtained for these coefficients were physically plausible and differed very little from each other.

3 Numerical results

We show in Fig. 1 a schematic representation of two experiments that yield both the resultants $\boldsymbol{R}_i^j$ in (29) and the displacements $\boldsymbol{u}^j$ in both (30) and (31). These experiments are carried out on a cylinder of square cross section containg an eccentric cylindrical inclusion of circular cross section. The length of a side of the square section is $\bar{\xi} = 50$ mm and the radius of the circular section is $r = 6$mm. The conditions on the boundary of the cylinder are the same ones considered for the experiments described in Section 2.1. Here, however, the resulting deformation fields are not homogeneous.

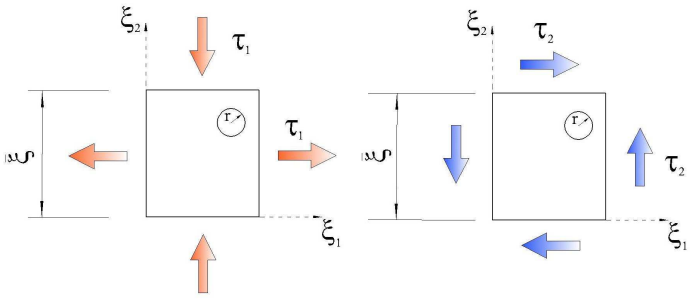

Figure 1: Bi-axial and shearing experiments on a cylinder containing an inclusion.

We have simulated numerically both experiments to obtain the resultant forces $\boldsymbol{R}_i^j$ and the displacements $\boldsymbol{u}^j$. For this, we use the Finite Element package *Ansys 5.5*[1] and assumed that the shear elastic moduli of both the matrix, which is the cylinder without the inclusion, and the inclusion are given by, respectively, $\mu_M = 36$ kPa and $\mu_I = C_R\,\mu_M$, where $C_R \geqslant 0$ is the shear modulus contrast ratio. Observe that $C_R = 0$ corresponds to an empty hole, $C_R = 1$ corresponds to a homogeneous cylinder, and $C_R > 1$ corresponds to an inclusion that is C_R times stiffer than the matrix. In Fig. 2 we show a mesh of finite elements used in the computation of both $\boldsymbol{u}^j$ and $\boldsymbol{R}_i^j$, where the inclusion is shown on the upper right side. In these simulations we have also obtained approximations for the pressure fields $\pi^j, j = 1, 2$.

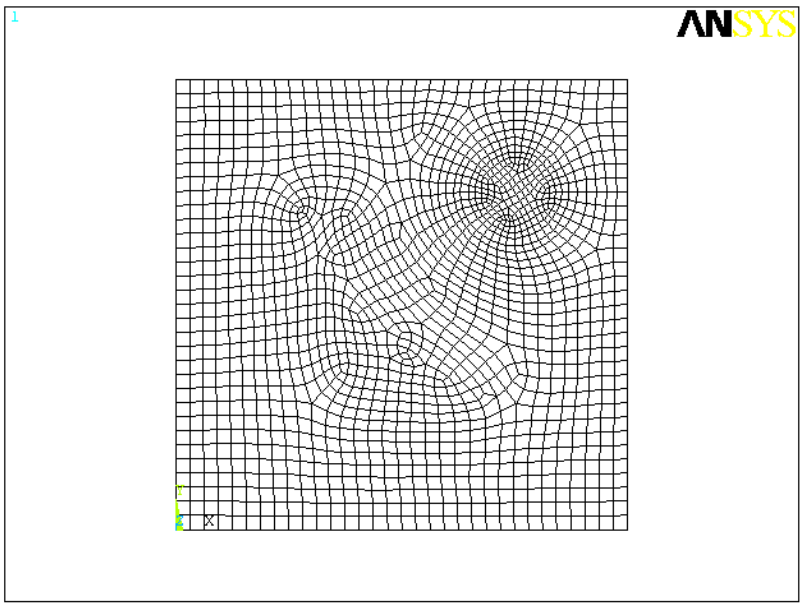

Figure 2: Non-uniform mesh of finite elements to dicretize the square cross section of a cylinder containing an eccentric inclusion.

With the vectors $\boldsymbol{u}^j$ and $\boldsymbol{R}_i^j$ computed from the numerical simulations above, we have solved the system given by (28) - (32) using the non-uniform mesh of Fig. 2 and computed approximations for both μ and $\pi^j, j = 1, 2$, from (26). We have verified that the approximations of π^j, $j = 1, 2$, are in very good agreement with the corresponding approximations obtained from the numerical simulations above.

[1] *Ansys 5.5* is proprietary software of Anys Inc., USA.

In the next two figures we show sequences of frames that use color maps to represent the distribution of the shear elastic modulus inside the cylinder of square cross section. Each frame has its own color map, which corresponds to a range of values for μ. The smallest and largest values of μ correspond to the colors at, respectively, the bottom and the top of the color map. The frames on the upper left corner in both figures contain exact values of μ and are used as reference frames to be compared with the other five frames. These five frames are obtained from different finite element meshes, which are represented in Tab. 1 by increasing numbers of nodes and elements. In particular, Fig. 2 corresponds to Mesh 5 in Tab. 1.

In Fig. 3 and Fig. 4 we consider the cases $C_R = 0$[2] and $C_R = 6$, respectively. Comparing the reference frame (a) in each figure with the other five frames of the same figure and observing the values in the corresponding legend, we note that μ_h, defined by (26.a), converges to μ as the mesh is refined. In both cases, $\mu_h \to 36$ kPa everywhere inside the matrix. Inside the inclusions, we see from Fig. 3 that $\mu_h \to 0$ kPa and from Fig. 4 that $\mu_h \to 216$ kPa.

Table 1: Finite element meshes for a cylinder with an eccentric inclusion.

Mesh	**Number of nodes**	**Number of elements**
1	733	668
2	931	866
3	1077	1012
4	1218	1153
5	1535	1470

Next, in Fig. 5 we consider an inclusion with a cross section having a complex geometry. The color maps of both Frame (a) and Frame (b) represent, respectively, the exact and the calculated values of μ inside the inclusion and the matrix. By comparing both frames, we see that our numerical approach yields accurate values for μ and is capable of reconstructing the geometry of the inclusion.

[2]Because of numerical difficulties experienced during the numerical simulations using *ANSYS 5.5*, we used $C_R = 10^{-25}$ and Poisson's ratio $\nu_I = 0.3$ for the inclusion, instead of $C_R = 0$ and $\nu_I = 0.5$.

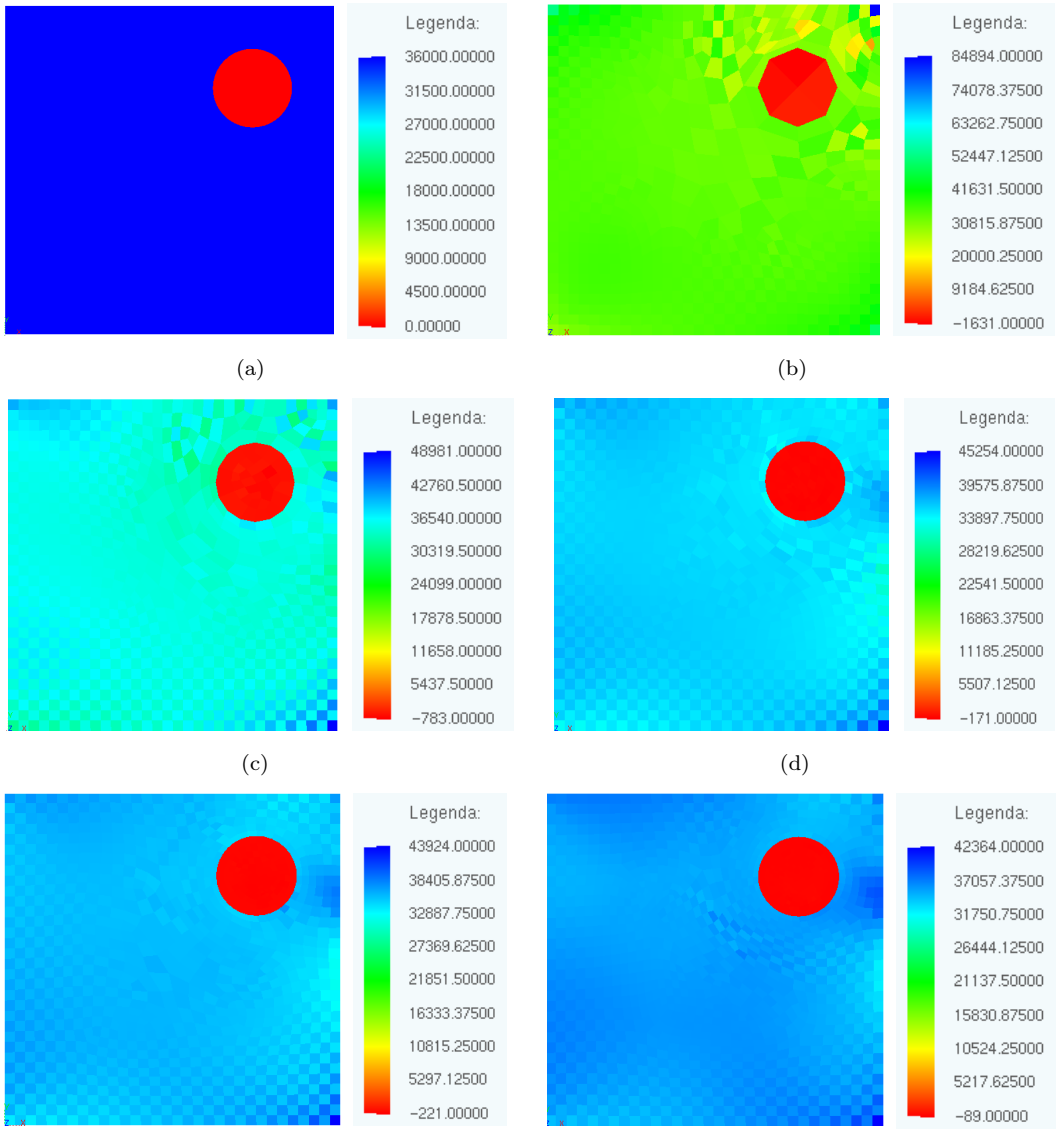

Figure 3: Reconstruction of μ in a cylinder containing an eccentric circular hole, ($C_R = 0$).

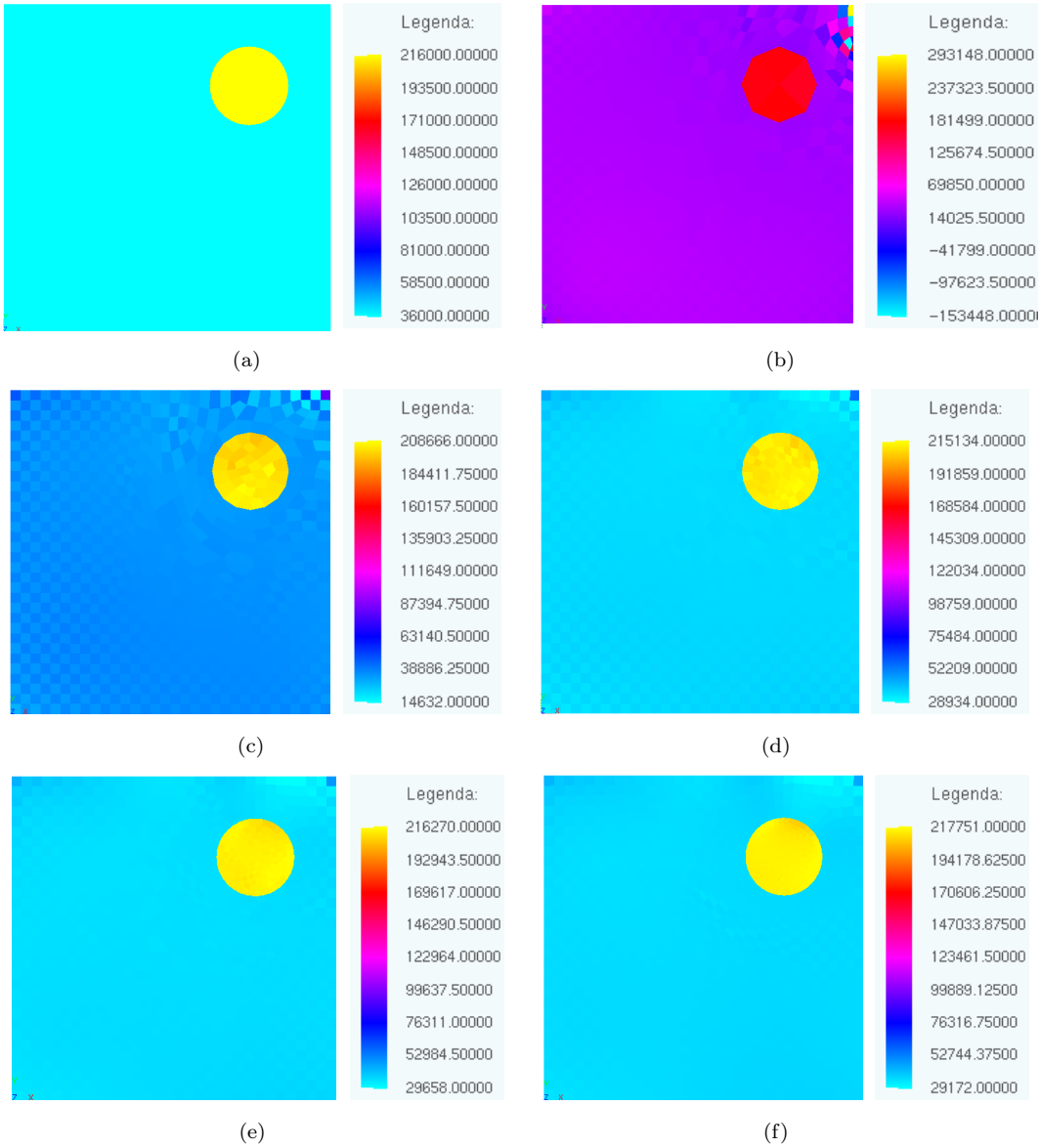

Figure 4: Reconstruction of μ in a cylinder containing an eccentric circular inclusion with $C_R = 6$.

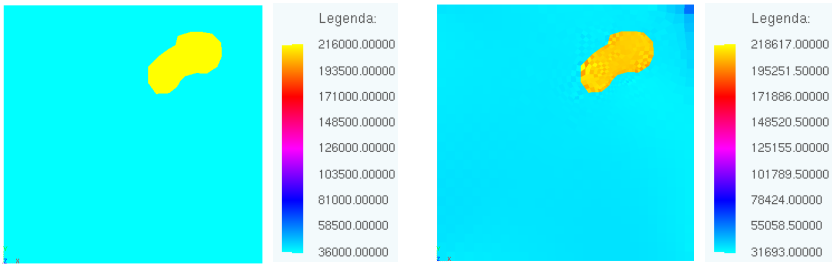

(a) (b)

Figure 5: Reconstruction of μ in a cylinder containing an inclusion with a complex geometry.

4 Conclusion

The theoretical approach used in this work to reconstruct the shear elastic modulus μ of an isotropic, incompressible, and linearly elastic solid in a state of plane strain together with the numerical method proposed in Aguiar and Prado [8], which is based on a Finite Element formulation described briefly in Section 2, yield very accurate results. In particular, these results are not sensitive to numerical errors due (i) numerical simulation of both experiments, which yield approximations to both $\boldsymbol{u}^1$ and $\boldsymbol{u}^2$ and to the corresponding resultant forces $\boldsymbol{R}_i^1$ and $\boldsymbol{R}_i^2$, i = 1, ..., r; (ii) finite element discretization of the inclusion, which has a non-polygonal geometry, using quadrilateral elements; (iii) use of finite elements to obtain the displacement fields $\boldsymbol{u}^1$ and $\boldsymbol{u}^2$ that may yield the locking effect, which appear in the numerical simulation of problems involving incompressible materials. See a discussion about this effect in Hughes [9].

We are now investigating the application of this numerical method (i) using regular meshes, instead of the non-uniform meshes used in this work; (ii) in the reconstruction of μ in problems that are more general than plane problems; (iii) using constitutive relations that take into account viscous and nonlinear behavior of living tissues.

Acknowledgements

The authors wish to acknowledge CAPES (Coordination for the Improvement of High Education Personnel) for its support of this research.

References

[1] Fung, Y.C., *Biomechanics: mechanical properties of living tissues*. Springer: New York, 2nd edition, 2004.
[2] Krouskop, T.A., Wheeler, T.M., Kallel, F. & Garra, B.S.T., Elastic moduli of breast and prostate tissues under compression. *Ultrasound Imaging*, **4(20)**, pp. 260–274, 1998.
[3] Mridha, M. & Ödman, S., Noinvasive method for the assessment of subcutaneous edema. *Med Biol Eng*

Comput, **24(4)**, pp. 393–398, 1986.
[4] Park, E. & Maniatty, A.M., Shear modulus reconstruction in dynamic elastography: time harmonic case. *Physics in Medicine and Biology*, **(51)**, pp. 3697–3721, 2006.
[5] Barbone, P.E. & Gokhale, N.H., Elastic modulus imaging: on the uniqueness and nonuniqueness of the eslastography inverse problem in two dimensions. *Inverse Problems*, **20**, pp. 283–296, 2004.
[6] McLaughlin, J.R. & Yoon, J.R., Unique identifiability of elastic parameters from time-dependent interior displacement measurement. *Inverse Problems*, **20**, pp. 25–45, 2004.
[7] Weinberger, H.F., *Partial differential equations with complex variables and transform methods*. John Wiley & Sons, Inc.: New York, USA, 1965.
[8] Aguiar, A.R. & Prado, E.B.T., A Finite Element Methodology to determine elastic parameters in biological tissues. *XXIX CILAMCE - Iberian Latin American Congress on Computational Methods in Engineering*, Maceió, 2008. University of Minnesota Supercomputing Institute Research Report UMSI 2008/100, September 2008 and CB number 2008-43.
[9] Hughes, T.J.R., *The Finite Element Method: Linear Static and Dynamic Analysis*. Prentice-Hall, Inc.: Englewood Cliffs, New Jersey, 1987.

Mechanics of Solids in Brazil 2009, H.S. da Costa Mattos & Marcílio Alves (Editors)
Brazilian Society of Mechanical Sciences and Engineering, ISBN 978-85-85769-43-7

Numerical simulation of soft-body impact on GFRP laminate composites: mixed SPH-FE and pure SPH approaches

Ricardo L. Azevedo
West Paraná State University, Cascavel/PR – Brazil
Marcílio Alves
Group of Solid Mechanics and Structural Impact, Department of Mechatronics and Mechanical System Engineering, University of São Paulo, São Paulo/SP – Brazil

Abstract

Impact events involving laminate composites had been largely studied through computational approaches, due mainly to the technical difficulties and high costs associated with experimental tests, and the availability of highly sophisticated computational codes. In the present work, medium-to-high velocities impact events of 'dummy birds' against balanced S2-Glass/Epoxy laminate composites are simulated through LS-Dyna explcit finite element package. Pure and mixed formulation coupling finite elements (FE) and smoothed particle hydrodynamics (SPH) techniques is adopted to describe the motion of the impacted composite plate and the soft body projectile, respectively. The severe distortions and the damage induced on the plate by the impact imply the remotion of some elements of the mesh, in order to become possible the continuity of the simulation without adoopting very reduced timesteps. An alternative approach consisting of SPH formulation of both projectile and target plate is adopted and comparisons between the these numerical procedures are made.

Keywords: impact, laminate composites, Finite Element Method, Smoothed Particle Hydrodynamics, LS-Dyna.

1 Introduction

The impact of birds with aircraft structures is one of the main threats for flight safety. Due the considerable presence of birds in the vicinity of airports a large number of these bird strikes occur around the world. In the last two decades a significant expansion of the use of fiber reinforced composite materials in aeronautical industry has been verified, aiming to obtain structures with advantageous strength/weight ratios. However, the damage induced by impact in composite materials is an aspect that inhibits the application of this kind of material, since it is well known that composites are very

Mechanics of Solids in Brazil 2009, H.S. da Costa Mattos & Marcílio Alves (Editors)
Brazilian Society of Mechanical Sciences and Engineering, ISBN 978-85-85769-43-7

susceptible to transverse impact. In the bird-aircraft impact the bird is characterized as a soft body, i.e. body with low rigidity/hardness, because the stresses generated are beyond the strength of the bird and generally below the strength of the target. Moreover, the bird behaves like a fluid in the impact event, and the effect are large area of the target [1]. Thus, the problem in consideration joins some very complex aspects, such as high strain rates, large deformations, complex constitutive relationships and damage/failure mechanisms, among others. Therefore, this complexity usually precludes the use of analytical solutions to solve this class of problems.

Considering that experimental tests ate both expensive and troublesome, computational methods have been extensively by the aircraft industry to minimize the number of experiments, aiming this way to reduce certification and development costs and support the design of efficient bird-proof structures. In this sense, nonlinear explicit codes based on Finite Element (FE) techniques have been successfully employed to a large number of problem in the field of Continuum Mechanics since late eighties. The LS-Dyna code [2] is a general purpose finite element code for non-linear structural dynamics, which has been largely employed to impact analysis [3–6]. Impact of bodies with low rigidity and hardness, as those considered in the bird impact analysis, has been treated in the aeronautical industry and research centers through the so-called 'substitute birds' [7, 8], materials whose mechanical behavior resembles real birds, with advantages in what it refers to the uniformity and repeatability of the experimental tests, usually conducted by using gas gun projectile launchers.

Recently, aiming to overcome the difficulties of Lagrangian description to handle large distortions of the mesh, it has been proposed in the literature the use of Smoothed Particle Hydrodynamics (SPH), a mesh less method developed initially to simulate astrophysical problems and later extended to several other applications in Computational Mechanics. Examples of the use of such technique, already incorporated to LS-Dyna [9], can be found in the works of Anghileri et al. [3] and Ryabov et al. [5]. Comparative studies of Lagrangian, Eulerian and SPH formulations have been presented by Schewer [10] and Buyuk et al. [11] in ballistic impact simulation, by Anghileri et al. [3] in fluid-structure interaction problems and, more recently, by Huertas [12] analyzing bird-strike events through LS-Dyna and three distinct formulations: Lagrangian, Arbitrary Lagrangian Eulerian (ALE) and SPH.

The present work presents a numerical simulation of the impact between a substitute bird and a glass fiber- reinforced polymer (GFRP), more specifically a S2-Glass/Epoxy composite plate, by using the LS-Dyna code. Due the lack of test data the material behavior of the idealized bird is approximated as that of the water, as suggested in the literature [4, 8]. Combinations of two different approaches to describe the motion of the bird are investigated, namely the classical Lagrangian FE and the SPH. The results obtained, as well as the computational performance of each method, are critically compared, and a qualitative comparison with experimental results obtained at Group of Solid Mechanics and Structural Impact (GMSIE/USP) is performed.

2 Problem description

The impact here considered is that of a circular cylindrical soft body, the plasticine ('play-doh' modeling compound) 'bird', which is horizontally launched on a vertically placed, circular composite plate, made of a continuous fiber-reinforced S2-Glass/Epoxy. The tested plate had a diameter of 250 mm

and a thickness of 4 mm, whereas the circular cylinder, with 50 mm of diameter and 100 mm of length, observed the ratio diameter-to-height suggested in the literature [8]. The plate was placed over a rigid circular ring, i.e. clamped boundary condition was assumed and an initial velocity of 115 ms^{-1} was provided to the impactor to start the analysis. In order to save processing time, the cylinder was initially placed very close to the plate in the beginning of the numerical analysis, i.e. 6 mm from plate upper surface to the bird lower surface. In the present work the commercial package LS-Dyna was used to obtain the transient dynamic response of the plate during impact. The main aspects of the numerical simulation are described in the next sections.

3 LS-Dyna's numerical solvers

LS-Dyna [2] is a general-purpose finite element package to non-linear, dynamic analysis of transient field problems. In the present work this code was adopted to solve the dynamic equilibrium equations, as well as the contact between the two deformable bodies. Regarding to the formulations, Eulerian approach with non-deformable mesh, Lagrangian approach with deformable mesh, and Smoothed Particle Hydrodynamics (a mesh-free method) are available in the version 970, which was used in this work. The kind of problem considered in the present work is traditionally analyzed by using the Lagrangian approach. However, aiming to circumvent the above mentioned difficulties of this formulation, in particular to handle large deformations of the mesh, the new alternative represented by SPH is also considered in this work. To allow the comparison the same code was used, the constitutive models were kept constant, and just minor changes were done in the geometric modeling in the two simulations.

In the traditional **Lagrangian** description, widely used in problems of Solid Dynamics, the FE mesh is attached to the material. Consequently this kind of description possesses limitations to contemplate severe distortions of the mesh, due to numerical inaccuracies that may to harm or even to make impracticable the simulation. In these cases, the occurrence of negative-volume errors and hour-glass modes appearance are often related with the entangling of the mesh. Furthermore, the explicit, conditionally stable nature of the central difference scheme, the time integration algorithm adopted in this work, can lead to very reduced time-steps, considerably increasing the computational cost of the problem. An alternative to remove too distorted elements from the simulation is the so-called 'element erosion', usually based on a user supplied criteria [2]. In LS-Dyna some of these criteria are maximum principal strain (tension), minimum principal strain (compression) and minimum allowable time step. The main drawback associated to these criteria is that they are ad hoc by nature, as observed by Schwer [10].

SPH, on the other hand, is a mesh less method where a set of particles with their respective masses provides the discretization of the continuum without any connectivity among the particles [9]. The particles are the basis of an interpolating scheme based on the kernel function and some conditions in setting the initial particle masses and coordinates are required: the array of particles needs to be regular, for instance. In this framework the conservation equations are equivalent to terms expressing inter-particular forces and the smoothing kernel is usually defined in terms of a cubic B-spline. Due to nonexistence of a mesh, SPH is not affected by the problems caused by distortions in

large deformation problems, as occurs in the traditional Lagrangian approach. Besides, this method shows another remarkable feature: a better representation of the fluid-like movement of projectiles with low rigidity/hardness, including their disintegration process. The compatibility between the SPH processor with the FE Lagrangian solver in LS-Dyna is ensured due the way as this new technique was implemented in the code, enabling the use of the classical LS-Dyna keywords (input data sets) and making easier the use of mixed approaches. On the other hand, there exist some remaining problems in the areas of accuracy and stability and of such formulation.

4 Numerical modeling methodology

As observed previously, both FE and SPH models were employed in the numerical simulations, either in isolated form or combined in a mixed approach. The contact-impact problem was modeled and solved on LS-Dyna version 970. All the numerical analysis were accomplished using a common PC (Pentium IV- 3 GHz CPU, 1024 MB RAM). A total of six different numerical experiments were conducted and are given in Tab. 1.

Table 1: Numerical models employed to simulate the soft body impact onto a composite plate.

TEST CASE	PLATE NODES	PLATE ELEMENTS	BIRD NODES	BIRD ELEMENTS	PLATE PARTICLES	BIRD PARTICLES
A1 (PURE FE)	**18635**	**14712**	**6825**	**5680**	**none**	**none**
A2 (PURE FE)	**18635**	**14712**	**15378**	**13840**	none	none
B1 (MIXED)	**18635**	**14712**	none	none	none	**6825**
B2 (MIXED)	**18635**	**14712**	none	none	none	**13325**
C1 (PURE SPH)	none	none	none	none	**19760**	**6825**
C2 (PURE SPH)	none	none	none	none	**162315**	**6825**

4.1 Pure Finite Element model

The FE model of the plate used 8-node (brick) finite elements with one integration point. Due the use of reduced integration, the 'Flanagan-Belytschko viscous form with exact volume integration' option was employed to stabilize the zero strain-energy ('hourglass') modes (Hallquist, 2006). The plate was modeled with four element layers through thickness and clamped boundary conditions were assumed in its boundary. To model the impacting body in Lagrangian description were used meshes with 6825 nodes/5680 elements to test case 'A1', Fig. 1a, and 15378 nodes/13840 elements to test case 'A2', resulting from previous sensitivity analysis [13]. Some values recommended in the literature [12] for element erosion were used to the bird part, as well as a limit to minimum allowable time step and

the failure criteria of the material model, as explained right after. These erosion procedures make the simulation more stable, but their use must be judicious in order to maintain coherence of the results [10].

4.2 Mixed model (FE + SPH)

In this simulation the plate was modeled by finite elements, whereas the bird model was generated with a set of equally spaced particles. As SPH was developed as an extra layer of the code, all LS-Dyna's features such as assignment of initial and boundary values, contact treatment and etc., can be used within the particles' context. Therefore the compatibility between FE and SPH in LS-Dyna's framework is complete, enabling mixed approaches. The same FE model employed previously to the composite plate was used again in the mixed model. The SPH parts of this model were comprised of 6825 and 13325 particles in the test cases 'B1', Fig. 1b, and 'B2', respectively. The SPH particles of model B1 were obtained from the bird mesh of model A1, whereas to model B2 a new set of particles was generated respecting the recommendation of to distribute the particles on a regular configuration [9].

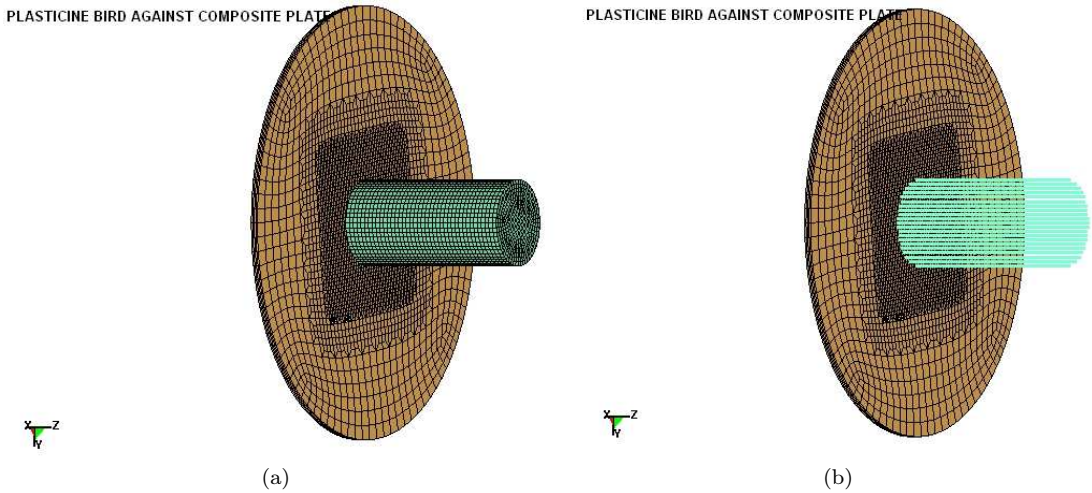

(a) (b)

Figure 1: Perspective view of two computational models: a) CASE A2 (Pure FE); b) CASE B1 (Mixed FE + SPH).

4.3 Pure SPH model

The last two simulations, i.e. test cases 'C1' and 'C2', were performed solely with SPH approach. Therefore both the plate and the impacting bird were discretized through sets of particles. The same

SPH model used before in the test case B1 was adopted to model the bird, whereas two different discretization levels were adopted to the plate: the first one containing 19760 particles (test case C2) and the second, more refined, with 19760 particles (test case C1). The particle approximation algorithm adopted was the code's standard gather form [9] and to all remaining SPH input parameters were used the code's defaults.

4.4 Contact/Impact interaction

In the simulations with pure FE model and mixed model, it was adopted the contact option *CONTACT_CONSTRAINT_NODES_TO_SURFACE with the code's default values. In these simulations the bird was considered as the 'slave' surface and the plate as 'master' surface for contact verification purposes, i.e. to handle the interaction between the two colliding parts. In the pure SPH simulations the contact is automatically verified and there is no need to specify a *CONTACT card, since the code assumes that two SPH parts will always interact (contact).

4.5 Material modeling

LS-Dyna's material library includes over 130 models to represent the mechanical behavior of the material to be modeled. Of course that the more complex the material model is, the greater the necessity of input material parameters. So the availability of these parameters is an important factor to be considered when choosing a determined material model, as observed by some authors [6]. Moreover, this fact can lead to the need of simplifications and estimations, strategy that were also adopted in the present work. Regarding to failure and erosion associated to each constitutive model, LS-Dyna proceeds as follows: each of the failure options is applied independently, and once any one of them is satisfied, the element is removed from the calculation [2].

4.5.1 Composite plate

This work used S2-Glass/Epoxy plain weave composite laminates (balanced 0/90 cross-plies) manufactured by the Mechanics of Composites Laboratory of Federal University of Minas Gerais [14]. All available material data resulting from mechanical characterization tests at GMSIE, i.e. compressive/tensile static tests on an Instron machine and dynamic tests on Split Hopkinson Pressure Bar [15], were used to provide the representation of the material properties, shown in Tab. 2. The *MAT_COMPOSITE_FAILURE_SOLID_MODEL, which is based on the Chang-Chang failure criterion [16] was selected. This material card allows to consider the reduction of material properties due the damage process and the inter-ply delamination in the failure process, and thus resembles the composite material behavior verified experimentally.

The above mentioned material model in not available in the code to SPH parts. Therefore the constitutive model *MAT_PLASTIC_KINEMATIC was adopted in the simulations 'C1' and 'C2', in which the plate is also modeled in the SPH framework. Again, the experimental results obtained with the composite material here considered were used. Table 3 presents a list of the LS-Dyna's required input parameters to this model. Although considerably simpler than the previous model, *MAT_PLASTIC_KINEMATIC has an remarkable feature: it permits to consider the strain rate

Table 2: Physical properties of composite panels – MAT_COMPOSITE_FAILURE_SOLID_MODEL constitutive model.

Mass density	1425 kgm^{-3}
Elastic Modulus at in-plane fill direction, E_1	17 GPa
Elastic Modulus at in-plane warp direction, E_2	17 GPa
Elastic Modulus at out-of-plane direction, E_3	17 GPa
Poisson's ratio, υ_{21}	0.12
Poisson's ratio, υ_{31}	0.40
Poisson's ratio, υ_{32}	0.40
Shear modulus (in-plane), G_{12}	6.1 GPa
Shear modulus (out-of-plane), G_{23}	6.1 GPa
Shear modulus (out-of-plane), G_{31}	6.1 GPa
Shear strength (in-plane), S	60 MPa
Shear strength at plane 1-3, S1	60 MPa
Shear strength at plane 2-3, S2	60 MPa
Compressive strength at in-plane fill direction, XXC	325 MPa
Compressive strength at in-plane warp direction, YYC	325 MPa
Compressive strength at out-of-plane direction, ZZC	325 MPa
Tensile strength at in-plane fill direction, XXT	325 MPa
Tensile strength at in-plane warp direction, YYT	325 MPa
Tensile strength at out-of-plane direction, ZZT	325 MPa

effects on the material properties, which plays an important role when this kind of material is simulated.

The strain rate parameters C and P of Cowper and Symonds model permit to the model to scale the static failure stress with the factor:

$$1 + \left(\dot{\varepsilon}/C\right)^{1/P} \tag{1}$$

This quite simple formulation, yet isotropic, allows to find the rupture stresses corresponding to each strain rate level. Other important parameter included in this model is the failure strain for eroding elements. Finally, the tangent modulus, obtained from the experimental stress-strain curve, permits to approximate the process of softening.

Table 3: Physical properties of composite panels – MAT_PLASTIC_KINEMATIC constitutive model.

Young's modulus, E	17 GPa
Yield stress, SIGY*	325 MPa
Tangent modulus, ETAN	-11459.16 Pa
Strain rate parameter for Cowper and Symonds model, C	1520.00
Strain rate parameter for Cowper and Symonds model, P	13.43
Poisson's ratio, PR	0.40

* actually the rupture stress, for composite materials are brittle and do not yield.

4.5.2 Plasticine cylinder

The substitute bird, made of plasticine compound, bahaves as a hydrodynamic material at higher pressures [17]. The selected material model to it was given by a combination of LS-Dyna's material card *MAT_NULL and the *EOS_LINEAR_POLYNOMIAL equation of state [2] as recommended in the literature to this kind of projectile [7, 8]. Thus, the pressure-dependent character of the material behavior is considered: at lower pressures the material behaves as isotropic elasto-plastic and at higher pressures as a hydrodynamic material, for which an equation of state relating the thermodynamic properties pressure and volume is adopted. An example of equation of state that has been largely used is the polynomial one, which was adopted in this work and has the following expression:

$$p = C_0 + C_1\mu + C_2\mu^2 + C_3\mu^3, \quad \mu = \rho/\rho_0 - 1 \tag{2}$$

where C_0, C_1, C_2 and C_3 are material constants, ρ is the current density and ρ_0 is the reference initial density. Difficulties in the measurement of these constants have motivated to adopt a material behavior similar to water, such that: C_0=C_2=C_3=0, C_1=2.2GPa. In these values may be recognized the bulk modulus of water, C_1. It is worthwhile to emphasize that the specimen employed in the gas-gun experimental tests with is about ten times lighter than those adopted adopted for the most part of the references, that is 1.82 kg, which is a requirement for the design of aircraft wing structures.

5 Results and discussion

Figures 2, 3 and 5 to 8 illustrate the final deformed configuration as calculated by the different simulations. As commonly observed in soft body impact events in this velocity range, the damaged area encloses a considerable portion of the plate, greater even than impactor's cross section, because these soft materials flows over the structure, spreading the impact area. This behavior is clearly noted in these simulations and the projectile's disintegration is adequately represented by the simulations.

For comparison purposes next are presented in Fig. 4 some pictures of the experimental test showing the final configuration of the plate after the gas gun test. An overall good agreement between the results of the two simulations is verified. It can be seen in Figs. 2 and 3 that some finite elements have been removed from the bird due the failure criterion adopted, which includes element deletion. At this stage of the simulation the presence of some very distorted elements in the plate description indicate the beginning of the numerical instabilities that will eventually interrupt the processing.

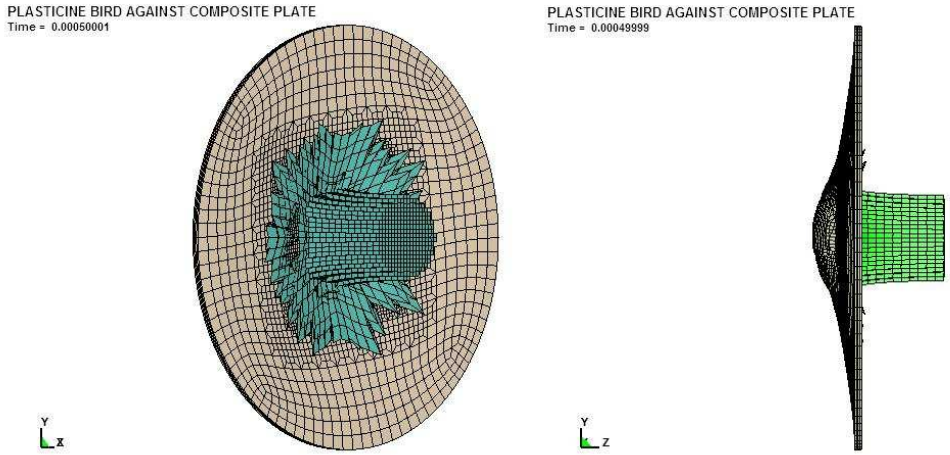

(a) (b)

Figure 2: Final deformed configuration to CASE A1: a) perspective view; b) lateral view.

Observing the Figs. 7 and 8, a different deformation profile is verified, which is probably related to differences in the simulations regarding to element erosion, that was not needed in pure SPH approaches (cases C1 and C2). A simple quantitative comparison between the simulations is presented in Fig. 9, where the time variation of the displacement of the plate's central node (at lower surface) is depicted, numerically confirms the above mentioned. Furthermore, it can be observed that simulations A1, A2, B1 and B2 furnished similar curves.

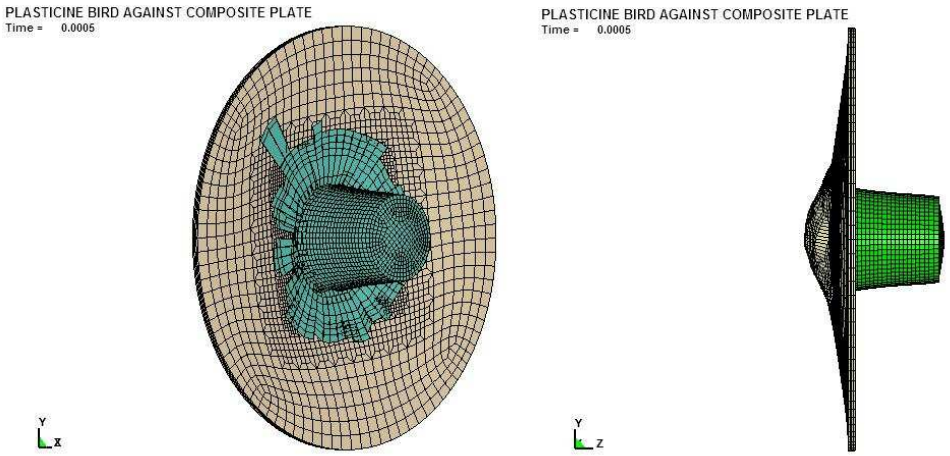

(a) (b)

Figure 3: Final deformed configuration to CASE A2: a) perspective view; b) lateral view.

Figure 4: Plate's deformed configurations after the gas gun impact test: total view (left) and zoom views (center and right).

Mechanics of Solids in Brazil 2009, H.S. da Costa Mattos & Marcílio Alves (Editors)
Brazilian Society of Mechanical Sciences and Engineering, ISBN 978-85-85769-43-7

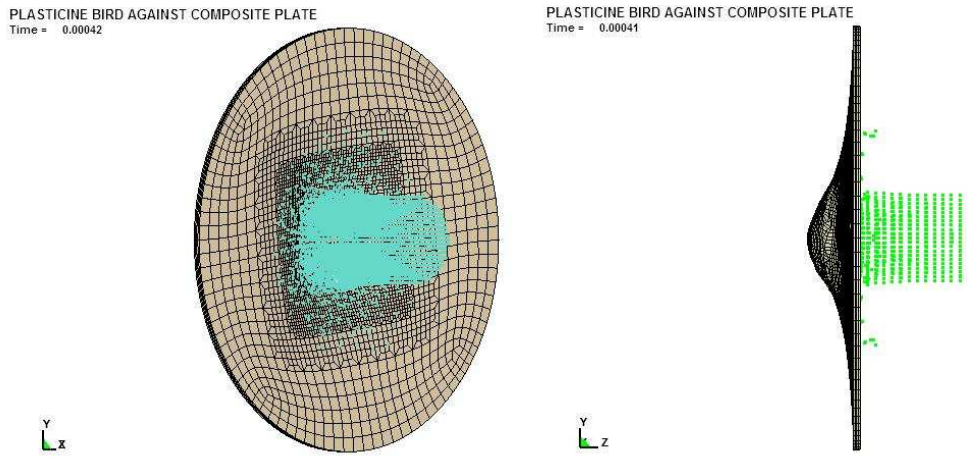

(a) (b)

Figure 5: Final deformed configuration to CASE B1: a) perspective view; b) lateral view.

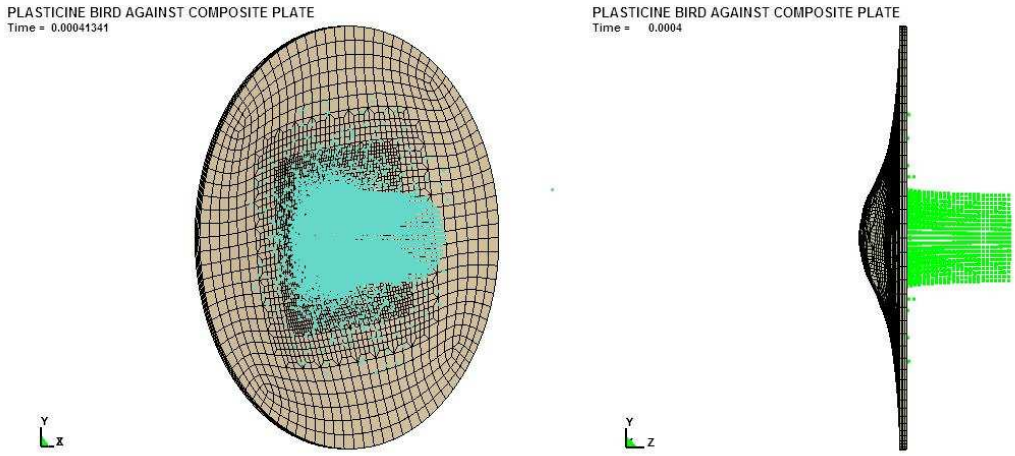

(a) (b)

Figure 6: Final deformed configuration to CASE B2: a) perspective view; b) lateral view.

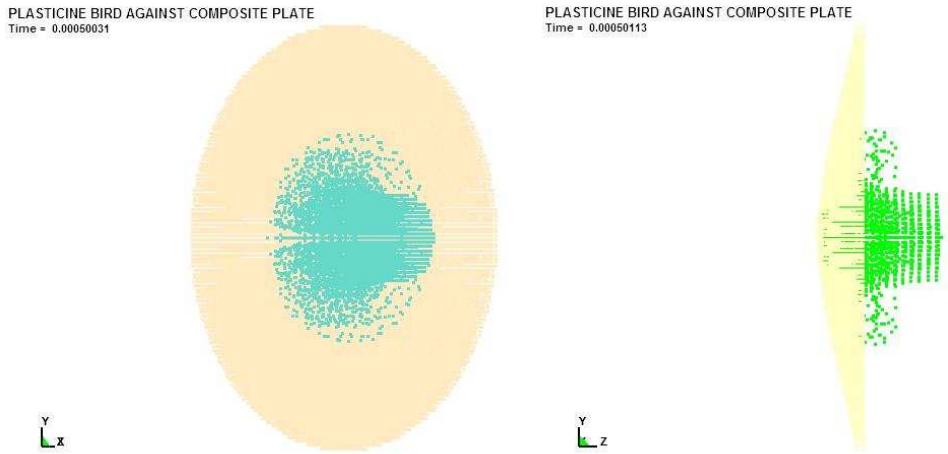

(a) (b)

Figure 7: Final deformed configuration to CASE C1: a) perspective view; b) lateral view.

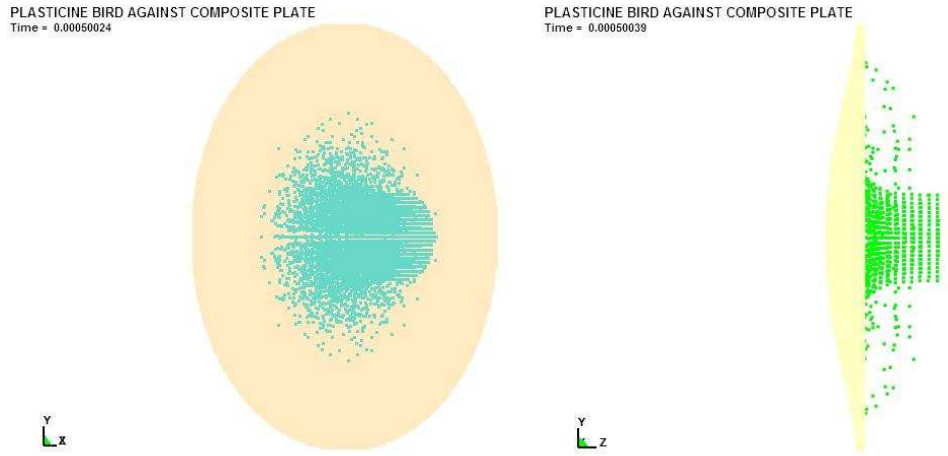

(a) (b)

Figure 8: Final deformed configuration to CASE C2: a) perspective view; b) lateral view.

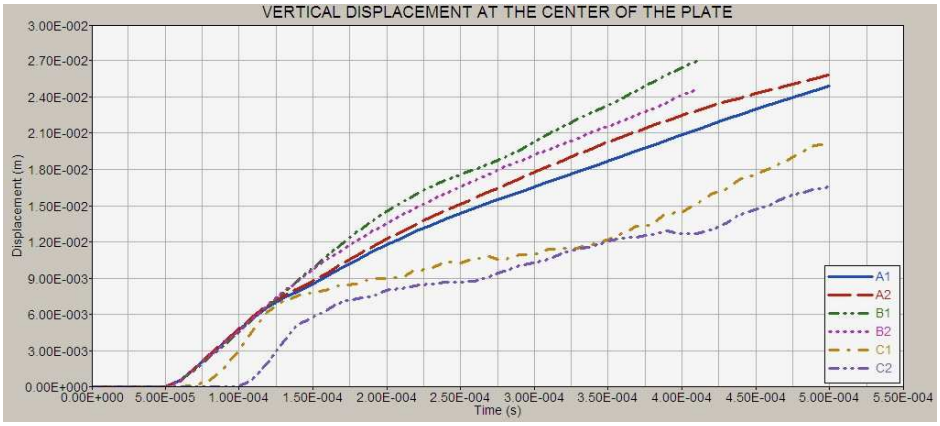

Figure 9: Curve displacement at plate's central node *versus* time to various test cases

The computational characteristics of the six simulations are presented in the Tabs. 4 and 5, in which it can be noted the way the timestep changed at every simulation, how the calculations ended, and the computational cost associated to all test cases. As expected, a considerable decreasing of stable timestep were verified in large-deformation simulations involving Lagrangian parts, whereas in the pure SPH runs the timestep remain almost constant. A normalized computational cost is defined to allow to compare the six test cases in a common basis, being the results presented in Tabs. 4 and 5.

6 Concluding remarks

In this work three numerical models to analysis the normal impact of idealized birds onto S2-Glass/Epoxy laminate composites have been developed by using LS-Dyna: finite element to both target and projectile in the first two analysis, finite element to target and smoothed particle hydrodynamics model to projectile in the second set, and a new approach: smoothed particle hydrodynamics to both domains in the third set. These models were qualitatively compared referring to a experimental test performed at GMSIE (USP) and advantages and disadvantages of the two models have been discussed. It was observed that LS-Dyna was able to capture the main patterns of the impact event and a reasonable qualitative correlation between numerical predictions and experimental results were obtained, although further improvements of the numerical models are necessary.

The LS-Dyna capacity to handle such complex problems with accuracy strongly depends on the knowledge of the material properties and the correct treatment of contact and failure phenomena. Despite these complexities, which are inherent to the problem, it can be considered that the obtained results are quite promising. Some issues like a better mechanical characterization of the materials, and additional instrumentation of the experimental tests with gas gun, allowing quantitative comparisons and aiming more integrated (numerical-experimental) approaches. Correlation for relevant impact

Table 4: Summary of the LS-Dyna's numerical analysis.

TEST CASE	INITIAL TIMESTEP (s)	FINAL TIMESTEP (s)	END TIME (s)	FINAL STATUS
A1	1.96E-07	1.53E-08	5.000E-04	normal termination
A2	1.96E-07	4.85E-09	5.000E-04	normal termination
B1	1.96E-07	5.87E-09	4.171E-04	interrupted(1)
B2	1.96E-07	4.94E-09	4.011E-04	interrupted(1)
C1	1.28E-06	1.28E-06	5.000E-04	normal termination
C2	6.44E-07	6.20E-07	5.000E-04	normal termination

(1)The reason of the interruption was the excess of brick elements eroded due to negative volume and a large number of failed elements as well. The reported 'end time' of these interrupted simulations mark the beginning of large variations in the ratio (total energy / initial energy), i.e. a considerable amount of energy loss, indicating numerical instabilities that generate non-physical results.

Table 5: Comparative of computational performance.

TEST CASE	ELAPSED TIME (s)	NUMBER OF NODES	NUMBER OF TIME STEPS	COMPUTATIONAL COST* (NORMALIZED)
A1	1662.00	25460	12699	1.25
A2	6168.00	34010	41925	1.00
B1	8834.00**	25460	11609	6.85
B2	6480.00***	31960	19242	2.33
C1	483.00	26585	391	9.02
C2	9169.00	169140	794	12.65

* COMPUTATIONAL COST = (elapsed time) / (total number of nodes) / (total number of time steps)
** simulation interrupted at time= 4.171E-04 s.
*** simulation interrupted at time= 4.011E-04 s.

parameters, such as inter-ply delamination area and contact forces are examples of such comparisons, that can be conducted when the suitable test data are available. These questions still remain open to be addressed as future works in this study. Additional theoretical studies regarding SPH approach are also needed, in oder to improve the accuracy of this promissing technique and to check the validity and feasibility of such numerical approach.

The SPH's computational cost was superior to that of FE analysis, although considering that the simulations ended at different times. As the size of the model is increased, the use of parallel processing may become mandatory due the large CPU requirements associated to the problem, specially if auto-adaptive analysis is adopted. This automatic adaption of mesh topology can be an alternative to overcome the limitation of Lagrangian formulation to follow large deformations, but is not applicable in LS-Dyna to all element types. The strategy of to remove the too distorted elements and replace them by SPH particles, already investigated by some authors, could provide to the model a good commitment beetween accuracy and computational efficiency but is not yet available in the code nowadays.

Acknowledgments

The first author wishes to thank Dr. James Kennedy and Dr. Leonard Schwer for their comments and suggestions offered at LS-Dyna discussion group at yahoo webpage.

References

[1] Abrate, S., Modeling of impact on composite structures. *Composite Structures*, **51**, pp. 129–138, 2001.
[2] Hallquist, J., *LS-DYNA3D Theoretical Manual*. Livermore Software Technology Corporation (LSTC): Livermore, 2006.
[3] Anghileri, M., Castelletti, L.M., Invernizzi, F. & Mascheroni, M., A survey of numerical models for hail impact analysis using explicit finite element codes. *International Journal of Impact Engineering*, **31**, pp. 929–944, 2005.
[4] Antoun, T.H., Gekfen, P.R., Holmes, B.S. & Kirkpatrick, S.W., Description of a six-inch gas gun facility for soft body impact. *Proceedings 43rd Annual Meeting of the Aeroballistic Range Association (ARA)*, 1992. Paper No. 50 (http://www.sri.com/poulter/composites/bird.html).
[5] Ryabov, A., Romanov, V., Kukanov, S., Shmotin, Y. & Chupin, P., Fan blade bird strike analysis using lagrangian, sph and ale formulations. *Proceedings of the 6th European LS-DYNA Users Conference*, 2007.
[6] Yen, C..F., Ballistic impact modeling of composite materials. *Proceedings of the 7th International LS-DYNA Users Conference*, 2002.
[7] Airoldi, A. & Cacchione, B., Modeling of impact forces and pressures in lagrangian bird strike analyses. *International Journal of Impact Engineering*, **32**, pp. 1651–1677, 2006.
[8] Johnson, A. & Holzapfel, M., Numerical prediction of damage in composite structures from soft body impacts. *Journal of Material Science*, **41**, pp. 6622–6630, 2006.
[9] Lacome, J.L., Smoothed particle hydrodynamics (sph): a new feature in ls-dyna. *Proceedings of the 7th International LS-DYNA Users Conference*, 2002.
[10] Schewer, L.E., Preliminary assessment of non-lagrangian methods for penetration/simulation. *Proceedings of the 8th International LS-DYNA Users Conference*, 2004.
[11] Buyuk, M., Kan, C.D.S., Bedewi, N.E., Durmus, A. & Ulku, S., Moving beyond the finite elements, a comparison between the finite element methods and meshless methods for a ballistic impact simulation. *Proceedings of the 8th International LS-DYNA Users Conference*, 2004.
[12] Huertas, C.A., *Robust Bird-Strike Modeling Using LS-DYNA*. Master's thesis, University of Puerto Rico,

2006.
[13] Azevedo, R.L. & Alves, M., Numerical simulation of bird strike impact against balanced fiberglass/epoxy composite plates. *Proceedings of the 19th International Congress of Mechanical Engineering*, Brasília (DF), Brasil, 2007.
[14] Ávila, A.F., Soares, M.I. & Silva Neto, A., An experimental investigation on nanocomposites under impact loading. *WIT Transactions on Engineering Sciences, Impact Loading of Lightweight Structures*, eds. M. Alves & N. Jones, pp. 89–102, 2005.
[15] Santiago, R.C., Azevedo, R.L., Alves, M. & Ávila, A.F., Mechanical characterization of glass/epoxy composite material with nanoclays. *Proceedings of the 19th International Congress of Mechanical Engineering*, Brasília (DF), Brasil, 2007.
[16] Chang, F.K. & Chang, K.Y., A progressive damage model for laminated composites containing stress concentrations. *Journal of Composite Materials*, **21**, pp. 834–855, 1987.
[17] Meyers, M.A., *Dynamic Behavior of materials*. John Wiley and Sons, Inc., 1994.

Mechanics of Solids in Brazil 2009, H.S. da Costa Mattos & Marcílio Alves (Editors)
Brazilian Society of Mechanical Sciences and Engineering, ISBN 978-85-85769-43-7

A dual finite visco-hypoelastic approach

Hilbeth P. Azikri de Deus
IF-SC - Santa Catarina Federal Institute of Education, Science and Technology, Joinville Campus, Department of Metal Mechanics, Joinville/SC – Brazil
Marcelo Krajnc Alves
UFSC - Federal University of Santa Catarina, Trindade Campus, Department of Mechanical Engineering, Florianópolis/SC – Brazil

Abstract

The objective of this work is to propose a dual finite deformation visco-hypoelasticity model and a numerical scheme for the analysis of polimeric materials. The proposed rate form of constitutive equation is formulated in terms of objective Green-Naghdi rate Kirchhoff stress tensor and Lagrangian logarithm (Hencky) strain tensor rate. The integration of the rate constitutive equation yields an integro-diferential form of constitutive equation. The material is assumed to be isotropic and the kernel functions, associated with the shear and bulk compliance modulus, are represented in Prony series. The problem is formulated within a Total Lagrangian descripton. The Galerkin finite element method is used for numerical approach. Finally some problem cases are solved, and the proposed model, the robustness and performance of the algorithms employed are tested.

Keywords: visco-hypoelasticity model, Kirchhoff stress tensor, Hencky strain tensor, Green-Naghdi rate.

1 Introduction

The materials are termed viscoelastic because they exhibit both solid- and fluid-like behaviour, and amongst examples of such media we find concrete and the thermoplastic polymers. The polymers consist of so called long chain molecules. They are easily moulded, lightweight and may be made strong plastics. The long chains, or backbones, are constructed by joining a great many hydrocarbon monomers together to form periodic sequences of specific arrangements of hydrogen and carbon atoms; this is then the long chain, the polymer.

Solid polymers can occur in the amorphous or crystalline state. Polymers in the amorphous state are characterized by a disordered arrangement of the macromolecular chains, which adopt conformations corresponding to statistical coils. The crystalline state is characterized by a long-range threedimensional order (order extending to distances of hundreds or thousands of times the molecular size of the

Mechanics of Solids in Brazil 2009, H.S. da Costa Mattos & Marcílio Alves (Editors)
Brazilian Society of Mechanical Sciences and Engineering, ISBN 978-85-85769-43-7

repeating unit). The macromolecular chains in this state adopt fixed conformations such as planar zigzag, or helical. These chains are aligned parallel to each other, forming a compact packing that gives rise to a three-dimensional order. Many polymers have the capability to crystallize. This capability basically depends on the structure and regularity of the chains and on the interactions between them. The term "semicrystal1ine state" should be used rather than crystalline state, because regions in which the chains or part of them have an ordered and regular spatial arrangement coexist with disordered regions typical of the amorphous state.

Viscoelastic behavior is typical of a number of materials such as polymers and plastics, as explained previously. These materials have memory, i.e. the stress depends on the entire history of the deformation and typically this memory fades with time. In dual formulation the strain can be represented as a functional of the stress history which, due to the requirement that the principle of material objectivity needs to be satisfied. This leads to reasonably complex relations even in the "simplest" of constitutive relations.

Later in this paper it describes a dual finite visco-hypoelastic model based in Hencky strain measure used in small strain contexts to the case of large deformation. The extension to the large deformation case is achieved by considering

a multiplicative decomposition of the deformation gradient and taking the logarithm strain measure with rotated Kirchhoff stress as the conjugated pair. Before presenting the model, this paper begins with a brief discussion about basic physical phenomena of creep and stress relaxation, typical for viscoelastic materials. The subsection 2.2 starts by a discussing the two more general categories of viscoelastic constitutive models: integral and differential models. In the subsection 2.3 are presented the derivation of our dual integral constitutive model. The section 3 presents the strong, weak (variational) formulation of the problem the numerical scheme. Finally the section 4 discusses the numerical applications.

2 Constitutive laws

Viscoelastic media are characterized by two basic phenomena: creep and stress relaxation. We consider both cases below.

2.1 Creep and relaxation

Consider a simple uniaxial bar of a viscoelastic material, subjected to an instantaneously applied and sustained tensile load as shown in figure 1.

Firstly imagine a qualitatively similar bar, again fixed at one end, to which an on/off axial step loading is applied at the other, that is, at $t_0 = 0$ the loading increases instantaneously to the constant value F and at $t^* > t_0$, F is removed as illustrated in figure. The bar now responds by extending in length and we denote this extension by $u(t)$. At the instant t_0+ there is again linear elastic behaviour and $u(t_0+)$ is therefore given by Hooke's law, but over the range $t \in (t_0, t^*)$, the bar will continue to extend, this behaviour is termed creep. If for arbitrarily large t^* this creep continues indefinitely then the material is a viscoelastic fluid, on the other hand if $u(t)$ approaches some constant value

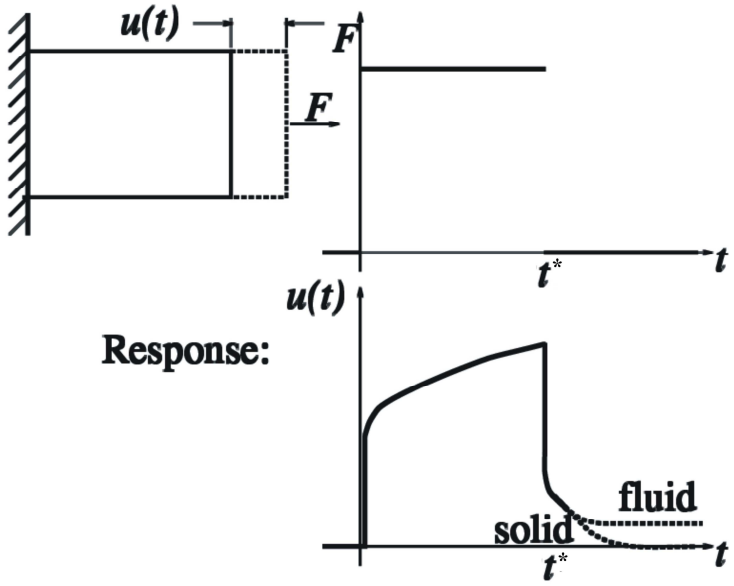

Figure 1: Schematic creep

then it is a viscoelastic solid. Upon removal of the load F at $t = t^*$ the material again displays elastic behaviour, there is an elastic recovery where u instantaneously snaps back to a lesser value.

Thereafter is another creep phase during which the material attempts to return to its original configuration. It can make a solid fluid distinction: if, as $t \to \infty$ we have $u \to 0$ then the material is a solid but if $u \to constant \neq 0$ then there is a permanent set within the bar caused by irreversible molecular flow during the initial creep phase and the material is a fluid.

The ability of a viscoelastic material to attempt to return to its original configuration even after inelastic deformation has taken place implies that it somehow has an internal record of its initial state. If this is the case then it seems plausible that it also keeps a record of all of its states up to the present time and for this reason viscoelastic materials are said to possess memory.

Now we think of the bar as being fixed rigidly at one end and, at some reference time $t = 0$, an instantaneous longitudinal displacement u, applied to the other as schematically shown in the figure 2.

In response an internal longitudinal stress σ is set up within the bar which at the instant, $t = 0+$, is given by Hooke's law, and so the instantaneous response of the material is linear elastic. Over time however the stress decreases monotonically to either the constant, nonzero, value σ_0 or to zero. In the former case the material is termed a viscoelastic solid whilst in the latter a viscoelastic fluid. This phenomena is known as stress relaxation.

Mechanics of Solids in Brazil 2009, H.S. da Costa Mattos & Marcílio Alves (Editors)
Brazilian Society of Mechanical Sciences and Engineering, ISBN 978-85-85769-43-7

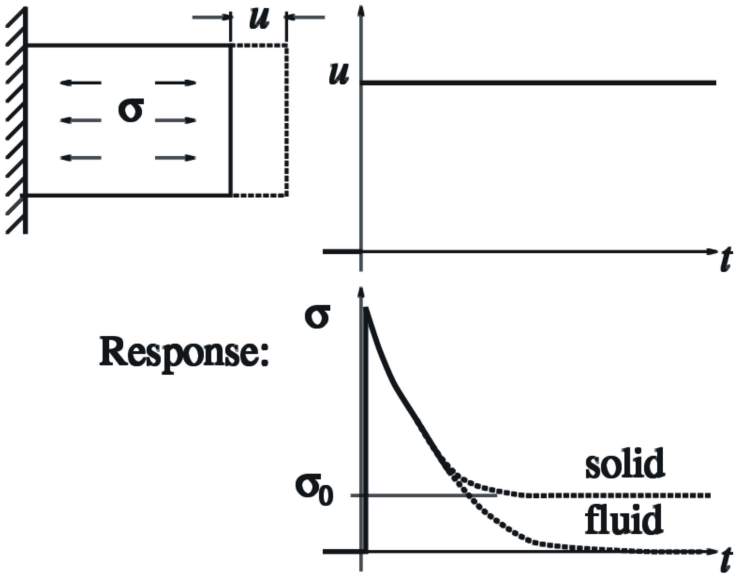

Figure 2: Schematic stress relaxation

2.2 Linear visco-hypoelastic constitutive model

As we have seen for an elastic solid, the stress is determined by the deformation of the material relative to a fixed reference configuration. However, it is. One blank line must be included above and bellow each equation. evident that several materials, exhibit viscoelastic characteristics, i.e. the magnitude of the measured stress depends on strain, strain rate, time and temperature as well, although we will not consider it here. In this sense the stress in viscoelastic materials can be represented as a functional of the history of the deformation. In other words, these materials have memory: the stress depends on the entire history of the motion, and typically this memory fades with time. There are a number of approaches for constructing constitutive models for the large strain viscoelastic deformation. Mathematical relations which describe how stress can depend on the history of the deformation are either given in integral form or in differential form. In integral form the stress at time t is given in terms of an expression which involves an integral over previous times. The integral in such an expression is known as a history integral. In contrast, the differential form of constitutive model the history of the deformation is taken into account by certain ordinary differential equations which describe how certain quantities known as internal variables evolve in time. For a more detailed presentation of both ways of representing viscoelastic constitutive models see, for example see the references Drozdov [1], Haupt [2], Johnson *et al.* [3], Reismann and Pawlik [4] and Truesdell and Noll [5].

The Boltzmann superposition principle follows by that in each strain step the stress evolution is given by Hooke's law. In this sense, the evolution in each strain step component is approximated with

a piecewise continuous step function. For sufficiently smooth fields, the general linear constitutive equation for the linear viscoelastic (small deformation) solid is given by

$$\sigma_{ij}(t) = D_{ijkl}(t - t_0)\varepsilon_{kl}(t_0) + \int_{t_0}^{t} D_{ijkl}(\mathbf{t} - \xi)\dot{\varepsilon}_{kl}(\xi)d\xi \tag{1}$$

or equivalently

$$\sigma_{ij}(t) = D_{ijkl}(t_0)\varepsilon_{kl}(t - t_0) - \int_{t_0}^{t} \dot{D}_{ijkl}(\mathbf{t} - \xi)\varepsilon_{kl}(\xi)d\xi \tag{2}$$

Considering now a viscoelastic isotropic material

$$D(t) = 2G(t)II_{DEV} + K(t)(I \otimes I) \tag{3}$$

in which

$$II_{DEV} = II - \frac{1}{3}(I \otimes I) \tag{4}$$

where I is the second order identity tensor and II is the fourth order identity tensor and the kernel functions are represented in terms of Prony series, which assumes that:

$$G(t) = G_\infty + \sum_{i=1}^{n_G} G_i \exp\left(-\frac{1}{\tau_i^G}\right) \tag{5}$$

$$K(t) = K_\infty + \sum_{i=1}^{n_K} K_i \exp\left(-\frac{1}{\tau_i^K}\right) \tag{6}$$

in which G_∞ and G_i are shear elastic moduli, K_∞ and K_i are bulk elastic moduli and τ_i^G and τ_i^K are the relaxation times for each Prony component. An a alternative formulation for the quasi-static rate model is the constitutive equation given in

$$\varepsilon_{ij}(t) = C_{ijkl}(t - t_0)\sigma_{kl}(t_0) + \int_{t_0}^{t} C_{ijkl}(\mathbf{t} - \xi)\dot{\sigma}_{kl}(\xi)d\xi \tag{7}$$

in which

$$C = \frac{B}{9}(I \otimes I) + \frac{J}{2}II_{DEV} \tag{8}$$

where B is the bulk compliance function and J is the shear compliance function with the kernel functions are represented in terms of Prony series, which assumes that:

$$B(t) = B_0 + \sum_{i=1}^{n_G} B_i \left(1 - \exp\left(-\frac{1}{\tau_i^B}\right)\right) \tag{9}$$

$$J(t) = J_0 + \sum_{i=1}^{n_G} J_i \left(1 - \exp\left(-\frac{1}{\tau_i^J}\right)\right) \tag{10}$$

in which J_0 and J_i are shear compliance moduli, B_0 and B_i are bulk compliance moduli and τ_i^B and τ_i^J are the relaxation times for each Prony component.

2.3 Finite visco-hypoelastic constitutive model

The Hencky's logarithmic strain measure model was proposed in 1938 to study elastic behaviour of rubbers at some simple finite deformation modes. The Hencky's logarithmic strain or natural strain has inherent advantages over other strain measures in his study of a priori constitutive inequalities and treated the Hencky strain, its rate and its work-conjugate stress as basic measures for strain, strain rates and stresses. The Hencky's logarithmic tensor E, based in Lagrangean formulation, can be defined in following way:

$$\begin{aligned} E(x_o, t) &= \frac{1}{2} \ln\left(C(x_o, t)\right); \\ &= \ln\left(U(x_o, t)\right) \end{aligned} \tag{11}$$

where U is the symetric positive defined second order tensor from polar decomposition of $F = RU$ (gradient of the deformation function). From the spectral decomposition:

$$U(x_o, t) = \sum_{i=1}^{n} \sqrt{\Lambda_i} \left(\varphi_i \otimes \varphi_i\right) \tag{12}$$

with $\{\Lambda_i\}_{i=1}^n$ and $\{\varphi_i\}_{i=1}^n$ are the eigenpairs of C. As pointed out by the famous Hill's work in 1978, the rate of stress work per unit of mass which is invariant under a change of strain measure and the reference configuration is used

to generate stress measures conjugate to the family of strain measures

$$\dot{W} = \frac{1}{\rho}\left(\sigma : D\right) = \frac{1}{\rho_o}\left(\tau : D\right) = \frac{1}{\rho_o}\left(P : \dot{F}\right) = \frac{1}{2\rho_o}\left(S : \dot{C}\right) \tag{13}$$

in which σ is the Cauchy stress tensor, τ is the Kirchhoff stress tensor, D is the infinitesimal deformation rate, P is the first Piola-Kirchhoff stress, F is the gradient of the deformation function, S is the second Piola-Kirchhoff stress, C is the right Cauchy-Green strain tensor and ρ_o and ρ being the reference and the current mass densities. Then, one follows that

Theorem 1 The rotated Kirchhoff stress tensor ($\bar{\tau} = R^T \tau R$) forms the conjugated stresstensor pair with the Hencky's logarithmic strain measure (E), under the isotropy hypothesis, i.e.

$$\dot{W} = \frac{1}{\rho_o}\left(\bar{\tau} : \dot{E}\right) \tag{14}$$

Proof We have

$$\rho_o \dot{W} = \tau : D = \bar{\tau} : \left(R^T D\, R\right)$$

Thus observing that $R^T D\, R$ can be rewritten as follow

$$R^T D\, R = \frac{1}{2}\left(U^{-1}\dot{U} + \dot{U}U^{-1}\right).$$

From the spectral decomposition, we have

$$\dot{E} = \frac{1}{2}\sum_{i=1}^{n}\left[\frac{\dot{\Lambda}_i}{\Lambda_i}\left(\varphi_i \otimes \varphi_i\right) + \ln\left(\Lambda_i\right)\left(\dot{\varphi}_i \otimes \varphi_i + \varphi_i \otimes \dot{\varphi}_i\right)\right]$$

and observing that $\varphi_i : \varphi_j = \delta_{ij}$ and $\dot{\varphi}_i : \varphi_i = \varphi_i : \dot{\varphi}_i = 0$, we conclude that

$$\tau : D = \bar{\tau} : \dot{E}. \tag{15}$$

By a similar way it follows in this unrotated configuration the constitutive equation may be rewritten as

$$E(t) = \bar{C}(t - t_0)\bar{\tau}(t_0) + \int_{t_0}^{t} \bar{C}(\mathbf{t} - \xi)\dot{\bar{\tau}}(\xi)d\xi \tag{16}$$

In order to generalize this constitutive equation to finite deformation problems, it is necessary to introduce the following definition

Definition 1 Let be v, A, and H (first order, second order and fourth order tensor respectively), one defines the pull back or bar transformation as

$$\bar{v}(t) = \Theta^T(t)\, v(t) \tag{17}$$

$$\bar{A}(t) = \Theta^T(t)\, A(t)\, \Theta(t) \tag{18}$$

$$\bar{H}(t) = \Theta^T(t)\, \Theta^T(t)\, H(t)\, \Theta(t)\, \Theta(t) \tag{19}$$

and from continuum mechanics

$$\bar{F}(t) = \Theta^T(t)\, F(t) \tag{20}$$

$$\bar{C}(t) = \Theta^T(t)\, C(t)\, \Theta(t) \tag{21}$$

These pull back (rotation neutralized) quantities with $\Theta(t)$ are used to define a convenient framework to perform the integration of the constitutive model. Indeed, the pull back Kirchhoff stress tensor can be defined as

$$\bar{\tau}(t) = \Theta^T(t)\,\tau(t)\,\Theta(t) \tag{22}$$

and one can show that

$$\dot{\bar{\tau}}(t) = \Theta^T(t)\,\overset{\cdot}{\breve{\tau}}(t)\,\Theta(t) \tag{23}$$

(for proof details see the reference Azikri de Deus [6]) where $\tau\breve{\cdot}(t)$ denotes the Green-Naghdi rate of the pull back Kirchhoff stress tensor, which is given by

$$\overset{\cdot}{\breve{\tau}} = \dot{\tau} - \Xi\tau + \tau\,\Xi \tag{24}$$

where $\Xi(t) = \dot{R}(t)\,R^T(t)$ (spin tensor). Let us define the rotation tensor $\Theta(t)$, as the solution to the following initial value problem:

Problem 1 Given $\Xi(t)$, find $\Theta(t)$ that solves

$$\dot{\Theta}(t)\,\Theta^T(t) = \Xi(t) \tag{25}$$

$$\dot{\Theta}(t) = \Xi(t)\,\Theta(t) \tag{26}$$

$$\Theta(0) = I \tag{27}$$

By simple observation, one can verify that the solution to the initial value problem is given by $\Theta(t) = R(t)$ (for more details see the references Azikri de Deus [6] and Truesdell and Noll [5]).

3 The finite visco-hypoelastic problem

The approach used here is the total Lagragian formulation. Considering the reference configuration Ω_o, defined at t_o, a bounded domain with a Lipschitz boundary $\partial\Omega_o$ subjected to a body force b defined on Ω_o, a prescribed surface traction defined on Γ_o^t and a prescribed displacement defined on Γ_o^u, where $\partial\Omega_o = \overline{\Gamma_o^t \cup \Gamma_o^u}$ and $\Gamma_o^t \cap \Gamma_o^u$.

Taking the motion function $\phi_t : \Re^3 \to \Re^3$ such that $x = \phi(x_o, t) = \phi_t(x_o) \;\therefore\; x_o = \phi_t^{-1}(x)$. It follows that the displacement field is defined as: $x = u(x_o, t) + x_o \;\therefore\; u_o(x_o, t) = \phi_t(x_o) - x_o = x - x_o = x - \phi_t^{-1}(x) = u(x_o, t)$. Thus, it is possible to announce the problem in the reference configuration as:

Problem 2 For each $t \in [0, t_f]$ determine $u_o(x_o, t)$ that solves the following boundary value problem stated as

$$div\,P(x_o, t) + \rho_o(x_o)\,b(x_o, t) = 0 \quad in \quad \Omega_o \tag{28}$$

$$P(x_o, t)\,n_o(x_o, t) = \bar{t}_o(x_o, t) \quad in \quad \Gamma_o^t \tag{29}$$

$$u_o(x_o, t) = \bar{u}_o(x_o) \quad in \quad \Gamma_o^u \tag{30}$$

with $b(x_o, t) \in L_2(\Omega_o)$ and $\bar{u}_o(x_o) \in H_{00}^{1/2}(\Gamma_o^u)$ for each $t \in [0, t_f]$.

Let us define now the following sets, for each time $t \in [0, t_f]$

$$Kin_o^u = \left\{ u_o : \Omega_o \to \Re^3 \,\middle|\, u_o \in H^1(\Omega_o),\, u_o(x_o,t) = \bar{u}_o(x_o)\ in\ \Gamma_o^u \right\} \tag{31}$$

$$Var_o^u = \left\{ \hat{v} : \Omega_o \to \Re^3 \,\middle|\, \hat{v} \in H^1(\Omega_o),\, \hat{v}(x_o) = 0\ in\ \Gamma_o^u \right\} \tag{32}$$

Thus it has the weak form of the problem

Problem 3 For each $t \in [0, t_f]$ determine $u_o(x_o, t) \in Kin_o^u$ such that

$$\int_{\Omega_o} P : \nabla \hat{v}\, d\Omega_o = \int_{\Omega_o} \rho_o b \cdot \hat{v}\, d\Omega_o + \int_{\Gamma_o^t} \bar{t}_o \cdot \hat{v}\, d\partial\Omega_o,\ \forall \hat{v} \in Var_o^u \tag{33}$$

For each $t \in [0, t_f]$, it can denoting

$$\Im(u_o; \hat{v}) = \int_{\Omega_o} P : \nabla \hat{v}\, d\Omega_o - \int_{\Omega_o} \rho_o b \cdot \hat{v}\, d\Omega_o - \int_{\Gamma_o^t} \bar{t}_o \cdot \hat{v}\, d\partial\Omega_o,\ \forall \hat{v} \in Var_o^u \tag{34}$$

Then, the problem can be stated as

Problem 4 For each $t \in [0, t_f]$ determine $u_o(x_o, t) \in Kin_o^u$ such that

$$\Im(u_o; \hat{v}) = 0,\ \forall \hat{v} \in Var_o^u \tag{35}$$

The problem above is approached by Newton method in association with Galerkin-FEM, and the incremental formulation follows from the schematic algorithm in Tab. 1

Table 1: Newton's Method Algorithm – Incremental Formulation.

For each time step $t = t_n$;
- (i) Initialize the iteration counter $k \leftarrow 0$;
- (ii) Initialize the variable vector $u_{n+1}^0 = u_n$;
- (iii) Compute the *residue vector*, $error = \|residue\ vector\|$;
- (vi) Do while ($error > tolerance$[1])
  - (1) Determine the tangent modulus $\left[\aleph(u_{n+1}^k)\right]_{ijkl} = \left.\frac{\partial P_{ij}}{\partial F_{kl}}\right|_{u=u_{n+1}^k}$
  - (2) Solve the problem $\int_{\Omega_o} \aleph(u_{n+1}^k) \nabla(\Delta u_{n+1}^k) : \nabla \hat{v} d\Omega_o = -\Im\left(u_{n+1_o}^k; \hat{v}\right),\ \forall \hat{v} \in Var_o^u$;
  - (3) Actualize the variable vector $u_{n+1}^{k+1} = u_{n+1}^k + \Delta u_{n+1}^k$;
  - (4) Compute the new *error*;
  - (5) Actualize $\Im\left(u_{n+1}^k; \hat{v}\right) \leftarrow \Im\left(u_{n+1}^{k+1}; \hat{v}\right)$ and $k \leftarrow k+1$;
- End Do while.

(1): previously defined.

4 Numerical examples

For these applications, one used a mesh with two six points triangular elements. The developed code is written in Fortran 90 and for post processing, it's used the GID 8.0 software. The global tolerance is 10^{-6}.

EXAMPLE 1: In this example, one is considered the plane strain state. The body is a rectangular shape, in which the dimentions are width $1\,(\times 25,4\,mm)$ and height $2\,(\times 25,4\,mm)$. Let be presented the following reference configuration $\Omega_o = \{(x,y)\,|0 < x < 1\,(\times 25,4\,mm)\ and\ 0 < y < 1\ \ (\times 25,4\,mm)\}$ under symmetry considerations. For the quasi-static problem one has the boundary conditions: $\bar{u}_x(0,y,t) = \bar{u}_y(0,y,t) = 0$, $\bar{u}_x(1,y,t) = 0.1\,t\,(\times\ 25,4\,mm)$ and the other conditions are tension free for $t \in [0,1]$ (see fig. 3). In this example one demonstrates the consistence of the numerical algorithm (code) by comparing the numerical solution against artificial exact solution. Invariably one design the loads and tractions so that the exact stretch have the form $x(t) = \lambda_1(t)\,x_o$ and $y(t) = \lambda_2(t)\,y_o$.

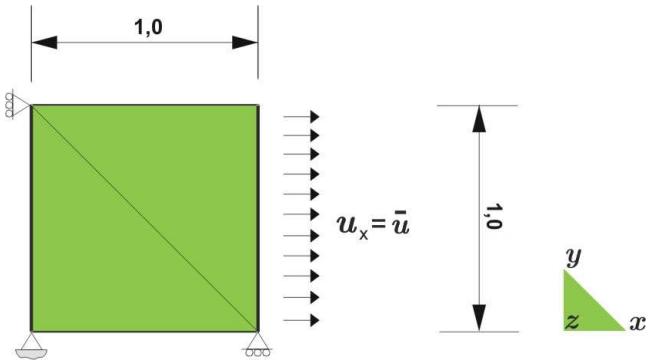

Figure 3: Traction test.

By a simple computation from the boundary condition and supposing

$$J(t) = 3,2386 \times 10^{-8}\left(1 - e^{\frac{1}{20,2599}t}\right) + 5,8578 \times 10^{-7}\,(\times 6,89\,kPa)^{-1} \tag{36}$$

one has that this block is composed by a polymer that has the following ralaxation function for B

$$B(t) = 4,7279 \times 10^{-8}\left(1 - e^{\frac{1}{19,8283}t}\right) + 8,7867 \times 10^{-7}\,(\times 6,89\,kPa)^{-1} \tag{37}$$

where the time scale is taken in days. In next figure (see fig. 4), one presents the time evolution of σ_{xx} in the body (constant profile along entire body).

One can observe the evolution of stress σ_{xx} component with the time for one day obeservation. Note that the numerical results are equal to the exact solution of the problem for each time step. The last figure shows the displacement profile on the deformed body (see fig. 5).

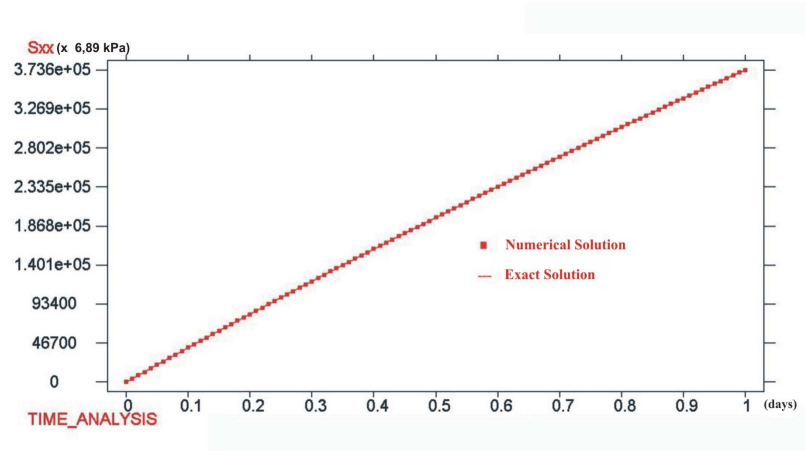

Figure 4: Tension (kPa) vs. time (days).

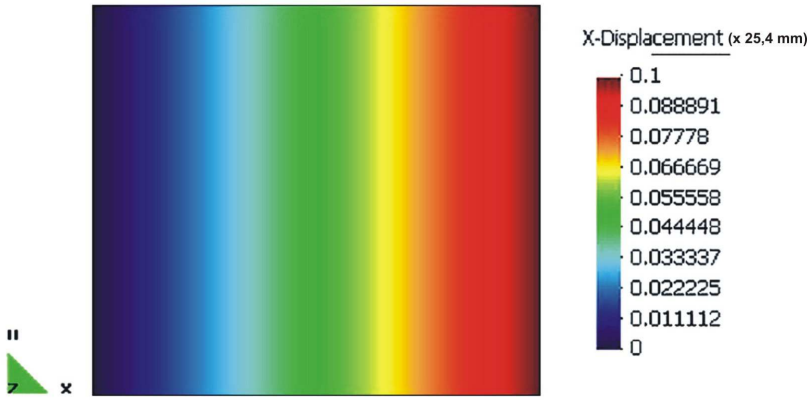

Figure 5: Displacement for $t = 1$ day.

EXAMPLE 2: In this example, one is considered the plane strain state. The body is a square shape $(2\,(\times 25,4\,mm) \times 2\,(\times 25,4\,mm))$ with a circular hole inside (radius $= 0,2\,(\times 25,4\,mm)$). This hole is placed at the geometrical center of square shape. For the quasi-static problem, the body is submited to prescribed displacement conditions on right and left (same value) side of the square shape and the other conditions are free stress. Motivated by numerical effort reduction, this problem is approached under simety considerations (1/4 of geometry - see fig. 6).

On the right side one has $\bar{u}_x(1, y, t) = 0.1\,t\,(\times 25,4\,mm)$ for $t \in [0, 1]$. The polymer is the same of

example 1 where the time scale is taken in days. In this example one is used 801 elements and 1682 nodes (see fig. 7).

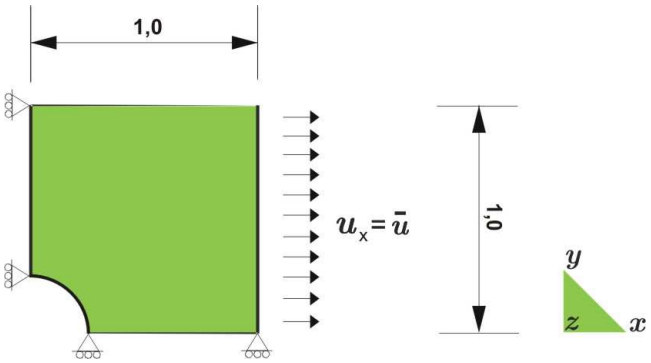

Figure 6: 1/4 Square shape with a circular hole.

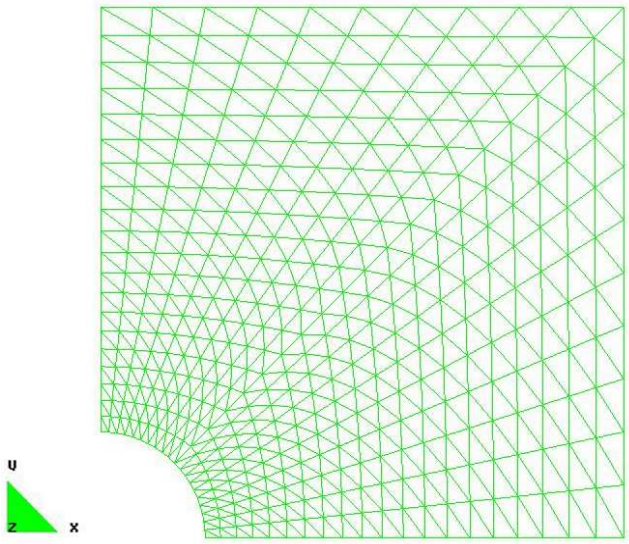

Figure 7: Tri 6 elements mesh.

The figure 8 shows the displacement field at the final observation instant. The figure 9 shows the stress σ_{xx} profile. Note that high stress levels are in top of the central hole. The figure 10 shows the

stress σ_{xy} profile, where higher stress levels are in top of the central hole and in the figure 11 is exposed the stress σ_{yy} profile. The high stress levels are too in top of the central hole.

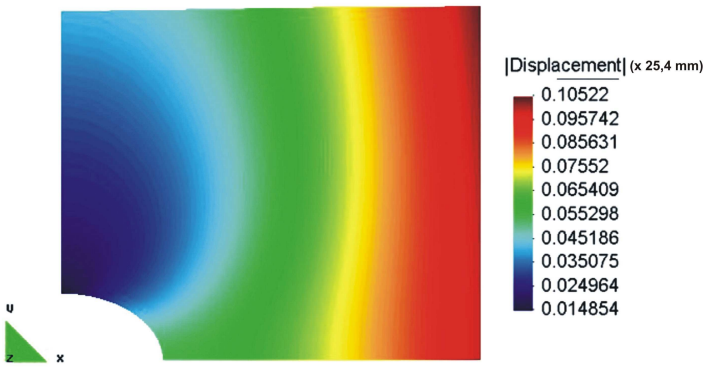

Figure 8: Displacement for $t = 1$ day.

Figure 9: σ_{xx} profile for $t = 1$ day.

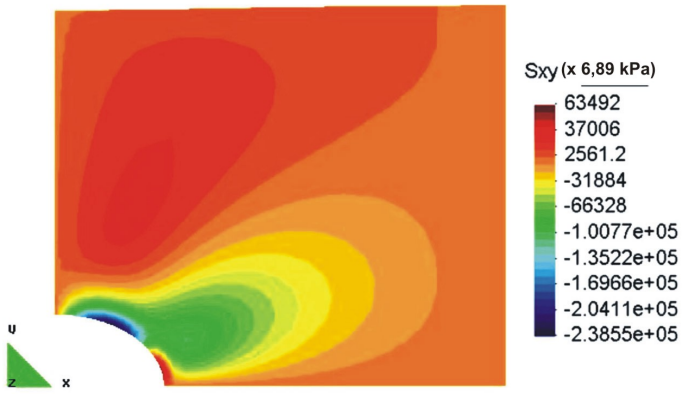

Figure 10: σ_{xy} profile for $t = 1$ day.

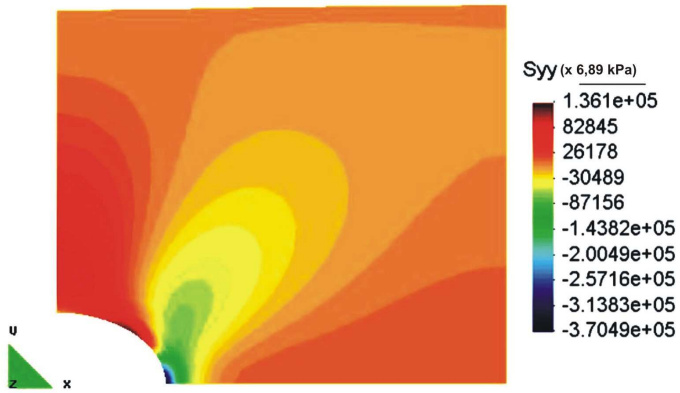

Figure 11: σ_{yy} profile for $t = 1$ day.

EXAMPLE 3: In this example, one is considered the plane strain state. The body is a complex geometry component (dimentions in inches). For the quasi-static problem, this body is submitted to prescribed displacement conditions on right side and the others condition are free stress conditions (see fig. 12).

On the right side one has $\bar{u}_x(1, y, t) = -0,3\,t\,(\times 25,4\,mm)$ for $t \in [0, 1]$. The polymer is the same of examples 1 and 2, where the time scale is taken in days. In this example one is used 337 elements and 755 nodes (see fig. 13).

The figure 14 shows the displacement field at the final observation instant. The figure 15 shows the stress σ_{xx} profile. Note that high stress levels are in upper right and low left of the central hole. The figure 16 shows the stress σ_{xy} profile, where higher stress levels are in upper right and low left of the central hole. In the figure 17 is exposed the stress σ_{yy} profile. The high stress levels are in upper left and low right of the central hole.

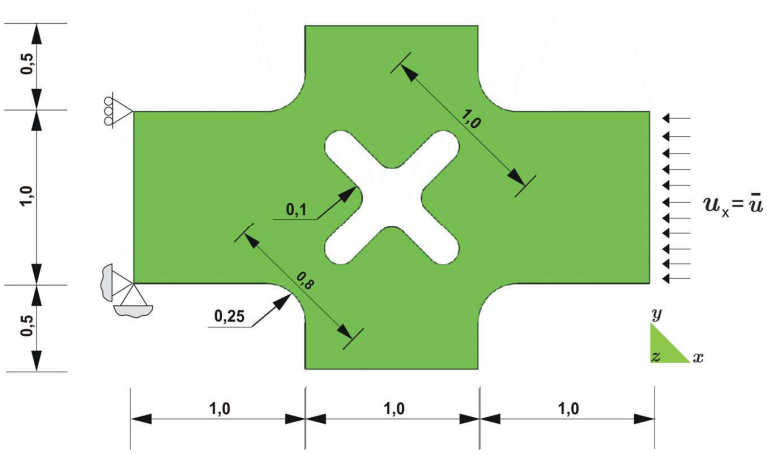

Figure 12: Problem sketch.

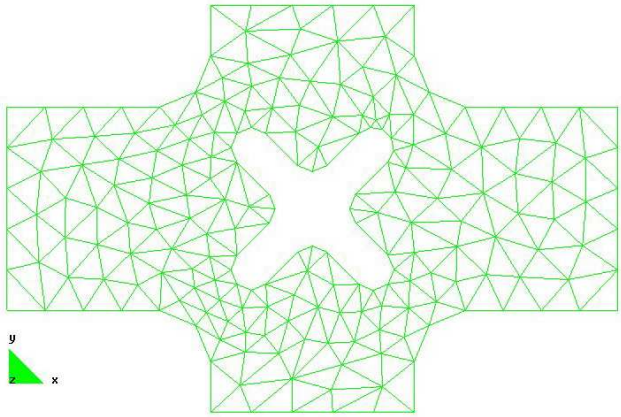

Figure 13: Tri 6 elements mesh.

Figure 14: Displacement for $t = 1$ day.

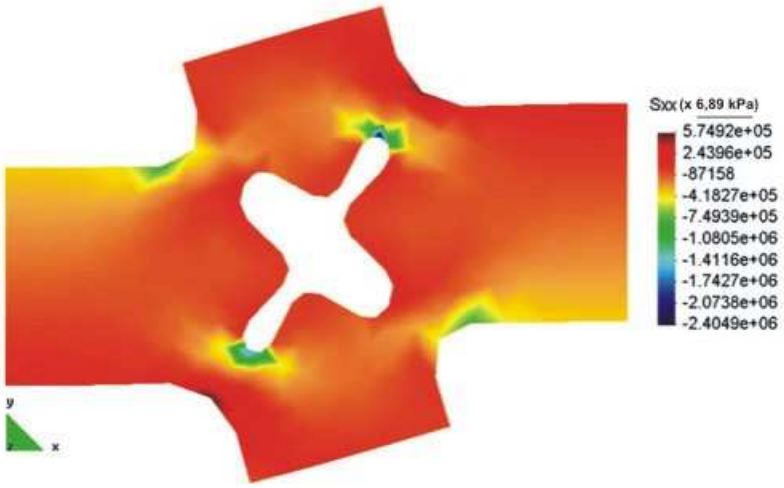

Figure 15: σ_{xx} profile for $t = 1$ day.

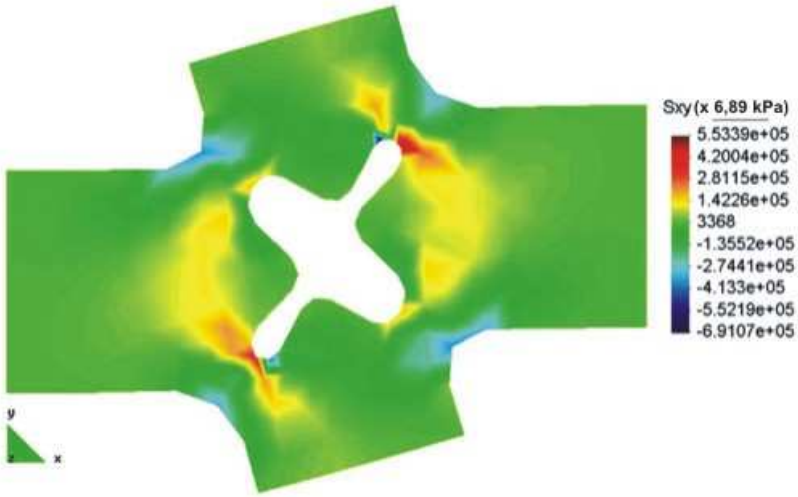

Figure 16: σ_{xy} profile for $t = 1$ day.

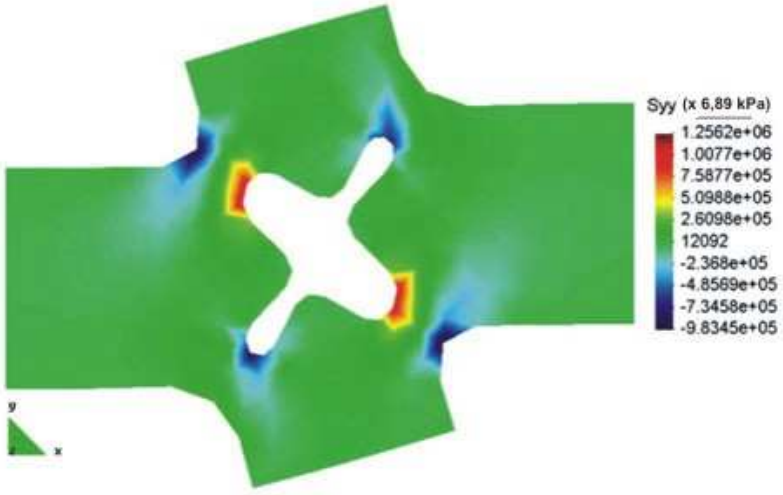

Figure 17: σ_{yy} profile for $t = 1$ day.

References

[1] Drozdov, A., *Finite Elasticity and Viscoelasticity: A Course in non-linear Mechanics of Solids*. World Scientific Publishing: New York, USA, 1996.
[2] Haupt, P., *Continuum Mechanics and Theory of Materials*. Springer-Verlag: Heidelberg, Germany, 2002.
[3] Johnson, A.R., Quigley, C.J., & Mead, J.L., Large strain viscoelastic constitutive models for rubber, part I: Formulations. *Rubber Chemistry and Technology*, **67**, pp. 904–917, 1994.
[4] Reismann, H. & Pawlik, P.S., *Elasticity: Theory and Applications*. John Wiley and Sons: New York, USA, 1980.
[5] Truesdell, C. & Noll, W., *The Non-Linear Fields Theories of Mechanics*. Springer-Verlag: Heidelberg, Germany, 2004.
[6] Azikri de Deus, H.P., *Computational Propositions and Aplications in Polymers*. Ph.D. thesis, Federal University of Santa Catarina, Florianpolis, Brazil, 2008.

Mechanics of Solids in Brazil 2009, H.S. da Costa Mattos & Marcílio Alves (Editors)
Brazilian Society of Mechanical Sciences and Engineering, ISBN 978-85-85769-43-7

An application for polymeric foams

Hilbeth P. Azikri de Deus
IF-SC - Santa Catarina Federal Institute of Education, Science and Technology, Joinville Campus, Department of Metal Mechanics, Joinville/SC – Brazil
Marcelo Krajnc Alves
UFSC - Federal University of Santa Catarina, Trindade Campus, Department of Mechanical Engineering, Florianópolis/SC – Brazil

Abstract

This work proposes a material model and algorithms for applications in polymeric foams. The constitutive relationship is given in association of work-conjugate pair Hencky strain deformation measure and rotated Kirchhoff stress tensor are proposed and explored. The viscoplastic model applied for polymeric foam is non associative, based on a modified von Mises model (by inclusion of the hydrostatic pressure) and incorporates a non linear isotropic hardening law. A regularization approach is proposed to guarantee that the relative density evolution is into the factible set Kρ. Various examples are presented along this work aiming to atest the models and implemented algorithms. The problem is formulated within a Total Lagrangian descripton. The Galerkin finite element method is used for numerical approach. Finally some problem cases are solved, and the proposed model, the robustness and performance of the algorithms employed are tested.

Keywords: polymeric foam, Kirchhoff stress tensor, Hencky strain tensor, viscoplasticity.

1 Introduction

Polymeric foams are widely used in industry and in domestic applications. These foams have a high energy absorption capacity, are useful for shock applications, acoustic and thermal insulating problems. For these reasons, they are used in aircraft and automotive industry, buildings and packaging. Combining good mechanical properties with low density, rigid polymer foams can also be used as structural materials.

The polymeric foams are made of a skeleton composed of open or closed cells, which represent the basic unit of these materials. The mechanical response of polymeric foams depend on the cells geometric characteristics, such as cell wall thickness, shape and size distributions, and on the intrinsic properties of the polymer in the cell wall. In order to model such complex materials, different constitutive relations have been proposed in the literature and are basically divided into two groups: complex

Mechanics of Solids in Brazil 2009, H.S. da Costa Mattos & Marcílio Alves (Editors)
Brazilian Society of Mechanical Sciences and Engineering, ISBN 978-85-85769-43-7

modeling approaches that proposes constitutive relation which describe the average behavior of the foam [1–5] or simpler models that try to represent the cells as an assemblage of structural elements (geometrically periodic cells) [6–9] and relate to analytically elastic material properties and yield stress to the foam relative density.

In order to properly use these materials, one must understand their microstructure/macroscopic mechanical property relationships. Indeed, the mechanical response of these materials depends on their geometrical characteristics, and on the intrinsic properties of the polymer in the cell wall. The geometrical characteristics are determined by the cell wall thickness, the size distribution and the cells shape.

In this work we consider a complex modeling approach and propose a hyperelastic-viscoplastic constitutive relation for modeling the behavior of open cell foam materials. Moreover, based on experimental results, we consider the hyperelastic response to depend on the relative density of the material [10, 11].

Among the various proposed constitutive relations, one can cite the power-law model, described in Chaboche and Rousselier [12], that is generally accepted to give good predictions for low strain rates. However, as the strain rate increases, such a model is unable to describe the observed decreasing strain rate dependence. Also, in the limit, with the increase of the strain rate, the model should be capable to account for a saturation of the material response, as observed experimentally. With the aim of incorporating this material behavior in a unified viscoplastic model, other propositions for the flow rule have been used in the literature. Examples include a hyperbolic sine function, see [13], an exponential function or the addition of a second power-law function to the flow law, as proposed by Chaboche [14]. Some models even combine plasticity with viscoplasticity in order to achieve these goals, as seen in Almroth *et al* [15]. Here, we make use of the constitutive equation proposed by Benallal, see [16], which can be applied for large strain rates and account for the saturation of the overstress where the strain rate is very high.

The proposed model is implemented in a Total Lagrangian framework that considers: a multiplicative decomposition of the deformation gradient, into a plastic and an elastic part and a constitutive relation given in terms of the logarithmic, or Hencky, strain measure and the rotated Kirchhoff stress. The advantage of choosing this conjugate stress-strain pair in the formulation of the constitutive relation is that it leads to a return mapping whose form is the same as the one derived in the small deformation plasticity framework. In addition, one consider the temperature to be low and the deformation rate to be sufficiently high in order to consider the existence of an elastic response and a yield function.

2 Theoretical approach

This paper proposes an elastoviscoplastic constitutive relation for the finite deformation of isotropic crushable polymeric foams, which incorporates the phenomena of creep, relaxation and deformation rate sensitivity in the response of the material.

The model considers the material to have a hardening behavior that is characterized by two curves: one for the compaction response and one for the uniaxial compressive test, which must be determined experimentally. In addition, as a result of experimental observation, the model incorporates a different

Mechanics of Solids in Brazil 2009, H.S. da Costa Mattos & Marcílio Alves (Editors)
Brazilian Society of Mechanical Sciences and Engineering, ISBN 978-85-85769-43-7

response in compression and tension and assumes the hyperelastic behavior to depend on the relative density of the material. In compression the ability of the material to deform volumetrically is enhanced by cell wall buckling processes as described by Gibson & Ashby [6] and Girson et al. [7].

It is assumed that the foam cell deformation is not recoverable instantaneously and can be seen as being viscoplastic. Under tension loading, the cell walls break readily so the tensile load bearing capacity of crushable foams may be considerably smaller than its compressive load bearing capacity.

3 Kinetics of deformation

The plasticity model presented in this paper considers the multiplicative decomposition of the deformation gradient F into an elastic part, F^e, and a viscoplastic part, F^{vp}, as illustrated in Fig. 1. Thus,

$$F = F^e F^{vp} \tag{1}$$

with $F = \nabla\phi(x_o, t)$, where ϕ is the deformation function.

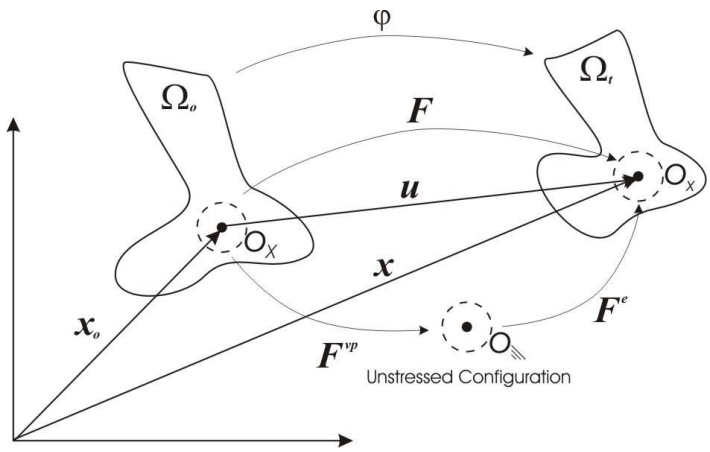

Figure 1: Kinematics of deformation.

However, since $F^e = R^e U^e$, $F^{vp} = R^{vp} U^{vp}$, $U^e = \sqrt{C^e} = \sqrt{F^{eT} F^e}$, $L^e = \dot{F}^e (F^e)^{-1}$, $L^{vp} = F^e \dot{F}^{vp} (F^{vp})^{-1} (F^e)^{-1}$ and $D = sym(L) = D^e + D^{vp}$, the deformation measure, given in terms of the logarithmic strain tensor, may be expressed as

$$\begin{aligned} E^e(x_o, t) &= \frac{1}{2} \ln \left(C^e(x_o, t) \right); \\ &= \ln \left(U^e(x_o, t) \right). \end{aligned} \tag{2}$$

Hill [17] pointed out that the stress-strain pairs must be such that the rate of work density remains preserved. The enforcement of this criterion together with the assumption of an isotropic response of the material leads to the identification of the conjugate stress measure, which is given by the rotated Kirchhoff stress,

$$\bar{\tau} = R^T \tau \, R \tag{3}$$

where τ is the Kirchhoff stress, $\tau = \det(F)\,\sigma$, with σ denoting the Cauchy stress [18, 19].

4 The Yield surface definition

To define the yield function, we introduce the following basic definitions:

- The deviatoric rotated Kirchhoff stress, given by:

$$\bar{\tau}^D = \bar{\tau} - \frac{1}{3} tr(\bar{\tau})\, I \tag{4}$$

- The von Mises effective rotated Kirchhoff stress, given by

$$q = \sqrt{\frac{3}{2} \bar{\tau}^D : \bar{\tau}^D} \tag{5}$$

- The hydrostatic pressure stress, given by

$$p = -\frac{1}{3} tr(\bar{\tau}^D) \tag{6}$$

Thus, from Eq. (4) and Eq.(6) we may express the rotated Kirchhoff stress as $\bar{\tau} = \bar{\tau}^D - p\, I$. Here, we consider the yield function for crushable foam materials, shown in Fig. 3, to be defined in terms of the Kirchhoff stress measure and given by

$$\tilde{\Im}(p, q, \bar{\varepsilon}_k) = \sqrt{q^2 + [\alpha(\bar{\varepsilon}_k)]^2 [p - p_o(\bar{\varepsilon}_k)]^2} - B(\bar{\varepsilon}_k) \tag{7}$$

in which $\alpha = \alpha(\bar{\varepsilon}_k)$ and $p_o = p_o(\bar{\varepsilon}_k)$ are functions of the internal variables $\bar{\varepsilon}_k$. The parameters o p_o and B of the yield ellipse are related to the yield strength in hydrostatic compression, p_c, and to the yield strength in hydrostatic tension, p_t, by

$$p_o = \frac{1}{2}(p_c - p_t), \;\; B = \alpha A = \alpha \frac{p_t + p_c}{2} \tag{8}$$

where p_c and p_t are positive numbers and A is the length of the (horizontal) p-axis of the yield ellipse (see Fig. 2 and Fig. 3).

The evolution of the yield ellipse is controlled by the volumetric compacting viscoplastic strain,

$$\bar{\varepsilon}_1 = \bar{\varepsilon}_v^{vp} = -\ln(J^{vp}), \;\; J^{vp} = \det(F^{vp}) \tag{9}$$

employed in the volumetric hardening model, and by the axial viscoplastic strain,

$$\bar{\varepsilon}_2 = \bar{\varepsilon}_a^{vp} = -\ln\left(\frac{L_f}{L_o}\right) \tag{10}$$

defined in a unilateral compression test, in which L_f is the unloaded length of the specimen, after the deformation has been applied, and L_o is the length of the initial configuration of the reference specimen. To define the hardening behavior, some experimental test data must be obtained, which comprise:

- A uniaxial compression test data
- A hydrostatic compression test data

These hardening curves must be experimentally evaluated and incorporated to the model. Here, we assume the hydrostatic tension strength, p_t , to be proportional to the hydrostatic compression strength, i.e.,

$$p_t = \alpha_p p_c \tag{11}$$

for some constant value $\alpha_p \in [5\%, 10\%]$, see Hanssen *et al* [20] and Hallquist [1]. In addition, we assume the hydrostatic compression strength, p_c , to evolve as a result of compaction (increase in density) or dilation (reduction in density) of the material, i.e.

$$p_c = p_c^o + H_p(\bar{\varepsilon}_v^{vp}) \tag{12}$$

where p_c^o is the initial hydrostatic compression yield strength and $H_p(\bar{\varepsilon}_v^{vp})$ is the hydrostatic compression strength hardening law, given in terms of the volumetric compacting viscoplastic strain.

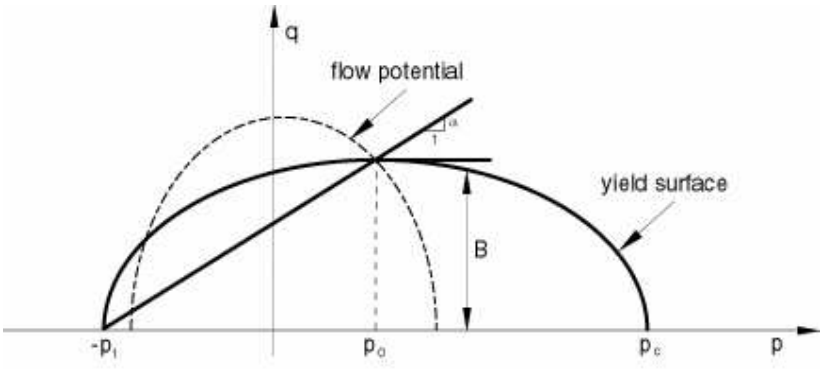

Figure 2: Yield surface.

In order to compute $\alpha(\bar{\varepsilon}_v^{vp}; \bar{\varepsilon}_a^{vp})$ different independent experimental test is required. Here, we employ a uniaxial compression tests. Notice that, different tests could also have been considered. Now, since

the type of impact loading that we want to simulate is dominated by a uniaxial compression type of loading, the best result for the analysis may be probably obtained by using a uniaxial compression test. From a uniaxial compression test we obtain

$$\bar{\sigma}_c(\bar{\varepsilon}_a^{vp}) = \bar{\sigma}_c^o + H(\bar{\varepsilon}_a^{vp}) \tag{13}$$

where $\bar{\sigma}_c^o$ is the initial yield stress, $H(\bar{\varepsilon}_a^{vp})$ is the strain hardening function and $\bar{\varepsilon}_a^{vp}$ is the equivalent viscoplastic strain. Now in a general 3D case, the axial viscoplastic strain is not well defined. However, the uniaxial test response may be incorporated indirectly by using the uniaxial relation

$$\bar{\varepsilon}_a^{vp} = \frac{\bar{\varepsilon}_c^{vp}}{(1-2\nu_p)} \tag{14}$$

Now, using (Eq.11-14), we can compute $\alpha(\bar{\varepsilon}_v^{vp}; \bar{\varepsilon}_a^{vp})$, as follows

$$\alpha(\bar{\varepsilon}_v^{vp}; \bar{\varepsilon}_a^{vp}) = \frac{\bar{\sigma}_c}{\left[p_c p_t - \frac{1}{3}\bar{\sigma}_c\,(p_c - p_t) - \frac{1}{9}\bar{\sigma}_c^2\right]^{\frac{1}{2}}} \tag{15}$$

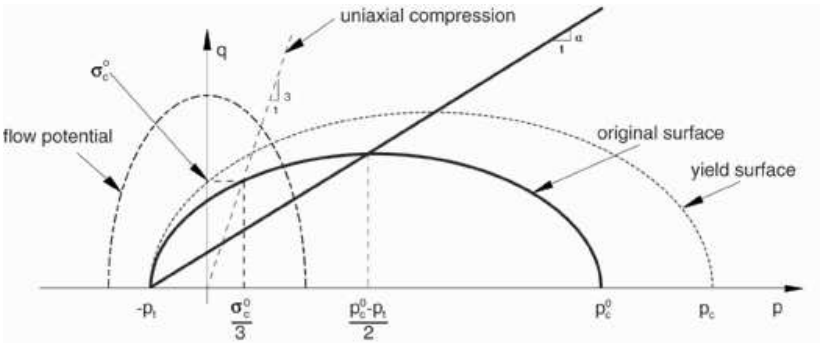

Figure 3: Volumetric hardening.

5 The non-associative viscoplastic flow potential

The viscoplastic strain rate for the volumetric hardening model is assumed to be given by

$$\bar{D}^{vp} = \dot{\lambda}\frac{\partial G}{\partial \bar{\tau}} \tag{16}$$

complemented by postulating a null viscoplastic spin, compatible with viscoplastic isotropy, i.e., $\bar{W}^{vp} = 0$ (null second order tensor). Here, $\dot{\lambda}$ is the viscoplastic multiplier which must satisfy: $\dot{\lambda} \geqslant 0$, which is given by a constitutive relation. The evolution of the viscoplastic deformation is computed as

$$\dot{F}^{vp} = \breve{D}^{vp} F^{vp} \tag{17}$$

where $\breve{L}^{vp} = (F^e)^{-1} L^{vp} F^e$ (unstressed local configuration) and $\breve{W}^{vp} = (U^e)^{-1} W^{vp} U^e = 0$ (null second order tensor). The viscoplastic flow potential (see Fig. 3) for this model is given by

$$G(p,q) = \sqrt{q^2 + \beta^2 p^2} \tag{18}$$

in which β is related to the plastic Poisson's ratio ν_p by

$$\beta = \frac{3}{\sqrt{2}} \sqrt{\frac{1-2\nu_p}{1+\nu_p}} \tag{19}$$

The usual assumption, for polymeric foams is to consider p $\nu = 0.0$. In the absence of the knowledge of the plastic Poisson's ratio, the consideration of a zero plastic Poisson's ratio is a reasonable assumption, as shown in Zhang *et al* [4], Gibson & Ashby [6] and Gilchrist & Mills [21].

6 Evolution law for the accumulated viscoplastic strain

In the case of viscoplastic materials, the viscoplastic multiplier λ is computed by solving a constitutive evolution equation. Here, we make use Benallal's model, see Lemaitre [16] for more details, given by

$$\dot{\bar{e}}^{vp} = \ln \left[\left(1 - \frac{\tilde{\Im}(p,q,\bar{\varepsilon}_k)}{K_v} \right)^{-M} \right] \tag{20}$$

where

$$\dot{\bar{e}}^{vp} = \left[\frac{2}{3} \left(\bar{D}^{vp} : \bar{D}^{vp} \right) \right]^{\frac{1}{2}} \tag{21}$$

Notice that, the evolution of the accumulated viscoplastic strain, which enables the determination of the viscoplastic multiplier, is based on a model that accounts for a saturation of the material response to the increase of the applied rate of deformation. In fact, we have that

$$\tilde{\Im}(p,q,\bar{\varepsilon}_k) = \sigma^v \geqslant 0 \tag{22}$$

where we denote σ v as the over stress measure, we obtain

$$\sigma^v = K_v \left[1 - \exp \left(\frac{\dot{\bar{e}}}{M} \right)^{-M} \right] \tag{23}$$

7 Hyperelastic response

Here, we consider the elastic response to be given, in terms of the logarithmic or Hencky strain tensor and therotated Kirchhoff stress, as

$$\bar{\tau} = 2\mu(\rho^*)E^e + \left[\kappa(\rho^*) - \frac{2}{3}\mu(\rho^*)\right] tr(E^e)\, I \tag{24}$$

where

$$\begin{aligned} \mu(\rho^*) &= \frac{E(\rho^*)}{2\,(1+\nu_o)}; \\ \kappa(\rho^*) &= \frac{E(\rho^*)}{3\,(1-2\nu_o)}, \end{aligned} \tag{25}$$

In which $E(\rho^*)$, is the Young modulus, I is the second order identity, tensor, $\kappa(\rho^*)$ is the bulk modulus, $\mu(\rho^*)$ is the Lamé's coefficient or the shear modulus and ρ^* denoting the relative density, which is defined by the ratio of the foam density, ρ , with the fully compact material density, ρ_M , i.e.,

$$\rho^* = \frac{\rho}{\rho_M} \tag{26}$$

The continuity equation may be written in terms of the relative density as

$$\rho_o^* = \det(F)\rho^* \tag{27}$$

in which $\rho_o^* = \rho_o^*(x_o)$ denotes the initial relative density, defined in the reference configuration, and $\rho^* = \rho^*(x_o, t)$ the actual relative density, defined at the reference configuration. Here, it's important to notice that the set of physical allowable relative densities, related to physical admissible deformation processes, is given by $K = \{\,\rho^* |\, 0 < \rho^* \leqslant 1\}$.

In order to impose implicitly these constraints, we will rewrite the Young modulus as

$$E(\rho^*) = [c(\rho^*)^\gamma + I_K(\rho^*)]\, E_M \tag{28}$$

where $I_K(\rho^*)$ represents the indicator set of K, i.e.,

$$I_K(\rho^*) = \begin{cases} 0,\ if\ \rho^* \in K_\rho; \\ \infty,\ if\ \rho^* \notin K_\rho. \end{cases} \tag{29}$$

This expression may be regularized by using a combined internal and external penalty approaches, i.e., we consider a differentiable function $\Psi_\eta(\rho^*)$ such that

$$I_K(\rho^*) = \lim_{\eta \to 0} [\Psi_\eta(\rho^*)] \tag{30}$$

Based on the above results, we consider the following constitutive relations

$$\Psi_\eta(\rho^*) = \eta\frac{1}{\rho^*} + \frac{1}{\eta}\left[\langle\rho^* - 1\rangle^+\right]^2 \tag{31}$$

and

$$E(\rho^*) = \left\{c(\rho^*)^\gamma + \eta\frac{1}{\rho^*} + \frac{1}{\eta}\left[\langle\rho^* - 1\rangle^+\right]\right\} E_M \tag{32}$$

with E_M representing the Young's modulus of the fully dense material respectively and η a penalty parameter.

8 Total Lagrangean formulation – weak form

The approach used here is the total Lagragean formulation. Considering the reference configuration Ω_o, defined at t_o, a bounded domain with a Lipschitz boundary $\partial\Omega_o$ subjected to a body force b defined on Ω_o, a prescribed surface traction defined on Γ_o^t and a prescribed displacement defined on Γ_o^u, where $\partial\Omega_o = \overline{\Gamma_o^t \cup \Gamma_o^u}$ and $\Gamma_o^t \cap \Gamma_o^u$.

Taking the motion function $\phi_t : \Re^3 \to \Re^3$ such that $x = \phi(x_o, t) = \phi_t(x_o) \;\therefore\; x_o = \phi_t^{-1}(x)$. It follows that the displacement field is defined as: $x = u(x_o, t) + x_o \;\therefore\; u_o(x_o, t) = \phi_t(x_o) - x_o = x - x_o = x - \phi_t^{-1}(x) = u(x_o, t)$. Thus, it is possible to announce the problem in the reference configuration as:

Problem 2 For each $t \in [0, t_f]$ determine $u_o(x_o, t)$ that solves the following boundary value problem stated as

$$div\, P(x_o, t) + \rho_o(x_o)\, b(x_o, t) = 0 \quad in \quad \Omega_o \tag{33}$$

$$P(x_o, t)\, n_o(x_o, t) = \bar{t}_o(x_o, t) \qquad in \quad \Gamma_o^t \tag{34}$$

$$u_o(x_o, t) = \bar{u}_o(x_o) \qquad in \quad \Gamma_o^u \tag{35}$$

with $b(x_o, t) \in L_2(\Omega_o)$ and $\bar{u}_o(x_o) \in H_{00}^{1/2}(\Gamma_o^u)$ for each $t \in [0, t_f]$.

Let us define now the following sets, for each time $t \in [0, t_f]$

$$Kin_o^u = \left\{u_o : \Omega_o \to \Re^3 \,\middle|\, u_o \in H^1(\Omega_o),\, u_o(x_o, t) = \bar{u}_o(x_o)\ in\ \Gamma_o^u\right\} \tag{36}$$

$$Var_o^u = \left\{\hat{v} : \Omega_o \to \Re^3 \,\middle|\, \hat{v} \in H^1(\Omega_o),\, \hat{v}(x_o) = 0\ in\ \Gamma_o^u\right\} \tag{37}$$

Thus it has the weak form of the problem

Problem 3 For each $t \in [0, t_f]$ determine $u_o(x_o, t) \in Kin_o^u$ such that

$$\int_{\Omega_o} P : \nabla\hat{v}\, d\Omega_o = \int_{\Omega_o} \rho_o b \cdot \hat{v}\, d\Omega_o + \int_{\Gamma_o^t} \bar{t}_o \cdot \hat{v}\, d\partial\Omega_o,\ \forall\hat{v} \in Var_o^u \tag{38}$$

For each $t \in [0, t_f]$, it can denoting

$$\Im\left(u_o;\hat{v}\right)=\int_{\Omega_o}P:\nabla\hat{v}\,d\Omega_o-\int_{\Omega_o}\rho_o b\cdot\hat{v}\,d\Omega_o\;-\int_{\Gamma_o^t}\bar{t}_o\cdot\hat{v}\,d\partial\Omega_o,\;\forall\hat{v}\in Var_o^u \tag{39}$$

Then, the problem can be stated as

Problem 4 For each $t\in[0,t_f]$ determine $u_o(x_o,t)\in Kin_o^u$ such that

$$\Im\left(u_o;\hat{v}\right)=0,\;\forall\hat{v}\in Var_o^u \tag{40}$$

The problem above is approached by Newton method in association with Galerkin-FEM, and the incremental formulation follows from the schematic algorithm in Tab. 1

Table 1: Newton's method algorithm – incremental formulation.

For each time step $t=t_n$;
(i) Initialize the iteration counter $k\leftarrow 0$;
(ii) Initialize the variable vector $u_{n+1}^0=u_n$;
(iii) Compute the *residue vector*, $error=\|residue\ vector\|$;
(iv) Do while ($error>tolerance$[1])
(1) Determine the tangent modulus $\left[\aleph(u_{n+1}^k)\right]_{ijkl}=\left.\frac{\partial P_{ij}}{\partial F_{kl}}\right|_{u=u_{n+1}^k}$
(2) Solve the problem $\int_{\Omega_o}\aleph(u_{n+1}^k)\nabla(\Delta u_{n+1}^k)\,:\nabla\hat{v}d\Omega_o=-\Im\left(u_{n+1_o}^k;\hat{v}\right),\;\forall\hat{v}\in Var_o^u$;
(3) Actualize the variable vector $u_{n+1}^{k+1}=u_{n+1}^k+\Delta u_{n+1}^k$;
(4) Compute the new *error*;
(5) Actualize $\Im\left(u_{n+1}^k;\hat{v}\right)\leftarrow\Im\left(u_{n+1}^{k+1};\hat{v}\right)$ and $k\leftarrow k+1$;
End Do while.

(1): previously defined.

9 Numerical examples

For these applications, one used a mesh with two six points triangular elements. The developed code is written in Fortran 90 and for post processing, it's used the GID 8.0 software. The global tolerance is 10-6.

EXAMPLE 1: Here, the simulation of a uniaxial compression test is presented. The specimen consists of a cylindrical bar with a radius R=28mm and a height of 50mm. The material parameters used in

this analysis are described in Table 2. The process consists is prescribing the displacement of the upper part of the specimen, with a total upsetting of $\bar{u} = -30\,mm$, applied in order to compress the body. Due to the axisymmetry condition, only half of the domain is modeled. Fig. 4 shows the displacement field, in the y-direction.

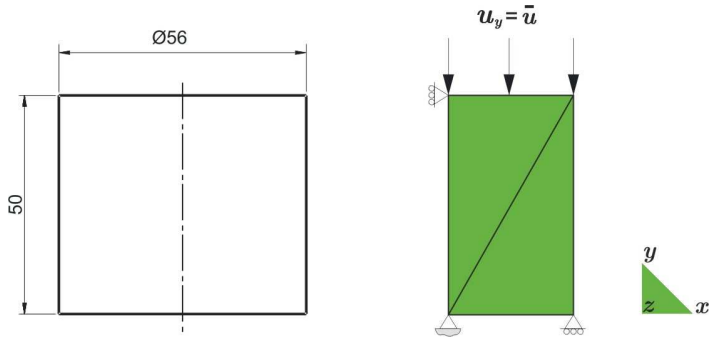

Figure 4: Compression test.

Table 2: Material Parameters(1).

$E_M = 928,09288\,MPa$	$\nu_p = 0,0$	$c = 0,3$
$\sigma_y^o = 0,10582\,MPa$	$\rho_o^* = 0,049\,MPa$	$M = 4,0$
$p_c^o = 0,04047\,MPa$	$\nu = 0,25$	$K_v = 0,005$
$\alpha_p = 0,1$	$\gamma = 1,54$	$\eta = 10^{-5}$

(1) see Zhang *et al* [4], Gibson & Ashby [6] and Gilchrist & Mills [21]

In next figures (see Fig. 5 and Fig. 6), one presents the time evolution of σ_{yy} in the body (constant profile along entire body) for two different rates. One can observe the evolution of stress σ_{yy} component in the observation time. Note that the numerical results shows good agreement to the experimental solution of the problem for load time step [4, 6, 21].

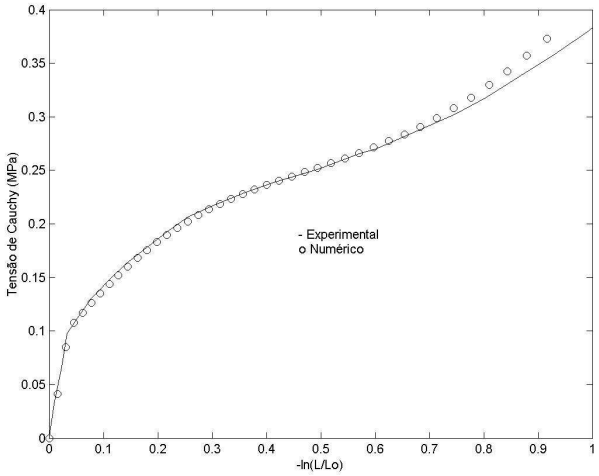

Figure 5: Compression test (0,0016 s^{-1}).

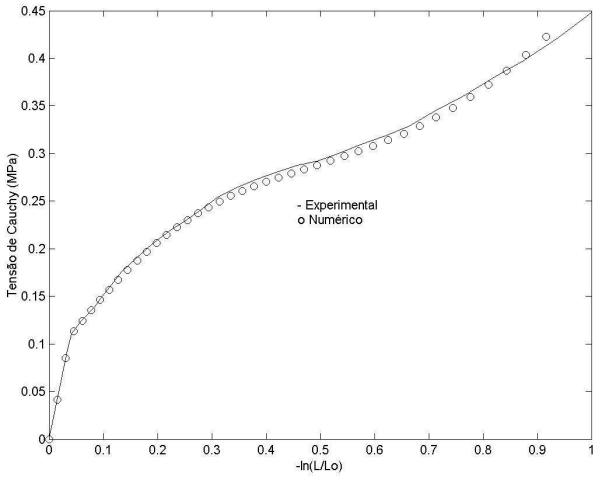

Figure 6: Compression test (0,08 s^{-1}).

At the final observation instant, we get the following results: $\bar{\varepsilon}_v^{vp} = \bar{\varepsilon}_a^{vp} = 0,90196$ (rate 0,0016 s^{-1}), $\bar{\varepsilon}_v^{vp} = \bar{\varepsilon}_a^{vp} = 0,90058$ (rate 0,08 s^{-1}), $\rho^* = 0,1216$ (rates 0,0016 s^{-1} and 0,08 s^{-1}) (constant profile along entire body – see Fig. 7).

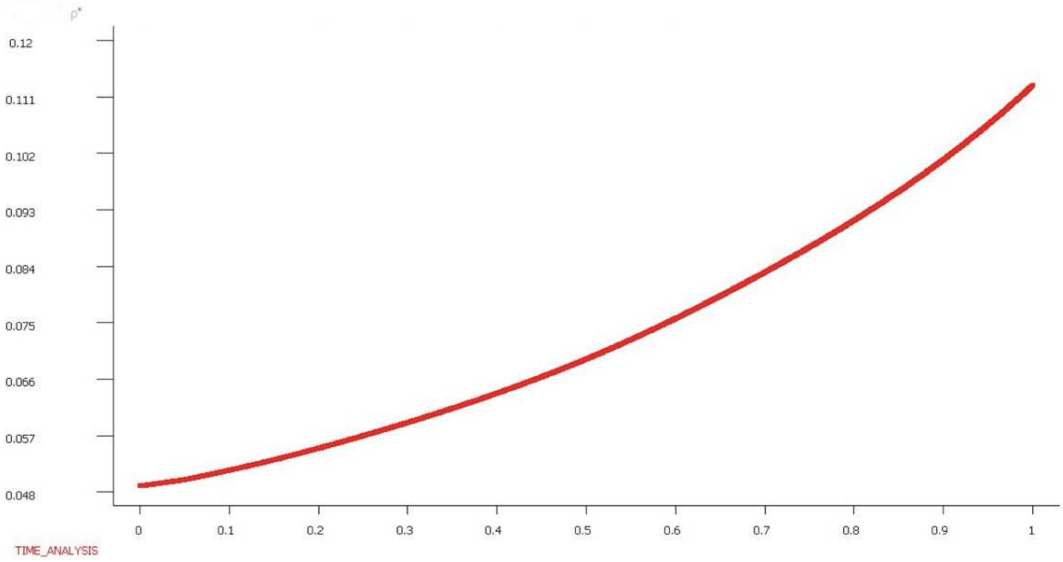

Figure 7: Relative density evolution.

EXAMPLE 2: This example considers an axisymmetric problem that consists of the upsetting of a conical slab, whose dimensions are: r1=90mm; r2=45mm and h=100mm. The analysis consists of prescribing the displacement of the upper wall, with a total upsetting of $\bar{u} = -50\,mm$, as shown in Fig. 8, and employs an integration mesh with 240 isoparametric tri-6 elements. Due to the axisymmetry condition, only half of the domain is modeled. Fig. 9 shows the displacement field, in the y-direction at the final observation instant (rates 0,0016 s^{-1} and 0,08 s^{-1}).

The Fig. 10 shows the Cauchy stress component σ_{xx} profile (rate 0,08 s^{-1}), Fig. 11 shows the Cauchy stress component σ_{xx} profile (rate 0,0016 s^{-1}),. Fig. 12 shows the Cauchy stress component σ_{xy} profile (rate 0,08 s^{-1}), Fig. 13 shows the Cauchy stress component σ_{xy} profile (rate 0,0016 s^{-1}), Fig. 14 shows the Cauchy stress component σ_{yy} profile (rate 0,08 s^{-1}), Fig. 15 shows the Cauchy stress component σ_{yy} profile (rate 0,0016 s^{-1}), Fig. 16 shows the relative density ρ^* profile (rates 0,08 s^{-1} and 0,0016 s^{-1}), and the Fig. 17 and Fig.18 show the equivalent von Misses stress profile for rates 0,08 s^{-1} and 0,0016 s^{-1}.

The evolutions of the Cauchy Stress versus the logarithm strain and of the relative density versus the volumetric plastic strain are shown in Figure 10, at points A and B. Point A is at the left upper

edge and B at the right upper edge of the mesh depicted in Figure 8. The sub indexes 1 and 2 refer to the solution obtained by using the FE and EFG methods respectively.

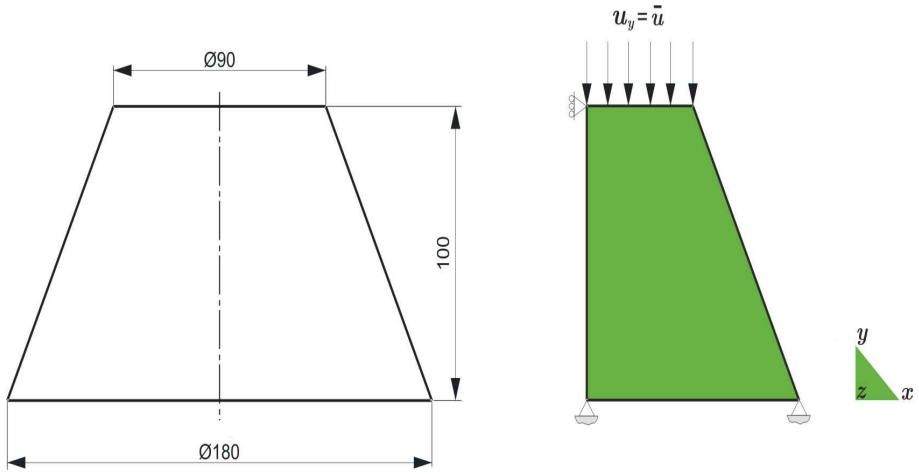

Figure 8: Conical slab.

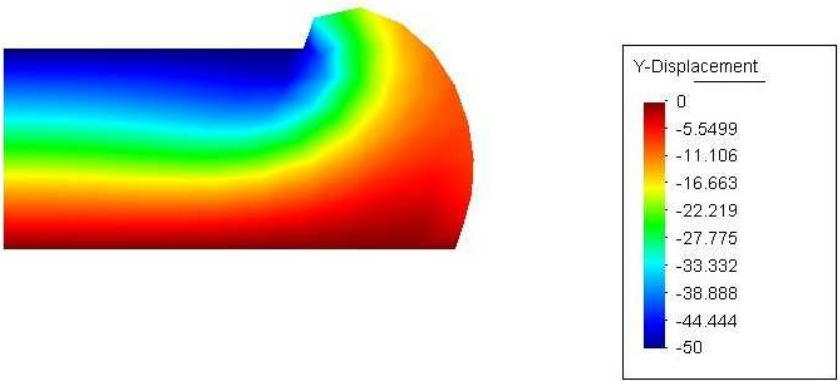

Figure 9: Y-displacement (mm).

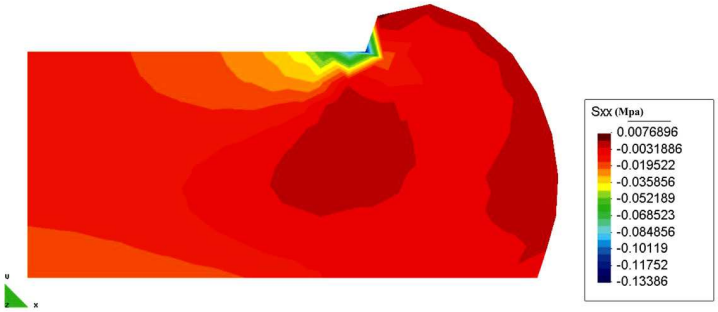

Figure 10: σ_{xx} profile $(0{,}08\mathrm{s}^{-1})$.

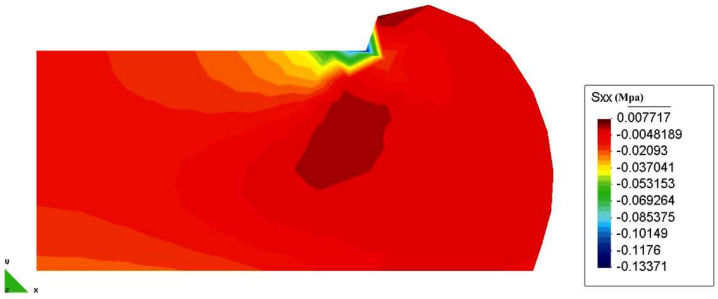

Figure 11: σ_{xx} profile $(0{,}0016\mathrm{s}^{-1})$.

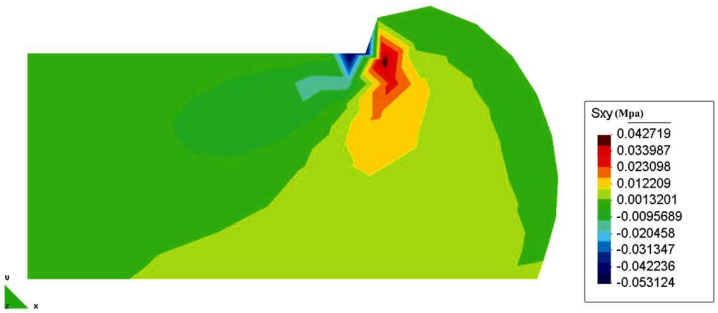

Figure 12: σ_{xy} profile $(0{,}08\mathrm{s}^{-1})$.

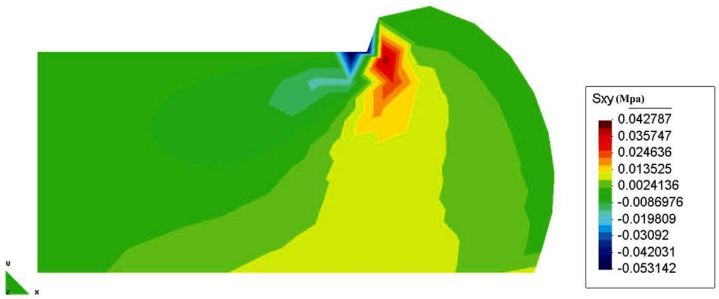

Figure 13: σ_{xy} profile $(0{,}0016\text{s}^{-1})$.

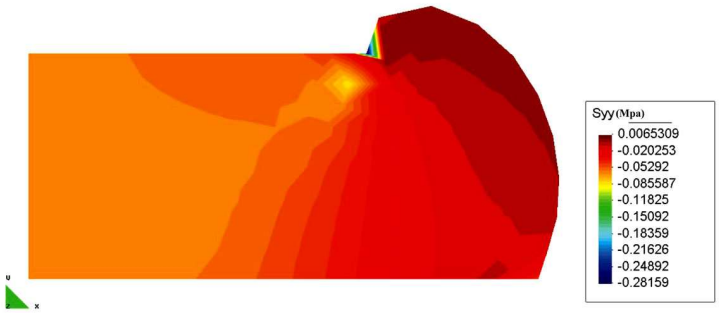

Figure 14: σ_{yy} profile $(0{,}08\text{s}^{-1})$.

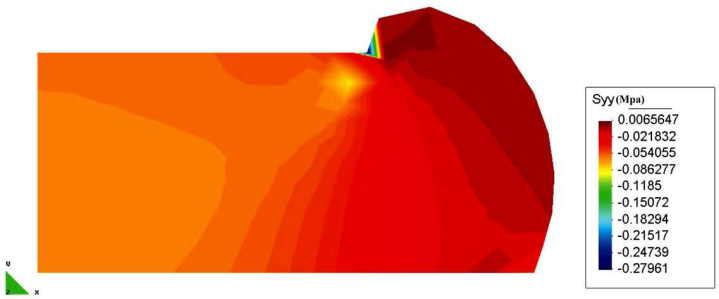

Figure 15: σ_{yy} profile $(0{,}0016\text{s}^{-1})$.

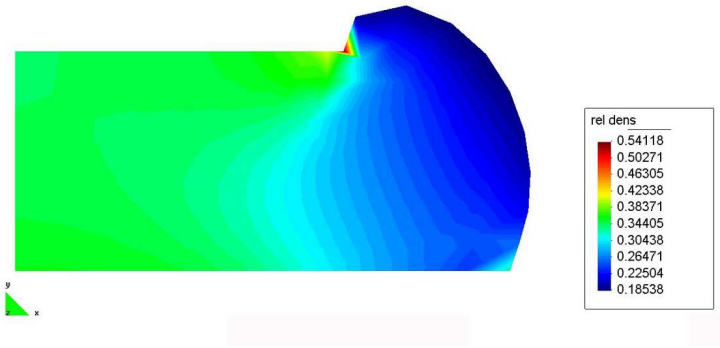

Figure 16: Relative density (0,0016 s^{-1} and 0,08 s^{-1}).

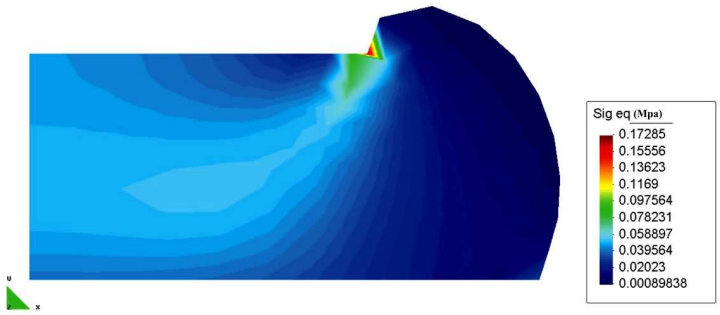

Figure 17: von Misses stress profile (0,08 s^{-1}).

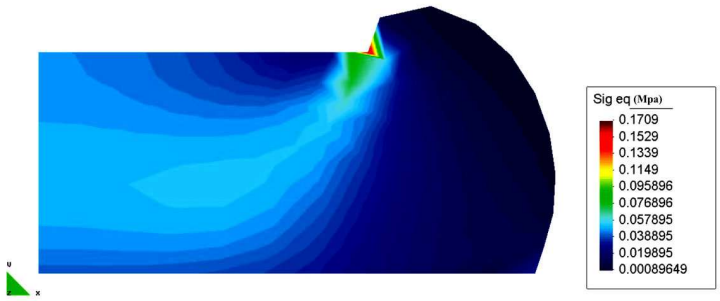

Figure 18: von Misses stress profile (0,0016s^{-1}).

10 Conclusions

The polymeric foam constitutive behavior is extremely complex on the micro structural scale. Cellular buckling under compression initiates a long stress plateau. Further compression causes stress build up due to foam consolidation.

A rate-dependent elasto-viscoplastic foam constitutive model, that features a single-surface yield criterion, has been developed. A non associated plastic flow law and the relative density dependence showed reasonable prediction for the responses of rigid polymeric foams under monotonic loading conditions.

The proposed polymeric foam model and the Galerkin-FEM algorithms was tested with a typical foam problem and has performed adequately. From the above considerations, one may conclude that the proposed model and numerical procedure showed to be adequate for the simulation of large strain behavior of polymeric crushable foams under monotonic loading conditions.

References

[1] Hallquist, J.O., *Theoritical Manual of LsDyna.* Livermore Software Technology Corporation, 1998.
[2] Hibbitt, H.D., *Models for crushable foams, version 6.5, ABAQUS theoretical Manual.* Karlsson and Sorensen Inc., 2000.
[3] Deshpande, V.S. & Fleck, N.A., Isotropic constitutive model for metallic foams. *J Mech Phys Solids*, **48**, pp. 1253–1276, 2000.
[4] Zhang, J., Kikuchi, N., Li, V.C., Yee, A.F. & Nusholtz, G.S., Constitutive modeling of polymeric foam material subjected to dynamic crash loading. *Int J Impact Engng*, **21(5)**, pp. 369–386, 1998.
[5] Zhang, J., Lin, Z., Wong, A., Kikuchi, N., Li, V.C., Yee, A.F. & Nusholtz, G.S., Constitutive modeling and material characterization of polymeric foams. *J Eng Mat Tech Trans ASME 119*, pp. 284–291, 1997.
[6] Gibson, L.J. & Ashby, M.F., *Cellular Solids: Structure and Properties.* Cambridge University Press, 1997.
[7] Gibson, L.J., Ashby, M.F., Zhang, J. & Triantafillou, T.C., Failure surfaces for cellular materials under multiaxial loads I: Modeling. *Int J Mech Sci*, **31(9)**, pp. 635–663, 1989.
[8] Gibson, L.J., Ashby, M.F., Zhang, J. & Triantafillou, T.C., Failure surfaces for cellular materials under multiaxial loads II: Comparisons of models with experiment. *Int J Mech Sci*, **31(9)**, pp. 665–678, 1989.
[9] Landro, L., Sala, G. & Olivieri, D., Deformation mechanisms and energy absorption of polystyrene foams for protective helmets. *Polymer Testing*, **21**, pp. 217–228, 2001.
[10] Roberts, A.P. & J., G.E., Elastic properties of model random three-dimensional open-cell solids. *Journal of the Mechanics and Physics of Solids*, **50**, pp. 33–55, 2002.
[11] Roberts, A.P. & J., G.E., Elastic moduli of model random three-dimensional closed-cell cellular solids. *Acta Materialia*, **49**, pp. 189–197, 2001.
[12] Chaboche, J.L. & Rousselier, G., On the plastic and viscoplastic constitutive equations – part I: rules developed with internal variable concept. *Journal of Pressure Vessel Technology*, **105**, pp. 153–158, 1983.
[13] Miller, A.K., Unified constitutive equations for creep and plasticity. *Elsevier applied Science*, 1987.
[14] Chaboche, J.L., Constitutive equations for cyclic plasticity and cyclic viscoplasticity. *Int J Plasticity*, **5**, pp. 247–302, 1989.
[15] Almroth, P., Hasselqvist, M., Simonsson, K. & Sjostrom, S., Viscoplastic-plastic modelling of in792. *Computational Materials Science*, **29**, pp. 437–445, 2004.

[16] Lemaitre, J.A., *A Course on Damage Mechanics*. Springer: Berlin, Germany, 1996.
[17] Hill, R., Aspects of invariance in solid mechanics. *Adv in Appl Mech*, **18**, pp. 1–75, 1978.
[18] Peric, D. & Owen, D.R.J., Finite-element applications to the nonlinear mechanics of solids. *Reports on Progress in Physics*, **61**, pp. 1495–1574, 1998.
[19] Weber, G. & Anand, L., Finite deformation constitutive equations and a time integration procedure for isotropic hyperelastic-viscoplastic solids. *Computer Methods in Applied Mechanics and Engineering*, **79**, pp. 173–202, 1990.
[20] G., H.A., S., H.O., H., L. & Ilstad, H., Validation of constitutive models applicable to aluminum foams. *International Journal of Mechanical Sciences*, 2001.
[21] A., G. & J., M.N., Impact deformation of rigid polymeric foams: experiments and FEA modeling. *International Journal of Impact Engineering*, **25**, pp. 767–786, 2001.

Mechanics of Solids in Brazil 2009, H.S. da Costa Mattos & Marcílio Alves (Editors)
Brazilian Society of Mechanical Sciences and Engineering, ISBN 978-85-85769-43-7

Some experimental results regarding creep behavior on synthetic materials used to produce offshore morring ropes

Fulvio E. G. Chimisso
POLICAB – Stress Analysis Laboratory, Engineering School, FURG – Federal University of Rio Grande/RS – Brazil

Abstract

With the development of oil fields in ultra deep waters, the replacement of steel ropes used to mooring floating structures by other with lesser linear weight, become a necessity. In shallow waters the drilling and production flotation units are anchored by conventional systems composed of steel chains and wire ropes in catenary geometric configurations. For deep and ultra deep waters the "taut-leg" system based on tightened synthetic ropes with lesser linear weight, was developed. Nowadays these ropes are made of polyester (PET) and they provide the necessary compliance to the taut-leg system by means of the natural mechanical properties of the fiber. Due to the appearance of other synthetic fibers in the market, which intend to improve the performance of the proper mooring system, it became necessary to analyze and verify the mechanical properties of these fibers. Research has been doing with HMPE - High Modulus Polyethylene, material with excellent mechanical behavior in tension and low density but with a inconvenient, to substitute polyester: significant creep at normal conditions of temperature. In this work, was analyzed the creep behavior for HMPE multifilament's, in low temperature. The specimens were submitted to constant load with temperature and displacement control. The obtained creep results were evaluated and compared to results obtained from multifilament specimens submitted to creep at environmental temperature.

Keywords: creep, synthetic ropes, polyethylene, low temperature.

1 Introduction

Nowadays in Brazil, the oil exploration is made each more in ultra deep waters, and, this situation had created a necessity of news mooring systems and materials for offshore platforms. As a result of these situation, the mooring conventional system (chain and steel ropes in a Catenary configuration) will be replaced by other mooring configurations with excellent flexibility and easy handling behavior like as the mooring system called "Taut-leg", where the steel ropes are replaced by synthetic ropes

Mechanics of Solids in Brazil 2009, H.S. da Costa Mattos & Marcílio Alves (Editors)
Brazilian Society of Mechanical Sciences and Engineering, ISBN 978-85-85769-43-7

that work with elastic strains. For this new mooring design, the exposition time with low variation of amplitude solicitation, shows the creep as a possible fail mode.

The polyester [1, 2], ordinary material used, is very efficient with excellent performance in stress, creep and fatigue work conditions [3, 4], but presents yet, the following inconveniences: density bigger than water and large diameters size. Research has been doing with HMPE - High Modulus Polyethylene, material with excellent mechanical behavior in tension and low density, to substitute polyester. Moreover, it was verified that at the environmental temperature, [5, 6], HMPE show large strain even with low constant tension load intensity. Some interesting works regarding HMPE creep behavior at environment temperature was write [7, 8] in recent times. However, considering what those ropes work submerged in approximately 200 meter deep waters and the water temperature in this environment is around 4º C, studies at normal temperature conditions become inappropriate. At the present time there are not many studies that check the behavior of HMPE fibers creep (mono or multifilament yarn) in low temperature. So, the current study about creep behavior in low temperature, becomes important. In the present study we consider two kind of HMPE: Dyneema SK 75 and Dyneema SK 78, manufactured by the DSM–Holland. The obtained HMPE multifilaments creep results in low temperature were evaluated and compared to results obtained from multifilament specimens submitted to creep at environmental (20º +/- 2ºC) temperature.

2 Polyester versus HMPE creep behavior

Just to compare the mechanical creep behavior between polyester and HMPE fibers, it has been obtained the tension rupture load and the linear weight of the multifilaments and their characterization in according to "OCIMF, 2000". It has been performed long term creep of the multifilaments using dead weights tests with constant load values of 30% of the YBL (Yarn Break Load), [6]. Table 1 show the average of the mechanical characteristics – 10 tests sample for each material.

The Table 1 shows the advantages of HMPE fibers regarding, tenacity and weight when compared with polyester fibers. The questions remain the creep behavior of both fibers. Figure 1 show the dead weights creep test device used to determine the creep behavior and figures 2 to 4 shows the creep behavior of HMPE 75, 78 and polyester when submitted at 30% of YBL, in tension.

Table 1: Tension tests.

Sample	HMPE SK78	HMPE SK75	POLYESTER
YBL (N)	540.70	532.25	171.10
Strain (%)	3.15	3.24	12.67
Linear weight (dtex)	1766	1760	2200
Tenacity (cN/dtex)	30.62	30.24	7.78

Figure 1: Dead weight creep test device

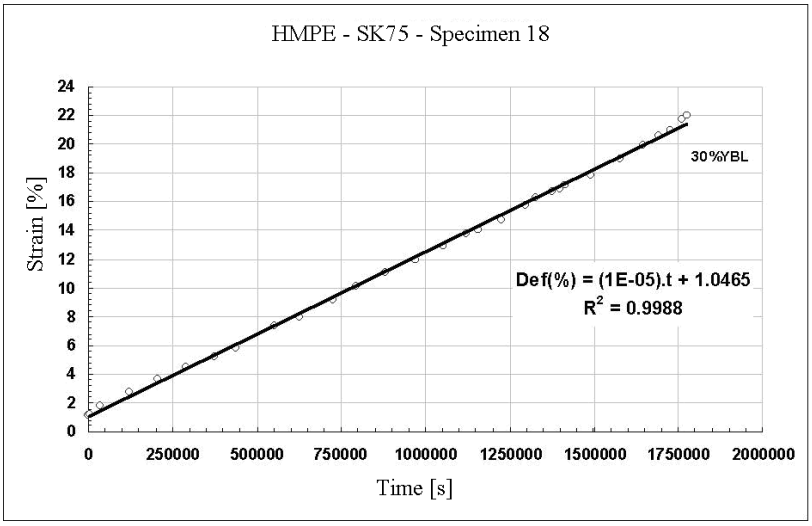

Figure 2: Creep behavior HMPE SK 75, 30%YBL.

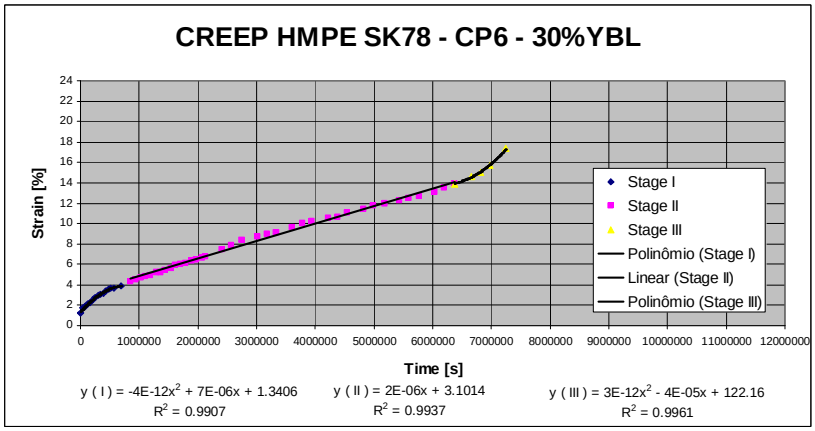

Figure 3: Creep behavior HMPE SK 78, 30%YBL.

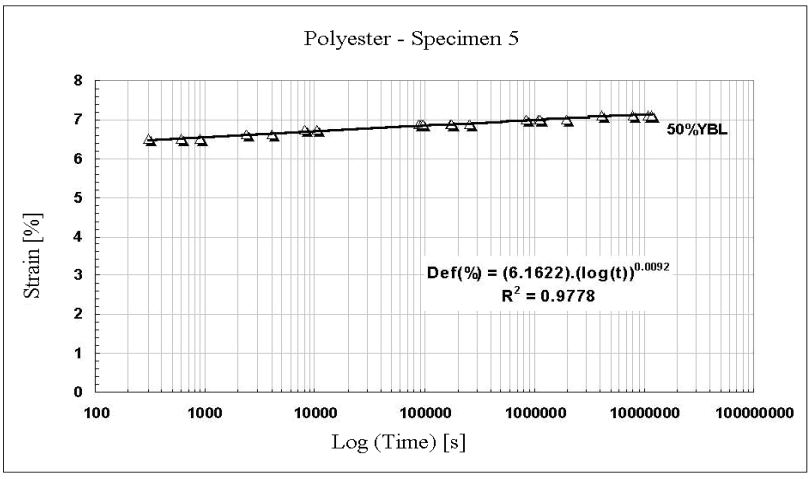

Figure 4: Creep behavior, Polyester, 30%YBL.

It is evident the good creep performance of polyester fibbers when compared with the HMPE fibbers. So, the use of HMPE was limited because the multifilaments showed high creep behavior in environment temperature.

But if we consider what the mooring rope work submerged, because the "taut-leg" anchoring configuration consist of a chain in superficial water plus synthetic rope submerged plus chain plus anchor in the bottom of the sea, maybe the behaviour will be change. The use of synthetic mooring ropes sub-

merged in deep water at temperature near 4 °C, perhaps will be introduce new possibilities regarding the HMPE creep behavior. This fact motivate the study of HMPE creep evolution at low temperature.

3 HMPE creep behavior in low temperature

3.1 Tensile tests

The new question introduced, is how creep behaviour change, if change, when the rope work at deep water temperature near 4° C. First it is necessary verify if the static mechanical behavior, like as break load and related strain, changes in low temperature. Two samples of 10 specimens of Dyneema SK 78 each was tested in tension: one at temperature of 4° +/- 1°C and the other at temperature of 20° +/- 2°C, both with relative humidity control (between 50 to 55%). The specimens and the tests were made in according to ASTM [9] with specimen length of 500 +/- 1 mm and speed test of 100 mm/min. The figures 5 and 6 shows the tests performed in a tensile test machine EMIC 2000L, with calibrate load cell.

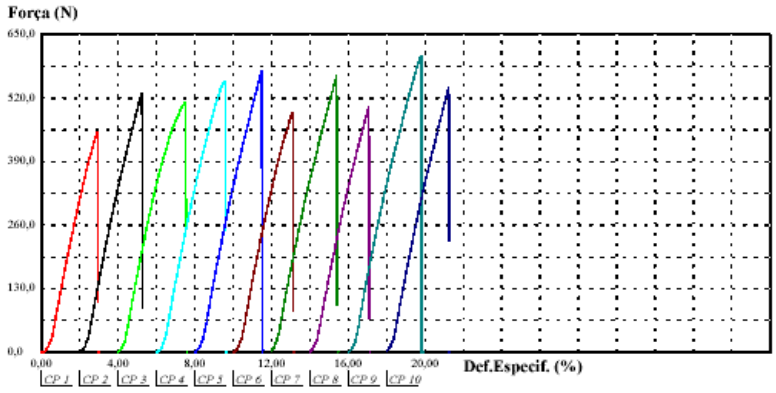

Figure 5: Dyneema SK78. Tensile multifilament break test (YBL) at 4 °C.

In the table 2 it is easy to see that no important changes happens in the averages of tensile mechanical properties data for tests at 20° +/- 2°C and tests at 4° +/- 1°C. So, it is possible follow to the creep tests at low temperature to verify possible mechanical behavior changes.

3.2 Creep tests device

To study the creep behavior of HMPE fibbers, was made an apparatus with appropriate devices, to simulate the real temperature at the bottom of the sea (or at more than 200 meters deep water). A cooling equipment [10], was used as volume of control to maintaining the temperature near the real

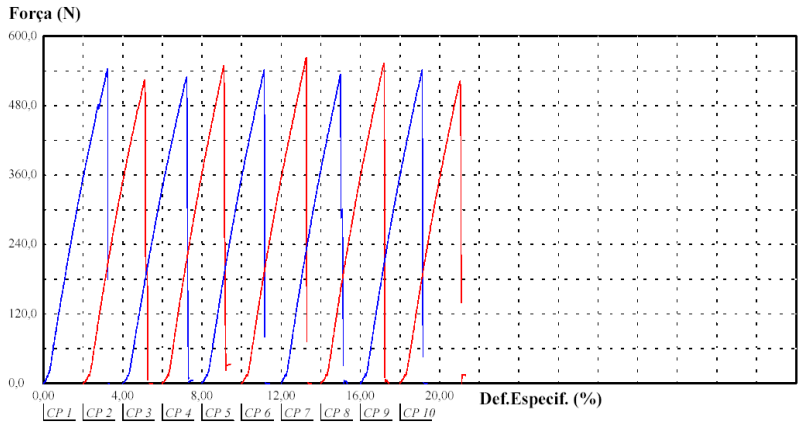

Figure 6: Dyneema SK78. Tensile multifilament break test (YBL) at 22 °C.

Table 2: HMPE SK78 average tensile tests at 20° +/- 2°C and 4° +/- 1°C

Material	YBL (N)	Strain (%)	Elongation at YBL (mm)
Dyneema SK78 at 20° +/- 2°C	540.70	3.15	15.75
Dyneema SK78 at 4° +/-1°C	541.00	3.37	16.83

temperature in the ocean deep water. We choose a fridge and made some mechanical modifications to improve their performance, like as: was installed a double glass door to reduce heat transfer between environment.

In the structure was also placed a temperature controller (on and off in the set point), to certify that the temperature will be around 4°C (+/- 0.5 °C). This equipment was designed for test three specimens, at same time, loaded with died weight, corresponding the value of 30 % of the multifilament YBL. Moreover, the specimens are clamped in terminations like sandwich, developed at POLICAB, [6], whose the main characteristics are not allow the slipping of fibres.

To determine the creep behavior, was used Linear Transducer (pneumatic cylinder of position). The measurement is without contact, and the transducer was protected by a body of aluminium. This transducer has a resolution of 0.01 mm and the measurement range of 250mm. Afterward, to evaluate the measurement, was fixed in the bottom of specimens, a magnet, showing each position and the related displacement of the specimens. This magnet, as we can see in Fig.7, doesn't enter in contact with the whole body transducer and thus not affecting the measurements.

The kit finally, was placed into the cold equipment on a fix support into the device like is shown in Fig.7. Figure 8 show the complete cold equipment.

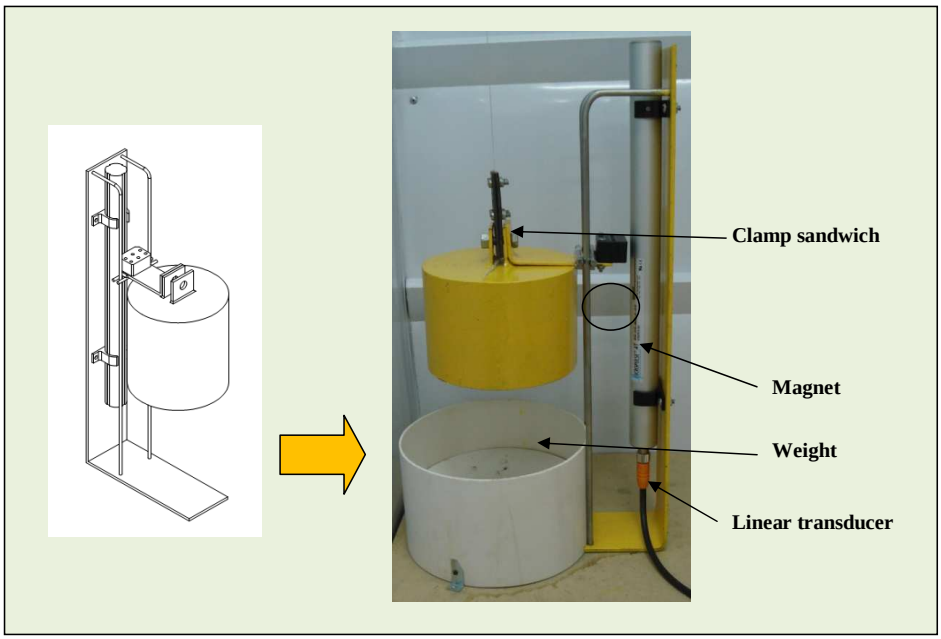

Figure 7: Creep device developed in the POLICAB.

3.3 Creep tests procedures

It is usual in mooring rope design consider the maximum tensile load applied in a rope equal to 30% of the break load in extreme work conditions. The extreme work conditions consider a storm condition. So, in this work was considered the extreme work conditions applied to the multifilament, to determine the creep load, like as 30% of YBL. Considering both HMPE SK75 and SK78 with approximately same YBL = 540.70, like is show in table 2, the weight of 30% of YBL = 162.21 N was considered for the following creep tests.

The initial procedure to assemble the specimens into the equipment considers the environmental temperature of 22 ºC. The room of the laboratory was maintained at approximately 20º +/-2 ºC and 55 +/- 2 % of relative humidity.

The choice of the length of the specimens was restricted to the inside height of the cold equipment in agreement with the ASTM length procedures [9]. The 890 +/- 1 mm length for each specimen was fixed on the structure.

After this, the load was slowly applied and turned on the cooling equipment to control the test temperature. Then the controller and measurement device were turned on too. The time counter started and the test go on. The dislocation of the magnet related to the initial length of the specimen provide the percentile elongation (displacement in percentile).

Figure 8: Creep cold equipment.

4 Results

The following figures and graphics show the tests made in low and environmental temperature regarding both materials Dyneema SK75 and SK78.

The figure 9 show and evaluate the creep behavior for the HMPE SK75 submitted at the same creep load (30% YBL) but in different temperature conditions. When the two creep graphs are compared, in the creep test at 22°C the material fail in 506 hours with 21.85% of strain and the creep test at 4°C not fail at the same time and show 2.86% of strain.

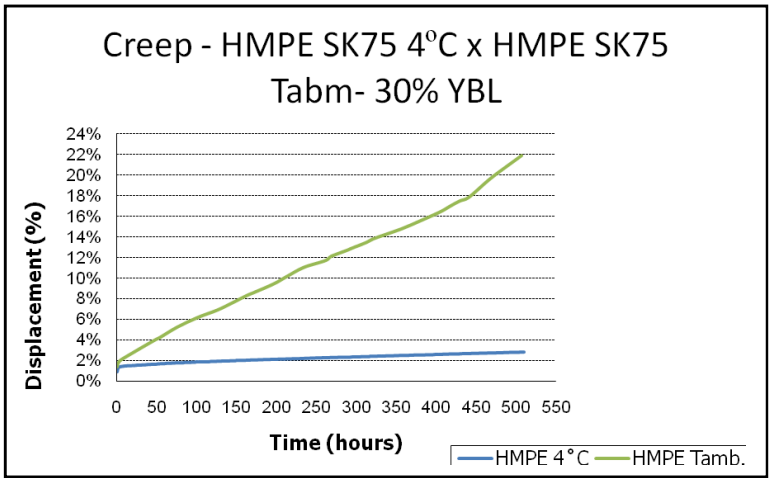

Figure 9: HMPE SK75. Creep at low and room temperature. 30% YBL.

The figure 10 show the creep behavior for 3 test specimens of Dyneema SK78, at low temperature. The 3 tests was stopped with 543 hours and shown an average strain of 1.85%.

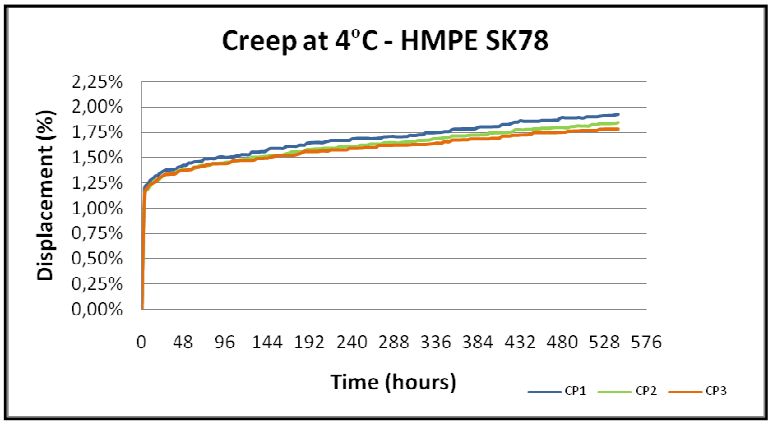

Figure 10: HMPE SK78. Creep at low temperature. 30% YBL.

In the figure 11 was compared the HMPE SK78 specimens creep behavior at room and low temperature test. The test at temperature room was stopped near 543 hours with 6.46% of strain (displacement).

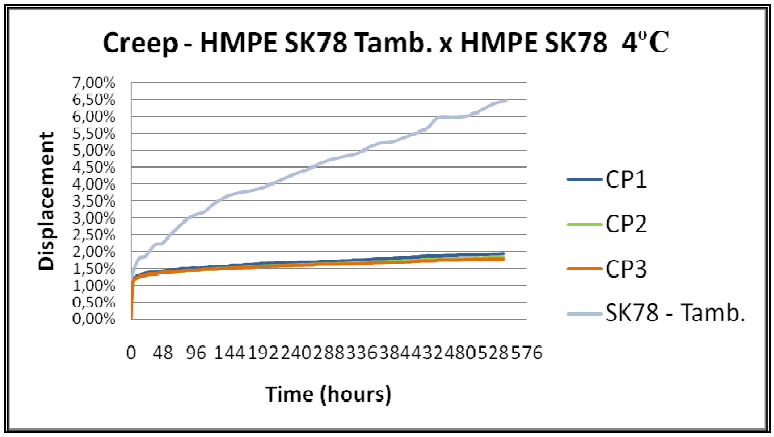

Figure 11: HMPE SK78. Creep at low temperature and room temperature. 30% YBL.

In the figure 12 was compared the creep behavior of both HMPE at low temperature. For sample was taken one specimen of SK 78 with 1.84% of strain for 543 hours of creep test and for the SK 75 was obtained 2.86 % of strain for the same time.

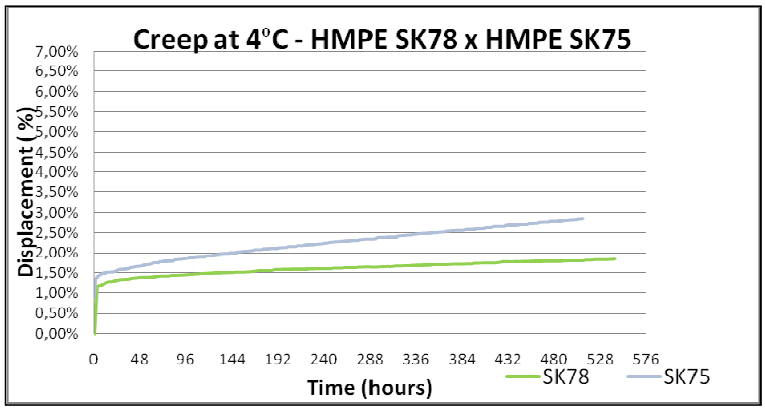

Figure 12: HMPE SK75 x SK78. Creep at low temperature. 30% YBL.

5 Concluding remarks

It is easy to see the best performance for both materials at low temperature, when are simulate the deep sea temperature conditions. The analysis of HMPE multifilament creep behavior at the simulated cold temperature to the deep water show a sensible decrease in strain (with the same load) when are compared with the strain behavior of the same material at environment or room temperature of 20º +/- 2ºC. It is possible to see that in low temperature, HMPE has a better mechanical behavior than the mechanical behavior at environment temperature.

This paper show the preliminary studies that was begin in the earliest months of 2008 [10]. The continuity of this experimental research points to more complete analysis of the same materials to give us parameters and conditions to best evaluate the creep phenomenon at low temperature.

It is important to obtain the complete curve of creep behavior even if expend very long time. Also, find the creep curves at sea water low temperatures for other kind of percentage of YBL (Yarn Break Load) like as 15%, 20% and 25% of YBL to verify other possibilities of mooring ropes use is an important data acquisition. Extend the research to others low temperatures, for sample 8 ºC, 10º C, and consecutively, to determine de variation of strain to temperature for a fixed YBL, turn more complete the experimental research.

Acknowledgements

The author would like to thank to his undergraduate students, Isabel Barreto Rochedo and Guilherme Augusto Chagas Vieira, to their dedication and study to develop their final work to obtain the Mechanical Engineer Degree, December 2008, entitled “An apparatus assembly for synthetic fiber creep analysis at low temperature”.

References

[1] Del Vecchio, C.J.M., *Light Weight Materials for Deep Water Moorings*. Ph.D. thesis, University of Reading, London, UK, 1992.

[2] Del Vecchio, C.J.M., Taut leg mooring systems based on polyester fiber ropes. petrobras experience and future developments. *International Conference on Mooring and Anchoring*, Aberdeen, UK, 1996.

[3] Bosman, R. & Cloos, P.J., Mooring with synthetic fiber ropes possible in all water depths. *Offshore*, p. 98, 1998.

[4] De Pellegrin, I., Manmade fiber ropes in deepwater mooring applications. *Offshore Technology Conference, OTC 10907*, USA, 1999.

[5] Lopes, A.C., *Análise de Fluência em Fibra de HMPE-SK75 para Cabos Utilizados na Ancoragem, tipo Taut-Leg, de Sistemas Flutuantes em Águas Profundas*. Master’s thesis, FURG, Rio Grande, 2003. Engenharia Oceânica.

[6] Silva, M. & Chimisso, F.E.G., Experimental creep analysis on HMPE synthetic fiber ropes for offshore mooring systems. *COBEM 18th International Congress of Mechanical Engineering*, Ouro Preto, Brazil, 2005.

[7] Smeets, P., Jacobs, M. & Mertens, M., Creep as a design tool for hmpe ropes in long term marine and

offshore applications. *MTS Oceans*, 2001.

[8] Sloan, F., Comparison of creep in HMPE and PET mooring lines. *IBC Mooring & Anchoring*, **draft B**, p. 13, 2002.

[9] *Standard Methods of Testing Tire Cords, Tire Cords Fabrics and Industrial Filament Yarns Made From Man-Made Organic-Base Fibers*, 1985.

[10] Rochedo, I.B., Vieira, G.A.C. & Chimisso, F.E.G., Creep analysis of HMPE multifilaments in low temperature. 7^{th} *Youth Symposium on Experimental Solid Mechanics*, Wojcieszyce, Poland, 2008.

Mechanics of Solids in Brazil 2009, H.S. da Costa Mattos & Marcílio Alves (Editors)
Brazilian Society of Mechanical Sciences and Engineering, ISBN 978-85-85769-43-7

Modelling the creep behaviour of HMPE fibers used in ultra-deep-sea mooring ropes

H.S. da Costa-Mattos
LMTA – Laboratório de Mecânica Teórica e Aplicada, Departamento de Engenharia Mecânica, Universidade Federal Fluminense, Niterói/RJ – Brazil
F.E.G. Chimisso
POLICAB – Laboratório de Análise de Tensões, Escola de Engenharia, Fundação Universidade Federal do Rio Grande, Rio Grande/RG – Brazil

Abstract

Due to its low density and high strength, HMPE (high modulus polyethylene) fibres are increasingly used in synthetic ropes for offshore mooring. Nevertheless, the occurrence of significant creep deformation at sea temperature is a major shortcoming for its practical use. The present paper is concerned with a methodology to predict creep lifetime of HMPE yarns in this macroscopic approach, besides the classical variables (stress, total strain), an additional scalar variable related with the damage induced by creep is introduced. An evolution law is proposed for this damage variable. The main goal is to present model equations that combine enough mathematical simplicity to allow their usage in engineering problems with the capability of describing a complex non-linear mechanical behaviour. The model prediction is compared with curves obtained experimentally at room temperature showing a good agreement.

Keywords: synthetic mooring ropes, continuum damage mechanics, creep, lifetime prediction.

1 Introduction

With the development of oil fields in ultra deep waters, the replacement of steel ropes used to mooring floating structures by other with lesser linear weight, become a necessity. In shallow waters the drilling and production flotation units are anchored by conventional systems composed of steel chains and wire ropes in catenary geometric configurations. For deep and ultra deep waters the "taut-leg" [1, 2] system based on tightened synthetic ropes with lesser linear weight was developed. Nowadays these ropes provide the necessary compliance to the taut-leg system by means of the natural mechanical properties of the fibres.

Most fibre ropes comprise a core to withstand tensile loads and an outer jacket, which often has

Mechanics of Solids in Brazil 2009, H.S. da Costa Mattos & Marcílio Alves (Editors)
Brazilian Society of Mechanical Sciences and Engineering, ISBN 978-85-85769-43-7

little tensile load bearing capability. Additional protective coatings or wrappings may be applied after rope manufacture. Typical rope construction types suitable for deepwater fibre moorings are wire rope constructions (WRC), and parallel strand types. The main structural levels in a fibre rope, although not all present in every construction, are: (i) Textile yarns, as made by the fibre producer and typically consisting of hundreds of individual filaments; (ii) Rope yarns, assembled from a number of textile yarns by the rope maker; (iii) Strands made up from many rope yarns; (iii) Sub-ropes of several strands; (v) The complete core rope assembly; (v) Rope, sub-rope and strand jackets.

Polymer based fibre ropes exhibit nonlinear behaviour and are subject to creep, potentially leading to creep rupture. Polyester ropes are not subject to significant creep at loads normally experienced in mooring applications. HMPE - High Modulus Polyethylene is a material with excellent mechanical behaviour in tension and lower density than polyester, but with significant creep at normal conditions of temperature. HMPE yarns creep substantially, although the rate of creep is very dependent on the particular HMPE yarn in question.

The analysis of creep phenomenon in HMPE synthetic ropes accounting for different rope constructions can be extremely complex. The mechanisms proposed so far to explain the damage initiation and propagation processes are not able to elucidate all aspects of the phenomenon in different geometry/material systems [3–9]. Despite the lack of definition of a basic theory for creep failure for such complex systems, the evaluation of the susceptibility to creep is a basic requirement for safe and economic operation, since creep rupture remains as one of the main limitations for the use of HMPE synthetic ropes for deep water mooring of FSOP units and floating platforms. This objective is accomplished by the execution of a set of laboratory tests taking as specimen a sub-system (yarn). Creep tests in textile yarns, as made by the fibre producer and typically consisting of hundreds of individual filaments, are frequently used in order to obtain more detailed information about the macroscopic creep behaviour of the fibres. These tests are so far the most important techniques used to rank the susceptibility of different materials in a specific temperature. However, it is necessary a large number of tests in order to provide basic parameters to be directly used in engineering design, mainly to estimate the influence of the load and temperature on the creep process. Hence, the determination of the creep behaviour of HPE yarns is up to now strongly dependent on these CL tests, what makes attempts to model these tests advisable.

The present paper is concerned with the phenomenological modelling of creep tests of HMPE yarns at room temperature. The goal is to propose a one-dimensional phenomenological elasto-viscoplastic model that combines enough mathematical simplicity to allow its usage in engineering problems with the capability of describing a complex non-linear mechanical behaviour. The main idea is to use such model to obtain the maximum information in order to rank the susceptibility of different materials to creep from a minimum set of laboratory tests, saving time and reducing experimental costs.

In this phenomenological approach, besides the classical variables for an isotropic elasto-viscoplastic material (stress, total strain, plastic strain), the basic idea is to introduce an auxiliary macroscopic variable $D \in [0, 1]$, related to the loss of stiffness of the specimen due to the damage (geometrical discontinuities induced by mechanical deformation and the simultaneous corrosion processes. If $D = 0$, the specimen is considered "virgin" and if $D = 1$, it is "broken" (it can no longer resist to mechanical loading). An evolution law is proposed for this damage variable. Examples are presented in order to

Mechanics of Solids in Brazil 2009, H.S. da Costa Mattos & Marcílio Alves (Editors)
Brazilian Society of Mechanical Sciences and Engineering, ISBN 978-85-85769-43-7

illustrate the main features of the model.

2 Material and experimental procedures

Long term creep tests were performed in multi-filaments of HMPE using an electromechanical test machine with special clamps for yarn tests in an atmosphere controlled room, with the following environmental conditions: 55 ± 2% of humidity and 20 ± 2 °C of temperature.

The HMPE fibre is produced from the ultra high molecular weight polyethylene (UHMW-PE) by the gelspinning process. In this process the molecules of UHMW-PE fibre are dissolved in a solvent. The obtained solution is successively pulled through small holes and afterwards solidified by cooling it. This process produces a fibre with a chemical structure composed by chains with a high molecular orientation degree (over 95%), as shown in Fig. 1. This molecular structure, with high crystalline degree (up to 85%) and a little amorphous content, gives the fibre a high modulus and a high rupture load.

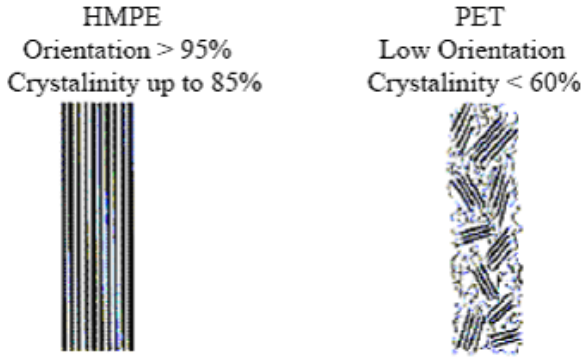

Figure 1: Orientation and Cristalinity representation of HMPE and Polyethylene fibres.

The stress σ at a given instant t can be defined as the rate between the applied tensile force $F(t)$ and the average yarn fibre area A_o

$$\sigma(t) = \frac{F(t)}{A_o} \; ; \; A_o = \frac{\rho_l}{\rho} \Rightarrow \sigma(t) = F(t)\left(\frac{\rho}{\rho_l}\right) \tag{1}$$

where ρ_l is the mass of fibre per unit length and ρ the mass density of fibre material. Since the mass density ρ is the same for a given polymer material, to define the stress of a general yarn regardless the number of fibres it is only necessary to consider the tensile force F divided by the mass of fibre per unit length ρ_l:

$$\hat{\sigma}(t) = \frac{\sigma(t)}{\rho} = \frac{F}{\rho_l} \tag{2}$$

The HMPE multi-filaments tested in this work have linear weight $\rho_l = 1760$ dtex (where 1 dtex = 1 g /10000m). dtex is the most used unit for linear density of a yarn in textile industry and hence it will be adopted on the present study. Each specimen with initial length $L_o = 500 \pm 1$mm was initially loaded at a rate $\alpha = 8{,}3$ N/sec until a limit constant load F_o. Fig. 2 shows the typical loading history the specimens are submitted to.

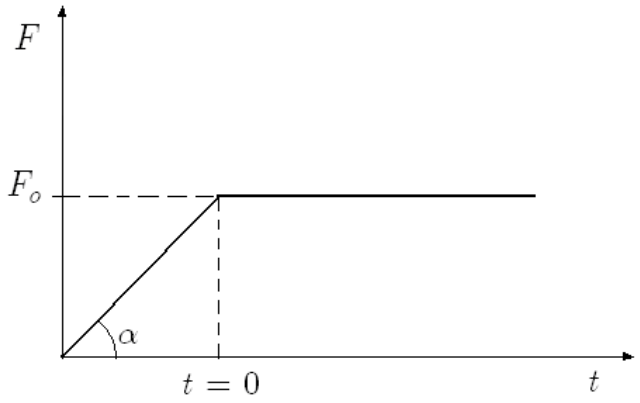

Figure 2: Typical loading history in a long term creep test.

The strain ε at a given instant t can be defined as the rate between the elongation $\delta(t)$ and the initial length L_o

$$\varepsilon(t) = \frac{\delta(t)}{L_o} \tag{3}$$

3 Results and discussion

3.1 Creep testing – Elongation curves at different load levels

Fig. 3 shows experimental creep curves at different load levels (level 1: $F_o = 86{,}3$ N; level 2: $F_o = 172{,}6$ N; level 3: $F_o = 345{,}3$ N; level 4: $F_o = 374$ N; level 5: $F_o = 402{,}7$ N; level 6: $F_o = 431{,}5$ N). The rupture force in a tensile test with prescribed load history $F(t) = \alpha t$ is dependent of the rate α. For a rate $\alpha = 8{,}3$ N/sec, the average rupture force (F_r/ρ_l) is 573,3 N (hence the rupture stress $\hat{\sigma}_r$ for any multi-filament of this particular HMPE is given by $(F_r/\rho_l) = 575{,}3/1760 \approx 0{,}33$ N/dtex). The load levels correspond, respectively, to 15%, 30%, 60%, 65%, 70% and 75% of the rupture force.

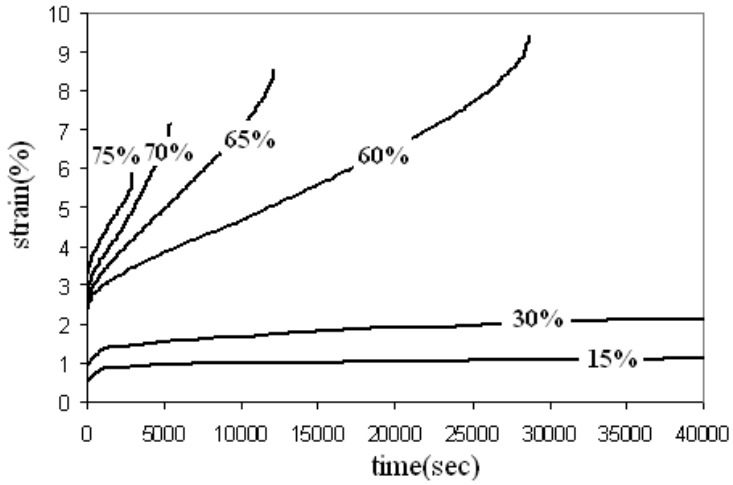

Figure 3: Experimental creep curves at different load levels.

From Fig. 3, it is possible to observe that a typical experimental curve shows three phases of behaviour: (i) a "primary" creep phase during which hardening of the material leads to a decrease in the rate of flow which is initially very high; (ii) a "secondary" creep phase during which the rate of flow is almost constant; (iii) a "tertiary" creep phase during which the strain rate increases up to fracture (see Fig. 4).

It can be verified that the load level strongly affects the creep deformation rate and creep lifetime. Table 1 presents the experimental lifetimes obtained for different load levels. The secondary creep rates ($\dot{\varepsilon}^s$) for different load levels are depicted in Table 2.

Table 1: Experimental creep lifetimes for different load levels. α = 8,3 N/sec.

F_o **(N)**	t_r **(sec)**
345,3	28.710
374,0	12.162
402,7	5.425
431,5	2.935

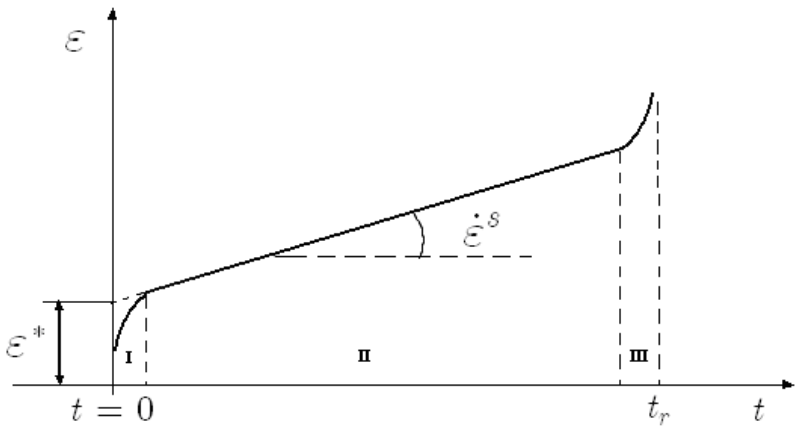

Figure 4: Typical experimental creep curve.

Table 2: Experimental secondary creep rate for different load levels. α = 8,3 N/sec.

F_o **(N)**	$(\dot{\varepsilon}^s)$ **(% sec^{-1})**
86,3	0,0000014
172,6	0,000094
345,3	0,00017
374,0	0,00039
402,7	0,00058
431,5	0,00074

The strain $\varepsilon*$ (Table 3) is related to the secondary creep and depends on the loading rate α and of the maximum force level F_o.

3.2 Modelling

In this paper, in order to provide a better understanding of the results from creep tests, a simple one-dimensional model is proposed. The main goal is to present model equations that combine enough mathematical simplicity to allow their usage in engineering problems with the capability of describing a complex non-linear mechanical behaviour. All the proposed equations can be developed from ther-

Table 3: Experimental values of $\varepsilon*$ for different load levels. α = 8,3 N/sec.

F_o **(N)**	$\varepsilon*$ **(%)**
86,3	0,50 1,02
172,6	0,68 1,73
345,3	0,70 2,79
374,0	0,78 3,05
402,7	0,74 3,18
431,5	0,75 3,37

modynamic arguments similar to Sampaio et al [10] and Costa-Mattos [11], that will not be discussed on this paper.

In order to build the model, it is considered as a system a tension specimen with gauge length L_o and a mass of fibre per unit length ρ_l submitted to a prescribed elongation $\delta(t)$. The following model is proposed to describe the creep damage behaviour of HMPE multi filaments:

$$F_o = (1 - D)\, \rho_l E\, (\varepsilon - \varepsilon_v) \tag{4}$$

$$\frac{d\varepsilon_v}{dt} = K\left[\exp(\tfrac{NF_o}{\rho_l}) - 1)\right] \tag{5}$$

$$\frac{dD}{dt} = \left(\frac{SF_o}{\rho_l(1-D)}\right)^R \tag{6}$$

where the variables ε, ε_v are defined as follows

$$\varepsilon = (\delta/L_o);\ \varepsilon_v = (\delta_v/L_o);\ \delta = \delta_e + \delta_v \tag{7}$$

with δ_e being the elastic or reversible part of δ and δ_v the irreversible parcel of δ. The basic idea is to introduce a macroscopic variable $D \in [0, 1]$, related to the loss of stiffness of the specimen due to creep damage. If $D = 0$, the specimen is considered "virgin" and if $D = 1$, it can no longer resist to mechanical loading. E, K, N, S, R, a, b are material constants which depend on the material. Eq. (4) will be called the state law and Eqs. (5), (6) the evolution laws.

Using boundary condition $D\,(t = 0) = 0$, it is possible to find the analytical solution of differential equation (6) that governs the damage evolution in a constant load (creep) test:

$$D(t) = 1 - \left[1 - \left(t\,(R+1)\left(\frac{SF_o}{\rho_l}\right)^R\right)\right]^{\frac{1}{R+1}} \tag{8}$$

Since rupture occurs when $D = 1$, it is possible to compute the time t_r until the rupture

$$D = 1 - \left(1 - \frac{t}{t_r}\right)^{\frac{1}{(R+1)}} \tag{9}$$

From the equations here proposed it is possible to observe that during the creep test the damage variable increases slowly until almost the end of the test ($t = t_r$) when it increases very fast until rupture($D = 1$), as it is shown in Fig.5.

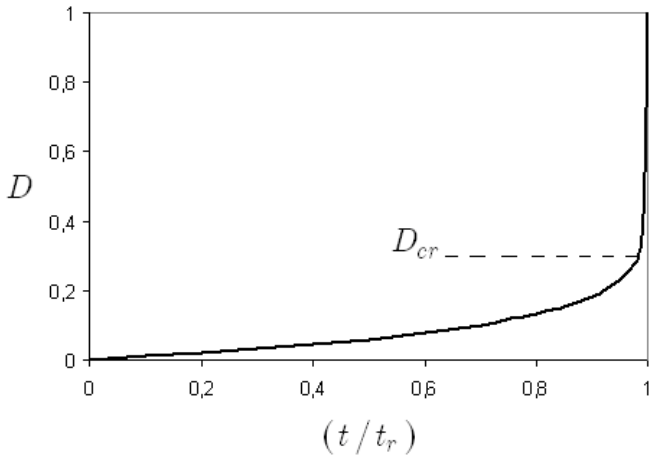

Figure 5: Damage evolution in a typical creep test.

If this kind of damage behaviour is observed, it is usual to consider a critical value D_{cr} of the damage variable, beyond which the evolution to the value toward $D = 1$ is so fast that it can be considered instantaneous. If, in a conservative approach, the failure is considered to occur when $D = D_{cr}$, the following expression is obtained

$$D = 1 - \left[1 - \left(\frac{t}{t_{cr} + \frac{(1+D_{cr})^{R+1}}{R+1}\left(\frac{SF_o}{\rho_l}\right)^{-R}}\right)\right]^{\frac{1}{R+1}} \tag{10}$$

with $t_{cr} = \frac{1-(1-D_{cr})^{R+1}}{R+1}\left(\frac{SF_o}{\rho_l}\right)^{-R}$

From Eq. (9) or (10), the curves of the damage evolution for creep tests under different conditions may be obtained. Examples of these curves are shown in the next section. As it is shown in the next section, the secondary and tertiary stages of the creep curve are fully described by this model. In this model, important parameters, such as steady state elongation rate, and time to failure are also taken into account.

The variables R and S can be identified experimentally from the lifetimes obtained in two creep tests at different load levels, since the behaviour of the $\log(t_r) \times \log(\sigma_0)$ curve is linear, as shown in Eq. (11)

$$t_r = \frac{1}{R+1}\left(\frac{SF_o}{\rho_l}\right)^{-R} = \underbrace{\left(\left(\frac{S}{\rho_l}\right)^{-R}\frac{1}{R+1}\right)}_{\alpha}(F_o)^{-R} \Rightarrow$$

$$\log(t_r) = \log(\alpha) - R\ \log(F_o) \tag{11}$$

Parameters K and N can be obtained from the secondary creep rate ($\dot{\varepsilon}^s$). Supposing that damage is negligible at secondary creep ($D \approx 0$) and that $\frac{d\varepsilon_v}{dt} \approx \frac{d\varepsilon}{dt} = \dot{\varepsilon}^s$ it is possible to obtain

$$\dot{\varepsilon}^s \approx\ K\left[\exp(\tfrac{NF_o}{\rho_l}) - 1)\right] \quad \text{at secondary creep} \tag{12}$$

K and N ca be identified using a minimum square technique. Nevertheless, for practical purposes, it is suggested to initially consider the law $\dot{\varepsilon}^s = \hat{K}\exp\left(\frac{\hat{N}F_o}{\rho_l}\right)$. $\hat{K}$ and $\hat{N}$ can be identified experimentally from the secondary creep strain rates obtained in two tests at different load levels, since the behaviour of the $\log(\dot{\varepsilon}^s) \times F_o$ curve is linear, as shown in Eq. (13)

$$\ln(\dot{\varepsilon}^s) =\ \ln(\hat{K}) + \left(\frac{\hat{N}}{\rho_l}\right)F_o \tag{13}$$

K and N are very close to $\hat{K}$ and $\hat{N}$, and can be approximated (from $\hat{K}$ and $\hat{N}$) using the following iterative procedure:

(a) $i = 0$
(b) $N^i = \hat{N};\ K^i = \hat{K}$;
(c) Compute K^{i+1} from $\ln(\dot{\varepsilon}^s) =\ \ln(K^{i+1}) + \ln\left[\exp(\frac{N^iF_o}{\rho_l}) - 1)\right]$
(d) Once K^{i+1} is known, compute N^{i+1} using $\ln(\dot{\varepsilon}^s) =\ \ln(K^{i+1}) + \ln\left[\exp(\frac{N^{i+1}F_o}{\rho_l}) - 1)\right]$
(e) $i = i + 1$
(f) If $i < i_{\max}$ go to (c). Else $K = K^{i+1}$ and $N = N^{i+1}$

$i_{\max}$ is the maximum allowed number of interactions (suggestion: $i_{\max} = 5$). More sophisticated convergence criteria can be adopted, but they will not be discussed on this paper.

The strain $\varepsilon*$ at instant $t = 0$ is supposed to be given by the following relation (Eq. 5)

$$\varepsilon* = \underbrace{\frac{F_o}{\rho_l E}}_{elasticity} + \underbrace{\left(\frac{a}{\rho_l}\right)^b (F_o)^b}_{primary\ creep} \tag{14}$$

The first parcel is the elastic deformation the second corresponds to the inelastic deformation after primary creep. Parameters a and b can be obtained from two creep tests at different load levels, since the behaviour of the $\log(\varepsilon*) \times \log(F_o)$ is linear, as shown in Eq. (15)

$$\ln\left(\varepsilon * - \frac{F_o}{\rho_l E}\right) = b\left[\ln\left(\frac{a}{\rho_l}\right) + \left(\frac{F_o}{\rho_l}\right)\right] \tag{15}$$

An explicit analytic expression for the creep deformation can be obtained using (5) and (9). Using these equations it is possible to obtain

$$\dot{\varepsilon}_v = \frac{K}{(1-D)}\left[\exp(\frac{NF_o}{\rho_l}) - 1)\right] \Rightarrow$$

$$\dot{\varepsilon}_v = \underbrace{K\left[\exp(N\sigma_o) - 1)\right]}_{\dot{\varepsilon}^s}\left(1 - \frac{t}{t_r}\right)^{-\left(\frac{1}{R+1}\right)} = \dot{\varepsilon}^s\left(1 - \frac{t}{t_r}\right)^{\underbrace{-\left(\frac{1}{R+1}\right)}_{\beta}}$$

with $\varepsilon_v(t=0) = \varepsilon*$. Hence

$$\int_{\varepsilon*}^{\varepsilon_v} d\varepsilon_v = \int_0^t \dot{\varepsilon}^s\left(1 - \frac{t}{t_r}\right)^{-\beta} dt \Rightarrow \varepsilon_v - \varepsilon* = \left(\tfrac{\dot{\varepsilon}^s t_r}{1-\beta}\right)\left[1 - \left(1 - \frac{t}{t_r}\right)^{(1-\beta)}\right] \Rightarrow$$

$$\varepsilon_v = \left(\tfrac{K[\exp(N\sigma_o)-1)]t_r}{1-\beta}\right)\left[1 - \left(1 - \frac{t}{t_r}\right)^{(1-\beta)}\right] + \varepsilon*$$

Finally, using (4), the following expression is obtained:

$$\varepsilon = \frac{F_o}{(1-D)\rho_l E} + \varepsilon_v \Rightarrow$$

$$\varepsilon = \frac{F_o}{\rho_l E}\left(1 - \frac{t}{t_r}\right)^{-\beta} + \left(\frac{K\left[\exp(\frac{NF_o}{\rho_l}) - 1)\right]t_r}{1-\beta}\right)\left[1 - \left(1 - \frac{t}{t_r}\right)^{(1-\beta)}\right] + \frac{F_o}{\rho_l E} + \left(\frac{aF_o}{\rho_l}\right)^b \tag{16}$$

3.3 Comparison with experimental results

In order to investigate the adequacy of the model presented here, samples of HMPE multi filaments were tested and the experimental results were checked with the model. The model parameters identified experimentally at room temperature are presented in Table 4

Table 4: Model parameters (HMPE at room temperature).

$\rho_l E$**[N]**	R **[sec]**	(S/ρ_l) **[N^{-1}]**	K **[sec^{-1}]**	(N/ρ_l) **[N^{-1}]**	(a/ρ_l) **[N^{-1}]**	b
165	10,314	$8{,}47 \times 10^{-4}$	$4{,}5 \times 10^{-7}$	$1{,}76 \times 10^{-2}$	$8{,}36 \times 10^{-4}$	0,26

The model prediction of secondary creep rate $\dot{\varepsilon}^s$ (Eq.12) for different load levels is presented in Fig. 6 and Table 5.

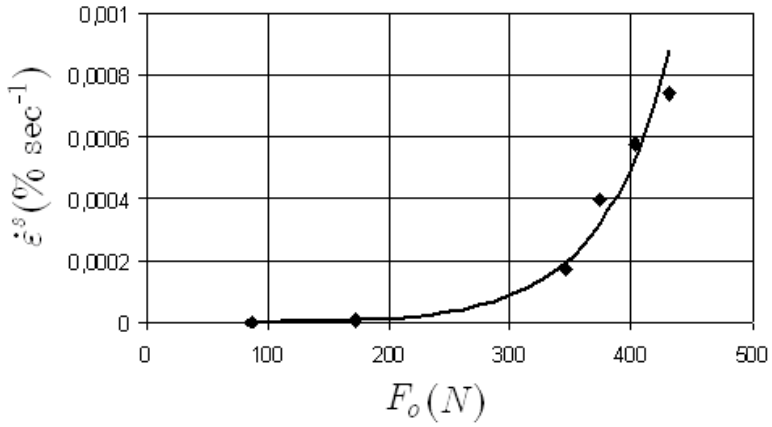

Figure 6: Secondary creep rate for different load levels. Comparison with experimental results. α = 8,3 N/sec.

Table 5: Secondary creep rate for different load levels. α = 8,3 N/sec.

F_o **(N)**	$\dot{\varepsilon}^s$ **(% sec^{-1}) experimental**	$\dot{\varepsilon}^s$ **(% sec^{-1}) model**
86,3	0,0000014	0,0000016
172,6	0,000094	0,0000089
345,3	0,00017	0,00019
374,0	0,00039	0,00032
402,7	0,00058	0,00053
431,5	0,00074	0,00088

The predicted values $\varepsilon*$ of the deformation at the beginning of the creep test using Eq. 14 is presented in Fig. 7 and Table 6.

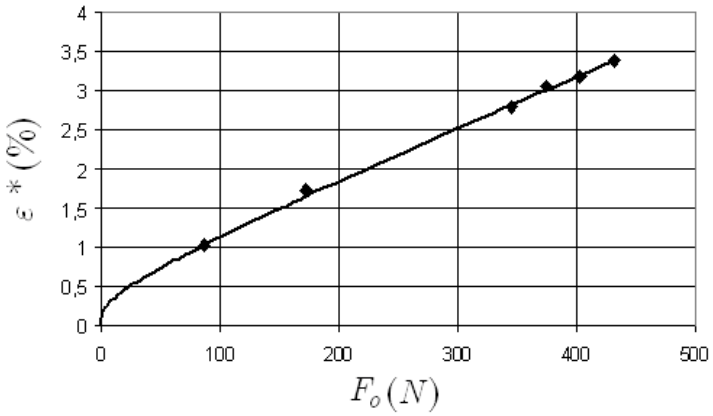

Figure 7: $\varepsilon*$ for different load levels. Comparison with experimental results.

Table 6: $\varepsilon*$ for different load levels.

F_o **(N)**	$\varepsilon*$ **(%) experimental**	$\varepsilon*$ **(%) Model**
86,3	1,02	1,02
172,6	1,73	1,64
345,3	2,79	2,80
374,0	3,05	3,00
402,7	3,18	3,18
431,5	3,37	3,38

The predicted creep lifetimes for different load levels using Eq. (9) are presented in Table 7 and Fig. 8.

Finally, Fig. 9 shows the theoretical and experimental creep curves at different load levels. The model prediction of the fracture time and elongation before rupture are in good agreement with the experimental results.

The initial stages of the creep curves are dependent on the loading history (stress and strain rates) adopted to reach the constant "initial" load F_o. Nevertheless, the final stages of the elongation-time curves (secondary and tertiary creep) seem to be little affected by this previous loading history.

Table 7: Creep lifetimes for different load levels.

F_o **(N)**	t_r **(sec) experimental**	t_r **(sec) model**
345,3	28710	28346
374,0	12162	12441
402,7	5425	5803
431,5	2935	2846

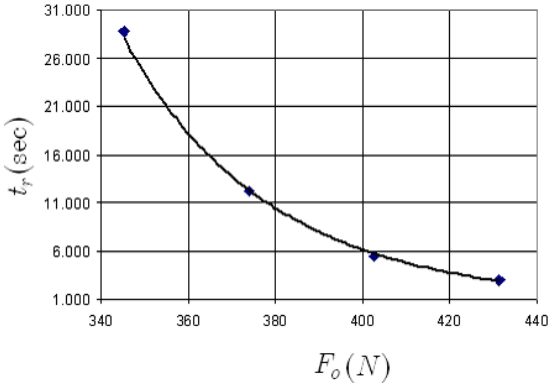

Figure 8: Creep lifetimes for different load levels. Comparison with experimental results.

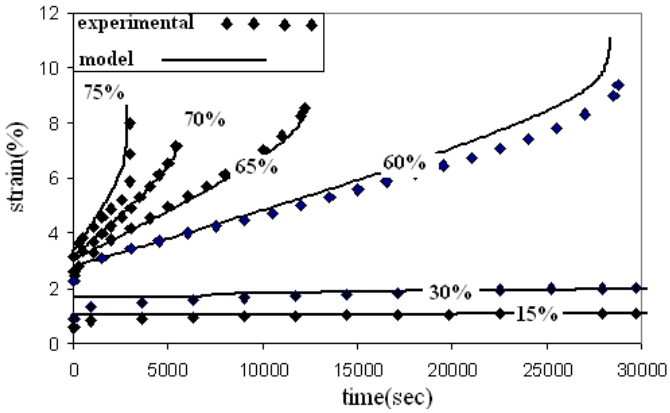

Figure 9: Creep curves at different load levels. Comparison with experimental results.

4 Conclusions

The proposed model equations combine enough mathematical simplicity to allow their usage in engineering problems with the capability to perform a physically realistic description of inelastic deformation, strain hardening, strain softening, strain rate sensitivity and damage observed in creep tests performed in HMPE multi filaments at different load levels. The main idea is to use the model to obtain the maximum information about macroscopic properties of HMPE yarns from a minimum set of laboratory tests. Only two creep tests are required to identify all the other material constants (two different load levels). The agreement between theory and experiment is very good in tests performed at 15%, 30%, 60%, 65%, 70% and 75% of the rupture load.

The present paper is a step towards the modelling of creep tests in HMPE ropes using Continuum Damage Mechanics. The analysis of creep behaviour of mooring lines accounting for the different rope constructions can be extremely complex. The mechanisms proposed so far to explain the damage initiation and propagation processes are not able to elucidate all aspects of the phenomenon in different geometry/material systems. However, in normal operation conditions, the tensile load in synthetic mooring ropes should be less than 15% of the MBL (minimum break load). For a storm condition, the maximum solicitation of a mooring line should not exceed 30% of MBL. Since the loads levels are not high in operation, it may be possible to adapt the proposed theory for yarns to ropes with complex geometric arrangements. In this case, the parameters E, K, N, S, R, a, b that appear in the theory would be geometry dependent to account for different possible sub-ropes arrangements. Heating and internal abrasion certainly reduce the lifetime but can be accounted in a thermodynamic framework. However, it is important to remark that further experimental work with HMPE ropes is still required in order to fully characterize the dependency of the parameters on the geometry.

References

[1] API-RP, *Recommended Practice for Design, Manufacture, Installation, and Maintenance of Synthetic Fiber Ropes for Offshore Mooring*, 2001.

[2] Bosman, R. & Cloos, P.J., Mooring with synthetic fiber ropes possible in all water depths. *DSM, 2003, High Performance Fibers BV – C. Design*, Offshore: Netherlands, p. 98, 1998.

[3] Schmidt, T.M., Bianchini, C., Forte, M.M.C., Amico, S.C., Voronoff, A. & Gonçalves, R.C.F., Socketing of polyester fibre ropes with epoxy resins for deep-water mooring applications. *Polymer Testing*, **25**, pp. 1044–1051, 2006.

[4] Pellegrin, I., Manmade fiber ropes in deepwater mooring applications. *Offshore Technology Conference*, Houston, pp. 1–9, 1999. OTC 10907.

[5] Sloan, F., Synthetics – the future for offshore platform moorings. *Sea Technol*, **40(4)**, p. 49, 1999.

[6] Hooker, J.G., *Synthetic fibre ropes for ultradeep water moorings in drilling and production applications*. Technical Paper Marlow Ropes, OMT: Singapore, 2000.

[7] Pearson, N.J., *Experimental snap loading of synthetic fiber ropes, Doctoral Thesis*. Virginia Polytechnic Institute and State University: Blacksburg, 2002.

[8] Petruska, D., Geyer, J., Macon, R., Craig, M., Ran, A. & Schulz, N., Polyester mooring for the mad dog spar – design issues and other considerations. *Ocean Eng*, **32(7)**, p. 767, 2005.

[9] Silva, M.O. & Chimisso, F.E.G., Experimental creep analysis on hmpe synthetic fiber ropes for offshore mooring systems. *Proceedings of the 18TH International Congress of Mechanical Engineering*, Ouro Preto, Brazil, 2005.
[10] Sampaio, E.M., Bastian, F.L. & Costa-Mattos, H.S., A simple continuum damage model for adhesively bonded butt joints. *Mechanics Research Communications*, **31(4)**, pp. 443–449, 2004.
[11] Costa-Mattos, H.S., Bastos, N. & Gomes, J.A.P., A simple model for slow strain rate and constant load corrosion tests of austenitic stainless steel in acid aqueous solution containing sodium chloride. *Corrosion Science*, **50**, pp. 2858–2866, 2008.

Modeling the damage behavior of superplastic materials

H.S. da Costa-Mattos
Laboratory of Theoretical and Applied Mechanics, Department of Mechanical Engineering, Universidade Federal Fluminense, Niterói/RJ – Brazil
G. Minak, F. Di Gioacchino, A. Soldà
Department of Mechanical Engineering and Materials Science, University of Bologna, Bologna – Italy

Abstract

The present paper is concerned with the modeling of superplasticity phenomenon in metallic materials using a continuum damage theory. The goal is to propose a one-dimensional phenomenological damage model, as simple as possible, able to perform a mathematically correct and physically realistic description of plastic deformations, strain hardening, strain softening, strain rate sensitivity and damage (nucleation and growth of voids) observed in tensile tests performed at different strain rates. Only two tensile tests at different controlled strain rates are necessary to obtain all the material parameters that appear in the theory. Examples concerning the modeling of tensile tests of a magnesium alloy at different strain rates are presented and analyzed. The results obtained show a very good agreement between experimental results and model prevision.

Keywords: superplasticity, strain rate sensitivity, magnesium alloy, tension/compression testing, continuum damage mechanics.

1 Introduction

A wide class of materials – metals, ceramics, intermetalics, nanocrystaline, etc – show superplastic behavior under special processing conditions. Although, up to now, there is no precise physical definition of superplasticity phenomenon in metallic materials, from a phenomenological point of view, superplasticity can be defined as very high deformations prior to local failure. In the case of tensile tests under controlled strain rate, this means very high elongations of the specimens before rupture. The deformation process is generally conducted at high temperature and the strain can be 10 times the obtained under room temperature. Superplastically deformed material in tensile tests gets thinner in a very uniform manner, rather than forming a 'neck' (a local narrowing) which leads to fracture.

The most important characteristic of a superplastic material is its high strain rate sensitivity of flow stress that confers a high resistance to neck development and results in the high tensile elongations

Mechanics of Solids in Brazil 2009, H.S. da Costa Mattos & Marcílio Alves (Editors)
Brazilian Society of Mechanical Sciences and Engineering, ISBN 978-85-85769-43-7

characteristic of superplastic behavior. Superplasticity is used to form directly complex objects, by the application of gas pressure or with a tool, and often with the help of dies, avoiding complicated and costly joining and machine steps. The applications of superplastic formations were originally limited to the aerospace industry, but it has recently been expanded to include the automobile industries as a result of breakthroughs in the range of materials that can be made superplastic.

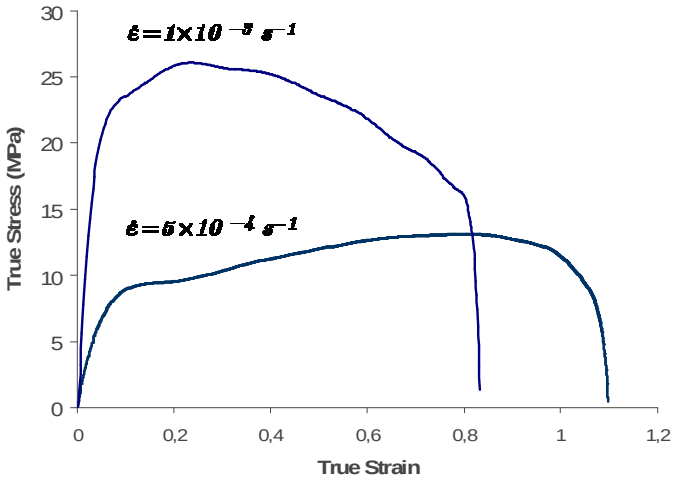

Figure 1: Strain hardening, strain softening, strain rate sensitivity and damage in AZ31B-F magnesium alloy at 400ºC.

The present paper is concerned with the modeling of such phenomenological behavior using a continuum damage theory. It is not the goal here to discuss the microscopic mechanisms of superplastic deformation. Most of the studies presented up to now in the literature are concerned with microstructural aspects of the phenomenon. In the case of superplasticity, the damage is mainly due to nucleation and growth of voids in the material. An interesting analysis of cavity initiation and growth can be found in Khaleel et al [1]. Other experimental works about superplastic behavior in magnesium alloys can be found in Kim et al [2]; Xin Wu and Yi Liu. [3]; Tan, [4]; Somekawa et al [5]; Lin et al [6]; Takuda et al [7]; Yin [8, 9]; Lee, et al [10].

2 Basic definitions

Let's consider a simple tension test in which the specimen has a gauge length L and cross section A_o submitted to a prescribed elongation $\Delta L(t)$. The force necessary to impose such elongation is noted $F(t)$.

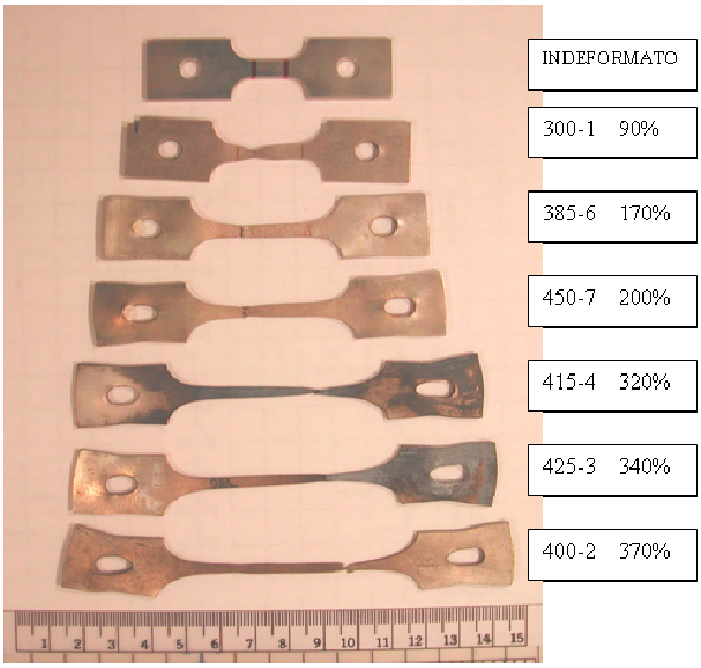

Figure 2: AZ31B-F magnesium alloy. Deformed specimens at different temperatures and strain rates.

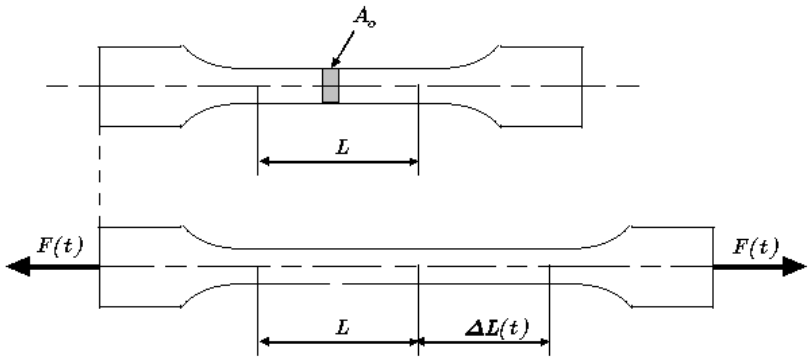

Figure 3: Specimen for a tensile test.

The so-called engineering strain ε and the engineering stress σ are defined as

Mechanics of Solids in Brazil 2009, H.S. da Costa Mattos & Marcílio Alves (Editors)
Brazilian Society of Mechanical Sciences and Engineering, ISBN 978-85-85769-43-7

$$\varepsilon(t) = \frac{\Delta L(t)}{L} \quad ; \quad \sigma(t) = \frac{F(t)}{A_o} \tag{1}$$

The so-called true strain ε_t and true stress σ_t are defined as

$$\varepsilon_t = \ln(1 + \varepsilon \quad ; \quad \sigma_t = \sigma(1 + \varepsilon) \tag{2}$$

From definitions (1) and (2) it is possible to obtain the following relations

$$\varepsilon_t = \ln(1 + \varepsilon) \;\Rightarrow\; \exp(\varepsilon_t) = \exp(\ln(1 + \varepsilon)) \;\Rightarrow \varepsilon = \exp(\varepsilon_t) - 1 \Rightarrow$$
$$\dot{\varepsilon} = \exp(\varepsilon_t)\dot{\varepsilon}_t \quad ; \quad \dot{\varepsilon}_t = \frac{\dot{\varepsilon}}{(1 + \varepsilon)} \tag{3}$$

The ASTM Standard E 2448-05 "Standard Test Method for Determining the Superplastic Properties of Metallic Sheet Materials" [11] describes the procedure for determining the superplastic forming properties (SPF) of a metallic sheet material. It includes tests both for the basic SPF properties and also for derived SPF properties. The test for basic properties encompasses effects due to strain hardening or softening.

3 Modeling the true stress against true strain curve without damage

The main idea of the model is to propose a very simple expression for the true stress σ_t *vs* true strain ε_t curve:

$$\textbf{HIP 1: } \sigma_t = a\ [1 - \exp(-b\varepsilon_t)]\,, \quad \text{with } a \text{ and } b \text{ being positive functions of } \varepsilon_t \text{ and } \dot{\varepsilon}_t \tag{4}$$

The dependency of the parameters a, b on ε_t and $\dot{\varepsilon}_t$ is the key to the definition of a physically realistic model. From experimental observations (see next section), it is possible to propose the following expression:

$$a(\varepsilon_t, \dot{\varepsilon}_t) \text{ is such that } \left[e^{(a-N_a)} - e^{(a_0-N_a)}\right] = \left[\dot{\varepsilon}_t \exp(\varepsilon_t)\right]^{K_a} \tag{5}$$

with a_o, K_a, N_a, being temperature dependent positive parameters. Since $\dot{\varepsilon} = \dot{\varepsilon}_t \exp(\varepsilon_t)$, a is constant in tensile tests with fixed value of the engineering strain rate $\dot{\varepsilon}$. Furthermore, it is easy to verify that $a = a_o$ when $\dot{\varepsilon} = 0$. From (5) it is possible to obtain the following relations:

$$\mathrm{e}^{\mathrm{a}}\mathrm{e}^{-\mathrm{N_a}} - \mathrm{e}^{\mathrm{a_o}}\mathrm{e}^{-\mathrm{N_a}} = \dot{\varepsilon}^{K_a} \Rightarrow$$
$$(\mathrm{e}^{\mathrm{a}} - \mathrm{e}^{\mathrm{a_o}})\,\mathrm{e}^{-\mathrm{N_a}} = \dot{\varepsilon}^{K_a} \Rightarrow$$
$$\ln(\mathrm{e}^{\mathrm{a}} - \mathrm{e}^{\mathrm{a_o}}) = K_a \ln(\dot{\varepsilon}) + N_a$$

If we define $\widehat{a} = \ln(\mathrm{e}^{\mathrm{a}} - \mathrm{e}^{\mathrm{a_o}})$, then

$$\mathrm{a} = \ln\left(e^{\widehat{a}} + \mathrm{e}^{\mathrm{a_o}}\right) \tag{6}$$

To simplify the model, it will be assumed from now on that $a_o = 0$, hence from (6):

$$a(\varepsilon_t, \dot{\varepsilon}_t) = \ln\left(e^{\widehat{a}} + 1\right) \quad \text{with} \quad \widehat{a} = K_a \ln(\dot{\varepsilon}) + N_a \tag{7}$$

The relation between coefficient a and the engineering strain rate $\dot{\varepsilon}$ is plotted below for the two different cases $a_o = 0$ and $a_o \neq 0$. It is evident that the obtained results differ only for lower strain rates.

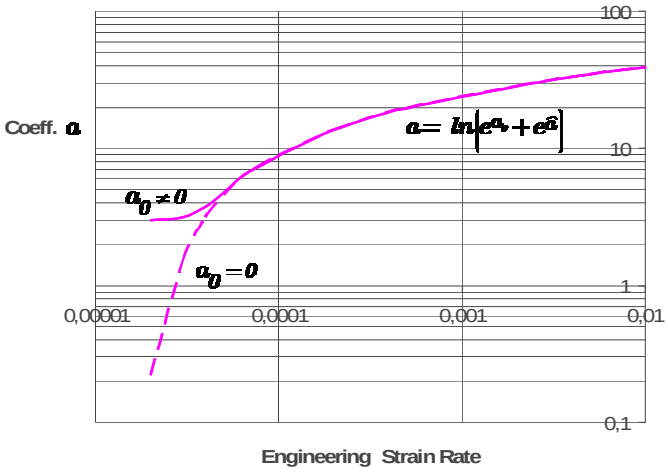

Figure 4: Variation of coefficient a with $a_0 = 0$ and $a_0 \neq 0$ for a magnesium alloy AZ31 at 375ºC.

Also from experimental observations, it is possible to propose:

$$b(\varepsilon_t, \dot{\varepsilon}_t) \text{ is such that } \left[e^{(ab - N_{ab})} - e^{(a_0 b_0 - N_a b)}\right] = \left[\dot{\varepsilon}_t \exp(\varepsilon_t)\right]^{K_{ab}} \tag{8}$$

with b_o, K_{ab}, N_{ab}, being temperature dependent positive parameters. Since $\dot{\varepsilon} = \dot{\varepsilon}_t \exp(\varepsilon_t)$, as shown for a, ab is constant in tensile tests with fixed value of the engineering strain rate $\dot{\varepsilon}$ and $ab = a_o b_o$ when $\dot{\varepsilon} = 0$. From (8) it is also possible to obtain the following relations:

$$\begin{aligned}
\mathrm{e^{ab}e^{-N_{ab}}} - \mathrm{e^{a_o b_o}e^{-N_{ab}}} &= \dot{\varepsilon}^{K_{ab}} \Rightarrow \\
\left(\mathrm{e^{ab}} - \mathrm{e^{a_o b_o}}\right)\mathrm{e^{-N_{ab}}} &= \dot{\varepsilon}^{K_{ab}} \Rightarrow \\
\ln\left(\mathrm{e^{ab}} - \mathrm{e^{a_o b_o}}\right) &= K_{ab}\ln(\dot{\varepsilon}) + N_{ab}
\end{aligned}$$

If we define $\widehat{ab} = \ln\left(\mathrm{e}^{\mathrm{ab}} - \mathrm{e}^{\mathrm{a_o b_o}}\right)$, then

$$ab = \ln\left(\mathrm{e} + \mathrm{e}^{\mathrm{a_o b_o}}\right) \quad \text{and} \quad \widehat{ab} = K_{ab}\ln\left(\dot{\varepsilon}\right) + N_{ab} \tag{9}$$

To simplify the model, it will be assumed from now on that $a_o b_o = 0$, hence:

$$ab(\varepsilon_t, \dot{\varepsilon}_t) = \ln\left(\mathrm{e}+1\right) \quad \text{with} \quad \widehat{ab} = K_{ab}\ln(\dot{\varepsilon}) + N_{ab} \tag{10}$$

Thus parameter $b(\varepsilon_t, \dot{\varepsilon}_t)$can now be expressed as ab and a ratio:

$$b(\varepsilon_t, \dot{\varepsilon}_t) = \frac{ab(\varepsilon_t, \dot{\varepsilon}_t)}{a(\varepsilon_t, \dot{\varepsilon}_t)} = \frac{\ln\left(\mathrm{e}+1\right)}{\ln\left(e^{\widehat{a}}+1\right)}$$

$$\text{with} \quad \widehat{a} = K_a\ln(\dot{\varepsilon}) + N_a \quad , \quad \widehat{ab} = K_{ab}\ln(\dot{\varepsilon}) + N_{ab} \tag{11}$$

Considering relation (3), it is easy to verify that b increases with increasing $\dot{\varepsilon}$ for $K_{ab} > K_a$ as shown in Fig.5 below

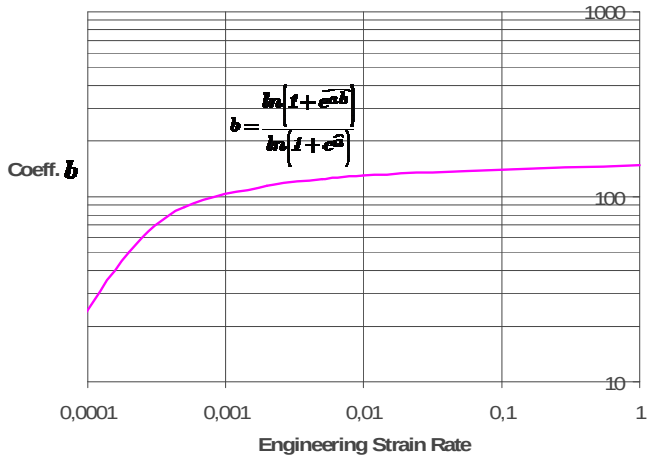

Figure 5: Variation of coefficient b for tensile tests at different strain rates ($K_{ab} > K_a$) for a magnesium alloy AZ31 at 375 ºC.

While b decreases with increasing $\dot{\varepsilon}$ for $K_{ab} < K_a$, Fig. 6.

Although expressions (5) and (8) are strongly non-linear, all parameters K_a, N_a, K_{ab}, N_{ab} can be identified from two tensile tests with constant engineering strain rates $\dot{\varepsilon}_1$ and $\dot{\varepsilon}_2$. In a tensile test with constant engineering stress rate $\dot{\varepsilon}_i$, from (4), true stress σ_t can be expressed as

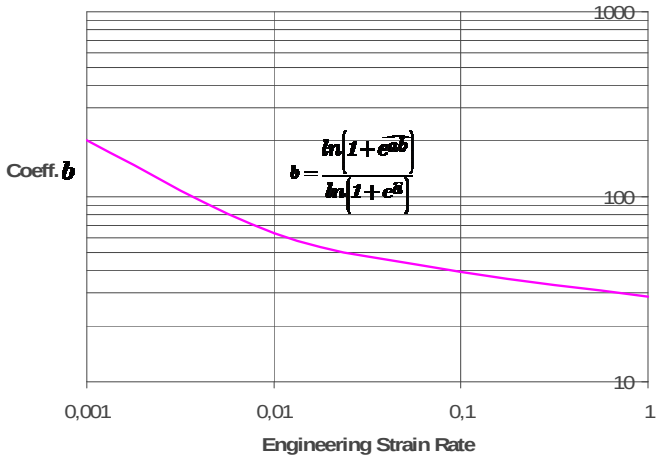

Figure 6: Variation of coefficient $b$for tensile tests at different strain rates ($K_{ab} < K_a$) for a magnesium alloy AZ31 at 500 °C.

$$\sigma_t = a_i \left[1 - \exp(-b_i \varepsilon_t)\right] \tag{12}$$

with

$$\widehat{a}_i = K_a \ln \left[\underbrace{\exp(\varepsilon_t)\ \dot{\varepsilon}_t}_{\dot{\varepsilon}_i} \right] + \mathrm{N}_a \tag{13a}$$

$$\widehat{a_i b_i} = K_{ab} \ln(\underbrace{\exp(\varepsilon_t)\ \dot{\varepsilon}_t}_{\dot{\varepsilon}_i}) + N_{ab} \tag{13b}$$

The parameters a_i and b_i can be identified from the true stress *vs* true strain curve obtained in a tensile test with constant engineering strain rate $\dot{\varepsilon}$ using a minimum squares curve fitting technique or using the following simpler procedure:

3.1 Identification of a_i

The parameter a_i can be identified from the true stress *vs* true strain curve. From (12), it is possible to obtain:

$$\lim_{\varepsilon_i \to \infty} (\sigma_t) = a_i \tag{14}$$

Hence, a_i is the maximum value of the stress σ_t.

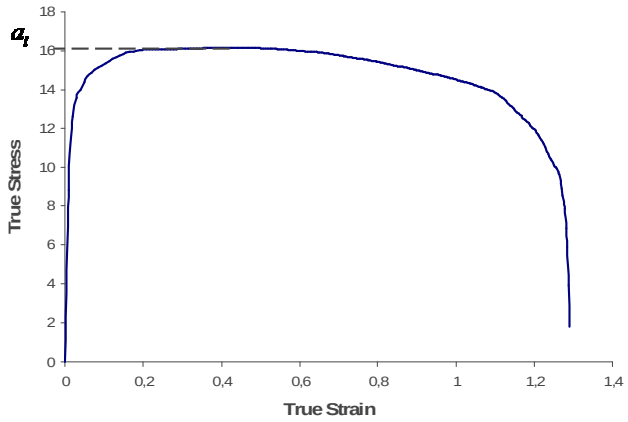

Figure 7: Identification of the parameter a_i from the true stress *vs* true strain curve.

3.2 Identification of b_i

From (12) it is also possible to verify that $\left.\frac{d\sigma_t}{d\varepsilon_t}\right|_{\varepsilon_t=0} = a_i b_i$

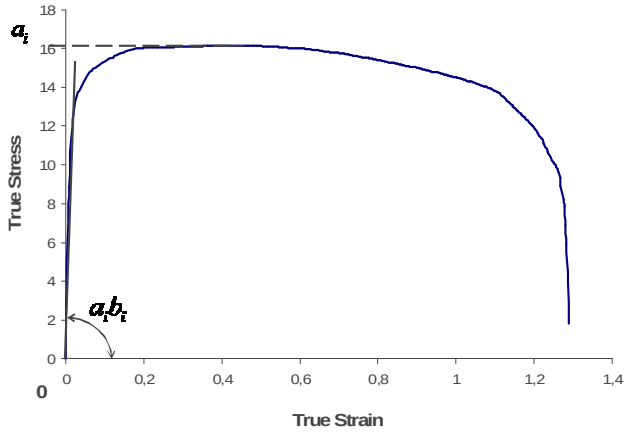

Figure 8: Identification of the parameter $a_i b_i$ from the true stress *vs* true strain curve.

Hence, once a_i is known, b_i can be identified from the initial slope of the true stress *vs* true strain curve. From (12) it is even possible to obtain

$$\exp(-b_i\varepsilon_t) = \left(\frac{a_i - \sigma_t}{a_i}\right) \quad \text{or,} \quad -b_i\varepsilon_t = \ln\left(\frac{a_i - \sigma_t}{a_i}\right)$$

Hence b_i can be approximated from the following expression:

$$b_i = -\left(\frac{1}{\varepsilon_t}\right)\ln\left(\frac{a_i - \sigma_t}{a_i}\right) \tag{15}$$

3.3 Identification of K_a, N_a, K_{ab}, N_{ab}

Once a_1, b_1 and a_2, b_2 are identified from two tensile tests with different engineering strain rates $\dot{\varepsilon}_1$ and $\dot{\varepsilon}_2$, the correspondent values of $\widehat{a}_1$, $\widehat{a}_2$ and $\widehat{a_1 b_1}$, $\widehat{a_2 b_2}$ are calculated from the definitions: $\widehat{a}_i = \ln\left(\mathrm{e}^{\mathrm{a_i}} - 1\right)$; $\widehat{a_i b_i} = \ln\left(\mathrm{e}^{\mathrm{a_i b_i}} - 1\right)$. These values permit to identified the parameters K_a, N_a, K_b, N_b as shown below.

From (13a) it is possible to obtain

$$\widehat{a_1} - K_a \ln(\dot{\varepsilon}_1) = N_a \tag{16}$$

and

$$-\left[\widehat{a_2} - K_a \ln(\dot{\varepsilon}_2) = N_a\right] \tag{17}$$

Hence, combining these equations it is possible to obtain

$$\widehat{a_1} - \widehat{a_2} = \mathrm{K_a}\left[\ln(\dot{\varepsilon}_1) - \ln(\dot{\varepsilon}_2)\right] \Rightarrow \mathrm{K_a} = \frac{\widehat{a_1} - \widehat{a_2}}{\ln(\dot{\varepsilon}_1) - \ln(\dot{\varepsilon}_2)} \tag{18}$$

The parameter K_a can be obtained from the following equation

$$N_a = -K_a \ln(\dot{\varepsilon}_1) \tag{19}$$

Once parameters K_a, N_a are known, it is possible to calculate $\widehat{a}_i$ for different strain rates and then obtain the correspondent a_i values from equation (7):

$$\mathrm{a_i} = \ln\left(1 + e^{\widehat{a_i}}\right) \tag{20}$$

With a similar procedure, from (13b), it is possible to verify that

$$\widehat{a_1 b_1} - K_{ab} \ln(\dot{\varepsilon}_1) = N_{ab} \tag{21}$$

and

$$-\left[\widehat{a_2 b_2} - K_{ab} \ln(\dot{\varepsilon}_2) = N_{ab}\right] \tag{22}$$

Hence, combining these equations it is possible to obtain

$$\widehat{a_1 b_1} - \widehat{a_2 b_2} = \mathrm{K_{ab}} \left[\ln\left(\dot{\varepsilon}_1\right) - \ln\left(\dot{\varepsilon}_2\right)\right] \Rightarrow \mathrm{K_{ab}} = \frac{\widehat{a_1 b_1} - \widehat{a_2 b_2}}{\ln\left(\dot{\varepsilon}_1\right) - \ln\left(\dot{\varepsilon}_2\right)} \tag{23}$$

Parameter N_{ab} can be obtained from the following equation

$$N_{ab} = -K_{ab} \ln\left(\dot{\varepsilon}_1\right) \tag{24}$$

Once parameters K_{ab}, N_{ab} are known, it is possible to calculate $\widehat{a_i b_i}$ for different strain rates and then obtain the correspondent $a_i b_i$ values from relation (10):

$$\mathrm{a_i b_i} = \ln\left(1 + e^{\widehat{a_i b_i}}\right) \tag{25}$$

Finally, it is possible to calculate b_i as $a_i b_i$ and a_i ratio.

$$b_i = \frac{a_i b_i}{a_i} \Rightarrow b_i = \frac{\ln\left(1 + e^{\widehat{a_i b_i}}\right)}{\ln\left(1 + e^{\widehat{a_i}}\right)} \tag{26}$$

3.4 Determination of material parameters for magnesium alloy AZ31 at 375°C with initial grain size d = 17μm

In this work, we examine the proposed constitutive equations for magnesium alloy AZ31 and identify the associated parameters. Magnesium alloys have recently attracted significant interest due to their excellent specific properties that make them potentially suitable candidates for replacing heavier materials in some automobile parts. Superplastic forming of Mg alloys is an alternative way of shaping these materials into complex geometries in one single operation. Thus, significant efforts are being lately devoted to understanding the underlying physical processes that take place during superplastic deformation of Mg alloys in order to improve their formability. The experimental results considered on this paper are taken from Del Valle et al. [12]. The Chemical Composition of an AZ31 magnesium alloy is presented on Table 1.

In order to identify the parameters that appear in the previous sections, two different series of experimental results referred to two tensile tests carried out at different strain rates ($\dot{\varepsilon}_1 = 0,0003$ (1/sec) and $\dot{\varepsilon}_2 = 0,01$ (1/sec)) have been considered.

For two different engineering strain rates $\dot{\varepsilon}_1 = 0,0003$ (1/sec) and $\dot{\varepsilon}_2 = 0,01$ (1/sec) we have

$$a_1 = 16,15 \text{ MPa} \; ; \; a_1 b_1 = 1130,5 \text{ MPa}; \; a_2 = 38,99 \text{ MPa} \; ; \; a_2 b_2 = 5068,7 \text{ MPa}.$$

From (18), (19), (23) and (24) it is possible to obtain

$$N_a = 0,251; \; K_a = 124,06 \; MPa; \; N_{ab} = 68.98; \; K_{ab} = 6,51 \; MPa$$

Table 1: Chemical Composition - Magnesium alloy AZ31.

Component	Value	Min	Max
Aluminum, Al		###	03:05
Calcium, Ca			00:04
Copper, Cu			00:05
Iron, Fe			0.005
Magnesium, Mg	97		
Manganese, Mn		###	
Nickel, Ni			0.005
Silicon, Si			00:01
Zinc, Zn		###	01:04

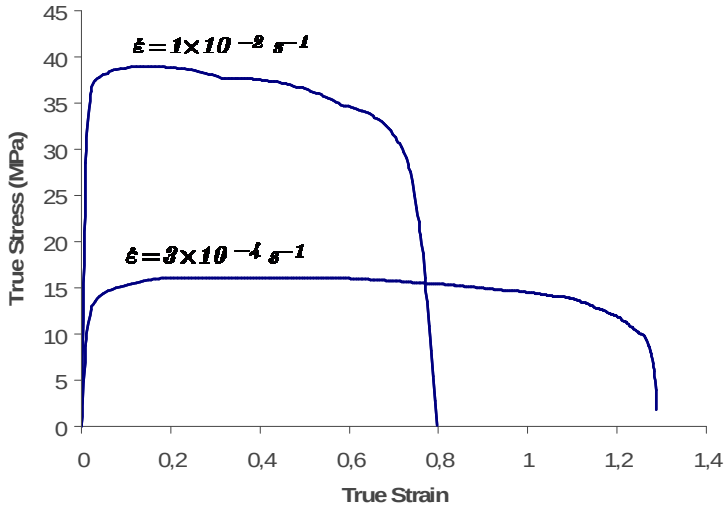

Figure 9: Magnesium alloy AZ31 at 375 ^{o}C. Two different strain rates $\dot{\varepsilon}_1 = 0,0003$ (1/sec) and $\dot{\varepsilon}_2 = 0,01$ (1/sec).

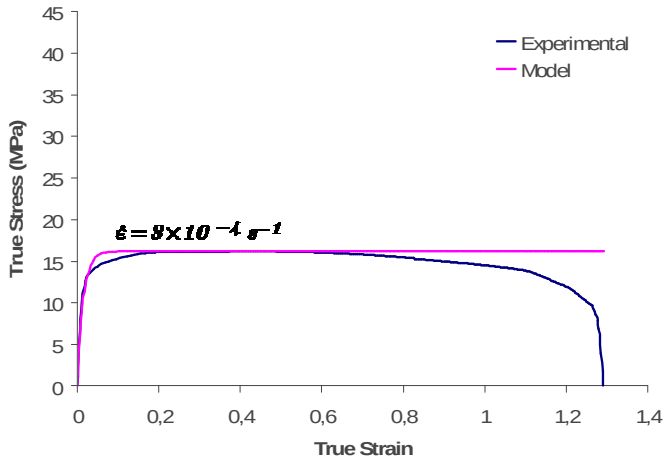

Figure 10: Stress-strain curve and model curve for $\dot{\varepsilon}_1 = 0,0003$ (1/sec).

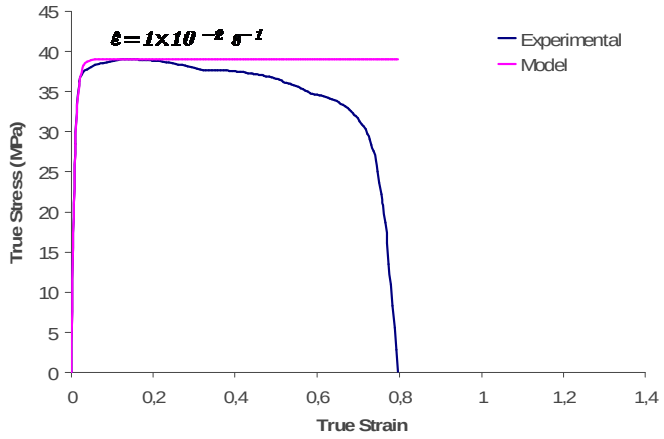

Figure 11: Stress-strain and model curve for $\dot{\varepsilon}_2 = 0,01$ (1/sec).

4 Modeling the true stress against true strain curve with damage

Only a few damage models were proposed for superplastic alloys, such as Chandra [13]. In the present paper it is introduced an auxiliary variable D that accounts for the nucleation and growth of voids observed in tensile tests performed at different strain rates.

$$\textbf{HIP 2: } \sigma_t = (1-D)\ a\ [1-\exp(-b\varepsilon_t)] \quad \text{with} \quad 0 \leqslant D \leqslant 1 \tag{27}$$

$$\textbf{HIP 3: } D = \begin{cases} 0, \text{ if } AUX > 1 \\ -\left[\dfrac{1}{b_d}\right] \ln(AUX), \text{ if } 0 < AUX < 1 \quad \text{with} \quad AUX = 1 - \left(\dfrac{\varepsilon_t - K_d/b}{a_d}\right) \\ 1, \text{ if } AUX < 0 \end{cases} \tag{28}$$

Where

$$a_d = -K_{a_d}(\dot{\varepsilon}) + N_{a_d}, \text{ and} \tag{29a}$$

$$\mathrm{a_d b_d} = K_{a_d b_d}[\dot{\varepsilon}]^{-N_{a_d b_d}} \tag{29b}$$

All parameters K_d, N_d, a_d, b_d can be identified from two tensile tests with constant engineering strain rates $\dot{\varepsilon}_1$ and $\dot{\varepsilon}_2$. Considering HIP 2. For a tensile test with constant stress rate $\dot{\varepsilon}_i$, the damage variable D can be expressed as $\frac{\sigma_t}{a[1-\exp(-b\varepsilon_t)]} = (1-D) \Rightarrow D = 1 - \frac{\sigma_t}{a[1-\exp(-b\varepsilon_t)]}$, after the softening behavior. Hence, the experimental curve D *vs* ε_t can be easily obtained.

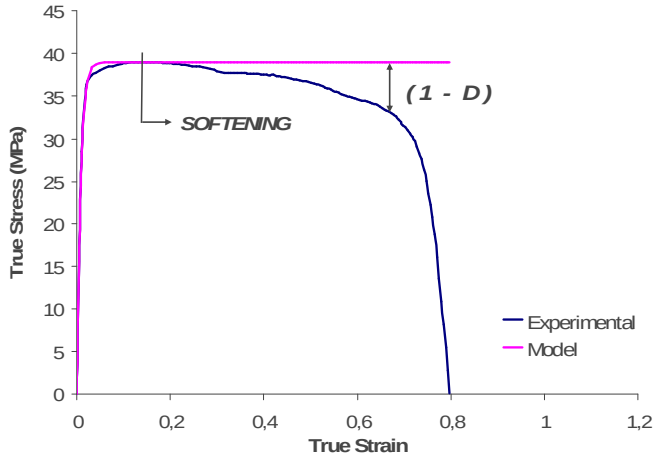

Figure 12: Experimental identification of the auxiliary variable D.

Since $\dot{\varepsilon} = \exp(\varepsilon_t)\dot{\varepsilon}_t$, it is possible to obtain from HIP 3

$$
\begin{aligned}
D = -\left[\frac{1}{b_d}\right] \ \ln\left[1 - \left(\frac{\varepsilon_t - \mathrm{K_d/b}}{a_d}\right)\right], \ \text{for } D \in [0,1) \Rightarrow \\
-b_d D = \ \ln\left[1 - \left(\frac{\varepsilon_t - \mathrm{K_d/b}}{a_d}\right)\right], \ \text{for } D \in [0,1) \Rightarrow \\
\exp(-b_d D) = \ 1 - \left(\frac{\varepsilon_t - \mathrm{K_d/b}}{a_d}\right), \ \text{for } D \in [0,1) \Rightarrow \\
\left(\frac{\varepsilon_t - \mathrm{K_d/b}}{a_d}\right) = \ 1 - \ \exp(-b_d D), \ \text{for } D \in [0,1) \Rightarrow \\
(\varepsilon_t - \mathrm{K_d/b}) = a_d\left[1 - \ \exp(-b_d D)\right], \ \text{for} D \in [0,1) \Rightarrow \\
\varepsilon_t \ = a_d\left[1 - \ \exp(-b_d D)\right] + \mathrm{K_d/b}
\end{aligned} \tag{30}
$$

Parameters a_i and b_i can be identified from the true stress *vs* true strain curve obtained in a tensile test with constant engineering strain rate $\dot{\varepsilon}$ using a minimum squares curve fitting technique or using the following simpler procedure. If $D = 0$, from (22) it is possible to obtain

$$\varepsilon_t = \frac{\mathrm{K_d}}{\mathrm{b}}$$

A "corrected curve" is obtained by eliminating the viscous term $\mathrm{K_d/b}$ from this curve.

$$(\varepsilon_t)_{\text{corrected}} \ = a_d\left[1 - \ \exp(-b_d D)\right] \tag{31}$$

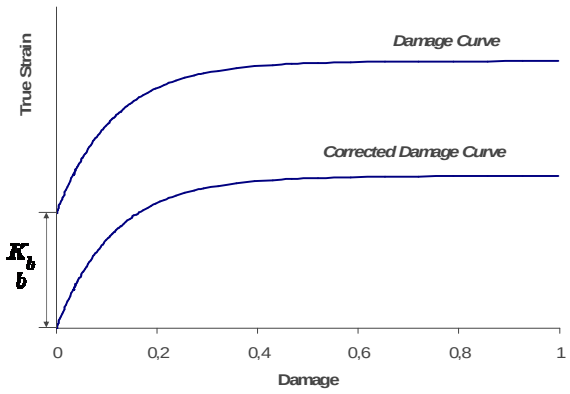

Figure 13: Damage curve and corrected damage curve obtained from a tensile test with constant engineering stress rate.

Parameters a_i and b_i can be identified from the true stress *vs* true strain curve using a minimum squares curve fitting technique or using the following simpler procedure.

4.1 Identification of a_d

From (31), it is possible to obtain:

$$\lim_{D\to 1}\left((\varepsilon_t)_{\text{corrected}}\right) = a_d \tag{32}$$

Hence, a_d is the value of the corrected strain $(\varepsilon_t)_{\text{corrected}}$ when $D \to 1$

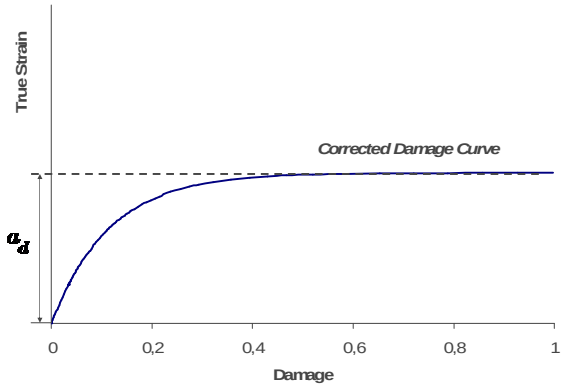

Figure 14: Experimental identification of a_d.

4.2 Identification of b_d

From (31) it is possible to verify that

$$\left.\frac{d(\varepsilon_t)_{\text{corrected}}}{dD}\right|_{D=0} = a_d b_d$$

Hence, once a_d is known, b_d can be identified from the initial slope of the true corrected damage curve. From (30) it is possible to obtain

$$\exp(-b_d D) = \left(\frac{a_d - (\varepsilon_t)_{\text{corrected}}}{a_d}\right) \quad \text{or,} \quad -b_d D = \ln\left(\frac{a_d - (\varepsilon_t)_{\text{corrected}}}{a_d}\right)$$

b_d can be approximated from the following expression:

$$b_d = -\left(\frac{1}{D}\right)\ln\left(\frac{a_d - (\varepsilon_t)_{\text{corrected}}}{a_d}\right) \tag{33}$$

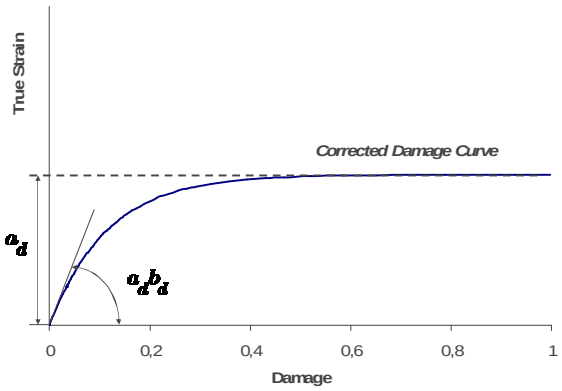

Figure 15: Identification of the parameter b_i from the true stress *vs* true strain curve.

4.3 Identification of K_{a_d}, N_{a_d}, $K_{a_d b_d}$, $N_{a_d b_d}$

Once a_{d_1}, b_{d_1} and a_{d_2}, b_{d_2} are identified from two tensile tests with different engineering strain rates $\dot{\varepsilon}_1$ and $\dot{\varepsilon}_2$, the parameters K_{a_d}, N_{a_d}, $K_{a_d b_d}$, $N_{a_d b_d}$ can also be identified.

From (29a) it is possible to obtain

$$-K_{a_d}\dot{\varepsilon}_1 + N_{a_d} = a_{d_1}$$

and

$$-\left[-K_{a_d}\dot{\varepsilon}_2 + N_{a_d} = a_{d_2}\right]$$

Hence, combining these equations it is possible to obtain

$$K_{a_d}\left(\dot{\varepsilon}_2 - \dot{\varepsilon}_1\right) = a_{d_1} - a_{d_2} \Rightarrow K_{a_d} = \frac{a_{d_1} - a_{d_2}}{\dot{\varepsilon}_2 - \dot{\varepsilon}_1} \tag{34}$$

The parameter N_{a_d} can be obtained from the following equation

$$N_{a_d} = a_{d_1} + K_{a_d}\dot{\varepsilon}_1 \tag{35}$$

While from (29b) we have

$$\ln(K_{a_d b_d}) + N_{a_d b_d}\ln(\dot{\varepsilon}_1) = \ln(a_{d_1} b_{d_1})$$

and

$$-\left[\ln(K_{a_d b_d}) + N_{a_d b_d}\ln(\dot{\varepsilon}_2) = \ln(a_{d_2} b_{d_2})\right]$$

which combined give $N_{a_d b_d}$

$$N_{a_d b_d}\left[\ln(\dot{\varepsilon}_1) - \ln(\dot{\varepsilon}_2)\right] = \left[\ln(a_{d_1} b_{d_1}) - \ln(a_{d_2} b_{d_2})\right] \Rightarrow N_{a_d b_d} = \frac{\left[\ln(a_{d_1} b_{d_1}) - \ln(a_{d_2} b_{d_2})\right]}{\left[\ln(\dot{\varepsilon}_1) - \ln(\dot{\varepsilon}_2)\right]} \tag{36}$$

The parameter $K_{a_d b_d}$ can be obtained from the following equation

$$K_{a_d b_d} = \frac{a_1}{(\dot{\varepsilon}_1)^{N_{a_d b_d}}} \tag{37}$$

4.4 Identification of K_d

The parameter K_d can be identified from the strain *vs* damage curves obtained in a tensile test with constant strain rates $\dot{\varepsilon}_1$ and $\dot{\varepsilon}_2$. The value η

$$\eta = \frac{K_d}{b}$$

can be obtained from both experimental damage curves, considering an avarage value. Hence, we have

$$K_d = \frac{b_1\eta_1 + b_2\eta_2}{2} \quad \text{and} \quad \eta_i = \frac{K_d}{b_i} \tag{38}$$

4.5 Determination of material parameters for magnesium alloy AZ31 at 375 ºC with initial grain size d = 17μm

The experimental damage curves shown in Fig 16 have been obtained for the investigated strain rates $\dot{\varepsilon}_1 = 0,0003$ (1/sec) and $\dot{\varepsilon}_2 = 0,01$ (1/sec).

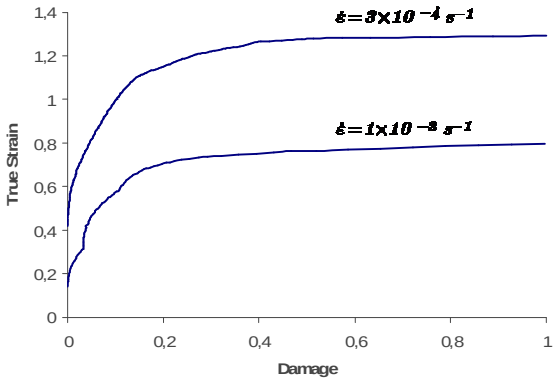

Figure 16: Damage curves for $\dot{\varepsilon}_1 = 0,0003$ (1/sec) and $\dot{\varepsilon}_2 = 0,01$ (1/sec).

For $\dot{\varepsilon}_1 = 0,0003$ (1/sec) the model curve which fits the experimental corrected damage curve gives $\eta_1 = 0,067$, $a_{d_1} = 1,12$ and $a_{d_1} b_{d_1} = 13,44$

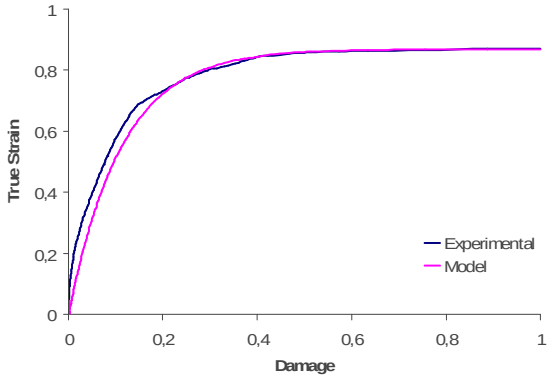

Figure 17: Corrected damage curve. Model and experiment. $\dot{\varepsilon}_1 = 0,003$ (1/sec).

While for $\dot{\varepsilon}_2 = 0,01$ (1/sec) the model curve gives $\eta_2 = 0,12$, $a_{d_2} = 0,72$ and $a_{d_2} b_{d_2} = 7,92$

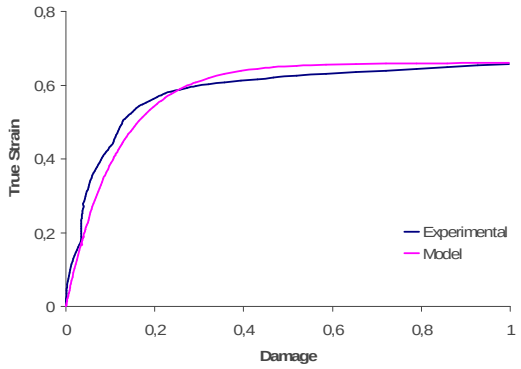

Figure 18: Corrected damage curve. Model and experiment. $\dot{\varepsilon}_2 = 0,01$ (1/sec).

Thus, from (34), (35), (36) and (37) it is possible to obtain $N_{a_d} = 1,16$; $K_{a_d} = -43,29$; $N_{a_d b_d} = -0,13$; $K_{a_d b_d} = 4,28$ while relation (38) gives $K_d = 8,71$. Hence, the following coefficients were identified for the examined magnesium alloy while the related model curves shown in figure 19 have been obtained.

$$a_1 = 16,20 \text{ MPa} \; ; \; a_1 b_1 = 1130,5 \text{ MPa} \; ; \; a_2 = 38,99 \text{ MPa} \; ; \; a_2 b_2 = 5068,7 \text{ MPa} \; ;$$
$$N_a = 68,92 \; ; \; K_a = 6,50 \; MPa \; ; \; N_{ab} = 10236 \; ; \; K_{ab} = 1122,1 \; MPa \; ; \; K_d = 8,71$$
$$a_{d_1} = 1,15 \; ; \; a_{d_1} b_{d_1} = 12,65 \; ; \; a_{d_2} = 0,73 \; ; \; a_{d_2} b_{d_2} = 7,92 \; ;$$
$$N_{a_d} = 1,16 \; ; \; K_{a_d} = -43,29 \; ; \; N_{a_d b_d} = -0,13 \; ; \; K_{a_d b_d} = 4,28$$

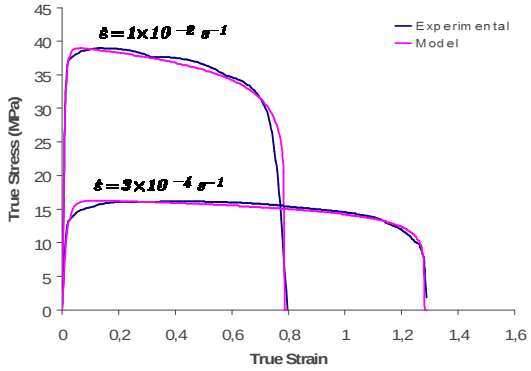

Figure 19: Stress-strain curve for $\dot{\varepsilon}_1 = 0,0003$ (1/sec) and $\dot{\varepsilon}_2 = 0,01$ (1/sec) for a magnesium alloy AZ31B-F at 375 °C.

5 Proposed model

From section (3) and (4) the model equations can be summarized as follows:

$$\sigma_t = (1 - D)\; a \;\; [1 - \exp(-b\varepsilon_t)] \quad \text{with} \quad 0 \leqslant D \leqslant 1$$

Where

$$D = \begin{cases} 0, \text{ if AUX} > 1 \\ -\left[\dfrac{1}{b_d}\right] \ln(AUX) \;\; , \text{ if } 0 < AUX < 1 \quad \text{with} \quad AUX = 1 - \left(\dfrac{\varepsilon_t \text{ - } \mathrm{K_d/b}}{a_d}\right) \\ 1, \text{ if } AUX < 0 \end{cases}$$

and

$$\ln(\mathrm{e^a} \text{ - } 1) = K_a \ln(\dot{\varepsilon}) + N_a, \quad \ln\left(\mathrm{e^{ab}} \text{ - } 1\right) = K_{ab} \ln(\dot{\varepsilon}) + N_{ab} \;, \quad \text{AUX} = 1 \text{ - } \left(\frac{\varepsilon_t \text{ - } [\mathrm{K_d}/b]}{a_d}\right) \;,$$
$$a_d = -K_{a_d}(\dot{\varepsilon}) + N_{a_d}, \quad \mathrm{a_d b_d} = K_{a_d b_d}[\dot{\varepsilon}]^{-N_{a_d b_d}}$$

Using the coefficient previously identified, it is now possible to predict the mechanical behavior of the same magnesium alloy deformed at the same conditions but at a different value of engineering strain rate.

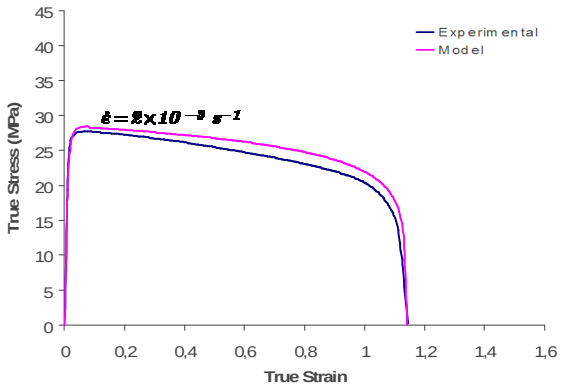

Figure 20: Stress-strain curve for $\dot{\varepsilon} = 0,002$ (1/sec) for a magnesium alloy AZ31 at 375 °C ($a_0 = a_0 b_0 = 0$).

Fig 20 shows the good approximation of the experimental true stress vs true strain curve achieved by the model curve for an intermediate strain rate $\dot{\varepsilon} = 0,002$ (1/sec).

Further good results have been observed applying the model to the step test experimental data taken from Del Valle [12] and referred to the same material tested in the previous tensile tests.

As shown in figure 21b, unrealistic previsions of the superplastic behavior can be observed for the lowest strain rates as $\dot{\varepsilon} = 0,000075$ (1/sec) $\dot{\varepsilon} = 0,00002$ (1/sec). Such limitation can be circumvented by taking the parameters a_o and b_o different from zero. When nonzero values are assumed for a_0 and b_0, good fitting curves can be obtained even for low values of strain rate as it can be seen in figure 22a-b.

The hypothesis of nonzero values for a_0 and b_0 suggest, as reported by literature, an evidence of some form of threshold stress for superplastic flow since dislocation activity is not normally observed at lower strain rates. Nevertheless, when tensile tests are carried out at such strain rates, grain grow and an associated hardening effect are usually observed. According to Del Valle [12], grain growth during tensile test at $\dot{\varepsilon} = 0,00005$ (1/sec) is reported. In this case model curve differs from experimental curve as show in fig 20.

The model seems then able to predict the experimental results obtained when grain growth is inhibited (step test), while it leads to results that disagree from experimetal ones when grain growth takes place.

This aspect suggests a possible application of the model to evaluate the hardening associated with grain growth during low strain rate tests.

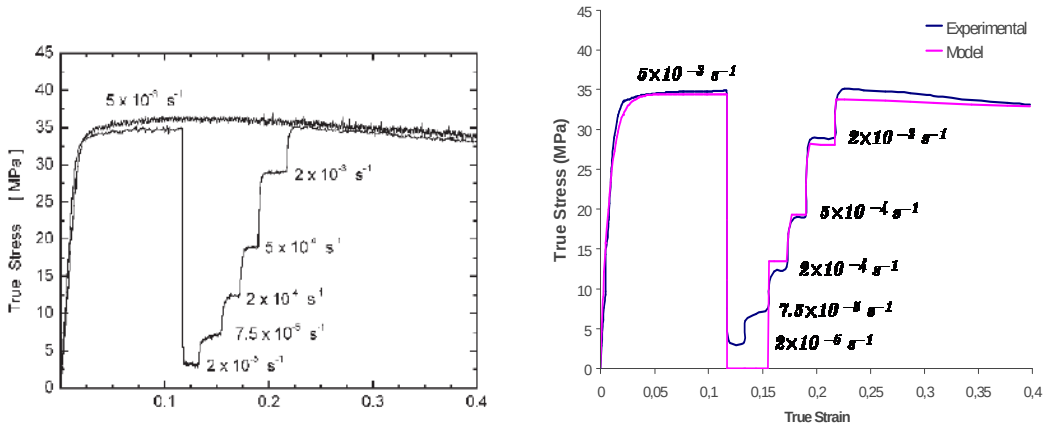

(a) (b)

Figure 21: Step Test curve from Del Valle [10] and model for a magnesium alloy AZ31 at 375 ºC ($a_0 = a_0 b_0 = 0$).

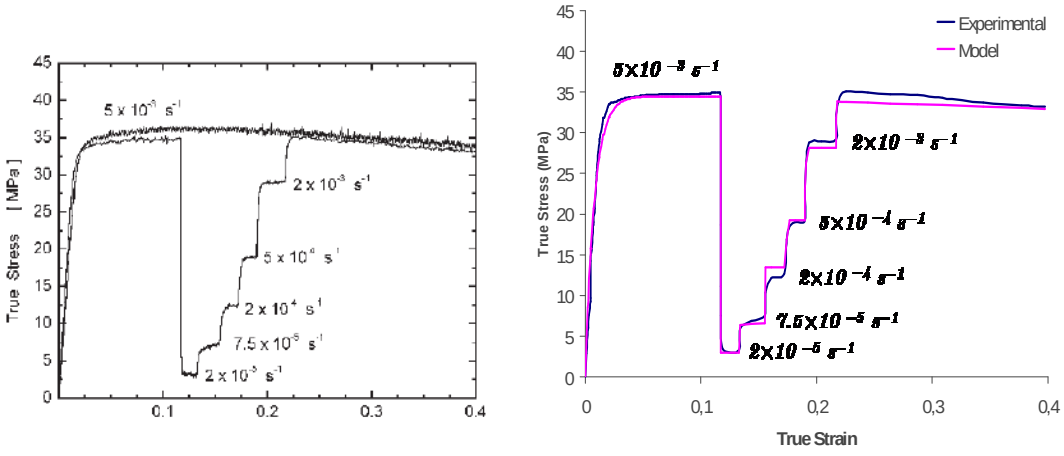

(a) (b)

Figure 22: Step Test curve from Del Valle [10] and model curve for a magnesium alloy AZ31 at 375 ºC ($a_0 = 3$, $a_0 b_0 = 135$).

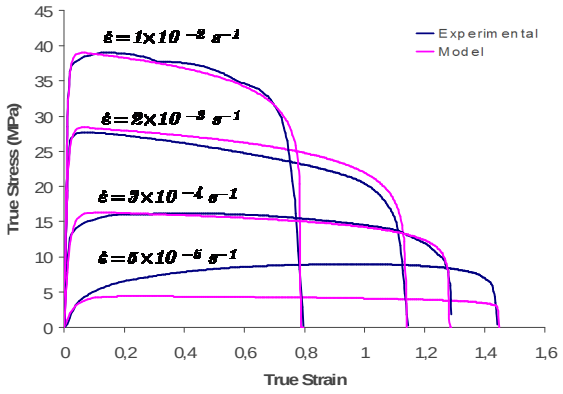

Figure 23: Stress-strain curve for different engineering strain rates for a magnesium alloy AZ31 at 375 ºC ($a_0 = 3$, $a_0 b_0 = 135$).

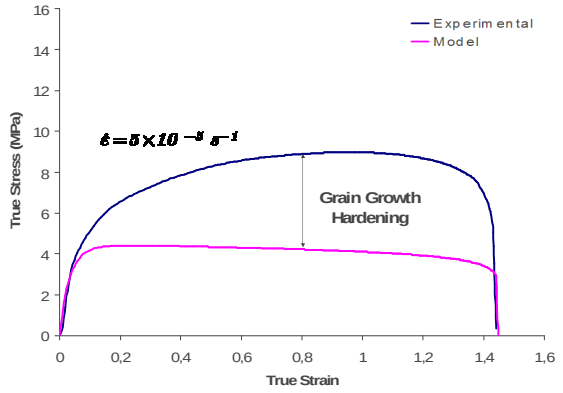

Figure 24: Evaluation of grain growth hardening from model and experimental curve for a magnesium alloy AZ31 at 375 ºC.

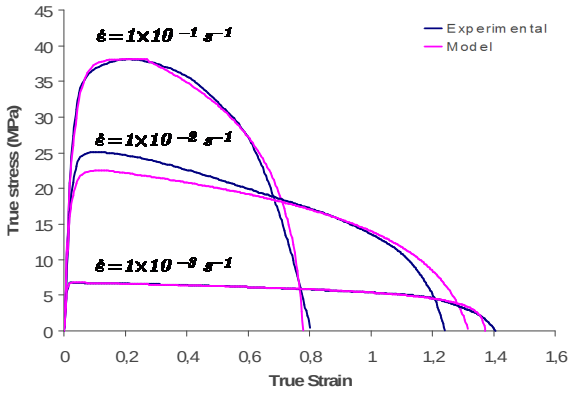

Figure 25: Stress-strain curve for different engineering strain rates for a magnesium alloy AZ31 at 500 °C.

Good predictions have also been obtained considering the experimental results from Xin Wu [3], referred to tensile tests carried out at 500 °C on AZ31 magnesium alloy with initial grain size d =300μm. In this case, the following coefficients were identified:

$$a_1 = 6,85 \text{ MPa} \; ; \; a_1 b_1 = 1370,0 \text{ MPa} \; ; \; a_2 = 38,12 \text{ MPa} \; ; \; a_2 b_2 = 1486,6 \text{ MPa} \; ;$$
$$N_a = 53,75 \; ; \; K_a = 6,79 \; MPa \; ; \; N_{ab} = 1545,0 \; ; \; K_{ab} = 25,33 \; MPa \; ; \; K_d = 9,16$$
$$a_{d_1} = 1,3 \; ; \; a_{d_1} b_{d_1} = 8,11 \; ; \; a_{d_2} = 0,53 \; ; \; a_{d_2} b_{d_2} = 1,89 \; ;$$
$$N_{a_d} = 1,30 \; ; \; K_{a_d} = -7,77 \; ; \; N_{a_d b_d} = -0,31 \; ; \; K_{a_d b_d} = 0,91$$

Figure 22 presents the experimental curves and model prevision for three different strain rates.

6 One-dimensional problem with compression

The previous model is only adequate for monotone problems ($\dot{\varepsilon} \geqslant 0$). In order to build a more general model, the first step is to include the possibility of non-monotone loadings. In this case, a new additional auxiliary variable must be considered – the cumulated plastic strain p, classically defined as follows:

$$p(t) = \int_{t=0}^{t} |\dot{\varepsilon}_t(\xi)| \; d\xi \Rightarrow \dot{p}(t) = |\dot{\varepsilon}_t(t)| \tag{39}$$

From definition (39) it is easy to verify that $p(t) = \varepsilon(t)$, in a tensile test with $\dot{\varepsilon}(t) \geqslant 0$. It is also possible to obtain that $p(t) = -\varepsilon(t)$ in a tensile test with $\dot{\varepsilon}(t) \leqslant 0$. Hence, the following model equations are proposed (the material parameters are the same from the model proposed in the last sections, and also their experimental identification)

$\sigma_t = (1-D)X$

Where

$\dot{X} = ab\dot{\varepsilon}_t - bX\dot{p}$

$p(t) = \int_{t=0}^{t} |\dot{\varepsilon}_t(\xi)| \; d\xi \Rightarrow \dot{p}(t) = |\dot{\varepsilon}_t(t)|$

$$D = \begin{cases} 0, \text{ if } AUX > 1 \\ -\left[\frac{1}{b_d}\right] \ln(AUX) \text{ , if } 0 < AUX < 1 \text{ with AUX = 1 - } \left(\frac{p - K_d/b}{a_d}\right) \\ 1, \text{ if } AUX < 0 \end{cases}$$

and

$\ln(\mathrm{e^a} - 1) = K_a \ln(\exp(p)\ \dot{p}) + N_a, \quad \ln\left(\mathrm{e^{ab}} - 1\right) = K_{ab} \ln(\exp(p)\ \dot{p}) + N_{ab},$

$\mathrm{AUX} = 1 - \left(\frac{\varepsilon_t - [\mathrm{K_d}/b]}{a_d}\right) , \quad a_d = -K_{a_d}(\exp(p)\ \dot{p}) + N_{a_d}, \quad \mathrm{a_d b_d} = K_{a_d b_d}[\exp(p)\ \dot{p}]^{-N_{a_d b_d}}$

To better understand the role of the variable X in the present model, it is interesting to verify the mechanical behavior described by the above presented equations in the case of monotone loading histories.

From the definition of the cumulated plastic strain p we have:

$$\dot{X} = ab\dot{\varepsilon}_t - bX\,|\dot{\varepsilon}_t| \tag{40}$$

In a tensile test with $\dot{\varepsilon}(t) \geqslant 0$ it is possible to obtain:

$$\dot{X} = ab\dot{\varepsilon}_t - bX\dot{\varepsilon}_t \Rightarrow \frac{dX}{d\varepsilon_t} = b\,(a - X) \tag{41}$$

Hence, for an initial condition $(X_\mathrm{i}, \varepsilon_i) \Rightarrow X = a + [(X_i - a)\ \exp(-b(\varepsilon_t - \varepsilon_i))]$, the true stress is given by the following expression:

$$\sigma_t = (1-D)\ \left(\ a + [(X_i - a)\ \exp(-b(\varepsilon_t - \varepsilon_i))]\ \right) \tag{42}$$

If $X_\mathrm{i} = 0$ and $\varepsilon_i = 0$, the above equation is the same proposed for the monotone case in section 4 (equation 23).

In a tensile test with $\dot{\varepsilon}(t) \leqslant 0$ it is also possible to obtain:

$$\dot{X} = ab\dot{\varepsilon}_t + bX\dot{\varepsilon}_t \Rightarrow \frac{dX}{d\varepsilon_t} = b(a + X) \tag{43}$$

Hence, for an initial condition $(X_\mathrm{i}, \varepsilon_i) \Rightarrow X = -a + [(X_i + a)\ \exp(b(\varepsilon_t - \varepsilon_i))]$, the true stress is given by the following expression:

$$\sigma_t = (1-D)\ \left(\ -a + [(X_i + a)\ \exp(b(\varepsilon_t - \varepsilon_i))]\ \right) \tag{44}$$

Figure 24 shows the stress-strain curve for a magnesium alloy AZ31B-F at 375 ºC considering the loading history presented at figure 26

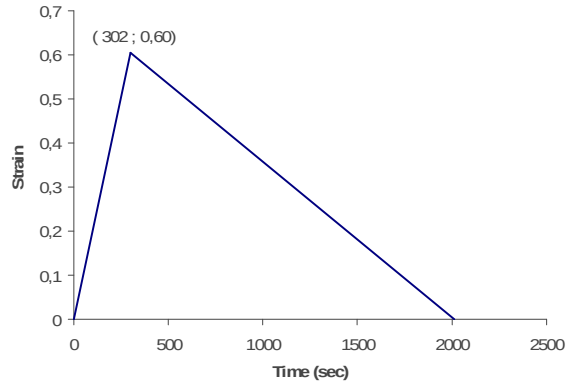

Figure 26: Non-monotone loading history.

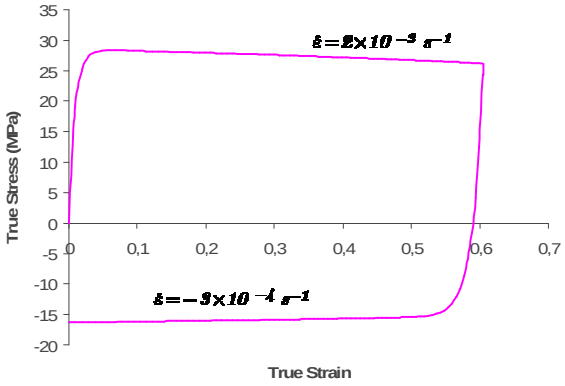

Figure 27: Stress-strain curve for the non-monotone loading history presented at figure 26, for a magnesium alloy AZ31B-F at 375 ºC.

7 Concluding remarks

The one-dimensional phenomenological damage model proposed on this paper is able to perform a mathematically correct and physically realistic description of plastic deformations, strain hardening, strain softening, strain rate sensitivity and damage observed in tensile tests performed at different strain rates and temperatures.

The identification of parameters that appear in the theory is discussed in detail and examples concerning the modeling of tensile tests of a magnesium alloy at different strain rates and temperatures

are presented and analyzed. It is necessary to perform only two tensile tests at different strain rates in order to identify the parameters that appear in the theory. The results obtained show a very good agreement between experimental results and model prevision for different strain rates.

Finally, it is important to observe that it is necessary to adapt such model to account for compression loading, what can be done through the introduction of a new auxiliary variable related to the cumulated plastic strain.

It is also necessary an adequate thermo mechanical framework in order to extend the proposed model to a tri-dimensional context, which is essential since one of the main practical motivation to study such alloys is the superplastic forming (SPF) of sheet metals. In a tri-dimensional context, the adequate choice of the measure of strain and of the objective time derivative is essential to build a physically realistic and mathematically correct model [14].

References

[1] Khaleel, M.A., Zbib, H.M. & Nyberg, E.A., Constitutive modeling of deformation and damage in superplastic materials. *International Journal of Plasticity*, **17**, pp. 277–296, 2001.

[2] Kim, W.J., Chung, S.W., Chung, C.S. & Kum, D., Superplasticity in thin magnesium alloy sheets and deformation mechanism maps for magnesium alloys at elevated temperatures. *Acta Mater*, **49**, pp. 3337–3345, 2001.

[3] Xin, W. & Yi, L., Superplasticity of coarse-grained magnesium alloy. *Scripta Materialia*, **46**, pp. 269–274, 2002.

[4] Tan, J.C. & Tan, M.J., Superplasticity in a rolled Mg-3Al-1Zn alloy by two-stage deformation method. *Scripta Materialia*, **47**, pp. 101–106, 2002.

[5] Somekawa, H., Hosokawa, H., Watanabe, H. & Higashi, K., Diffusion bonding in superplastic magnesium alloys. *Materials Science and Engineering*, **A339**, pp. 328–333, 2003.

[6] Lin, H.K., Huang, J.C. & Langdon, T.G., Relationship between texture and low temperature superplasticity in an extruded AZ31 Mg alloy processed by ECAP. *Materials Science and Engineering*, **A402**, pp. 250–257, 2005.

[7] Takuda, H., T., M., Kinoshita, T. & Shirakawa, N., Modelling of formula for flow stress of a magnesium alloy AZ31 sheet at elevated temperatures. *Journal of Materials Processing Technology*, **164-165**, pp. 1258–1262, 2005.

[8] Yin, D.L., Zhang, K.F. & Wang, G.F., Microstructure evolution and fracture behavior in superplastic deformation of hot-holled AZ31 Mg alloy sheet. *Materials Science Forum*, **475-479**, pp. 2923–2926, 2005.

[9] Yin, D.L., Zhang, K.F., Wang, G.F. & Han, W.B., Superplasticity and cavitation in AZ31 Mg alloy at elevated temperatures. *Materials Letters*, **59**, pp. 1714–1718, 2005.

[10] Lee, B.H., Shin, K.S. & Lee, C.S., High temperature behavior of AZ31 Mg alloy. *Materials Science Forum*, **475-479**, pp. 2927–2950, 2005.

[11] ASTM Standard E 2448-05, *Standard Test Method for Determining the Superplastic Properties of Metallic Sheet Materials.*

[12] Del Valle, J.A., Pérez-Prado, M.T. & Ruano, O.A., Deformation mechanisms responsible for the high ductility in a Mg AZ31 alloy analyzed by electron backscattered diffraction. *Metallurgical And Materials Transactions A*, **Volume 36A**, pp. 1427–1438, 2005.

[13] Chandra, N., Constitutive behavior of superplastic materials. *International Journal of Non-Linear*

Mechanics, **37**, pp. 461–484., 2002.

[14] Costa-Mattos, H., A thermodynamically consistent constitutive theory for fluids. *International Journal of Non-linear Mechanics*, **33(1)**, pp. 97–110, 1998.

Mechanics of Solids in Brazil 2009, H.S. da Costa Mattos & Marcílio Alves (Editors)
Brazilian Society of Mechanical Sciences and Engineering, ISBN 978-85-85769-43-7

A simple methodology to repair localized corrosion damage in metallic pipelines with epoxy resins

H.S. da Costa-Mattos, J.M.L. Reis, R.F. Sampaio
Laboratory of Theoretical and Applied Mechanics, Department of Mechanical Engineering, Universidade Federal Fluminense, Niterói/RJ – Brazil
V.A. Perrut
Research and Development Center - CENPES, Petróleo Brasileiro S.A. – PETROBRAS, Ilha do Fundão/RJ – Brazil

Abstract

The present work is concerned with the analysis of epoxy repair systems for metallic pipelines undergoing elastic or inelastic deformations with localized corrosion damage that impair the serviceability. In the case of trough-thickness damage, the main focus is to assure an adequate application of the epoxy filler in such a way the pipe wont leak after repair. Such a procedure can be used or not associated with a composite sleeve that assures a satisfactory level of structural integrity. Examples concerning the use of repair systems in different damage situations are presented and analyzed showing the possibilities of practical use of the proposed methodology.

Keywords: corroded pipelines, epoxy repair systems, polymer matrix composites.

1 Introduction

Corroded pipelines with part-wall metal loss defects can be repaired or reinforced with a composite sleeve system. In these systems, a piping or vessel segment is reinforced by wrapping it with concentric coils of composite material after the application of epoxy filler in the corrosion defect. Nevertheless, so far, composite repair systems are not effective for through-thickness corrosion defects because generally they cannot avoid leaking. Information about requirements and recommendations for the qualification, design, installation, testing and inspection for the external application of composite repairs to corroded or damaged pipeline in petroleum, petrochemical and natural gas industries can be found in Jaske et al [1] or in the ISO Technical Specification 24817 [2]. Composite repair systems (patches) are also used in aircraft industry to repair cracks in order to extend the service life of metallic components [3, 4]. In this case, the size of the patch and bonding properties are very important. In the case of

Mechanics of Solids in Brazil 2009, H.S. da Costa Mattos & Marcílio Alves (Editors)
Brazilian Society of Mechanical Sciences and Engineering, ISBN 978-85-85769-43-7

corroded pipelines conveying liquids, the geometry of the composite repair is simpler (a sleeve), but the main difficulties are the definition of the adequate composite thickness to assure a satisfactory level of structural integrity and to avoid leaking in the case of through-thickness defects.

The present paper is concerned with the analysis of epoxy repair systems for metallic pipelines undergoing elastic or inelastic deformations with localized corrosion damage that impair the serviceability. In the case of through-wall corrosion damage, the focus is to assure that the pipe wont leak after repair. The main motivation for the study presented on this paper are corrosion defects in produced water pipelines used in offshore oil exploitation. Since offshore platforms are hydrocarbon atmospheres, any repair method using equipment that may produce heat and/or sparkling is forbidden.

The damages derived from corrosion process in produced water pipelines in platforms cause very important economical losses because the operation must be stopped while the repair is being performed. The rehabilitation of this kind of corroded pipeline may eventually require an industrial climber and hence the application of the repair system must be as simple as possible. Although the operation pressure of these pipelines is not very high, the water temperature is between 60°C to 90°C, which can be a major shortcoming for the use of polymeric material as repair systems. Initially, it is presented in this paper a simple methodology to define the necessary thickness of the composite sleeve to assure the safe operation of corroded pipelines with part-wall metal loss defects. As a second step, it is presented a complementary procedure to repair through-thickness corrosion defects in pipelines using epoxy resins. The objective is to assure the pipeline wont leak under the operation pressure and temperature. Hydrostatic tests were carried out with water at room temperature and at 80°C to validate epoxy repair systems applied in offshore produced water pipelines. Examples concerning the use of repair systems in different damage situations are presented and analyzed showing the possibilities of practical use of the proposed methodology.

2 Mechanical analysis of composite sleeve reinforcement systems

The present section is concerned with the analysis of composite sleeve reinforcement systems for metallic pipelines undergoing elastic or inelastic deformations with localized part-wall metal loss that impair the serviceability. Different commercial repair systems based in fiber reinforced composite materials can be found: (a) dry fiberglass fabric to be wrapped with impregnation of liquid resin, (b) ready pre-cured layers ready to wrap around the pipe, (c) Flexible resin pre-impregnated bandage to be wrapped with water. No matter the application procedure, the basic idea of the reinforcement technique is to transfer the hoop stress in the pipe wall due to the internal pressure to the composite sleeve.

Most of the studies about these systems are concerned with the materials (matrix, fibers, adhesive) and application procedures. Only a few studies are concerned with the mechanical analysis of the repair system [5–9]. The main goal of this section is to summarize a new methodology, as simple as possible, to define the minimum thickness of composite material to assure: (a) the safety of repairs under operation conditions and/or (b) the lifetime extension under operation conditions. Such methodology, although simple, is able to account for different failure mechanisms (plasticity, corrosion, etc.).

Mechanics of Solids in Brazil 2009, H.S. da Costa Mattos & Marcílio Alves (Editors)
Brazilian Society of Mechanical Sciences and Engineering, ISBN 978-85-85769-43-7

2.1 Basic model – Pipe without localized damage

In a first step towards a simplified mechanical analysis of composite sleeve reinforcement systems, no localized imperfections or damage are considered. The pipe-composite sleeve system is modeled as two concentric cylinders, open at the ends, under internal pressure – an internal thin-walled cylinder with elastic-plastic behavior and a sleeve with orthotropic elastic behavior. The internal cylinder has an inner radius r_i and external radius r_o. The cylinder can be considered thin-walled if the wall thickness t is less than about 1/10 of the internal radius ($t < r_i/10$). The sleeve has an internal radius r_o and external radius r_e. The system is subjected to an internal pressure P_i as shown in Fig.1.

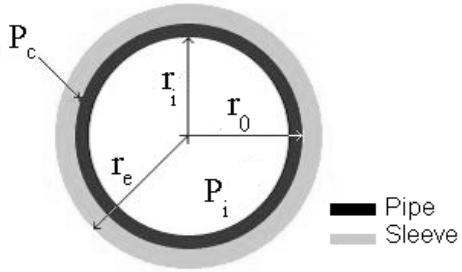

Figure 1: Pipe and sleeve with internal pressure.

The contact pressure between the pipe and the sleeve will be noted P_c. Assuming that the radial displacement in the contact surface is the same for both cylinders, it is possible to obtain analytical expressions for the stress, strain and displacement fields. With this expressions, it can be obtained the minimum composite sleeve thickness in order to verify a given safety criterion.

Generally unidirectional glass reinforced epoxy is used for the sleeve (epoxy resin is the matrix and the reinforcement is glass fiber). Neglecting a decrease in time of the polymer composite strenght due to the environment, a closed-form of the radial displacement u_r in the sleeve can be obtained (see appendix)

$$u_r(r) = -BKr^{-K}\left(\frac{1}{E_{\theta\theta}} + \frac{\nu_{r\theta}}{E_{rr}}\right) + CKr^{K}\left(\frac{1}{E_{\theta\theta}} - \frac{\nu_{r\theta}}{E_{rr}}\right) \tag{1}$$

With

$$K = \sqrt{\frac{E_\theta}{E_r}} \tag{2}$$

$$B = \left(\frac{-P_c r_e^{(K-1)}}{\left[r_o^{-(K+1)} r_e^{(K-1)} - r_o^{(K-1)} r_e^{-(K+1)}\right]}\right) \tag{3}$$

$$C = \left(\frac{-P_c r_e^{-(K+1)}}{\left[r_o^{-(K+1)} r_e^{(K-1)} - r_o^{(K-1)} r_e^{-(K+1)} \right]} \right) \tag{4}$$

P_c is the contact pressure between the sleeve and pipe, E_θ the extensional modulus in the tangential direction and E_r the extensional modulus in the radial direction and $\nu_{r\theta}$ the coefficient relating contraction in the circumferential direction to extension in the radial direction. The radial displacement in the sleeve is a function of the contact pressure P_c which is not known "a priori". If the pipe wall is thin, it can be shown that the stress component σ_θ and the radial displacement u_r are approximated by the following expressions (see appendix)

$$\sigma_\theta = \frac{P_i r_i - P_c r_o}{r_o - r_i} \tag{5}$$

$$u_r = r \left[\frac{\sigma_\theta}{E} + \left\langle \frac{\sigma_\theta - \sigma_y}{K} \right\rangle^{\frac{1}{N}} \right] \tag{6}$$

where E is the Young modulus of the pipe material, σ_y the yield stress, K and N are material parameters that characterize the plastic behavior of the material. K is the coefficient of plastic resistance and N is the hardening exponent. The angular brackets have the following meaning: $\langle x \rangle = \max\{0, x\}$. The term (σ_θ / E) corresponds to the elastic deformation and the term $\left\langle \frac{\sigma_\theta - \sigma_y}{K} \right\rangle^{1/N}$ to the plastic deformation in the pipe. From the practical point of view, it is important to define the sleeve thickness in order to assure a given maximum hoop stress criterion in the pipe

$$\sigma_\theta < \sigma_{\max} \text{ in the pipe} \tag{7}$$

In this case, since the minimum contact (external) pressure $(P_c)_{min}$ acting on the pipe necessary to assure (7) can be obtained analytically

$$\sigma_\theta = \frac{P_i r_i - (P_c)_{\min} r_o}{r_o - r_i} = \sigma_{\max} \Rightarrow (P_c)_{\min} = \frac{P_i r_i - \sigma_{\max}(r_o - r_i)}{r_o} \tag{8}$$

the minimum sleeve thickness to assure (7) may be obtained from the following compatibility condition

$$[u_r(r = r_o)]_{pipe} - \hat{u} = [u_r(r = r_o)]_{sleeve} \tag{9}$$

where $\hat{u}$ is the radial displacement of the external surface of the pipe due to the internal pressure P_{apl} the pipe was submitted to when the reinforcement was applied

$$\hat{u} = r_o \left[\frac{\hat{\sigma}_\theta}{E} + \left\langle \frac{\hat{\sigma}_\theta - \sigma_y}{K} \right\rangle^{\frac{1}{N}} \right] \text{ with } \hat{\sigma}_\theta = \frac{P_{apl}\ r_i}{r_o - r_i} \tag{10}$$

Compatibility condition (9) assures that the radial displacement of outer surface of the pipe and the inner surface of the sleeve must be the same (contact surface). Using this condition and considering eqs. (1) - (4) and (8) it comes that the minimum external radius $(r_e)_{\min}$ to assure the constraint (7) is the root of the function Φ

$$\Phi(r_e) = r_o \overbrace{\left[\frac{\sigma_{\max}}{E} + \left\langle \frac{\sigma_{\max} - \sigma_y}{K} \right\rangle^{\frac{1}{N}}\right]}^{[u_r(r=r_o)]_{pipe}} - \hat{u} - \overbrace{\left[B(r_e)\sqrt{\frac{E_\theta}{E_r}}\, r_o^{-\sqrt{\frac{E_\theta}{E_r}}} \left(\frac{1}{E_\theta} + \frac{\nu_{r\theta}}{E_r}\right) + C(r_e)\sqrt{\frac{E_\theta}{E_r}}\, r_o^{\sqrt{\frac{E_\theta}{E_r}}} \left(\frac{1}{E_\theta} - \frac{\nu_{r\theta}}{E_r}\right)\right]}^{[u_r(r=r_o)]_{sleeve}} \tag{11}$$

Where

$$B(r_e) = \left(\frac{-(P_c)_{\min} r_e^{(K-1)}}{\left[r_o^{-(K+1)} r_e^{(K-1)} - r_o^{(K-1)} r_e^{-(K+1)}\right]} \right) \tag{12}$$

$$C(r_e) = \left(\frac{-(P_c)_{\min} r_e^{-(K+1)}}{\left[r_0^{-(K+1)} r_e^{(K-1)} - r_0^{(K-1)} r_e^{-(K+1)}\right]} \right) \tag{13}$$

$$(P_c)_{\min} = \frac{P_i r_i - \sigma_{\max}(r_0 - r_i)}{r_0} \tag{14}$$

The internal pressure P_{apl} the pipe is submitted to when the sleeve is applied is one of the most important variables in the application of reinforcement systems. The wrong choice of this pressure may result in ineffective reinforcements as it is discussed in Costa-Mattos et al [8]. If $P_{apl\mathrm{B}B}$ is closer to P_i, the reinforcement must be very thick and will only share hoop stresses with the sleeve when a pressure surge above the value P_i occurs. Most of commercial repair systems recognize that reducing pressure during repair is a good practice but this pressure reduction is not quantified and is not a mandatory requirement. The choice of $\sigma_{\max}$ is also very important in order to define the role of the sleeve reinforcement [8]. The most obvious choice is the von Mises criterion. The pipe won't be submitted to permanent deformation provided the hoop stress is smaller than the yield stress

$$\sigma_\theta < \sigma_y \Rightarrow \sigma_{\max} = \sigma_y \tag{15}$$

2.2 Accounting for a localized corrosion damage

The expressions presented up to now are valid only if there are no localized imperfections or damage in the pipe section. In this section, a simple procedure to account for a localized damage is proposed. The basic idea is to suppose the maximum hoop stress close to a localized imperfection can be approximated considering the tangential stress for an undamaged cylinder corrected by a factor η which is a function of the geometry

$$\sigma_\theta = \eta \ (\sigma_\theta)_{undamaged} = \eta \ \frac{P_i r_i - P_c r_o}{r_o - r_i} \tag{16}$$

Most "engineering safety criteria" for thin-walled pipelines consider expressions similar to (16) and the only basic difference is the definition of how the "correction factor" η depends on the geometry. Generally these criteria have the following form

$$\sigma_\theta = \eta \ \frac{P_i r_i - P_c r_o}{r_o - r_i} < \hat{\sigma}_{\max} \tag{17}$$

where $\hat{\sigma}_{\max}$ is a material constant. If a criterion like (17) is considered, the same equations proposed in the last section can be used taking $\sigma_{\max} = \frac{\hat{\sigma}_{\max}}{\eta}$

$$\sigma_\theta = \frac{P_i r_i - P_c r_o}{r_o - r_i} < \frac{\hat{\sigma}_{\max}}{\eta} = \sigma_{\max} \tag{18}$$

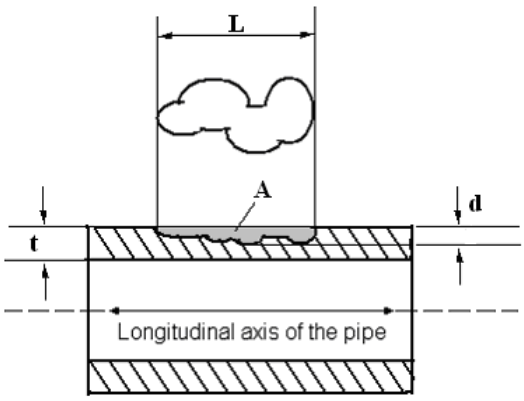

Figure 2: Metal loss in the pipe.

The adequate choice of the sleeve thickness assures that the maximum hoop stress verifies safety condition (17). The most widely used criteria for assessment of corrosion defects under internal pressure loading is a family of criteria described in Stephens and Francini [10] as the effective area methods. These include the ASME B31G criterion [11], the RSTENG 0.85 criterion (also Known as the modified B31G criterion). These criteria were developed in the beginning of the late 1960s and early 1970s to evaluate the serviceability of corroded gas transmission lines. The basic empirical assumption is that the strength loss due to corrosion is proportional to the amount of metal loss measured axially along the pipe. Other approaches can be considered (damage mechanics, assume that corrosion defects are blunt and hence they all fail by plastic collapse, etc.) but will not be discussed in the present paper. Other studies can be found in literature but in all of then the resulting metal loss is treated as a part-through defect in the pipe [12].

The effective area methods assume that the maximum depth profile lies in one plane along the axis of the pipe. To accommodate the irregular nature of most corrosion defects, a profile of the defect is measured and the deepest points are translated to a single axial plane for analysis, as illustrated in Fig. 2. These criteria may be expressed in the following form

$$\sigma_\theta < \bar{\sigma}\left[\frac{1-(A/A_o)}{1-(A/A_o)(M^T)^{-1}}\right] \Rightarrow \sigma_{\max} = \bar{\sigma}\left[\frac{1-(A/A_o)}{1-(A/A_o)(M^T)^{-1}}\right] \tag{19}$$

A is the area of defect in the longitudinal plane through the wall thickness, $A_o = Lt$ is the original cross-sectional area, M^T is the Folias factor for a through-wall defect, $\hat{\sigma}_{\max} = \bar{\sigma}$ in this case is the "flow stress", which is a computed parameter that is between the material's yield stress and ultimate strength. The B31G criterion assumes conservatively that $\bar{\sigma} = 1.1\,\sigma_y$ and also that the corrosion defect has a parabolic shape (this approximation results in the expression $A = (2/3)Ld$). Lastly, the B31G criterion uses a simplified two-term form of the Folias bulging factor that is applicable to $\left(L/\sqrt{2r_it}\right)^2 \leqslant 20.0$ and $(d/t) < 0.175$. Hence, from (19), it comes that

$$\begin{gathered}\sigma_\theta < 1.1\sigma_y\left[\frac{1-(2/3)(d/t)}{1-(2/3)(d/t)(M_1^T)^{-1}}\right];\ M_1^T = \sqrt{1+0.8\left(\frac{L}{2r_it}\right)^2} \\ \Rightarrow \sigma_{\max} = 1.1\sigma_y\left[\frac{1-(2/3)(d/t)}{1-(2/3)(d/t)(M_1^T)^{-1}}\right]\end{gathered} \tag{20}$$

The modified B31G criterion may be expressed in the following form

$$\sigma_\theta < \bar{\sigma}\left[\frac{1-0.85(d/t)}{1-0.85(d/t)(M_2^T)^{-1}}\right] \Rightarrow \sigma_{\max} = \bar{\sigma}\left[\frac{1-0.85(d/t)}{1-0.85(d/t)(M_2^T)^{-1}}\right] \tag{21}$$

with

$$\bar{\sigma} = \sigma_y + 68.94 \text{ MPa} \tag{22}$$

In this criterion the flow stress $\bar{\sigma}$ is given by the less conservative expression (22). In addition, rather than the parabolic shape resulting in the "2/3" area factor, this criterion utilizes the more accurate three-term expression (22) for the Folias bulging factor. These changes result in less conservative and more reliable estimates of failure pressure than the B31G criterion.

3 Epoxy repair systems for localized trough-thickness corrosion damage

In the present section it is proposed a complementary procedure to repair leaking defects in pipes using epoxy resins. The objective is to assure the pipe wont leak under the operation pressure and temperature. Composite sleeves can assure a satisfactory level of structural integrity for part-through corrosion defects but are not necessarily effective to avoid leakage for localized through-thickness corrosion defects. The repair methodology proposed in this section can be used or not associated with a composite sleeve in order to improve the effectiveness of the epoxy repair system.

The experimental set up at the laboratory was conceived to approximate a real repair operation, where the resin has to be applied in field conditions (which affect the quality of the resulting epoxy repair).

3.1 Defect sizing

The defect sizing is important to define limits to an effective use of the repair procedure. The dimension of the defect should be determined by the smaller ellipse with one axis parallel to the axis of the pipe that fully contains the area of the flaw (see Fig 3).

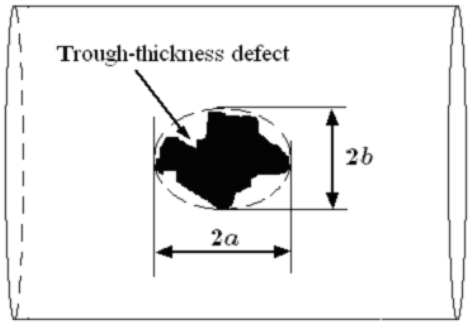

Figure 3: Defect sizing.

The maximum allowable defect size for the proposed repair procedure is defined by the semi major axis a of the ellipse which is given by:

$$a_{\max} \leqslant \max\left\{\frac{R}{10}, t\right\} \tag{23}$$

where R is the inner radius of the pipe and t the wall thickness. That means the maximum allowable dimension for the semi major axis a is the biggest value between the wall thickness t and $1/10$ of the inner radius R.

3.2 Proposed repair procedure

The repair methodology can be described as follows:

3.2.1 Surface preparation

Surface treatments often involve chemicals reactions, which produce surfaces modifications on adherends, or mechanical procedures, which improve adhesion by increasing mechanical interlocking of the adhesive to the adherend. By this way, the primary objective of a surface treatment is to increase the

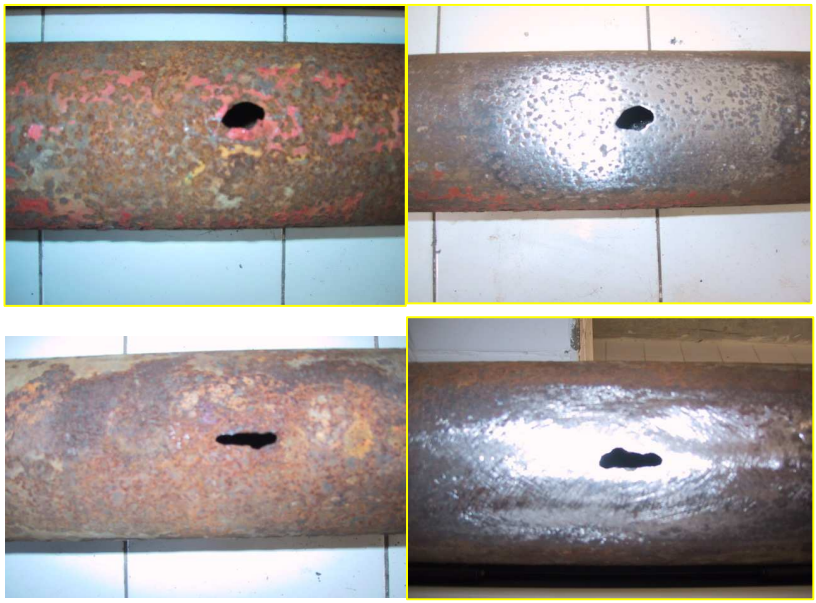

Figure 4: Surface preparation.

surface energy of the adherend as much as possible and/or improve the contact between the adhesive/adherend by increasing the contact area. Roughness or an increase in the surface area has been shown good results in improving adhesion. Subsequently, a relationship exists between good adhesion and bond durability.

In order to obtain the previous properties, sanding with sand paper 120 or 150 is used to achieve a white metal appearance and to remove some of the existing oxide layer. A final rinse with solvent was made to provide a free of oil, grease and dirt surface. After that the adhesive was mixed according to manufacture procedure and then the pipe was repaired. It is important to remark that, in a real situation, eventually the pipe is so corroded that sand paper should be used with extreme care (see Fig 4). Besides, since offshore platforms are hydrocarbon atmospheres, any method to mechanically rough up the surface (sandblasting, cutting, grinding) that may produce heat and sparkling is inadequate.

3.2.2 Introduction of a plastic cap inside the pipeline to avoid spilling of epoxy resin and application of the epoxy adhesive

A plastic cap with elliptical shape must be used to avoid resin to spill inside the pipe. Since the plastic material is very deformable, it is easy to introduce the cap inside the pipe. The cap is maintained in possition using a simple system of nylon strings (Fig. 5).

The cap should ensure internal layer of adhesive with approximately the same thickness of the

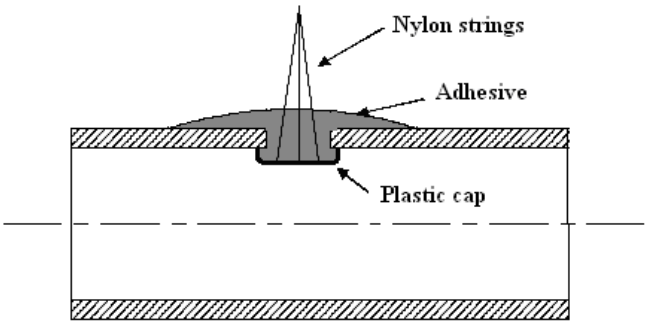

Figure 5: Plastic cap to avoid adhesive spilling.

pipe wall and with average dimension twice the size of the defect The Epoxy adhesive layer applied externally should have proximally 5 times the ellipse size. The thickness of this first layer must be at least equal to the thickness of the pipe. The epoxy layer should have a smooth boundary for improved performance and thickness higher than the pipe wall (see Fig 6). After application of the first layer, wait, according to manufacturer, the epoxy polymerization (maximum desirable 20 min), cut the the nylon strings at the surace and apply a second layer of adhesive without sanding the first one.

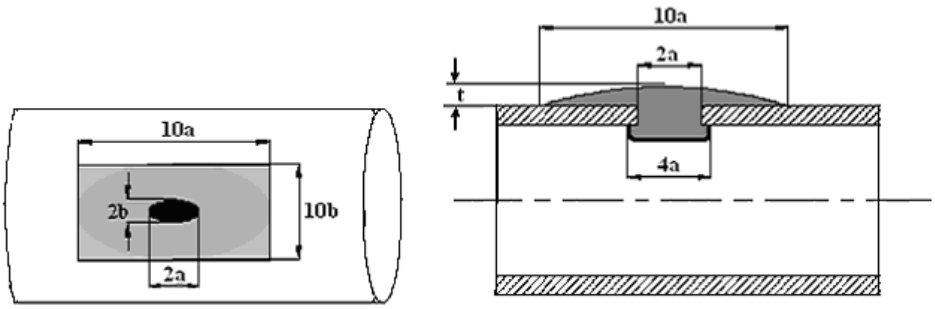

Figure 6: External epoxy adhesive layer.

For through-thickness defects with $a \leqslant 5mm$, it may be difficult to introduce the rubber cap and a metallic wedge should be used instead (Fig. 7). The following steps of the repair procedure are exactly the same if the wedge or caps are used.

3.2.3 Application of a composite sleeve

The repair procedure is considered safe, even without a composite sleeve when

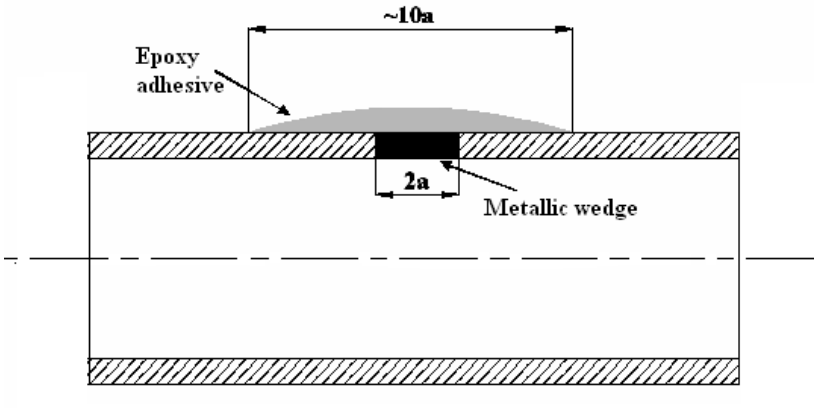

Figure 7: Metallic wedge for smaller defects.

$$\left(1+2\tfrac{a}{b}\right)\left(\frac{P_i r_i}{t}\right) \geqslant \sigma_y \tag{24}$$

where a and b are, respectively, the semi major and the semi minor axis of the ellipse (see section 3.1). r_i is the inner radius of the pipe, t the wall thickness and σ_y the yielding stress of the pipe material.

If constraint (24) is not verified, the suggestion is to apply the epoxy resin as described on this paper and then apply a composite material sleeve to restrain the plastic strain and to assure a satisfactory level of structural integrity. The adequate thickness of the sleeve is the biggest value between the thickness recommended by ISO/TS 24817 and the one obtained using the procedure presented in section 2 with

$$\sigma_{\max} = \frac{\sigma_y}{\left(1+2\tfrac{a}{b}\right)} \tag{25}$$

The stress distribution in a general through-thickness corrosion defect is very complex, but, if the size of the defect is limited, a rough estimative of the magnitude of the permanent deformations close to the defect can be performed. The term in the left side of Eq. (24) is the maximum stress in a thin-walled infinite plate with an elliptical defect with semi axis a and b subjected to traction of a uniform force per unit area $S = (P_i r_i/t)$ (see Fig. 8). The stress concentration factor in this case is $K_t = \left(1+2\tfrac{a}{b}\right)$. Criterion (24) states that the permanent deformation close to the defect in the pipe can be neglected when $K_t S$ is smaller than the yielding stress σ_y.

If (24) is verified, immediately after the application of the second epoxy layer, a rubber sheet should be applied over the repair around the perimeter and a simple metallic clamp, similar to those used for garden hoses, is attached (Fig. 9).

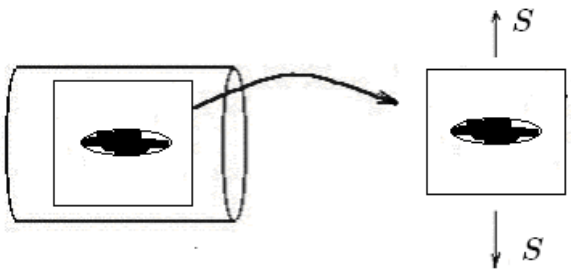

Figure 8: Equivalent system.

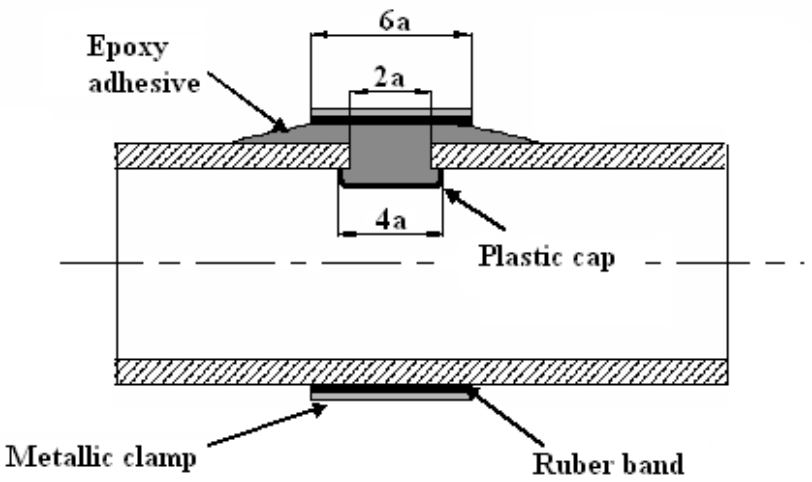

Figure 9: Complete repair system.

The clamp is not used to improve the level of structural integrity of the pipe, but to avoid the two major failure mechanisms of the adhesive repair shown in Fig. 10, mainly at the beginning of operation when the resin may not be fully cured.

In the following sections it is presented an analysis of the performance of two different commercial epoxy resins using the repair procedure defined in the previous sections.

In the following sections it is presented an analysis of the performance of two different commercial epoxy resins using the repair procedure defined in the previous sections.

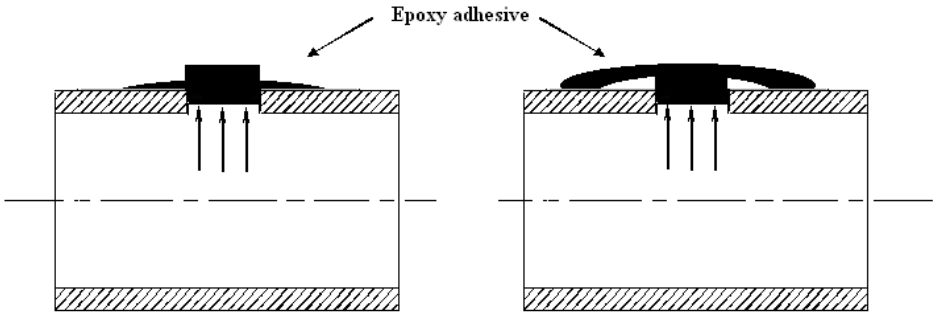

Figure 10: Types of brutal failures of the adhesive layer.

4 Materials and methods

Two different commercial fast curing epoxy resins were considered to perform the repair of through-thickness damages in metallic pipes using the methodology proposed in the previous section. Both are two-component systems consisting of a base and solidifier. The first one (System I) is conceived for leak repair on tanks and pipes as well as for other emergency applications. The product is based on a silicon steel alloy blended within high molecular weight polymers and oligomers and it is partly cured (machining and/or light loading) after 35 minutes at 25°C and it is fully cured after 1 hour at this temperature. Further technical data for System I is presented in table 1.

The second one (System II) is also a polymer-based system especially developed for repair consisting of a mixture of epoxy resin and aluminum powder and it is partly cured (machining and/or light loading) after 18 minutes at 25°C and it is fully cured after 40 minutes at this temperature. Further technical data for System II is presented in table 2.

The hydrostatic tests were performed at two different temperatures – room temperature and 80°C. An experimental set up was conceived to check the effectiveness of the methodology, trying to approximate a real repair operation. API 5L grade B steel pipes, normally used in offshore platform for produced water, were used to build the specimens for hydrostatic tests. Five different specimens were used:

1: 2”diameter schedule 80 pipe with a circular hole of 3 mm;
2: 2” diameter schedule 80 pipe with a circular hole of 10 mm;
3: 12” diameter, schedule 20, 1300 mm length pipe with a circular hole of 10 mm;
4: 12” diameter, schedule 20, 1300 mm length pipe with a circular hole of 30 mm;
5: 3,5” diameter, schedule 20, 1000 mm length pipes taken from the field with real corrosion defects (see Fig 4).

Initially all the repaired specimens (no composites sleeves were used) with the two systems were submitted to a classical hydrostatic test at room temperature to evaluate its strength and effectiveness. The maximum allowable time for each repair was 1 hour and all tests began exactly 1 hour and 15 minutes after the beginning of the procedure. In such tests, the pipe pressure is raised up to 30 kg/cm^2

and held at this level for an hour. After five cycles, if the repair did not fail brutally, the specimen is unloaded and inspected to check eventual small leaks or reinforcement rebounding.

As a second step, the repaired specimens (no sleeves were used, only the clamp) were submitted to 5 pressure cycles (1 hour at 30 kg/cm^2) but the water temperature inside the specimen was 80ºC. This temperature level was chosen in order to simulate average offshore fluid condition. The fluid temperature of 80ºC is reached at atmospheric pressure. Only after temperature stabilization, the internal pressure is increased. After each pressure cycle the specimen is cooled to room temperature. Hence, each specimen is also submitted to 5 temperature cycles during testing. Once again the maximum allowable time for each repair was 1 hour and all tests began exactly 1 hour and 15 minutes after the beginning of the repair.

5 Results and discussion

All repairs performed with Systems I and II using the proposed methodology resisted the 5 pressure cycles with water at room temperature - 5 different tests/repairs for each specimen (1), (2), (3), (4) and (5). The repairs resisted a so high pressure level that it was not possible to obtain the failure pressure – the pipe caps were not conceived to burst tests and they deform plastically and fail before the repairs. Fig. 11 shows a type 5 specimen before and after the repair procedure (internal pressure of 30 kg/cm^2).

If the proposed procedure is not adopted (mainly the use of the plastic cap), the repair may not be able to resist the loading. Table 3 shows the failure pressure obtained for specimen (2) – 2" diameter schedule 80 pipe with a circular hole of 10 mm – repaired using system I if no cap and clamp are used.

All repaired pipes with system II at 80ºC resisted to 5 cycles. In order to decide whether a given epoxy system can be used at higher temperatures we suggest to use the same conditions adopted in the ISO Technical Specification 24817 for composite sleeves - For a design temperature greater than 40ºC the repair system shall not be used at a temperature higher than the glass transition (*Tg*) less 30ºC. For repair systems where a *Tg* cannot be measured, the repair system shall not be used above a heat distortion temperature (HDT) less 20ºC. For repair systems, which do not exhibit a clear transition point, i.e. a significant reduction in mechanical properties at elevated temperatures, then an upper temperature limit, *Tm*, shall be defined (or quoted) by the repair supplier.

It is interesting to remark that the adhesive system A behaves surprisingly well if the proposed repair procedure is adopted, even at temperatures above the heat distortion temperature. All repairs resisted to 5 cycles at $80_{P}{}^{oP}$C in tests performed with the specimens (1), (2) and (3). Nevertheless, all repairs performed in pipes taken from the field with real corrosion defects (specimen type 5) failed.

6 Concluding remarks

The present work is a first step toward the definition of safer and more reliable procedures to apply epoxy repair systems in metallic pipelines with localized corrosion damage.

In the case of part-through corrosion damage, it is proposed a simplified methodology that can

Figure 11: 3,5" diameter, schedule 20, 1000 mm length pipe with real corrosion defect before and after repair.

be used as an auxiliary tool in the design of epoxy repair systems. This methodology can be helpful to define the pressure of application and sleeve thickness necessary to assure safer and more reliable repair systems.

In the case of through-thickness damage, the idea is to perform an adequate application of the epoxy filler in a way the pipe won't leak and to use eventually the composite sleeve as a complementary procedure that will assure a satisfactory level of structural integrity. The internal pressure of the fluid acting in the bottom of the repair and the external pressure done by the clamp (or the sleeve) dilate the epoxy system in the interior of the hole enhancing sealing. The suggestion is to apply the epoxy resin as described on this paper and then apply a composite material sleeve, with the normalized thickness, to restrain the plastic strain and to assure a satisfactory level of structural integrity. The main requirements to the epoxy resins to be used as repair systems for such kind of localized corrosion damage are: fast curing and high heat distortion temperature. The full validation

of this simplified repair methodology still requires an extensive program of experimental investigation, mainly concerning repair lifetime: fatigue, creep, ageing, resistance to UV degradation and weathering.

References

[1] Jaske, C.A., Hart, B.O. & Bruce, W.A., *Pipeline Repair Manual.* Pipeline Research Council International, Inc.: Virginia, 2006.
[2] ISO Technical Specification 24817, *Petroleum, petrochemical and natural gas industries. Composite repairs for pipework. Qualification and design, installation, testing and inspection*, 2006.
[3] Ouinas, D., Sahnoune, M., Benderdouche, N. & BachirBouiadjra, B., Sif analysis for notched cracked structure repaired by composite patching. *Materials and Design*, 2008. Doi:10.1016/j.matdes.2008.11.014.
[4] Ouinas, D., Bachir Bouiadjra, B., Achour, B. & Benderdouche, N., Modelling of a cracked aluminium plate repaired with composite octagonal patch in mode I and mixed mode. *Materials and Design*, **30**, pp. 590–595, 2009.
[5] Chapetti, M.D., Otegui, J.L., Manfredi, C. & Martins, C.F., Full scale experimental analysis of stress states in sleeve repairs of gas pipelines. *Int J Pressure Vessels Piping*, **78**, pp. 379–387, 2001.
[6] Otegui, J.L., Cisilino, A., Rivas, A.E., Chapetti, M. & Soula, G., Influence of multiple sleeve repairs on the structural integrity of gas pipelines. *Int J Pressure Vessels Piping*, **79**, pp. 759–765, 2002.
[7] Cisilino, A.P., Chapetti, M.D. & Otegui, J.L., Minimum thickness for circumferential sleeve repair fillet welds in corroded gas pipelines. *Int J Pressure Vessels Piping*, **79**, pp. 67–76, 2002.
[8] Costa-Mattos, H., Sampaio, R.F., Reis, J.M.L. & Perrut, V.A., Rehabilitation of corroded steel pipelines with epoxy repair systems. *Solid Mechanics In Brazil*, eds. M. Alves & H. Costa Mattos, Brazilian Society of Mechanical Sciences and Engineering Symposium Series: São Paulo, pp. 485–496, 2007.
[9] Goertzen, W.K. & Kessler, M.R., Dynamic mechanical analysis of carbon/epoxy composites for structural pipeline repair. *Composites Part B*, **38**, pp. 1–9, 2007.
[10] Stephens, D.R. & Francini, R.B., A review and evaluation of remaining strength criteria for corrosion defects in transmission pipelines. *ETCE2000/OGPT-10255, Proceedings of ETCE/OMAE2000 Joint Conference, Energy for the New Millennium*, New Orleans, USA, 2000.
[11] The American Society of Mechanical Engineers, New York, *Manual for Determining the Remaining Strength of Corroded Pipelines. A Supplement to ASME B31 Code for Pressure Piping, ASME B31G-1991 (Revision of ANSI/ASME B31G-1984)*, 1991.
[12] Duane, S.C. & Roy, J.P., Prediction of the failure pressure for complex corrosion defects. *Int J Pressure Vessels Piping*, **79**, pp. 279–287, 2002.

Appendix: Thin-walled elastic orthotropic and thin-walled elasto-plastic cylinders under pressure – closed-form expressions for stress, strain and displacements

A.1 Thick-walled elastic orthotropic cylinder under pressure

In the present study it is considered an elastic cylinder with inner radius r_i and external radius r_e submitted, respectively, to an internal pressure P_o and to an external pressure P_1 as shown in Fig. 12.

The model equations for this problem, using a cylindrical coordinates system are:

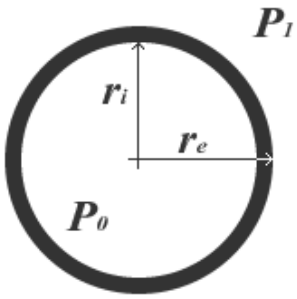

Figure 12: Pipe under external and internal pressure.

Balance of Linear momentum: Under the hypothesis of a plane state of stress and neglecting body forces, the balance of linear momentum for a pipe in static equilibrium can be expressed as

$$\frac{\partial \sigma_r}{\partial r} + \frac{1}{r}\frac{\partial \sigma_{r\theta}}{\partial \theta} + \frac{\sigma_r - \sigma_\theta}{r} = 0 \quad ; \quad \frac{1}{r}\frac{\partial \sigma_\theta}{\partial \theta} + \frac{\partial \sigma_{r\theta}}{\partial r} + \frac{2\sigma_{r\theta}}{r} = 0 \tag{A.1}$$

where σ_r and σ_θ are, respectively, the radial and tangential components of the stress tensor.

Constitutive equations: Assuming a linear orthotropic elastic behavior, the constitutive equations can be expressed as follows

$$\varepsilon_r = \frac{1}{E_r}\sigma_r - \frac{\nu_{r\theta}}{E_r}\sigma_\theta \quad ; \quad \varepsilon_\theta = -\frac{\nu_{r\theta}}{E_r}\sigma_r + \frac{1}{E_\theta}\sigma_\theta \quad ; \quad \varepsilon_{r\theta} = \frac{1}{2G_{r\theta}}\sigma_{r\theta} \tag{A.2}$$

where ε_r is the radial strain and ε_θ the tangential strain. E_θ the extensional modulus in the tangential direction and E_r the extensional modulus in the radial direction and $\nu_{r\theta}$ the coefficient relating contraction in the circumferential direction to extension in the radial direction. $G_{r\theta}$ is the shear modulus.

Geometric relations:

$$\varepsilon_\theta = \frac{u_r}{r} + \frac{1}{r}\frac{\partial u_\theta}{\partial \theta} \quad ; \quad \varepsilon_r = \frac{\partial u_r}{\partial r} \quad ; \quad \varepsilon_{r\theta} = \frac{1}{2}\left(\frac{1}{r}\frac{\partial u_r}{\partial \theta} + \frac{\partial u_\theta}{\partial r} - \frac{u_\theta}{r}\right) \tag{A.3}$$

where u_r is the radial displacement and u_θ the tangencial displacement.

In order to adequately model the problem, besides eqs. (A.1) - (A.3), it is necessary to provide the adequate set of boundary conditions:

$$\sigma_r|_{r=r_i} = -P_0 \quad ; \quad \sigma_r|_{r=r_e} = -P_1 \tag{A.4}$$

Equations (A.1) - (A.4) govern the behavior of an elastic orthotropic pipe. Such problem can be solved using the Airy stress function method. In this method, it is supposed to exist a differentiable function $\phi(r,\theta)$, called Airy function, such that

$$\sigma_r = \frac{1}{r}\frac{\partial \phi}{\partial r} + \frac{1}{r^2}\frac{\partial^2 \phi}{\partial \theta^2} \quad ; \quad \sigma_\theta = \frac{\partial^2 \phi}{\partial r^2} \quad ; \quad \sigma_{r\theta} = -\frac{\partial}{\partial r}\left(\frac{1}{r}\frac{\partial \phi}{\partial \theta}\right) \tag{A.5}$$

It is easy to verify that, if all relations in (A.5) are valid, then eqs. (A.1) are automatically satisfied. Assuming radial symmetry ($\phi(r,\theta) = \varphi(r)$), eqs. (A.5) can be reduced to:

$$\sigma_r = \frac{1}{r}\frac{d\varphi}{dr} \quad ; \quad \sigma_\theta = \frac{d^2\varphi}{dr^2} \quad ; \quad \sigma_{r\theta} = 0 \tag{A.6}$$

Introducing (A.6) in the constitutive equations (A.2), it is possible to obtain:

$$\varepsilon_r = \frac{1}{E_r}\frac{1}{r}\frac{d\varphi}{dr} - \frac{\nu_{r\theta}}{E_r}\frac{d^2\varphi}{dr^2} \quad ; \quad \varepsilon_\theta = -\frac{\nu_{r\theta}}{E_r}\frac{1}{r}\frac{d\varphi}{dr} + \frac{1}{E_\theta}\frac{d^2\varphi}{dr^2} \quad ; \quad \varepsilon_{r\theta} = 0 \tag{A.7}$$

The choice of a function $\varphi(r)$ that satisfies the boundary conditions (A.4) is not enough to assure the existence of strain fields u_r, u_θ that satisfy the geometric relations (A.3). Assuming that, due to the symmetry, $u_\theta = 0$, the geometric relations can be reduced to

$$\varepsilon_\theta = \frac{u_r}{r} \quad ; \quad \varepsilon_r = \frac{\partial u_r}{\partial r} \tag{A.8}$$

Once ε_θ is obtained from the second equation in (A.7), it is possible to determine u_r from the first geometric relation in (A.8). Using the geometric relations (A.8) it is simple to verify that the strain components ε_r and ε_θ must satisfy the following relation, called the compatibility equation of the problem

$$\frac{\partial \varepsilon_\theta}{\partial r} = \frac{1}{r}\left(\varepsilon_r - \varepsilon_\theta\right) \tag{A.9}$$

Hence, to make an adequate choice of φ and to satisfy the geometric relations, it is necessary to verify the compatibility equation (A.9). Introducing (A.7) in (A.9), it is possible to obtain

$$\frac{1}{E_\theta}\left[\frac{d^3\varphi}{dr^3} + \frac{1}{r}\frac{d^2\varphi}{dr^2}\right] - \frac{1}{E_r}\frac{1}{r^2}\frac{d\varphi}{dr} = 0 \tag{A.10}$$

The function φ that correspond to the solution of the problem (A.1)-(A.4) must be a solution of the ordinary differential equation (A.10). To solve this equation, it is interesting to perform the following change of variables: $r = e^t$. In this case, it is possible to obtain

$$\frac{d\varphi}{dr} = \frac{d\varphi}{dt}\frac{dt}{dr} = \frac{d\varphi}{dt}e^t \tag{A.11}$$

$$\frac{d^2\varphi}{dr^2} = \frac{d}{dr}\left(\frac{d\varphi}{dr}\right) = \frac{d}{dt}\left(\frac{d\varphi}{dt}e^t\right) = e^t\left(\frac{d^2\varphi}{dt^2} - \frac{d\varphi}{dt}\right) \tag{A.12}$$

$$\frac{d^3\varphi}{dr^3} = \frac{d}{dr}\left(\frac{d^2\varphi}{dr^2}\right) = \frac{d}{dt}\left[\left(\frac{d^2\varphi}{dt^2} - \frac{d\varphi}{dt}\right)e^t\right] = e^{-3t}\left(\frac{d^3\varphi}{dt^3} - 3\frac{d^2\varphi}{dt^2} + 2\frac{d\varphi}{dt}\right) \tag{A.13}$$

Using (A.11) - (A.13) and (A.10) it is possible to obtain the following linear ordinary differential equation

$$\frac{1}{E_\theta}\left[\frac{d^3\varphi}{dt^3} - 2\frac{d^2\varphi}{dt^2} + \frac{d\varphi}{dt}\right] - \frac{1}{E_r}\frac{d\varphi}{dt} = 0 \tag{A.14}$$

The general solution for Eq. (A.14) is

$$\varphi = \hat{A} + \hat{B}r^{\left(1-\sqrt{\frac{E_\theta}{E_r}}\right)} + \hat{C}r^{\left(1+\sqrt{\frac{E_\theta}{E_r}}\right)} \tag{A.15}$$

where $\hat{A}$, $\hat{B}$ and $\hat{C}$ are constants to be obtained from the boundary conditions. Finally, using (A.6) and (A.15), it is easy to verify that the stress components corresponding to that Airy function are

$$\sigma_r(r) = \frac{1}{r}\frac{d\varphi}{dr} = \hat{B}\left(1-\sqrt{\frac{E_\theta}{E_r}}\right) r^{-\left(\sqrt{\frac{E_\theta}{E_r}}+1\right)} + \hat{C}\left(1+\sqrt{\frac{E_\theta}{E_r}}\right) r^{\left(\sqrt{\frac{E_\theta}{E_r}}-1\right)} \tag{A.16}$$

$$\sigma_\theta(r) = \frac{d^2\varphi}{dr^2} = -\hat{B}\left(1-\sqrt{\frac{E_\theta}{E_r}}\right)\sqrt{\frac{E_\theta}{E_r}} r^{-\left(\sqrt{\frac{E_\theta}{E_r}}+1\right)} + \hat{C}\left(1+\sqrt{\frac{E_\theta}{E_r}}\right)\sqrt{\frac{E_\theta}{E_r}} r^{\left(\sqrt{\frac{E_\theta}{E_r}}-1\right)} \tag{A.17}$$

And, from the boundary conditions, it comes that

$$\hat{B} = \frac{P_1 r_i^{\left(\sqrt{\frac{E_\theta}{E_r}}-1\right)} - P_0 r_e^{\left(\sqrt{\frac{E_\theta}{E_r}}-1\right)}}{\left(1-\sqrt{\frac{E_\theta}{E_r}}\right)\left[r_i^{-\left(\sqrt{\frac{E_\theta}{E_r}}+1\right)} r_e^{\left(\sqrt{\frac{E_\theta}{E_r}}-1\right)} - r_i^{\left(\sqrt{\frac{E_\theta}{E_r}}-1\right)} r_e^{-\left(\sqrt{\frac{E_\theta}{E_r}}+1\right)}\right]} \tag{A.18}$$

$$\hat{C} = \frac{P_1 r_i^{-\left(\sqrt{\frac{E_\theta}{E_r}}+1\right)} - P_0 r_e^{-\left(\sqrt{\frac{E_\theta}{E_r}}+1\right)}}{\left(1-\sqrt{\frac{E_\theta}{E_r}}\right)\left[r_i^{\left(\sqrt{\frac{E_\theta}{E_r}}-1\right)} r_e^{-\left(\sqrt{\frac{E_\theta}{E_r}}+1\right)} - r_i^{-\left(\sqrt{\frac{E_\theta}{E_r}}+1\right)} r_e^{\left(\sqrt{\frac{E_\theta}{E_r}}-1\right)}\right]} \tag{A.19}$$

The radial displacement u_r is obtained from the second constitutive relation in (A.2)

$$u_r(r) = \left(1-\sqrt{\frac{E_\theta}{E_r}}\right)\left[-\hat{B}\sqrt{\frac{E_\theta}{E_r}} r^{-\sqrt{\frac{E_\theta}{E_r}}}\left(\frac{1}{E_\theta}+\frac{\nu_{r\theta}}{E_r}\right) + \hat{C}\sqrt{\frac{E_\theta}{E_r}} r^{\sqrt{\frac{E_\theta}{E_r}}}\left(\frac{1}{E_\theta}-\frac{\nu_{r\theta}}{E_r}\right)\right] \tag{A.20}$$

A.2 Thin-walled elasto-plastic cylinder under pressure

The study of a composite sleeve – metallic pipe system under an internal pressure P_i, as it is shown if Fig. 3 can be performed using the above equations, considering the pipe as an isotropic material, the glove as an anisotropic material and using the following compatibility relation to determine the contact pressure

$$[u_r(r=r_o)]_{pipe} - \hat{u} = [u_r(r=r_o)]_{sleeve} \tag{A.21}$$

Nevertheless, it is possible to show that, if the wall thickness t of the metallic pipe is less than about $1/10$ of the internal radius ($t < r_i/10$, the simplifying hypothesis of thin-walled structures can be adopted, since the computed contact pressure between pipe and sleeve are the same. In this case, it is considered only the tangential (hoop) stress component σ_θ, which has a very simple expression

$$\sigma_\theta = \frac{P_0 r_i - P_1 r_e}{r_e - r_i} \tag{A.22}$$

The advantage of using the thin-wall theory is that an inelastic behavior of the pipe can be easily included in the analysis. For a thin-walled metallic pipe undergoing inelastic deformations at room temperature, the elastic stress-strain relation is given by

$$\sigma_\theta = E(\varepsilon_\theta - \varepsilon_\theta^p) \tag{A.23}$$

with ε_θ^p being the tangential component of the plastic deformation. Besides this classic relation, it is necessary to give additional information about the relation between the stress the plastic deformation and. The following relation is is adequate to model monotonic loading histories in metallic materials

$$\sigma_\theta = \sigma_y + K\,(\varepsilon_\theta^p)^N, \text{ if } \quad \sigma_\theta > \sigma_y \quad \Rightarrow \quad \varepsilon_\theta^p = \left\langle \frac{\sigma_\theta - \sigma_y}{K} \right\rangle^{\frac{1}{N}} \tag{A.24}$$

$\langle x \rangle = Max\{0, x\}$. σ_y is the yielding stress. K and n are positive constants that characterize the plastic behavior of the material. From (A.24) it is easy to verify that $\varepsilon_\theta^p = 0$ if $\sigma_\theta < \sigma_y$. It also follows that $\varepsilon_\theta = \frac{\sigma_\theta}{E} + \varepsilon_\theta^p$. Assuming that $\varepsilon_\theta \approx \frac{u_r}{r_i}$, it is possible to obtain the following expression for the radial displacement

$$u_r = r_i \left[\frac{\sigma_\theta}{E} + \left\langle \frac{\sigma_\theta - \sigma_y}{K} \right\rangle^{\frac{1}{N}} \right], \forall r \tag{A.25}$$

Mechanics of Solids in Brazil 2009, H.S. da Costa Mattos & Marcílio Alves (Editors)
Brazilian Society of Mechanical Sciences and Engineering, ISBN 978-85-85769-43-7

A finite strain rod model that incorporates general cross section deformation and its implementation by the Finite Element Method

Evandro R. Dasambiagio, Paulo M. Pimenta
and Eduardo M. B. Campello

Department of Structural and Geotechnical Engineering, Polytechnic School at the University of São Paulo, São Paulo/SP – Brazil

Abstract

A fully nonlinear geometrically-exact multi-parameter rod model is presented in this work for the analysis of beam structures undergoing arbitrarily large 3-D deformations. Our approach accounts for in-plane distortions of the cross-sections as well as for out-of-plane cross-sectional warping by means of cross-sectional degrees-of-freedom within the rod theory. With such a kinematical description, fully three-dimensional finite-strain constitutive equations are permitted in a totally consistent way. Proper representation of profile (distortional) deformations, which are typical of cold-formed thin-walled beam structures, may be attained and we believe this is a major feature of our formulation. The model is implemented via the finite element method and numerical examples are shown to assess the performance of the scheme.

Keywords: rods, cross-sectional deformations, finite rotations, finite strains, Finite Element Method.

1 Introduction

The main purpose of this work is to (i) present a fully nonlinear geometrically-exact multi-parameter rod model that allows for cross-sectional deformations and (ii) develop its finite element implementation. The formulation can be understood as an extension of our earlier works in [1–4], as presented in [5], in the sense that the restrictions to a rigid cross-section and to a St.-Venant-type elastic warping are now removed from the theory. The ideas for the kinematical description were first set by the authors in [6], however at that time only the general theoretical grounds were discussed and no numerical results were attained. In the present work, we exploit and further develop the concepts presented therein and derive the complete rod theory, together with its numerical implementation via the finite element method and related examples.

We follow a cross-section resultant approach and define the cross-sectional quantities in terms of first Piola-Kichhoff stresses and deformation gradient strains, based on the concept of a cross-section

Mechanics of Solids in Brazil 2009, H.S. da Costa Mattos & Marcílio Alves (Editors)
Brazilian Society of Mechanical Sciences and Engineering, ISBN 978-85-85769-43-7

director. Besides practical importance, the use of cross-sectional resultants simplifies the derivation of equilibrium equations and the enforcement of boundary conditions, in either weak and strong senses. In addition, the corresponding tangent of the weak form is obtained in a more expedient way, rendering always symmetric for hyperelastic materials and conservative loadings even far from equilibrium states.

The definition of a cross-section director plays a central role in our formulation. Accordingly, it allows for the introduction of independent degrees-of-freedom pertaining to the cross-sections to describe both the in-plane cross-sectional distortions and the out-of-plane cross-sectional warping. Fully three-dimensional finite-strain constitutive equations can therefore be adopted with no additional considerations nor condensations. This is a remarkable feature and up to our knowledge makes our model the first rod formulation as to permit general 3-D material laws for arbitrarily large strains. Hyperelasticity and finite elastoplasticity are thus made possible in a consistent way within the context of rods.

The Euler-Rodrigues formula is used to describe finite rotations in a total Lagrangean framework. We assume a straight reference configuration for the rod axis, but initially curved rods can also be considered if regarded as a stress-free deformed state from the straight position (see the ideas of [7, 8]).

Altogether, the present assumptions provide a consistent basis to the computational simulation of profile (distortional) deformations, which are typical of cold-formed thin-walled rod structures. We believe this is one of the major contributions of our work. For a historical background on the subject, we address the interested reader to the papers from [1, 2, 9–18] and references therein.

Throughout the text, italic Latin or Greek lowercase letters ($a, b, \ldots, \alpha, \beta, \ldots$) denote scalar quantities, bold italic Latin or Greek lowercase letters ($\boldsymbol{a}$, $\boldsymbol{b}$, $\ldots \boldsymbol{\alpha}, \boldsymbol{\beta}, \ldots$) denote vectors, bold italic Latin or Greek capital letters ($\boldsymbol{A}$, $\boldsymbol{B}$, $\ldots$) denote second-order tensors, bold calligraphic Latin capital letters ($\boldsymbol{\mathcal{A}}$, $\boldsymbol{\mathcal{B}}$, $\ldots$) denote third-order tensors and bold blackboard Latin capital letters ($\mathbb{A}$, $\mathbb{B}$, $\ldots$) denote fourth-order tensors in a three-dimensional Euclidean space. Vectors and matrices built up of tensor components on orthogonal frames (e.g. for computational purposes) are expressed by boldface upright Latin letters ($\mathbf{A}, \mathbf{B}, \ldots \mathbf{a}, \mathbf{b}, \ldots$). Summation convention over repeated indices is adopted in the entire text, with Greek indices ranging from 1 to 2 and Latin indices from 1 to 3.

2 The multi-parameter rod theory with general cross-sectional deformations

2.1 Kinematics

It is assumed at the outset that the rod is straight at the initial configuration, which is used as reference. Initially curved rods can be mapped by standard isoparametric means, or can be regarded as a stress-free deformed state from the straight reference position (see [7, 8]).

Let $\{\boldsymbol{e}_1^r, \boldsymbol{e}_2^r, \boldsymbol{e}_3^r\}$ be a local orthonormal system in the reference configuration, with $\boldsymbol{e}_3^r$ placed along the rod axis as depicted in Fig. 1. Cross-sectional planes in this configuration are uniquely defined by the vectors $\boldsymbol{e}_\alpha^r$. The position of the rod material points in the reference configuration can be described by

$$\boldsymbol{\xi} = \boldsymbol{\zeta} + \boldsymbol{a}^r, \tag{1}$$

where

$$\boldsymbol{\zeta} = \zeta \boldsymbol{e}_3^r, \quad \zeta \in \Omega = [0, \ell] \tag{2}$$

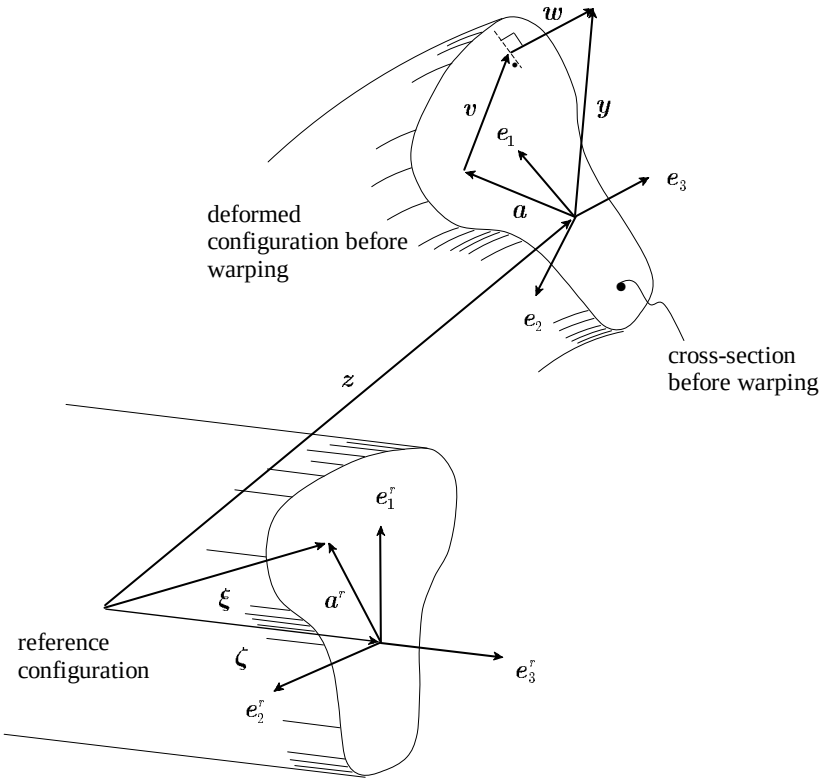

Figure 1: Rod description and basic kinematical quantities.

defines a point on the rod axis and

$$\boldsymbol{a}^r = \xi_\alpha \boldsymbol{e}_\alpha^r \tag{3}$$

is the cross-section director at this point. The axis-coordinate ζ defines the rod length ℓ in the reference configuration. Observe that $\{\xi_1, \xi_2, \zeta\}$ sets a three-dimensional Cartesian frame.

Let now $\{\boldsymbol{e}_1, \boldsymbol{e}_2, \boldsymbol{e}_3\}$ be a local orthonormal system on the current configuration, with $\boldsymbol{e}_\alpha$ attached to the cross-sectional plane before its warping. The rotation of the cross-section in the 3-D space is described by a rotation tensor $\boldsymbol{Q} = \hat{\boldsymbol{Q}}(\zeta)$, such that $\boldsymbol{e}_i = \boldsymbol{Q}\boldsymbol{e}_i^r$. In the current configuration, the position $\boldsymbol{x}$ of the material points (see Fig. 1) is given by the vector field

$$\boldsymbol{x} = \boldsymbol{z} + \boldsymbol{y} \ , \tag{4}$$

where $\boldsymbol{z} = \hat{\boldsymbol{z}}\,(\zeta)$ represents the current position of a point on the rod axis and $\boldsymbol{y}$ the position of the remaining points on the cross-section relative to the axis. We assume that the cross-sections are first rigidly rotated from the reference configuration, then undergo an in-plane deformation and then are warped in the out-of-plane direction, so that the vector $\boldsymbol{y}$ can be decomposed as follows

$$\boldsymbol{y} = \boldsymbol{a} + \boldsymbol{v} + \boldsymbol{w} \ . \tag{5}$$

Here,

$$\boldsymbol{a} = \boldsymbol{Q}\boldsymbol{a}^{r} \tag{6}$$

is the current cross-section director, representing the rotational part of the deformation,

$$\boldsymbol{v} = v_\beta \boldsymbol{e}_\beta \tag{7}$$

is the vector of in-plane (or transversal) displacements, describing the in-plane distortions of the cross-section, and

$$\boldsymbol{w} = w\boldsymbol{e}_3 \tag{8}$$

is the vector of out-of-plane displacements, embodying the cross-sectional warping. Notice that first-order shear deformations are accounted for, since $\boldsymbol{e}_3$ is not necessarily coincident with the deformed axis.

Several kinematical assumptions are possible for the vector of transversal displacements $\boldsymbol{v}$. Let $\boldsymbol{r} = \hat{\boldsymbol{r}}\,(\zeta)$ be a vector that collects the n_v cross-sectional transverse degrees-of-freedom, necessary to describe the cross-sectional in-plane distortions. We assume here that $\boldsymbol{v}$ is a linear function[1] of $\boldsymbol{r}$ such that

$$\boldsymbol{v} = \left(\boldsymbol{e}_\beta \otimes \boldsymbol{\phi}_\beta\right) \boldsymbol{r} \ , \tag{9}$$

where $\boldsymbol{\phi}_\beta = \hat{\boldsymbol{\phi}}_\beta\,(\xi_\alpha)$ are two vectors of cross-sectional shape functions describing the transversal distribution of the components of $\boldsymbol{v}$ on the cross-section. From (7), these components are given by

$$v_\beta = \boldsymbol{\phi}_\beta \cdot \boldsymbol{r} \ . \tag{10}$$

A number of expressions are possible for $\boldsymbol{\phi}_\beta$, according to the degree of refinement desired for the representation of the cross-sectional distortions. Here we adopt

[1] Nonlinear relations may be necessary for the modeling of local buckling in cold-formed thin-walled metallic profiles. This will be addressed in a forthcoming paper.

Mechanics of Solids in Brazil 2009, H.S. da Costa Mattos & Marcílio Alves (Editors)
Brazilian Society of Mechanical Sciences and Engineering, ISBN 978-85-85769-43-7

$$\boldsymbol{\phi}_1 = \begin{bmatrix} \xi_1 \\ 1/2\xi_1^2 \\ \xi_1\xi_2 \end{bmatrix} , \quad \boldsymbol{\phi}_2 = \begin{bmatrix} \xi_2 \\ \xi_1\xi_2 \\ 1/2\xi_2^2 \end{bmatrix} \quad \text{and} \quad \boldsymbol{r} = \begin{bmatrix} r_1 \\ r_2 \\ r_3 \end{bmatrix} , \tag{11}$$

with quadratic functions on the two local directions $\boldsymbol{e}_\beta$, as this is the simplest kinematical assumption valid for both membrane and bending dominated deformations in isotropic materials. Notice that in this case $n_v = 3$, i.e. three cross-sectional transverse degrees-of-freedom are necessary for the complete description. It is not difficult to realize that r_1 is important for stretching-dominated situations, while r_2 and r_3 are imperative for the bending-dominated ones. Other possibilities for $\boldsymbol{\phi}_\beta$ are discussed in detail in [6].

There is also a number of possible kinematical assumptions for the out-of-plane displacements $\boldsymbol{w}$ due to warping. Analogously to (9), let us write these displacements as

$$\boldsymbol{w} = (\boldsymbol{e}_3 \otimes \boldsymbol{\psi})\, \boldsymbol{p} \,, \tag{12}$$

where $\boldsymbol{p} = \hat{\boldsymbol{p}}\,(\zeta)$ is a vector that collects the n_w cross-sectional out-of-plane degrees-of-freedom describing the warping of the cross-section, and $\boldsymbol{\psi} = \hat{\boldsymbol{\psi}}\,(\xi_\alpha)$ is a vector of corresponding warping shape functions ψ_w. According to (12) the component w of (8) on the current local system is given by

$$w = \boldsymbol{\psi} \cdot \boldsymbol{p} \,. \tag{13}$$

Consideration of $\boldsymbol{w}$ is of central importance in torsion- and other shear-dominated deformations. Again, several expressions are possible for $\boldsymbol{\psi}$ and aiming simplicity (but without loss of generality) we assume here that

$$\boldsymbol{\psi} = [\xi_1\xi_2] \quad \text{and} \quad \boldsymbol{p} = [p] \,, \tag{14}$$

i.e. $n_w = 1$ and $p = \hat{p}\,(\zeta)$ is the only cross-sectional degree-of-freedom describing the warping deformation. It is not difficult to realize that in this case p represents the warping magnitude and $\psi = \xi_1\xi_2$ is the warping shape. Adoption of such a simple shape function for description of the warping may be understood as the simplest choice possible within the theory, and is valid as a first approximation for the warping of any type of cross-section (notice that for rectangular sections the choice in (14) corresponds to the St.-Venant warping function from the Saint-Venant's torsion theory). More elaborated sets for (14) are discussed in [6].

According to Fig. 1, the displacements of the points on the rod axis can be computed by

$$\boldsymbol{u} = \boldsymbol{z} - \boldsymbol{\zeta} \,. \tag{15}$$

The rotation tensor $\boldsymbol{Q}$, describing the rotation of the cross-sections, may be expressed in terms of the Euler rotation vector $\boldsymbol{\theta}$, by means of the well-known Euler-Rodrigues formula

$$\boldsymbol{Q} = \boldsymbol{I} + h_1\,(\theta)\, \boldsymbol{\Theta} + h_2\,(\theta)\, \boldsymbol{\Theta}^2 \,. \tag{16}$$

In this case, $\theta = \|\boldsymbol{\theta}\|$ is the true rotation angle and

$$h_1(\theta) = \frac{\sin\theta}{\theta} \quad \text{and} \quad h_2(\theta) = \frac{1}{2}\left(\frac{\sin\theta/2}{\theta/2}\right)^2 \tag{17[2]}$$

are two trigonometric functions, with $\boldsymbol{\Theta} = \text{Skew}(\boldsymbol{\theta})$ as the skew-symmetric tensor whose axial vector is $\boldsymbol{\theta}$. Altogether, the components of $\boldsymbol{u}$, $\boldsymbol{\theta}$, $\boldsymbol{r}$ and $\boldsymbol{p}$ on a global Cartesian system constitute the $3+3+n_v+n_w$ parameters (or cross-sectional degrees-of-freedom) of this rod model.

From differentiation of (4) with respect to $\boldsymbol{\xi}$ one can evaluate the deformation gradient $\boldsymbol{F}$. After some algebra one gets

$$\boldsymbol{F} = \boldsymbol{x}_{,\alpha} \otimes \boldsymbol{e}_\alpha^r + \boldsymbol{x}' \otimes \boldsymbol{e}_3^r, \tag{18}$$

where we have used the notation $(\bullet)_{,\alpha} = \partial(\bullet)/\partial\xi_\alpha$ and $(\bullet)' = \partial(\bullet)/\partial\zeta$ for derivatives. With the aid of (4) through (8), the derivatives in (18) are

$$\boldsymbol{x}_{,\alpha} = \boldsymbol{a}_{,\alpha} + \boldsymbol{v}_{,\alpha} + \boldsymbol{w}_{,\alpha} \quad \text{and} \quad \boldsymbol{x}' = \boldsymbol{z}' + \boldsymbol{a}' + \boldsymbol{v}' + \boldsymbol{w}' \,, \tag{19}$$

in which

$$\begin{aligned}
&\boldsymbol{a}_{,\alpha} = \boldsymbol{Q}\boldsymbol{e}_\alpha^r \,, \quad \boldsymbol{v}_{,\alpha} = \left(\boldsymbol{\phi}_{\beta,\alpha}\cdot\boldsymbol{r}\right)\boldsymbol{Q}\boldsymbol{e}_\beta^r \,,\\
&\boldsymbol{w}_{,\alpha} = \left(\boldsymbol{\psi}_{,\alpha}\cdot\boldsymbol{p}\right)\boldsymbol{Q}\boldsymbol{e}_3^r \,, \quad \boldsymbol{a}' = \boldsymbol{Q}\left(\boldsymbol{\kappa}^r\times\boldsymbol{a}^r\right) \,,\\
&\boldsymbol{v}' = \boldsymbol{Q}\left[\left(\boldsymbol{\phi}_\beta\cdot\boldsymbol{r}'\right)\boldsymbol{e}_\beta^r + \boldsymbol{\kappa}^r\times\boldsymbol{v}^r\right] \quad \text{and}\\
&\boldsymbol{w}' = \boldsymbol{Q}\left[\left(\boldsymbol{\psi}\cdot\boldsymbol{p}'\right)\boldsymbol{e}_3^r + \boldsymbol{\kappa}^r\times\boldsymbol{w}^r\right] \,,
\end{aligned} \tag{20}$$

with

$$\boldsymbol{v}^r = v_\beta\boldsymbol{e}_\beta^r = \boldsymbol{Q}^T\boldsymbol{v} \quad \text{and} \quad \boldsymbol{w}^r = w\boldsymbol{e}_3^r = \boldsymbol{Q}^T\boldsymbol{w} \,. \tag{21}$$

Still in (20), the following vector has been introduced

$$\boldsymbol{\kappa}^r = \boldsymbol{\Gamma}^T\boldsymbol{\theta}' \,, \tag{22}$$

in which

$$\boldsymbol{\Gamma} = \boldsymbol{I} + h_2(\theta)\,\boldsymbol{\Theta} + h_3(\theta)\,\boldsymbol{\Theta}^2 \tag{23}$$

and

$$h_3(\theta) = \frac{1-h_1(\theta)}{\theta^2} \,. \tag{24}$$

Vector $\boldsymbol{\kappa}^r$ in (22) can be regarded as the back-rotated counterpart of $\boldsymbol{\kappa} = \text{axial}(\boldsymbol{K}) = \boldsymbol{\Gamma}\boldsymbol{\theta}'$, where $\boldsymbol{K} = \boldsymbol{Q}'\boldsymbol{Q}^T$ is a skew-symmetric tensor that shows up in the derivation of expressions (20). One can understand $\boldsymbol{K}$ as the tensor describing the specific rotations of the cross-sections.

[2]Singularities in $h_1(\theta)$ and $h_2(\theta)$ at $\theta = 0$ are straighforwardly removable.

Thus, the deformation gradient may be rewritten as

$$\boldsymbol{F} = \boldsymbol{Q}\left(\boldsymbol{I} + \boldsymbol{\gamma}_\alpha^r \otimes \boldsymbol{e}_\alpha^r + \boldsymbol{\gamma}_3^r \otimes \boldsymbol{e}_3^r\right) = \boldsymbol{Q}\boldsymbol{F}^r \ , \tag{25}$$

where $\boldsymbol{F}^r = \boldsymbol{I} + \boldsymbol{\gamma}_\alpha^r \otimes \boldsymbol{e}_\alpha^r + \boldsymbol{\gamma}_3^r \otimes \boldsymbol{e}_3^r$ is called the back-rotated deformation gradient and

$$\begin{aligned} \boldsymbol{\gamma}_\alpha^r &= \left(\boldsymbol{\phi}_{\beta,\alpha} \cdot \boldsymbol{r}\right) \boldsymbol{e}_\beta^r + \left(\boldsymbol{\psi}_{,\alpha} \cdot \boldsymbol{p}\right) \boldsymbol{e}_3^r \quad \text{and} \\ \boldsymbol{\gamma}_3^r &= \boldsymbol{\eta}^r + \boldsymbol{\kappa}^r \times \boldsymbol{y}^r + \left(\boldsymbol{\phi}_\beta \cdot \boldsymbol{r}'\right) \boldsymbol{e}_\beta^r + \left(\boldsymbol{\psi} \cdot \boldsymbol{p}'\right) \boldsymbol{e}_3^r \ . \end{aligned} \tag{26}$$

Here,

$$\boldsymbol{\eta}^r = \boldsymbol{Q}^T \boldsymbol{z}' - \boldsymbol{e}_3^r \ , \tag{27}$$

and $\boldsymbol{y}^r$ is the back-rotated counterpart of $\boldsymbol{y}$, i.e.

$$\boldsymbol{y}^r = \boldsymbol{a}^r + \boldsymbol{v}^r + \boldsymbol{w}^r = \boldsymbol{Q}^T \boldsymbol{y} \ . \tag{28}$$

It will be clear on next section that vectors $\boldsymbol{\eta}^r$ of (27) and $\boldsymbol{\kappa}^r$ of (22) can be understood as generalized cross-sectional strains.

The material velocity gradient is given by time differentiation of (25) (denoted by a superposed dot) as follows

$$\dot{\boldsymbol{F}} = \boldsymbol{\Omega}\boldsymbol{F} + \boldsymbol{Q}\left(\dot{\boldsymbol{\gamma}}_\alpha^r \otimes \boldsymbol{e}_\alpha^r + \dot{\boldsymbol{\gamma}}_3^r \otimes \boldsymbol{e}_3^r\right) \ , \tag{29}$$

where $\boldsymbol{\Omega} = \dot{\boldsymbol{Q}}\boldsymbol{Q}^T$ represents the cross-section spin tensor. The spin axial vector $\boldsymbol{\omega}$ is obtained in a similar way as to obtain the axial vector of $\boldsymbol{K}$, i.e. $\boldsymbol{\omega} = \text{axial}\left(\boldsymbol{\Omega}\right) = \boldsymbol{\Gamma}\dot{\boldsymbol{\theta}}$. Derivatives $\dot{\boldsymbol{\gamma}}_i^r$ of (29) are computed directly from (26), what yields

$$\begin{aligned} \dot{\boldsymbol{\gamma}}_\alpha^r &= \left(\boldsymbol{e}_\beta^r \otimes \boldsymbol{\phi}_{\beta,\alpha}\right) \dot{\boldsymbol{q}} + \left(\boldsymbol{e}_3^r \otimes \boldsymbol{\psi}_{,\alpha}\right) \dot{\boldsymbol{p}} \quad \text{and} \\ \dot{\boldsymbol{\gamma}}_3^r &= \dot{\boldsymbol{\eta}}^r + \dot{\boldsymbol{\kappa}}^r \times \boldsymbol{y}^r + \left[\left(\boldsymbol{\kappa}^r \times \boldsymbol{e}_3^r\right) \otimes \boldsymbol{\psi}\right] \dot{\boldsymbol{p}} + \left(\boldsymbol{e}_3^r \otimes \boldsymbol{\psi}\right) \dot{\boldsymbol{p}}' + \\ &\quad + \left[\left(\boldsymbol{\kappa}^r \times \boldsymbol{e}_\beta^r\right) \otimes \boldsymbol{\phi}_\beta\right] \dot{\boldsymbol{r}} + \left(\boldsymbol{e}_\beta^r \otimes \boldsymbol{\phi}_\beta\right) \dot{\boldsymbol{r}}' \ . \end{aligned} \tag{30}$$

In order to fully evaluate expressions (30), the time derivatives $\dot{\boldsymbol{\eta}}^r$ and $\dot{\boldsymbol{\kappa}}^r$ are needed. From (27) and (22), after some algebra it is possible to arrive at

$$\dot{\boldsymbol{\eta}}^r = \boldsymbol{Q}^T\left(\dot{\boldsymbol{u}}' + \boldsymbol{Z}'\boldsymbol{\Gamma}\dot{\boldsymbol{\theta}}\right) \quad \text{and} \quad \dot{\boldsymbol{\kappa}}^r = \boldsymbol{Q}^T\left(\boldsymbol{\Gamma}'\dot{\boldsymbol{\theta}} + \boldsymbol{\Gamma}\dot{\boldsymbol{\theta}}'\right) \ , \tag{31}$$

where $\boldsymbol{Z}' = \text{Skew}\left(\boldsymbol{z}'\right)$ and

$$\begin{aligned} \boldsymbol{\Gamma}' = {} & h_2\left(\theta\right)\boldsymbol{\Theta}' + h_3\left(\theta\right)\left(\boldsymbol{\Theta}\boldsymbol{\Theta}' + \boldsymbol{\Theta}'\boldsymbol{\Theta}\right) + \\ & + h_4\left(\theta\right)\left(\boldsymbol{\theta} \cdot \boldsymbol{\theta}'\right)\boldsymbol{\Theta} + h_5\left(\theta\right)\left(\boldsymbol{\theta} \cdot \boldsymbol{\theta}'\right)\boldsymbol{\Theta}^2 \ . \end{aligned} \tag{32}$$

Notice that in (32) $\boldsymbol{\Theta}' = \text{Skew}\left(\boldsymbol{\theta}'\right)$ and

$$h_4(\theta) = \frac{h_1(\theta) - 2h_2(\theta)}{\theta^2} \quad \text{and} \quad h_5(\theta) = \frac{h_2(\theta) - 3h_3(\theta)}{\theta^2} \tag{33[3]}$$

are two additional trigonometric functions.

2.2 Statics

Let the 1st Piola-Kirchhoff stress tensor be written as

$$\boldsymbol{P} = \boldsymbol{Q}\left(\boldsymbol{\tau}_\alpha^r \otimes \boldsymbol{e}_\alpha^r + \boldsymbol{\tau}_3^r \otimes \boldsymbol{e}_3^r\right) . \tag{34}$$

The quantities $\boldsymbol{\tau}_i^r$ are back-rotated stress vectors and act on cross-sectional planes whose normals on the reference configuration are $\boldsymbol{e}_i^r$. Expression (34) motivates the definition of a back-rotated 1st Piola-Kirchhoff stress tensor $\boldsymbol{P}^r$, such that

$$\boldsymbol{P}^r = \boldsymbol{Q}^T\boldsymbol{P} = \boldsymbol{\tau}_\alpha^r \otimes \boldsymbol{e}_\alpha^r + \boldsymbol{\tau}_3^r \otimes \boldsymbol{e}_3^r . \tag{35}$$

With the expressions for $\boldsymbol{P}$ and $\dot{\boldsymbol{F}}$, it is not difficult to show that the rod internal power per unit reference volume may be written as

$$\boldsymbol{P} : \dot{\boldsymbol{F}} = \boldsymbol{\tau}_\alpha^r \cdot \dot{\boldsymbol{\gamma}}_\alpha^r + \boldsymbol{\tau}_3^r \cdot \dot{\boldsymbol{\gamma}}_3^r , \tag{36}$$

where property $\boldsymbol{P}\boldsymbol{F}^T : \boldsymbol{\Omega} = 0$, arising from the local moment balance equation, was utilized. Introducing (30) into (36) and performing some manipulation with the cross products, one gets

$$\begin{aligned} \boldsymbol{P} : \dot{\boldsymbol{F}} = {} & \boldsymbol{\tau}_3^r \cdot \dot{\boldsymbol{\eta}}^r + \left(\boldsymbol{y}^r \times \boldsymbol{\tau}_3^r\right) \cdot \dot{\boldsymbol{\kappa}}^r + \\ & + \left[\left(\boldsymbol{\tau}_\alpha^r \cdot \boldsymbol{e}_3^r\right)\boldsymbol{\psi}_{,\alpha} + \left(\boldsymbol{\tau}_3^r \cdot \boldsymbol{\kappa}^r \times \boldsymbol{e}_3^r\right)\boldsymbol{\psi}\right] \cdot \dot{\boldsymbol{p}} + \left[\left(\boldsymbol{\tau}_3^r \cdot \boldsymbol{e}_3^r\right)\boldsymbol{\psi}\right] \cdot \dot{\boldsymbol{p}}' + \\ & + \left[\left(\boldsymbol{\tau}_\alpha^r \cdot \boldsymbol{e}_\beta^r\right)\boldsymbol{\phi}_{\beta,\alpha} + \left(\boldsymbol{\tau}_3^r \cdot \boldsymbol{\kappa}^r \times \boldsymbol{e}_\beta^r\right)\boldsymbol{\phi}_\beta\right] \cdot \dot{\boldsymbol{r}} + \left[\left(\boldsymbol{\tau}_3^r \cdot \boldsymbol{e}_\beta^r\right)\boldsymbol{\phi}_\beta\right] \cdot \dot{\boldsymbol{r}}' . \end{aligned} \tag{37}$$

Integration of (37) over the cross-section provides

$$\int_A \left(\boldsymbol{P} : \dot{\boldsymbol{F}}\right) dA = \boldsymbol{n}^r \cdot \dot{\boldsymbol{\eta}}^r + \boldsymbol{m}^r \cdot \dot{\boldsymbol{\kappa}}^r + \boldsymbol{\pi} \cdot \dot{\boldsymbol{p}} + \boldsymbol{\alpha} \cdot \dot{\boldsymbol{p}}' + \boldsymbol{\rho} \cdot \dot{\boldsymbol{r}} + \boldsymbol{\beta} \cdot \dot{\boldsymbol{r}}' , \tag{38}$$

in which

$$\begin{aligned} & \boldsymbol{n}^r = \textstyle\int_A \boldsymbol{\tau}_3^r dA , \quad \boldsymbol{m}^r = \textstyle\int_A \left(\boldsymbol{y}^r \times \boldsymbol{\tau}_3^r\right) dA , \\ & \boldsymbol{\pi} = \textstyle\int_A \left[\left(\boldsymbol{\tau}_\alpha^r \cdot \boldsymbol{e}_3^r\right)\boldsymbol{\psi}_{,\alpha} + \left(\boldsymbol{\tau}_3^r \cdot \boldsymbol{\kappa}^r \times \boldsymbol{e}_3^r\right)\boldsymbol{\psi}\right] dA , \quad \boldsymbol{\alpha} = \textstyle\int_A \left[\left(\boldsymbol{\tau}_3^r \cdot \boldsymbol{e}_3^r\right)\boldsymbol{\psi}\right] dA , \\ & \boldsymbol{\rho} = \textstyle\int_A \left[\left(\boldsymbol{\tau}_\alpha^r \cdot \boldsymbol{e}_\beta^r\right)\boldsymbol{\phi}_{\beta,\alpha} + \left(\boldsymbol{\tau}_3^r \cdot \boldsymbol{\kappa}^r \times \boldsymbol{e}_\beta^r\right)\boldsymbol{\phi}_\beta\right] dA \quad \text{and} \\ & \boldsymbol{\beta} = \textstyle\int_A \left[\left(\boldsymbol{\tau}_3^r \cdot \boldsymbol{e}_\beta^r\right)\boldsymbol{\phi}_\beta\right] dA \end{aligned} \tag{39}$$

are the generalized cross-sectional stresses energetically conjugated to the cross-sectional strains $\boldsymbol{\eta}^r$, $\boldsymbol{\kappa}^r$, $\boldsymbol{p}$, $\boldsymbol{p}'$, $\boldsymbol{r}$ and $\boldsymbol{r}'$. In this case, $\boldsymbol{n}^r$ is said to be the back-rotated cross-sectional forces and $\boldsymbol{m}^r$ the back-rotated cross-sectional moments (notice the effect of the in-plane-distortions and of the out-of-plane

[3]The singularities in $h_4(\theta)$ and $h_5(\theta)$ are also removable.

warping on the definition of $\boldsymbol{m}^r$). Vector $\boldsymbol{\pi}$ represents the axial bi-shears, $\boldsymbol{\alpha}$ the axial bi-moments, $\boldsymbol{\rho}$ the transversal bi-shears and $\boldsymbol{\beta}$ the transversal bi-moments.

It is important to remark that $\boldsymbol{\tau}_i^r$, $\boldsymbol{\gamma}_i^r$, $\boldsymbol{n}^r$, $\boldsymbol{m}^r$, $\boldsymbol{\eta}^r$, $\boldsymbol{\kappa}^r$, $\boldsymbol{p}$, $\boldsymbol{r}$, $\boldsymbol{\pi}$, $\boldsymbol{\alpha}$, $\boldsymbol{\rho}$ and $\boldsymbol{\beta}$ are not affected by superimposed rigid body motions and in this sense entirely fulfill objectivity requirements. We now collect these cross-sectional quantities into three vectors, as displayed below

$$\boldsymbol{\sigma} = \begin{bmatrix} \boldsymbol{n}^r \\ \boldsymbol{m}^r \\ \boldsymbol{\pi} \\ \boldsymbol{\alpha} \\ \boldsymbol{\rho} \\ \boldsymbol{\beta} \end{bmatrix}, \quad \boldsymbol{\varepsilon} = \begin{bmatrix} \boldsymbol{\eta}^r \\ \boldsymbol{\kappa}^r \\ \boldsymbol{p} \\ \boldsymbol{p}' \\ \boldsymbol{r} \\ \boldsymbol{r}' \end{bmatrix} \quad \text{and} \quad \boldsymbol{d} = \begin{bmatrix} \boldsymbol{u} \\ \boldsymbol{\theta} \\ \boldsymbol{p} \\ \boldsymbol{r} \end{bmatrix}. \tag{40}$$

Note that both $\boldsymbol{\sigma}$ and $\boldsymbol{\varepsilon}$ have $6 + 2\,(n_v + n_w)$ elements, whilst $\boldsymbol{d}$ encompasses the $6 + n_v + n_w$ cross-sectional degrees-of-freedom. Definitions in (40) allow us to write (38) as follows

$$\int_A \left(\boldsymbol{P} : \dot{\boldsymbol{F}}\right) dA = \boldsymbol{\sigma} \cdot \dot{\boldsymbol{\varepsilon}}\,. \tag{41}$$

Here, the time derivative $\dot{\boldsymbol{\varepsilon}}$ may be written in a very compact manner as

$$\dot{\boldsymbol{\varepsilon}} = \boldsymbol{\Psi}\boldsymbol{\Delta}\dot{\boldsymbol{d}}\,, \tag{42}$$

where

$$\boldsymbol{\Psi} = \begin{bmatrix} \bar{\boldsymbol{\Psi}} & \boldsymbol{O}_{6\times 2(n_v+n_w)} \\ \boldsymbol{O}_{2(n_v+n_w)\times 9} & \boldsymbol{I}_{2(n_v+n_w)} \end{bmatrix} \quad \text{and} \quad \boldsymbol{\Delta} = \begin{bmatrix} \bar{\boldsymbol{\Delta}} & \boldsymbol{O}_{9\times n_w} & \boldsymbol{O}_{9\times n_v} \\ \boldsymbol{O}_{n_w\times 9} & \boldsymbol{I}_{n_w} & \boldsymbol{O}_{n_w\times n_v} \\ \boldsymbol{O}_{n_w\times 9} & \boldsymbol{I}_{n_w}\frac{\partial}{\partial\zeta} & \boldsymbol{O}_{n_w\times n_v} \\ \boldsymbol{O}_{n_v\times 9} & \boldsymbol{O}_{n_v\times n_w} & \boldsymbol{I}_{n_v} \\ \boldsymbol{O}_{n_v\times 9} & \boldsymbol{O}_{n_v\times n_w} & \boldsymbol{I}_{n_v}\frac{\partial}{\partial\zeta} \end{bmatrix} \tag{43}$$

are respectively a $[6 + 2\,(n_v + n_w)]\times[9 + 2\,(n_v + n_w)]$ linear operator and a $[9 + 2\,(n_v + n_w)]\times(6 + n_v + n_w)$ differential operator. In (43) one has

$$\bar{\boldsymbol{\Psi}} = \begin{bmatrix} \boldsymbol{Q}^T & \boldsymbol{O} & \boldsymbol{Q}^T\boldsymbol{Z}'\boldsymbol{\Gamma} \\ \boldsymbol{O} & \boldsymbol{Q}^T\boldsymbol{\Gamma} & \boldsymbol{Q}^T\boldsymbol{\Gamma}' \end{bmatrix}_{6\times 9} \quad \text{and} \quad \bar{\boldsymbol{\Delta}} = \begin{bmatrix} \boldsymbol{I}\frac{\partial}{\partial\zeta} & \boldsymbol{O} \\ \boldsymbol{O} & \boldsymbol{I}\frac{\partial}{\partial\zeta} \\ \boldsymbol{O} & \boldsymbol{I} \end{bmatrix}_{9\times 6}, \tag{44}$$

which correspond exactly to $\boldsymbol{\Psi}$ and $\boldsymbol{\Delta}$ of [1–4].

With (41) at hand, the rod internal power on a domain $\Omega = [0, \ell]$ is then given by

$$P_{int} = \int_{\Omega} (\boldsymbol{\sigma} \cdot \dot{\boldsymbol{\varepsilon}})\, d\zeta \ . \tag{45}$$

The external power on the same domain $\Omega = [0, \ell]$ can be expressed by

$$P_{\text{ext}} = \int_{\Omega} \left(\int_{\Gamma} \boldsymbol{t} \cdot \dot{\boldsymbol{x}} d\Gamma + \int_{A} \boldsymbol{b} \cdot \dot{\boldsymbol{x}} dA \right) d\zeta \ , \tag{46}$$

where Γ is the contour of a cross-section, $\boldsymbol{t}$ is the external surface traction per unit reference area and $\boldsymbol{b}$ is the vector of body forces per unit reference volume. By time differentiation of (4), one has

$$\dot{\boldsymbol{x}} = \dot{\boldsymbol{u}} + \boldsymbol{\omega} \times \boldsymbol{y} + \left(\boldsymbol{e}_{\beta} \otimes \boldsymbol{\varphi}_{\beta} \right) \dot{\boldsymbol{r}} \ + (\boldsymbol{e}_3 \otimes \boldsymbol{\psi})\, \dot{\boldsymbol{p}} \ , \tag{47}$$

which can be introduced into (46) so that

$$P_{\text{ext}} = \int_{\Omega} \left(\bar{\boldsymbol{q}} \cdot \dot{\boldsymbol{d}} \right) d\zeta \ , \tag{48}$$

where

$$\bar{\boldsymbol{q}} = \begin{bmatrix} \bar{\boldsymbol{n}} \\ \bar{\boldsymbol{\mu}} \\ \bar{\boldsymbol{\alpha}} \\ \bar{\boldsymbol{\beta}} \end{bmatrix} \ . \tag{49}$$

In this expression the following generalized external forces have been introduced

$$\begin{aligned} &\bar{\boldsymbol{n}} = \textstyle\int_{\Gamma} \boldsymbol{t} d\Gamma + \int_{A} \boldsymbol{b} dA \ , \\ &\bar{\boldsymbol{\mu}} = \boldsymbol{\Gamma}^{T} \bar{\boldsymbol{m}} \ , \quad \text{with} \quad \bar{\boldsymbol{m}} = \textstyle\int_{\Gamma} \boldsymbol{y} \times \boldsymbol{t} d\Gamma + \int_{A} \boldsymbol{y} \times \boldsymbol{b} dA \ , \\ &\bar{\boldsymbol{\alpha}} = \textstyle\int_{\Gamma} (\boldsymbol{e}_3 \cdot \boldsymbol{t})\, \boldsymbol{\psi} d\Gamma + \int_{A} (\boldsymbol{e}_3 \cdot \boldsymbol{b})\, \boldsymbol{\psi} dA \quad \text{and} \\ &\bar{\boldsymbol{\beta}} = \textstyle\int_{\Gamma} (\boldsymbol{e}_{\beta} \cdot \boldsymbol{t})\, \boldsymbol{\phi}_{\beta} d\Gamma + \int_{A} (\boldsymbol{e}_{\beta} \cdot \boldsymbol{b})\, \boldsymbol{\phi}_{\beta} dA \ , \end{aligned} \tag{50}$$

where $\bar{\boldsymbol{n}}$ is the applied external force, $\bar{\boldsymbol{m}}$ the applied external moment, $\bar{\boldsymbol{\alpha}}$ the applied external axial bi-moments and $\bar{\boldsymbol{\beta}}$ the applied external transversal bi-moments, all per unit length of the rod axis in the reference configuration.

2.3 Equilibrium

In the same way as to obtain (45), one can have the expression for the rod internal virtual work on a domain $\Omega = [0, \ell]$ as follows

$$\delta W_{int} = \int_{\Omega} (\boldsymbol{\sigma} \cdot \delta \boldsymbol{\varepsilon})\, d\zeta \ , \quad \text{with} \quad \delta \boldsymbol{\varepsilon} = \boldsymbol{\Psi} \boldsymbol{\Delta} \delta \boldsymbol{d} \ . \tag{51}$$

The external virtual work on the same domain $\Omega = [0, \ell]$ may be evaluated similarly to (48), i.e.

$$\delta W_{\text{ext}} = \int_{\Omega} (\bar{\boldsymbol{q}} \cdot \delta \boldsymbol{d})\, d\zeta \,, \tag{52}$$

so that the rod local equilibrium can be stated by means of the virtual work theorem in a standard way:

$$\delta W = \delta W_{\text{int}} - \delta W_{\text{ext}} = 0 \quad \text{in } \Omega, \quad \forall \delta \boldsymbol{d} \,. \tag{53}$$

Introducing (51) and (52) into this expression, and performing partial integration on the terms with $\delta \boldsymbol{u}'$, $(\boldsymbol{\Gamma} \delta \boldsymbol{\theta})'$, $\delta \boldsymbol{p}'$ and $\delta \boldsymbol{r}'$, the following local equilibrium equations in Ω are obtained by standard arguments of variational calculus

$$\boldsymbol{n}' + \bar{\boldsymbol{n}} = \boldsymbol{o} \,, \tag{54a}$$

$$\boldsymbol{m}' + \boldsymbol{z}' \times \boldsymbol{n} + \bar{\boldsymbol{m}} = \boldsymbol{o} \,, \tag{54b}$$

$$\boldsymbol{\alpha}' - \boldsymbol{\pi} + \bar{\boldsymbol{\alpha}} = \boldsymbol{o} \quad \text{and} \tag{54c}$$

$$\boldsymbol{\beta}' - \boldsymbol{\rho} + \bar{\boldsymbol{\beta}} = \boldsymbol{o} \,. \tag{54d}$$

Here,

$$\boldsymbol{n} = \boldsymbol{Q}\boldsymbol{n}^r \quad \text{and} \quad \boldsymbol{m} = \boldsymbol{Q}\boldsymbol{m}^r \tag{55}$$

are the true cross-sectional force and couple resultants with respect to the current configuration. Equations (54a) and (54b) could be obtained by Statics as well.

The essential boundary conditions emanating from (53) are prescribed in terms of $\boldsymbol{d}$, i.e. $\boldsymbol{u}$, $\boldsymbol{\theta}$, $\boldsymbol{p}$ and $\boldsymbol{r}$. On the other hand, the natural boundary conditions are prescribed in terms of the static quantities $\boldsymbol{n}$, $\boldsymbol{\mu} = \boldsymbol{\Gamma}^T \boldsymbol{m}$, $\boldsymbol{\alpha}$ and $\boldsymbol{\beta}$. We draw the attention of the reader to fact that the pseudo-moment $\boldsymbol{\mu} = \boldsymbol{\Gamma}^T \boldsymbol{m}$ must be prescribed, and not purely $\boldsymbol{m}$ as one would expect.

2.4 Tangent of the weak form

The Gateaux derivative of δW in (53) with respect to $\boldsymbol{d}$, after some laborious manipulation, leads to the tangent bilinear form

$$\delta\,(\delta W) = \int_{\Omega} \left[(\boldsymbol{\Psi}\boldsymbol{\Delta}\delta\boldsymbol{d}) \cdot (\boldsymbol{D}\boldsymbol{\Psi}\boldsymbol{\Delta}\delta\boldsymbol{d}) + (\boldsymbol{\Delta}\delta\boldsymbol{d}) \cdot (\boldsymbol{G}\boldsymbol{\Delta}\delta\boldsymbol{d}) - \delta\boldsymbol{d} \cdot (\boldsymbol{L}\delta\boldsymbol{d}) \right] d\Omega \,, \tag{56}$$

in which

$$\boldsymbol{D} = \frac{\partial \boldsymbol{\sigma}}{\partial \boldsymbol{\varepsilon}} \,, \quad \boldsymbol{G} = \begin{bmatrix} \bar{\boldsymbol{G}} & \boldsymbol{O}_{9\times 2(n_v+n_w)} \\ \boldsymbol{O}_{2(n_v+n_w)\times 9} & \boldsymbol{O}_{2(n_v+n_w)\times 2(n_v+n_w)} \end{bmatrix} \quad \text{and} \quad \boldsymbol{L} = \frac{\partial \bar{\boldsymbol{q}}}{\partial \boldsymbol{d}} \,. \tag{57}$$

Operators $\boldsymbol{D}$ and $\boldsymbol{G}$ represent the constitutive contribution and the geometrical effects of the internal forces on the tangent operator, respectively. It is worth mentioning that operator $\bar{\boldsymbol{G}}$ in (57) is identical

to $\boldsymbol{G}$ of [1, 2] (where it was first derived, see appendix A for more details), what remarkably means that the consideration of cross-sectional in-plane distortions and out-of-plane warping does not introduce any additional geometric terms into (56). Consequently, $\boldsymbol{G}$ is a function of $\boldsymbol{n}^r$, $\boldsymbol{m}^r$, $\boldsymbol{u}$ and $\boldsymbol{\theta}$ only, remaining always symmetric even far from equilibrium states. Operator $\boldsymbol{L}$, however, stands for the geometrical effects of the external forces and depends directly on the character of the external loading, as one can see in (57)[4]. The bilinear form (56) is therefore symmetric whenever $\boldsymbol{D} = \boldsymbol{D}^T$ and $\boldsymbol{L} = \boldsymbol{L}^T$, i.e. whenever the material is hyperelastic (or whenever the stress integration algorithm for inelastic materials possesses a potential) and the external loading is locally conservative.

We introduce now the following tensors of elastic (or algorithmic) tangent moduli

$$\frac{\partial \boldsymbol{\tau}_i^r}{\partial \boldsymbol{\gamma}_j^r} = \boldsymbol{C}_{ij} \ . \tag{58}$$

With the aid of (58), together with the derivatives

$$\begin{aligned}
&\frac{\partial \boldsymbol{\gamma}_\alpha^r}{\partial \boldsymbol{\eta}^r} = \boldsymbol{O} \ , && \frac{\partial \boldsymbol{\gamma}_3^r}{\partial \boldsymbol{\eta}^r} = \boldsymbol{I} \ , \\
&\frac{\partial \boldsymbol{\gamma}_\alpha^r}{\partial \boldsymbol{\kappa}^r} = \boldsymbol{O} \ , && \frac{\partial \boldsymbol{\gamma}_3^r}{\partial \boldsymbol{\kappa}^r} = -\boldsymbol{Y}^r , \\
&\frac{\partial \boldsymbol{\gamma}_\alpha^r}{\partial \boldsymbol{p}} = \boldsymbol{e}_3^r \otimes \boldsymbol{\psi}_{,\alpha} \ , && \frac{\partial \boldsymbol{\gamma}_3^r}{\partial \boldsymbol{p}} = (\boldsymbol{\kappa}^r \times \boldsymbol{e}_3^r) \otimes \boldsymbol{\psi} \ , \\
&\frac{\partial \boldsymbol{\gamma}_\alpha^r}{\partial \boldsymbol{p}'} = \boldsymbol{O} \ , && \frac{\partial \boldsymbol{\gamma}_3^r}{\partial \boldsymbol{p}'} = \boldsymbol{e}_3^r \otimes \boldsymbol{\psi} \ , \\
&\frac{\partial \boldsymbol{\gamma}_\alpha^r}{\partial \boldsymbol{r}} = \boldsymbol{e}_\beta^r \otimes \boldsymbol{\phi}_{\beta,\alpha} \ , && \frac{\partial \boldsymbol{\gamma}_3^r}{\partial \boldsymbol{r}} = \left(\boldsymbol{\kappa}^r \times \boldsymbol{e}_\beta^r\right) \otimes \boldsymbol{\phi}_\beta \quad \text{and} \\
&\frac{\partial \boldsymbol{\gamma}_\alpha^r}{\partial \boldsymbol{r}'} = \boldsymbol{O} \ , && \frac{\partial \boldsymbol{\gamma}_3^r}{\partial \boldsymbol{r}'} = \boldsymbol{e}_\beta^r \otimes \boldsymbol{\phi}_\beta \ ,
\end{aligned} \tag{59}$$

where $\boldsymbol{Y}^r = \text{Skew}\,(\boldsymbol{y}^r)$, one can obtain the elements of $\boldsymbol{D}$ (see appendix B) by the chain rule. We remark that $\boldsymbol{D}$ is symmetric as long as

$$\boldsymbol{C}_{ij} = \boldsymbol{C}_{ji}^T \ . \tag{60}$$

3 Elastic constitutive equations

We assume the rod is made of a hyperelastic material that may undergo arbitrarily large strains. With this assumption, the developments presented in this section are general in the sense that they are derived for fully three-dimensional finite strain constitutive models. These achievements are only possible due to the three-dimensional character of our rod theory, which allows for a complete three-dimensional state of deformation for a point within the rod body. Objectivity requirements (in the

[4] More details on the operator $\boldsymbol{L}$ can be found in appendix C.

sense of [19, 20]) are automatically fulfilled by the use of objective strain measures. Extension to finite elastoplasticity is straightforward once a stress integration scheme within a time step is at hand.

3.1 General hyperelastic materials

We write the symmetric Green-Lagrange strain tensor as

$$\boldsymbol{E} = \frac{1}{2}\left(\boldsymbol{C} - \boldsymbol{I}\right) \ , \tag{61}$$

where

$$\boldsymbol{C} = \boldsymbol{F}^T\boldsymbol{F} = \left(\boldsymbol{F}^r\right)^T\boldsymbol{F}^r \tag{62}$$

is the right Cauchy-Green strain tensor. The second Piola-Kirchhoff stress tensor $\boldsymbol{S}$ is energetically conjugated to $\boldsymbol{E}$ and is such that $\boldsymbol{P} = \boldsymbol{F}\boldsymbol{S}$, or equivalently

$$\boldsymbol{P}^r = \boldsymbol{F}^r\boldsymbol{S}. \tag{63}$$

A general hyperelastic material can be fully described by a specific strain energy function $\psi = \hat{\psi}\left(\boldsymbol{E}\right)$, such that $\boldsymbol{S}$ is given by

$$\boldsymbol{S} = \frac{\partial\psi}{\partial\boldsymbol{E}} \ . \tag{64}$$

As a consequence, a fourth-order tensor of elastic tangent moduli for the pair $\{\boldsymbol{S}, \boldsymbol{E}\}$ can be defined as

$$\mathbb{D} = \frac{\partial\boldsymbol{S}}{\partial\boldsymbol{E}} = \frac{\partial^2\psi}{\partial\boldsymbol{E}^2} \ . \tag{65}$$

With the aid of the following third-order tensors

$$\boldsymbol{\mathcal{B}}_i = \frac{\partial\boldsymbol{E}}{\partial\boldsymbol{\gamma}_i^r} \ , \tag{66}$$

the relations

$$\boldsymbol{\tau}_i^r = \boldsymbol{\mathcal{B}}_i^T\boldsymbol{S} \tag{67}$$

can be readily derived from (63). From these last three expressions, and from (58), we arrive at

$$\boldsymbol{C}_{ij} = \boldsymbol{\mathcal{B}}_i^T\mathbb{D}\boldsymbol{\mathcal{B}}_j + \left(\boldsymbol{e}_i^r \cdot \boldsymbol{S}\boldsymbol{e}_j^r\right)\boldsymbol{I} \ , \tag{68}$$

with which $\boldsymbol{D}$ can be computed.

3.2 Isotropic hyperelastic materials

For isotropic hyperelasticity, the strain energy function ψ can be written in terms of the invariants of the right Cauchy-Green strain tensor $\boldsymbol{C}$. We adopt here the following set of invariants

$$I_1 = \boldsymbol{I} : \boldsymbol{C} \,, \quad I_2 = \frac{1}{2}\boldsymbol{I} : \boldsymbol{C}^2 \quad \text{and} \quad J = \det \boldsymbol{F} \,, \tag{69}$$

with which we write $\psi = \hat{\psi}\,(I_1, I_2, J)$. Using (63) and (64), the back-rotated first Piola-Kirchhoff stress tensor is then obtained via

$$\boldsymbol{P}^r = 2\boldsymbol{F}^r \left(\frac{\partial \psi}{\partial \boldsymbol{C}} \right) \,, \tag{70}$$

what yields

$$\boldsymbol{P}^r = \frac{\partial \psi}{\partial J} J (\boldsymbol{F}^r)^{-T} + 2\boldsymbol{F}^r \left(\frac{\partial \psi}{\partial I_1}\boldsymbol{I} + \frac{\partial \psi}{\partial I_2}\boldsymbol{C} \right) \tag{71}$$

if the chain rule is applied with the derivatives

$$\frac{\partial J}{\partial \boldsymbol{C}} = \frac{1}{2} J \boldsymbol{C}^{-1} \,, \quad \frac{\partial I_1}{\partial \boldsymbol{C}} = \boldsymbol{I} \quad \text{and} \quad \frac{\partial I_2}{\partial \boldsymbol{C}} = \boldsymbol{C} \,. \tag{72}$$

Conversely, as one can readily verify, if we write the back-rotated deformation gradient as

$$\boldsymbol{F}^r = \boldsymbol{f}_i^r \otimes \boldsymbol{e}_i^r \,, \tag{73}$$

where $\boldsymbol{f}_i^r = \boldsymbol{e}_i^r + \boldsymbol{\gamma}_i^r$ (see expression (25)), then

$$\begin{aligned} & J = (\boldsymbol{f}_1^r \times \boldsymbol{f}_2^r) \cdot \boldsymbol{f}_3^r \,, \\ & J(\boldsymbol{F}^r)^{-T} = \boldsymbol{g}_i^r \otimes \boldsymbol{e}_i^r \quad \text{and} \\ & \boldsymbol{F}^r \boldsymbol{C} = \left(\boldsymbol{f}_i^r \cdot \boldsymbol{f}_j^r \right) \boldsymbol{f}_i^r \otimes \boldsymbol{e}_j^r \,, \end{aligned} \tag{74}$$

in which

$$\boldsymbol{g}_1^r = \boldsymbol{f}_2^r \times \boldsymbol{f}_3^r \,, \quad \boldsymbol{g}_2^r = \boldsymbol{f}_3^r \times \boldsymbol{f}_1^r \quad \text{and} \quad \boldsymbol{g}_3^r = \boldsymbol{f}_1^r \times \boldsymbol{f}_2^r \,. \tag{75}$$

Introducing (74) into (71), one arrives at the following expression for the vector-columns of $\boldsymbol{P}^r$:

$$\boldsymbol{\tau}_i^r = \frac{\partial \psi}{\partial J}\boldsymbol{g}_i^r + 2\frac{\partial \psi}{\partial I_1}\boldsymbol{f}_i^r + 2\frac{\partial \psi}{\partial I_2}\left(\boldsymbol{f}_j^r \otimes \boldsymbol{f}_j^r \right) \boldsymbol{f}_i^r \,. \tag{76}$$

3.3 A neo-Hookean isotropic hyperelastic material

A simple poly-convex neo-Hookean material as proposed in [20, 21] is represented by the specific strain energy function

$$\psi\left(J, I_1\right) = \frac{1}{2}\lambda\left[\frac{1}{2}\left(J^2-1\right) - \ln J\right] + \frac{1}{2}\mu\left(I_1 - 3 - 2\ln J\right) \ , \tag{77}$$

in which λ and μ are material parameters (or Lamé coefficients). With this expression at hand, from (76) we get

$$\tau_i^r = \frac{1}{J}\left[\lambda\frac{1}{2}\left(J^2-1\right) - \mu\right]\boldsymbol{g}_i^r + \mu\boldsymbol{f}_i^r \ , \tag{78}$$

and then the tangent tensors of (58) are given by

$$\begin{aligned}\boldsymbol{C}_{ij} = &\left[\tfrac{1}{2}\lambda\left(1+\tfrac{1}{J^2}\right) + \tfrac{1}{J^2}\mu\right]\boldsymbol{g}_i^r\otimes\boldsymbol{g}_j^r + \mu\,\delta_{ij}\boldsymbol{I} + \\ &- \tfrac{1}{J}\left[\lambda\tfrac{1}{2}\left(J^2-1\right) - \mu\right]\varepsilon_{ijk}\,\mathrm{Skew}\left(\boldsymbol{f}_k^r\right) \ .\end{aligned} \tag{79}$$

Here, $\delta_{ij} = \boldsymbol{e}_i^r\cdot\boldsymbol{e}_j^r$ and $\varepsilon_{ijk} = \boldsymbol{e}_i^r\cdot\boldsymbol{e}_j^r\times\boldsymbol{e}_k^r$ are the usual Kronecker and permutation symbols, respectively. From (79), the constitutive matrix $\boldsymbol{D}$ can be computed.

4 Finite Element implementation

The description of the rod deformation generates a boundary value problem whose weak form (53) can be solved by several approximation techniques. We adopt here a Galerkin type of approximation, the trial functions of which are to be supplied by the finite element method. We write the finite element interpolation in a particular element e, $e = 1, \ldots N_e$, as follows

$$\boldsymbol{d} = \mathbf{N}\mathbf{p}_e \ , \tag{80}$$

where $\mathbf{N}$ is the matrix of element shape functions and $\mathbf{p}_e$ the vector of element nodal degrees-of-freedom. The vector of the residual nodal forces for a particular element is then obtained from (80) into (53), and after some algebra one gets

$$\mathbf{P}_e = \int_{\Omega_e}\left[\mathbf{N}^T\bar{\boldsymbol{q}} - \left(\boldsymbol{\Psi}\boldsymbol{\Delta}\mathbf{N}\right)^T\boldsymbol{\sigma}\right]\,d\zeta \ , \tag{81}$$

in which Ω_e is the element domain. The element tangent stiffness matrix is obtained by inserting (80) into (56), leading to

$$\mathbf{k}_e = \int_{\Omega_e}\left[\left(\boldsymbol{\Psi}\boldsymbol{\Delta}\mathbf{N}\right)^T\boldsymbol{D}\left(\boldsymbol{\Psi}\boldsymbol{\Delta}\mathbf{N}\right) + \left(\boldsymbol{\Delta}\mathbf{N}\right)^T\boldsymbol{G}\left(\boldsymbol{\Delta}\mathbf{N}\right) - \mathbf{N}^T\boldsymbol{L}\mathbf{N}\right]\,d\zeta \ . \tag{82}$$

Here it is important to remark that the linearization stated in (82) can be performed either before or after discretization. Assemblage of the global residual forces and of the global tangent stiffness may be done as usual by means of

$$\mathbf{R} = \sum_{e=1}^{N_e} \mathbf{A}_e^T \mathbf{P}_e \quad \text{and} \quad \mathbf{K} = \sum_{e=1}^{N_e} \mathbf{A}_e^T \mathbf{k}_e \mathbf{A}_e \ , \tag{83}$$

respectively, where $\mathbf{A}_e$ is the connectivity matrix relating the element nodal degrees-of-freedom $\mathbf{p}_e$ with the whole domain nodal degrees-of-freedom $\mathbf{r}$, i.e.

$$\mathbf{p}_e = \mathbf{A}_e \mathbf{r} \ . \tag{84}$$

Equilibrium is then stated by vanishing the global residual forces,

$$\mathbf{R}(\mathbf{r}) = \boldsymbol{o} \ , \tag{85}$$

what can be iteratively solved by the Newton method for the free degrees-of-freedom.

5 Numerical examples

The finite element expressions derived on the previous section were implemented into a finite element code and in the present section we assess the performance of our formulation by means of two numerical examples. Standard quadratic shape functions of Lagrangian type are adopted to construct $\mathbf{N}$. Reduced gaussian quadrature for computation of (81) and (82) is utilized, whereas integration of the constitutive equation over the cross-sections (i.e. integration of the expressions in appendix B) is performed using a 2×2 gaussian scheme. We remark that several other examples can be found in [5].

5.1 Example 1: pure stretching of a bar

A straight rod with free ends and rectangular cross-section $b \times h$ is subjected to a large tensile normal force $P = 3.75 \times 10^6$ as depicted in Fig. 2. With this example we want to show the ability of the formulation in capturing Poisson's effect when finite stretching occurs. The rod is discretized using four 3-noded elements along with symmetry conditions. We adopt $\nu = 0.499999$ in order to simulate incompressibility. In Fig. 2 one can see the deformed configuration obtained in true scale, and the final dimensions of the cross-sections are also shown (no in-plane distortion is observed as only homothetic deformation occurs). We remark that the rod volume is perfectly preserved, with $J = \det \boldsymbol{F} = 1.0$ being exactly attained in all elements at every converged configuration of the Newton iterations.

5.2 Example 2: pure bending of a bar

The simply supported rod with geometric and material properties shown in Fig. 3 is subjected to a pair of external bending moments M at both ends. The right end support is free to move in the horizontal direction and we apply M such that the rod undergoes a complete round-turn. Discretization is performed using four 3-noded elements, the same as in the previous example. In Fig. 4 one can see a graph of the end moments M against (i) the rotations θ in radians of the right-end section, (ii) the horizontal displacements u of the right-end and (iii) the mid-span vertical displacements v. A plot of

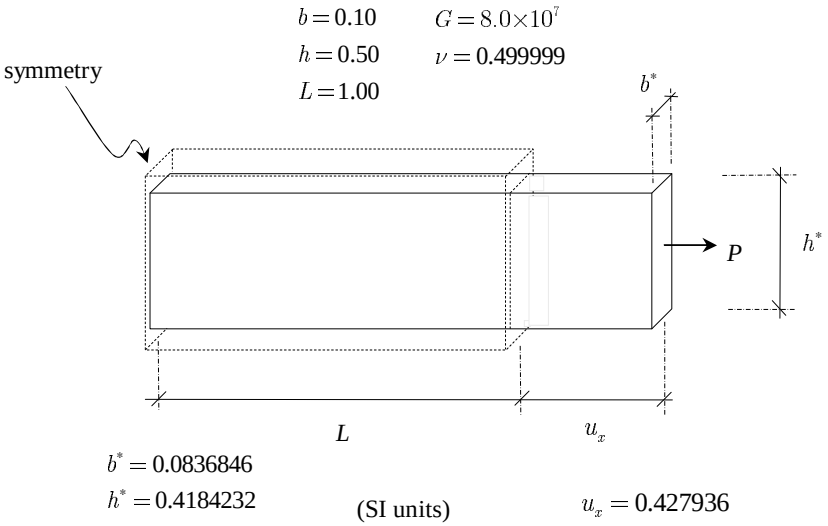

Figure 2: Pure stretching of a bar.

the deformed cross-sections is shown in Fig. 5 for $M = 1.4875 \times 10^6$, where a slight amplification factor is adopted to make the in-plane deformations visible. Notice that the deformation of the cross-sections is nearly the same along the rod's length. Notice, also, that the upper portion of the sections remains distented whereas the bottom part is shortened, as expected. Excellent convergence is found within the Newton solution procedure.

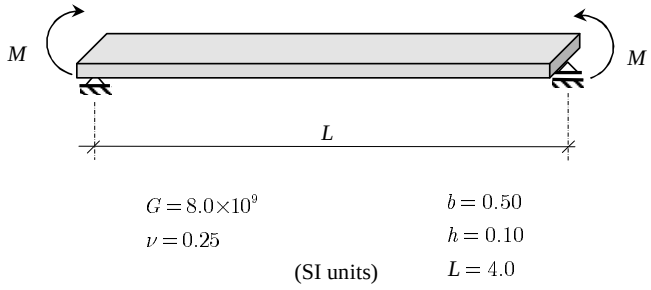

Figure 3: Pure bending of a bar.

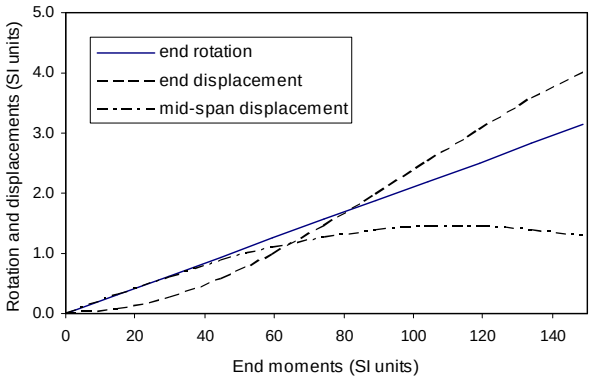

Figure 4: Displacements and rotation at pure bending of a bar.

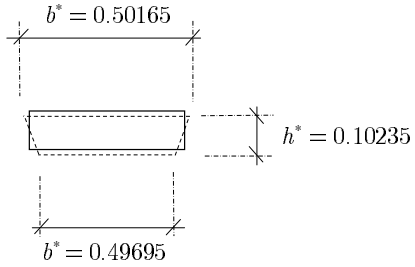

Figure 5: Cross section in-plane deformation at final moment for the pure bending of a bar.

6 Conclusions

In this work we revisit the geometrically-exact six-parameter rod model presented in [1–4] and extend it to a multi-parameter formulation that allows for general cross-sectional in-plane distortions and general out-of-plane warping. We start from the ideas set by the authors in [6], and derive the complete rod theory together with its numerical implementation via the finite element method. The key aspects are the definition of additional degrees of freedom pertaining to the cross-sections and the concept of a cross-section director. We follow a stress-resultant approach, with the cross-sectional resultants being defined based on first Piola-Kirchhoff stresses and deformation gradient strains. Finite rotations are described in a total Lagrangian way. The theory allows for a complete three-dimensional state of deformation for a point within the rod body and for this reason fully 3-D finite strain constitutive equations are possible to be adopted without any condensation. This is a remarkable feature and up to our knowledge makes our model the first rod formulation as to permit general 3-D material laws for arbitrarily large strains. The present assumptions provide a consistent basis to the computational simulation of profile (distortional) deformations, which are typical of cold-formed thin-walled rod

structures, and we believe this is one of the main contributions of our work. Several other examples presented in [5] further illustrate the robustness of the formulation.

Acknowledgements

First author acknowledges the University of São Paulo. Material support from IBNM (*Institut für Baumechanik und Numerische Mechanik*) of the Leibniz University of Hannover and from FAPESP (*Fundação de Amparo à Pesquisa do Estado de São Paulo*) under the grant 05/52453-2 are gratefully acknowledged by the second and third authors. Second author also acknowledges fellowship funding from CNPq (*Conselho Nacional de Desenvolvimento Tecnológico*) under the grant 305822/2006-3 and the *Mercator Gastprofessur* from DFG (*Deutsche Forschungsgemeinschaft*), which made possible his stay at the IBNM on a leave from the University of São Paulo.

References

[1] Pimenta, P.M. & Yojo, T., Geometrically-exact analysis of spatial frames. *Appl Mech Reviews, ASME*, **46(11)**, pp. 118–128, 1993.

[2] Pimenta, P.M., On a geometrically-exact finite-strain rod model. *Proceedings of the 3rd Pan-American Congress on Applied Mechanics, III PACAM*, São Paulo, 1993.

[3] Campello, E.M.B., *Análise não-linear de perfis metálicos conformados a frio*. Master's thesis, Escola Politécnica da Universidade de São Paulo, São Paulo, 2000. (in portuguese).

[4] Pimenta, P.M. & Campello, E.M.B., Geometrically nonlinear analysis of thin-walled space frames. *Proceedings of the Second European Conference on Computational Mechanics, II ECCM*, Cracow, 2001.

[5] Pimenta, P.M., Dasambiagio, E.R. & Campello, E.M.B., A truly finite strain rod model and its finite element implementation. *Submitted to journal Comput Meth Appl Mech Engrg*, 2009.

[6] Pimenta, P.M. & Campello, E.M.B., A fully nonlinear multi-parameter rod model incorporating general cross-sectional in-plane changes and out-of-plane warping. *Lat Amer J Solid Struct*, **1(1)**, pp. 119–140, 2003.

[7] Pimenta, P.M., Geometrically exact analysis of initially curved rods. *Advances in Computational Techniques for Structural Engineering*, Edinburgh, volume 1, pp. 99–108, 1996.

[8] Pimenta, P.M. & Campello, E.M.B., Shell curvature as an initial deformation: A geometrically-exact finite element approach. *Int J Numer Meth Engrg*, 2009. Published online, DOI 10.1002/nme.2528.

[9] Simo, J.C., A finite strain beam formulation. part I: The three-dimensional dynamic problem. *Comput Meth Appl Mech Engrg*, **49**, pp. 55–70, 1985.

[10] Simo, J.C. & Vu-Quoc, L., A three-dimesional finite strain rod model. part II: Computational aspects. *Comput Meth Appl Mech Engrg*, **58**, pp. 79–116, 1986.

[11] Cardona, A. & Geradin, M., A beam finite element non-linear theory with finite rotations. *Int J Numer Meth Engrg*, **26**, pp. 2403–38, 1988.

[12] Simo, J.C. & Vu-Quoc, L., A geometrically exact rod model incorporating shear and torsion-warping deformation. *Int J Solid Structures*, **27**, pp. 371–393, 1991.

[13] Ibrahimbegović, A. & Taylor, R.L., On the role of frame-invariance in structural mechanics models at finite rotations. *Comp Meth Appl Mech Engrg*, **191**, pp. 5159–5176, 2002.

[14] Crisfield, M.A. & Jelenić, G., Objectivity of strain measures in the geometrically-exact three-dimensional

beam theory and its finite element implementation. *Proc R Soc Lond*, **455**, pp. 1125–1147, 1999.
[15] Gruttmann, F. & Wagner, W., Geometrical and material nonlinear three-dimensional beams – theory and numerics. *Proceedings of the ECCM'99*, ed. W. Wunderlich, Munich, 1999.
[16] Jelenic, G. & Saje, M., A kinematically exact space finite strain beam model – finite element formulation by generalized virtual work principle. *Comput Meth Appl Mech Engrg*, **120**, pp. 131–161, 1995.
[17] Betsch, P. & Steinmann, P., Frame-indifferent beam finite elements based upon the geometrically-exact beam theory. *Int J Numer Methods Engrg*, **54**, pp. 1775–1788, 2002.
[18] Gruttmann, F., Sauer, R. & Wagner, W., A geometrical nonlinar eccentric 3D beam element with arbitrary cross-sections. *Comput Meth Appl Mech Engrg*, **160**, pp. 383–400, 1998.
[19] Bertram, A., *Elasticity and Plasticity of Large Deformations – An Introduction*. Springer-Verlag: Berlin-Heidelberg-New York, 2005.
[20] Ciarlet, P.J., *Mathematical Elasticity*, volume 1. North Holland, Amsterdam, 1988.
[21] Simo, J.C. & Hughes, T.J.R., *Computational Inelasticity*. Springer-Verlag: New York, 1998.

Appendix A

Tangent operator $\bar{\boldsymbol{G}}$ in (57) has the following structure

$$\bar{\boldsymbol{G}} = \begin{bmatrix} \boldsymbol{O} & \boldsymbol{O} & \boldsymbol{G}^{u'\theta} \\ \boldsymbol{O} & \boldsymbol{O} & \boldsymbol{G}^{\theta'\theta} \\ \boldsymbol{G}^{\theta u'} & \boldsymbol{G}^{\theta\theta'} & \boldsymbol{G}^{\theta\theta} \end{bmatrix} . \tag{86}$$

In order to derive the elements of (86), the following result is obtained by differentiation

$$\frac{\partial(\boldsymbol{\Gamma}^T\boldsymbol{t})}{\partial\boldsymbol{\theta}} = \boldsymbol{\Gamma}^T\frac{\partial\boldsymbol{t}}{\partial\boldsymbol{\theta}} + \boldsymbol{V}(\boldsymbol{\theta},\boldsymbol{t}) , \tag{87}$$

where $\boldsymbol{t}$ is a generic vector and

$$\begin{aligned} \boldsymbol{V}(\boldsymbol{\theta},\boldsymbol{t}) = h_2(\theta)\boldsymbol{T} + h_3(\theta)(\boldsymbol{T}\boldsymbol{\Theta} - 2\boldsymbol{\Theta}\boldsymbol{T}) + \\ -h_4(\theta)(\boldsymbol{\Theta}\boldsymbol{t}\otimes\boldsymbol{\theta}) + h_5(\theta)\left(\boldsymbol{\Theta}^2\boldsymbol{t}\otimes\boldsymbol{\theta}\right) , \end{aligned} \tag{88}$$

with $\boldsymbol{T} = \text{skew}(\boldsymbol{t})$. One can show that property

$$\boldsymbol{V}(\boldsymbol{\theta},\boldsymbol{t}) = \boldsymbol{V}^T(\boldsymbol{\theta},\boldsymbol{t}) + \boldsymbol{\Gamma}^T\boldsymbol{T}\boldsymbol{\Gamma} \tag{89}$$

holds for $\boldsymbol{V}(\boldsymbol{\theta},\boldsymbol{t})$, and this is a crucial result in proving the symmetry of (86). With the aid of (87) and (88) it is possible to write

$$\begin{aligned} &\boldsymbol{G}^{u'\theta} = \left(\boldsymbol{G}^{\theta u'}\right)^T = -\boldsymbol{N}\boldsymbol{\Gamma} , \\ &\boldsymbol{G}^{\theta\theta'} = \left(\boldsymbol{G}^{\theta'\theta}\right)^T = \boldsymbol{V}(\boldsymbol{\theta},\ \boldsymbol{m}) \quad \text{and} \\ &\boldsymbol{G}^{\theta\theta} = \left(\boldsymbol{G}^{\theta\theta}\right)^T = \boldsymbol{\Gamma}^T\boldsymbol{Z}'\boldsymbol{N}\boldsymbol{\Gamma} - \boldsymbol{V}(\boldsymbol{\theta},\ \boldsymbol{z}'\times\boldsymbol{n}) + \boldsymbol{V}'(\boldsymbol{\theta},\ \boldsymbol{\theta}',\ \boldsymbol{m}) - \boldsymbol{\Gamma}'^{\mathrm{T}}\boldsymbol{M}\boldsymbol{\Gamma} , \end{aligned} \tag{90}$$

in which $\boldsymbol{N} = \text{Skew}(\boldsymbol{n})$, $\boldsymbol{M} = S\text{kew}(\boldsymbol{m})$ and

$$\begin{aligned}\boldsymbol{V}'(\boldsymbol{\theta},\ \boldsymbol{\theta}',\ \boldsymbol{m}) = {} & h_3(\theta)\left(\boldsymbol{M}\boldsymbol{\Theta}' - 2\boldsymbol{\Theta}'\boldsymbol{M}\right) - h_4(\theta)\left(\boldsymbol{\Theta}'\boldsymbol{m}\otimes\boldsymbol{\theta} + \boldsymbol{\Theta}\boldsymbol{m}\otimes\boldsymbol{\theta}_{,\alpha}\right) + \\ & + h_5(\theta)\left(\left(\boldsymbol{\Theta}'\boldsymbol{\Theta} + \boldsymbol{\Theta}\boldsymbol{\Theta}'\right)\boldsymbol{m}\otimes\boldsymbol{\theta} + \boldsymbol{\Theta}^2\boldsymbol{m}\otimes\boldsymbol{\theta}'\right) + \\ & + (\boldsymbol{\theta}\cdot\boldsymbol{\theta}')\left[h_4(\theta)\,\boldsymbol{M} + h_5(\theta)\left(\boldsymbol{M}\boldsymbol{\Theta} - 2\boldsymbol{\Theta}\boldsymbol{M}\right)\right] + \\ & + (\boldsymbol{\theta}\cdot\boldsymbol{\theta}')\left[-h_6(\theta)\left(\boldsymbol{\Theta}\boldsymbol{m}\otimes\boldsymbol{\theta}\right) + h_7(\theta)\left(\boldsymbol{\Theta}^2\boldsymbol{m}\otimes\boldsymbol{\theta}\right)\right]\ .\end{aligned}$$

Here the following trigonometric functions have been introduced

$$h_6(\theta) = \frac{h_3(\theta) - h_2(\theta) - 4h_4(\theta)}{\theta^2} \quad \text{and} \quad h_7(\theta) = \frac{h_4(\theta) - 5h_5(\theta)}{\theta^2}\ . \tag{91[5]}$$

Appendix B

Tangent operator $\boldsymbol{D}$ in (57) has following structure

$$\boldsymbol{D} = \begin{bmatrix} \frac{\partial \boldsymbol{n}^r}{\partial \boldsymbol{\eta}^r} & \frac{\partial \boldsymbol{n}^r}{\partial \boldsymbol{\kappa}^r} & \frac{\partial \boldsymbol{n}^r}{\partial \boldsymbol{p}} & \frac{\partial \boldsymbol{n}^r}{\partial \boldsymbol{p}'} & \frac{\partial \boldsymbol{n}^r}{\partial \boldsymbol{r}} & \frac{\partial \boldsymbol{n}^r}{\partial \boldsymbol{r}'} \\ \frac{\partial \boldsymbol{m}^r}{\partial \boldsymbol{\eta}^r} & \frac{\partial \boldsymbol{m}^r}{\partial \boldsymbol{\kappa}^r} & \frac{\partial \boldsymbol{m}^r}{\partial \boldsymbol{p}} & \frac{\partial \boldsymbol{m}^r}{\partial \boldsymbol{p}'} & \frac{\partial \boldsymbol{m}^r}{\partial \boldsymbol{r}} & \frac{\partial \boldsymbol{m}^r}{\partial \boldsymbol{r}'} \\ \frac{\partial \boldsymbol{\pi}}{\partial \boldsymbol{\eta}^r} & \frac{\partial \boldsymbol{\pi}}{\partial \boldsymbol{\kappa}^r} & \frac{\partial \boldsymbol{\pi}}{\partial \boldsymbol{p}} & \frac{\partial \boldsymbol{\pi}}{\partial \boldsymbol{p}'} & \frac{\partial \boldsymbol{\pi}}{\partial \boldsymbol{r}} & \frac{\partial \boldsymbol{\pi}}{\partial \boldsymbol{r}'} \\ \frac{\partial \boldsymbol{\alpha}}{\partial \boldsymbol{\eta}^r} & \frac{\partial \boldsymbol{\alpha}}{\partial \boldsymbol{\kappa}^r} & \frac{\partial \boldsymbol{\alpha}}{\partial \boldsymbol{p}} & \frac{\partial \boldsymbol{\alpha}}{\partial \boldsymbol{p}'} & \frac{\partial \boldsymbol{\alpha}}{\partial \boldsymbol{r}} & \frac{\partial \boldsymbol{\alpha}}{\partial \boldsymbol{r}'} \\ \frac{\partial \boldsymbol{\rho}}{\partial \boldsymbol{\eta}^r} & \frac{\partial \boldsymbol{\rho}}{\partial \boldsymbol{\kappa}^r} & \frac{\partial \boldsymbol{\rho}}{\partial \boldsymbol{p}} & \frac{\partial \boldsymbol{\rho}}{\partial \boldsymbol{p}'} & \frac{\partial \boldsymbol{\rho}}{\partial \boldsymbol{r}} & \frac{\partial \boldsymbol{\rho}}{\partial \boldsymbol{r}'} \\ \frac{\partial \boldsymbol{\beta}}{\partial \boldsymbol{\eta}^r} & \frac{\partial \boldsymbol{\beta}}{\partial \boldsymbol{\kappa}^r} & \frac{\partial \boldsymbol{\beta}}{\partial \boldsymbol{p}} & \frac{\partial \boldsymbol{\beta}}{\partial \boldsymbol{p}'} & \frac{\partial \boldsymbol{\beta}}{\partial \boldsymbol{r}} & \frac{\partial \boldsymbol{\beta}}{\partial \boldsymbol{r}'} \end{bmatrix}\ . \tag{92}$$

The elements of (92) are displayed next.

[5]The singularities in $h_6(\theta)$ and $h_7(\theta)$ are also removable.

$$
\begin{aligned}
\frac{\partial \boldsymbol{n}^r}{\partial \boldsymbol{\eta}^r} &= \int_A \boldsymbol{C}_{33} dA \,, \\
\frac{\partial \boldsymbol{n}^r}{\partial \boldsymbol{\kappa}^r} &= -\int_A \boldsymbol{C}_{33} \boldsymbol{Y}^r dA \,, \\
\frac{\partial \boldsymbol{n}^r}{\partial \boldsymbol{p}} &= \int_A \left[\boldsymbol{C}_{3\alpha} \left(\boldsymbol{e}_3^r \otimes \boldsymbol{\psi}_{,\alpha} \right) + \left(\boldsymbol{C}_{33} \left(\boldsymbol{\kappa}^r \times \boldsymbol{e}_3^r \right) \right) \otimes \boldsymbol{\psi} \right] dA \,, \\
\frac{\partial \boldsymbol{n}^r}{\partial \boldsymbol{p}'} &= \int_A \boldsymbol{C}_{33} \left(\boldsymbol{e}_3^r \otimes \boldsymbol{\psi} \right) dA \,, \\
\frac{\partial \boldsymbol{n}^r}{\partial \boldsymbol{r}} &= \int_A \left[\left(\boldsymbol{C}_{3\gamma} \boldsymbol{e}_\beta^r \right) \otimes \boldsymbol{\phi}_{\beta,\gamma} + \left(\boldsymbol{C}_{33} \left(\boldsymbol{\kappa}^r \times \boldsymbol{e}_\beta^r \right) \right) \otimes \boldsymbol{\phi}_\beta \right] dA \,, \\
\frac{\partial \boldsymbol{n}^r}{\partial \boldsymbol{r}'} &= \int_A \left(\boldsymbol{C}_{33} \boldsymbol{e}_\beta^r \right) \otimes \boldsymbol{\phi}_\beta dA \,, \\
\frac{\partial \boldsymbol{m}^r}{\partial \boldsymbol{\eta}^r} &= \int_A \boldsymbol{Y}^r \boldsymbol{C}_{33} dA \,, \\
\frac{\partial \boldsymbol{m}^r}{\partial \boldsymbol{\kappa}^r} &= -\int_A \boldsymbol{Y}^r \boldsymbol{C}_{33} \boldsymbol{Y}^r dA \,, \\
\frac{\partial \boldsymbol{m}^r}{\partial \boldsymbol{p}} &= \int_A \left[(\boldsymbol{Y}^r \boldsymbol{C}_{3\alpha} \boldsymbol{e}_3^r) \otimes \boldsymbol{\psi}_{,\alpha} + (\boldsymbol{Y}^r \boldsymbol{C}_{33} (\boldsymbol{\kappa}^r \times \boldsymbol{e}_3^r)) \otimes \boldsymbol{\psi} + (\boldsymbol{e}_3^r \times \boldsymbol{\tau}_3^r) \otimes \boldsymbol{\psi} \right] dA \,, \\
\frac{\partial \boldsymbol{m}^r}{\partial \boldsymbol{p}'} &= \int_A (\boldsymbol{Y}^r \boldsymbol{C}_{33} \boldsymbol{e}_3^r) \otimes \boldsymbol{\psi} dA \,, \\
\frac{\partial \boldsymbol{m}^r}{\partial \boldsymbol{r}} &= \int_A \left[\left(\boldsymbol{Y}^r \boldsymbol{C}_{3\gamma} \boldsymbol{e}_\beta^r \right) \otimes \boldsymbol{\phi}_{\beta,\gamma} + \left(\boldsymbol{Y}^r \boldsymbol{C}_{33} \left(\boldsymbol{\kappa}^r \times \boldsymbol{e}_\beta^r \right) \right) \otimes \boldsymbol{\phi}_\beta + \left(\boldsymbol{e}_\beta^r \times \boldsymbol{\tau}_3^r \right) \otimes \boldsymbol{\phi}_\beta \right] dA \,, \\
\frac{\partial \boldsymbol{m}^r}{\partial \boldsymbol{r}'} &= \int_A \left(\boldsymbol{Y}^r \boldsymbol{C}_{33} \boldsymbol{e}_\beta^r \right) \otimes \boldsymbol{\phi}_\beta dA \,, \\
\frac{\partial \boldsymbol{\pi}}{\partial \boldsymbol{\eta}^r} &= \int_A \left[\boldsymbol{\psi}_{,\alpha} \otimes \left(\boldsymbol{C}_{\alpha 3}^T \boldsymbol{e}_3^r \right) + \boldsymbol{\psi} \otimes \left(\boldsymbol{C}_{33}^T \left(\boldsymbol{\kappa}^r \times \boldsymbol{e}_3^r \right) \right) \right] dA \,, \\
\frac{\partial \boldsymbol{\pi}}{\partial \boldsymbol{\kappa}^r} &= \int_A \left[\boldsymbol{\psi}_{,\alpha} \otimes \left(\boldsymbol{Y}^r \boldsymbol{C}_{\alpha 3}^T \boldsymbol{e}_3^r \right) + \boldsymbol{\psi} \otimes \left(\boldsymbol{Y}^r \boldsymbol{C}_{33}^T \left(\boldsymbol{\kappa}^r \times \boldsymbol{e}_3^r \right) \right) + \boldsymbol{\psi} \otimes \left(\boldsymbol{e}_3^r \times \boldsymbol{\tau}_3^r \right) \right] dA \,, \\
\frac{\partial \boldsymbol{\pi}}{\partial \boldsymbol{p}} &= \int_A \left[\left(\boldsymbol{e}_3^r \cdot \boldsymbol{C}_{\alpha\beta} \boldsymbol{e}_3^r \right) \left(\boldsymbol{\psi}_{,\alpha} \otimes \boldsymbol{\psi}_{,\beta} \right) + \left(\boldsymbol{e}_3^r \cdot \boldsymbol{C}_{\alpha 3} \left(\boldsymbol{\kappa}^r \times \boldsymbol{e}_3^r \right) \right) \left(\boldsymbol{\psi}_{,\alpha} \otimes \boldsymbol{\psi} \right) \right] dA + \\
&\quad + \int_A \boldsymbol{\psi} \otimes \left(\boldsymbol{\kappa}^r \times \boldsymbol{e}_3^r \right) \left[\boldsymbol{C}_{3\alpha} \left(\boldsymbol{e}_3^r \otimes \boldsymbol{\psi}_{,\alpha} \right) + \boldsymbol{C}_{33} \left(\boldsymbol{\kappa}^r \times \boldsymbol{e}_3^r \right) \otimes \boldsymbol{\psi} \right] dA \,, \\
\frac{\partial \boldsymbol{\pi}}{\partial \boldsymbol{p}'} &= \int_A \left[\left(\boldsymbol{\psi}_{,\alpha} \otimes \boldsymbol{e}_3^r \right) \boldsymbol{C}_{\alpha 3} \left(\boldsymbol{e}_3^r \otimes \boldsymbol{\psi} \right) + \boldsymbol{\psi} \otimes \left(\boldsymbol{\kappa}^r \times \boldsymbol{e}_3^r \right) \boldsymbol{C}_{33} \left(\boldsymbol{e}_3^r \otimes \boldsymbol{\psi} \right) \right] dA \,,
\end{aligned}
\tag{93}
$$

$$
\begin{aligned}
\frac{\partial \boldsymbol{\pi}}{\partial \boldsymbol{r}} &= \int_A \left(\boldsymbol{\psi}_{,\alpha} \otimes \boldsymbol{e}_3^r\right) \left[\boldsymbol{C}_{\alpha\gamma} \left(\boldsymbol{e}_\beta^r \otimes \boldsymbol{\phi}_{\beta,\gamma}\right) + \boldsymbol{C}_{\alpha 3} \left(\boldsymbol{\kappa}^r \times \boldsymbol{e}_\beta^r\right) \otimes \boldsymbol{\phi}_\beta\right] dA + \\
&\quad + \int_A \boldsymbol{\psi} \otimes \left(\boldsymbol{\kappa}^r \times \boldsymbol{e}_3^r\right) \left[\boldsymbol{C}_{3\gamma} \left(\boldsymbol{e}_\beta^r \otimes \boldsymbol{\phi}_{\beta,\gamma}\right) + \boldsymbol{C}_{33} \left(\kappa^r \times \boldsymbol{e}_\beta^r\right) \otimes \boldsymbol{\phi}_\beta\right] dA \,, \\
\frac{\partial \boldsymbol{\pi}}{\partial \boldsymbol{r}'} &= \int_A \left[\left(\boldsymbol{\psi}_{,\alpha} \otimes \boldsymbol{e}_3^r\right) \boldsymbol{C}_{\alpha 3} \left(\boldsymbol{e}_\beta^r \otimes \boldsymbol{\phi}_\beta\right) + \boldsymbol{\psi} \otimes \left(\boldsymbol{\kappa}^r \times \boldsymbol{e}_3^r\right) \boldsymbol{C}_{33} \left(\boldsymbol{e}_\beta^r \otimes \boldsymbol{\phi}_\beta\right)\right] dA \,, \\
\frac{\partial \boldsymbol{\alpha}}{\partial \boldsymbol{\eta}^r} &= \int_A \left(\boldsymbol{\psi} \otimes \boldsymbol{e}_3^r\right) \boldsymbol{C}_{33} dA \,, \\
\frac{\partial \boldsymbol{\alpha}}{\partial \boldsymbol{\kappa}^r} &= -\int_A \left(\boldsymbol{\psi} \otimes \boldsymbol{e}_3^r\right) \boldsymbol{C}_{33} \boldsymbol{Y}^r dA \,, \\
\frac{\partial \boldsymbol{\alpha}}{\partial \boldsymbol{p}} &= \int_A \left(\boldsymbol{\psi} \otimes \boldsymbol{e}_3^r\right) \left[\boldsymbol{C}_{3\alpha} \left(\boldsymbol{e}_3^r \otimes \boldsymbol{\psi}_{,\alpha}\right) + \boldsymbol{C}_{33} \left(\boldsymbol{\kappa}^r \times \boldsymbol{e}_3^r\right) \otimes \boldsymbol{\psi}\right] dA \,, \\
\frac{\partial \boldsymbol{\alpha}}{\partial \boldsymbol{p}'} &= \int_A \left(\boldsymbol{\psi} \otimes \boldsymbol{e}_3^r\right) \boldsymbol{C}_{33} \left(\boldsymbol{e}_3^r \otimes \boldsymbol{\psi}\right) dA \,, \\
\frac{\partial \boldsymbol{\alpha}}{\partial \boldsymbol{r}} &= \int_A \left(\boldsymbol{\psi} \otimes \boldsymbol{e}_3^r\right) \left[\boldsymbol{C}_{3\gamma} \left(\boldsymbol{e}_\beta^r \otimes \boldsymbol{\phi}_{\beta,\gamma}\right) + \boldsymbol{C}_{33} \left(\boldsymbol{\kappa}^r \times \boldsymbol{e}_\beta^r\right) \otimes \boldsymbol{\phi}_\beta\right] dA \,, \\
\frac{\partial \boldsymbol{\alpha}}{\partial \boldsymbol{r}'} &= \int_A \left(\boldsymbol{\psi} \otimes \boldsymbol{e}_3^r\right) \boldsymbol{C}_{33} \left(\boldsymbol{e}_\beta^r \otimes \boldsymbol{\phi}_\beta\right) dA \,, \\
\frac{\partial \boldsymbol{\rho}}{\partial \boldsymbol{\eta}^r} &= \int_A \left[\left(\boldsymbol{\phi}_{\delta,\alpha} \otimes \boldsymbol{e}_\delta^r\right) \boldsymbol{C}_{\alpha 3} + \boldsymbol{\phi}_\delta \otimes \left(\boldsymbol{\kappa}^r \times \boldsymbol{e}_\delta^r\right) \boldsymbol{C}_{33}\right] dA \,, \\
\frac{\partial \boldsymbol{\rho}}{\partial \boldsymbol{\kappa}^r} &= \int_A \left[-\left(\boldsymbol{\phi}_{\delta,\alpha} \otimes \boldsymbol{e}_\delta^r\right) \boldsymbol{C}_{\alpha 3} \boldsymbol{Y}^r - \boldsymbol{\phi}_\delta \otimes \left(\boldsymbol{\kappa}^r \times \boldsymbol{e}_\delta^r\right) \boldsymbol{C}_{33} \boldsymbol{Y}^r + \boldsymbol{\phi}_\beta \otimes \left(\boldsymbol{e}_\beta^r \times \boldsymbol{\tau}_3^r\right)\right] dA \,, \\
\frac{\partial \boldsymbol{\rho}}{\partial \boldsymbol{p}} &= \int_A \left(\boldsymbol{\phi}_{\delta,\alpha} \otimes \boldsymbol{e}_\delta^r\right) \left[\boldsymbol{C}_{\alpha\beta} \left(\boldsymbol{e}_3^r \otimes \boldsymbol{\psi}_{,\beta}\right) + \boldsymbol{C}_{\alpha 3} \left(\left(\boldsymbol{\kappa}^r \times \boldsymbol{e}_3^r\right) \otimes \boldsymbol{\psi}\right)\right] dA + \\
&\quad + \int_A \boldsymbol{\phi}_\delta \otimes \left(\boldsymbol{\kappa}^r \times \boldsymbol{e}_\delta^r\right) \left[\boldsymbol{C}_{3\alpha} \left(\boldsymbol{e}_3^r \otimes \boldsymbol{\psi}_{,\alpha}\right) + \boldsymbol{C}_{33} \left(\boldsymbol{\kappa}^r \times \boldsymbol{e}_3^r\right) \otimes \boldsymbol{\psi}\right] dA \,, \\
\frac{\partial \boldsymbol{\rho}}{\partial \boldsymbol{p}'} &= \int_A \left[\left(\boldsymbol{\phi}_{\delta,\alpha} \otimes \boldsymbol{e}_\delta^r\right) \boldsymbol{C}_{\alpha 3} \left(\boldsymbol{e}_3^r \otimes \boldsymbol{\psi}\right) + \boldsymbol{\phi}_\delta \otimes \left(\boldsymbol{\kappa}^r \times \boldsymbol{e}_\delta^r\right) \boldsymbol{C}_{33} \left(\boldsymbol{e}_3^r \otimes \boldsymbol{\psi}\right)\right] dA \,, \\
\frac{\partial \boldsymbol{\rho}}{\partial \boldsymbol{r}} &= \int_A \left(\boldsymbol{\phi}_{\delta,\alpha} \otimes \boldsymbol{e}_\delta^r\right) \left[\boldsymbol{C}_{\alpha\gamma} \left(\boldsymbol{e}_\beta^r \otimes \boldsymbol{\phi}_{\beta,\gamma}\right) + \boldsymbol{C}_{\alpha 3} \left(\boldsymbol{\kappa}^r \times \boldsymbol{e}_\beta^r\right) \otimes \boldsymbol{\phi}_\beta\right] dA + \\
&\quad + \int_A \boldsymbol{\phi}_\delta \otimes \left(\boldsymbol{\kappa}^r \times \boldsymbol{e}_\delta^r\right) \left[\boldsymbol{C}_{3\gamma} \left(\boldsymbol{e}_\beta^r \otimes \boldsymbol{\phi}_{\beta,\gamma}\right) + \boldsymbol{C}_{33} \left(\boldsymbol{\kappa}^r \times \boldsymbol{e}_\beta^r\right) \otimes \boldsymbol{\phi}_\beta\right] dA \,, \\
\frac{\partial \boldsymbol{\rho}}{\partial \boldsymbol{r}'} &= \int_A \left[\left(\boldsymbol{\phi}_{\delta,\alpha} \otimes \boldsymbol{e}_\delta^r\right) \boldsymbol{C}_{\alpha 3} \left(\boldsymbol{e}_\beta^r \otimes \boldsymbol{\phi}_\beta\right) + \boldsymbol{\phi}_\delta \otimes \left(\boldsymbol{\kappa}^r \times \boldsymbol{e}_\delta^r\right) \boldsymbol{C}_{33} \left(\boldsymbol{e}_\beta^r \otimes \boldsymbol{\phi}_\beta\right)\right] dA \,, \\
\frac{\partial \boldsymbol{\beta}}{\partial \boldsymbol{\eta}^r} &= \int_A \left(\boldsymbol{\phi}_\beta \otimes \boldsymbol{e}_\beta^r\right) \boldsymbol{C}_{33} dA \,,
\end{aligned}
\tag{94}
$$

$$
\begin{aligned}
\frac{\partial \boldsymbol{\beta}}{\partial \boldsymbol{\kappa}^r} &= -\int_A \left(\boldsymbol{\phi}_\beta \otimes \boldsymbol{e}_\beta^r\right) \boldsymbol{C}_{33} \boldsymbol{Y}^r dA \,, \\
\frac{\partial \boldsymbol{\beta}}{\partial \boldsymbol{p}} &= \int_A \left(\boldsymbol{\phi}_\beta \otimes \boldsymbol{e}_\beta^r\right) \left[\boldsymbol{C}_{3\alpha} \left(\boldsymbol{e}_3^r \otimes \boldsymbol{\psi}_{,\alpha}\right) + \boldsymbol{C}_{33} \left(\boldsymbol{\kappa}^r \times \boldsymbol{e}_3^r\right) \otimes \boldsymbol{\psi}\right] dA \,, \\
\frac{\partial \boldsymbol{\beta}}{\partial \boldsymbol{p}'} &= \int_A \left(\boldsymbol{\phi}_\beta \otimes \boldsymbol{e}_\beta^r\right) \boldsymbol{C}_{33} \left(\boldsymbol{e}_3^r \otimes \boldsymbol{\psi}\right) dA \,, \\
\frac{\partial \boldsymbol{\beta}}{\partial \boldsymbol{r}} &= \int_A \left(\boldsymbol{\phi}_\alpha \otimes \boldsymbol{e}_\alpha^r\right) \left[\boldsymbol{C}_{3\gamma} \left(\boldsymbol{e}_\beta^r \otimes \boldsymbol{\phi}_{\beta,\gamma}\right) + \boldsymbol{C}_{33} \left(\boldsymbol{\kappa}^r \times \boldsymbol{e}_\beta^r\right) \otimes \boldsymbol{\phi}_\beta\right] dA \quad \text{and} \\
\frac{\partial \boldsymbol{\beta}}{\partial \boldsymbol{r}'} &= \int_A \left(\boldsymbol{\phi}_\alpha \otimes \boldsymbol{e}_\alpha^r\right) \boldsymbol{C}_{33} \left(\boldsymbol{e}_\beta^r \otimes \boldsymbol{\phi}_\beta\right) dA \,.
\end{aligned} \tag{95}
$$

Appendix C

Tangent operator $\boldsymbol{L}$ has following structure

$$
\boldsymbol{L} = \begin{bmatrix}
\dfrac{\partial \bar{\boldsymbol{n}}}{\partial \boldsymbol{u}} & \dfrac{\partial \bar{\boldsymbol{n}}}{\partial \boldsymbol{\theta}} & \dfrac{\partial \bar{\boldsymbol{n}}}{\partial \boldsymbol{p}} & \dfrac{\partial \bar{\boldsymbol{n}}}{\partial \boldsymbol{r}} \\
\dfrac{\partial \bar{\boldsymbol{\mu}}}{\partial \boldsymbol{u}} & \dfrac{\partial \bar{\boldsymbol{\mu}}}{\partial \boldsymbol{\theta}} & \dfrac{\partial \bar{\boldsymbol{\mu}}}{\partial \boldsymbol{p}} & \dfrac{\partial \bar{\boldsymbol{\mu}}}{\partial \boldsymbol{r}} \\
\dfrac{\partial \bar{\boldsymbol{\alpha}}}{\partial \boldsymbol{u}} & \dfrac{\partial \bar{\boldsymbol{\alpha}}}{\partial \boldsymbol{\theta}} & \dfrac{\partial \bar{\boldsymbol{\alpha}}}{\partial \boldsymbol{p}} & \dfrac{\partial \bar{\boldsymbol{\alpha}}}{\partial \boldsymbol{r}} \\
\dfrac{\partial \bar{\boldsymbol{\beta}}}{\partial \boldsymbol{u}} & \dfrac{\partial \bar{\boldsymbol{\beta}}}{\partial \boldsymbol{\theta}} & \dfrac{\partial \bar{\boldsymbol{\beta}}}{\partial \boldsymbol{p}} & \dfrac{\partial \bar{\boldsymbol{\beta}}}{\partial \boldsymbol{r}}
\end{bmatrix} . \tag{96}
$$

For instance, semi-tangential external moments are conservative moments characterized by the following time derivative

$$
\dot{\bar{\boldsymbol{m}}} = \frac{1}{2} \boldsymbol{\omega} \times \bar{\boldsymbol{m}} \,. \tag{97}
$$

For this type of loading the only nonzero submatrix of $\boldsymbol{L}$ is

$$
\frac{\partial \bar{\boldsymbol{m}}}{\partial \boldsymbol{\theta}} = \mathrm{Sym}\left(\boldsymbol{V}\left(\boldsymbol{\theta}, \bar{\boldsymbol{m}}\right)\right) \,. \tag{98[6]}
$$

In contrast, for a constant eccentric force $\bar{\boldsymbol{n}}$ whose moment is $\bar{\boldsymbol{m}} = \boldsymbol{s} \times \bar{\boldsymbol{n}}$ (with $\boldsymbol{s}$ as the eccentricity vector), this submatrix is given by

$$
\frac{\partial \bar{\boldsymbol{m}}}{\partial \boldsymbol{\theta}} = \boldsymbol{\Gamma}^T \mathrm{Sym}\left(\boldsymbol{S}\bar{\boldsymbol{N}}\right) \boldsymbol{\Gamma} + \mathrm{Sym}\left(\boldsymbol{V}\left(\boldsymbol{\theta}, \bar{\boldsymbol{m}}\right)\right) \,, \tag{99}
$$

where $\boldsymbol{S} = \mathrm{Skew}(\boldsymbol{s})$ and $\bar{\boldsymbol{N}} = \mathrm{Skew}(\bar{\boldsymbol{n}})$.

[6]The operator $\mathrm{Sym}\,(\bullet)$ extracts the symmetric part of $(\bullet)$, i.e. $\mathrm{Sym} = \frac{1}{2}\left[(\bullet) + (\bullet)^T\right]$.

Shape memory alloy helical springs: modeling, simulation and experimental analysis

Ricardo Alexandre Amar de Aguiar
CEFET/RJ - Department of Mechanical Engineering, Rio de Janeiro/RJ – Brazil

Juliana Hoyer Insaurrauld Pereira, Cristina Gomes de Souza
CEFET/RJ - PPTEC / Department of Mechanical Engineering, Rio de Janeiro/RJ – Brazil

Pedro Manuel Calas Lopes Pacheco
CEFET/RJ - PPEMM / Department of Mechanical Engineering, Rio de Janeiro/RJ – Brazil

Marcelo Amorim Savi
COPPE/UFRJ - Department of Mechanical Engineering, Rio de Janeiro/RJ – Brazil

Abstract

Shape memory alloys (SMAs) are metallic materials that have the capability to recover its original shape eliminating residual deformations when subjected to adequate thermal process. This behavior is related to phase transformation induced by stress or temperature and several alloys present this behavior. During the phase transformation process of a SMA component, large loads and/or displacements can be generated in a relatively short period of time making this component an interesting mechanical actuator. Because of such remarkable properties, SMAs have found a number of applications in different areas. The present contribution deals with the modeling, simulation and experimental analysis of SMA helical springs. Basically, it is assumed a one-dimensional constitutive model to describe its thermomechanical shear behavior and, afterwards, helical springs are modeled by considering classical approach. A numerical method based on the operator split technique is developed. SMA helical spring thermomechanical behavior is investigated through experimental tests performed at different loads. Numerical results show that the model is in close agreement with those obtained by experimental tests.

Keywords: shape memory alloy, modeling, helical spring, experimental analysis.

Mechanics of Solids in Brazil 2009, H.S. da Costa Mattos & Marcílio Alves (Editors)
Brazilian Society of Mechanical Sciences and Engineering, ISBN 978-85-85769-43-7

1 Introduction

Shape memory alloys (SMAs) present complex thermomechanical behaviors related to different physical processes. The most common phenomena presented by this class of material are the pseudoelasticity, the shape memory effect, which may be one-way (SME) or two-way (TWSME), and the phase transformation due to temperature variation. Besides these phenomena, there are more complicated effects that have significant influence over its overall thermomechanical behavior – for instance: plastic behavior, tension-compression asymmetry, plastic-phase transformation coupling, transformation induced plasticity, thermomechanical coupling, among others [1, 2]. The remarkable properties of SMAs are attracting much technological interest, motivating different applications in several fields of sciences and engineering. Aerospace, biomedical, and robotics are some areas where SMAs have been applied [3–15].

SMAs have the capability to generate large strains associated with phase transformation induced by stress and/or temperature variations [3, 16]. During the phase transformation process of a SMA component, large loads and/or displacements can be generated in a relatively short period of time making this component an interesting mechanical actuator. Basically, SMA presents two possible phases: martensite and austenite. Martensitic phase may appear in variants induced by different kinds of stress fields [17]. Several alloys can develop strains associated with phase transformation but only those that can develop large strains are of commercial interest, as nickel-titanium (NiTi) and copper base alloys (CuZnAl and CuAlNi).

SME occurs at low temperatures, below a critical temperature where twined martensite phase is the only stable phase in a stress-free state (M_F). Figure 1a presents a stress-strain curve for the shape memory effect at a constant temperature. For this situation the nonlinear behavior in the loading process is associated with phase transformation related to the conversion from twinned to detwinned martensite ($O \rightarrow A \rightarrow B$). After the unloading process (C), some amount of residual strain remains (ϵ_R), meaning that the reverse transformation is not completed. The shape memory effect takes place by heating the alloy at a temperature above a critical temperature (A_F) where austenitic phase is the only stable phase in a stress-free state. This temperature change controls the transformation from detwinned martensite to austenite and promotes the residual strain recovery. Figure 1b presents a diagram that illustrates the shape memory effect. M_S and M_F are the temperatures at which the formation of martensite starts and ends, respectively, while A_S and A_F are the temperatures at which the formation of austenite starts and ends, respectively.

The complex thermomechanical behavior of SMAs makes their modeling a difficult task. This may introduce difficulties in the evaluation of SMA applications. SMA springs are an important actuator that can be used in different kinds of application. There are some efforts to model the SMA helical springs thermomechanical behavior [18–20]. In the present contribution, it is proposed a model that may be useful for engineering purposes. Basically, a constitutive model originally proposed for one-dimensional tensile-compressive behavior [2, 21–23] is employed to describe the shear behavior. Afterwards, it is developed a SMA helical spring model by assuming that the spring wire presents a homogeneous phase transformation. An experimental apparatus is developed in order to characterize the thermomechanical behavior of SMA helical springs through load-displacement tests. Finally,

Mechanics of Solids in Brazil 2009, H.S. da Costa Mattos & Marcílio Alves (Editors)
Brazilian Society of Mechanical Sciences and Engineering, ISBN 978-85-85769-43-7

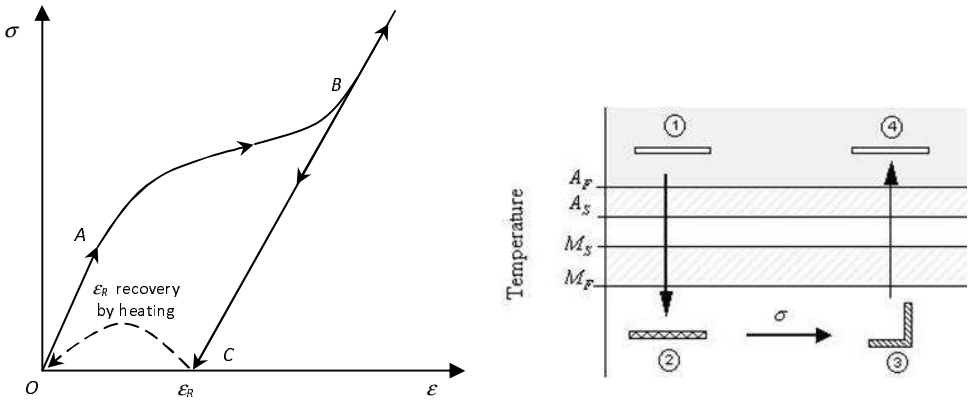

Figure 1: Shape memory effect (SME). Stress-strain curve (a) and a diagram to illustrate the shape memory effect (*b*).

numerical simulations are carried out showing that the proposed model is in close agreement with experimental tests.

2 Constitutive model

There are different ways to describe the thermomechanical behavior of SMAs [24]. Here, a constitutive model that is built upon the Fremond's model [25, 26] and previously presented in different references [2, 21–23] is employed. This model considers different material properties and four macroscopic phases for the description of the SMA behavior. The model also considers plastic strains and plastic-phase transformation coupling, which turns possible the two-way shape memory effect description. Moreover, the original model also contemplates tension-compression asymmetry.

Besides strain (ϵ) and temperature (T), the model considers four more state variables associated with the volumetric fraction of each phase: β_1 is associated with tensile detwinned martensite, β_2 is related to compressive detwinned martensite, β_3 represents austenite and β_4 corresponds to twinned martensite. Actually, the original model also includes other variables related to plastic phenomenon, which are beyond the scope of this contribution.

Although this one-dimensional constitutive model is originally proposed to describe tension-compression behavior, it has been noted that experimental torsion test curves presented in different references [27, 28] indicate that these curves are qualitatively similar to those obtained in tension tests performed in Ni-Ti and other SMAs. Based on this observation, this constitutive model is employed to describe the pure shear stress states, replacing the stress, strain, and elastic modulus respectively by the shear stress τ, shear strain γ, and shear modulus G.

In order to obtain the constitutive equations a free energy potential is proposed concerning each isolated phase. After this definition, a free energy of the mixture can be written weighting each energy function with its volumetric fraction. With this assumption, it is possible to obtain a complete set of constitutive equations that describes the thermomechanical behavior of SMAs as presented bellow:

$$\tau = G\gamma + (\alpha + G\alpha_h)(\beta_2 - \beta_1) \tag{1}$$

$$\dot{\beta}_1 = \frac{1}{\eta_1}\left\{ \alpha\gamma + \Lambda_1 + \left(2\,\alpha_h\alpha + G\,\alpha^2\right)(\beta_2 - \beta_1) + \alpha_h G\,\gamma - \partial_1 J_\pi \right\} + \partial_1 J_\chi \tag{2}$$

$$\dot{\beta}_2 = \frac{1}{\eta_2}\left\{ -\alpha\gamma + \Lambda_2 - \left(2\,\alpha_h\alpha + G\,\alpha^2\right)(\beta_2 - \beta_1) - \alpha_h G\,\gamma - \partial_2 J_\pi \right\} + \partial_2 J_\chi \tag{3}$$

$$\dot{\beta}_3 = \frac{1}{\eta_3}\left\{ -\frac{1}{2}\,(G_A - G_M)\,[\gamma + \alpha_h(\beta_2 - \beta_1)]^2 + \Lambda_3 - \partial_3 J_\pi \right\} + \partial_3 J_\chi \tag{4}$$

where $G = G_M + \beta_3\,(G_A - G_M)$ is the shear modulus. Note that subscript "A" refers to austenitic phase, while "M" refers to martensite. Parameters α and α_h are respectively associated with the vertical and horizontal sizes of the stress-strain hysteresis loop. The terms $\partial_n J_\pi$ (n = 1,2,3) are sub-differentials of the indicator function J_π with respect to βn [29]. The indicator function J_π $(\beta_1, \beta_2, \beta_3)$ is related to a convex set π, which provides the internal constraints related to the phases' coexistence. Concerning the evolution equations of volumetric fractions, η_1, η_2 and η_3 represent the internal dissipation related to phase transformations. Moreover, $\partial_n J_\chi$ (n = 1,2,3) are sub-differentials of the indicator function J_χ with respect to $\dot{\beta}_n$ [29]. This indicator function is associated with the convex set χ, which establishes conditions for the correct description of internal sub-loops due to incomplete phase transformations and also avoids phase transformations $M+ \rightarrow M$ or $M- \rightarrow M$ [23].

Concerning the parameters definition, linear temperature dependent relations are adopted for Λ_1, Λ_2 and Λ_3 as follows:

$$\Lambda_1 = \Lambda_2 = -L_0^M + \frac{L^M}{T_M}(T - T_M) \qquad \Lambda_3 = -L_0^A + \frac{L^A}{T_M}(T - T_M) \tag{5}$$

where T_M is the temperature below which the martensitic phase becomes stable, L_0^M, L^M, L_0^A and L^A are parameters related to critical stress for phase transformation.

In order to contemplate different characteristics of the kinetics of phase transformation for loading and unloading processes, it is possible to consider different values to the parameters η_n (n = 1,2,3), which are related to internal dissipation: η_n^L and η_n^U during loading and unloading process, respectively. For more details about the constitutive model, see Paiva *et al.* [22].

3 Shape memory alloy helical spring

The modeling of the restoring force produced by a shape memory alloy spring is done considering a helical spring with diameter D, built with N coils with a wire diameter d. It is assumed that the

longitudinal force, F, is resisted by the torsional shear stress developed on the circular cross section of the helical shaped wire (Fig. 2) [30].

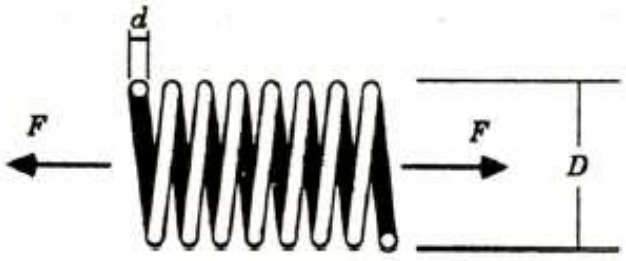

Figure 2: Helical spring.

$$F = \frac{4\pi}{D}\int_0^{d/2} \tau\, r^2 dr \tag{6}$$

where r is the radial coordinate along the wire cross section. It is also assumed that the shear strain is linearly distributed along the wire cross section, from what follows the kinematics relation

$$\gamma = \frac{d}{\pi D^2 N} u \tag{7}$$

where u is the spring displacement.

By combining these equations, and performing the integration, assuming that the wire presents a homogeneous phase transformation through the wire cross section, we obtain:

$$F(u, T, \beta_i) = \frac{\pi\, d^3}{6D}\left[\left(\frac{d}{\pi\, D^2 N} G\right) u + (\alpha + G\alpha_h)\,(\beta_2 - \beta_1)\right] \tag{8}$$

This equation together with those that describes the volume fraction evolution establishes a proper description of the thermomechanical behavior of SMA helical springs.

4 Experimental procedure

The characterization of the SMA helical springs is obtained through load-displacement tests using the tensile test device shown in Fig. 3. This device is composed by a rigid frame that has a load cell (Alfa SV-20 with 20 N capacity) fixed at the top. An SMA spring is connected to the load cell and the other end is attached to the rod of a resistive displacement transducer (Gefran PY-1-F-100 with 100 mm span). Both transducers are connected to a data acquisition system (HBM Spider 8). A

fluid reservoir is attached to the other end of the transducer rod in order to produce the mechanical loadings. The load is prescribed to the SMA spring by controlling the fluid level of the reservoir which is done by changing the vertical position of a second fluid reservoir that is connected to the first by a tube. This configuration allows one to apply precise loading and unloading conditions to the spring element. Temperature variations are induced in the SMA helical spring through joule effect by the application of an electrical current using a stabilized current source (Minipa MPL-1303). The thermomechanical tests developed are composed by two stages: (1) a mechanical loading-unloading followed by a (2) thermal heating-cooling. The first stage promotes a residual strain that is eliminated during the second stage. Three different levels of loads are considered: 3 N, 3.5 N and 4 N. The heating SMA helical spring to a temperature above A_F is performed by applying an electrical current of 1.2 A. All tests are performed at room temperature (22°C).

The SMA helical is built with NiTi that is in martensitic phase at room temperature. The spring has an external diameter of 6 mm, a wire diameter of 0.75 mm, 20 active coils and an activation temperature in the range of 45-55°C.

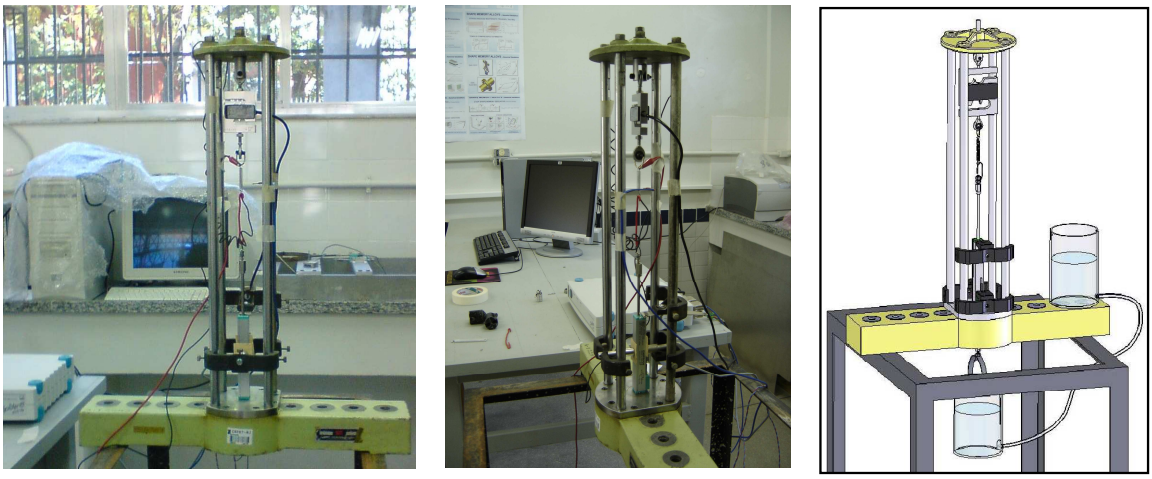

Figure 3: Tensile test device for thermomechanical characterization of the SMA helical springs.

Figure 4 shows the spring load-displacement curves for three different load levels revealing the SME. At the beginning of the test, the SMA helical spring is at room temperature (22°C), a situation where martensitic phase is stable. In order to assure that each test is done with a spring where its wire section has a homogeneous twinned martensitic phase distribution, the following process is applied. Initially, all mechanical loads are removed and then, an electric current of 1.2 A is applied to the spring. Finally, the spring is subjected to cooling prescribed in order to allow a thermal equilibrium with the medium. After this initial treatment, a mechanical loading is applied promoting the formation of detwined martensite that remains after the mechanical load removal causing a residual displacement. At this

point, an electric current of 1.2 A is applied and the SMA helical spring recovers part of the residual displacement developed during the loading stage. A residual load with a magnitude of approximately 1 N is still present at the end of the unloading as a consequence of the devices attached to the spring (resistive displacement transducer, fluid reservoir, etc). A loading rate of approximately 2.7 x 10^{-2} N/s is used in the developed tests.

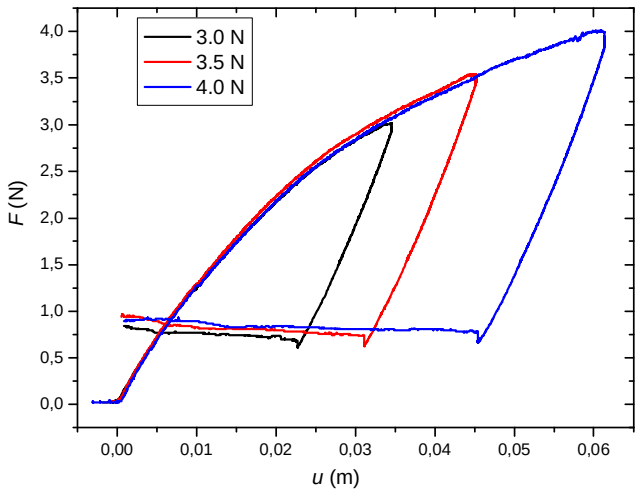

Figure 4: Experimental data related to the spring load-displacement curve for three load levels.

Experimental data is used to match parameters of the proposed model. In the beginning of the test, phase transformation does not take place and the initial slope of the load-displacement curve can be used to obtain $G = 8.5$ GPa. The residual displacement is also employed to match parameters related to phase transformations.

5 Numerical simulations

The operator split technique [31] associated with an iterative numerical procedure is developed in order to deal with the nonlinearities of the formulation. The procedure isolates the sub-differentials and uses the implicit Euler method combined with an orthogonal projection algorithm [2] to evaluate evolution equations. Orthogonal projections assure that volume fractions of the macroscopic phases obey the imposed constraints. In order to satisfy constraints, values of volume fractions must stay inside or on the boundary the tetrahedron shown in Fig. 5 that establishes the phase coexistence conditions.

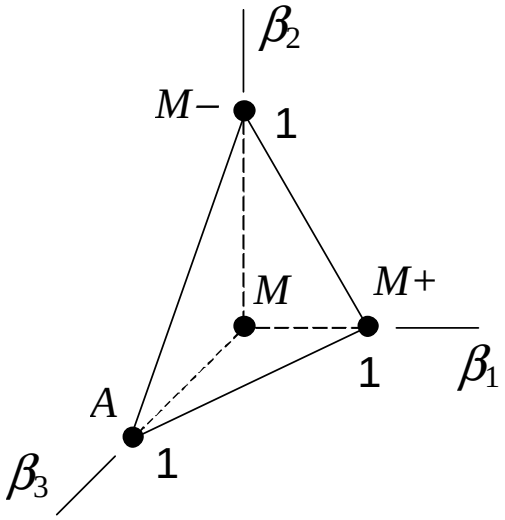

Figure 5: Tetrahedron of the constraints related to phase coexistence.

Numerical simulations are now focused on establishing a comparison with experimental tests. It is considered a helical spring with the same characteristics described in the previous section. Parameters experimentally matched from experimental tests are presented in Table 1.

Table 1: SMA parameters.

G_A(GPa)	G_M(GPa)	α(MPa)	γ_R	T_M (K)
16	8.5	30	0.030	318
L_0^M(MPa)	L^M(MPa)	L_0^A(MPa)	L^A(MPa)	
0.7	9.5	0.03	27	
$\eta_{1,2}^L$(MPa.s)	$\eta_{1,2}^U$(MPa.s)	η_3^L(kPa.s)	η_3^U(kPa.s)	
200	200	150	150	

Figure 6 shows thermomechanical loading that represents the experimental tests: a mechanical loading-unloading followed by a thermal heating-cooling. Figures 7 and 8 present the force-displacement curves and the volume fraction time evolution, respectively, for the three loading levels applied in the experimental tests (3 N, 3.5 N and 4 N). The force-displacement curves have the same behavior

observed in experimental tests, presenting a residual displacement and a load when the mechanical loading-unloading process is finished. Figure 8 allows a better comprehension of the phase transformation process related to this thermomechanical loading process. Initially, martensitic reorientation takes place due to mechanical loading, changing twinned to detwinned martensite. The final state for each of the three load levels is the following: 0.25 for $F = 3$ N, 0.40 for $F = 3.5$ N and 0.60 for $F = 4$ N. Afterwards, during the heating-cooling process, there is an austenitic formation during the heating stage followed by twinned martensite formation during the cooling stage.

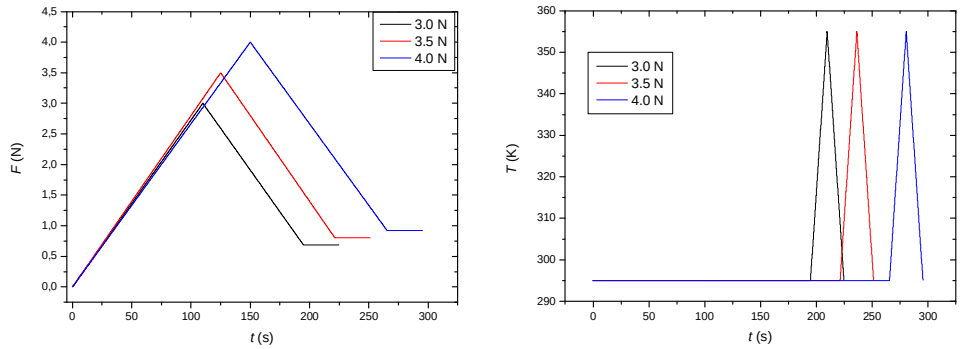

(a) (b)

Figure 6: Thermomechanical loading for three loading levels. (a) Mechanical and (b) thermal loadings.

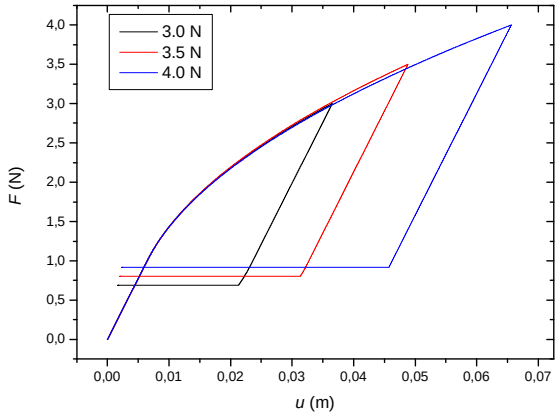

Figure 7: Spring load-displacement curve for three load levels: Numerical simulation.

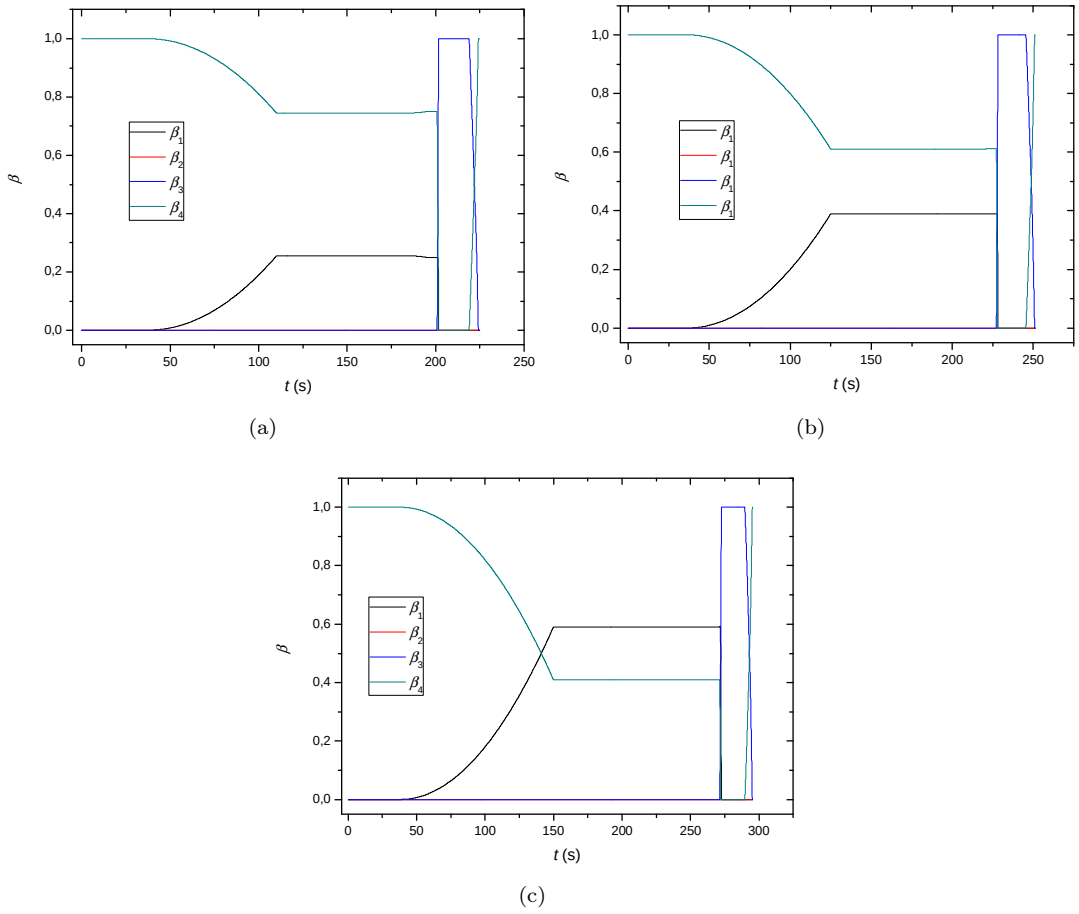

Figure 8: Volume fraction time evolution. (a) $F = 3$ N, (b) $F = 3.5$ N and (c) $F = 4$ N.

In order to establish a comparison between numerical and experimental tests Fig. 9 presents a direct comparison of the load-displacement curves obtained for three load levels analyzed. Results show that model results are in close agreement with experimental tests.

6 Conclusion

This contribution analyses the quasi-static response of shape memory alloy helical springs described by a one-dimensional constitutive model that includes four macroscopic phases in the formulation (three variants of martensite and an austenitic phase) and is used to describe the thermomechanical

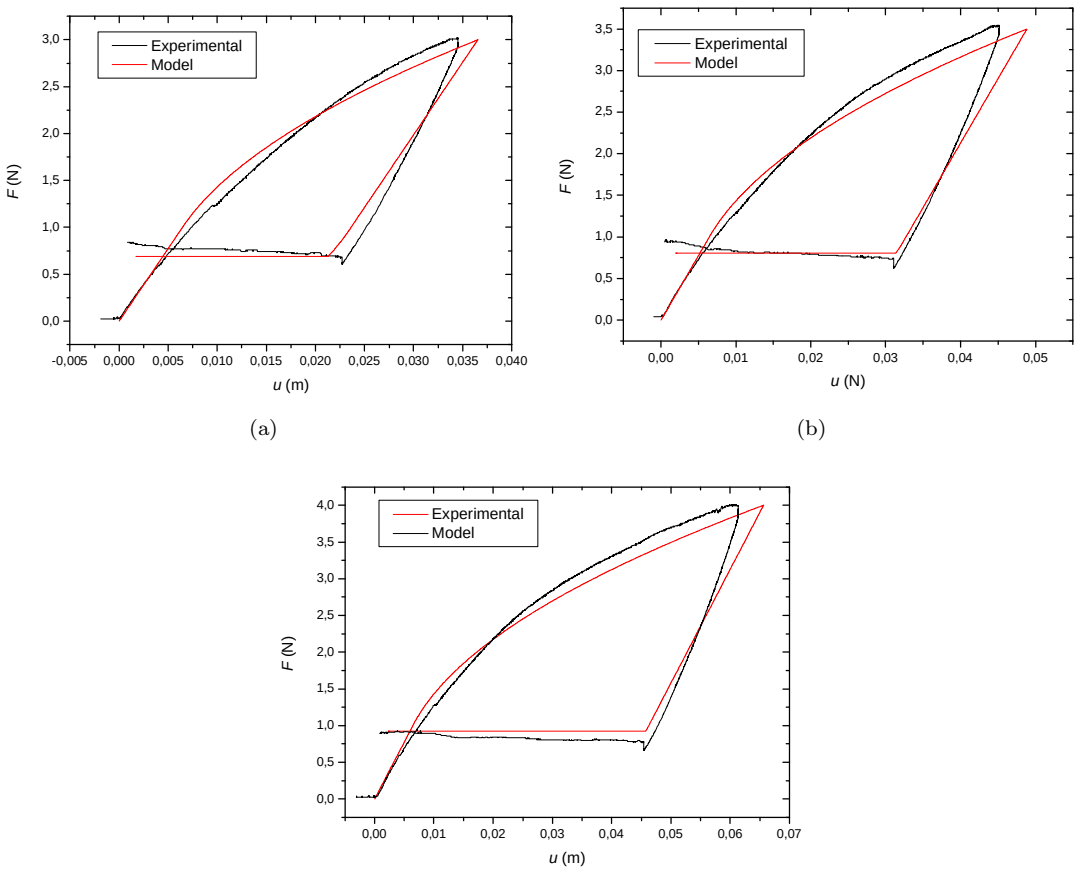

Figure 9: Comparison between experimental and numerical tests of an SMA spring. Load-displacement curve for three load levels. (a) $F = 3$ N, (b) $F = 3.5$ N and (c) $F = 4$ N.

shear behavior of SMA helical springs. A numerical method based on the operator split technique is employed. An experimental apparatus is developed in order to characterize the thermomechanical behavior of SMA helical springs through load-displacement tests. Numerical results show that the proposed model is in close agreement with experimental data obtained and can be used for the design of actuator using SMA helical springs. It is important to highlight that the hypotheses that phase transformation occurs in a homogeneous way at the SMA wire is realistic providing good results.

Acknowledgements

The authors would like to acknowledge the support of the Brazilian Research Agency CNPq and the State Research Agency FAPERJ.

References

[1] Tanaka, K., A phenomenological description on thermomechanical behavior of shape memory alloys. *Journal of Pressure Vessel Technology*, **112**, pp. 158–163, 1990.
[2] Savi, M.A., Paiva, A., Baêta-Neves, A.P. & Pacheco, P.M.C.L., Phenomenological modeling and numerical simulation of shape memory alloys: A thermo-plastic-phase transformation coupled model. *Journal of Intelligent Material Systems and Structures*, **13(5)**, pp. 261–273, 2002.
[3] Rogers, C.A., Intelligent materials. *Scientific American*, pp. 122–127, 1995.
[4] Birman, V., Review of mechanics of shape memory alloys structures. *Applied Mechanics Rev*, **50(11)**, pp. 629–645, 1997.
[5] Pacheco, P.M.C.L. & Savi, M.A., A non-explosive release device for aerospace applications using shape memory alloys. *Proceedings of XIV the Brazilian Congress of Mechanical Engineering (COBEM 97 - ABCM)*, Bauru, Brazil, 1997.
[6] Pacheco, P.M.C.L. & Savi, M.A., Modeling a shape memory release device for aerospace applications. *Revista de Engenharia e Ciências Aplicadas, UNESP*, 2000.
[7] van Humbeeck, J., Non-medical applications of shape memory alloys. *Materials Science and Engineering A*, **273-275**, pp. 134–148, 1999.
[8] La Cava, C.A.P.L., Pacheco, P.M.C.L. & Savi, M.A., Modelagem de um dispositivo de pré-carga com memória de forma para juntas flangeadas. *CONEM 2000 – Congresso Nacional de Engenharia Mecânica*, Natal-RN, 2000.
[9] Webb, G., Wilson, L., D.C., Lagoudas & Rediniotis, O., Adaptive control of shape memory alloy actuators for underwater biomimetic applications. *AIAA Journal*, **38(2)**, pp. 325–334, 2000.
[10] Denoyer, K.K., Scott Erwin, R. & Rory Ninneman, R., Advanced smart structures flight experiments for precision spacecraft. *Acta Astronautica*, **47**, pp. 389–397, 2000.
[11] Garner, L.J., Wilson, L.N., Lagoudas, D.C. & Rediniotis, O.K., Development of a shape memory alloy actuated biomimetic vehicle. *Smart Materials and Structures*, **9(5)**, pp. 673–683, 2001.
[12] Machado, L.G. & Savi, M.A., Odontological applications of shape memory alloys. *Revista Brasileira de Odontologia*, **59(5)**, pp. 302–306, 2002. (in portuguese).
[13] Machado, L.G. & Savi, M.A., Medical applications of shape memory alloys. *Brazilian Journal of Medical and Biological Research*, **36(6)**, pp. 683–691, 2003.
[14] Machado, L.G., Savi, M.A. & Pacheco, P.M.C., Nonlinear dynamics and chaos in coupled shape memory oscillators. *International Journal of Solids and Structures*, **40**, pp. 5139–5156, 2003.
[15] Wang, Z.G., Zu, X.D., Feng, X.D., Zhu, S., Bao, J.W. & Wang, L.M., Characteristics of two-way shape memory TiNi springs driven by electrical current. *Materials and Design*, **25**, pp. 699–703, 2004.
[16] Hodgson, D.E., Wu, M.H. & Biermann, R.J., Shape memory alloys. *ASM Handbook*, **2**, pp. 887–902, 1992.
[17] Zhang, X.D., Rogers, C.A. & Liang, C., Modeling of two-way shape memory effect. *ASME - Smart Structures and Materials*, **24**, pp. 79–90, 1991.
[18] Toi, Y., Lee, J.B. & Taya, M., Finite element análisis of superelastic, large deformation behavior of shape memory alloy helical springs. *Computer and Structures*, **82**, pp. 1685–1693, 2004.

[19] Savi, M.A. & Braga, A.M.B., Chaotic vibrations of an oscillator with shape memory. *Journal of the Brazilian Society of Mechanical Sciences and Engineering*, **XV(1)**, pp. 1–20, 1993.
[20] Tobushi, H. & Tanaka, K., Deformation of a shape memory alloy helical spring - (Analysis based on stress-strain-temperature relation). *JSME International Journal Series I - Solid Mechanics Strength of Materials*, **34(1)**, pp. 83–89, 1991.
[21] Baêta-Neves, A.P., Savi, M.A. & Pacheco, P.M.C.L., On the fremond's constitutive model for shape memory alloys. *Mechanics Research Communications*, **31(6)**, pp. 677–688, 2004.
[22] Paiva, A., Savi, M.A., Braga, A.M.B. & Pacheco, P.M.C.L., A constitutive model for shape memory alloys considering tensile-compressive asymmetry and plasticity. *International Journal of Solids and Structures*, **42(11-12)**, pp. 3439–3457, 2005.
[23] Savi, M.A. & Paiva, A., Describing internal subloops due to incomplete phase transformations in shape memory alloys. *Archive of Applied Mechanics*, **74(9)**, pp. 637–647, 2005.
[24] Paiva, A. & Savi, M.A., An overview of constitutive models for shape memory alloys. *Mathematical Problems in Engineering*, **2006**, pp. 1–30, 2006. Article ID56876.
[25] Fremond, M., Matériaux à mémoire de forme. *C R Acad Sc Paris*, **Tome 34, s.II(7)**, pp. 239–244, 1987.
[26] Fremond, M., *Shape memory alloy: A thermomechanical macroscopic theory*. CISM courses and lectures, Springer Verlag, 1996.
[27] Jackson, C.M., Wagner, H.J. & Wasilewski, R.J., 55-Nitinol - The alloy with a memory: Its physical metallurgy, properties, and applications. *NASA-SP-5110*, 1972.
[28] Manach, P.Y. & Favier, D., Shear and tensile thermomechanical behavior of near equiatomic niti alloy. *Materials Science and Engineering A*, **222**, pp. 45–57, 1997.
[29] Rockafellar, R.T., *Convex analysis*. Princeton Press, 1970.
[30] Shigley, J.E. & Mischke, C.R., *Mechanical Engineering Design*. McGraw-Hill, 6th edition, 2001.
[31] Ortiz, M., Pinsky, P.M. & Taylor, R.L., Operator split methods for the numerical solution of the elasto-plastic dynamic problem. *Computer Methods of Applied Mechanics and Engineering*, **39**, pp. 137–157, 1983.

Mechanics of Solids in Brazil 2009, H.S. da Costa Mattos & Marcílio Alves (Editors)
Brazilian Society of Mechanical Sciences and Engineering, ISBN 978-85-85769-43-7

Crack propagation tests: analytical and numerical approaches

Silvio de Barros
Nucleo de Estudos e Pesquisas em Materiais NEPEM-UFPB, Joao Pessoa/PB – Brazil
Laurent Champaney
LMT, Cachan Cedex – France

Abstract

Crack propagation tests are often used to identify adhesion parameters,helping to evaluate the quality of bonded joints. The critical energy release rate G_C is one of the basics parametres that caracterizes a bonded joint. One can predict the behavior of the bonded plates during a crack propagation test by obtaining the propagation curves for a given G_C value. This paper aims to consider the usefullness of two methods for obtaing such curves. In a classic analytical approach, the adhesion between the plates is considered perfect. In such case the interface stiffness is not taken into account, where both plates behave as one when the joint is undamage and as two separated plates in the cracked zone. The second approach is numerical. The bonded interface is now consider elastic. The interface stiffiness is also a parametre that caracterize the bonded joint. With the aide of the finit element code Cast3m, a diferent method is proposed to obtain the propagation curves. A good quality of fitting was achieved when both analytical and numerical based values are compared. Finally, some exemples applying numerical method are presented to show the advantage of such approach.

Keywords: bonded joints, adhesive, mechanical tests, propagation curves.

1 Introduction

In the last years, industrial use of adhesive has been growing over other conventional joining techniques. This growth can be mainly explained by the low weight among other engineering effectiveness of this type of structural joint.

Crack propagation tests are normally used to identify the adhesion parameters, helping to evaluate the quality of bonded joints [1, 2]. In classic tests, a initial crack between two bonded plates propagates when a flexure load is applied. This tests are classified by the propagation modes defined in the fracture mechanics theory. In Fig. 1, DCB (Double Cantilever Beam) and ENF (End Notched Flexure) are pure

Mechanics of Solids in Brazil 2009, H.S. da Costa Mattos & Marcílio Alves (Editors)
Brazilian Society of Mechanical Sciences and Engineering, ISBN 978-85-85769-43-7

mode I and pure mode II tests, respectively. There are also some tests that combine pure propagation modes, as the MMF (Mixed Mode Flexure).

The critical energy release rate G_c is one of the basics parametres caracterizing a bonded joint. One can predict the behavior of the bonded plates during a crack propagation test by obtaining the propagation curves for a given G_c value.

Two diferents methods to obtain this curves are considered here. In an classic analytical approach, the adhesion between the plates is considered perfect. In such case the interace stiffness is not taken into account. Both plates behave as one when the joint is undamage and as two separated plates in the cracked zone. By applying the classic beam theory one can study the behavior of the plates during the delamination in the framework of the Linear Elastic Fracture Mechanics. This approach was originally presented by Allix, Ladeveze and Corigliano [3]. They have showed how to calculate the stability conditions for load and displacement control, wich is very important to identify snap-back problems.

The second approach is numerical. The bonded interface is now consider elastic. The interface stiffiness is also a parametre that caracterize the bonded joint. The propagation curves are abtained with the aide of the finit element code Cast3M, developed by the CEA (*Commisariat a l'Energie Atomique*, France), by taking the structural response for a given value of initial crack at a time.

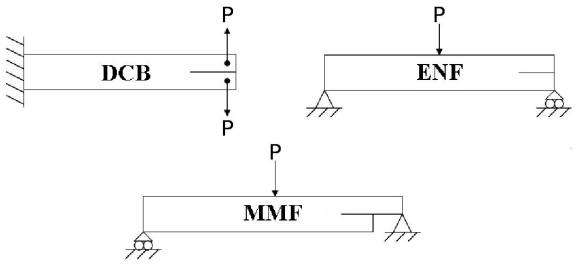

Figure 1: Crack propagation tests.

2 Analytical approach

The critical energy release rates G_c can be derived from linear beam theory using the classical Irwin-Kies expression for the fracture energy [4]:

$$G_c = \frac{P^2}{2B}\frac{dC}{da} \tag{1}$$

where P is the load applied to the specimen, B the specimen width and a the crack length.

The compliance C is defined as:

$$C = \frac{u}{P} \tag{2}$$

where u is the displacement.

Allix, Ladeveze and Corigliano [3] presents the expressions for the compliance and the propagation curves for DCB and ENF specimens (Tab. 1). In this table the expressions for a mixed mode test (MMF) were found following the same methode presented by Allix, Ladeveze and Corigliano [3]. The expressions were calculated for two beans of length L, width B, thickness H, Young's modulus E and moment of inertia of section I.

Table 1: Compliance and propagation curves for pure mode tests

Test	a	C	*f(P,u)*
DCB	$0 \leq a \leq L$	$\frac{2a^3}{3EI}$	$u = \frac{1}{3P^2}\sqrt{EI}\left(BG_c\right)^{3/2}$
ENF	$0 \leq a \leq L/2$	$\frac{L^3+12a^3}{384EI}$	$u = \frac{PL^3}{384EI} + \frac{16}{P^2}\sqrt{EI}\left(\frac{BG_c}{3}\right)^{3/2}$
ENF	$L/2 \leq a \leq L$	$\frac{L^3+3(L-a)^3}{96EI}$	$u = \frac{PL^3}{96EI} - \frac{16}{P^2}\sqrt{EI}\left(\frac{BG_c}{3}\right)^{3/2}$
MMF	$0 \leq a \leq L/2$	$\frac{L^3+28a^3}{384EI}$	$u = \frac{PL^3}{384EI} + \frac{112}{3P^2}\sqrt{EI}\left(\frac{BG_c}{7}\right)^{3/2}$
MMF	$L/2 \leq a \leq L$	$\frac{2L^3-7(L-a)^3}{96EI}$	$u = \frac{PL^3}{48EI} - \frac{112}{3P^2}\sqrt{EI}\left(\frac{BG_c}{7}\right)^{3/2}$

Figure 2 shows the crack propagation curves for a MMF test and the lines that mark the stability zones for load control ($0.5L < a < L$) and for displacement control ($0.261L < a < L$). The curves were obtained using the following values: $Gc = 0.4$ N/mm; $E = 81000$ MPa; $L = 120$ mm; $B = 20$ mm and $H = 3$ mm.

3 Numerical approach

Flexure tests can also be studied by numerical simulations [5, 6]. The simplest way to simulate a flexure test is to use a finite elements model with an elastic interface representing the adhesive. The simulations here were performed in Cast3M software developed by the CEA - (*Commisariat a l'Energie Atomique*, France). The elastic interface behavior can be simulated in this software, in which the elastic stiffness is defined by the constants *k(i)* (i = 1,2 or 3). The use of a simple elastic interface does not allow observing the evolution of the crack automatically. It should be necessary to use a damage interface model to be able to represent a crack propagation through the interface[7]. However, when sharp snap-back problems are encountered in the structural response it's necessary to follow some special procedures to overcome it [8]. In this work we propose to obtain the propagation curves by using simple elastic interface and by taking the structural response for a given value of initial crack

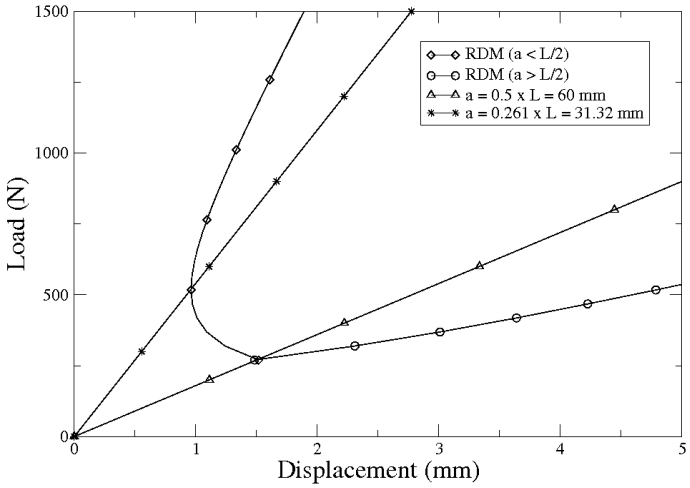

Figure 2: Crack propagation curves and stability zones for a MMF test.

at a time. Figure 3 is a scheme representing the crack evolution. The energy G necessary to make a crack propagate represented by the gray area is calculated by Eq. (3).

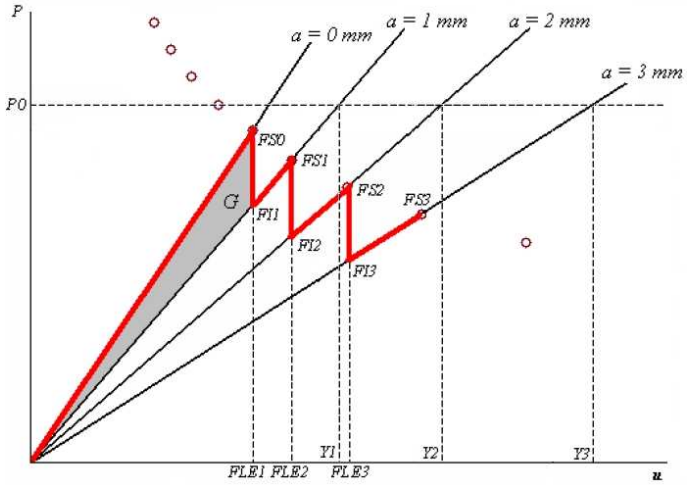

Figure 3: Crack propagation scheme.

Mechanics of Solids in Brazil 2009, H.S. da Costa Mattos & Marcílio Alves (Editors)
Brazilian Society of Mechanical Sciences and Engineering, ISBN 978-85-85769-43-7

$$G = \frac{FLE(i)}{2}\left(FS(i-1) - FI(i)\right) \tag{3}$$

Index i represents the instant observed in relation to the initial crack length a. For instance, *FLE(2)* and *FS(1)* represent the displacement and load at the time the crack advances from 1mm to 2mm, and *FI(2)* is the load at the time when energy begins to accumulate again, to make the crack advance from 2mm to 3mm. The 1mm crack step is used as a reference to simplify analysis, however, from the numerical standpoint, smaller steps can be used.

With the FE model it is possible to obtain the displacement *Y(i)* corresponding to a load *P0* applied for a given crack length a. The propagation curve for a given critical energy value G_c is the curve that contains all the *FS(i)* points. Based on Fig. 3, the following relations can be written:

$$\frac{F1}{Y(i)} = \frac{FS(i)}{FLE(i+1)} = \frac{FI(i)}{FLE(i)} = R(i) \tag{4}$$

Using Eq. (3) one can find all displacements *FLE(i)* for each value of the rigidity *R(i)*:

$$FLE(i) = \sqrt{\frac{2G_c}{R(i-1) - R(i)}}$$

A routine was performed in CAST3M to calculate loads *FS(i)* and *FI(i)* and the displacements *FLE(i)* and *Y(i)* for a given load *P0*. Figure 4 shows some examples of curves obtained in an ENF test for different values of G_c. The curves were obtained using the following values: $k(i) = 10^{17} N/m^3$; $E = 81000$ MPa; $L = 120$ mm; $B = 20$ mm and $H = 3$ mm.

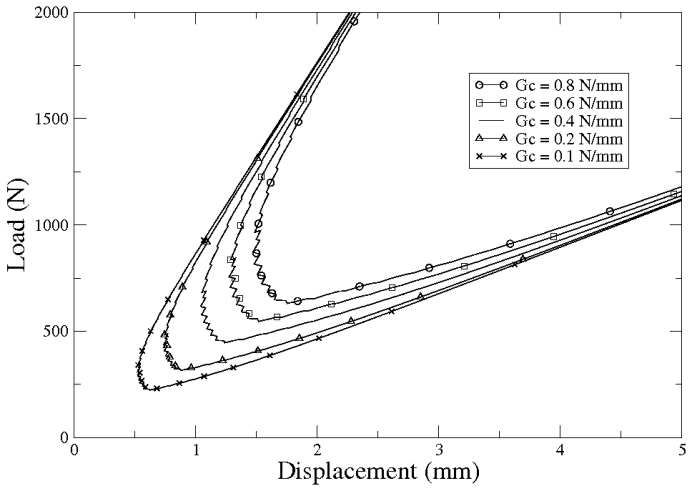

Figure 4: Crack propagation curves.

4 Comparison of results

The graph in Fig. 5 compares the numerically obtained curve to those obtained analytically for a ENF test. The two methods present very close curves, with a small difference when the crack enters the stability zone for displacement control ($a = 41.64mm$). This difference is due to the fact that the analytic method considers that the plates behave like two beams without any contact in the crack region, while the finite elements model takes the unilateral contact between the plates in the crack region into account.

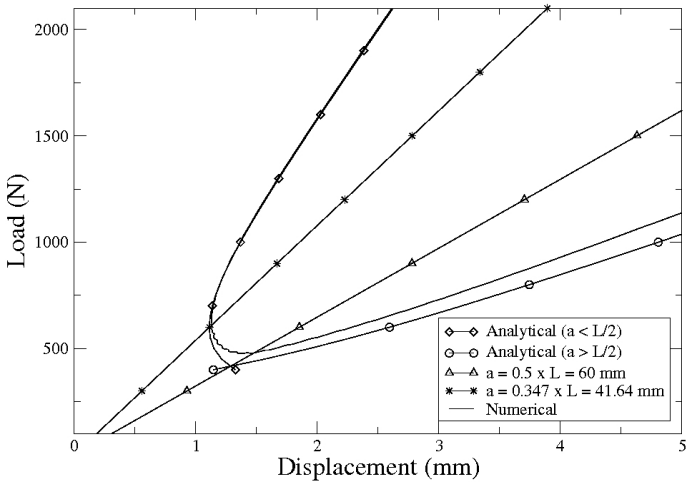

Figure 5: Analytical and numerical curves for ENF tests.

Figures 6 and 7 confirms the good agreement between the two methods now for mode I and mixed mode tests.

5 Different test geometries

More than an easier method to obtain propagation curves, the numerical method presented here is an important tool to selection of optimized adhesion tests geometries. The Tapered Double Cantilever Beam test (TDCB) is a good example of the difficulties associated with the analytical approach due to the complexity of its geometry [9]. Qiao, Wang and Davalos [10] have shown that it can be even more complex in the case of different materials for adherend and contour portions. With the numerical method presented here, it is possible to obtain the propagation curves for TDCB tests with the same material or different materials as well. One can also study the influence of the specimen geometry by changing the FE mash (Fig. 8). Figure 9 shows an example of propagation curves for TDCB tests with

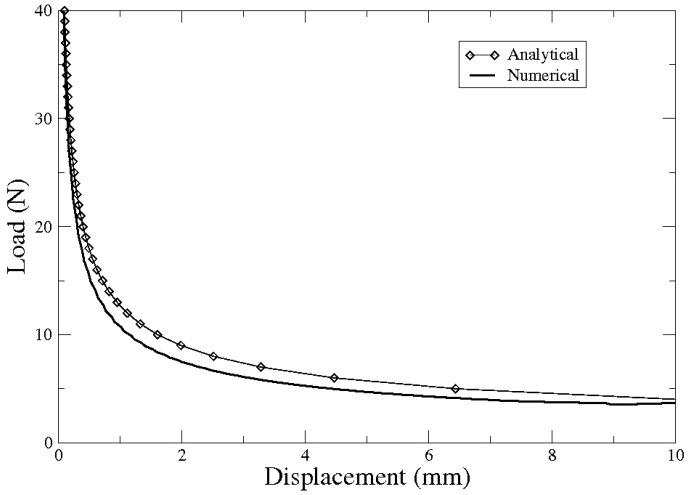

Figure 6: Analytical and numerical curves for DCB tests.

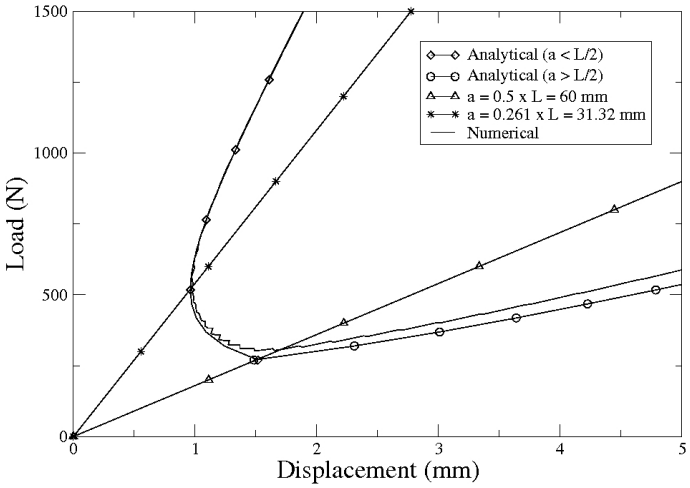

Figure 7: Analytical and numerical curves for MMF tests.

different values of the H1. The curves were obtained using the following values: $k(i) = 10^{17} N/m^3$; E = 81000 MPa; $L1$ = 300 mm; $L2$ = 40 mm; $H2$ = 15 mm and width B = 20 mm. One can see the rigidity increasing specially for a crack lenght bigger than $L2$. Also, the closest $H1$ is to $H2$ the closest the curve is to a DCB test one.

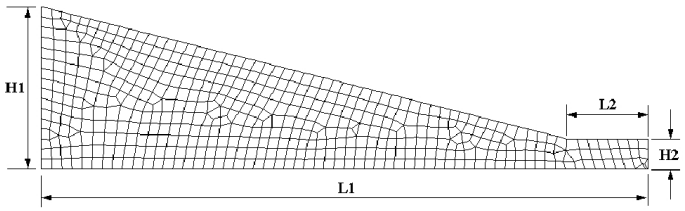

Figure 8: TDCB FE mash.

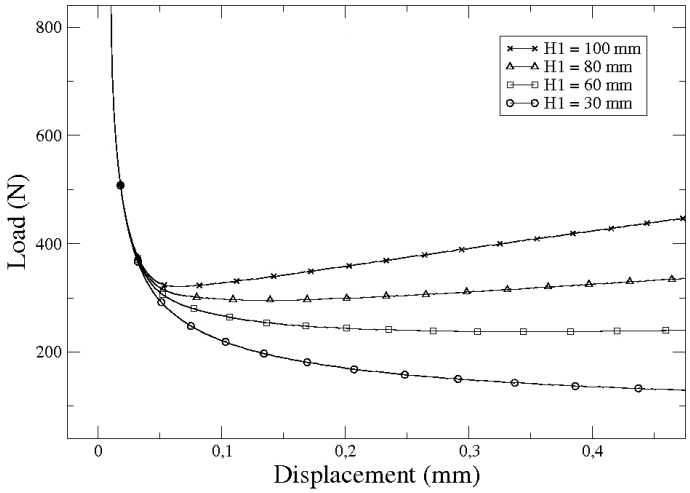

Figure 9: Crack propagation curves for TDCB tests.

6 Interface stiffness

Damage interface models usually take the interface stiffness redution as a parameter to indicate the degradation of the interface [11–14]. The problem using this models is to obtain the initial value of the stiffness. It is impossible to obtain the undamaged interface stiffness from classical mechanical tests with accuracy. Figure 10 shows the propagations curves for a ENF test by changing the interface stiffness in the FE model. For the values of $k(i)$ above $10^4 N/m^3$, one cannot see the difference because the curves are too close. Usually, the interface stiffness is higher than such value. That is why an ultrasonic method was proposed to measure it [15].

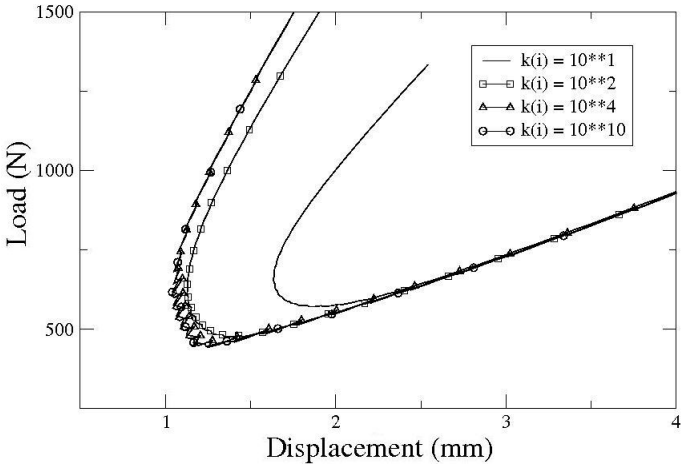

Figure 10: Influence of the interface stiffness.

7 Conclusion

The crack propagation in adhesion tests was studied in the framework of linear elastic fracture mechanics by two different and complementary approaches. The first, purely analytical, allows the equations of propagation curves to be obtained. The second is numerical and allows taking elastic interface stiffness into account. It was seen that the two approaches generate compatible results. The results obtained in an initial analysis using the methods presented here, provide an idea of the behavior of bonded plates before to perform the mechanical tests. The prior knowledge of the stability zones allows planning the test so that the crack propagation occurs in a stable manner. It can be done by using a correct value for the initial crack length. The advantage of the numerical method is that it can supply the propagation curves easier than the analytical. It can also be used for more complex geometries different from the classical tests. Depending on the specimen used in the test, the analytical calculation may take a lot of work or even be imprecise when the profiles used are no longer in the domain of the classical beam theory.

Responsibility notice

The author(s) is (are) the only responsible for the printed material included in this paper.

References

[1] Jangblad, D., Prediction of the failure loads of adhesive single lap joints using a fracture mechanics evaluation technique. *Mechanical behavoir of adhesive joints*, eds. G. Verchery & A.H. Cardon, Pluralis,

pp. 293–306, 1987.

[2] Ladeveze, P., Allix, O., Gornet, L., Leveque, D. & Perret, L., A computational damage mechanics approach for laminates: identification and comparison with experimental results. *Damage Mechanics in Engineering Materials*, eds. G. Voyiadjis et al., Elsevier, pp. 481–500, 1998. Proceedings of McNu97.

[3] Allix, O., Ladeveze, P. & Corigliano, A., Damage analysis of interlaminar fracture specimens. *Composites Structures*, **31**, pp. 61–74, 1995.

[4] Irwin, G.R. & Kies, J.A., Critical energy release rate analysis of fracture strength. *Welding Journal Research Supplement*, **33**, pp. 193–198, 1954.

[5] Alfano, G., On the influence of the shape of the interface law on the application of cohesive-zone models. *Composites Science and Technology*, **66**, pp. 723–730, 2005.

[6] Corigliano, A., Formulation, identification and use of interface models in the numerical analysis of composite delamination. *Int J Solids Struct*, **30(20)**, pp. 2779–2811, 1993.

[7] Valoroso, N. & Champaney, L., A damage-mechanics-based approach for modelling decohesion in adhesively bonded assemblies. *Engineering Fracture Mechanics*, **73**, pp. 2774–2801, 2006.

[8] Qiu, Y., Crisfield, M.A. & Alfano, G., An interface element formulation for the simulation of delamination with buckling. *Engineering Fracture Mechanics*, **68**, pp. 1755–1776, 2001.

[9] Blackman, B.R.K., Hadavinia, H., Kinloch, A.J., Paraschi, M. & Williams, J.G., The calculation of adhesive fracture energies in mode i: revisiting the tapered double cantilever beam (TDCB) test. *Engineering Fracture Mechanics*, **70**, pp. 233–248, 2003.

[10] Qiao, P., Wang, J. & Davalos, J.F., Tapered beam on elastic foundation model for compliance rate change of TDCB specimen. *Engineering Fracture Mechanics*, **70**, pp. 339–353, 2003.

[11] Mi, Y., Crisfield, M.A., Davies, G.A.O. & Hellweg, H.B., Progressive delamination using interface elements. *Journal of Composite Materials*, **32(14)**, pp. 1246–1272, 1998.

[12] Allix, O. & Corigliano, A., Geometrical and interfacial non-linearities in the analysis of delamination in composites. *International Journal of Solids and Structures*, **36(15)**, pp. 2189–2216, 1999.

[13] Ortiz, M. & Pandolfi, A., Finite-deformation irreversible cohesive elements for three-dimensional crack-propagation analysis. *International Journal for Numerical Methods in Engineering*, **44(9)**, pp. 1267–1282, 1999.

[14] Ladeveze, P., Allix, O., Deu, J.F. & Leveque, D., A mesomodel for localisation and damage computation in laminates. *Computer Methods in Applied Mechanics and Engineering*, **183**, pp. 105–122, 2000.

[15] Vlasie, V., De Barros, S., M. Rousseau, M., Champaney, L., Duflo, H. & Morvan, B., Mechanical and acoustical study of structural bond: comparison theory/numerical simulations/experiment. *European Journal of Mechanics A/Solids*, **25**, pp. 464–482, 2006.

Load measurements in reinforced concrete columns

Jaime Tupiassú Pinho de Castro, Ronaldo Domingues Vieira
Department of Mechanical Engineering, Pontifical Catholic University of Rio de Janeiro, Rio de Janeiro/RJ – Brazil
Rafael Araújo de Sousa
Department of Civil Engineering, Pontifical Catholic University of Rio de Janeiro, Rio de Janeiro/RJ – Brazil
Marco Antonio Meggiolaro, José Luiz de França Freire
Department of Mechanical Engineering, Pontifical Catholic University of Rio de Janeiro, Rio de Janeiro/RJ – Brazil

Abstract

Particularly careful strain measurements made on several reinforced concrete columns yielded much higher values than initially expected, causing great concern since their final objective was to evaluate the forces that were loading the columns. Indeed, some loads calculated from the measured strain in a standard linear elastic way appear to be larger than the column's ultimate design load. However, despite its widespread use in structural design, such linear elastic calculations do not include the very significant influence of concrete creep on the columns strain state, a phenomenon that is only implicitly considered by the "allowable stresses" specified in their design codes. Since this procedure is inappropriate for experimental stress analysis purposes, a relatively simple viscoelastic model is proposed to describe the concrete long term stress-strain behavior. This model is extended to describe the reinforced columns behavior, and then qualified by fitting it to concrete column creep data from the literature, proving that despite their high value the measured strains were indeed compatible with the columns load history.

Keywords: concrete creep, residual stresses, time-dependent strain measurements.

1 Introduction

A large and very busy subway station was suffering important structural modifications to serve as the main commuting point between an existing line and a new one under construction. That station was originally conceived as a crossing point, but in its original plan the new subway line would have two parallel tunnels to hold its two railways, and its structure was accordingly built several years ago.

Mechanics of Solids in Brazil 2009, H.S. da Costa Mattos & Marcílio Alves (Editors)
Brazilian Society of Mechanical Sciences and Engineering, ISBN 978-85-85769-43-7

However, that original plan had to be changed, as the new line was being dug by a machine which opened a larger hole to hold the two railways inside a single tunnel. Consequently, several columns of that veteran station should be removed and properly replaced to allow the passage of the digging machine, and the settlement of the new line with its adjacent railways. Moreover, this unusual task should be fulfilled without interrupting the old line regular transportation services. To assure the safety of this process, load measurements were specified in all the columns that would be removed or could be affected during the station upgrade.

Direct load measurements were impossible in this case, not only because the reinforced concrete columns were built into the subway station structure, but also because it should continuously support the existing line traffic without interruptions during the whole construction campaign of the new line. In view of this limitation, residual or resident strain measurements by localized stress releases were proposed as an alternative method for indirectly measuring the required loads, which should of course be calculated from the strain measurements by using the appropriate columns stiffness properties.

The approximately 1.2m diameter concrete columns were reinforced by some 30 or more vertical steel rods, tied in a standardized way. The rods diameters were either 16, 20 or 24mm, depending on the column design load. The steel rods had a minimum yield strain $\epsilon_{Ymin} > 2500\mu m/m$, and were distributed more or less circumferentially near the columns perimeter in approximately uniform intervals. But there was no warranty about the depth of the rods, nor about the thickness of the concrete layer which covered them. This thickness, as it was later on verified, indeed varied significantly from column to column, and even around a same column.

To avoid the uncertainty associated with residual strain measurements made on concrete layers of varying thickness, four small windows were opened on most columns, to expose a small portion of some of their steel reinforcing bars, see Figure1. The windows on the columns surfaces were spaced at approximately 90^o and opened in a same transversal plane. The reinforcing bars were strain-gaged and then sectioned to alleviate their service strains. Note that instead of using only three co-planar measurement points, which is the minimum number required to separate the normal from the bending strains, whenever possible four reinforcing bars were instrumented in each column to provide some measurement redundancy. This conservative practice is strongly recommendable, not only to avoid losing important information in case of an eventual gage problem, but also to provide some insight on the measurement dispersion. Due to the severe structural risk problem associated with the columns removal, this measurement service was made with particular care by highly trained personnel.

In a few columns, only three windows could be opened, due to access limitations, losing in this way the redundancy discussed above, but still allowing the separation of the normal from the bending loads. The windows were typically around 200mm high, and their depth and horizontal size were kept as small as possible (around 150mm wide with a 50 to 100mm depth, see Fig.1) to allow the preparation of the rod's surface for bonding the strain gage, and the subsequent cut of the lower part of the exposed rod by a 125mm abrasive wheel.

A carefully grounded small plane recess was introduced at the superior part of each exposed rod inside the small windows opened around the column, which surface was later on finished by hand using a 220 grid sand paper. In most cases, these plane recesses were about 8 to 12mm wide and 40 to 60mm long. After proper cleaning the sanded recess surface, a uniaxial strain gage was bonded on

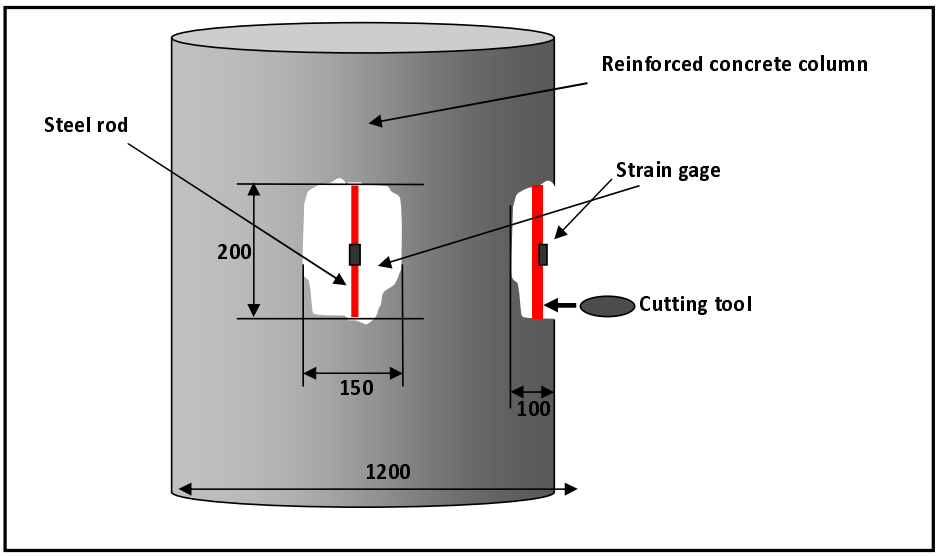

Figure 1: Sketch of the residual or resident strain measurement procedure.

it using a cyanoacrilate adhesive. The gages were then connected to a three wire shielded cable, and finally protected by a neutral silicone rubber barrier.

To make the residual strain measurements, after having bonded, cabled and protected all the four gages (or three, if one side of the column was not accessible) of a column, they were simultaneously connected to a precision four channel portable strain indicator, and properly balanced. Then the lower part of the rods were slowly cut by the abrasive wheel, always in several steps to allow for proper water cooling during the progressive cutting, in order to avoid overheating the gage (this task was easily achieved by holding the rods with a bare hand). The cuts were always performed at least 100mm (or more than 4 to 5 rod diameters) from the gage, and the strain readings were only made after the complete stabilization of their (small) thermal transients.

It is worth mentioning that if the concrete layers over the rods were sufficiently thick, or if the columns were made of non-reinforced concrete, the rod sectioning method could be substituted by the tick-tack-toe method proposed elsewhere [1].

Despite all the care, the measured results turned out to be much higher than initially expected, a big problem for the engineers in charge of the expansion project. Thus, the first reaction of the experts on concrete structures, who should in principle provide the columns stiffness properties necessary for the loadings calculations, was to question the accuracy of the strain measurements. This questioning was an irrefutable and welcome challenge for the measuring team, whose solution turned out to be quite interesting, as shown in the following sections.

Mechanics of Solids in Brazil 2009, H.S. da Costa Mattos & Marcílio Alves (Editors)
Brazilian Society of Mechanical Sciences and Engineering, ISBN 978-85-85769-43-7

2 Strain measurements

Before starting any analysis, it is important to point out that the released strain measured in any steel rod of a reinforced concrete column can in general be due to the superposition of several mechanisms, namely:

1. the rod service stress, which is caused by the column load (remembering that this load, whose evaluation is the final objective of such a measurement, generally has both a compression and a bending component);
2. concrete creep under the service load (the steel rods do not creep significantly at room temperature, but their strain also increase as time passes by to maintain their geometrical compatibility with the slowly creeping concrete);
3. concrete shrinkage during its cure (whose consequences are similar to creep);
4. residual stresses introduced during the rods' manufacturing (e.g. by non-uniform plastic deformations and/or heat treatments);
5. residual stresses introduced during the mounting of the reinforcement (by bending, torsion and/or tying of the reinforcing rods);
6. concrete removal to expose the rod for the measuring process (the load carried by that small volume is partially transferred to the exposed rod); and
7. rod cross section decrease during the preparation of its surface for bonding the gage (if the rod load is constant, its stress and strain increase as the cross section decreases).

The severance of any rod interrupts its force path and, as a result, completely releases all these strain components under the gage, no matter which mechanisms caused them. This strain alleviation can be correlated with the rod stress, and thus with the forces that were imposed in the rod to cause it, if:

1. it can be supposed that the stress caused by the load in the rod is uniaxial, a quite reasonable assumption in such a slender member built into a concrete column of a much larger diameter; and
2. all the other strain parcels can be neglected or properly evaluated.

Since the rod sectioning cuts where always made several rod diameters from the gages, the residual stresses eventually (and usually) introduced during the rods manufacture, which are of course self-equilibrating in any cross section, should not significantly affect the gage measurements according to Saint Venant's principle. Consequently, component 4 of the above list could be safely neglected when analyzing the total released strain.

As all 4 (or 3) gages of a given column were continuously monitored during the cutting process, it could be observed that cutting a rod did not influence the others, whose signals remained balanced within the strain indicator noise level (always less than (5μm/m). Therefore, the column stiffness loss introduced by alleviating the instrumented rods was negligible, and so was the 6th listed component of the total rod strain.

All the exposed rods were checked for lateral displacements and/or rotations after the cuts, but they maintained the alignment in almost all cases, evidence that the mounting stresses which could cause the 5th listed strain component were also negligible.

Mechanics of Solids in Brazil 2009, H.S. da Costa Mattos & Marcílio Alves (Editors)
Brazilian Society of Mechanical Sciences and Engineering, ISBN 978-85-85769-43-7

Finally, the effect of the rod cross section reduction, necessary for mounting the gage, could easily be accounted for, as schematized in Figure 2. The grinding of a short and small plane recess on the rods surface was needed to bond the gage (because reinforced rods have a very rough surface and a helical external thread for improving their adherence to the concrete), but they not only reduced the rod cross section, as they also introduced some local bending due to the eccentricity of their (assumed) pure compression load.

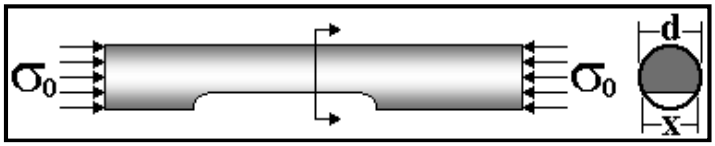

Figure 2: The small recess for bonding the gages introduces some bending strains in the rod.

The exposed part of the rod is really loaded under displacement control, since its strain is imposed by the rest of the column, which is much stiffer than the rods. However, since the recess was small and short, it can be modeled as if it was loaded under a pure axial load which induced a stress σ_0 on its section.

Thus, if σ_0 is the pure nominal compression stress acting on the original section of a reinforcing rod of diameter d and area $A_0 = \pi d^2/4$, x is the width of the recess, and $A = d^2(\alpha - \sin\alpha\cdot\cos\alpha)/4$ is the area of the plane recess section, where $\alpha = \pi\ asin(x/d)$, then the stress σ under the gage (which has a normal and a bending component) is given by (see Figure 3):

$$\sigma = \frac{32\sigma_0 A_0}{3d^2}\left\{\frac{\frac{(\sin\alpha)^3}{(\alpha-\sin\alpha\cdot\cos\alpha)}\left[\frac{2(\sin\alpha)^3}{3(\alpha-\sin\alpha\cdot\cos\alpha)}-\cos\alpha\right]}{\alpha-\sin\alpha\cdot\cos\alpha+2(\sin\alpha)^3\cdot\cos\alpha-\frac{16(\sin\alpha)^6}{9(\alpha-\sin\alpha\cdot\cos\alpha)}}+\frac{1}{A}\right\} \tag{1}$$

The mean value of the released strains measured after having cut more than 100 reinforcing rods of 28 different columns was $\epsilon_m = 1325\mu m/m$, and the maximum was $\epsilon_{max} = 2600\mu m/m$. Thus, most measured strains were still within the linear elastic range of the steel rods, except for ϵ_{max} that was slight above ϵ_{Ymin}. But they indeed seem to be too large for the concrete, whose ultimate design strain is generally taken as $\epsilon_U = 2000\mu m/m$. No prudent structural engineer would ever want to approach such a value under the maximum load conceived for his or her design. Even after considering the recess correction, which decreased the measured strain values in average by 20%, in a first look they still seems to imply that the columns were or could be unsafe. But there was no other evidence of such a problem, since no cracking, screaking or any other warning was ever emitted by the columns, even after opening the windows to expose the rods. As a result, it was much simpler to just dismiss the measurements, assuming they were simply wrong.

On the other hand, there was no evidence of any problem with the measured strains. The measurements followed reliable and very well established procedures, including electrical tests of the reading

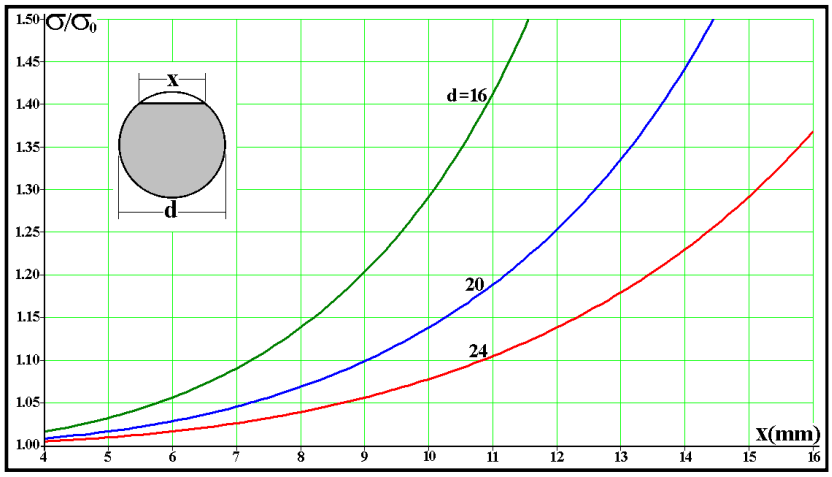

Figure 3: Ratio σ/σ_0 as a function of the recess width x for the three rod diameters: this effect is not negligible in most cases, and it must be accounted for in the load analysis.

equipment with high precision resistors and operational tests of the installed gages, always generating consistent checks. Moreover, as the tests were made by veteran engineers with a long practical experience in the field and a sound theoretical background, their qualitative opinion is an asset that cannot be ignored. Therefore, something had to be done to make sense out of these two apparently incompatible, but very strong evidences, as explained below.

3 The viscoelastic behavior of concrete

Concrete is made by mixing gravel, sand and a calcium silicate cement powder, which are all ceramic materials, with water, which hydrates and hardens the cement to form a rock-like composite. Therefore, it may sound strange to talk about concrete creep at room temperature. Nevertheless, concrete can creep a lot. For example, Figure 4 shows some concrete creep data presented by Leeth [2]. According to Buyukozturk [3], concrete creep is influenced by factors that can be internal, dependent on the concrete composition (such as concentration, stiffness, grading, distribution and permeability of the aggregate, water/cement ratio, cement type, etc.), or external, dependent on structural parameters (size, shape, environment, loading, etc.). Moreover, creep strains are linearly proportional to the stress typically if $\sigma < f'_c/2$, where f'_c is the concrete compressive strength, usually measured after a 28 day curing time.

The three curves shown in Figure 4 show only the creep strains measured under 2.1, 4.2 and *6.3MPa*, which after 600 days are ϵ_{cr} = *446*, 872 and *1325μm/m* (but the total strain has also an initial elastic part $\epsilon_{el} = \sigma/E$ = *100*, 200 and *300μm/m*, respectively.) Therefore, the creep strains are certainly not negligible in these tests. Moreover, these creep strains are indeed linearly proportional to the stresses,

as shown in Figure 5, where the curves obtained under 2.1 and *4.2MPa* practically coincide with the *6.3MPa* curve when multiplied by 3 and 1.5, respectively.

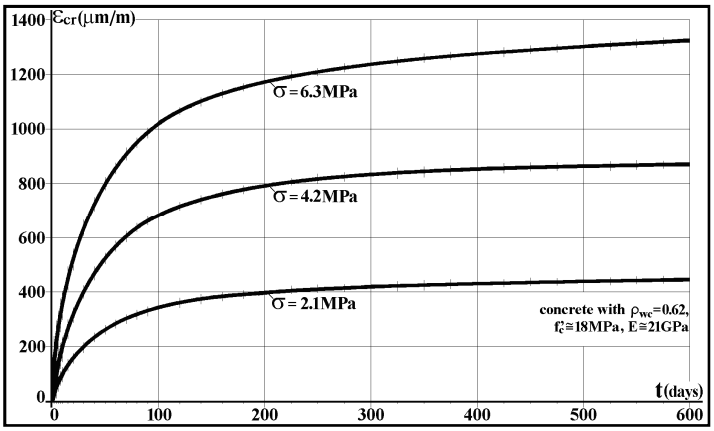

Figure 4: Time variation of creep strains under compressive stresses (plotted as positives for convenience) for a concrete with compressive strength $f'_c = 18MPa$, Young's modulus $E_{c28} \cong 1.36(\rho_c^3 \cdot f'_c)^{0.5} \cong 21GPa$ (both measured, as usual, 28 days after casting), water/cement ratio ρ_{wc} = *0.62*, and density $\rho_c \cong$ *2.3*.

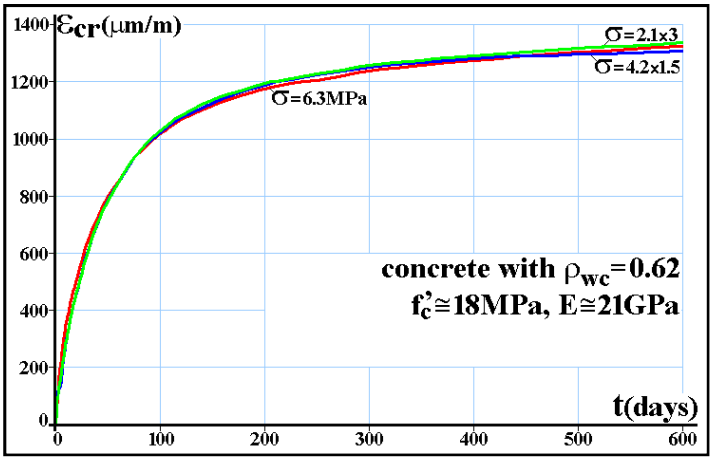

Figure 5: The concrete whose creep curves are shown in Figure 4 is indeed a linear viscoelastic material, since the 3 curves practically coincide when properly scaled by a **6.3/**σ factor.

The next step is to find a proper rheological model to reproduce all these curves, which should not include the elastic strains as they show only the creep strains. A first option could be to try to fit the data by a Kelvin-Voigt equation, but as the experimental creep data does not show a horizontal asymptote, at least another damper is needed in the model.

A generic non-linear curve can be fitted to a set of data by minimizing its mean square deviation from that set using, for example, the Levenberg-Marquardt (LM) algorithm [4, 5]: given a set of m points (x_i, y_i), $i = 1, \cdots, m$, LM searches for the parameter vector $p = [p_1, p_2, \cdots, p_n]^T$ (where T means transpose) containing the n constants of the specified $f(x_i, p)$ function which minimizes the sum of the square deviations:

$$S(p) = \sum_{i=1}^{m} [y_i - f(x_i, p)]^2 \tag{2}$$

The LM algorithm can be applied to non-linear vectorial functions, whereas x_i can be a scalar for one-variable functions, or a vector for functions of more than one variable. But in the following formulation, $f(x_i, p)$ and y_i are supposed scalars. It is didactic to present a few practical applications of such functions, for example, in fatigue: when using Paris' rule $da/dN = f(x_i, p) = A \cdot \Delta K^m$, $x_i = \Delta K$ and $p = [A_p, m]^T$; whereas for Walker's rule $da/dN = f(x_i, p) = A_w \Delta K^{m_w} K_{\max}^{p_w}$, $x_i = [\Delta K, K_{max}]^T$ and $p = [A_w, m_w, p_w]^T$; and for Coffin-Manson's rule $\Delta\epsilon = f(x_i, p) = (2\sigma_c/E)(2N)^b + (2\epsilon_c)(2N)^c$, $x_i = N$ and $p = [\sigma_c, E, b, \epsilon_c, c]^T$.

LM is an iterative procedure, which depends on an initial estimate for the vector p, which for highly non-linear functions needs to be fairly close to the final solution to guarantee convergence. However, this normally is not the case when fitting data obtained in mechanical tests. In each iteraction, p is replaced by a new estimate $p + q$. To find the vector $q = [q_1, q_2, \cdots, q_n]^T$, the functions $f(x_i, p + q)$ are approximated by their linearizations, given by

$$f(x_i, p + q) \cong f(x_i, p) + J(x_i, p) \cdot q \tag{3}$$

where J is the Jacobian of f with respect to p:

$$J(x_i, p) = \left[\frac{\partial f(x_i, p)}{\partial p_1}, \frac{\partial f(x_i, p)}{\partial p_2}, ..., \frac{\partial f(x_i, p)}{\partial p_n} \right] \tag{4}$$

In the case discussed here, as f is scalar, the Jacobian results in the gradient of f with respect to p. When the sum of the deviations $S(p)$ is minimum, the gradient of S with respect to q is equal to zero. Therefore, applying equation (2) at $S(p + q)$, and making $\partial S/\partial q = 0$, results in

$$\sum_{i=1}^{m} \{J(x_i, p)^T \cdot J(x_i, p)\} \cdot q = \sum_{i=1}^{m} \{J(x_i, p)^T \cdot [y_i - f(x_i, p)]\} \tag{5}$$

In this manner, the correction vector $q$can be obtained in each iteraction by:

$$q = \left[\sum_{i=1}^{m} J(x_i,p)^T \cdot J(x_i,p)\right]^{-1} \cdot \sum_{i=1}^{m} \{J(x_i,p)^T \cdot [y_i - f(x_i,p)]\} \tag{6}$$

All the m experimental data points can be stacked in an $m \times n$ matrix J_t and in an $m \times 1$ error vector e_t, defined as:

$$J_t(p) \equiv \begin{bmatrix} J(x_1,p) \\ J(x_2,p) \\ \vdots \\ J(x_m,p) \end{bmatrix} \tag{7}$$

Then, equation (6) can be rewritten as:

$$q = (J_t^T J_t)^{-1} J_t^T \cdot e_t \equiv pinv(J_t) \cdot e_t \tag{8}$$

where $pinv(J_t)$ is known as the pseudo-inverse of J_t, with $pinv(J_t) \equiv (J_t{}^T J_t)^{-1} J_t{}^T$. After finding q in each iteraction and summing it to the current p estimate, the algorithm continues updating p until the correction q has absolute value smaller than a given tolerance.

If f varies linearly with p, then J does not depend on p, and the algorithm converges in only one iteration. Even when J depends on p, the use of a log-log scale usually guarantees convergence in a few iterations. It is advisable to monitor the value of the deviation sum $S(p)$, which should always decrease at each iteration. If $S(p)$ increases in some iteration, a possibility when working with highly non-linear functions, it is necessary to introduce a positive damping term λ in the pseudo-inverse:

$$q = (J_t^T J_t + \lambda I)^{-1} J_t^T \cdot e_t \tag{9}$$

where I is the identity matrix $n \times n$. The damping factor λ is updated at each iteration. If the $S(p)$ reduction is too high, smaller values are chosen for λ to avoid that the algorithm becomes unstable. On the other hand, if $S(p)$ decreases too slowly, λ is increased to accelerate the convergence of the iterative calculations.

Marquardt [5] recommends that damping be introduced in the numerical calculation algorithm for calculating the correction vector q by guessing an initial value $\lambda = \lambda_0 > 0$ and a correction factor $v > 1$, e.g. $\lambda = 1$ and $v = 2$. At each iteration, q is calculated using a damping factor λ/v. If $S(p + q) < S(p)$, then this q is summed to p, $\lambda = \lambda/v$ is chosen as the new factor, and a new iteration is made. In the opposite case, q is recalculated using λ. If $S(p + q) < S(p)$, then this q is summed to p, λ is maintained, and a new iteration begins. If in both cases $S(p + q) \geq S(p)$, then q is recalculated with damping factors $\lambda \cdot v^k$, $k = 1, 2, \cdots$, at each new iteration until obtaining $S(p + q) < S(p)$. When this occurs, then this q is summed to p, $\lambda = \lambda \cdot v^k$ is chosen as the new damping factor, and the iterations continue. With this procedure, the algorithm stability is guaranteed.

As shown in Figure 6, two viscoelastic models are used to fit the average of the curves shown in Figure 5, using the above procedures. The first model is Kelvin-Voigt's, with its 2 parameters k and

c obtained by minimizing the mean square error, generating curve 1. The second is a Kelvin-Voigt model in series with a damper, generating curves 2 and 3, either by applying the same method or by visually re-fitting the parameters c_1, c_2 and k_2, respectively. The introduction of a damper in series with the Kelvin-Voigt element improves the data fitting, but the "optimum" mathematical adjustment is not as good as the old-fashioned eye-ball data fitting used to obtain curve 3. This visual tuning of the parameters generated by LM is a much recommended procedure, since there is no substitute for a well trained human judgment: the eye-ball fitting does not minimize the least square error, however it ended up fitting better the long-term creep behavior, especially after 500 days. But such a refinement by man-machine interaction is only possible after knowing the mathematically optimized parameters. In these cases, it is a particularly powerful tool when working with non-linear functions.

The LM generated curve 1 parameters are $k = 5GPa$ and $c = 21.6GPa{\cdot}s$, whereas for curve 2 the optimum parameters are $c_1 = 1.196TPa{\cdot}s$, $k_2 = 5.8GPa$ and $c_2 = 18.92GPa{\cdot}s$. The subjective final visual adjustment of curve 3 generates $c_1 = 1.814TPa{\cdot}s$, $k_2 = 5.8GPa$ e $c_2 = 21.6GPa{\cdot}s$. But to model the total concrete strain, another spring $k_1 = 21GPa$ in series with the damper c_1 must be used to simulate the elastic modulus $E_{c_{28}}$estimated above, see Figure 7.

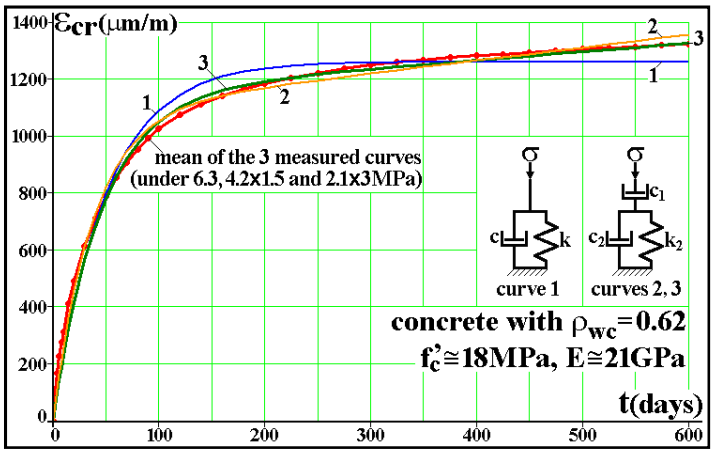

Figure 6: Fitting of the concrete creep data presented in Figure 5.

This 4-element Burger model shown in Figure 7 is capable of reproducing well the long term mechanical behavior of the concrete whose creep data is given in Figure 4. However, to model a reinforced concrete column under pure compression, it is necessary to use still another spring in parallel with the Burgers model, to describe the effect of the steel rods. Only one spring is needed because the steel creep can be neglected at room temperature. Also, this spring is in parallel with the concrete model because both see the same strains to maintain geometric compatibility inside the column.

Therefore, if A_s is the total area of the reinforcing steel rods and A_c is the concrete area in a column whose cross section area $A = A_s + A_c$, then $fa_s = A_s/A$ and $(1 - fa_s)$ are the area fractions of the steel

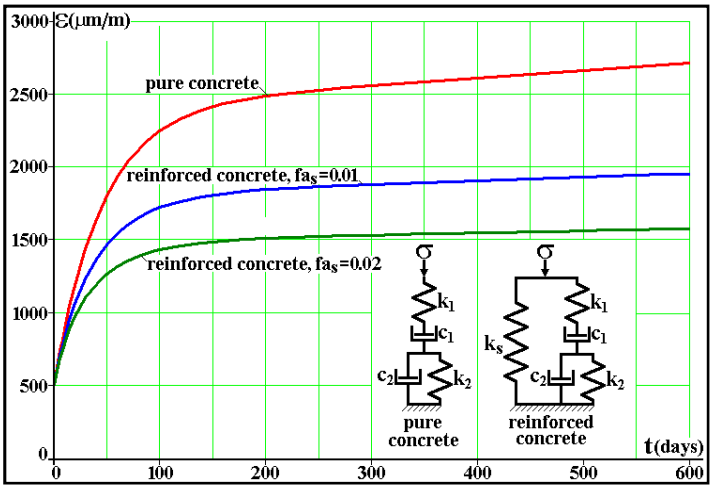

Figure 7: Strain histories $\epsilon(t)$ estimated by equation (10) for a pure concrete and for two steel reinforced concrete columns with steel area fractions $fa_s = 1\%$ and $fa_s = 2\%$, when they are loaded by a fixed force that causes an initial strain $\epsilon_0 = 500\mu m/m$. The concrete is modeled as a linear viscoelastic Burgers' material with constant parameters $k_1 = 21GPa$, $c_1 = 1.814TPa{\cdot}s$, $k_2 = 5.8GPa$ e $c_2 = 21.6GPa{\cdot}s$, whereas the steel reinforcement is modeled as a Hookean material with $k_s = 200GPa$.

and the concrete in the column. If F is the force (supposed constant) which loads the column; E_s is the steel elastic modulus (which does not creep) and $E_c(t)$ is the (variable) creep modulus of the concrete; $\sigma_s(t)$ and $\sigma_c(t)$ are the stresses on the rods and on the concrete (both vary in time, since the concrete creep transfers loads to the steel reinforcing rods); and $\epsilon(t)$ is the column strain (which also varies as time passes by), then it is trivial to show that the compressive force in the column is $F = \sigma_s(t){\cdot}A_s + \sigma_c(t){\cdot}A_c = \epsilon(t){\cdot}[E_s{\cdot}A_s + E_c(t){\cdot}A_c]$, therefore:

$$\varepsilon(t) = \frac{F}{E_s A_s + E_c(t) A_c} = \frac{F/A}{fa_s k_s + \frac{(1-fa_s)}{1/k_1 + t/c_1 + [1-\exp(-k_2 t/c_2)]/k_2}} \tag{10}$$

It is also easy to show that the equivalent stress in the column is given by:

$$\sigma = F/A = \varepsilon(0)[fa_s k_s + (1-fa_s)k_1] = \varepsilon_0[fa_s k_s + (1-fa_s)k_1] \tag{11}$$

The steel area in a reinforced concrete column is typically 1 to 2% of its total area. Knowing that the (elastic) ultimate strain in reinforced concrete structural design is usually assumed as $2000\mu m/m$, a column designed for an initial strain $\epsilon_0 = 500\mu m/m$ can thus be considered representative of the problems found in practice. Using this value, Figure 7 shows the strain time variations expected from a pure concrete column (with $f'_c = 18MPa$ and all the viscoelastic properties obtained above), and

from two reinforced concrete columns, one with a steel area fraction $fa_s = 0.01$ and the other with $fa_s = 0.02$.

Figure 7 demonstrates that strains in the order of $\epsilon_{max} = 1500$ to $2000\mu m/m$ are certainly not incompatible with typical working loads applied on reinforced columns made out of the concrete whose creep strains are described by Figure 4. But this figure does not include several important details about the concrete properties, which had to be estimated in order to generate the information that supports this claim, a fact that decreases its power. However, a quite comprehensive report by Ziehl et al. [6] presents several such details, removing any doubts about the adequacy of this approach.

Ziehl and his colleagues studied if reinforced concrete columns with steel area fractions $fa_s < 1\%$, the minimum steel fraction required by the American standard [7, 8], could be used for structural purposes. They said that those existing minimum fa_s requirements for columns were developed to prevent yielding of the reinforcement resulting from creep deformations in the concrete; that the tests used to support this limit were conducted decades ago, when steel yield strengths for reinforcing bars were approximately half of what is common today; and that a substantial reduction in the column steel area fraction might be possible with present-day materials, resulting in economic savings.

Ziehl et al. have cast several *203mm* (*8"*) diameter by *1219mm* (*4'*) long cylindrical columns made out of two concretes with nominal compressive strengths (at 28 days) of 28 and *56MPa* (4 and *8ksi*), with three steel fractions fa_s (0.36, 0.54, and *0.72%*). They have subjected them to a constant axial load $F = 0.4 \cdot f'_c \cdot A$ (the maximum load allowed by ACI [8] and AASHTO [9] standards) in reduced-humidity enclosures, and measured their long-term axial deformations using electronic and mechanical strain gages. The load was applied through coil springs, to provide the necessary compliance. Unloaded specimens were used to monitor temperature and shrinkage-related deformations. They presented plots of measured strain versus time, and compared the experimental results with an empirical model reported by the ACI Committee 209 [7].

The columns were cast in cardboard molds, which were stripped five days after having poured the concrete. These columns were loaded between 14 and *28 days* after casting. To determine the material properties, *4×8* and *6×12* inch test cylinders were also cast for every group of columns. These cylinders were tested for modulus of elasticity and compressive strength at 7, 14, 28, and *56 days* after casting. The steel rods were tested for yield and ultimate strengths. Dehumidifiers were used to keep the relative humidity and temperature generally between 30 and *60%* and 10 and 43^oC. The period required to load the columns for a length of time sufficient for the rate of creep to approach nearly zero was initially estimated to be close to two years, but in practice it was 15 to 18 months, depending on the specimens. Ziehl's report is particularly meticulous, and should be consulted for further details on concrete specifications and experimental procedures. Figures 8-11 show how the technique discussed above can quite reasonably fit some of their data.

4 Conclusions

A relatively simple linear viscoelastic model was proposed to describe concrete creep, and extended to model the behavior of reinforced columns under axial loading. The model treats the concrete as a Burgers' solid, composed by a Maxwell's element with a spring k_1 (which represents its short term

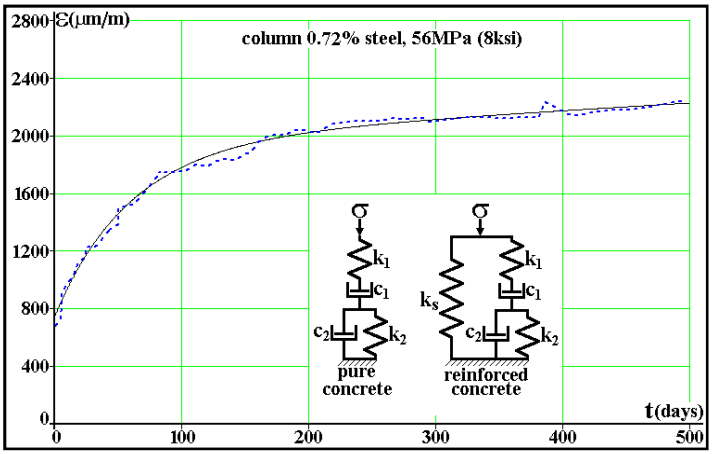

Figure 8: Total (elastic plus creep) strain history $\epsilon(t)$ estimated by equation (10) for a reinforced concrete column with f'_c= *56MPa* and steel area fraction fa_s = *0.72%*, loaded by a fixed force that induces an initial (elastic) strain ϵ_0 = *800μm/m* (curve generated by using the fitted viscoelastic parameters k_1 = *37.54GPa*, c_1 = *40TPa·day*, k_2 = *19GPa* and c_2 = *1.2TPa·day*.)

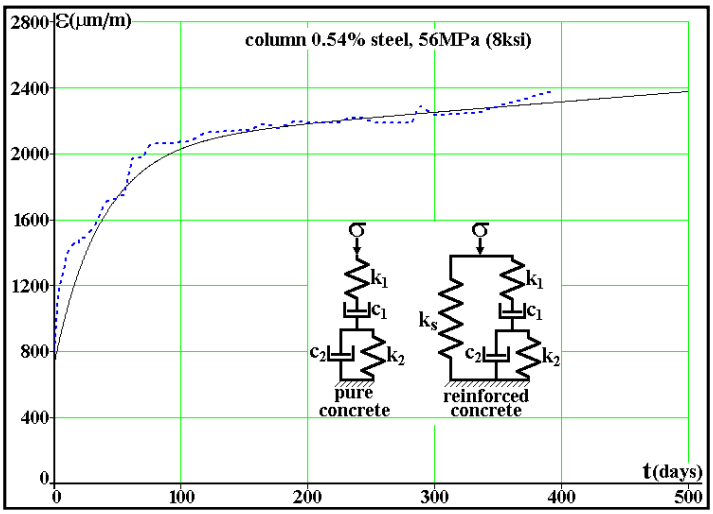

Figure 9: Strain history $\epsilon(t)$ for a f'_c= *56MPa* reinforced concrete column with steel area fraction fa_s = *0.54%*, loaded by a force that causes an initial strain ϵ_0 = *800μm/m* (curve generated using k_1 = *24.87GPa*, c_1 = *80TPa·day*, k_2 = *6.5GPa* and c_2 = *340GPa·day*.)

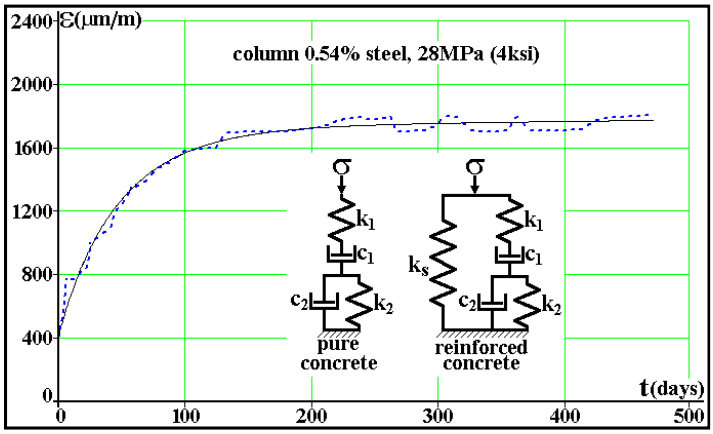

Figure 10: Strain history $\epsilon(t)$ for a f'_c= *28MPa* reinforced concrete column with steel area fraction fa_s = *0.54%*, loaded by a fixed force that induces an initial strain ϵ_0 = *400μm/m* (k_1 = *24.87GPa*, c_1 = *80TPa·day*, k_2 = *6.5GPa* and c_2 = *340GPa·day*.)

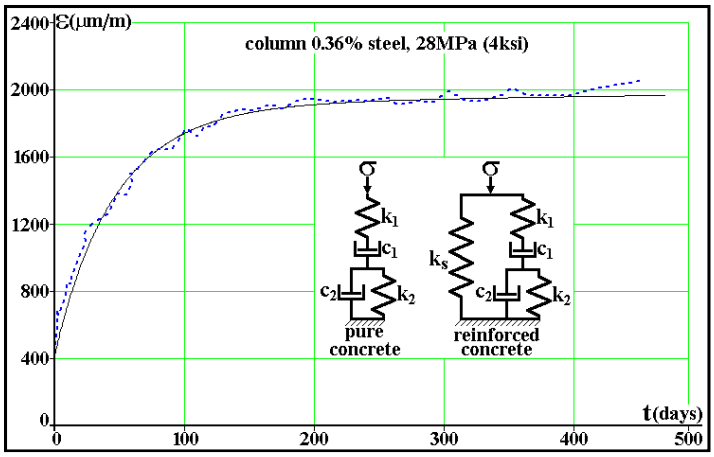

Figure 11: Strain history $\epsilon(t)$ for a f'_c= *28MPa* reinforced concrete column with steel area fraction fa_s = *0.36%*, loaded by a fixed force that induces an initial strain ϵ_0 = *400μm/m* (k_1 = *24.87GPa*, c_1 = *70TPa·day*, k_2 = *6GPa* and c_2 = *300GPa·day*.)

elastic modulus) and a damper c_1, in series with a Kelvin-Voigt element whose spring is k_2 and the damper is c_2. The reinforcing steel is modeled by a spring k_s in parallel with the concrete. This model satisfactorily fitted creep data measured in reinforced concrete column obtained from the literature, demonstrating its potential to explain why the residual strains measured in instrumented rods of the

subway station columns were so high when compared with the nominal design strains. Therefore, this procedure can be recommended to deal with similar load measurement problems.

Acknowledgements

Some of the authors have been partially supported by research scholarships provided by the Brazilian National Research Council, CNPq.

References

[1] Vieira, R., Castro, J.T.P. & Freire, J.L.F., A new technique for measuring loads in concrete columns. *Proceedings of the VI COTEQ*, 2002. In CD (in Portuguese).
[2] Leet, K., *Reinforced Concrete Design*. McGraw-Hill, 2nd edition, 1982.
[3] Buyukozturk, O., Creep and shrinkage deformation. *MIT 1054/1541 Mechanics and Design of Concrete Structures Course Notes*, 2004.
[4] Levenberg, K., A method for the solution of certain non-linear problems in least squares. *Quarterly of Applied Mathematics*, **2**, pp. 164–168, 1944.
[5] Marquardt, D., An algorithm for least-squares estimation of nonlinear parameters. *SIAM Journal on Applied Mathematics*, **11**, pp. 431–441, 1963.
[6] Ziehl, P.H., Cloyd, J.E. & Kreger, M.E., Evaluation of minimum longitudinal reinforcement requirements for reinforced concrete columns. Technical Report Report FHWA/TX-02/1473-S, 1998.
[7] ACI, *ACI 209-R86: Prediction of Creep, Shrinkage, and Temperature Effects in Concrete Structures*, 1986.
[8] ACI, *ACI 318-95: Building Code Requirements for Reinforced Concrete and Commentary*, 1995.
[9] AASHTO - American Association of State Highway and Transportation Officials, Washington, DC, *Standard Specification for Highway Bridges*. 15th edition, 1992.

Application of hybrid van der Pol-Rayleigh oscillators for modeling of a bipedal robot

Armando Carlos de Pina Filho
Universidade Federal do Rio de Janeiro, Urban Engineering Program, Polytechnic School, Technology Center, Rio de Janeiro/RJ – Brazil
Max Suell Dutra
Universidade Federal do Rio de Janeiro, Mechanical Engineering Program, COPPE, Technology Center, Rio de Janeiro/RJ – Brazil

Abstract

A large number of degrees of freedom is involved in human locomotion and well-coordinated movements of these degrees of freedom is essential. The main part of this coordination occurs in the central nervous system, which generates signals according to the desired gait. Nervous networks in the spinal marrow, known as central pattern generators (CPGs), are capable to produce rhythmic movements. A set of nonlinear oscillators can be used in control systems of locomotion as pattern generator, providing approximate trajectories for the legs. The objective of this work is the application of a coupled hybrid van der Pol-Rayleigh oscillators system for modeling of a bipedal robot. We analyzed a 2D model, with the three most important determinants of gait, that performs movements in the sagittal plane. Using oscillators with integer relation of frequency, we determined the response as a function of time and the stable limit cycles of the network formed by three oscillators, showing the behavior of knee and hip angles. From plotted graphics, the system provided excellent results when compared to experimental analysis, and we concluded that the use of coupled hybrid van der Pol-Rayleigh oscillators can represent an excellent method to signal generation, allowing their application for feedback control of a walking machine, presenting optimized functioning in relation to the systems that use only van der Pol or Rayleigh oscillators.

Keywords: CPG, gait, locomotion, oscillator, control.

1 Introduction

The objective of the study of mechanical limbs is not only to construct autonomous robots, but also to help in the rehabilitation of people that suffered some accident. The study of locomotion is inserted in this context, and the same one has been intensively studied since the second half of twenty century. The biped gait is one of the most complex in Nature. It requires not only an adequate physical structure,

Mechanics of Solids in Brazil 2009, H.S. da Costa Mattos & Marcílio Alves (Editors)
Brazilian Society of Mechanical Sciences and Engineering, ISBN 978-85-85769-43-7

but also an extremely accurate control system. Locomotion of humans and animals, performed by rhythmic and synchronized movements, involves a very large number of degrees of freedom, becoming essential a good coordination between them. The main part of this coordination is performed by spinal marrow, which generates signals according to the movement pattern of the desired gait [1]. This process of signal generation can be modeled by a pattern generator, which can be designed as a network of nonlinear oscillators [2–5].

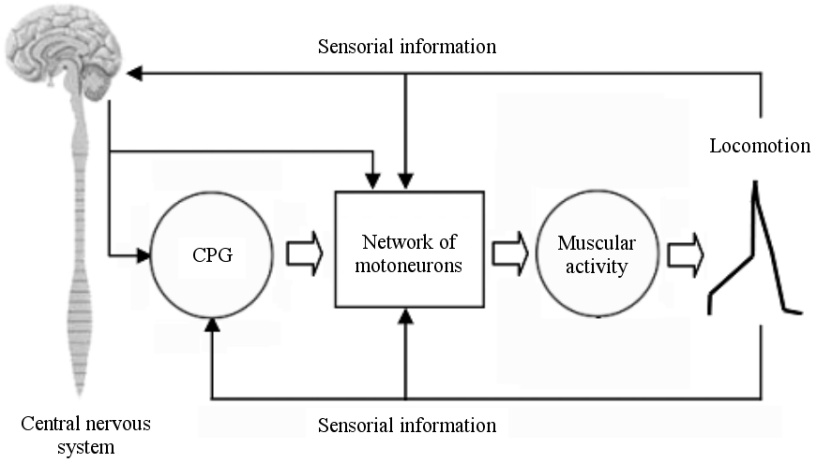

Figure 1: Control system of human locomotion.

Figure 1 presents a diagram of the control system of human locomotion controlled by the central nervous system, in which the CPG supplies a series of pattern curves. This information is passed to the muscles by means of a network of motoneurons, and the muscular activity performing the locomotion. Sensorial information about the environment conditions or some disturbance are supplied as feedback of the system, providing a fast action of the CPG, which to adjust the gait to the new situation [6].

Oscillators can be used in locomotor control systems similar to the patterns generator of the human gait, providing approach trajectories of the legs. Each pattern of movement requires a set of oscillator parameters and couplings. The gait can be modified by changing some parameters. Some kind of supervisory controller could be imagined, which would deliver and calculate the parameters for the pattern generator with a desired motion. The pattern of movement depends upon the parameters of the oscillators as well as the coupling between the oscillators. The generated signals can be used as reference trajectories for feedback control of a walking machine.

Mechanics of Solids in Brazil 2009, H.S. da Costa Mattos & Marcílio Alves (Editors)
Brazilian Society of Mechanical Sciences and Engineering, ISBN 978-85-85769-43-7

2 Description of the mechanical model

A feasible modeling of bipedal locomotion is made by reducing the number of degrees of freedom, since there are more than 200 involved in the human locomotion. According to Saunders et al. [7], the most important determinants of gait are: the compass gait, that is performed with stiff legs like an inverted pendulum; the pelvic rotation about a vertical axis; the pelvic tilt; the knee flexion of the stance leg, which effects combined with pelvic rotation and pelvic tilt achieve minimal vertical displacement of the center of gravity; the plantar flexion of the stance ankle; and the lateral displacement of the pelvis.

In order to further simplify the investigation, a 2D model that performs only movements in the sagittal plane will be considered. This model, presented in Fig. 2, characterizes the three most important determinants of gait: 1 (compass gait), 4 (knee flexion of the stance leg), and 5 (plantar flexion of stance ankle). The model does not take into account the motion of the joints necessary for the lateral displacement of the pelvis, the pelvic rotation, and the pelvic tilt.

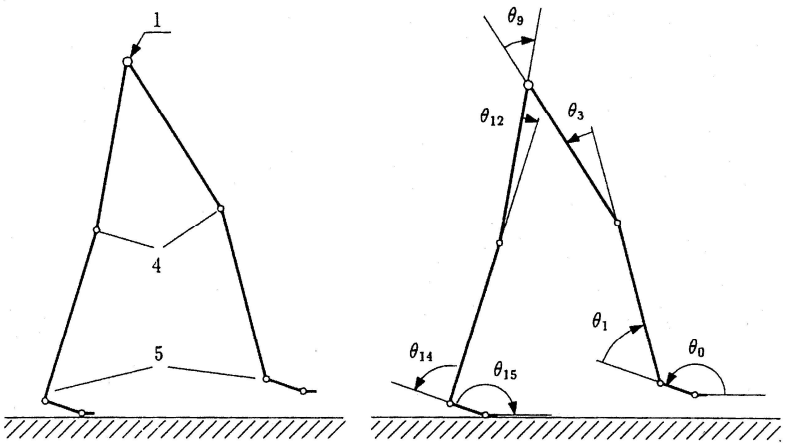

Figure 2: 2D model with the three most important determinants of gait and the relative angles.

The model used rigid-body assumption, where the natural structural movements of the skin and muscles, as well as bone deformities, are disregarded. The walking period can be divided into two intervals: single support phase (SSP), where one of the legs perform the movement of balance while the other is responsible for the support (the extremity of the support leg is assumed to be not sliding); and double support phase (DSP), where the transition of the legs occurs, i.e., the balance leg becomes the support leg and the other leg prepares to initiate the balance movement.

3 Central Pattern Generator (CPG)

The first indications that the spinal marrow could contain the basic nervous system necessary to generate locomotion date to the beginning of 20th century. According to Mackay-Lyons [8], nervous networks in the spinal marrow are capable to produce rhythmic movements, such as swimming, walking, and jumping, even when isolated of the brain and sensorial inputs. These specialized nervous systems are known as *nervous oscillators* or *central pattern generators* (CPGs).

Some significant works about vertebrate locomotion controlled by CPG include Grillner [9], Pearson [10], and Collins and Richmond [11]. Human locomotion is controlled, in a way, by a CPG, which is evidenced in works of Calancie et al. [12], and Dimitrijevic et al. [13].

Nonlinear oscillators system can be used as a central pattern generator. A great number of studies about the application of this principle has been performed, specially the application in hexapodal [14], quadrupedal [11] and bipedal models [15–18]. In this work the CPG is formed by a set of hybrid van der Pol-Rayleigh oscillators, where each oscillator generates angular reference signals for the motion of a single link (knees and hip).

4 Hybrid van der Pol-Rayleigh oscillator

A hybrid oscillator have characteristics of two types of oscillators and whose equation presents a combination of terms of these oscillators. Considering the equations of van der Pol:

$$\ddot{x} - \varepsilon \left(1 - p(x - x_0)^2\right) \dot{x} + \Omega^2 (x - x_0) = 0 \; \varepsilon, p \geqslant 0 \tag{1}$$

and Rayleigh:

$$\ddot{x} - \delta \left(1 - q\dot{x}^2\right) \dot{x} + \Omega^2 (x - x_0) = 0 \; \delta, q \geqslant 0 \tag{2}$$

the equation of hybrid oscillator that will be used in the analysis is:

$$\ddot{x} - \varepsilon \left(1 - p(x - x_0)^2\right) \dot{x} - \delta \left(1 - q\dot{x}^2\right) \dot{x} + \Omega^2 (x - x_0) = 0 \; \varepsilon, p, \delta, q \geqslant 0 \tag{3}$$

where ϵ, p, δ, q and Ω are the parameters of the oscillator. Using $y = \dot{x}$, we have the following autonomous system:

$$\begin{cases} \dot{x} = y \\ \dot{y} = \varepsilon \left(1 - p(x - x_0)^2\right) y + \delta \left(1 - qy^2\right) y - \Omega^2 (x - x_0) \end{cases} \tag{4}$$

Choosing values for ϵ, p, δ, q, Ω and x_0, using a program that integrates ordinary differential equations (ODE), it is possible to plot the graphic representation of x and $\dot{x}$ as functions of time and the trajectory in the phase space.

Setting $\epsilon = p = \delta = q = \Omega = 1$ and $x_0 = 0$, and using the Matlab, the graphic representation illustrating the hybrid van der Pol-Rayleigh oscillator behavior was generated (Fig. 3 and 4). Figure

3 shows the periodic movement of the oscillator and the limit cycle, while Fig. 4 presents the phase portrait.

An interesting characteristic of the hybrid oscillator is that depending on the relation between the values of ϵ and δ, it assumes a similar behavior to the van der Pol oscillator or Rayleigh oscillator. More details about the characteristics and behavior of each oscillators with limit cycle cited here are described in Hebisch [19].

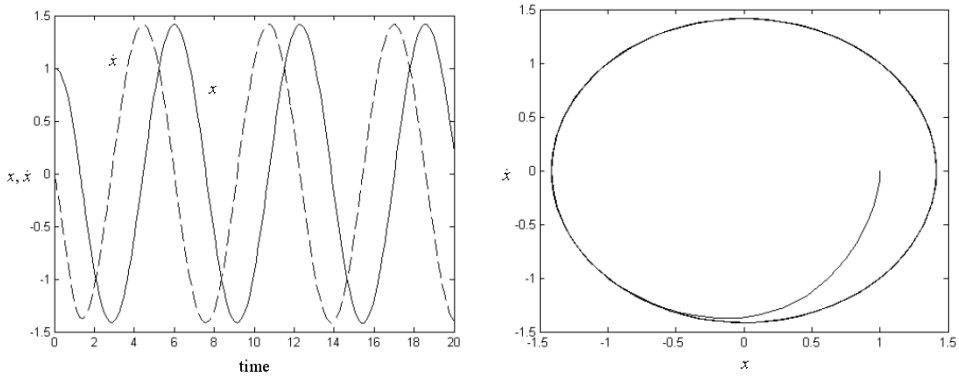

Figure 3: Graphical representation of x and $\dot{x}$ as a function of time, and the limit cycle.

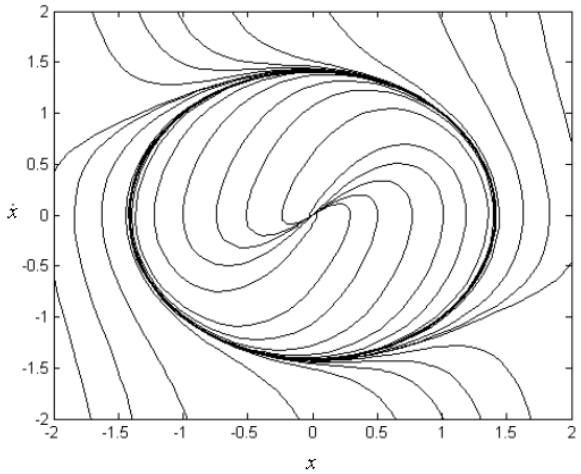

Figure 4: Phase portrait of the hybrid van der Pol-Rayleigh oscillator.

5 Coupled oscillators system

Taking into consideration the model shown in Fig. 2, the hip angle θ_9 and the knee angles θ_3 and θ_{12} will be determined by a nonlinear oscillators system. Experimental studies of human locomotion [20] and Fourier analysis of these data [21] show that the motion of knees and hip angles can be described very precisely by their fundamental harmonic, whether the biped is in DSP or SSP. Figure 5 shows the experimental results where θ_{3m}, θ_{9m} and θ_{12m} represent the curves built by means of experimental studies and θ_{3h}, θ_{9h} and θ_{12h} represent the approximation of these curves using the Fourier analysis. A set of three coupled oscillators was used to generate the angles θ_3, θ_9 and θ_{12}. These oscillators are mutually coupled by terms that determine the influence of one oscillator on the others (Fig. 5).

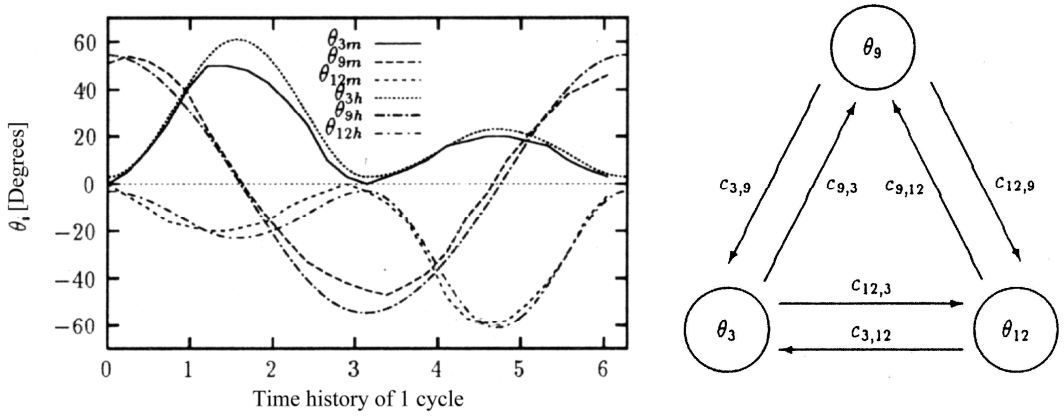

Figure 5: Experimental results and approximation using Fourier analysis, and coupled oscillators system.

5.1 Oscillators with the same frequency

A network of n-coupled hybrid van der Pol-Rayleigh oscillators is considered. From Eq. (3) and adding a coupling term that relates the velocities of the oscillators, we have:

$$\ddot{\theta}_i - \varepsilon_i \left[1 - p_i(\theta_i - \theta_{io})^2\right] - \delta_i \left(1 - q_i \dot{\theta}_i^2\right) \dot{\theta}_i + \Omega_i^2 \left(\theta_i - \theta_{io}\right) - \sum_{j=1}^{n} c_{i,j} \left(\dot{\theta}_i - \dot{\theta}_j\right) = 0 \; i = \; 1, \, 2, \, ..., \; n \quad (5)$$

where ϵ_i, p_i, δ_i, q_i, Ω_i and $c_{i,j}$ are the parameters of this system.

For small values of parameters determining the model nonlinearity, we will assume that the response is approximated by low frequency components from full range of harmonic response. Therefore, periodic solutions can be expected, which can be approximated by:

$$\theta_i = \theta_{io} + A_i \cos(\omega t + \alpha_i) \tag{6}$$

We desired to determine the values of the parameters q_i, p_i e Ω_i. In this case all oscillators have the same frequency ω. Deriving Eq. (6) and inserting the solutions in Eq. (5), by the method of harmonic balance [22], the following nonlinear equation system is obtained:

$$\begin{cases} A_i\left(\Omega_i^2-\omega^2\right)\ \cos\alpha_i + A_i\omega\left[\varepsilon_i\left(1-\frac{A_i^2 p_i}{4}\right)+\delta_i\left(1-\frac{3\omega^2 A_i^2 q_i}{4}\right)\right]\ sen\alpha_i + \omega\sum_{j=1}^{n} c_{i,j}\left(A_i sen\alpha_i - A_j sen\alpha_j\right)=0 \\ A_i\left(\omega^2-\Omega_i^2\right)\ \mathrm{sen}\alpha_i + A_i\omega\left[\varepsilon_i\left(1-\frac{A_i^2 p_i}{4}\right)+\delta_i\left(1-\frac{3\omega^2 A_i^2 q_i}{4}\right)\right]\ \cos\alpha_i + \omega\sum_{j=1}^{n} c_{i,j}\left(A_i\cos\alpha_i - A_j\cos\alpha_j\right)=0 \end{cases} \tag{7}$$

Moreover, it is possible to verify the following relation proposal by Hebisch [19]:

$$q_i = \frac{\varepsilon_i p_i}{\delta_i \omega^2} \tag{8}$$

Then, substituting the value of q_i in Eq. (7) and solving, the parameters p_i and Ω_i are:

$$p_i = \frac{1}{A_i^2} + \frac{\delta_i}{A_i^2\varepsilon_i} + \frac{1}{A_i^3\varepsilon_i}\sum_{j=1}^{n} c_{i,j}\left[A_i - A_j\cos(\alpha_i-\alpha_j)\right]\ \ i=\ 1,\ 2,\ ...,\ n \tag{9}$$

$$\Omega_i = \sqrt{\omega^2 - \frac{\omega}{A_i}\sum_{j=1}^{n} A_j c_{i,j} sen(\alpha_i-\alpha_j)}\ \ i=\ 1,\ 2,\ ...,\ n \tag{10}$$

Given the amplitude A_i and A_j, phase α_i and α_j, the frequency ω and the chosen values of ϵ_i, δ_i and $c_{i,j}$, the value of the parameters q_i, p_i and Ω_i can be calculated.

5.2 Oscillators with integer relation of frequency

Nonlinear oscillators with frequency ω can be synchronized with other oscillators with frequency $n\omega$, where n is an integer. In analyzing human gait, we can observe that some degrees of freedom have twice the frequency of the others ($n = 2$), that can be seen in Fig. 5.

Therefore, a network of coupled hybrid van der Pol-Rayleigh oscillators can be described as:

$$\ddot{\theta}_h - \varepsilon_h[1-p_h(\theta_h-\theta_{ho})^2]\,\dot{\theta}_h - \delta_h\left(1-q_h\dot{\theta}_h^2\right)\ \dot{\theta}_h + \Omega_h^2\left(\theta_h-\theta_{ho}\right) - \sum_{i=1}^{m} c_{h,i}\left[\dot{\theta}_i\left(\theta_i-\theta_{io}\right)\right] - \sum_{k=1}^{n} c_{h,k}\left(\dot{\theta}_h-\dot{\theta}_k\right)=0 \tag{11}$$

where $c_{h,i}\left[\dot{\theta}_i\left(\theta_i-\theta_{io}\right)\right]$ is responsible for the coupling between two oscillators with different frequencies, while $c_{h,k}\left(\dot{\theta}_h-\dot{\theta}_k\right)$ effects the coupling between two oscillators with the same frequencies.

Using a similar assumption as applied in Section 5.1. we have:

$$\theta_h=\theta_{ho}+A_h\,\cos\left(2\omega t+\alpha_h\right) \tag{12}$$

$$\theta_i=\theta_{io}+A_i\,\cos\left(\omega t+\alpha_i\right) \tag{13}$$

$$\theta_k=\theta_{ko}+A_k\,\cos\left(2\omega t+\alpha_k\right) \tag{14}$$

Deriving Eq. (12) -(14) and inserting the solutions in Eq. (11), a nonlinear equation system is obtained, and solving this system, the parameters p_h and Ω_h are:

$$p_h=\frac{1}{A_h^2}+\frac{\delta_h}{A_h^2\varepsilon_h}+\frac{1}{4A_h^3\varepsilon_h}\sum_{i=1}^{m}A_i^2c_{h,i}\cos\left(\alpha_h-2\alpha_i\right)+\frac{1}{A_h^3\varepsilon_h}\sum_{k=1}^{n}c_{h,k}\left[A_h-A_k\cos\left(\alpha_h-\alpha_k\right)\right] \tag{15}$$

$$\Omega_h=\sqrt{4\omega^2+\frac{\omega}{2A_h}\sum_{i=1}^{m}A_i^2c_{h,i}sen\left(\alpha_h-2\alpha_i\right)-\frac{2\omega}{A_h}\sum_{k=1}^{n}A_kc_{h,k}sen\left(\alpha_h-\alpha_k\right)} \tag{16}$$

Given the amplitude A_h, A_i and A_k, phase αh, αi and αk, the frequency ω and the chosen values of ϵh, δh, ch,i and ch,k, the value of these parameters qh, ph and Ωh can be calculated.

6 Analysis of the system and results

Considering the oscillators system presented in Fig. 5, from Eq. (11) the system can be described as:

$$\ddot{\theta}_3-\varepsilon_3[1-p_3(\theta_3-\theta_{3o})^2]\;\dot{\theta}_3-\delta_3\left(1-q_3\dot{\theta}_3^2\right)\;\dot{\theta}_3+\Omega_3^2\left(\theta_3-\theta_{3o}\right)-c_{3,9}\left[\dot{\theta}_9\left(\theta_9-\theta_{9o}\right)\right]-c_{3,12}\left(\dot{\theta}_3-\dot{\theta}_{12}\right)=0 \tag{17}$$

$$\ddot{\theta}_9-\varepsilon_9[1-p_9(\theta_9-\theta_{9o})^2]\;\dot{\theta}_9-\delta_9\left(1-q_9\dot{\theta}_9^2\right)\;\dot{\theta}_9+\Omega_9^2\left(\theta_9-\theta_{9o}\right)-c_{9,3}\left[\dot{\theta}_3\left(\theta_3-\theta_{3o}\right)\right]-c_{9,12}\left[\dot{\theta}_{12}\left(\theta_{12}-\theta_{12o}\right)\right]=0 \tag{18}$$

$$\ddot{\theta}_{12}-\varepsilon_{12}[1-p_{12}(\theta_{12}-\theta_{12o})^2]\;\dot{\theta}_{12}-\delta_{12}\left(1-q_{12}\dot{\theta}_{12}^2\right)\;\dot{\theta}_{12}+\Omega_{12}^2\left(\theta_{12}-\theta_{12o}\right)-c_{12,9}\left[\dot{\theta}_9\left(\theta_9-\theta_{9o}\right)\right]-c_{12,3}\left(\dot{\theta}_{12}-\dot{\theta}_3\right)=0 \tag{19}$$

The synchronized harmonic functions, corresponding to the desired movements, can be written as:

$$\theta_3=\theta_{3o}+A_3\;\cos\left(2\omega t+\alpha_3\right) \tag{20}$$

$$\theta_9=A_9\;\cos\left(\omega t+\alpha_9\right) \tag{21}$$

$$\theta_{12}=\theta_{12o}+A_{12}\;\cos\left(2\omega t+\alpha_{12}\right) \tag{22}$$

Considering $\alpha_3=\alpha_9=\alpha_{12}=0$ and deriving Eq. (20)-(22), inserting the solution in Eq. (17)-(19), the necessary parameters of the oscillators (q_i, p_i and Ω_i, $i\in\{3,9,12\}$) can be determined. Then:

$$p_3 = \frac{4c_{3,12}\left(A_3 - A_{12}\right) + 4A_3\left(\varepsilon_3 + \delta_3\right) + A_9^2 c_{3,9}}{4A_3^3\varepsilon_3} \tag{23}$$

$$\Omega_3 = 2\omega \tag{24}$$

$$q_3 = \frac{\varepsilon_3 p_3}{4\delta_3\omega^2} \tag{25}$$

$$p_9 = \frac{1}{A_9^2} + \frac{\delta_9}{A_9^2\varepsilon_9} \tag{26}$$

$$\Omega_9 = \omega \tag{27}$$

$$q_9 = \frac{\varepsilon_9 p_9}{\delta_9\omega^2} \tag{28}$$

$$p_{12} = \frac{4c_{12,3}\left(A_{12} - A_3\right) + 4A_{12}\left(\varepsilon_{12} + \delta_{12}\right) + A_9^2 c_{12,9}}{4A_{12}^3\varepsilon_{12}} \tag{29}$$

$$\Omega_{12} = 2\omega \tag{30}$$

$$q_{12} = \frac{\varepsilon_{12} p_{12}}{4\delta_{12}\omega^2} \tag{31}$$

From Eq. (17)-(19) and Eq. (23)-(31), and using the Matlab, the graphs shown in Fig. 6 and 7 were generated; they present, respectively, the behavior of the angles as a function of time and the stable limit cycles of the oscillators.

These results were obtained using the parameters shown in Tab. 1, as well as the initial values provided by Tab. 2. All values were experimentally determined.

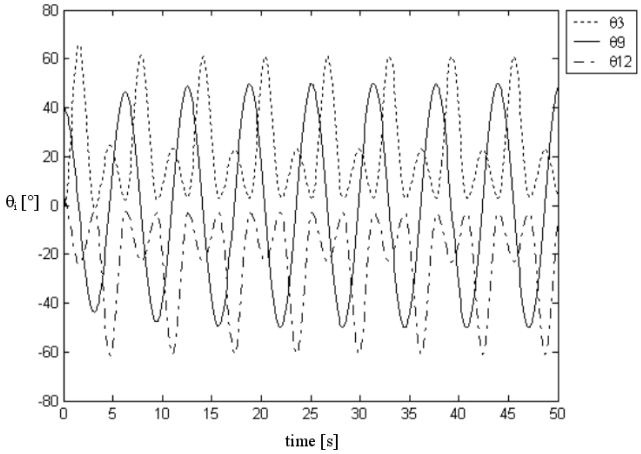

Figure 6: Behavior of θ_3, θ_9 and θ_{12} as a function of time.

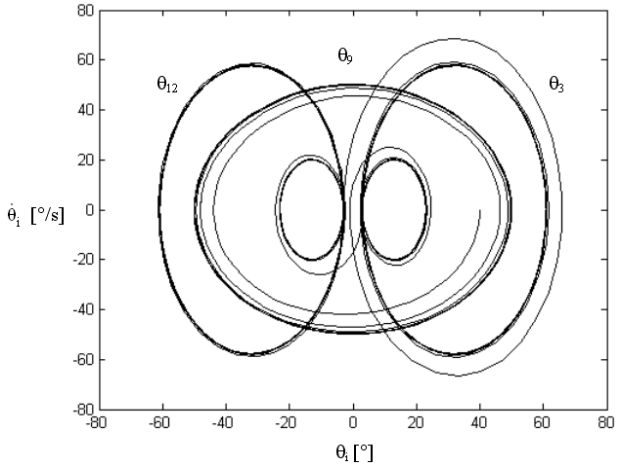

Figure 7: Trajectories in the phase space (stable limit cycles).

Table 1: Parameters of hybrid van der Pol-Rayleigh oscillators.

$c_{3,9}$	$c_{9,3}$	$c_{3,12}$	$c_{12,3}$	$c_{9,12}$	$c_{12,9}$	ϵ_3	ϵ_9	ϵ_{12}	δ_3	δ_9	δ_{12}
0.001	0.001	0.1	0.1	0.001	0.001	0.01	0.1	0.01	0.01	0.1	0.01

Table 2: Experimental initial values.

Cycle	A_3	A_9	A_{12}	θ_{3o}	θ_{9o}	θ_{12o}
$0 < \omega t \leq \pi$	-29	50	10	32	0	-13
$\pi < \omega t \leq 2\pi$	-10	50	29	13	0	-32

In Fig. 7 the great merit of this oscillator can be observed, i.e., if an impact occurs and the angle of one joint is not the correct or desired, it returns after a small number of periods to the desired trajectory. Considering, for example, a frequency equal to 1 s^{-1} and null initial velocities, with arbitrary initial values: θ_3 = -3°, θ_9 = 40° and θ_{12} = 3°, after some cycles we have: θ_3 = 3°, θ_9 = 50° and θ_{12} = -3°.

Comparing the results supplied for the coupling system using hybrid van der Pol-Rayleigh oscillators with the experimental results presented in recent work about human gait [23], it is verified that the coupling system supplies similar results, which confirms the possibility of using coupled hybrid van der Pol-Rayleigh oscillators in the modeling of the CPG. Figures 8 and 9 present the results comparison.

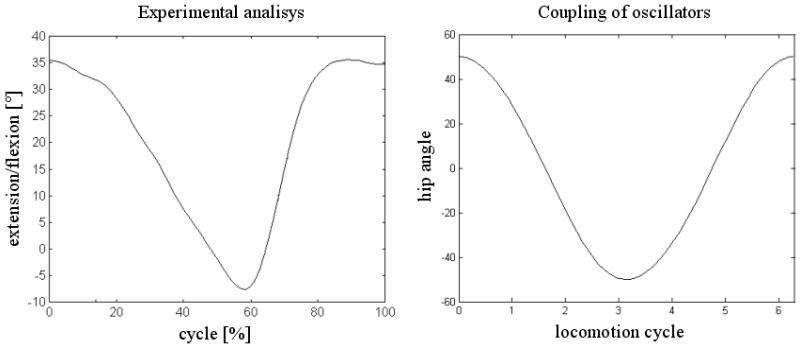

Figure 8: Behavior of the hip angle in the course of one locomotion cycle.

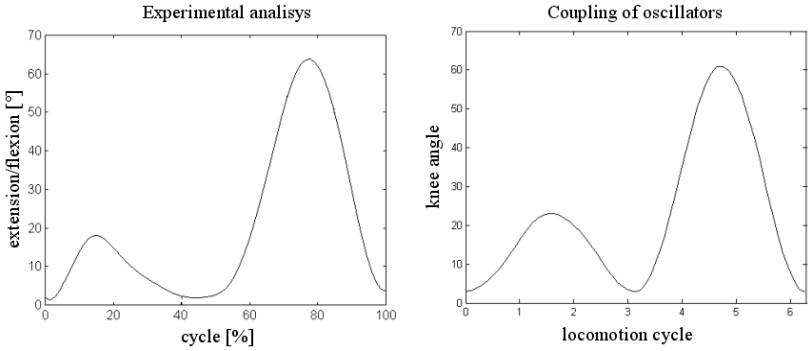

Figure 9: Behavior of the knee angle in the course of one locomotion cycle.

An interesting characteristic of the hybrid oscillators, verified in the course of the tests, is the fact of it to recover the periodicity of the movement faster than the van der Pol oscillators, using similar parameters. Therefore, if a small disturbance occurs and the angle of a joint is not the correct or desired, it is return more quickly to the desired trajectory. This difference in the recovery time is most significant in relation to the hip angle, but for the angles of the knees a small advantage for the hybrid oscillator still exists. The same advantage also exists in relation to Rayleigh oscillators, since the behavior of these is similar to van der Pol oscillators.

Finally, applying the system to the bipedal robot, we obtained the response shows in Fig. 10, which represents the gait with a step length of 0.63 m. The model have identical legs with 0.37 m for femur and tibia, and 0.11 for feet. Other step lengths and gaits can be simulated by changing some system parameters.

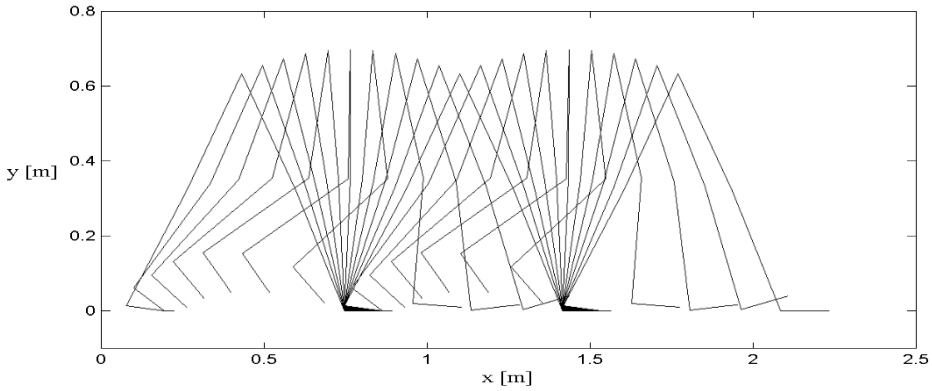

Figure 10: Stick diagram showing the gait with a step length of 0.63 m.

7 Conclusion

The results presented in this work and their analysis and discussion lead us to the following conclusions about the modeling of a bipedal robot using hybrid van der Pol-Rayleigh oscillators: (1) The use of these oscillators can represent an excellent way to signal generation, allowing their application for feedback control of a walking machine by synchronization and coordination of the lower extremities, presenting optimized functioning in relation to the systems that use only van der Pol or Rayleigh oscillators. (2) The model is able to characterize three of the six most important determinants of human gait. (3) By changing a few parameters in the oscillators, modification of the step length and gait frequency can be obtained. The gait frequency can be modified by means of Eq. (20)-(22) by choosing a new value for ω. The step length can be modified by changing the angles θ_9 and θ_{12}, with the parameters q_i, p_i e Ω_i, $i \in \{3, 9, 12\}$, being responsible for the gait transitions.

Acknowledgements

The author Armando Carlos de Pina Filho would like to express your gratitude to FAPERJ (Fundação Carlos Chagas Filho de Amparo à Pesquisa do Estado do Rio de Janeiro), Brazilian governmental entity promoter of the scientific and technological development, for the financial support for purchase of the equipment used in the course of this present research.

References

[1] Grillner, S., Control of locomotion in bipeds, tetrapods and fish. *Handbook of physiology*, American Physical Society: College Park, MD, pp. 1179–1236, 1981.
[2] Pavlidis, T., *Biological Oscillators.* Academic Press, Inc.: New York, 1973.

[3] Johnsson, A., Zur biophysik biologischer oszillatoren. *Biophisik*, Springer Verlag, 1978.
[4] Dutra, M.S., Modeling of a bipedal locomotor using nonlinear oscillators. *International Journal of Intelligent Mechatronics Design and Production*, **2(2)**, 1997.
[5] Pina Filho, A.C.d., *Study of Mutually Coupled Nonlinear Oscillators Applied in the Locomotion of a Bipedal Robot, D.Sc. Thesis*. Universidade Federal do Rio de Janeiro, COPPE/PEM: Brazil, 2005.
[6] Ivanenko, Y.P., Grasso, R., Zago, M., Molinari, M., Scivoletto, G., Castellano, V., Macellari, V. & Lacquaniti, F., Temporal components of the motor patterns expressed by the human spinal cord reflect foot kinematics. *Journal of Neurophysiology*, **90**, pp. 3555–3565, 2003.
[7] Saunders, J.B., Inman, V. & Eberhart, H.D., The major determinants in normal and pathological gait. *J Bone Jt Surgery*, **35A**, 1953.
[8] Mackay-Lyons, M., Central pattern generation of locomotion: A review of the evidence. *Physical Therapy*, **82(1)**, 2002.
[9] Grillner, S., Neurobiological bases of rhythmic motor acts in vertebrates. *Science*, **228**, pp. 143–149, 1985.
[10] Pearson, K.G., Common principles of motor control in vertebrates and invertebrates. *Annu Rev Neurosci*, **16**, pp. 265–297, 1993.
[11] Collins, J.J. & Richmond, S.A., Hard-wired central pattern generators for quadrupedal locomotion. *Biological Cybernetics*, **71**, pp. 375–385, 1994.
[12] Calancie, B., Needham-Shropshire, B., Jacobs, P., Willer, K., Zych, G. & Green, B.A., Involuntary stepping after chronic spinal cord injury. evidence for a central rhythm generator for locomotion in man. *Brain*, **117(Pt 5)**, pp. 1143–1159, 1994.
[13] Dimitrijevic, M.R., Gerasimenko, Y. & Pinter, M.M., Evidence for a spinal central pattern generator in humans. *Annals of the New York Academy of Sciences*, **860**, pp. 360–376, 1998.
[14] Collins, J.J. & Stewart, I., Hexapodal gaits and coupled nonlinear oscillators models. *Biological Cybernetics*, **68**, pp. 287–298, 1993.
[15] Bay, J.S. & Hemami, H., Modelling of a neural pattern generator with coupled nonlinear oscillators. *IEEE Trans Biomed Eng*, **34**, pp. 297–306, 1987.
[16] Zielinska, T., Coupled oscillators utilised as gait rhythm generators of a two-legged walking machine. *Biological Cybernetics*, **74**, pp. 263–273, 1996.
[17] Dutra, M.S., Pina Filho, A.C.d. & Romano, V.F., Modeling of a bipedal locomotor using coupled nonlinear oscillators of Van der Pol. *Biological Cybernetics*, **88(4)**, pp. 286–292, 2003.
[18] Pina Filho, A.C.d., Dutra, M.S. & Raptopoulos, L.S.C., Modeling of a bipedal robot using mutually coupled Rayleigh oscillators. *Biological Cybernetics*, **92(1)**, pp. 1–7, 2005.
[19] Hebisch, H., Vergleich verschiedener nichtlinearer schwinger als bausteine für einen bewegungsmustergenerator, diplomarbeit fachgebiet mechanik. *Universität-GH Duisburg, Germany*, 1992.
[20] Braune, W. & Fischer, O., *The Human Gait*. Springer Verlag: Berlin, 1987.
[21] Dutra, M.S., *Bewegungskoordination und Steuerung einer zweibeinigen Gehmaschine*. Shaker Verlag: Aachen, Germany, 1995.
[22] Nayfeh, A.H. & Mook, D.T., *Nonlinear oscillations*. John Wiley & Sons, Inc., pp. 59–61, 1979.
[23] Raptopoulos, L.S.C., *Estudo e Desenvolvimento de Equipamento de Baixo Custo para Análise da Marcha de Amputados, D.Sc. Thesis*. Universidade Federal do Rio de Janeiro, COPPE/PEM: Brazil, 2003.

Study of flexible wall acoustic cavities using Beam Finite Element

Soraya Mendes de Souza, Lineu José Pedroso
Brasília University - UnB, Faculty of Technology, Civil Engineering Department, Brasília/DF – Brazil

Abstract

The problems related to coupled fluid-structure are found in various fields of engineering. Technology enhancements, new materials, and the development of various sectors of industry led to the raise of complex problems, involving, for example, those related to acoustic-mechanical coupling, which appear in cases of cavities containing fluid, limited by elastic walls. This work analyses some cases of coupled fluid-structure problems on acoustic cavities with flexible walls, using two classic Eulerian formulations to fluid-structure interaction problems: U-ϕ-P_0 and U-P, represented, respectively, by the programs: FEDYFE (GDFE/UnB) and ANSYS. The theoretical formulation and the finite element discretization are presented for the first formulation, not both. In this fluid-structure interaction problem, the solid will be treated using beam finite elements, while for the fluid 2D acoustic fluid finite elements are used. Cases involving free vibration for coupled systems in 2D, for conditions of regular contour of the cavity with walls open and/or closed, rigid and/or flexible were studied. The frequencies and the vibration modes obtained have presented a good agreement when compared with the two numerical methods, both for the uncoupled and coupled problems. Analytical solutions are also used and indicate good agreement with these results.

Keywords: fluid-structure, finite element, vibration modes, cavity, beam.

1 Introduction

The coupled problems related to fluid-structure can be found in various branches of engineering. The studies of these problems can appear in several cases of cavities containing fluid and it is associated to structures that can be elastic, flexible/rigid, as well as in pipe with fluid on the outside/inside, and so on. Generally, the coupled systems are characterized by axisymmetric and ill-conditioned matrices. The elements of the global matrix are represented by physical and geometrical constant of the domains involved, which have very different magnitudes, which complicates the resolution of these systems. Therefore, a segment of the literature related to the subject is dedicated to the study of simplified models, to make them more applicable and to produce satisfactory results.

Mechanics of Solids in Brazil 2009, H.S. da Costa Mattos & Marcílio Alves (Editors)
Brazilian Society of Mechanical Sciences and Engineering, ISBN 978-85-85769-43-7

The formulation used considers the fluid as acoustic (without flow), which makes the model more simplified. The movements are small around a position of equilibrium, where there are only waves of pressure. Among the classic formulations that deal with the coupled problem of fluid-structure has been: 1) The Lagrangian has been used, for example, by Zienkiewicz and Bettess [1], Wilson and Khalvati [2] and others; 2) the Eulerian has been caracterized by the pressure, a displacement or velocity potencial for the fluid, and the displacement as variable for the solid, such as described by Zienkiewicz and Newton [3], Daniel [4, 5], Everstine [6], Sandberg [7], Sandberg, Hansson and Gustavsson [8] and others.

This work presents the implementation of a Bernoulli beam element in the code FEDYFE (Finite Elements in Dynamics and Fluid-Structure) which was developed by a research Group for Dynamic and Fluid-Structure at UnB (GDFE). This code is based on the symmetrical potencial formulation (U-ϕ-P_0), proposed by the Olson and Bathe [9] and adapted by Barbosa [10]. The FEDYFE code uses simple triangular elements of the plane stress state, as well as triangular elements with linear interpolation for the fluid.

The implementation of the beam element in the FEDYFE code is done by simply replacing the stiffness and mass matrices of the triangular element of the plane stress state with the stiffness and mass matrices of the Bernoulli's beam element. The frequencies and vibration modes obtained by FEDYFE were compared with results of the ANSYS [11] software, that uses other Eulerian formulation (U-P). This formulation was also used by Sousa Jr [12] and Souza [13]. Despite the formulations of the coupled problem are different, the numerical results provided by the two softwares were satisfactory when compared with each other.

This work selects two cases of coupling, considering the beam element: The Case 1 shows a simple supported beam with open square cavity and Case 2 corresponds to a simple supported beam with closed square cavity. The results of frequencies and coupled vibration modes obtained by the FEDYFE code were compared with their output of the ANSYS [11]. These results presented a good agreement for cases of reservoir with flexible bottom which were analyzed. Moreover, the frequencies and uncoupled numeric vibration modes of the structure were also compared with the analytical solution given by Cough and Penzien [14], showing satisfactory values.

2 Coupled problem formulation (U-ϕ-P_0)

The formulation in question, proposed by Olson and Bathe [9], considers as the main hypotheses for the solid domain linear elastic behavior, isotropic and homogenous material with constant elasticity module and small displacements. It is assumed that the fluid is inviscid, compressible and having an adiabatic behavior. The variational analysis of the dynamic problem for the solid is given by:

$$\Pi_s = \int \left[\frac{1}{2} \int \varepsilon^T C_s \varepsilon dS - \frac{1}{2} \int \rho \dot{u}^T \dot{u} dS - \int u^{IT} f^I dI \right] dt \tag{1}$$

where:

C_s = material stress-strain matrix.

ρ_s = density of solid; u = displacement vector.

Mechanics of Solids in Brazil 2009, H.S. da Costa Mattos & Marcílio Alves (Editors)
Brazilian Society of Mechanical Sciences and Engineering, ISBN 978-85-85769-43-7

f^I = surface (interface) force vector.

The first variation of the functional of the Eq. (1), dismembering surface forces (f^I) into fluid interface forces (f^F) and general external forces (f^E) will lead as to the Eq. (2). The Eq. (2) corresponds to the principle of virtual work for the solid.

$$\int \delta\varepsilon^T C_s \varepsilon dS + \int \rho \delta u^T \ddot{u} dS = \int \delta u^{IT} f^E dI + \int \delta u^{IT} f^F dI \tag{2}$$

The functional of the acoustic problem is given by:

$$\Pi_f = \int \left[\frac{1}{2} \int \frac{1}{\beta} \left(P_0 - \rho_f \dot{\phi} \right)^2 dF - \frac{1}{2} \int \rho_F \nabla\phi \nabla\phi dF - \int \left(P_0 - \rho_f \dot{\phi}^I \right) u_N dI \right] dt \tag{3}$$

where:

ρ_f = density of fluid.

ϕ = velocity potential in the fluid.

u_N = externally imposed displacement, normal to the fluid boundary and positive acting into the fluid.

β = bulk modulus of fluid.

P_0 = hydrostatic pressure

Doing Eq. (3) stationary in relation to the ϕ and P_0, we get:

$$\begin{aligned} &\int \frac{1}{\beta} \delta P_0 P_0 dF - \int \frac{\rho_F}{\beta} \delta P_0 \dot{\phi} dF + \int \frac{\rho_F}{\beta} \delta\phi \dot{P}_0 dF - \int \frac{\rho^2{}_F}{\beta} \delta\phi \ddot{\phi} dF - \int \rho_F \nabla\delta\phi . \nabla\phi dF \\ &= \int \delta P_0 u_N dI + \int \rho_F \delta\phi^I \ddot{u}_N dI \end{aligned} \tag{4}$$

Obtaining the expressions of both domain and considering that they have the same interface I, therefore the Eq. (5) allows the coupling between these domains:

$$f^F = n \left(P_0 - \rho_F \dot{\phi}^I \right) \tag{5}$$

Replacing the Eq. (5) with Eq. (2), we obtain the final coupled equation for the solid:

$$\int \delta\varepsilon^T C_s \varepsilon dS - \int \rho \delta u^T \ddot{u} dS = \int \delta u^{IT} f^E dI - \int \delta u^{IT} n P_0 dI + \int \rho_F \delta u^{IT} n \dot{\phi}^I dI \tag{6}$$

Where the fluid displacements are related to solid displacements at the interface I:

$$u_N = n^T u^I \tag{7}$$

Applying the Eq. (7) into Eq. (4), we get to the coupling expression for the fluid:

$$\int \frac{1}{\beta}\delta P_0 P_0 dF - \int \frac{\rho_F}{\beta}\delta P_0 \dot{\phi} dF + \int \frac{\rho_F}{\beta}\delta\phi \dot{P}_0 dF - \int \frac{\rho^2{}_F}{\beta}\delta\phi\ddot{\phi} dF - \int \rho_F \nabla\delta\phi.\nabla\phi dF$$
$$= \int \frac{1}{\beta}\delta P_0 n^T u^I dI + \int \rho_F \delta\phi^I n^T \dot{u}^I dI \tag{8}$$

Therefore, the Eq. (6) and the Eq. (8) describe the fluid-structure coupling in variational terms.

2.1 Discretization used beam element

The classic beam element used to present two nodes and two degrees of freedom per node (V_1, θ_1, V_2, θ_2), as shown in Fig. 1:

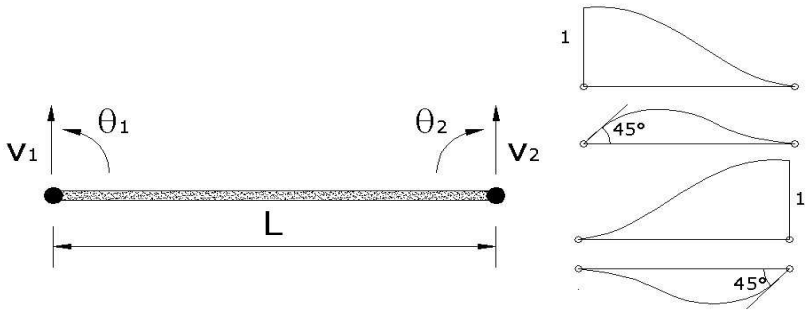

Figure 1: Beam element and shape functions.

The expression which provides the displacement in the inner part of the element is obtained by the shape functions (N) in Eq. (9):

$$V(x) = N_1 V_1 + N_2\theta_1 + N_3 V_2 + N_4\theta_2 = NV^e \tag{9}$$

The shape functions for the beam element are:

$$N_1 = \left[\frac{2x^3}{L^3} - \frac{3x^2}{L^2} + 1\right] \qquad N_3 = \left[\frac{3x^2}{L^2} - \frac{2x^3}{L^3}\right]$$
$$N_2 = \left[x - \frac{2x^2}{L} + \frac{x^3}{L^2}\right] \qquad N_4 = \left[\frac{x^3}{L^2} - \frac{x^2}{L}\right] \tag{10}$$

The vector deformation can be expressed in terms of nodal displacements, as:

$$\varepsilon = BV^e \tag{11}$$

where B is the matrix of the derivatives of the shape functions.

The stiffness and mass matrices are given by the expressions $K_{SS} = \int B^T C_s B dV$ and $M_{SS} = \int \rho N^T N dS$, respectively. By replacing the shape function (10) in these expressions, we obtain the stiffness and mass classic matrices of a beam finite element, which are represented by Eq. (12) and Eq. (13):

$$K_{SS} = \frac{2EI}{L^3} \begin{bmatrix} 6 & 3L & -6 & 3L \\ 3L & 2L^2 & -3L & L^2 \\ -6 & -3L & 6 & -3L \\ 3L & L^2 & -3L & 2L^2 \end{bmatrix} \tag{12}$$

where:
E = Young' modulus of the element.
I = moment of inertia.
L = length of the element.

$$M_{SS} = \frac{\rho AL}{420} \begin{bmatrix} 156 & 22L & 54 & -13L \\ 22L & 4L^2 & 13L & -3L^2 \\ 54 & 13L & 156 & -22L \\ -13L & -3L^2 & -22L & 4L^2 \end{bmatrix} \tag{13}$$

where:
ρ = density of the solid.
A = cross sectional area of the element.
L = length of the element.

3 Results

3.1 Case 1: 2D cavity-beam with open boundary condition

Figure 2 illustrates the case 1. This example is a simple supported beam at the bottom, coupled to a square cavity of rigid side walls with an opening at the top, ie, a reservoir with rigid walls, without cover and flexible bottom. The physical and geometrical properties are showed as follows:

A) Analytical uncoupled frequencies and vibration modes for the structure

The frequencies and structure modes that describe the behavior of bending to a simple supported beam are defined by the Eq. (14) and Eq. (15), respectively:

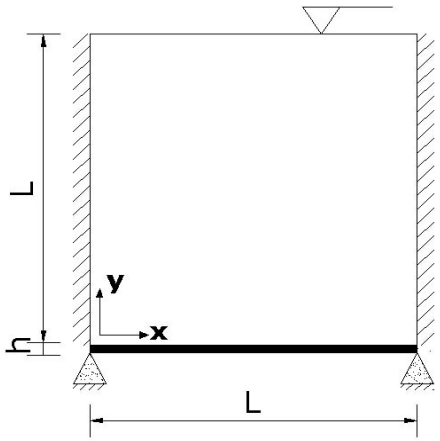

**** Solid domain:***

$L_x = 10m;\ b = 1m;\ h = 1m;$

$E = 2{,}1x10^{11}\,\frac{N}{m^2};\ \nu = 0{,}3;$

$\rho_s = 7800\,\frac{Kg}{m^3};$

**** Fluid domain:***

$L_Y = 10m;\ \beta = 2{,}25x10^9\,\frac{N}{m^2};$

$\rho_f = 1000\,\frac{Kg}{m^3};\ c = 1500\,\frac{m}{s};$

Figure 2: Case 1 - Open cavity with a simple supported beam at the bottom.

Description

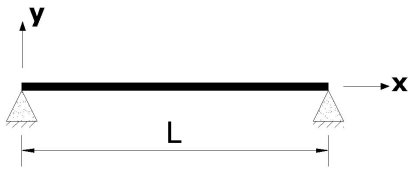

$$\textbf{Frequency (Hz):}\quad f_i = \frac{(i\pi)^2}{2\pi L^2}\left(\frac{EI}{m}\right)^{1/2} \qquad i = 1, 2, 3... \tag{14}$$

$$\textbf{Mode:}\quad y = \sin\frac{i\pi x}{L} \tag{15}$$

where:

EI = bending stiffness.

m = mass of beam per unit length.

L = length of the element.

Figure 3 corresponds to the first four vibration bending modes for the simple supported beam with values of normalized displacement (y) in the direction (x).

B) Uncoupled numeric results (FEDYFE and ANSYS) for the structure

The mesh used in the discretization for the beam contains 20 elements with 21 nodes, that has two nodes for the finite element. There is a correlation between the modal deformed obtained by FEDYFE (Fig. 4) and ANSYS (Fig. 5), with their respective analytical vibration modes, as showed in Fig. 3.

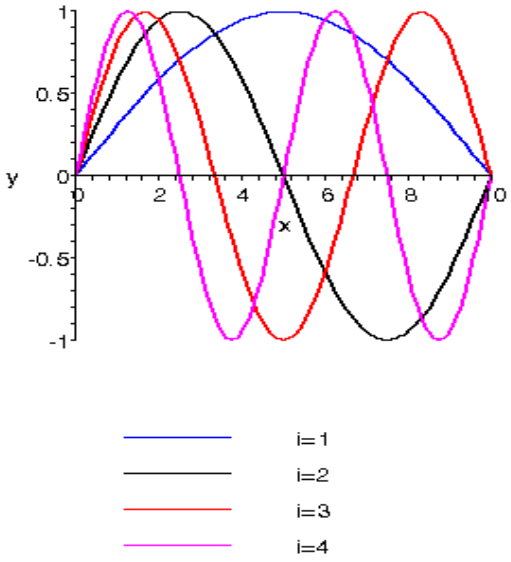

Figure 3: Analytic vibration modes for the simple supported beam.

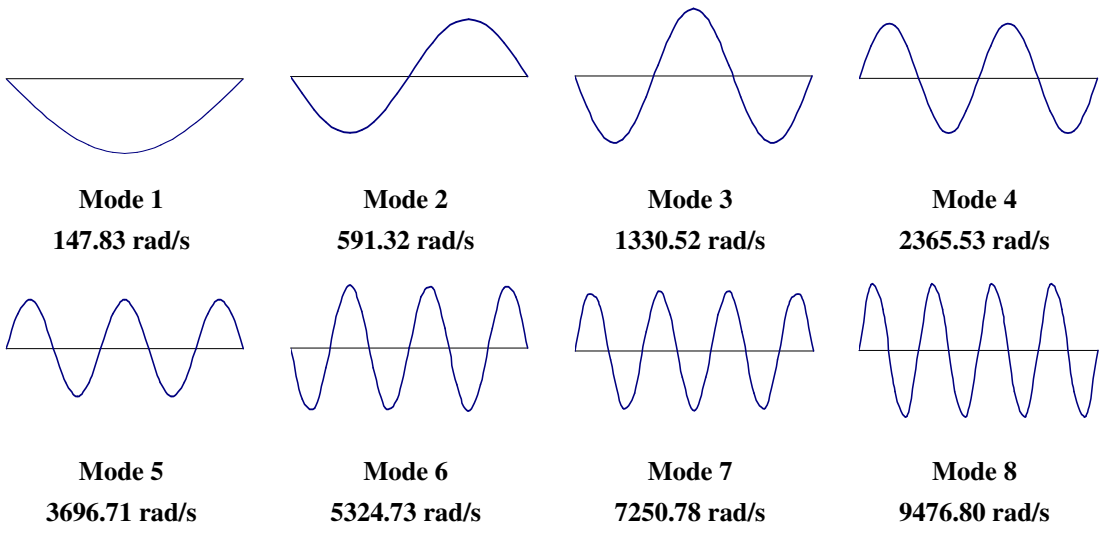

Figure 4: Numeric vibration modes for the simple supported beam obtained by the FEDYFE code.

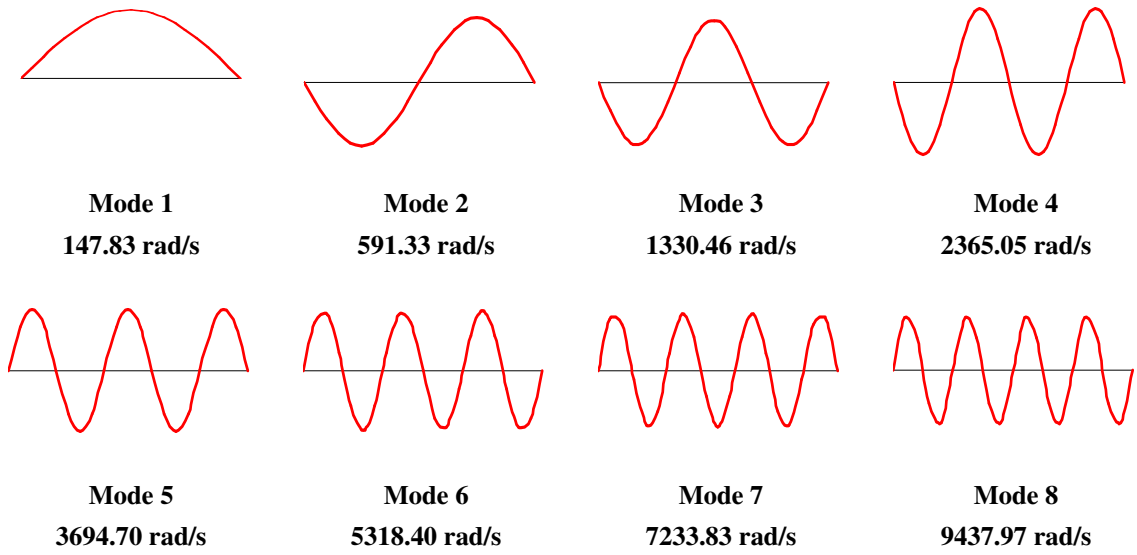

Figure 5: Numeric vibration modes for the simple supported beam obtained by the ANSYS software.

Table 1 summarizes the uncoupled numerical results for the structure obtained by FEDYFE and ANSYS softwares, as well as analytical results and the percentage of error between them.

C) Coupled numeric results (FEDYFE and ANSYS) for the Case 1

The discretization of the domain fluid consists of the 800 triangular linear elements with 441 nodes, while the beam has 20 elements with 21 nodes. In the coupled region, it used 20 interface elements with 21 nodes. Figure 6 shows the mesh used for the coupled case 1.

Table 2 shows the comparison of coupled frequencies obtained by the ANSYS and FEDYFE softwares, considering the open 2D cavity-beam problem, as illustrated in Fig. 2. Note that FEDYFE and ANSYS softwares present a good agreement in the results.

Figure 7 and Figure 8 illustrate the first five coupled modes of the 2D acoustic cavity-beam problem, respectively, got by the FEDYFE and ANSYS softwares. The frequencies and vibration modes showed a good agreement when compared with each other.

The analysis and interpretation of the modal forms associated to the fluid-structure coupled problem with acoustic cavities present some special characteristics: the appearance of modes with different nature and dominance, such as: added mass mode (MA), structure dominant modes (DE) and cavity dominant modes (DC). These modes present typical aspects of uncoupled modal deformed of the structure or the cavity, as analyzed by Souza [13].

The mode 1 represents the typical added mass mode with frequency lower (MA). In this case, the

Table 1: Analytic and numeric uncoupled frequencies for the structure in rad/s.

Mode	UNCOUPLED STRUCTURE				
	Analytic Eq. (14)	**Numeric FEDYFE**	**Numeric ANSYS**	**Error (%) FEDYFE**	**Error (%) ANSYS**
1	147.83	147.83	147.83	0.00	0.00
2	591.33	591.32	591.33	0.00	0.00
3	1330.5	1330.52	1330.46	0.00	0.00
4	2365.33	2365.53	2365.05	0.01	0.01
5	3695.83	3696.71	3694.70	0.02	0.03
6	5321.99	5324.73	5318.40	0.05	0.07
7	7243.67	7250.78	7233.83	0.10	0.14
8	9461.31	9476.80	9437.97	0.16	0.25
9	11974.48	12005.65	11922.34	0.26	0.44
10	14783.30	14841.35	14676.26	0.39	0.72

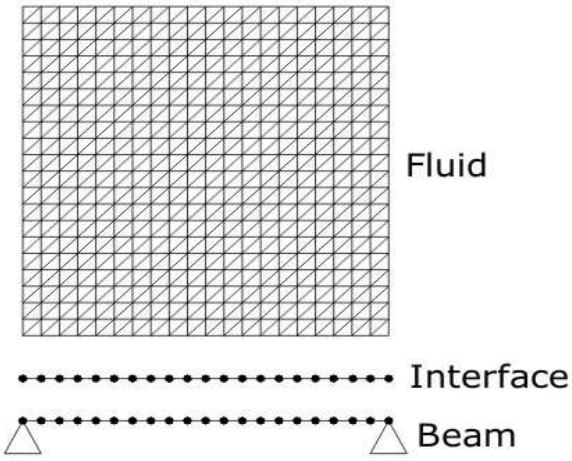

Figure 6: Mesh used in the discretization of the coupled case 1.

structure presents the first modal deformed for the cavity with incompressible fluid ($\omega_1 L/c = 0.65 < 1$). The modal deformed of the fluid presents a linear evolution.

Table 2: Comparison of coupled numeric frequencies obtained by the ANSYS and FEDYFE softwares for the Case 1.

		ω - rad/s	
	Mode	**ANSYS**	**FEDYFE**
Beam + Fluid	1	98.32	98.51
	2	315.61	316.16
	3	446.04	448.85
	4	620.58	625.67
	5	736.39	736.68
	6	885.87	889.83
	7	957.49	960.48
	8	1,127.83	1,140.48
	9	1,209.01	1,210.16
	10	1,291.76	1,296.81

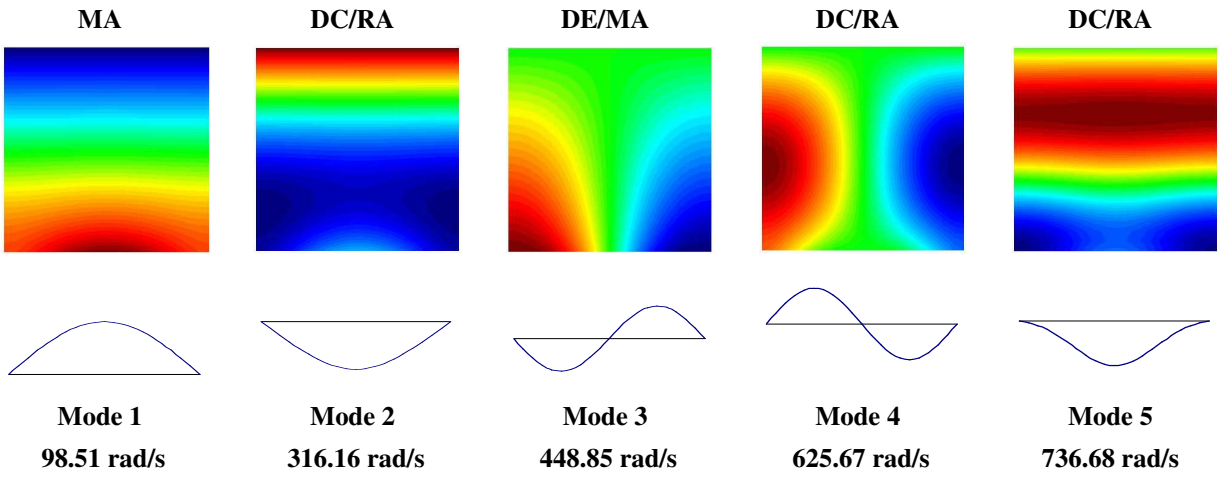

Figure 7: Representation of coupled vibration modes obtained by FEDYFE for Case 1.

The modes 2, 4 and 5 characterize the cavity modes with added stiffness (DC/RA). They reproduce the shape of the 2D uncoupled cavity modes with values higher than those uncoupled frequencies. The

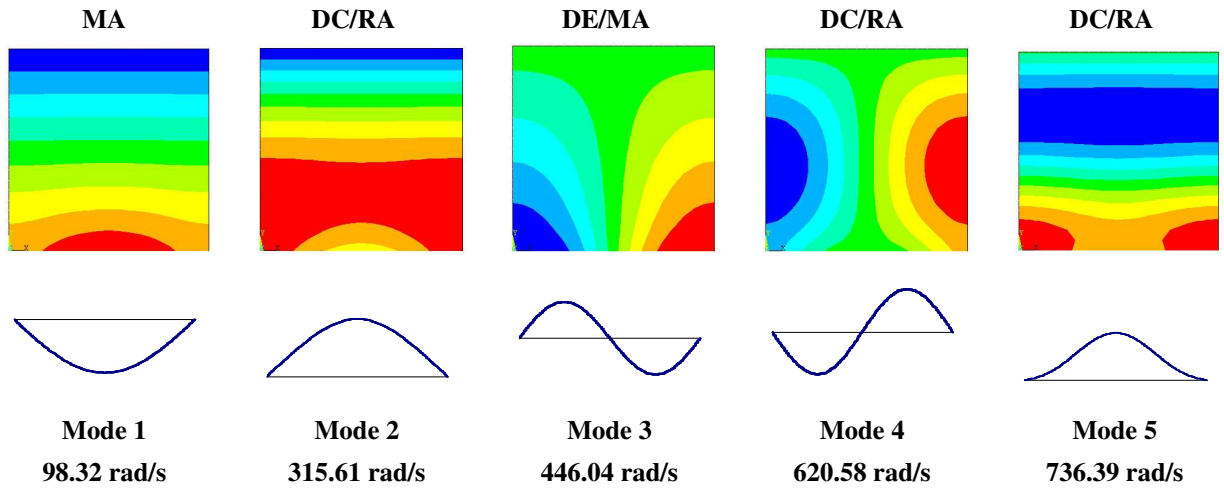

Figure 8: Representation of coupled vibration modes obtained by ANSYS for Case 1.

structure follows the modal forms of pressure, it conforms to those and follows some of its typical and well defined deformed, as shown and interpreted by Souza [13].

The mode 3 presents the characteristic of the structure dominant modes (structure modal form) with added mass (DE/MA). The coupled frequencies have values lower than uncoupled frequencies for the structure. The fluid is attached to the structure deformed. There isn't excitement of the modal forms of the cavity, because the fluid is disturbed only in the area of interface with the beam and acts with added mass in the structure.

3.2 Case 2: 2D acosutic cavity-beam with closed boundary condition

The case 2 has the same physical and geometrical characteristic of case 1, as illustrated in the Fig. 2, the exception of this example is a closing at the upper part of the cavity, as shown in Fig. 9.

A) Coupled numeric results (FEDYFE and ANSYS) for Case 2

The mesh used in the discretization for case 2 is the same mesh for case 1, as shown in Fig. 6. The difference is that model is closed at the top, while that one in case 1 is open at the top ($p = 0$).

Table 3 summarizes the coupled numerical results of the problem in Fig. 9, calculated by the ANSYS and FEDYFE softwares. There is a good correlation between these numerical results.

Furthermore, the first five frequencies correspond to Tab. 3, the FEDYFE code generates the first five coupled modes to the problem of case 2, as illustrated in Fig. 10. Thus, these modes present an excellent agreement when compared with the results provided by the ANSYS software, as illustrated in Fig. 11.

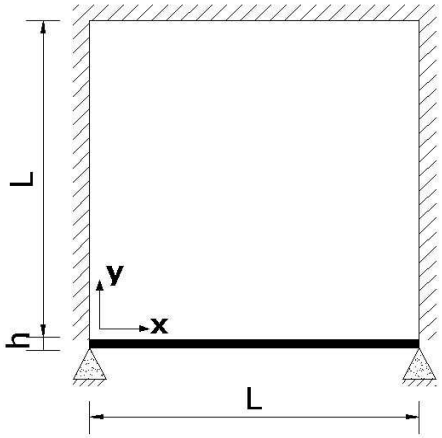

**** Solid domain:***

$$L_x = 10m;\ b = 1m;\ h = 1m;$$

$$E = 2{,}1x10^{11}\frac{N}{m^2};\ \nu = 0{,}3;$$

$$\rho_s = 7800\frac{Kg}{m^3};$$

**** Fluid domain:***

$$L_Y = 10m;\ \beta = 2{,}25x10^9\frac{N}{m^2};$$

$$\rho_f = 1000\frac{Kg}{m^3};\ c = 1500\frac{m}{s};$$

Figure 9: Case 2 - Closed cavity with a simple supported beam at the bottom.

Table 3: Comparison of coupled numeric frequencies got from the ANSYS and FEDYFE softwares for Case 2.

		ω - rad/s	
	Mode	**ANSYS**	**FEDYFE**
Beam + Fluid	1	0.0	0.0
	2	177.74	178.29
	3	431.05	431.68
	4	513.44	516.14
	5	544.13	546.76
	6	726.59	730.77
	7	930.35	931.84
	8	969.49	969.94
	9	1,038.23	1,043.74
	10	1,084.26	1,084.66

Observe that there is a zero frequency mode (low frequency) and modal deformed with constant pressure throughout the cavity, as described in zero mode (M0). As the cavity is closed and symmetric, we can easily observe the presence of this mode, which in the ANSYS software appears with a residue of low pressure in the cavity (small change in pressure).

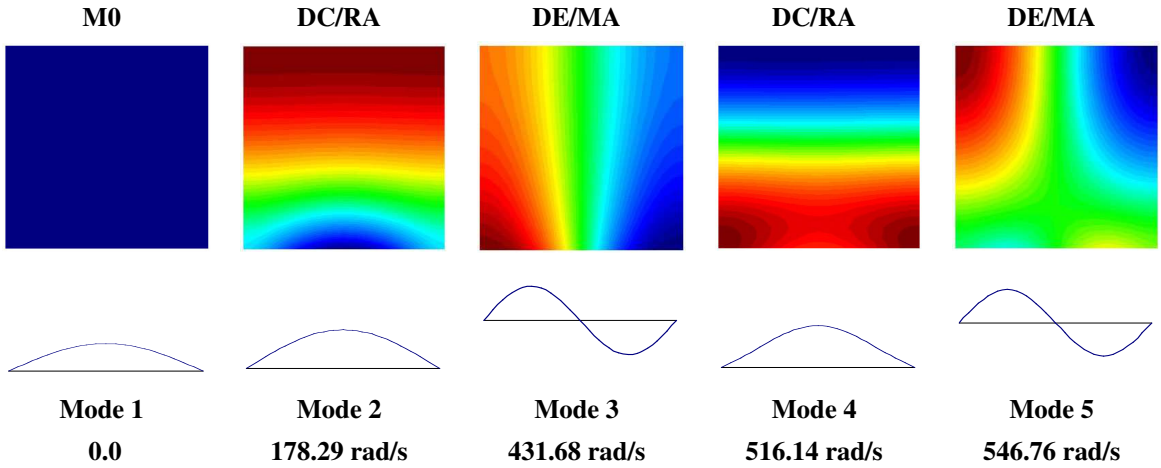

Figure 10: Representation of coupled vibration modes obtained by FEDYFE software for Case 2.

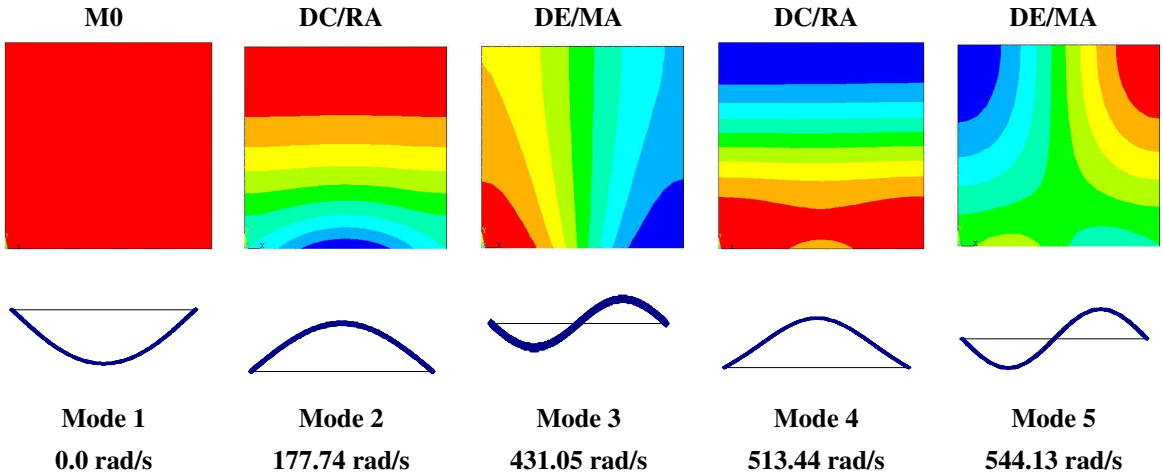

Figure 11: Representation of coupled vibration modes obtained by ANSYS software for Case 2.

Using the same methodology proposed by Souza [13], we observe the rising of modes with characteristic of the structure and the cavity. They reproduce the same typical vibration modes for the structure and cavity uncoupled problem.

The structure dominant mode with added mass (DE/MA) is characterized by disturbed fluid that acts with the effect of added mass in the structure. It has the value of coupled frequency lower than uncoupled frequency for the structure. In this problem, the modes 3 and 5 represent the structure dominant modes with added mass.

The cavity dominant mode with added stiffness (DC/RA) is characterized by frequency higher than those obtained for the uncoupled problem (cavity and structure). This is due to the increasing of stiffness in the coupled system. In this example, the DC/RA mode is represented by the modes 2 and 4. There is a clear correlation in the characteristics of coupled modes with the uncoupled cavity mode for the frequencies of the cavity. We suggest reading Souza [13], for better understanding of the methodology used to identify coupled modes.

4 Conclusion

In this work, the fluid-structure coupled problems using the beam element through the potential symmetrical formulation, obtained by the use of the FEDYFE software, showed excellent results, both for the values of the frequencies and for the fluid-structure coupled vibration modes, considering the open and closed cavities.

When a 2D acoustic cavity-beam coupled problem was used, there were modes difficult to identify (structure and cavity), because the beam element accentuates the effects of bending, which disturb the pattern of coupled deformed modal, in particular, in the cavity domain.

The frequencies and vibration modes results of the FEDYFE code showed good agreement compared with the ANSYS software, even though they have different Eulerian formulations. Therefore, these results validate the implementations made in the FEDYFE code. The interpretation and methodology used to identify the coupled vibration modes in the cavity-beam problem follow the same procedure developed by Souza (2007) for the finite element of plane stress state.

Acknowledgements

The authors wish to thank CNPq and CAPES for material (equipment) and financial support (scholarships) provided during this research.

References

[1] Zienkiewicz, O.C. & Bettess, P., Fluid-structure dynamic interaction and wave forces. an introduction to numerical treatment. *International Journal Methods in Engineering*, **13**, pp. 1–16, 1978.

[2] Wilson, E.L. & Khalvati, M., Finite elements for the dynamic analysis of fluid-solid systems. *International Journal for Numerical Methods in Engineering*, **19**, pp. 1657–1668, 1983.

[3] Zienkiewicz, O.C. & Newton, R., Coupled vibrations of a structure submerged in a compressible fluid. *Symposium on Finite Element Techniques*, Stuttgart, 1969.
[4] Daniel, W.J.T., Modal methods in finite element fluid-structure eingenvalue problems. *International Journal Methods in Engineering*, **15**, pp. 1161–1175, 1980.
[5] Daniel, W.J.T., Performance of reduction methods for fluid-structure and acoustic eigenvalue problems. *International Journal Methods in Engineering*, **15**, pp. 1585–1594, 1980.
[6] Everstine, C.G., Finite element formulations of structural acoustics problems. *Computers & Structures*, **65(3)**, pp. 307–321, 1997.
[7] Sandberg, G., A new strategy for solving fluid-structure problems. *International Journal Methods in Engineering*, **38**, pp. 357–370, 1995.
[8] Sandberg, G., Hansson, P. & Gustavsson, M., Domain decomposition in acoustic and structure-acoustic analysis. *Computer Methods in Applied Mechanics and Engineering*, **190**, pp. 2979–2988, 2001.
[9] Olson, L.C. & Bathe, K.J., Analysis of fluid-structure interaction. a direct symmetric coupled formulation based on the fluid velocity potencial. *Computers & Structures*, **21(1/2)**, pp. 21–32, 1985.
[10] Barbosa, A., *Uma Formulação Potencial Simétrica para o Cálculo Estático e Dinâmico de Problemas de Interação Fluido-Estrutura*. Departamento de Engenharia Civil e Ambiental, Universidade de Brasília, 1998. Dissertação de Mestrado em Estruturas e Construção Civil, Publicação E.DM-008A/98.
[11] Swanson Analysis Systems, Inc., Houston, PA, *ANSYS Version 5.4*, 1997.
[12] Sousa Jr, L.C., *Uma Aplicação dos Métodos dos Elementos Finitos e Diferenças Finitas à Interação Fluido-Estrutura*. Departamento de Engenharia Civil e Ambiental, Universidade de Brasília: DF, p. 197p., 2006. Dissertação de Mestrado em Estruturas e Construção Civil, Publicação E.DM-008/06.
[13] Souza, S.M., *Contribuição para uma Metodologia de Análise Acoplada Fluido-Estrutura para Cavidades Acústicas de Paredes Flexíveis*. Departamento de Engenharia Civil e Ambiental, Universidade de Brasília, 2007. Dissertação de Mestrado em Estruturas e Construção Civil, Publicação E.DM-004A/07.
[14] Clough, R.W. & Penzien, J., *Dynamic of structures*. MacGraw-Hill: New York, 2nd edition, 1960.

Load-elongation characteristics of high tenacity polyamide yarns

Cesar J. M. Del Vecchio, José Márcio Carter
Petrobras – Centro de Pesquisa e Desenvolvimento Leopoldo Américo Miguez de Mello, Rio de janeiro/RJ – Brazil

Abstract

Synthetic fibre ropes are extensively used in a number of applications related the production of oil in deep and ultra-deep water, for example in moorings and in the installation of equipment on the sea floor. The ability to build a tether with quasi-static and dynamic load-elongation characteristics that best suits each application is used by the engineer to optimize the performance of the system being designed. Tether properties can be estimated based on yarn properties and the geometric construction of the tether. Since the basic constituent of the ropes, that is the yarns, are non-linear viscoelastic, cyclic load-elongation properties are a function of frequency, mean load and load amplitude. The paper describes the load-elongation behaviour of high tenacity nylon yarns in cyclic conditions relevant for deepwater moorings and for the connection of two deepwater units one to each other by means of these tensile elements. Load control and elongation control, including slack conditions are reported.

Keywords: fibre rope, nylon, load-elongation, mooring, deep water.

1 Introduction

The use of synthetic fibre ropes is well established in deep water moorings [1] (% YBLWet). The ability to tailor load-extension characteristics to the required response of the tether is the most important characteristic of fibre ropes. For example, the use of high efficiency polyester ropes suits very well the taut leg mooring of Floating Production Units [2].

Typical deepwater mooring ropes have breaking loads ranging from 5MN to 20MN. The basic building unit of these ropes is an industrial yarn with breaking load of the order of 100N and rope making consists of a sequence of twisting and/or braiding operations.

Properties of ropes are derived from the properties of their constituent yarns and of the geometry of the construction. High tensile efficiency ropes are obtained by using quite long twisting and/or braiding pitches and high tenacity yarns.

Mechanics of Solids in Brazil 2009, H.S. da Costa Mattos & Marcílio Alves (Editors)
Brazilian Society of Mechanical Sciences and Engineering, ISBN 978-85-85769-43-7

Tenacity is the standard way of assessing the strength of textile products such as yarn and fibre ropes. Tenacity is measured by dividing the breaking load of the component by its mass per unit length and is expressed in N/tex in the International System of Units. Tex is a mass per unit length of 1g/km. In textile practice modulus is also presented normalized by mass per unit length (in N/tex) instead of by cross sectional area as usual in other engineering areas.

Table 1 shows typical properties of some industrial yarns used for rope making [2]. As mentioned above the choice of a yarn to make a mooring rope is decided considering several characteristics of which load-extension properties and cost are probably the most important.

Table 1: Typical properties of most widely used rope making yarns

Material	Tensile Strength (GPa)	Tenacity (N/tex)	Failure strain (%)	Density (g/cm^3)	Moisture Absorption (%)
nylon 6	0.9	0.81	23	1.14	4.5
nylon 6.6	1.0	0.88	19	1.14	4.5
Polyester	1.1	0.82	11.0	1.38	0.4
Aramid	2.8	1.95	3.6	1.44	7.0
HMPE	2.6	2.65	3.5	0.97	0.0

Offshore moored Units respond to mean environmental load by offsetting horizontally from their base position until the mooring system generates restoring force to balance these loads, but their response to waves and the dynamic components of wind and current is more complex. For the sake of better understanding one can consider the dynamics of the vessel as consisting of a low frequency resonant response excited by currents and winds and a high frequency response to waves.

The limits, both static and dynamic, for these movements is typically given by what it is acceptable for the pipes that connect the Unit to the seafloor bringing or taking fluids from various equipments such as wellheads, manifolds, etc. Since hydrodynamic forces from waves are of a cyclic nature and very strong to be restricted by a deepwater mooring system, in general a mooring system should be compliant to these loads.

All steel mooring systems draw their compliance from the catenary shape they assume in their free length. Fibre ropes can be designed, in deep water, to use their axial compliance for this purpose. However the non-linear viscoelastic behaviour of yarns and consequently ropes interacts with the loading on the moored Unit in a quite complex way making the design of mooring systems based on fibre ropes substantially different from the design of systems base in all steel components.

A Full understanding of the behaviour of fibre ropes is essential for the design of the mooring system since the response of the system is a function of load-elongation characteristics. On the other

hand rope must be fit for the long term response in fatigue, creep as well as environmentally assisted degradation.

The application envisaged presently is the use of fibre ropes to link two offshore units moored in deep water at an approximate distance of 50m. The ropes restrict relative movement making it viable to have a foot bridge and a bundle of flexible pipe jumpers between the units.

This is a new application for fibre ropes and the combined system consisting of the two units show other responses in addition to the individual response of each moored unit as described above.

Preliminary design exercises for this application have shown that high efficiency polyester fibre ropes are too stiff, resulting in very high fatigue loads and in the ropes becoming slack. It was then decided to study the use of high efficiency nylon ropes. Another option would be to use ropes made of Polyester fibres with lower modulus.

Load extension properties of mooring size ropes in high efficiency constructions can be estimated from yarn characteristics, therefore this paper presents a study of the load-extension characteristics of some high tenacity nylon yarns relevant to this application.

2 Materials and methods

It was decided to evaluate three high tenacity yarns, two of them are nylon 6.6 and one is a nylon 6 yarn. All yarns are manufactured by Polyamide High Performance Fibres. Table 2 shows basic data for them.

Table 2: Linear density and breaking properties of polyamide yarns studied

Manufacturer Identification	Type	Linear Density tex	Tenacity (dry) N/tex	Elongation at break (dry) %	Tenacity (wet) N/tex
140HRT	6.6	210.5	0.832	19.8	0.765
142HRT	6.6	211	0.95	18.0	0,867
540T	6	190	0.768	23.5	0.711
HPPIY Spec.AA	PET	111	0.700	22.0	0.700

Tensile tests were performed in the yarns after 12 hours immersion to characterize their wet breaking strength, since in the application ropes will be wet and it is well known that nylon yarn behave differently in the wet condition. Table 2, above, also shows breaking tenacity measured for the wet yarns.

For load-elongation measurement yarns were terminated by gluing with epoxy resin between acrylic tabs. Free length between tabs was 190mm. This was considered the gauge length.

Tests were performed in a 100kN MTS load frame using a 2500N load cell. The load cell was verified with dead weights to check its calibration and stability since loading was between zero and 91N. Extension was measured with the 150mm range LVDT mounted in the servo-hydraulic cylinder. This is acceptable since all fixtures in the load path are at least two orders of magnitude stiffer than the yarns tested.

Since loading in the application envisaged sometimes is controlled by force and sometimes is controlled by extension test were performed both in load and in displacement control. This allowed the determination of the yarn characteristics in the slack condition.

For the sake of comparison a limited number of tests were performed in a high tenacity low modulus polyester (PET) yarn manufactured by Zhejiang Unifull Industrial Fibre Co., which has similar breaking tenacity and elongation. Basic properties of this yarn are also shown in Tab. 2.

All load-extension measurements were performed with the yarns wet after immersion for 12 hours. For tests performed in load-control minimum load varied from 2 to 40% of the wet breaking load of each yarn (YBLWet) and maximum load varied between 10 and 50% of YBLWet. Yarns were cycled at 0.1Hz, which is a typical frequency for the response of the current application. Since the response varies substantially in the first few cycles, results are presented for a single cycle after 50 to 100 cycles, as needed to obtain a steady response.

3 Results

Figure 1 shows a typical plot of load versus strain after 100 cycles, in the form of a hysteresis loop. The graph gives us an idea of the non linear behaviour of the yarn as well as the significant amount of energy dissipated in each cycle.

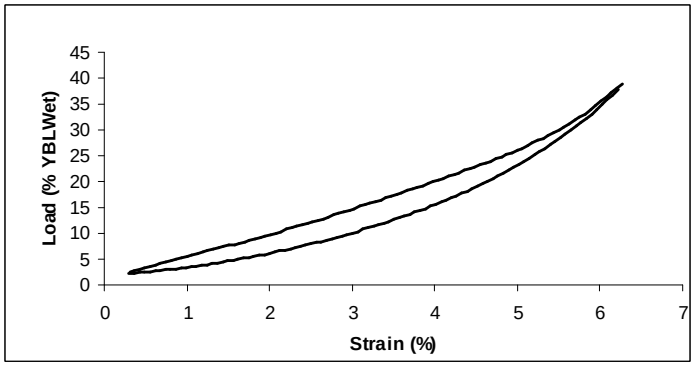

Figure 1: Load versus strain plot of a nylon 142HRT yarn cycled between 2 and 40% of the average wet breaking load of the yarn at 0.1Hz (100^{th} cycle)

Table 3 shows the secant modulus for each loading condition, for tests performed under load control respectively for yarns 140HRT, 142HRT and 540T.

Table 3: Secant modulus for nylon yarns after 100 cycles

Load Limits (%)	140HRT Modulus (N/tex)	142HRT Modulus (N/tex)	540T Modulus (N/tex)
2 - 10	2,34	2,45	1,83
2 - 20	3,12	3,34	2,49
10 - 20	5,10	5,77	4,79
2 - 30	3,88	4,21	3,50
10 - 30	5,77	6,50	5,22
20 - 30	7,89	9,24	7,42
10 - 40	7,36	7,24	6,48
20 - 40	8,61	9,77	8,75
30 - 40	10,36	12,02	10,40
10 - 50	7,43	7,98	7,11
20 - 50	9,64	10,35	9,20
30 - 50	11,07	13,20	11,10
40 - 50	12,75	15,83	12,71

Table 4 shows yarn modulus normalized by YBLWet. These figures were obtained by dividing the secant modulus (in N/tex) by YBLWet (in N) and multiplying by the mass per unit length (in tex).

This is another way of normalizing modulus which it is quite useful for the designer of the mooring system. It represents the force, in number of times the breaking load, one must apply to the component to double its length. It provides a direct way to compare modulus of components that have the same breaking load.

Figures 2 and 3 show the result of cycling yarns 142HRT and 540T up to 30% of YBLWet from the unloaded condition. It can be seen that load-elongation characteristics are similar if the yarns had the same breaking load. However the higher hysteresis presented by the 142HRT yarn is noticeable.

Table 4: Secant modulus of nylon yarns presented as load/strain normalized by the breaking load of each yarn

Load Limits (%)	140HRT Modulus (N/N)	142HRT Modulus (N/N)	540T Modulus (N/N)
2 - 10	3,05	2,83	2,57
2 - 20	4,08	3,85	3,50
10 - 20	6,67	6,66	6,75
2 - 30	5,07	4,86	4,92
10 - 30	7,54	7,50	7,35
20 - 30	10,31	10,66	10,44
10 - 40	9,62	8,36	9,13
20 - 40	11,25	11,28	12,31
30 - 40	13,55	13,87	14,63
10 - 50	9,71	9,21	10,00
20 - 50	12,61	11,94	12,95
30 - 50	14,47	15,23	15,62
40 - 50	16,67	18,26	17,88

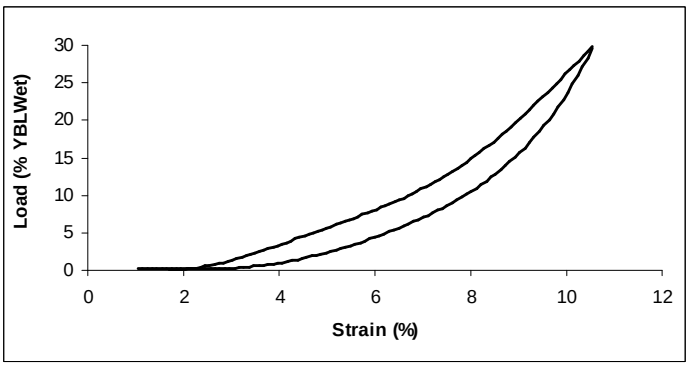

Figure 2: Load-strain plot of a nylon 142HRT yarn cycled between a slack condition and 30% of the average wet breaking load of the yarn at 0.1Hz (50^{th} cycle)

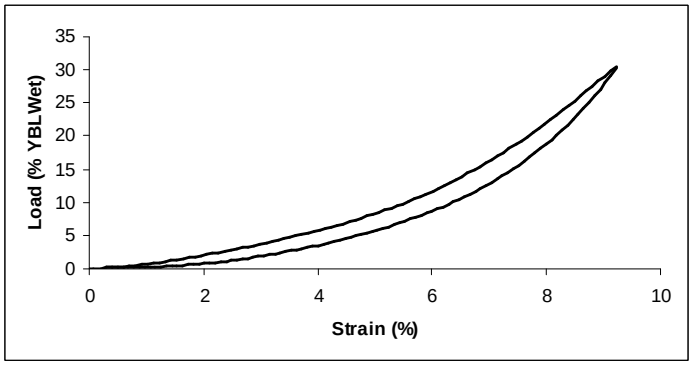

Figure 3: Load-strain plot of a nylon 540T yarn cycled between a slack condition and 30% of the average wet breaking load of the yarn at 0.1Hz (50^{th} cycle)

4 Discussion

It was possible to characterize the load-extension behaviour of nylon yarns that are good candidates for making ropes to be used to connect floating units moored in deep water.

A usual way of translating yarn modulus is by a linear regression in terms of load range and load range (peak to peak). Tab. 5 shows the coefficients of such regressions for the three nylon yarns studied, as well as the square of the coefficient of correlation (R^2). The fit selected forces the intercept to be at the point (0, 0, 0).

Table 5: Regression of Modulus (N/tex) as a function of Mean load (% YBLWet) and Load range (% YBLWet)

Yarn	Mean load coefficient	Load range coefficient	R2
140HRT	0.297346	-0.021043	0.9963
142HRT	0.367327	-0.064195	0.9973
540T	0.302957	-0.042311	0.9982

Modulus of high efficiency fibre ropes can be estimated based on the modulus of their constituent yarn and rope geometry. Typically moduli of such ropes vary from 0.75 to 0.8 of the modulus of the yarns for high tenacity PET fibre. Its is reasonable to expect that high tenacity nylon yarns such as those tested show a similar behaviour. Verifying this hypothesis is one of the subjects of ongoing work.

Figure 4 shows results (raw data) for yarns 142HRT, 540T and the PET yarn cycled between the slack condition and 30% of YBLWet plotted together. Although the PET yarn has failure strain in the same range of the nylon yarns it can be seen that the near zero load is very different. The nylon yarn show an almost asymptotic behaviour to the X axis and one would expect that a high efficiency rope made with this yarn shows no impact when being loaded from a slack condition. On the other hand, a PET rope of a similar construction will certainly show impact loading in the same condition.

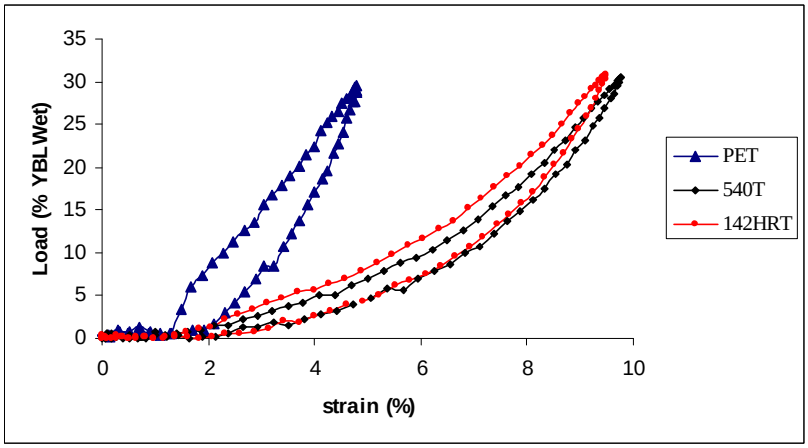

Figure 4: Load-strain plot of nylons 540T and 142HRT yarns and of the high elongation PET yarn cycled between a slack condition and 30% of the average wet breaking load of each yarn at 0.1Hz (50^{th} cycle)

5 Conclusions

High tenacity nylon yarns showed load-extension behaviour, characterized by the secant modulus after some 100 stabilization cycles, that can be represented as a linear function of mean load and load range. Mean load is the dominant factor, the influence of load range being one order of magnitude smaller.

It is reasonable to expect that high efficiency ropes made with these yarns show modulus between 0.75 and 0.8 of the modulus of the yarns used. This approximation can be used for preliminary design analyses.

All nylon yarns showed asymptotic behaviour as loading approaches zero, as opposed to the typical behaviour of PET yarns. Considering that rope constructional stretch adds tensile compliance to the yarn it can be concluded the high efficiency nylon ropes should not show impact when loaded from the slack condition. This characteristic is very interesting in the application of connecting two units moored in deepwater.

6 Further work

The time history of the movement between two units moored in deepwater, connected by cables, is random in nature, therefore its computer simulation would be much easier if load-extension behaviour of the connecting ropes could be represented by a single curve giving an instantaneous modulus at each load. The assembly of such a "master curve" is the subject of present ongoing work.

Load-extension behaviour must be characterized in ropes in order to verify how modulus varies with rope construction and to check the hypothesis that rope modulus is in the range of 75 to 80% of yarn modulus. It is believed that this can be done on model ropes with breaking loads of a few tens of kN.

Preliminary computer simulations have shown that cycling amplitudes are substantial in the application envisaged, therefore fatigue performance of the candidate ropes shall be obtained and compared with the service load history. Although this could be addressed initially with small ropes, some testing in full size ropes will be required. To the best knowledge of the authors, no such data is available in the literature for high tensile efficiency ropes based on high tenacity nylon yarns.

Acknowledgements

We acknowledge the permission of Petróleo Brasileiro S.A.- PETROBRÁS to publish this paper. We also acknowledge the help of Carlos Eduardo Chiapim, Almir Cardoso, Daniel Adolpho da Silva Júnior, Benedito Nogueira and Edilson Botelho in conducting laboratory testing and Sérgio Damasceno Soares in generating the graphs presented.

References

[1] Bureau Veritas, *Certification of Fibre Ropes for Deepwater Offshore Service*. Guidance Note NI 432 DTO R01E: Paris, France, 2007.

[2] Del Vecchio, C.J.M., *Light Weight Materials for Deep Water Moorings*. Reading: UK, 1992.

Modeling and simulation of macro-crack initiation and propagation in elastic structures using a gradient-enhanced continuum damage model

S.M.P. Domingues, H.S. da Costa-Mattos
Laboratory of Theoretical and Applied Mechanics, Department of Mechanical Engineering, Universidade Federal Fluminense, Niterói/RJ – Brazil
F. A. Rochinha
Program of Mechanical Engineerin, Universidade Federal do Rio de Janeiro - COPPE/UFRJ, Rio de Janeiro/RJ – Brazil

Abstract

In order to avoid the loss of well-posedness in the post-localization range, some continuum damage theories introduce higher order gradients of the damage variable in the constitutive model. This paper discuss the possibility of structural failure prediction of quasi-brittle materials through a special kind of gradient-enhanced damage theory in which the material is considered to possess a substructure or microstructure. In these theories the microscopic movements are accounted for by the damage variable and a reformulation of the kinematics (to include the possible "micromotions") and of some basic governing principles of the classical Continuum Mechanics is necessary. The theory allows an adequate description of the strain-softening and localization behavior due to the material degradation. Within this framework, a numerically predicted macro-crack is the set of points in the structure where the damage variable has reached its critical value. A simple numerical technique, based on the finite element method, is proposed to approximate the solution of the resulting nonlinear problems. The main features of such kind of approach are discussed through examples concerning macro-crack initiation and propagation in plates under different loading conditions.

Keywords: Damage Mechanics, Finite Elements, quasi-brittle materials, crack initiation, crack propagation.

1 Introduction

Continuum Damage Mechanics uses a phenomenological approach to model the effect of microscopic geometric discontinuities induced by the deformation process (micro-cracks, micro-voids, etc.) on the macroscopic behavior of a structure. In continuum damage theories, an internal variable related to the growth and coalescence of micro defects before the macroscopic crack initiation (whose definition

Mechanics of Solids in Brazil 2009, H.S. da Costa Mattos & Marcílio Alves (Editors)
Brazilian Society of Mechanical Sciences and Engineering, ISBN 978-85-85769-43-7

and physical interpretation may vary from one model to the other) is introduced and the problem becomes to establish the constitutive relations for the damage variable as a function of the other state variables.

In the last few years, many different continuum damage theories for quasi-brittle materials have been proposed. Since the damage propagation generally leads to a local softening behaviour, the models based on a local approach, see Kachanov (1986) and Lemaitre and Chaboche [1], may lead to a physically unrealistic description of strain localization phenomena. In general, due to the loss of ellipticity of the governing equations in the post-localization range, the resulting mathematical problems may present an infinity number of solutions with discontinuous fields of displacement gradients what leads to numerical difficulties of mesh-dependence [2–5]. Some alternative approaches to the local damage theories have been proposed in the last years, see Saouridis and Mazars (1988); Bazant and Cedolin [6]; Costa-Mattos et al [7]; Frémond and Nedjar [8], Oller et al (2005), Khoei and Karimi [9], Peyrot et al [10], for example. Other approaches to the simulation of strain localization and fracture such as Ruter and Stein (2005), Carpinteri and Brighenti (2008), Brighenti [11], Lorentz [12] can be found in recent literature.

The present paper deals with an alternative theory in which the continuum is supposed to possess a substructure or microstructure. Since damage results from microscopic movements, it is proposed a reformulation of the kinematics and of some basic governing principles of the classical Continuum Mechanics in order to account for such "micro-movements". The constitutive equations are developed within a thermodynamic framework. The basic assumption is that the free energy is supposed to depend not only on the strain and the damage variable but on the damage gradient as well. Besides, to account for microscopic effects, the power of the internal forces depends not only on the velocity and its gradient, but also on the damage velocity and its gradient. The main goal is to present a numerical technique as simple as possible for approximating the resulting nonlinear mathematical problems. A splitting technique allows studying the coupled nonlinear problem through a sequence of simpler linear problems. This technique requires, at each time step, the solution of two problems: one similar to an equilibrium problem in linear elasticity and the other similar to a heat transfer problem in a rigid body.

The possibilities and main features of such kind of approach are discussed through examples concerning "crack" initiation and propagation in plates with brittle-elastic behavior under different loading conditions. The theory allows an adequate description of the strain-softening and localization behaviors due to the material degradation. The additional balance equation that governs the evolution of the damage variable prevents the occurrence of discontinuous damage gradients and, consequently, the occurrence of discontinuous displacement gradients. This fact allows an adequate simulation of severe local deformations without the numerical difficulties of mesh-dependence that arise in local continuum damage models.

2 Modeling

A body is defined as a set of material points B which occupies a region Ω of the Euclidean space at the reference configuration. In this theory, besides the classical variables that characterize the

Mechanics of Solids in Brazil 2009, H.S. da Costa Mattos & Marcílio Alves (Editors)
Brazilian Society of Mechanical Sciences and Engineering, ISBN 978-85-85769-43-7

kinematics of a continuum medium (displacements and velocities of material points), an additional scalar variable $\beta \in [0,1]$, is introduced. A point, in such continuum theory, is representative of a given "volume element" of the real material and it is endowed with a microstructure that accounts for the kinetic energy and internal power of the microscopic motions associated to the microscopic geometric discontinuities (density of micro-cracks or cavities). This variable is related with the microscopic motions or links between material points and can be interpreted as a measure of the damage state of the "volume element". If $\beta = 1$, all the links are preserved and the initial material properties are preserved. If $\beta = 0$, a local rupture is considered since all the links between material points have been broken. Since the degradation is an irreversible phenomenon, the rate $\dot{\beta}$ must be negative or equal to zero.

In the next sections the basic principles that govern the evolution of this kind of continuum are summarized. A more detailed presentation of these basic principles can be found in Costa-Mattos and Sampaio [13]. For the sake of simplicity, the hypothesis of quasi-static and isothermal processes is adopted throughout this paper. Besides, it is also assumed the hypothesis of small deformation and, consequently, the conservation of mass principle is automatically satisfied.

2.1 Principle of virtual power

In this work an arbitrary part P of the body B that occupies a region $\Omega \subset R^3$ at the reference configuration is taken as a mechanical system. By definition, the boundary of the region Ω will be called Γ. It is considered with respect to P the space V_u of all fields $\hat{\boldsymbol{u}}$ of possible velocities and the space V_β of all fields $\hat{\beta}$ of possible rates of the damage variable. V_u is called the space of virtual velocities and V_β the space of virtual damage rates.

The power of the external forces$P_{ext}(P, \hat{\boldsymbol{u}}, \hat{\beta})$, for a given virtual field of velocity $\hat{\boldsymbol{u}} \in V_u$ and for a given virtual field $\hat{\beta} \in V_\beta$ is defined as:

$$P_{ext}(P, \hat{\boldsymbol{u}}, \hat{\beta}) = P^u_{ext}(P, \hat{\boldsymbol{u}}) + P^D_{ext}(P, \hat{\beta}) \tag{1}$$

$$P^u_{ext}(P, \hat{\boldsymbol{u}}) = \int_\Omega (\boldsymbol{b} \cdot \hat{\boldsymbol{u}}) dV + \int_\Gamma (\boldsymbol{g} \cdot \hat{\boldsymbol{u}}) dA;\ P^\beta_{ext}(P, \hat{\beta}) = \int_\Omega (p\hat{\beta}) dV + \int_\Gamma (q\hat{\beta}) dA \tag{2}$$

where $(\boldsymbol{b}, \boldsymbol{g})$ are called the external forces and (p, q) the external microscopic forces. The external forces are of two kinds: contact forces $\boldsymbol{g}$ applied on the boundary Γ and volume (or body) forces $\boldsymbol{b}$ applied on Ω. Similarly, the microscopic forces are of two kinds: contact microscopic forces q applied on Γ and microscopic volume forces p applied on Ω. The power of the microscopic forces must be introduced in the theory in order to take into account the non mechanical actions that affect the cohesion state of the material even if there is no mechanical deformation.

In Continuum Mechanics it is usual to consider a first order gradient theory in which the power of the internal forces is supposed to be a function of the velocity and its gradient. In this theory, similarly as in Costa-Mattos and Sampaio [13] and Frémond, and Nedjar [8], the power of the internal forces is also supposed to be a function of β and $\boldsymbol{\nabla}\beta$. On the assumption that, for a fixed instant t, the

power of the internal forces can be expressed as a linear functional on $V_u \times V_\beta$, it may be shown that $P_{int}(P, \hat{\boldsymbol{u}}, \hat{\beta})$ must have the following form:

$$P_{int}(P, \hat{\boldsymbol{u}}, \hat{\beta}) = P^u_{int}(P, \hat{\boldsymbol{u}}) + P^\beta_{int}(P, \hat{\beta}) \tag{3}$$

$$P^u_{int}(P, \hat{\boldsymbol{u}}) = -\int_\Omega (\sigma \cdot \boldsymbol{\nabla}\hat{\mathbf{u}}) dV ; P^\beta_{int}(P, \hat{\beta}) = -\int_\Omega (\boldsymbol{H}.\boldsymbol{\nabla}\hat{\beta} + M\hat{\beta}) dV \tag{4}$$

with $\boldsymbol{\sigma}$, $\boldsymbol{H}$, M being the internal forces. $\boldsymbol{\sigma}$ is a second order tensor, $\boldsymbol{H}$ a vector and M a scalar. $\boldsymbol{\sigma}$ is the classical stress tensor and ($\boldsymbol{H}$,M) are internal microscopic forces. Similar additional internal forces also arise in classical microstructure theories such as Mindlin [14], Toupin [15], Goodman and Cowin (1972). Using the previous definitions, and assuming the hypothesis of slow deformations (hence, neglecting inertial effects) the principle of virtual power may be stated as follows:

"A given part P of B that occupies region Ω of the space at the reference configuration, is at equilibrium if the stress tensor$\boldsymbol{\sigma}$, the internal microscopic forces ($\boldsymbol{H}$,M), the external forces ($\boldsymbol{b}, \boldsymbol{g}$), the microscopic external forces (p, q) are such that

P1 - $P_{int}(P, \hat{\boldsymbol{u}}, \hat{\beta}) + P_{ext}(P, \hat{\boldsymbol{u}}, \hat{\beta}) = 0 \ \forall\ \hat{\boldsymbol{u}} \in V_u, \ \forall\ \hat{\beta} \in V_\beta$, *hence*

$$\begin{gathered}\int_\Omega [\boldsymbol{\sigma}.(\boldsymbol{\nabla}\hat{\boldsymbol{u}}) - \boldsymbol{b}.\hat{\boldsymbol{u}}]\, dV - \int_{\Gamma_2} [\boldsymbol{g}.\hat{\boldsymbol{u}}]\, dA + \int_\Omega [\boldsymbol{H} \cdot \boldsymbol{\nabla}\hat{\beta} + F\hat{\beta} - p\hat{\beta}] dV - \int_\Gamma \left[q\hat{\beta}\right] dA = 0 \\ \forall\ \hat{\boldsymbol{u}} \in V_u, \ \forall\ \hat{\beta} \in V_\beta\end{gathered} \tag{5}$$

P2 - $P_{int}(P, \hat{\boldsymbol{u}}, \hat{\beta}) = 0$ *for a rigid body motion (i.e. when $\hat{\boldsymbol{u}}(\boldsymbol{x}) = \boldsymbol{A}(\boldsymbol{x} - \boldsymbol{x_o}) + \boldsymbol{c_o}$ and $\hat{\beta}(\boldsymbol{x}) = 0$, with $\boldsymbol{x} \in \Omega$, $\boldsymbol{A}$ being an antisymmetrical tensor and $\mathbf{c_o}$ the velocity of a reference point $\boldsymbol{x_o} \in \Omega$)."*

Under suitable regularity assumption, it can be proved that P1 implies the following local expressions:

$$div\ \boldsymbol{\sigma} + \boldsymbol{b} = \mathbf{0} \ \ in\ \ \Omega, \ \ \boldsymbol{\sigma}.\mathbf{n} = \mathbf{f} \ \ in\ \Gamma \ \ ; \ \ div\ \mathbf{H} - M + p = 0\ in\ \Omega, \ \ \mathbf{H}.\boldsymbol{n} = q\ in\ \Gamma \tag{6}$$

where $\boldsymbol{n}$ is the unit outward normal to the surface Γ. It can also be proved that P2 implies the symmetry of the stress tensor.

2.2 Constitutive equations

Under the hypothesis of small deformations and isothermal processes, the free energy of a quasi-brittle material is supposed to be a function of the deformation ε, the damage variable β and its gradient $\boldsymbol{\nabla}\beta$. In order to resume the presentation, the thermodynamic framework used to obtain the constitutive equations is not presented in this paper. The final relations are the following:

$$\boldsymbol{\sigma} = \left(\frac{\beta \mathrm{E}}{\mathbf{1} + \nu}\right) \left[\frac{\nu}{1 - 2\nu} tr(\varepsilon)\mathbf{1} + \varepsilon\right] = \beta\, [\lambda\, tr(\varepsilon)\mathbf{1} + 2\mu\varepsilon] \tag{7}$$

$$F = \left[\frac{1}{2}\lambda\, tr(\varepsilon)^2 + \mu\, \varepsilon.\varepsilon\right] - w + \lambda_\beta + C\dot{\beta} + \lambda_{\dot{\beta}} \tag{8}$$

$$\boldsymbol{H} = k(\boldsymbol{\nabla}\beta) \tag{9}$$

Where E is the Young modulus, ν is the Poisson's ratio, λ and μ are the Lamé constants. The terms λ_β and $\lambda_{\dot\beta}$ are Lagrange multipliers associated, respectively, to the constraints $\beta \geq 0$ and $\dot\beta \leq 0$, they are such that: $\lambda_\beta \leq 0$, $\beta\,\lambda_\beta = 0$ and $\lambda_{\dot\beta} \leq 0$, $\dot\beta\,\lambda_{\dot\beta} = 0$.

2.3 Mechanical problem

Neglecting the external microscopic forces p and q, the following integral formulation for the quasi-static evolution problem can be obtained introducing constitutive equations (7) - (9) in (5)

"Let a body B that occupies a region $\Omega \subset R^3$ with a sufficiently regular boundary Γ be subjected at each time instant t to external forces – a contact force $\boldsymbol{g}$: $\Gamma_2 \subset \Gamma \rightarrow R^3$, and a body force $\boldsymbol{b}(t)$: $\Omega \rightarrow R^3$ – and to prescribed displacements $\bar{\boldsymbol{u}}(t)$ and damage fields $\bar\beta(t)$ in $\Gamma_1 \subset \Gamma$, where $\Gamma = \Gamma_1 \cup \Gamma_2$ and $\Gamma_1 \cap \Gamma_2 = \varnothing$. Find the displacement field $\boldsymbol{u}(t)$: $\Omega \rightarrow R^3$ with $\boldsymbol{u}(t)|_{\Gamma_1} = \bar{\boldsymbol{u}}(t)$ and the field $\beta(\boldsymbol{x}, t)$: $\Omega \rightarrow R$ with $\beta(t)|_{\Gamma_1} = \bar\beta(t)$, such that, for all time instant $t \in [0, \tau]$

$$\begin{array}{c} a_\varepsilon(\boldsymbol{u}, \hat{\boldsymbol{u}}, \beta) - l_\varepsilon(\hat{\boldsymbol{u}}) = 0 \\ a_\beta(\beta, \hat\beta) + l_\beta(\boldsymbol{u}, \hat\beta) + \mathrm{c}_\beta(\dot\beta, \hat\beta) + \Lambda_\beta(\beta, \hat\beta) + \Lambda_{\dot\beta}(\dot\beta, \hat\beta) = 0 \end{array} \qquad \forall\ \hat u \in V_u,\ \forall\ \hat\beta \in V_\beta \tag{10}$$

with the initial condition $\beta(t = 0) = 1$ and subjected to the constraints: $\dot\beta \leq 0$, $\beta \geq 0$"

a_ε, l_ε, a_β, l_β and c_β are defined as follows:

$$a_\varepsilon(\boldsymbol{u}, \hat{\boldsymbol{u}}, \beta) = \int_\Omega \beta[\lambda\, div\boldsymbol{u}\, div\hat{\boldsymbol{u}} + 2\mu\ \boldsymbol{\nabla u}.\boldsymbol{\nabla}\hat{\mathbf{u}}]dV \tag{11}$$

$$l_\varepsilon(\hat{\boldsymbol{u}}) = \int_\Omega [\boldsymbol{b}.\hat{\boldsymbol{u}}]\, dV + \int_{\Gamma_2} [\boldsymbol{g}.\hat{\boldsymbol{u}}]\, dA \tag{12}$$

$$a_\beta(\beta, \hat\beta) = \int_\Omega \left[k\nabla\beta.\nabla\hat\beta\right] dV \tag{13}$$

$$l_\beta(\hat\beta, \boldsymbol{u}) = \int_\Omega \hat\beta\ [\frac{1}{2}\lambda\ (div\boldsymbol{u})^2 + \mu\ \boldsymbol{\nabla u}.\boldsymbol{\nabla u} - w + \lambda_\beta + \lambda_{\dot\beta}]dV \tag{14}$$

$$c_\beta(\hat\beta, \dot\beta) = \int_\Omega \left[C\dot\beta\hat\beta\right] dV \tag{15}$$

$$\Lambda_\beta(\hat\beta, \beta) = \int_\Omega \left[\lambda_\beta\hat\beta\right]\ dV;\ \ \lambda_\beta \leq 0,\ \beta\lambda_\beta = 0 \tag{16}$$

$$\Lambda_{\dot\beta}(\hat\beta, \dot\beta) = \int_\Omega \left[\lambda_{\dot\beta}\hat\beta\right]\ dV;\ \ \lambda_{\dot\beta} \leq 0,\ \dot\beta\lambda_{\dot\beta} = 0 \tag{17}$$

3 Numerical approximation of the integral problem

The abstract mathematical problem (10) is similar to the one that arises in the study of heat transfer in elastic bodies undergoing small transformations. Hence, numerical strategies adopted for the solution of coupled heat transfer problems can be easily adapted to this case [16, 17]. This coupled nonlinear problem can be solved through a strategy in which the semi-discrete problem that results from a spatial discretization is splitted in a sequence of two linear systems of ordinary differential equations, which are in turn solved by standard time integration techniques. Such a staggered scheme can be viewed as a product formula algorithm, exactly as in the classical method of fractional steps [18, 19].

3.1 Semi-discrete problem

The solution of the damage evolution problem is based on a spatial discretization leading to a semi-discrete version (a nonlinear system of ordinary differential equations). This system of differential equations is approximated through a sequence of two linear problems, which are in turn solved by standard time integration techniques. Let's consider V_u^m a m-dimensional sub-space of the space V_u, generated by a finite set of base functions $\boldsymbol{N}_i (1 = 1, \ldots, m)$ and V_β^m a n-dimensional subspace of the space V_β, generated by a finite set of base functions $\varphi_i (1 = 1, \ldots, n)$. These base functions allow the construction the approximations $\boldsymbol{u}_m$ and β_n for $\boldsymbol{u}$ and β:

$$\boldsymbol{u}_m(\boldsymbol{x}, t) = \sum_{i=1}^{m} (w_i(t)\boldsymbol{N}_i(\boldsymbol{x})) + \bar{\boldsymbol{u}}(t) \text{ and } \beta_n(\boldsymbol{x}, t) = \sum_{i=1}^{n} (\zeta_i(t)\varphi_i(\boldsymbol{x})) + \bar{\beta}(t) \tag{18}$$

Where $\bar{\boldsymbol{u}}(t)$ and $\bar{\beta}(t)$ are given functions satisfying the boundary conditions imposed in Γ_1. The spaces V_u^m and V_β^n may have different dimension ($m \neq n$). Nevertheless, to simplify the presentation, from now on, both spaces are supposed to have the same dimension ($m = n$). The semi-discrete problem is obtained by replacing $\boldsymbol{u}$ by $\boldsymbol{u}_m$ and β by β_m in the governing equations presented in (10). It can be verified that the resulting semi-discrete problem is a nonlinear system of first order ordinary differential equation with the following form:

$$[\mathbf{K}(\boldsymbol{\beta})]\,\mathbf{U} = \mathbf{R};\ [\mathbf{C}]\,\dot{\boldsymbol{\beta}} + [\mathbf{A}]\,\boldsymbol{\beta} + [\mathbf{F}(\mathbf{U})] + \left[\boldsymbol{\Upsilon}_\beta(\dot{\boldsymbol{\beta}})\right] + \left[\boldsymbol{\Upsilon}_{\dot{\beta}}(\dot{\boldsymbol{\beta}})\right] = \mathbf{0} \tag{19}$$

where

$$\left.\begin{array}{c} \mathbf{U} = \{w_1, w_2, ..., w_m\}\ ;\ \boldsymbol{\beta} = \{\zeta_1, \zeta_2, ..., \zeta_m\}\ ;\ \dot{\boldsymbol{\beta}} = \left\{\dot{\zeta}_1, \dot{\zeta}_2, ..., \dot{\zeta}_m\right\} \\ [\mathbf{K}(\boldsymbol{\beta})]_{ij} = a_\varepsilon(\mathbf{N}_i, \mathbf{N}_j, \beta_m)\ ;\ [\mathbf{C}]_{ij} = c_\beta(\varphi_i, \varphi_j)\ ;\ [\mathbf{A}]_{ij} = a_\beta(\varphi_i, \varphi_j) \\ [\mathbf{R}]_i = \mathbf{l}_\varepsilon(\mathbf{N}_i)\ ;\ \ [\boldsymbol{F}(\boldsymbol{U})]_i = l_\beta(\varphi_i, \boldsymbol{u}_m) \\ \left[\boldsymbol{\Upsilon}_{\boldsymbol{\beta}}(\dot{\boldsymbol{\beta}})\right]_i = \Lambda_\beta(\varphi_i, \beta_m)\ \ ;\ \left[\boldsymbol{\Upsilon}_{\dot{\boldsymbol{\beta}}}(\dot{\boldsymbol{\beta}})\right]_i = \Lambda_{\dot{\beta}}(\varphi_i, \dot{\beta}_m), \quad i, j = 1, ..., m \end{array}\right\} \tag{20}$$

If the base function are chosen following the classical Finite Element technique, the parameters w_i (i=1,...,m) at a given instant t can be associated to the components of the displacement $\boldsymbol{u}$ at the nodal points and the parameters ζ_i (i=1,...,m) to the value of the auxiliary variable β at the

nodal points. From now on, it is supposed that the Finite Element technique is adopted and that the parameters w_i and ζ_i can have such physical interpretation. Nevertheless, the notation will be kept intentionally general and abstract, since any adequate choice of base functions (such as in the element-free Galerkin method [20]) can also be adopted alternatively in the semi-discretization.

3.2 Operator splitting technique applied to semi-discrete problem

A splitting Technique is used to approximate the nonlinear semi-discrete problem through a sequence of simpler linear problems. In the following, it is considered a time step Δt and the notation: $t_n = (n\ \Delta t)$ and $y(t_n) = y^n$. If all the fields are known at a given instant t_n, the nodal variables β^{n+1} and $\mathbf{U}^{n+1}$ can be approximated by solving the following sequence of linear problems

i) β^{n+1} is the solution of

$$[\mathbf{C}]\left\{\theta\boldsymbol{\beta}^{n+1} + (1-\theta)\boldsymbol{\beta}^{n}\right\} + \Delta t\,[\mathbf{A}]\left\{\theta\boldsymbol{\beta}^{n+1} + (1-\theta)\boldsymbol{\beta}^{n}\right\} + \Delta t\,[\mathbf{F}(\mathbf{U}^{n})] = \mathbf{0}$$

ii) Projection 1: if $\beta_i^{n+1} \geq \beta_i^n \rightarrow \beta_i^{n+1} = \beta_i^n;\ \ i = 1, \ldots, m$

iii) Projection 2: if $\beta_i^{n+1} < \delta \Rightarrow \beta_i^{n+1} = \beta_i^n$

iv) $\mathbf{U}^{n+1}$ is the solution of $\left[\mathbf{K}(\boldsymbol{\beta}^{n+1})\right]\ \boldsymbol{U}^{n+1} = \boldsymbol{R}^{n+1}$

Projection technique adopted in step (ii) aims to assure that the constraint $\dot{\beta} \leq 0$ is verified in all nodal points. Projection technique adopted in step (iii) assures that $\beta \geq 0$ in all nodal points. $\delta > 0$ is the smallest admissible numerical value of the damage variable β. The choice of δ depends on the precision of the machine, but it is suggested $10^{-6} \leq \delta \leq 10^{-5}$. θ defines the integration method: $\theta = 0$, forward Euler; $\theta = 1$, backward Euler and $\theta = 1/2$, trapezoidal rule. A similar procedure to approximate $\boldsymbol{\beta}^{n+1}$ and $\mathbf{U}^{n+1}$ can be considered using a different sequence of linear problems:

i) $\mathbf{U}^{n+1}$ is the solution of $[\mathbf{K}(\boldsymbol{\beta}^{n})]\ \boldsymbol{U}^{n+1} = \boldsymbol{R}^{n+1}$

ii) $\boldsymbol{\beta}^{n+1}$ is the solution of $[\mathbf{C}]\left\{\theta\boldsymbol{\beta}^{n+1} + (1-\theta)\boldsymbol{\beta}^{n}\right\} + \Delta t\,[\mathbf{A}]\left\{\theta\boldsymbol{\beta}^{n+1} + (1-\theta)\boldsymbol{\beta}^{n}\right\} +$
$$+\Delta t\left\{\theta\,[\mathbf{F}(\mathbf{U}^{n})] + (1-\theta)\left[F(U^{n+1})\right]\right\} = \mathbf{0}$$

iii) Projection 1: if $\beta_i^{n+1} \geq \beta_i^n \rightarrow \beta_i^{n+1} = \beta_i^n;\ \ i = 1, \ldots, m$

iv) Projection 2: if $\beta_i^{n+1} < \delta \Rightarrow \beta_i^{n+1} = \beta_i^n$

A reasonable criterion to verify if the approximation of a given problem is adequate is to compare the different solutions obtained using these two different procedures. Generally they are very close, even if sufficiently small time interval is considered.

4 Results and discussion

A local governing equation for the damage variable β can be obtained introducing (8), (9) into the second expression in (6):

$$C\dot{\beta} = k\ \Delta\beta + w - \left[\frac{1}{2}\lambda\ tr(\varepsilon)^2 + \mu\ \varepsilon.\varepsilon\right] - \lambda_\beta - \lambda_{\dot{\beta}} \tag{21}$$

Eq. (21) is similar to the heat transfer equation for elastic bodies undergoing small transformations. Parameter C plays the same role than the specific heat (the smaller is C the bigger is the damage variation for a given supply of mechanical power). k has a similar role than the thermal conductivity (the smaller is k, the more localized is the damage). The main difference is the limit defined by parameter w – at a given material point, $\dot{\beta} \neq 0$ only if $\left[\frac{1}{2}\lambda\, tr(\varepsilon)^2 + \mu\, \varepsilon.\varepsilon\right] > w$. Hence, it is necessary a minimum strain energy w in order to have a local evolution of the damage variable.

As a first step to assess the main features of the modeling, a one-dimensional problem is considered in the next section. The main goal is to study the influence of the material parameters on the material behavior through a simple example. The features of the numerical solution strategy are discussed in three other examples concerning the crack initiation and propagation in plates under different conditions.

4.1 A non-homogeneous one-dimensional problem

In this first example, it is considered a bar of length L, submitted to the following boundary conditions

$$u_x(x=0,t)=0, u_x(x=L,t)=\alpha t \text{ and } \beta(x=0,t)=1, \beta(x=L,t)=1, \forall t \tag{22}$$

Neglecting the weight of the bar ($\boldsymbol{b}=\mathbf{0}$) and assuming it is not submitted to external microscopic forces ($p=q=0$), the local governing equations can be expressed as follows in a one-dimensional context

$$\frac{\partial \sigma_{xx}}{\partial x} = 0 \tag{23a}$$

$$\frac{\partial u_x}{\partial x} = \frac{\sigma_{xx}}{E\beta} \tag{23b}$$

$$\frac{\partial \beta}{\partial t} = \begin{cases} -\frac{1}{C}\left\langle \frac{1}{2E}\left(\frac{\sigma_{xx}}{\beta}\right)^2 - w - k\frac{\partial^2 \beta}{\partial x^2}\right\rangle, \text{ if } 0<\beta\leq 1 \\ 0, \text{ if } \beta = 0 \end{cases} \tag{23c}$$

Defining the dimensionless variables $(\sigma^*, x^*, u^*, t^*)$ and the dimensionless quantities (C_1, C_2):

$$\sigma^* = \frac{\sigma_{xx}}{E}, x^* = \frac{x}{L} u^* = \frac{u_x}{L}, t^* = \frac{E}{C}t, C_1 = \frac{w}{E}, C_2 = \frac{k}{L^2 E} \tag{24}$$

problem (22), (23) can be re-written as follows:

$$\frac{\partial \sigma^*}{\partial x^*} = 0 \tag{25a}$$

$$\frac{\partial u^*}{\partial x^*} = \frac{\sigma^*}{\beta} \tag{25b}$$

$$\frac{\partial \beta}{\partial t^*} = \begin{cases} -\left\langle \frac{1}{2}\left(\frac{\sigma^*}{\beta}\right)^2 - C_1 - C_2\frac{\partial^2 \beta}{\partial (x^*)^2}\right\rangle, \text{ if } 0<\beta\leq 1 \\ 0, \text{ if } \beta = 0 \end{cases} \tag{25c}$$

with

$$\begin{aligned} &u^*(x^*=0,t^*)=0,\ u^*(x^*=1,t^*)=\hat{\alpha}t^*=\left(\tfrac{\alpha C}{EL}\right)t^* \\ &\beta(x^*=0,t^*)=1,\ \beta(x^*=1,t^*)=1 \end{aligned} \qquad \forall t \tag{26}$$

This simple one-dimensional example shows that the model accounts for the size effect through the parameter C_2 (the behavior of the structure will depend on the length L). Although the (dimensionless) axial stress component σ^* is constant along the bar, it will undergo a non homogeneous deformation due to the damage. Fig. 1 shows the distribution of the axial strain component $\varepsilon = \frac{\partial u^*}{\partial x^*}$ at instant $t^* = 3.555 \times 10^5$ for two different values of the parameter C_2 considering $C_1 = 5 \times 10^{-7}$ and $\hat{\alpha} = 10^{-8}$. It can be observed that the smaller is C_2 (or k), the more localized is the deformation at the middle of the bar.

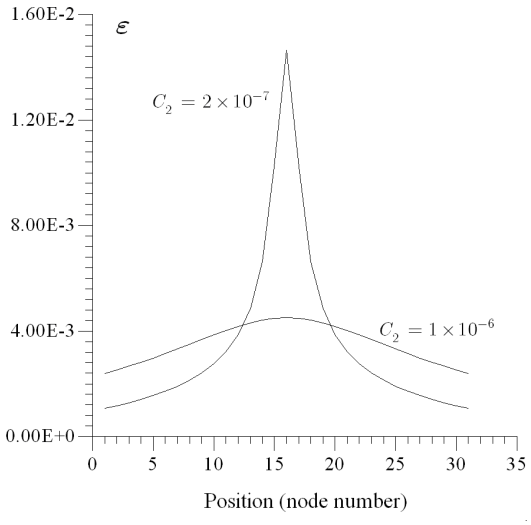

Figure 1: Distribution of the axial deformation along the bar for two different values of C_2.

Fig. 2 shows the influence of the parameter C_2 on the (dimensionless) axial stress versus axial strain curve at the point $x^* = 1/2$, taking $C_1 = 5 \times 10^{-7}$ and $\hat{\alpha} = 10^{-8}$. Parameter w (or the dimensionless parameter C_1) is related to the minimum strain energy necessary to start the damage evolution at a given point. In the one-dimensional case it corresponds to the area of the linear portion of the stress-strain curve, see Fig 3.

Parameter C (or the dimensionless parameter $\hat{\alpha}$) has a similar role than the specific heat in a one dimensional heat transfer problem in an elastic bar. Fig. 4 shows the (dimensionless) axial stress versus axial strain curve at the point $x^* = 1/2$, taking $C_2 = 2 \times 10^{-7}$, $C_1 = 5 \times 10^{-7}$ and different values of $\hat{\alpha}$.

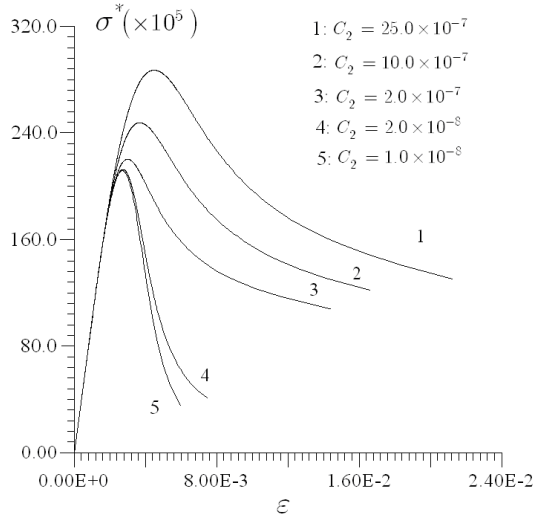

Figure 2: Influence of the parameters C_2 on the structure behavior.

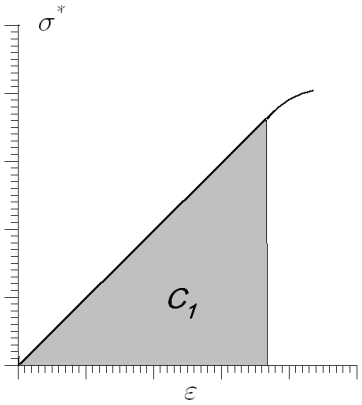

Figure 3: Definition of the parameter C_1.

4.2 Square plate with transverse hole submitted to prescribed axial displacement

In order to assess the features of the modeling, it is analyzed a square plate (200 mm x 200 mm) with a central circular hole with 50 mm radius, submitted to prescribed displacement $\hat{u}(t) = \alpha t$, $\alpha = 2.5\times10^{-3}\ mm/s$, at the extremities (Fig. 5). The goal is to study the "crack" initiation on such kind of structure. The material properties are: E=27.0GPa, $\nu = 0.2$, $k = 0.2$ MPa.mm^2, $C = 1.0\times10^{-8}$ MPa.s and $w = 5.0\times10^{-8}$ MPa. The prescribed displacement and the adopted time step are respectively

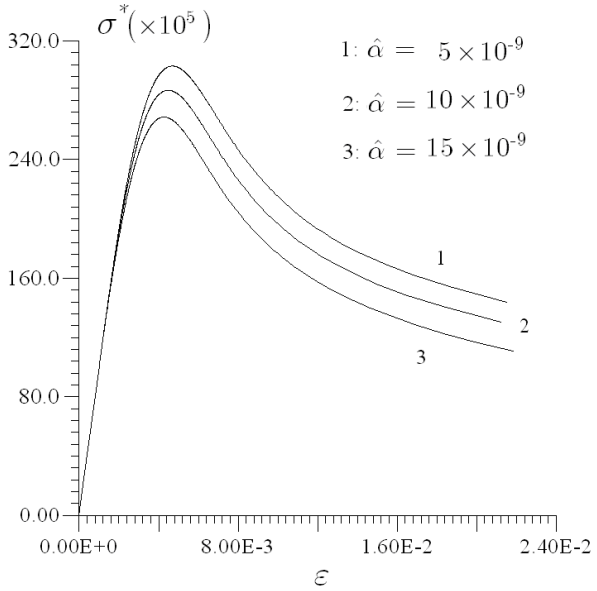

Figure 4: Influence of the parameters $\hat{\alpha}$ on the structure behavior.

given by $u(L,t) = \alpha t$, ($\alpha = 5.0 \times 10^{-3}\ mm/s$). Plane state of strain is assumed and isoparametric bi-linear quadrilateral finite elements are adopted with time step $\Delta t = 1.0 \times 10^{-4}\ s$.

The evolution of the variable $D = (1-\beta)$ on the plate is depicted in Fig. 6. Considering a numerically predicted macro-crack the set of points in the structure where the damage variable has reached a given critical value, it can be observed a straight "macro-crack" initiation and propagation orthogonally to the load direction. The region where the material is completely damaged ($\beta = 0$ or, equivalently, $D = 1$) is not limited to a column of elements as it happens in a mesh dependent problem.

Fig. 7 presents the damage and axial stress fields at instant t = 3.0 s. In this theory, the stress at the tip of the "crack" is zero (since $\beta = 0$) and the higher stress concentration (but with a finite value) occurs a little ahead of the "crack" tip.

Fig. 8 shows the distribution of the longitudinal displacement along the plate at three different time steps. As it can be verified, after instant t=3.35 s, total failure occurs and the "broken" part of the plate almost undergoes a rigid body motion.

The external tensile force F versus prescribed displacement $\hat{h}$ curves for the four different meshes in Fig. 10 are presented in Fig. 9. The softening behavior is almost the same for all the meshes showing that numerical difficulties of mesh-dependence due to the loss of ellipticity of the governing equations in the post-localization range are not observed in this case.

Fig. 12 allows to observe the damage propagation along the horizontal lines A (y = 53.0 mm) and B (y = 60.0 mm), defined in Fig 11. The shapes of the curves and the damage levels at different points along those lines are almost the same for different meshes.

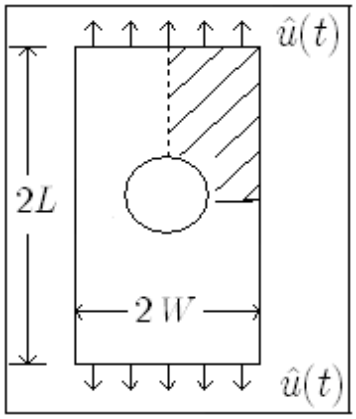

Figure 5: Plate with central circular hole.

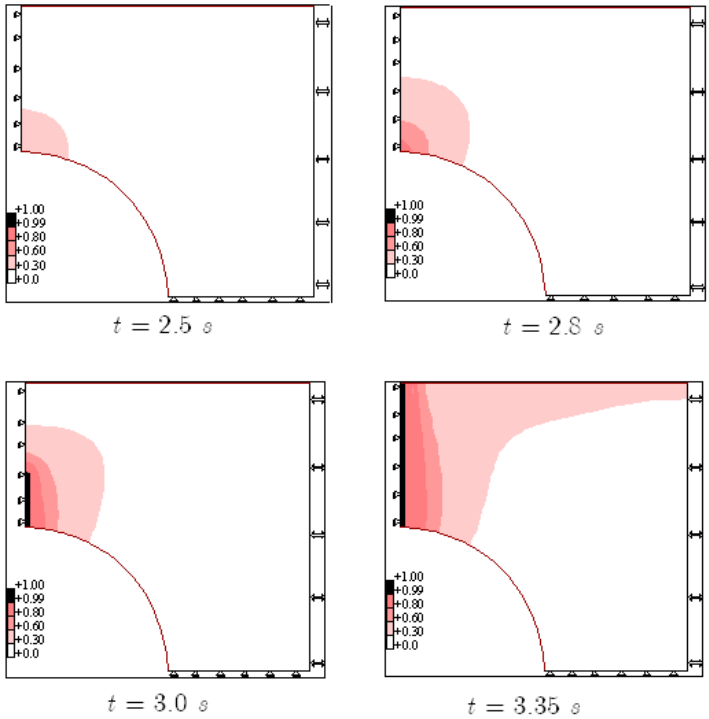

Figure 6: Plate with central circular hole. Damage distribution at different instants.

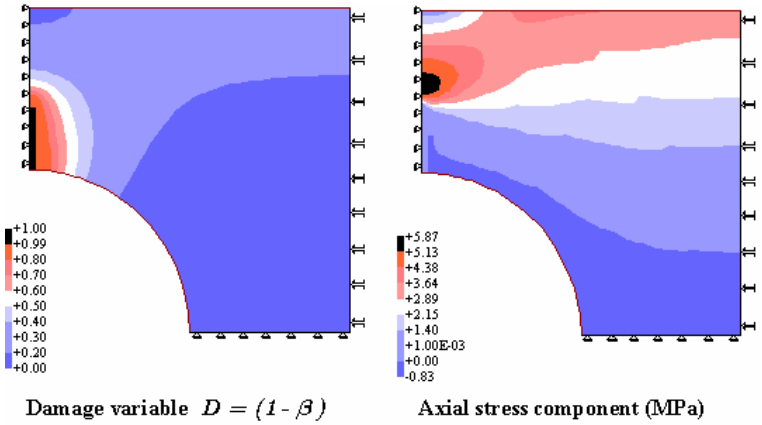

Figure 7: Plate with central circular hole. Damage and axial stress distribution. $t = 3.0\ s$.

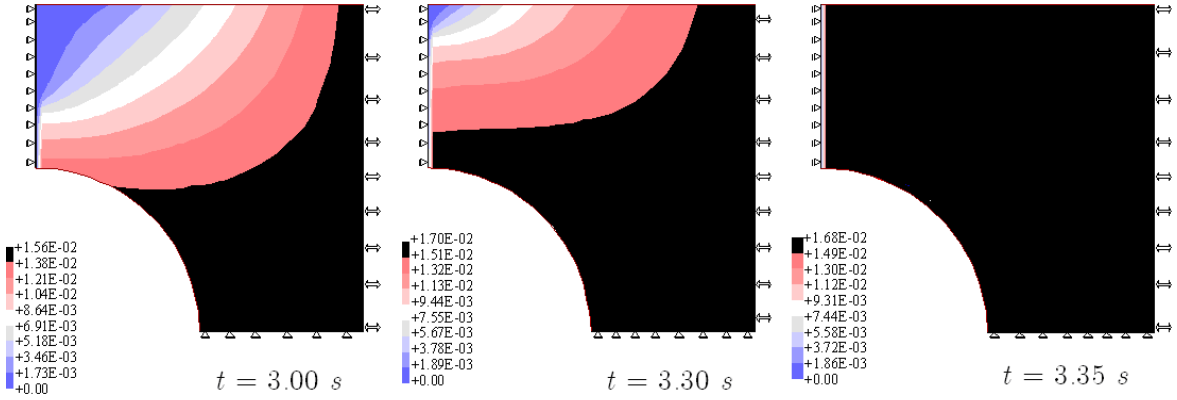

Figure 8: Plate with central circular hole. Distribution of the longitudinal displacement along the plate at three different time steps.

The performance of the proposed algorithm is also checked by comparing the distribution of variable β and longitudinal displacement u obtained using different time steps Δt and the same spatial discretization, mesh-2 (Fig. 9). Backward Euler ($\theta = 1$) time integration scheme was employed. The time increments considered in the simulations are 0.1 s, 0.01 s, 0.001 s, 0.0005 s and 0.0001 s. The distribution of the variables β and u along the line B, at instant $t =$ 3.0s, is presented in Fig 13. The curves obtained using time increments Δt=0.0005s and Δt=0.0001s are indiscernible within the precision of the figure.

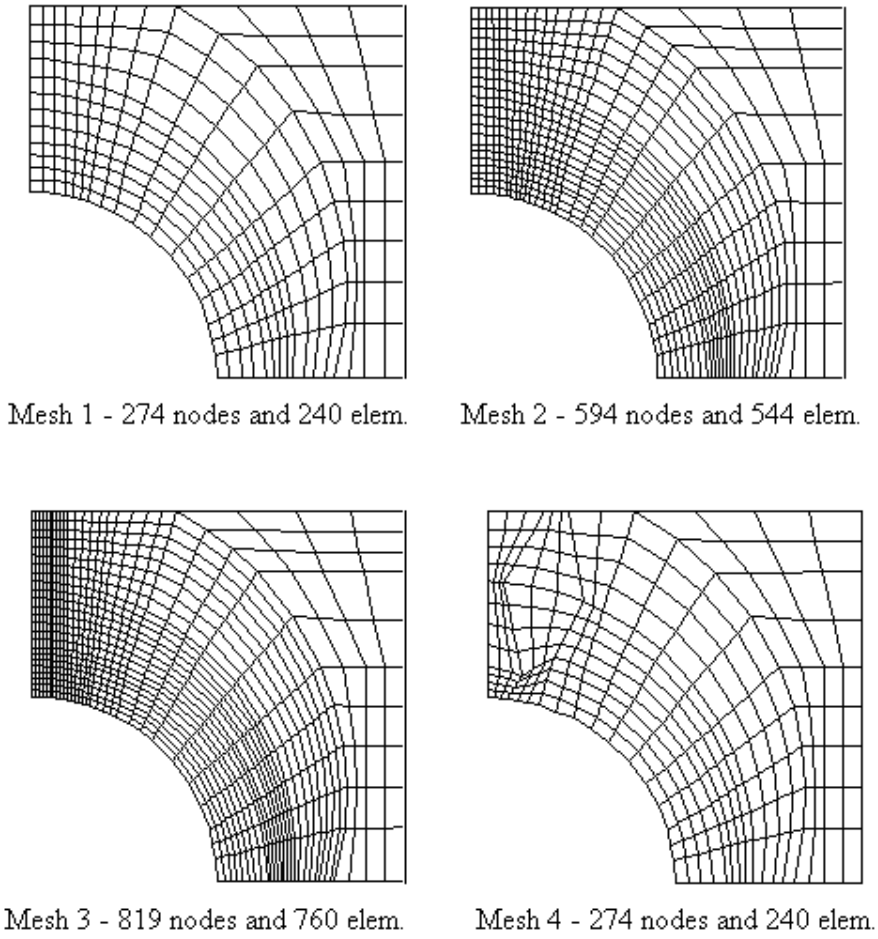

Figure 9: Plate with central circular hole. Analysis of mesh dependence - Different meshes considered.

4.3 Double-edge-cracked plate submitted to a prescribed axial displacement

It is considered in this section a double-edge-cracked plate (25 mm x 10 mm), with initial crack length of 4 mm, loaded with a prescribed displacement $\hat{u}(t) = \alpha t$, $\alpha = 5.0 \times 10^{-3}\ mm/s$, at both sides (Fig. 14). In this case, the goal is to perform the analysis of a "crack" propagation. The material properties are the same than the previous example. Plane state of strain is assumed and isoparametric bilinear quadrilateral finite elements are used with a time step $\Delta t = 1.0 \times 10^{-4}$.

Fig. 15 shows the damage field $D = (1 - \beta)$ on the plate at three different time steps. Fig. 16 shows the longitudinal displacement along the plate. As it can be verified, after instant t=1.577s, total failure occurs and the "broken" part of the plate undergoes a rigid body motion.

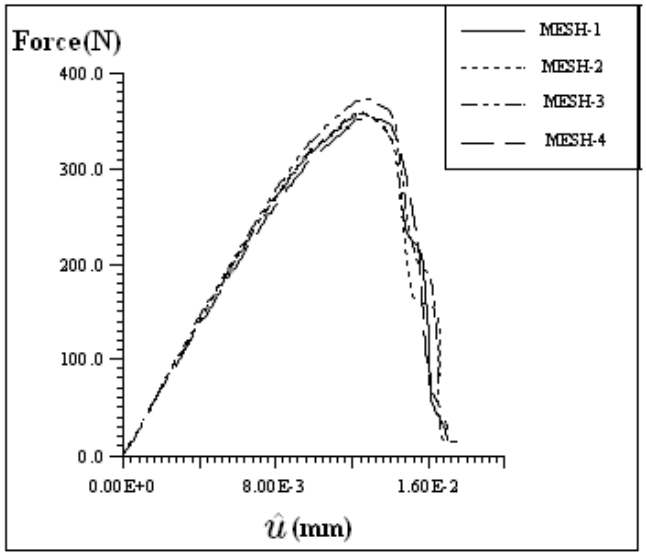

Figure 10: Plate with central circular hole. Tensile force versus displacement $\hat{u}$.

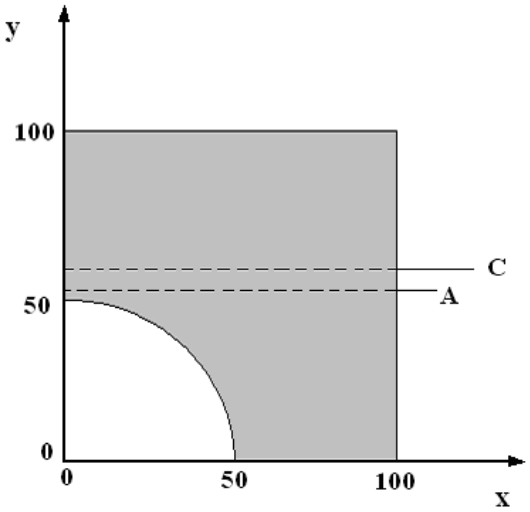

Figure 11: Plate with central circular hole. Longitudinal lines A and B.

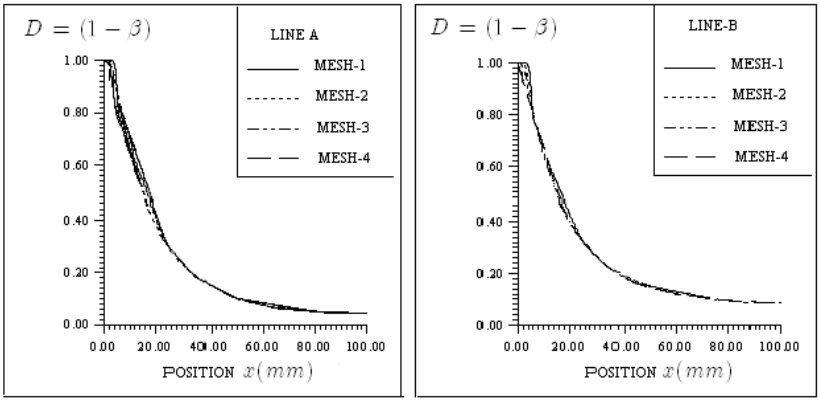

Figure 12: Plate with central circular hole. Damage along lines A and B.

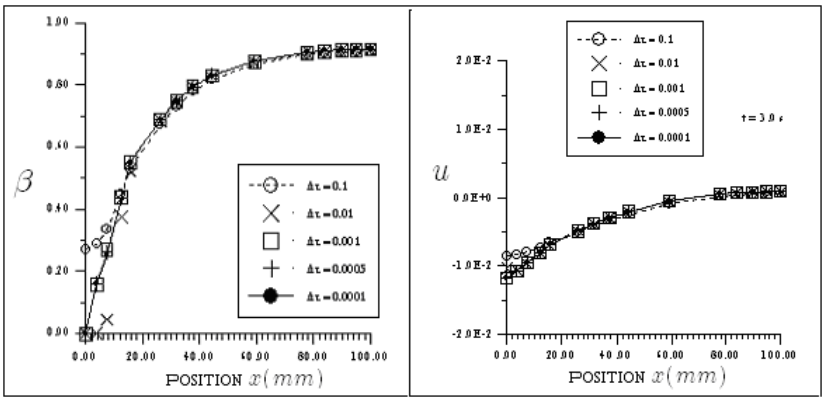

Figure 13: Plate with central circular hole. Distribution of variables β and u along the line along line B, at t = 3.0s

The external tensile force F versus prescribed displacement $\hat{u}$ curves for the three different meshes in Fig. 17 are presented in Fig. 18. Mesh-1 has 340 nodes and 304 elements, mesh-2 has 500 nodes and 456 elements and mesh-5 has 252 nodes and 221 elements. Mesh 3 is deliberately distorted to check the sensitivity of the numerical solution to the choice of the mesh. The softening behavior is almost the same for all the meshes showing that numerical difficulties of mesh-dependence are not observed in this case.

Fig. 19 shows the damage distribution at instant t_f when total failure occurs for the 3 different meshes. The damage distribution is practically the same for all the meshes.

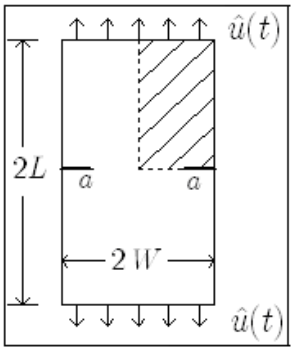

Figure 14: Double-edge-cracked plate.

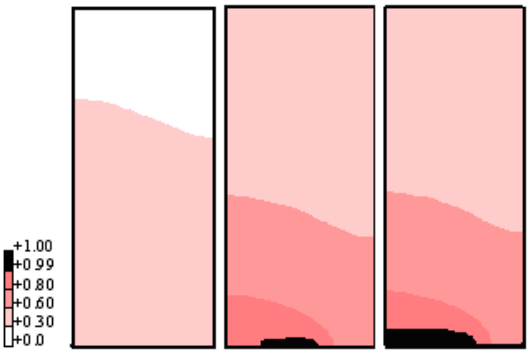

Figure 15: Double-edge-cracked plate. Damage distribution at instants t = 1.3 sec, t = 1.575 sec and t =1.577sec.

4.4 Rectangular plate, clamped at the ends and submitted to a prescribed axial displacement

It is considered in this section a rectangular plate (200mm x 100 mm) clamped at the ends and submitted to a prescribed axial displacement $\hat{u}(t) = \alpha t$, $\alpha = 1.0\text{x}10^{-2} mm/s$, at the extremities (Fig. 20). The material parameters are: E=50.0GPa, ν=0.2, $C = 1.0 \times 10^{-3}$ MPa.s and $w = 2.5 \times 10^{-2}$ MPa. In this case, the goal is to perform the analysis of a "crack" initiation and propagation in a complex mode.

Fig 21 shows the vertical displacement along the plate at the moment total failure occurs, considering two different values of the parameter k: 1 MPa.mm^2 (t=30 s) and 0.5 MPa.mm^2 (t = 24 s). Initially a "macro-crack" appears on the left corner at the bottom of the plate initially propagates orthogonally to the load direction and then changes the direction of propagation until total failure occurs (with two regions almost undergoing a rigid body motion). The "macro-crack" can be associated to the zone of

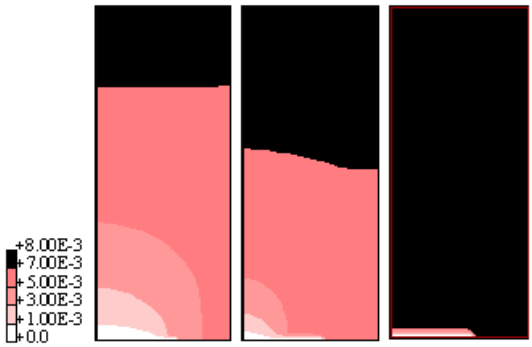

Figure 16: Double-edge-cracked plate. Longitudinal displacement (mm) at instants t = 1.3 s, t = 1.575 s and t = 1.577s.

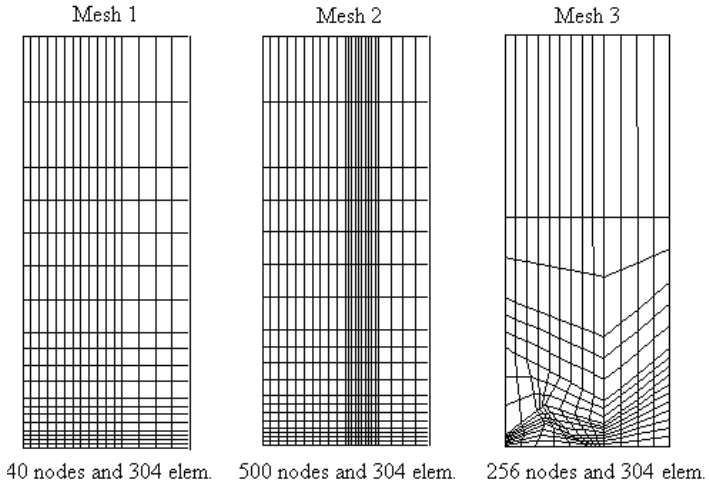

Figure 17: Double-edge-cracked plate – Different meshes considered.

transition between regions I and II where the material can no longer resist to mechanical solicitations. If a constant k=0.5 MPa.mm^2 is considered instead of k=1 MPa.mm^2, the fracture is more localized.

5 Conclusion

In the present paper it is proposed a framework, as simple as possible, to perform structural integrity analysis of quasi-brittle structures undergoing general loading (degradation due to the deformation process, crack initiation, crack propagation, total rupture) using a gradient-enhanced continuum dam-

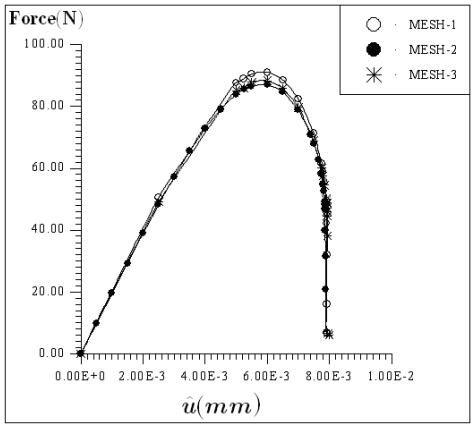

Figure 18: Double-edge-cracked plate. Tensile force versus displacement $\hat{u}$.

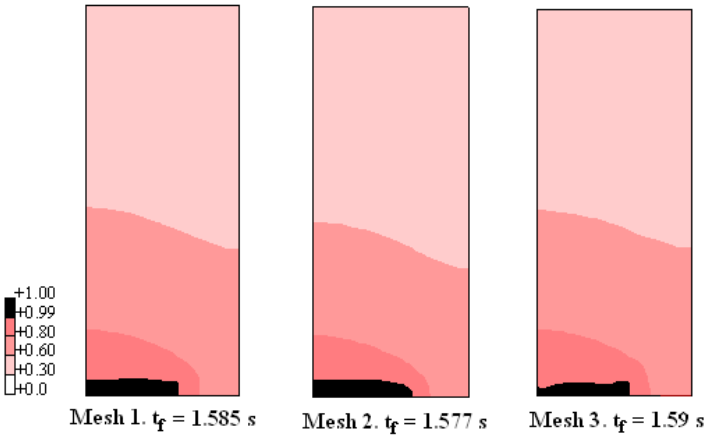

Figure 19: Double-edge-cracked plate. Damage distribution at the instant t_f when total failure occurs.

age model. A simple numerical technique was proposed to approximate the solution of the resulting nonlinear mathematical problem without the necessity of radical modification of an ordinary finite element code. The basic idea is to consider a splitting technique that transforms the global nonlinear problem in a sequence of linear problems that can be approximated using classical The basic idea is to consider a splitting technique that transforms the global nonlinear problem in a sequence of linear problems that can be approximated using classical discretization techniques. The Finite Element technique was adopted to obtain the semi-discrete problem. Nevertheless, the notation was kept intentionally general and abstract, since any adequate choice of base functions (such as in the element-free

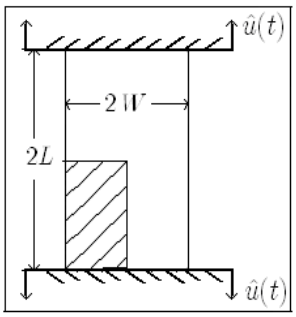

Figure 20: Clamped plate.

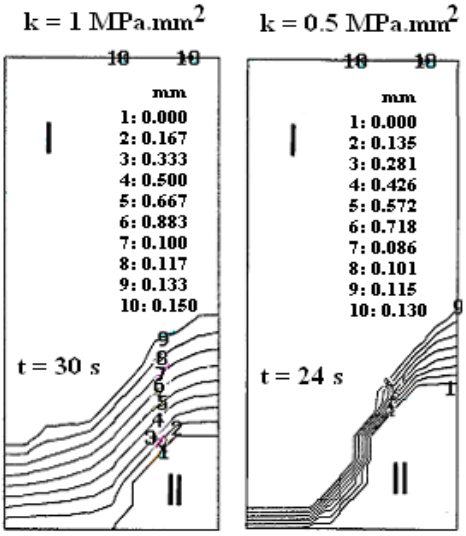

Figure 21: Clamped plate. Longitudinal displacement (mm) for two different values of k.

Galerkin method) can also be adopted alternatively in the semi-discretization. The numerical results are indiscernible within the precision of the figures if different time integration techniques (different values of θ) were adopted or different splitting techniques (section 3.2) were applied to the semi-discrete problem.

The theory allows a correct qualitative description of the strain-softening phenomena, is valid for any kind of geometry and for any kind of external loading, and can be seen as a first step towards a reasonably simple and practical tool to model the fracture of quasi-brittle structures(ceramics, concretes, rocks, glasses, etc.). Within this framework of microstructure theory, more sophisticated

boundary conditions for the damage variable can be considered to include adherence, for instance, through the external contact microscopic force.

References

[1] Lemaitre, J. & Chaboche, J.L., *Mechanics of Solids Materials*. Cambridge University Press, 1990.

[2] Knowles, J.K. & Sternberg, E., On the failure of ellipticity and the emergence of discontinuous deformation gradients in plane finite elastostatics. *J Elasticity*, **8**, pp. 329–379, 1978.

[3] Pietruszczak, S.T. & Mroz, Z., Finite element analysis of the deformation of strain-softening materials. *Int J Numer Meth Engng*, **17**, pp. 327–334, 1981.

[4] Needleman, A., Material rate dependence and mesh sensitivity in localization problems. *Comput Meth Appl Mech Engng*, **67**, pp. 69–87, 1988.

[5] Bazant, Z.P. & Pijaudier Cabot, G., Nonlocal continuum damage, localization, instability and convergence. *ASME J Appl Mech*, **55**, pp. 287–293, 1988.

[6] Bazant, Z.P. & Cedolin, L., *Stability of structures - elastic, inelastic and damage theories*. Oxford University Press, 1991.

[7] Costa-Mattos, H.S., N., M.E. & M., F., A simple model of the mechanical behavior of ceramic-like materials. *Int J Solid and Struct*, **24**, pp. 3185–3200, 1992.

[8] Frémond, M. & Nedjar, B., Damage, gradient of damage and principle of virtual power. *Int J Solids Structures*, **33(8)**, pp. 1083–1103, 1996.

[9] Khoei, A.R. & Karimi, K., An enriched-FEM model for simulation of localization phenomenon in cosserat continuum theory. *Comp Materials Science*, **44**, pp. 733–749, 2008.

[10] Peyrot, I., Bouchard, P.O., Bay, F., Bernard, F. & Garcia-Diaz, E., Numerical aspects of a problem with damage to simulate mechanical behavior of a quasi-brittle material. *Comp Materials Science*, **40**, pp. 327–340, 2007.

[11] Brighenti, R., A new discontinuous FE formulation for crack path prediction in brittle solids. *Int J Solid and Struct*, **45**, pp. 6501–6517, 2008.

[12] Lorentz, E., A mixed interface finite element for cohesive zone models. *Comput Methods Appl Mech Engrg*, **198**, pp. 302–317, 2008.

[13] Costa Mattos, H.S. & Sampaio, R., Analysis of the fracture of brittle elastic materials using a continuum damage model. *Struct Eng and Mechanics*, **3(5)**, pp. 411–427, 1995.

[14] Mindlin, R.D., Microstructure theories in linear elasticity. *Arch Rat Mech Anal*, **16**, pp. 51–78, 1964.

[15] Toupin, R.A., Theories of elasticity with couple-stress. *Arch Rat Mech Anal*, **17**, pp. 85–112, 1964.

[16] Armero, F. & Simo, J.C., A new unconditionally stable fractional step methods for non-linear coupled thermomechanical problems. *Int J Numerical Methods in Engineering*, **35**, pp. 737–766, 1992.

[17] Simo, J.C. & Miehe, C., Associative coupled thermoplasticity at finite strains: formulation, numerical analysis and implementation. *Comput Meth Appl Mech Engng*, **98**, pp. 41–104, 1992.

[18] Yanenko, N.N., *The Method of Fractional Steps*. Springer-Verlag: New York, 1980.

[19] Chorin, A.J., Hughes, T.J.R., McCracken, M.F. & Marsden, J.E., Product formula and numerical algorithms. *Communications on Pure and Applied Mathematics*, **31**, pp. 205–256, 1978.

[20] Belytschko, T., Lu, Y.Y. & Gu, L., Element free Galerkin methods. *Int J for Numerical Methods in Engineering*, **37**, pp. 229–256, 1994.

A continuum model for hydrogen diffusion in a hollow cylinder

Fernando P. Duda, Nélio Achão Filho
Universidade Federal do Rio de Janeiro - COPPE - PEM, Rio de Janeiro – Brazil
Angela C. Souza, Leandro S. Costa
Universidade Federal Fluminense - TEM - PGMEC, Rio de Janeiro – Brazil

Abstract

This paper presents the formulation of a coupled continuum model for deformation and solute diffusion applied in a cylindrical geometry. The formulation is carried out within the framework of the multifield continuum mechanics, where, in addition to the standard fields, extra fields are introduced in order to describe diffusion processes. The theory is singled out and subjected to a numerical implementation based on the finite element method, backward Euler scheme and an operator-split algorithm. A numerical example is given to illustrate the capabilities of the theory to describe the process of constant surface potential.

Keywords: multifield continuum mechanics, solute diffusion in solids.

1 Introduction

In 1878 [1] introduced the idea of a solid which also contains fluid components, whereby a fluid can enter into, move independently through and distort the solid, which otherwise is conserved and behaves elastically. As indicated by [2], a genuine example of this kind of body is provided by interstitial solid solutions at sufficiently low temperatures, with host and interstitial species playing the role of solid and fluids, respectively. Additional examples can be found in the fields of geology, polymer science and metallurgy, as pointed out by [3], who extended Gibbs' idea by allowing solid diffusion. This extension is basic for the modern understanding of equilibrium and diffusion kinetics in solid solutions under stress (see [4] and [5]) as well as for the unified treatment of atomic transport given by [6] (see also [7]).

Particularly, hydrogen in metals provides a large topic of material science, which has attracted considerable interest due to its several applications, such as palladium and palladium-alloy membranes used for hydrogen separation and purification, as described by [8]. These membranes provide this efficient application based on the high solubility and very fast diffusion of the hydrogen in metal-

Mechanics of Solids in Brazil 2009, H.S. da Costa Mattos & Marcílio Alves (Editors)
Brazilian Society of Mechanical Sciences and Engineering, ISBN 978-85-85769-43-7

hydrogen systems. The experiments are generally performed by using tubular membranes, where the initiations of permeation is obtained by gaseous atmospheres of hydrogen at the external surface. [9] have investigated the effect of chemical stress on diffusion in a hollow cylinder for plane strain case, and [10] have concluded that the geometric approximation of modeling thin cylindrical membranes as planar structures fails in the presence of stress-induced diffusion. Some specific boundary conditions have been investigated in the diffusion-induced stress in a hollow cylinder by [11].

Specifically, the purpose of this work is to present a framework based on the formalism of continuum mechanics for the description of solute diffusion, solid-induced deformation applied in a cycilindrical geometry. In accordance with the formalism of modern continuum mechanics (see [6]), we elaborate the framework by introducing the following ingredients: basic balances; free energy imbalance (the second law of thermodynamics) and constitutive theory. We consider as basic the balances of mass for solid and solute, and the balances of forces conjugated to the selected independent kinematical fields, namely solid displacement, solute flow and solute density. The free energy imbalance accounts for energy inflow due to both power expended by all external forces and solute supply, a contribution through which the chemical potential is introduced. The constitutive theory is based upon the following assumptions: additive decomposition of the solid strain into its elastic and solute-induced parts; the dissipation is due degradation and diffusion; the set of constitutive variables includes elastic strain and solute density. Finally, the underlying governing equations of the framework are obtained by merging the aforementioned ingredients. In particular, the equation for the solute flux follows from the corresponding conjugated force balances, whereas the equation for the chemical potential follows from the solute density conjugated force balance.

The present development is similar to that used by [12] in that the solute density and solute flow are considered as independent kinematical descriptors. In particular, the use of the solute density as an independent degree of freedom was inspired on [13] (see also [14]). A preliminary version of this work was presented by the authors in [15].

2 The continuum model

2.1 Preliminaries

Let us consider a continuum hollow cylinder $\mathcal{C}$ with inner radius R_i, outer radius R_e and lenght L. The cylindrical coordinates system standard are (r, θ, z), but for simplicity the hollow cylinder can be treated as an one-dimensional problem, so that we consider only the radial coordinate r.

Therefore, a generic scalar field quantity $\alpha(r,t)$ has temporal derivative denoted by: $\dot{\alpha} := \dfrac{\partial \alpha}{\partial t}$ and its gradient is defined as: $\nabla \alpha := \dfrac{\partial \alpha}{\partial r}\,\mathbf{e}_r$, where $\mathbf{e}_r$ is the unity vector in the radial direction.

A generic vector field $\mathbf{v}(r,t)$, defined as: $\mathbf{v}(r,t) := v(r,t)\,\mathbf{e}_r$, has the temporal derivative given by: $\dot{\mathbf{v}} := \dfrac{\partial v}{\partial t}\,\mathbf{e}_r$, and its gradient is given by:

Mechanics of Solids in Brazil 2009, H.S. da Costa Mattos & Marcílio Alves (Editors)
Brazilian Society of Mechanical Sciences and Engineering, ISBN 978-85-85769-43-7

$$\nabla \mathbf{v} := \begin{bmatrix} \dfrac{\partial v}{\partial r} & 0 & 0 \\ 0 & \dfrac{v}{r} & 0 \\ 0 & 0 & 0 \end{bmatrix} \tag{1}$$

and the divergence is given by:

$$\operatorname{Div} \mathbf{v} := \frac{\partial v}{\partial r} + \frac{v}{r} \tag{2}$$

A generic tensor field $\mathbf{S}(r,t)$ is given by:

$$\mathbf{S} := \begin{bmatrix} S_r & 0 & 0 \\ 0 & S_\theta & 0 \\ 0 & 0 & S_z \end{bmatrix} \tag{3}$$

and the divergence is given by:

$$\operatorname{Div} \mathbf{S} := \begin{bmatrix} \dfrac{\partial S_r}{\partial r} + \dfrac{S_r - S_\theta}{r} \\ 0 \\ 0 \end{bmatrix} \tag{4}$$

We consider that $\mathcal{C}$ contains two components, one that is conserved and acts as a framework through which the other moves independently. For definiteness we name them solid and solute, respectively, whose densities per unit lattice volume are denoted by $\rho_S(r,t)$ and $\rho(r,t)$. For posterior reference we define the solute concentration c as:

$$c := \frac{\rho}{\rho_S}. \tag{5}$$

Besides, the solid can undergo deformation, described by strain tensor field $\mathbf{E}(r,t)$ and the displacement field $\mathbf{u}(r,t) := u(r,t)\,\mathbf{e}_r$, given by:

$$\mathbf{E} := \frac{1}{2}(\nabla \mathbf{u} + \nabla \mathbf{u}^T) \quad \longrightarrow \quad \begin{bmatrix} E_r & 0 & 0 \\ 0 & E_\theta & 0 \\ 0 & 0 & 0 \end{bmatrix} := \begin{bmatrix} \dfrac{\partial u}{\partial r} & 0 & 0 \\ 0 & \dfrac{u}{r} & 0 \\ 0 & 0 & 0 \end{bmatrix} \tag{6}$$

2.2 Basic laws

Since the solid is conserved, it follows from its mass balance that $\dot{\rho}_S = 0$. Therefore we assume henceforth that ρ_S is given. On the other hand, the mass balance for the solute yields the local field equation:

$$\dot{\rho} = -\mathrm{Div}\,\mathbf{J} + h, \tag{7}$$

where $\mathbf{J}$ is the vector field that represents the solute flux and h the external solute supply. The latter is assumed to be given but otherwise arbitrary.

Now we use the principle of virtual to power to obtain the field equations and the boundary conditions corresponding to the basic force balances of the theory. Firstly, we have to decide on which kinematical description to be adopted and then to prescribe two functionals, namely the virtual power of the external forces and the virtual power of the internal forces ([16]). These are considered below.

We consider $\mathbf{u}$, ρ and $\mathbf{J}$ as independent kinematical descriptors and, for a fixed time, we define a generalized virtual velocity $\bar{\mathbf{v}}$ as the list $(\bar{\mathbf{u}}, \bar{\rho}, \bar{\mathbf{J}})$ of smooth time independent fields on $\mathcal{C}$. The set of virtual velocities is denoted by $\mathcal{V}$, which is assumed to contain the realizable velocity $\mathbf{v} = (\dot{\mathbf{u}}, \dot{\rho}, \mathbf{J})$. We remark that $\mathbf{J}$ is a rate-type variable.

For any part $\mathcal{P} = (R_1, R_2)$ of $\mathcal{C}$ we adopt the following prescriptions for the virtual power of the external and internal forces expended on an arbitrary virtual velocity $\bar{\mathbf{v}}$:

- Virtual power of the external forces

$$P_e(\mathcal{P}, \bar{\mathbf{v}}) := \int_{\mathcal{P}} \mathbf{s}^e \cdot \bar{\mathbf{v}}\, dV + \int_{\partial\mathcal{P}} \mathbf{t} \cdot \bar{\mathbf{v}}\, dA, \tag{8}$$

  where the smooth vector fields $\mathbf{t}$ and $\mathbf{s}^e$ describe contact and body interactions, respectively. The infinitesimal quantities are: $dV := r\, dr\, d\theta\, dz$ and $dA := (R_i \text{ or } R_e)\, d\theta\, dz$.
- Virtual power of the internal forces

$$P_i(\mathcal{P}, \bar{\mathbf{v}}) := -\int_{\mathcal{P}} \left(\mathbf{S} \cdot \nabla \bar{\mathbf{v}} + \mathbf{s}^i \cdot \bar{\mathbf{v}} \right) dV, \tag{9}$$

  where the smooth tensor field $\mathbf{S}$ and vector field $\mathbf{s}^i$ describe internal interactions.

The four-tuple lists of quantities denoted by $\mathbf{S} = (\mathbf{T}, \Gamma, \Lambda)$, $\mathbf{s}^i = (\mathbf{b}^i, \gamma^i, \lambda^i)$ and $\mathbf{s}^e = (\mathbf{b}^e, \gamma^e, \lambda^e)$ are related to the fields $\mathbf{u}$, ρ and $\mathbf{J}$, respectively. The Principle of Virtual Power (see, for instance, [16]) states that for each part $\mathcal{P}$:

$$P_i(\mathcal{P}, \bar{\mathbf{v}}) + P_e(\mathcal{P}, \bar{\mathbf{v}}) = 0 \quad \forall\, \bar{\mathbf{v}} \in \mathcal{V}. \tag{10}$$

The above statement in addition with standard arguments, furnishes the field equation:

$$\mathrm{Div}\mathbf{S} - \mathbf{s}^i + \mathbf{s}^e = \mathbf{0} \text{ in } \mathcal{C} \quad \mathbf{s} = \mathbf{S}\mathbf{n} \text{ in } \partial\mathcal{C}, \tag{11}$$

with the understanding that above equations hold componentwise. Therefore, we arrive at the following set of force balances with the corresponding field equations:

- displacement-conjugated force balance

$$\mathrm{Div}\mathbf{T} - \mathbf{b}^i + \mathbf{b}^e = \mathbf{0} \text{ in } \mathcal{C} \quad \mathbf{t} = \mathbf{T}\mathbf{n} \text{ in } \partial\mathcal{C}, \tag{12}$$

where $\mathbf{T}$, $\mathbf{b}^e$ and $\mathbf{b}^i$ are the motion conjugated stress tensor, external body force and internal body force, respectively, whereas $\mathbf{t}$ is the tractions at the boundary of $\mathcal{C}$. It can be shown that $\mathbf{b}^i$ is equal to zero since the internal power must be frame invariant;

- solute-conjugated force balance

$$\mathrm{Div}\Gamma - \gamma^i + \gamma^e = 0 \text{ in } \mathcal{C} \quad \gamma = \Gamma \cdot \mathbf{n} \text{ in } \partial\mathcal{C}, \tag{13}$$

where Γ, γ^e and γ^i are the solute density conjugated stress vector, external body force and internal body force, respectively, whereas γ is the tractions at the boundary of $\mathcal{C}$;

- flux-conjugated force balance

$$\mathrm{Div}\Lambda - \lambda^i + \lambda^e = \mathbf{0} \text{ in } \mathcal{C} \quad \lambda = \Lambda\mathbf{n} \text{ in } \partial\mathcal{C}, \tag{14}$$

where Λ, λ^e and λ^i are the flux conjugated stress tensor, external body force and internal body force, respectively, whereas λ is the tractions at the boundary of $\mathcal{C}$;

2.2.1 Free energy imbalance

We also consider as basic a mechanical version of the second law of thermodynamics, namely the free energy imbalance. It asserts that (see [6]):

$$\frac{d}{dt}\int_{\mathcal{P}} \psi \, dV \leq P_e(\mathcal{P}, \mathbf{v}) + \int_{\mathcal{P}} \mu h \, dV, \tag{15}$$

where ψ is the free energy density, $P_e(\mathcal{P}, \mathbf{v})$ the power expended by all external forces and μ is the chemical potential. After using the principle of virtual power, this version localizes into the dissipation inequality:

$$\dot{\psi} \leq \mathbf{T} \cdot \dot{\mathbf{E}} + \Gamma \cdot \nabla\dot{\rho} + (\gamma^i + \mu)\,\dot{\rho} + (\Lambda + \mu\mathbf{I}) \cdot \nabla\mathbf{J} + \lambda^i \cdot \mathbf{J} \tag{16}$$

3 Constitutive theory

The first constitutive assumption adopted here is the additive decomposition of the strain $\mathbf{E}$,

$$\mathbf{E} = \mathbf{E}_e + \mathbf{E}_s, \tag{17}$$

into its elastic $\mathbf{E}_e$ and solute induced $\mathbf{E}_s$ parts, the latter given by:

$$\mathbf{E}_s = \eta\,(c - c_r)\mathbf{I}, \tag{18}$$

where η is a positive parameter and c_r a reference concentration. It follows then that the dissipation inequality (16) can be written as:

$$\dot{\psi} \leq \mathbf{T} \cdot \dot{\mathbf{E}}_e + \Gamma \cdot \nabla \dot{\rho} + \left(\gamma^i + \mu + \frac{\eta \operatorname{tr} \mathbf{T}}{\rho_S} \right) \dot{\rho} + (\Lambda + \mu \mathbf{I}) \cdot \nabla \mathbf{J} + \lambda^i \cdot \mathbf{J} \tag{19}$$

Based on the inequality (16), we consider constitutive equations of the form:

$$\psi = \hat{\psi}(\mathsf{p}), \quad \mathbf{T} = \hat{\mathbf{T}}(\mathsf{p}), \quad \Gamma = \hat{\Gamma}(\mathsf{p}), \quad \gamma^i + \mu + \frac{\eta \operatorname{tr} \mathbf{T}}{\rho_S} = \hat{\gamma}(\mathsf{p}), \quad \Lambda + \mu \mathbf{I} = \hat{\Lambda}(\mathsf{p}), \quad \lambda^i = \hat{\lambda}^i(\mathsf{p}), \tag{20}$$

where p represents the list of constitutive variables. We assume that:

$$\mathsf{p} := (\underbrace{\mathbf{E}_e, \rho}_{\mathsf{e}}, \mathbf{J}) \tag{21}$$

where e and $\mathbf{J}$ stand for equilibrium and non-equilibrium, or dissipative, variables. We assume that the response functions in (20) are smooth.

Following the Coleman-Noll procedure (see, for instance, [17]), we require that the constitutive responses must be such that the dissipation inequality (16) holds identically for whatever $(\dot{\mathsf{e}}, \dot{\mathbf{J}}, \nabla \dot{\rho}, \nabla \mathbf{J})$ at whatever $(\mathsf{e}, \mathbf{J})$. Hence we conclude that:

- the constitutive function $\hat{\psi}$ is independent of the non-equilibrium variable $\mathbf{J}$, i.e., $\hat{\psi}(\mathsf{e}, \mathbf{J}) = \hat{\psi}(\mathsf{e})$;
- the equilibrium relations

$$\hat{\mathbf{T}} = \frac{\partial \hat{\psi}}{\partial \mathbf{E}_e}, \quad \hat{\Gamma} \equiv 0, \quad \hat{\gamma} = \frac{\partial \hat{\psi}}{\partial \rho}, \quad \hat{\Lambda} \equiv 0 \tag{22}$$

  hold;
- the internal dissipation inequality

$$\hat{\lambda}^i(\mathsf{p}) \cdot \mathbf{J} \geq 0 \tag{23}$$

  must hold for whatever $\mathbf{J}$.

Therefore, the constitutive theory is characterized by the constitutive functions $\hat{\psi}$ and $\hat{\lambda}^i$. The former is independent of $\mathbf{J}$, whereas the later must comply with (23).

The cylinder is considered in a fixed reference configuration at uniform temperature T with constant value for the solid density ρ_S. The densities ρ_S and ρ are given in terms of number of atoms or molecules per unit lattice volume, consequently, the solute concentration $c = \dfrac{\rho}{\rho_S}$ is measured in number of solute atoms per number of solid atoms. Hence, we assume the following free energy and dissipative response:

i) Free energy response:

$$\hat{\psi}(\mathbf{E}_e, \rho) = \frac{\bar{\lambda}}{2} (\operatorname{tr} \mathbf{E}_e)^2 + \bar{\mu} |\mathbf{E}_e|^2 + k_B T \rho \left(\ln \left(\frac{\rho}{\rho_S} \right) - 1 \right), \tag{24}$$

where the first two terms correspond to the classical elastic strain energy, and $\bar{\lambda}$ and $\bar{\mu}$ are the Lame parameters. The last term represents the classical entropic contribution to the free

energy of a dilute ideal interstitial solid solution, where k_B is Boltzmann's constant and T is the absolute temperature.

ii) Dissipative response:

$$\hat{\lambda} = \frac{1}{M\rho}, \tag{25}$$

where the positive parameter M is the solute mobility.

4 Governing equations

Henceforth we consider the notation for the hollow cylinder as described in the Preliminaries Section, and we assume that $\gamma^e = \lambda^e = 0$. The governing equations for the fields u, μ, ρ and J are obtained through the combination of the aforementioned basic balances and constitutive theory. We also consider the previous definitions related with the gradient and divergent of the scalar, vector and stress fields.

Remark the following relations:

$$E_r = \frac{\partial u}{\partial r}, \quad E_\theta = \frac{u}{r}, \quad c = \frac{\rho}{\rho_S}, \quad D = M\, k_B\, T, \tag{26}$$

where D is the diffusion coeficient.

- The equation for the displacement u is the following:

$$\frac{\partial T_r}{\partial r} + \frac{T_r - T_\theta}{r} + b^e = 0, \tag{27}$$

where:

$$\begin{aligned} T_r &= \bar{\lambda}\,(E_r + E_\theta) + 2\bar{\mu}E_r - \eta(3\bar{\lambda} + 2\bar{\mu})(c - c_r), \\ T_\theta &= \bar{\lambda}\,(E_r + E_\theta) + 2\bar{\mu}E_\theta - \eta(3\bar{\lambda} + 2\bar{\mu})(c - c_r), \\ T_z &= \bar{\lambda}\,(E_r + E_\theta) - \eta(3\bar{\lambda} + 2\bar{\mu})(c - c_r), \end{aligned} \tag{28}$$

- The equation for the chemical potential μ is the following:

$$\mu = k_B T \ln c - \frac{\eta\,(T_r + T_\theta + T_z)}{\rho_S} \tag{29}$$

- the equation for the solute flux J is the following:

$$J = -D\frac{\partial \rho}{\partial r} + \frac{D\,\eta}{k_B T \rho_S}\rho\frac{\partial}{\partial r}(T_r + T_\theta + T_z) \tag{30}$$

- the equation for the solute density ρ is the following:

$$\dot{\rho} = -\frac{\partial J}{\partial r} - \frac{J}{r} + h, \tag{31}$$

with J given by (30).

Observe that, from (29), the chemical potential depends on the solute density and the hydrostatic stress. From (30), we can observe a generalization of Ficks Law, since the solute flux may be driven by the solute density and stress gradients. The prescription of μ implies the prescription of ρ, and vice versa. As pointed out by [4] and [5], when chemical equilibrium prevails at the boundary a constant value for the chemical potential must be prescribed. This does not mean a constant value for ρ, since by (29) the chemical potential may involve not only ρ but also stress and elastic strain.

With the above assumptions, the linear elasticity coupled with the diffusion problem can be stated as follows:

Problem:

Given: Boundary/initial conditions, material and geometrical parameters, body force density, external solute supply and reference concentration,

Find: The displacement u and the solute density ρ, satisfying the following equations:

$$\begin{cases} \dfrac{\partial T_r}{\partial r} + \dfrac{T_r - T_\theta}{r} + b^e = 0, \\ \dot{\rho} + \dfrac{\partial J}{\partial r} + \dfrac{J}{r} = h, \end{cases} \tag{32}$$

where:

$$\begin{aligned} T_r &= \bar{\lambda}\,(E_r + E_\theta) + 2\bar{\mu}E_r - \eta(3\bar{\lambda} + 2\bar{\mu})\left(\frac{\rho}{\rho_S} - c_r\right), \\ T_\theta &= \bar{\lambda}\,(E_r + E_\theta) + 2\bar{\mu}E_\theta - \eta(3\bar{\lambda} + 2\bar{\mu})\left(\frac{\rho}{\rho_S} - c_r\right), \\ J &= -D\frac{\partial \rho}{\partial r} + \frac{D\,\eta}{k_B T \rho_S}\rho\,\frac{\partial (T_r + T_\theta + T_z)}{\partial r}. \end{aligned} \tag{33}$$

The equation for the stress components $(33)_{1,2,3}$ show that stress-assisted diffusion favors solute migration from lower to higher stressed locations. The relation $(33)_3$ shows that diffusion is driven by the solute concentration and hydrostatic stress, then the solute flows from a region of higher to a region of lower concentration. The opposite effect occurs with respect to hydrostatic stress.

Based on the above equations (32), the treatment of boundary conditions at ends $r = R_i$ and $r = R_e$ would be the following: for the equation $(32)_1$, the boundary condition involves the prescription of the displacement or traction, and the boundary condition associated to the equation $(32)_2$ involves the prescription of either ρ or J. Actually, in this article, the bondary contitions related with the force balance equation $(32)_1$ are standard. Therefore, for the solute density equation $(32)_2$ we have considered the chemical potential μ constant at both surfaces. However, because the chemical potential

depends explicitly on the trace of stress (see equation (29)), that envolves its dependency on the solute concentration field, the boundary condition for this equation is time dependent.

5 Weak form

Now we briefly describe the steps involved in the construction of the numerical model, which is based on the finite element method, backward Euler scheme and an operator-split algorithm.

The governing equations (32) in their weak forms, are:

Given: Boundary/initial conditions, material and geometrical parameters, body force density and reference concentration,

Find: u and ρ satisfying the following equations:

$$\begin{aligned}
&\int_{R_i}^{R_e} \left(T_r \frac{\mathrm{d}v}{\mathrm{d}r} + T_\theta \frac{v}{r} - b^e v \right) r \,\mathrm{d}r + p_i \, R_i - p_e \, R_e = 0 \quad \forall \; v \; \in \; V^0, \\
&\int_{R_i}^{R_e} \left(J \frac{\mathrm{d}\varphi}{\mathrm{d}r} - \dot{\rho}\varphi + h\varphi \right) r \,\mathrm{d}r + J(R_i) \, R_i - J(R_e) \, R_e = 0 \quad \forall \; \varphi \; \in \; V^0,
\end{aligned} \tag{34}$$

where:

$$\begin{aligned}
&V^0 \text{ is the appropriate functional space,} \\
&p_i \text{ and } p_e \text{ are the internal and external pressure,} \\
&T_r = \bar{\lambda} \, (E_r + E_\theta) + 2\bar{\mu} E_r - \eta(3\bar{\lambda} + 2\bar{\mu}) \left(\frac{\rho}{\rho_S} - c_r \right), \\
&T_\theta = \bar{\lambda} \, (E_r + E_\theta) + 2\bar{\mu} E_\theta - \eta(3\bar{\lambda} + 2\bar{\mu}) \left(\frac{\rho}{\rho_S} - c_r \right), \\
&J = -D \frac{\partial \rho}{\partial r} + \frac{D \, \eta}{k_B T \rho_S} \rho \, \frac{\partial (T_r + T_\theta + T_z)}{\partial r}.
\end{aligned} \tag{35}$$

The solution and test spaces (functional spaces) are approximated by finite dimensional spaces by using the finite element method. The approximated fields are denoted by u_h, ρ_h, v_h and φ_h.

$$\begin{aligned}
&\int_{R_i}^{R_e} \left((T_r)_h \, \frac{\mathrm{d}v_h}{\mathrm{d}r} + (T_\theta)_h \, \frac{v_h}{r} - (b^e)_h \, v_h \right) r \,\mathrm{d}r + (p_i) \, R_i - (p_e) \, R_e = 0, \\
&\int_{R_i}^{R_e} \left(J_h \, \frac{\mathrm{d}\varphi_h}{\mathrm{d}r} - \dot{\rho}_h \, \varphi_h + h_h \, \varphi_h \right) r \,\mathrm{d}r + J(R_i) \, R_i - J(R_e) \, R_e = 0.
\end{aligned} \tag{36}$$

Or, in a simplified notation, we have the following semi-discrete systems of equations that represent the system in (36):

$$\begin{aligned} \mathbf{F}_u(\mathbf{u},\rho) &= \mathbf{0} \\ \mathbf{F}_\rho(\mathbf{u},\rho,\dot{\rho},) &= \mathbf{0} \end{aligned} \tag{37}$$

where $\mathbf{u}$ and ρ are vectors containing the unknown nodal values for u_h and ρ_h. The functions $\mathbf{F}_u$ and $\mathbf{F}_\rho$, viewed as vector valued, have the same dimensions of $\mathbf{u}$ and ρ, respectively. The temporal discretization of this set of equations is carried out by using the Euler implicit method. This results in the following set of equations for each time instant t_k:

$$\begin{aligned} \mathbf{F}_u(\mathbf{u}^k,\rho^k) &= \mathbf{0}, \\ \mathbf{F}_\rho(\mathbf{u}^k,\rho^k,\dot{\rho}^k) &= \mathbf{0}, \end{aligned} \tag{38}$$

where, for a time dependent function f, f^k and $\dot{f}^k$, which is given by:

$$\dot{f}^k = \frac{f^k - f^{k-1}}{t_k - t_{k-1}}, \tag{39}$$

are approximations to $f(t_k)$ and $\dot{f}(t_k)$, respectively.

The computational problem is to determine $\mathbf{u}^k$ and ρ^k given ρ^{k-1}. This is solved by using a staggered scheme comprising the following steps:

i) assume ρ^{k-1} as trial solutions for ρ^k;

ii) obtain the trial solution for $\mathbf{u}^k$ by solving $(38)_1$;

iii) update the trial solution for ρ^k by solving $(38)_2$;

iv) if convergence is attained, update $\mathbf{u}^k$ and ρ^k using their trials, otherwise, go to Step (ii) repeating the next steps.

Each subproblem is solved for its primitive variable while holding that of the other subproblems equal to their current trials. In the Step (iii), the mechanical stress is obtained from the displacement and concentration through a direct computation followed by nodal averaging.

6 Numerical example

In this section solutions to the initial boundary value problem of transient hydrogen diffusion coupled with elasticity are presented in a hollow cylinder, with inner radius $R_i = 150$ mm and outer radius $R_e = 190$ mm. Plane strain was assumed and the system's temperature was 300 K. The material used in the simulations was high strenght steel and the properties are listed in Table 1 see [18]).

The units used are: the solid density ρ_S is measured in host lattice atoms (Fe) per volume, i.e., (Fe/m^3), and the hydrogen density ρ is measured in hydrogen atoms (H) per volume, i.e., (H/m^3).

The solute concentration $c = \frac{\rho}{\rho_S}$, is, then, measured in hydrogen atoms (H) per host lattice atoms (Fe), i.e., H/Fe.

We assumed that the cylinder is under a prescribed constant pressure on the internal and external surface: $p_i = 100.0\,\text{MPa}$, $p_e = 50.0\,\text{MPa}$, respectively. As well as, the boundary condition for the solute density equation is the constant chemical potential $\mu = -2.0\text{x}10^{-20}$ Joule/H on both surfaces. These conditions were adopted in order to mimic the situation described in [11].

Table 1: Material properties of high strenght steel with internal hydrogen.

$\bar{\lambda}$	119.0 GPa
$\bar{\mu}$	79.0 GPa
D	$1.0\text{x}10^{-8}$ m^2/s
ρ_S	$8.454\text{x}10^{28}$ Fe/m^3
$k_B\,T$	$4.14\text{x}10^{-21}$ Joule/H
η	0.0937 Fe/H

The displacement field with different times are plotted in Figure 1. The blue line corresponds to initial instant, when the diffusion process had not started, and the cylinder is only under internal and external pressure, and the black line corresponds to the final instant of the simulation.

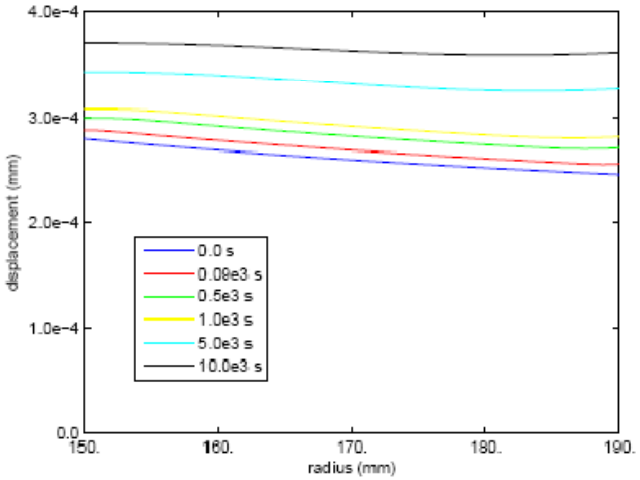

Figure 1: The displacement field

The solute concentration distribution with different times are plotted in Figure 2. Initially no solute atom is in the solid, that corresponds to blue line. The solute diffuses from both outer and inner surfaces into the middle of the cylinder, and then the concentration increases with an increase in time.

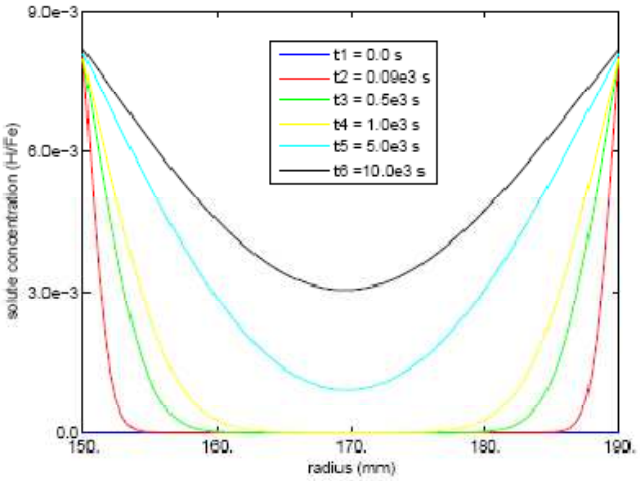

Figure 2: The solute distribution

As shown in Figure 3 the radial stress component is compressive in all instants and everywhere, the curves do not differ significantly and have the maximum value at inner surface whereas the internal pressure is higher than the external pressure.

The circumferential stress component, shown in Figure 4, is tensile everywhere. It is interesting to observe that at the beginning of the process the curves are close the blue one, that represents to initial instant.

Almost the same situation we find in the distribution of the axial stress component, shown in Figure 5, at the beginning of the process the curves are close to the initial instant, and all curves are almost symmetric with respect to the middle of cylinder. This component is compressive in the region near both surfaces and tensile in the middle region of cylinder. The distribution of the trace of the stress is quite similar, but all curves and everywhere the trace corresponds to tensile stress, shown in Figure 6.

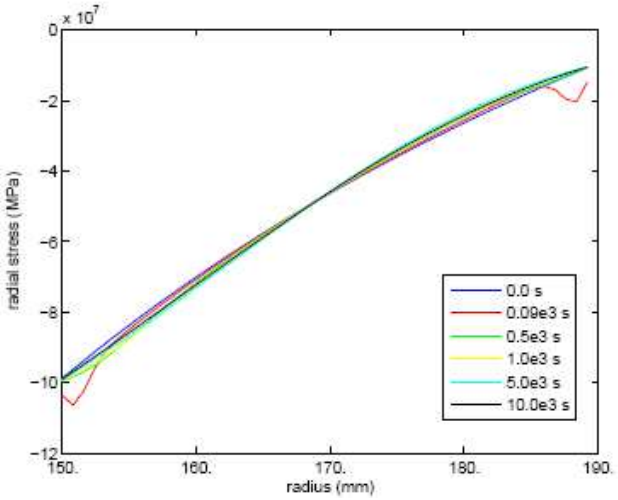

Figure 3: The radial stress component profiles

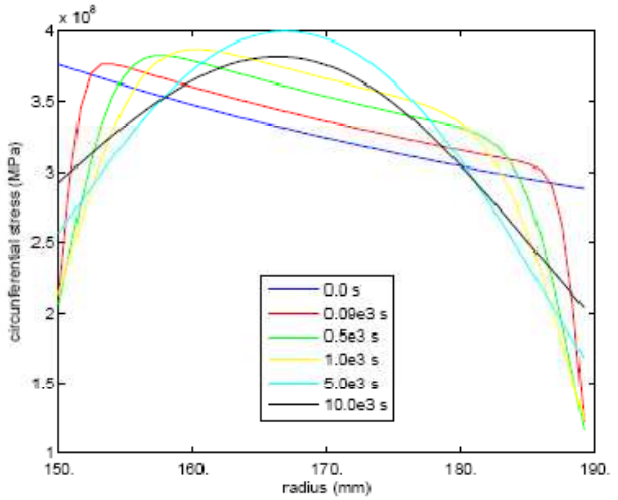

Figure 4: The circumferential stress component profiles

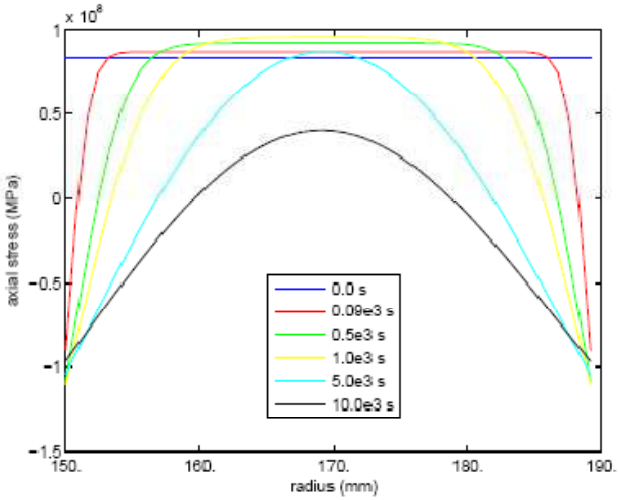

Figure 5: The axial stress component profiles

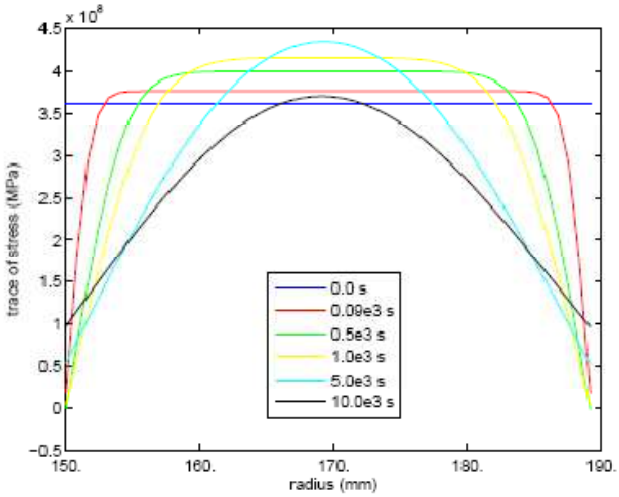

Figure 6: The trace of stress profiles

Acknowledgements

Duda F.P. gratefully acknowledges the support by CNPq (485866/2006-4, 484579/2006-1 and 201080/2008-7) and FAPERJ (E-26/171.599/2004). Souza A.C. gratefully acknowledges the support by the FAPERJ (E-26/170.292/2006) and CAPES (0720/08-9).

References

[1] Gibbs, J.W., *The Scientific Papers of J. Williard Gibbs, Volume One, Thermodynamics*. Ox Bow press, 1993.

[2] Li, J.C.M., Oriani, R.A. & Darken, L.S., The thermodynamics of stressed solids. *Z physik Chem Neue Folg*, **Bd. 49**, pp. 271–290, 1966.

[3] Larché, F.C. & Cahn, J.W., A linear theory of thermochemical equilibrium of solids under stress. *Acta Metallurgica*, **21**, pp. 1051–1063, 1973.

[4] Larché, F.C. & Cahn, J.W., The effect of self-stress on diffusion in solids. *Acta Metallurgica*, **30**, pp. 1835–1845, 1982.

[5] Larché, F.C. & Cahn, J.W., The interactions of composition and stress in crystalline solids. *Acta Metallurgica*, **33**, pp. 331–357, 1985.

[6] Fried, E. & Gurtin, M., Coherent solid-state phase transitions with atomic diffusion: A thermomechanical treatment. *J Statistical Physics*, **95(5-6)**, pp. 1361–1427, 1999.

[7] Fried, E. & Gurtin, M., A unified treatment of evolving interfaces accounting for small deformations and atomic transport with emphasis on grain-boundaries and epitaxy. *Advances in Applied Mechanics*, **40**, pp. 1–177, 2004.

[8] Buxbaum, R.E. & Kinney, A.B., Hydrogen transport through tubular membranes of palladium-coated tantalum and niobium. *Ind Eng Chem Res*, **35**, pp. 530–537, 1996.

[9] Wang, W.L., Lee, S. & Chen, J.R., Effect of chemical stress on diffusion in a hollow cylinder. *J Appl Physics*, **91**, pp. 9584–9590, 2002.

[10] Adrover, A., Giona, M., Capobianco, L., Tripoli, P. & Violante, V., Stress induced diffusion of hydrogen in metallic membranes: cylindrical vs. planar formulation I. *J Alloy and Compounds*, **358**, pp. 268–280, 2003.

[11] Lee, S., Wang, W.L. & Chen, J.R., Diffusion-induced stress in a hollow cylinder. *Mat Sci Eng*, **A285**, pp. 186–194, 2000.

[12] Fried, E. & Sellers, S., Theory for atomic diffusion on fixed and deformable crystal lattices. *J Elasticity*, **59**, pp. 67–81, 2000.

[13] Gurtin, M.E., Generalized Ginzburg-Landau and Cahn-Hilliard equations based on a microforce balance. *Physica D*, **92**, pp. 178–192, 1996.

[14] Podio-Guidugli, P., Models of phase segregation and diffusion of atomic species on a lattice. *Ricerche di Matematica*, **55**, pp. 105–118, 2006.

[15] Duda, F.P., Souza, A.C., aes, L.J.G. & Barbosa, J.M., An one dimensional coupled model for deformation, degradation and solute diffusion in elastic solids. *Mechanics of Solids in Brazil*, eds. M. Alves & H.S. da Costa Mattos, Brazilian Society of Mechanical Sciences and Engineering, 2007.

[16] Germain, P., The method of virtual power in continuum mechanics. part 2: Microstructure. *SIAM J Appl Math*, **25(3)**, 1973.

[17] Silhavy, M., *The Mechanics and Thermodynamics of Continuous Media*. Springer-Verlag: Berlin, 1997.

[18] Taha, A. & Sofronis, P., A micromechanics approach to the study of hydrogen transport and embrittlement. *Eng Fracture Mechanics*, **68**, pp. 803–937, 2001.

Mechanics of Solids in Brazil 2009, H.S. da Costa Mattos & Marcílio Alves (Editors)
Brazilian Society of Mechanical Sciences and Engineering, ISBN 978-85-85769-43-7

An energy-based approach for estimates of the stress-strain fields near crack-like notches

Jorge Alberto Rodríguez Durán
Fluminense Federal University, Volta Redonda School of Industrial and Metallurgical Engineering, RJ – Brazil

Abstract

Estimates of the elastic-plastic stress-strain distribution near cracks and crack-like notches under maximum load and in plane stress were made using a modified form of the Equivalent Strain Energy Density Hypothesis (here denoted as the GM approach). According to this hypothesis both, the elastic W_S and the elastic-plastic W_σ strain energy densities, have approximately the same value in the region ahead of a crack/crack-like notch. In the present paper, the W_S was estimated integrating the stress-strain relations in the linear-elastic regime. Using the classical linear elastic fracture mechanics, the principal stresses in the solution for W_S were left in terms of the well known stress intensity factor. This parameter is believed to be the characteristic variable for crack-like notches. On the other hand, the W_σ was estimated by integration of the bi-axial constitutive relation for a strain-hardening material using the deformation plasticity theory. Equating the expressions for both energies, an implicit relation for the maximum stress (σ_{1max}) as a function of the distance from the crack tip (r) and the ratio between the two non-zero principal stresses (λ), was obtained. A computer code was developed to numerically solve this implicit relation for σ_{1max} at discrete values of r and for $0.2 \leq \lambda \leq 1$. One fixed K value and three structural materials were considered for the simulation. The resultant matrix of estimated values for maximum stress field within the plastic zone is presented in various non-dimensional plots. The λ parameter did not exhibit a strong influence in the crack/notch stress-strain tip fields. For comparison, the classical HRR solution for elastic-plastic stress fields in cracks was also plotted in the same graph and good agreement was found with the GM approach. The results can be easily extended to cyclic loading for using in fatigue design.

Keywords: strain energy density, linear elastic fracture mechanics, crack-like notches.

1 Introduction

Fracture and fatigue behavior of structures with cracks and notches primarily depends on the stress-strain fields in the vicinity of these discontinuities. For cracks and in small scale yielding conditions, the crack tip stress-strain fields according to the classical Linear Elastic Fracture Mechanics (LEFM) do control the fatigue and fracture process, as has been amply demonstrated by the practice of engineering

Mechanics of Solids in Brazil 2009, H.S. da Costa Mattos & Marcílio Alves (Editors)
Brazilian Society of Mechanical Sciences and Engineering, ISBN 978-85-85769-43-7

in the last decades. This happens in spite of the existence of a small volume of material in front of the crack (plastic zone) where the stresses are well above the yield point.

The analysis of stress in notches, needed almost exclusively for fatigue design purposes, is performed with the help of the fatigue stress concentration factor k_f. Again the material behavior is assumed to be linear elastic and the little plasticity, if present, is believed to be confined at a pretty small region that it can be neglected. By increasing the nominal stress by a factor of k_f (or by decreasing the strength) it is possible to obtain the characteristic variable (maximum local stress) at the tip of the notch.

Despite the success of the above engineering solutions, many attempts were and are made to find and use in design the stress-strain fields within the plastic zones. A closed form solution for cracks was developed by Hutchinson [1] and Rice & Rosengren [2] and named *HRR* solution since then. For notches, approximate methods were also developed, the two most used being due to the works of Neuber [3] and Glinka [4]. Both of the approaches, however, return only scalar values for stress and strain at the tip of the notch and not the stress-strain fields ahead of the notch. In many cases the stress-strain field is an important parameter. For example, the fatigue limit in sharp notches, according to the line method [5], is believed to be the average stress range over certain critical distance, also called the process zone. The present paper deals with the analogies between crack and notches so as to develop a new method to estimate the monotonic stress-strain fields near crack-like notches in plane stress and on the crack plane.

2 Approximate methods to calculate inelastic stress and strain at the tip of notched members (for elastic nominal stress only)

Notched engineering members are often subjected to nominal stresses that causes localized yielding. For elastic behavior the values of local strain and stress (ϵ, σ) can be estimated on the basis of the theoretical stress (the same as strain) concentration factor k_t. At the notch tip a uniaxial state of stress exists. For this reason, after yielding, i.e., when the product $k_t \cdot \sigma_n > S_y$, where σ_n is the nominal stress and S_y the yield strength, the localized stresses and strains at the notch tip continue to vary according to the monotonic stress-strain response of the material, which means that the stress diminishes and the strain grows. In these cases it is necessary to define separate stress k_σ and strain k_ϵ concentration factors as follows:

$$k_\sigma = \frac{\sigma}{\sigma_n}, \qquad k_\varepsilon = \frac{\varepsilon}{\varepsilon_n} \tag{1}$$

As in the case of stress, ϵ_n is the nominal strain. Some approximate methods have been developed for estimating these notch stresses and strains. Among them, Neuber [3] and Glinka [4] rules are the most widely used and are well described in textbooks like Dowling [6]. Neuber's rule can be mathematically represented by the following equation:

$$k_t = \sqrt{k_\sigma \, k_\varepsilon} \tag{2}$$

Mechanics of Solids in Brazil 2009, H.S. da Costa Mattos & Marcílio Alves (Editors)
Brazilian Society of Mechanical Sciences and Engineering, ISBN 978-85-85769-43-7

For localized yielding and uniaxial state of stress $\epsilon_n = \sigma_n/E$, where E is the elasticity modulus, applies. One equation relating the product of local stress and strain and the nominal stress times the stress concentration factor can be obtained substituting this relation in Eq. (1) and the result in Eq. (2):

$$\begin{aligned} k_t = \sqrt{k_\sigma \, k_\varepsilon} = \sqrt{\frac{\sigma}{\sigma_n} \, \frac{\varepsilon}{\varepsilon_n}} = \sqrt{\frac{\sigma}{\sigma_n} \, \frac{E\,\varepsilon}{\sigma_n}} \\ \sigma\,\varepsilon = \frac{(k_t\,\sigma_n)^2}{E} \end{aligned} \tag{3}$$

Equation (3) means that, knowing few properties of materials (E, H, n), (being H and n the strength coefficient and the strain hardening exponent, respectively), the true stress-strain curve, the applied load and the theoretical stress concentration factor, it is possible to obtain a solution for the local stress and strain at the tip of the notch (σ_{tip} and ϵ_{tip}). In $\epsilon\sigma$ coordinates, Eq. (3) is a hyperbola ($(kt{\cdot}\sigma_n)^2/E$ is a constant) whose intersection with equations that model the monotonic or cyclic stress-strain behavior of material, Ramberg-Osgood $\epsilon = \sigma/E + (\sigma/H)^{(1/n)}$ e.g., returns the desired values stress and strain at the notch tip.

On the other hand, Glinka's approach [4] is based on the equivalence between the plastic W_σ and the elastic strain energy density W_S at the notch tip and can be mathematically enunciated as in Eq. (4):

$$\frac{(k_t\,\sigma_n)^2}{2\,E} = \frac{\sigma^2}{2\,E} + \frac{\sigma}{n+1}\left(\frac{\sigma}{H}\right)^{\frac{1}{n}} \tag{4}$$

Using some type of iteration or numerical method it is possible to solve Eq. (4) for local stress at the notch tip σ_{tip}. Local strains ϵ_{tip} are then obtained by substituting the local stress in the stress-strain curve of the material. This method generally gives estimates of local strains and stresses lower than those obtained by Neuber's rule. It is worthy to mention that both, Neuber's and Glinka's methods, in the form of Eq. (3) and Eq. (4) are only valid while the nominal stress σ_n is under the yield strength S_y of material. It should be emphasized that the results corresponds only to the tip of notches.

3 Modifications proposed to Glinka's method to calculate inelastic stress-strain fields at notched members

Moving into the interior of the notch the state of stress becomes biaxial or triaxial. Suppose that we are only interested in the crack plane and in the surface of the solid, thereby dealing with plane stress. Some modifications are necessary to Glinka's approach in order to deal with this bi-axial stress state. The elastic strain energy density W_S in terms of principal stresses and in plane stress is [7]:

$$W_S = \frac{1}{2\,E}\left(\sigma_{1e}^2 + \sigma_{2e}^2 - 2\,\nu\,\sigma_{1e}\,\sigma_{2e}\right) \tag{5}$$

The subscript e in Eq. (5) denotes an elastic stress. For simplicity's sake we have considered that the non-zero components of principal stresses are σ_1 and σ_2. To express W_S as a function of the

distance r from the notch tip we recall that, for crack-like notches, close relationship exists between stress concentration analysis and crack analysis, the latter realized by means of fracture mechanics [8]. In fact, on the crack/notch plane ($\theta = 0$) and in accordance with the classical Irwin's solution [9] for the stress tensor at the crack tip, $\tau_{xy} = 0$ and both σ_x and σ_y are the same and also main stresses ($\sigma_x = \sigma_y = \sigma_{1e} = \sigma_{2e}$). For maximum load Eq. 5 then becomes:

$$W_S = \frac{(1-\nu)}{E}\,\sigma_{1e}^2 \tag{6}$$

The plastic zone size in $\theta = 0$ for materials with a power-hardening stress-strain curve was derived (from *HRR* solution) by Rice [10] and Schwalbe [11]:

$$r_{y\_sh} = \frac{1}{(1+n)\,\pi}\left(\frac{K}{S_y}\right)^2 \tag{7}$$

In Eq. (7) K is the well known stress intensity factor of fracture mechanics. As r_{y_sh} by Eq. (7) is $2/(1+n)$ times the plastic zone size r_y deducted from Irwin's solution $r_y = 1/(2\pi)\cdot(K/S_y)^2$, the elastic stress field near a crack tip and consequently the elastic strain energy density should be increased by a factor of $\sqrt{2/(1+n)}$:

$$W_S = \frac{2}{(1+n)}\,\frac{(1-\nu)}{E}\,\sigma_{1e}^2\,(K,r) \tag{8}$$

For now let the W_S as a function of σ_{1e} which in turn is a function of K and r. According to the strain energy density hypothesis *SEDH*, in small scale yielding, the strain energy density inside the notch/crack plastic zone W_σ can be calculated on the basis of a linear elastic analysis, it means $W_S = W_\sigma$. The term W_σ is the area under the strain-stress curve, provided this curve represents the true behavior of material under the actual state of stress. For plane stress, proportional loading (which means that principal stresses maintain constant ratios) and using the deformation plasticity theory, a useful relationship between the elastic-plastic principal strain ϵ_1 and the elastic-plastic principal stress σ_1 can be obtained, for a Ramberg-Osgood type stress-strain curve of material, as described in Dowling [6]:

$$\varepsilon_1 = (1-\lambda\,\nu)\,\frac{\sigma_1}{E} + (1-0.5\,\lambda)\,\left(1-\lambda+\lambda^2\right)^{\frac{1-n}{2n}}\left(\frac{\sigma_1}{H}\right)^{\frac{1}{n}} \tag{9}$$

The parameter λ in Eq. (9) is defined as the ratio between principal (in plane) stresses $\lambda = \sigma_2/\sigma_1$. Figure 1 shows an example of the estimates effects that different λ ratios have on the stress-strain curve of a steel with $E = 207\ GPa$, $H = 1655\ MPa$ and $n = 0.131$. In this case, only for maximum clarity purposes in the graph, the range of λ has been defined between $-1 \leq \lambda \leq 1$.

Each point in the plastic zone (at different distances r from the notch/crack tip) will behave according to Eq. (9) which is shown in Figure 2 as function of r. Also shown in the figure is the area corresponding to the elastic-plastic strain energy density W_σ. The available expression for the stress-strain curve is in the form $\epsilon_1 = f(\sigma_1)$, so we need to calculate first the complementary strain energy density $W_\sigma{}^*$ by simple integration:

$$W_\sigma * = \int_0^{\sigma_{1\max}(r)} \varepsilon_1(r)\, d\sigma_1(r) \tag{10}$$

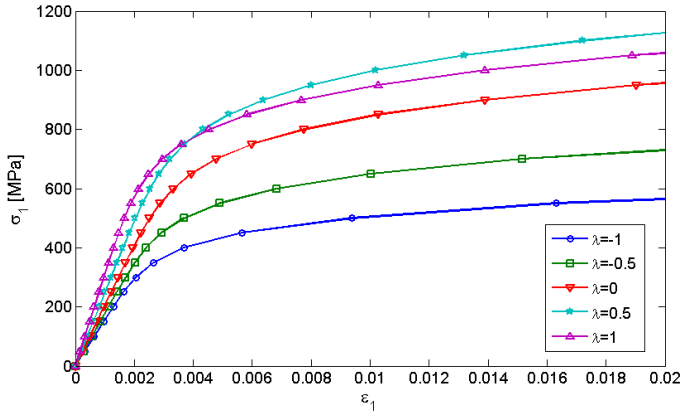

Figure 1: Effect of the ratio between principal stresses $\lambda = \sigma_2/\sigma_1$ on a Ramberg-Osgood stress-strain curve according to Eq. (9) for a steel ($\nu \cong$ *1/3*) with *E = 207 GPa*, *H = 1655 MPa* and *n = 0.131*.

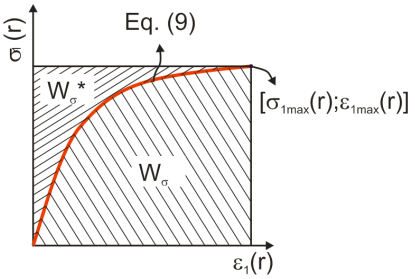

Figure 2: Elastic-plastic strain energy density W_σ and the complementary energy $W\sigma*$ at each point (r fixed) within the plastic zone of a crack/notch. The elastic-plastic behavior of material is in accordance with the deformation plasticity theory.

Since proportional loading has been assumed λ = *constant*, the stress σ_2 grows in the same proportion as does σ_1 between zero and σ_{1max}. By substituting Eq. (9) into Eq. (10) and performing the integration comes up to:

$$W_\sigma* = (1-\lambda\,\nu)\,\frac{\sigma^2_{1\,\max}(r)}{2\,E} + \frac{n\,(1-0.5\,\lambda)\,\left(1-\lambda+\lambda^2\right)^{\frac{1-n}{2n}}}{(1+n)\,H^{\,1/n}}\sigma^{\frac{1}{n}+1}_{1\,\max}(r) \tag{11}$$

From Figure 2 the total area for maximum load is:

$$\sigma_{1\,\max}(r)\,\cdot\,\varepsilon_{1\,\max}(r) = W_\sigma + W_\sigma* \tag{12}$$

In Eq. (12) ϵ_{1max}*(r)* = ϵ_{1max} *(*σ_{1max}*(r))* from Eq. (9). Performing the required substitutions and manipulating gives the desired elastic-plastic strain energy density for plane stress:

$$W_\sigma = \frac{(1-\lambda\nu)}{2\,E}\sigma^2_{1\,\max}(r) + \frac{(1-0.5\,\lambda)\,\left(1-\lambda+\lambda^2\right)^{\frac{1-n}{2n}}\,\sigma_{1\,\max}(r)}{(1+n)}\left(\frac{\sigma_{1\,\max}(r)}{H}\right)^{\frac{1}{n}} \tag{13}$$

Equation (13) reduces, as expected, to the right hand side of Eq. (4) for the uniaxial state of stress (λ = *0*) existent at the crack/notch tip (*r* = *0*). Equating the Eq. (8) with Eq. (13) it is possible to obtain, for maximum load, an expression for the principal elastic-plastic stress-strain field σ_{1max}*(r)* within the plastic zone:

$$\begin{aligned}\frac{2}{(1+n)}\,\frac{(1-\nu)}{E}\sigma^2_{1e}(K,r) &= \frac{(1-\lambda\nu)}{2\,E}\sigma^2_{1\,\max}(r) + \ldots \\ \ldots + \frac{(1-0.5\,\lambda)\,\left(1-\lambda+\lambda^2\right)^{\frac{1-n}{2n}}\,\sigma_{1\,\max}(r)}{(1+n)}&\left(\frac{\sigma_{1\,\max}(r)}{H}\right)^{\frac{1}{n}}\end{aligned} \tag{14}$$

A non-singular expression for σ_{1e}*(K,r)* which, in turn, depends on the applied nominal stress, is needed. The following section is dedicated to this problem.

4 Non-singular elastic stress fields on the crack plane

The elastic singularity of Irwin's solution was completely resolved by Creager & Paris's solution [12]:

$$\begin{aligned}\sigma_y\,(r)\,|_{\theta=0} &= \frac{K}{\sqrt{2\,\pi\,r}}\left[1+\frac{\rho}{2\,r}\right] \\ \sigma_{tip} = k_t\cdot\sigma_n &= \sigma_y|_{\substack{r=\rho/2\\ \theta=0}} = \frac{2\,K}{\sqrt{\pi\rho}}\end{aligned} \tag{15}$$

This equation, however, depends on the notch/crack tip radius ρ. In order to eliminate this parameter we use a procedure already discussed in Durán et al. [13]. First, an expression for crack tip opening displacement *CTOD* is needed. This can be obtained by doubling the displacement u_y of a physical crack of effective size (a + r_{y_sh}) [14]:

$$u_y = \frac{4}{E'} K \sqrt{\frac{r_{y\_sh}}{2\,\pi}} \tag{16}$$

where $E' = E$ for plane stress and $E' = E/(1-\nu^2)$ for plane strain. Substitution of Eq. (7) into Eq. (16) and doubling the result gives the CTOD for a strain hardening material:

$$CTOD = 2\,u_y = \frac{8}{E'} K \sqrt{\frac{K^2}{2\,\pi\,(1+n)\,\pi\,S_y^2}} = \frac{8\,K^2}{\pi\,E'\,S_y} \sqrt{\frac{1}{2\,(1+n)}} \tag{17}$$

Now using the relation $\rho = CTOD/2$, the elastic stress distribution in the plastic zone for $\theta = 0$, or equivalently, the elastic point stresses as function of the distance from crack-tip $\sigma_y(r) = k_t \cdot \sigma_n$, as predicted by Creager & Paris [12] can be obtained for a given K:

$$\begin{aligned} \frac{\rho}{2} &= \frac{CTOD}{4} = \frac{2\,K^2}{\pi\,E'\,S_y} \sqrt{\frac{1}{2\,(1+n)}} \\ \sigma_y\,(r) &= \frac{K}{\sqrt{2\,\pi\,r}} \left(1 + \frac{\rho}{2\,r}\right) = \frac{K}{\sqrt{2\,\pi\,r}} \left(1 + \frac{2}{r}\,\frac{K^2}{\pi\,E'\,S_y} \sqrt{\frac{1}{2\,(1+n)}}\right) \end{aligned} \tag{18}$$

Obviously the $\sigma_y(r)$ is the $\sigma_{1e}(K,r)$ we are interested in for using in Eq. (14). After substitution of Eq. (18) into Eq. (14) we have an analytical implicit expression for the principal elastic-plastic stress field $\sigma_{1max}(r)$ within the plastic zone and for a given λ ratio:

$$\begin{aligned} &\frac{(1-\nu)}{(1+n)\;E}\,\frac{K^2}{\pi\,r} \left(1 + \frac{2}{r}\,\frac{K^2}{\pi\,E\,S_y} \sqrt{\frac{1}{2\,(1+n)}}\right)^2 = \frac{(1-\lambda\nu)}{2\,E} \sigma_{1\,\max}^2\,(r) + \ldots \\ &\ldots + \frac{(1-0.5\,\lambda)\,\left(1-\lambda+\lambda^2\right)^{\frac{1-n}{2n}}\,\sigma_{1\,\max}\,(r)}{(1+n)} \left(\frac{\sigma_{1\,\max}\,(r)}{H}\right)^{\frac{1}{n}} \end{aligned} \tag{19}$$

Note that for plane stress we use $E' = E$. Theoretically Eq. (18) would be valid only for distances $r > \rho/2$ from the crack tip. Like the *HRR* solution, however, inelastic stress-strain from Eq. (19) in the region of crack-tip blunting ($r < 2CTOD$) would not be valid because of the very intense deformation that there exists, which invalidates any analysis based on the consideration of small-scale yielding.

5 Results

A computer code was developed for numerically solving the Eq. 19 at discrete values of r ($2\,CTOD \leq r \leq r_{y\_sh}$) and for $0.2 \leq \lambda \leq 1$. Each element of the matrix of σ_{1max} values with r columns and λ rows are then substituted into the Eq. (9) to obtain, if desired, the corresponding $\epsilon_{1max}(r,\lambda)$ values. Only stress fields are presented in this work.

Non-dimensional plots of stress fields against the distance from the crack/notch tip were used in order to evaluate the approach developed in this paper. The well established *HRR* solution

$\sigma_y/S_y=(r_{y\_sh}/r)^{(n/n+1)}$ was also plotted for comparison. In this paper we are dealing only with crack-like notches. Consequently, there is an associated stress intensity factor K which include parameters like the nominal stress σ_n, the size of the notch a and the geometry factor F. By fixing a K value, for example, $K = 20\ MPa.m^{1/2}$, the plots become independent of these parameters. Figures 3 - 5 show the stress fields as predicted by the Glinka modified (*GM*) approach (this paper) for extreme values of λ and its comparison with the well known *HRR* solution. Note that for plane stress with $\sigma_3 = 0$, the parameter λ should be always greater than zero.

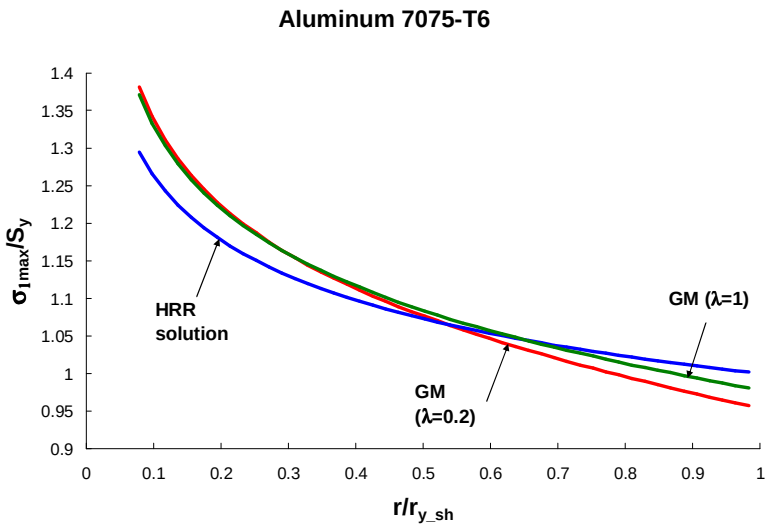

Figure 3: Stress field within the plastic zone for a crack/notch with $K = 20\ MPa.m^{1/2}$ in a Aluminum 7075 T-6 part as predicted by Glinka modified (*GM*) approach (this paper) for extreme values of $\lambda = \sigma_2/\sigma_1$ and comparison with the well known *HRR* solution.

6 Discussion

As already mentioned, Glinka's approach [4] has its main field of application in finding approximate values of the stress-strain at the notch tip after yielding. Both, Neuber and Glinka's approaches are also adapted for alternate loading and then used in low cycle fatigue design. In high cycle fatigue, however, the well known notch sensitivity phenomenon causes the fatigue limit not to be determined only by the maximum stress value at the notch tip, mainly for crack-like notches. Knowing the stress fields in these cases are of major importance. The basic idea under the extension of the Glinka approach deep inside of the plastic zone, as was done in this paper, and therefore dealing with stress fields in place of scalar values at the tip of the notches, is for its use in high cycle fatigue design. The preliminary

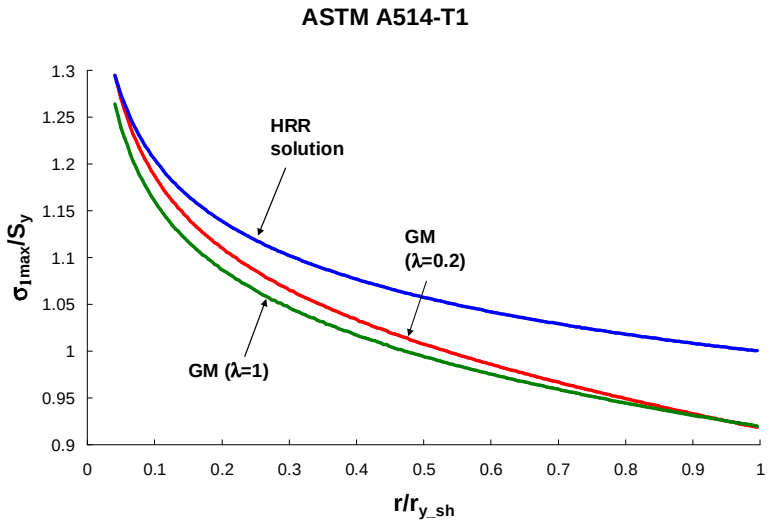

Figure 4: Stress field within the plastic zone for a crack/notch with $K = 20\ MPa.m^{1/2}$ in a ASTM A514-T1 steel part as predicted by Glinka modified (*GM*) approach (this paper) for extreme values of $\lambda = \sigma_2/\sigma_1$ and comparison with the well known *HRR* solution.

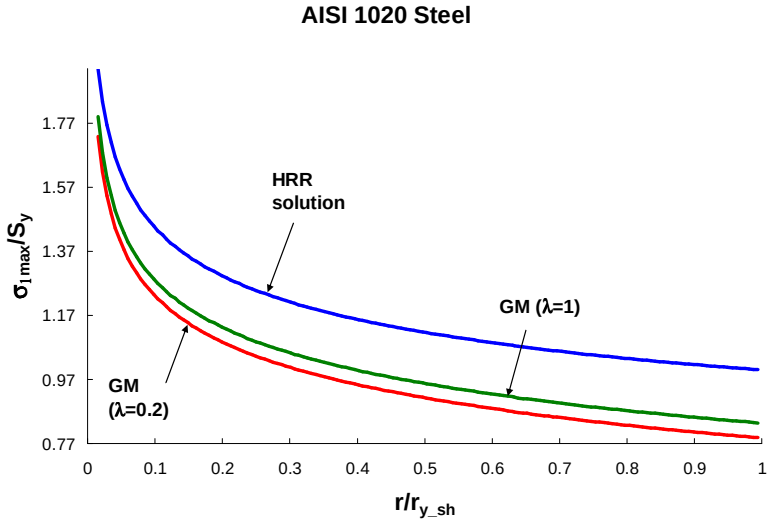

Figure 5: Stress field within the plastic zone for a crack/notch with $K = 20\ MPa.m^{1/2}$ in a AISI 1020 Steel part as predicted by Glinka modified (*GM*) approach (this paper) for extreme values of $\lambda = \sigma_2/\sigma_1$ and comparison with the well known *HRR* solution.

results showed in this work for monotonic loading and the possibility of extending them for fatigue loading constitute a good and encouraging sign.

The *GM* approach is strongly dependent on some properties of materials, as can be seen in Eq. (19). Of course, non-dimensional plots avoid, in part, this dependence. The strain hardening exponent n is a non-dimensional quantity so that normalized plots are still functions of the materials involved. Three materials were used in the simulation and its properties were taken mainly from Dowling [6]. These properties are summarized in table 1.

Table 1: Properties of the three materials used for simulation in the present paper [6].

Material	True Fracture		Strength Coefficient H [MPa]	Strain Hardening Exponent n
	Strength [MPa]	Strain		
Aluminum 7075-T6	744	0.41	827	0.113
ASTM A514-T1	1213	1.08	1103	0.088
AISI 1020 steel	713	0.96	737	0.19

Besides the reasonably good agreement between the *HRR* solution and the *GM* method showed in Figs. 3-5, the most interesting fact to note after analyzing these figures is that the *GM* approach has a normalized stress gradient similar to the *HRR* solution in all the graphs. According to the *HRR* solution this gradient is *n/(n+1)* while the *GM* approach (Eq. (19)) does not have an explicit form of this parameter. This is an excellent indication about the quality on the predictions of the stress fields by the proposed method.

It should be noted that there was almost no influence of λ parameter in the results. Glinka [15] has already used the *SEDH* so as to get the stress field inside the plastic zone. Although he used a somewhat different approach, the expression for the stress field he got was independent of the λ parameter. It is worthy to remember that nowadays the widespread use of modern and efficient computers facilitates the solution of equations like Eq. 19 and the understanding of effects such as the influence of λ parameter on the estimates of stress fields in crack-like notches.

7 Conclusion

After some modifications to the equivalent strain energy density hypothesis, a new method to estimate the stress fields in crack-like notches has been developed. Good agreement was found when comparing the results with a well established analytical solution. The most encouraging result obtained in the present paper is related to the fact that the normalized stress field gradient by the *GM* method is very similar to that of the *HRR* solution, with differences as low as *15 %* in some cases.

References

[1] Hutchinson, J.W., Singular behavior at the end of a tensile crack in a hardening material. *Journal of the Mechanics and Physics of Solids*, **16(1)**, pp. 13–31, 1968.

[2] Rice, J.R. & Rosengren, G.F., Plane strain deformation near a crack tip in a power law hardening material. *Journal of the Mechanics and Physics of Solids*, **16(1)**, pp. 1–12, 1968.

[3] Neuber, H., Theory of stress concentration for shear-strained prismatical bodies with nonlinear stress-strain law. *Transactions of ASME, Journal of Applied Mechanics*, **28**, pp. 544–550, 1961.

[4] Glinka, G., Energy density approach to calculation of inelastic strain-stress near notches and cracks. *Engineering Fracture Mechanics*, **22(3)**, pp. 485–508, 1985.

[5] Taylor, D., A mechanistic approach to critical-distance methods in fatigue. *Fatigue and Fracture of Eng Materials and Structures*, **24**, pp. 215–224, 2001.

[6] Dowling, N.E., *Mechanical Behavior of Materials*. Pearson Prentice Hall, Inc: New Jersey, U.S.A., 3rd edition, 2007.

[7] Norton, R.L., *Machine Design: An Integrated Approach*. Prentice Hall Inc.: New Jersey, 2nd edition, 2000.

[8] Tada, H., Paris, P.C. & Irwin, G.R., *The Stress Analysis of Cracks Handbook*. St Louis Missouri, 2nd edition, 1985.

[9] Irwin, G.R., Analysis of stresses and strains near the end of a crack traversing a plate. *Transactions of ASME, Journal of Applied Mechanics*, **24(3)**, pp. 361–364, 1957.

[10] Rice, J.R., Mechanics of crack tip deformation and extension by fatigue. *ASTM STP 415, Fatigue Crack Propagation*, pp. 247–311, 1967.

[11] Schwalbe, K.H., Approximate calculation of fatigue crack growth. *Engineering Fracture Mechanics*, **9(4)**, pp. 381–395, 1973.

[12] Creager, M. & Paris, P.C., Elastic field equations for blunt cracks with reference to stress corrosion cracking. *International Journal of Fracture Mechanics*, **3**, pp. 247–252, 1967.

[13] Durán, J.A.R., Castro, J.T.P. & Payão, J.C., Fatigue crack propagation prediction by cyclic plasticity damage accumulation models. *Fatigue and Fracture of Engineering Materials and Structures*, **26**, pp. 137–150, 2003.

[14] Anderson, T.L., *Fracture Mechanics. Fundamentals and Applications*. Taylor & Francis Group: Florida, U.S.A., 3rd edition, 2005.

[15] Glinka, G., Relations between the strain energy density distribution and elastic-plastic stress-strain fields near cracks and notches and fatigue life calculation. *Low Cycle Fatigue, ASTM STP 942*, eds. H.D. Solomon, G.R. Halford, L.R. Kaisand et al., American Society for Testing and Materials: Philadelphia, pp. 1022–1047, 1988.

Natural vibration frequency of classic MEMS structures

Zacarias E. Fabrim
PGCIMAT, UFRGS, Porto Alegre, RS, Brazil
Wang Chong, Manoel Martín Pérez Reimbold
DeTec, UNIJUI, Ijuí, RS, Brazil

Abstract

This work addresses the determination of natural frequencies of three typical MEMS (Microelectromechanical Systems) microresonators comb-drive. The microstructures are understood as modular systems, composed by rigid masses coulped to elastic beam elements. The structure stiffness is calculated on the base of deflection deformation energy of elastic beams. The equivalent mass is given by the equality of the kinetic energy of the microstructure system with the one of a simple mass-spring system in harmonic vibration. Then the natural frequencies are obtained analytically in terms of the structure sizes and materials parameters. Numerical modal analysis with the software ANSYS showed good agreement with analytical results. Also it was discussed the influence of the rigidities of structural elements such as plates and beams on the frequencies and vibration modes. To achieve the expected frequencies and vibration modes its important the rigidity of microstructures and stiffness of elastic elements, therenfore the plates and beams shall be move in the same plane as expected. The methods presented in this work could be good for the determination of dynamic parameters of various MEMS structures.

Keywords: MEMS comb-drive, natural frequency, equivalent stiffness, equivalent mass.

1 Introduction

Microelectromechanical Systems (MEMS) are micro-manufactured structures, enabling functions of control, sensing and actuation [1]. The dynamic behavior of mechanical structures of MEMS has influence on the electrical responses through energy transduction principle [2]. Therefore, the determination of mechanical parameters such as elasticity, natural frequency and damping are of great technological importance to characterization and optimization of these devices. In this work we present a method under the framework of solid vibration theory [3] and strength of materials to determine natural frequency of laterally drive resonator MEMS *comb-drive* [4]. The analytical results are compared with numerical ones of finite element method (FEM) using the commercial software ANSYS. Three typical structures of MEMS (Figure 1) are analyzed: Typology 1 (T1), composed of two cantilever beams and

Mechanics of Solids in Brazil 2009, H.S. da Costa Mattos & Marcílio Alves (Editors)
Brazilian Society of Mechanical Sciences and Engineering, ISBN 978-85-85769-43-7

a central mass (Fig. 1 (a)), Typology 2 (T2), four cantilever beams and a central mass (Fig. 1(b)) and Typology 3, a central mass, two lateral masses and eight beams (Fig 1 (c)).

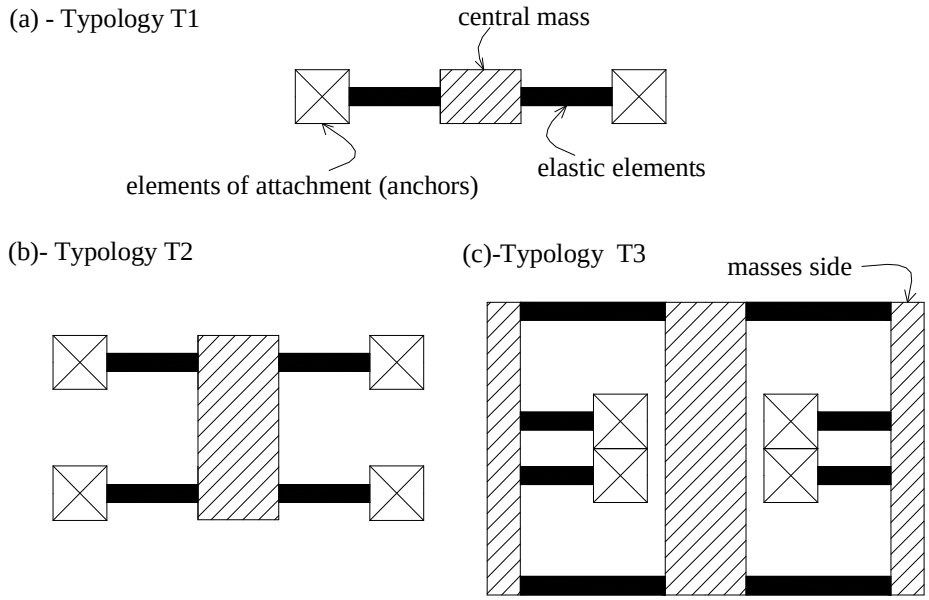

Figure 1: Typologies examined and basic elements: central mass, anchors, elastic elements and masses side.

2 Methodology

The natural frequency of a mass-spring system is expressed by the Equation (1):

$$f_n = \frac{1}{2\pi}\sqrt{\frac{k}{m}} \tag{1}$$

where k is the stiffness constant and m the mass.

Planar MEMS resonators are made of continuous structures in which the determination of resonant frequency is relatively complex. However, it is possible to substitute the original system for a simple mass-spring system by calculating structure stiffness and kinetic energy once are establish a kinematical equality for the displacements of systems, typology and mass spring (Fig. 2).

The total kinetic energy of a typology structure can be obtained by the sum of kinetic energy of the *mass-beam* elements. As the symmetry of structural geometry and boundary conditions, the

parameters K and M_E can be calculated considering the typologies as modular systems, composed by coupling of basic mass-beam elements, as illustrated in the Figure 3.

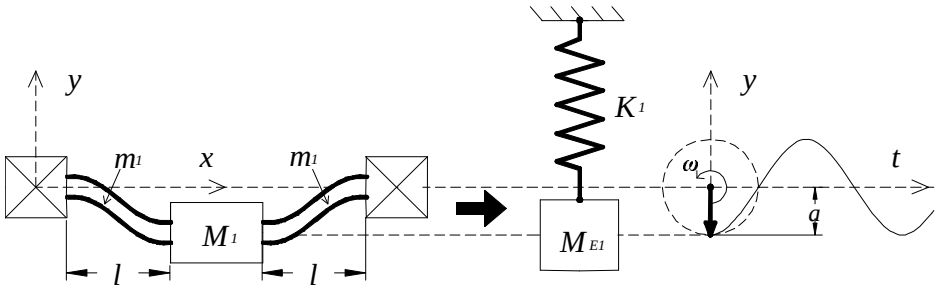

Figure 2: Kinematical equivalency between original system of typology T1 with a mass-spring system; m_1 is the mass of elastic element, M_1 is the mass of rigid element, K_1 the stiffness constant of spring, M_{E1} the equivalent mass, ω is the angular speed, a the maximal displacement and t time.

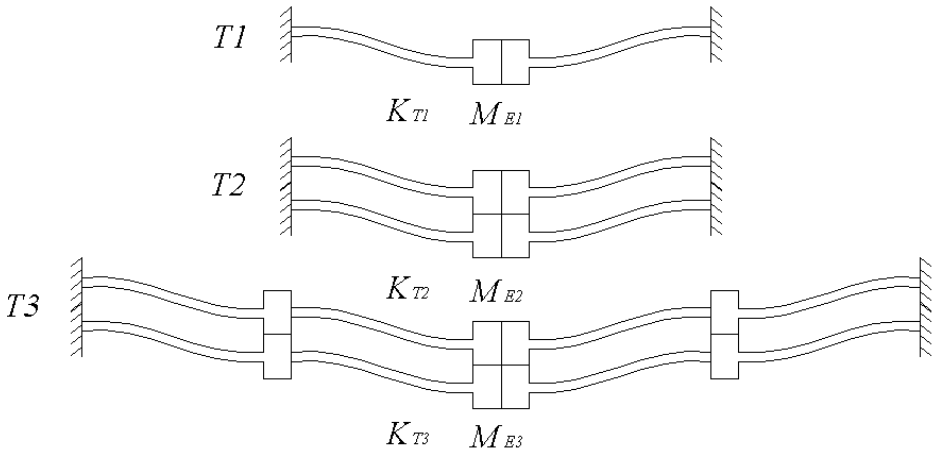

Figure 3: Modular structures of T1, T2 and T3.

3 Stiffness constant of mass beam element

The total stiffness constant of one typology, K, is obtained by the deflection of the beam end subjected to a concentrated force and connected to the central mass. The displacements in direction y are given as the deflection curve of the elastic beam. The concepts of connecting beams in series and in parallel allow the stiffness of modular systems to be a function of several basic mass-beam elements. The stiffness constant of a basic mass-beam element illustrated in the Fig. 4 is obtained by division of the force by the displacement at the position in the direction of the applied force, that is $K_e = P_e / |y_B|$.

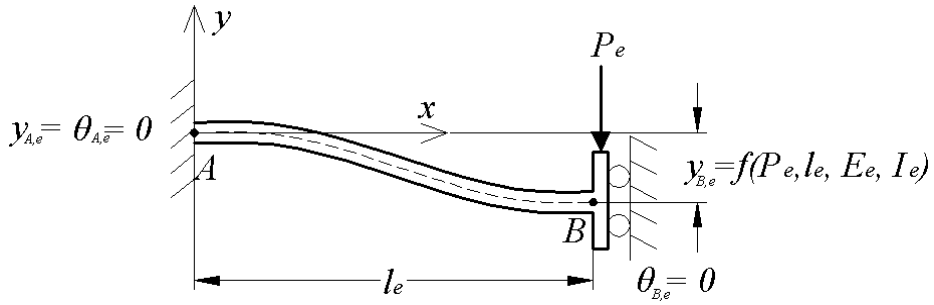

Figure 4: Load, deflection and boundary conditions for the elastic element beam AB. The displacement y_B will be a function of load P_e, length l_e, elasticity module E_e and inertial moment of the transversal section I_e.

When the force P_e is applied, the energy potential is stored in the form of elastic deformation energy in the entire beam. According to the elastic beam theory, the deflection curve is given by:

$$y(x) = -\frac{P_e\, x^2}{E_e I_e 6}\left(\frac{3}{2} l_e\, x\right) \tag{2}$$

From above, we can get the stiffness constant of basic element beam:

$$K_e = \frac{12 E_e I_e}{l_e^3} \tag{3}$$

4 Equivalent mass of mass-beam element

A simple method to obtain the equivalent mass, M_E, is to make a kinematics analogy between the original system and the equivalent system (Fig. 5). The equivalence principle will be that the original system and equivalent system have the same dynamic effect, i.e. the same kinetic energy. The kinetic energy of the original system can be obtained by the sum of the kinetic energy of moving parts.

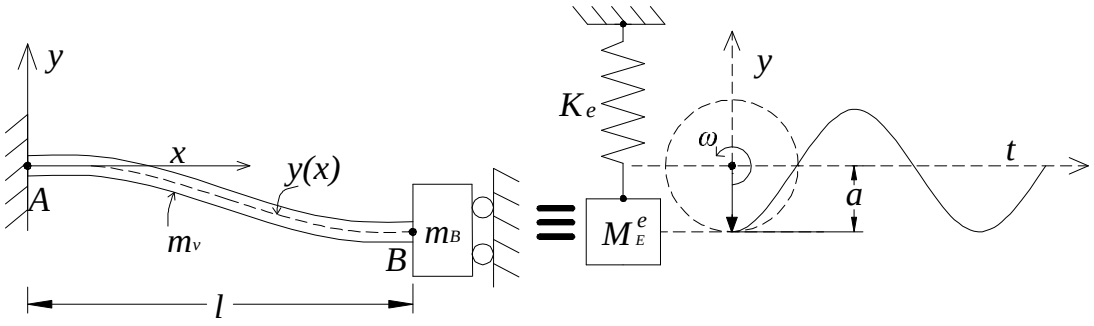

Figure 5: Equivalence between the basic mass-beam element to a simple mass-spring. m_v - beam mass and m_B - rigid mass.

We separate the kinetic energy of vibration elements into two components: $E_C^{m_B}$, kinetic energy of the rigid body at the end of the beam and E_C^l, kinetic energy of the elastic beam. For the rigid body:

$$E_C^{m_B} = \frac{1}{2} m_B v_B^2 \tag{4}$$

The kinetic energy of the elastic beam AB can be described by the sum of the kinetic energy of the small elements, that is:

$$E_C^l = \frac{1}{2} \sum_{i=1}^{n} v_i^2 \Delta m_i \cong E_C^l(t) = \frac{\rho \mathrm{A}}{2} \int_0^l v(x,t)^2 dx \tag{5}$$

where A is the area of cross section of the beam and ρ the density of the material, supposedly constants. Assuming that the beam movement in the direction y is of the form described as the static deflection curve, Eq. (2), the total kinetic energy of vibration elements is

$$E_C^e = E_C^{m_B} + E_C^l = \frac{P^2 l^6}{288 E^2 I^2} \omega^2 \cos^2(\omega t + \theta) \left(\frac{13 m_v}{35} + m_B \right) \tag{6}$$

where θ is the phase angle and ω the angular velocity of vibration. From above, we get the mass equivalent of the basic element of Figure 7 by assuming that the mass spring system vibrates with the magnitude equal to the maximum deflection:

$$M_E^e = \left(\frac{13 m_v}{35} + m_B \right) \tag{7}$$

5 Analytical results

We obtained the stiffness constant of each typology using the stiffness constant of the basic beam element (Eq. (3)) and the equivalent stiffness concept of beams connected in series and in parallel. The separation of a continuous structure into same modular elements, shown as Figure 5, simplifies the calculation of equivalent stiffness and equivalent mass of a typology.

The natural frequency of each typology is obtained through substituting the equivalent stiffness and equivalent mass into the Equation (1). Tab. 1 lists the analytic results of stiffness constant, K, equivalent mass M_E and natural frequency f_n in terms of the dimensions, mass e materials of typologies.

Table 1: Systematization of analytic results: stiffness constant, equivalent mass and natural frequency. Where $w, h$and l are the width, thickness and length respectively; M_V is the mass of all beams of a given type; M_C is the central mass; M_L is the sum of the two lateral bodies of the typology T3.

Typology	K		M_E	f_n
T1	$\frac{24EI}{l^3}$	$\frac{2Ehw^3}{l^3}$	$\frac{13M_V}{35} + M_C$	$\frac{1}{2\pi}\sqrt{\frac{2Ehw^3}{l^3\left(\frac{13M_V}{35} + M_C\right)}}$
T2	$\frac{48EI}{l^3}$	$\frac{4Ehw^3}{l^3}$	$\frac{13M_V}{35} + M_C$	$\frac{1}{2\pi}\sqrt{\frac{4Ehw^3}{l^3\left(\frac{13M_V}{35} + M_C\right)}}$
T3	$\frac{24EI}{l^3}$	$\frac{2Ehw^3}{l^3}$	$\frac{12}{35}M_V + M_C + \frac{M_L}{4}$	$\frac{1}{2\pi}\sqrt{\frac{2Ehw^3}{l^3\left(\frac{12}{35}M_V + M_C + \frac{M_L}{4}\right)}}$

6 FEM simulation

Using the software ANSYS, we got the natural frequencies from modal analysis. The simulations were conducted for silicon monocrystalline microstructures (Tab. 2). The parameters of size, mass and excitement harmonic are presented in Tab. 3.

We are interested in frequencies of resonance and respective modes of vibration. Two cases for T3 were simulated: T3 (a) and T3 (b), having differences in the dimensions and weight of the lateral and central masses, but same masses. However, the dimensions, weights and thicknesses of beams are same for each case, so that their analytical results are identical. Since obtaining of analytical formulations considered the central mass and lateral masses as lumped ones, no deformation energy of these elements was considered. The purpose of making comparison between two conceptions of T3

is to check the influence of the rigidity of mass central and lateral masses on the vibration modes and respective natural frequencies.

Table 2: Mono-crystalline silicon data.

Description	*Symbol*	*Value*	*Conversion*
Young Module	E	140 [GPa]	1,4 x 10^5 [kg.μm^{-1}.s^{-1}]
Density	ρ	2,33 [g.cm^{-3}]	2,33 x 10^{-15} [kg.μm^{-3}]

Table 3: Dimensions and loading.

Description	*Symbol*	*Value*
Length of the beams	l	200 μm
Width of the beams	w	2 μm
Thickness of the all structure	h	2,1 μm
Central mass	M_C	5,0887 x 10^{-11} kg
Lateral mass of T3	M_L	2.6911 x 10^{-12}kg
Harmonic excitement amplitude	F_0	0,14 μN

Fig. 6 shows the graphic results of the ANSYS for the first mode of vibration of T1 and T2. It can be seen that the deflections of beams are in agreement with the analytical models for the first mode of vibration, that is, the deflection curves of the two beams are close well to the curve described by the Eq. (2).

The modal analysis of T3 (a) showed a distinct behavior from T1 and T2. The first mode (the left illustration in Fig. 7) is characterized by a rotational movement around the mass center; also the strain of sidebars is considerable. For T3 (a), the vibration mode that best matches the analytical models was the 3 rd mode, as shown by the right illustration in Figure 7. However with the size of T3 (b), the first mode of vibration was in agreement with the analytical result (Figure 8).

The numerical and analytical results of natural frequency are compared in Table 4. We can see good coincidences between the analytical results and the numerical ones, except for T3(a). The large difference for T3 (a) is owing to the low rigidity of the lateral rods, whose horizontal displacement x is greater than the one of T3(b) (Figure 9).

Calculation of elastic strain energy confirmed that the lateral rods of T3(a) have experienced notable deformation. The ratio of the elastic strain energy of the lateral rods to the total elastic strain energy

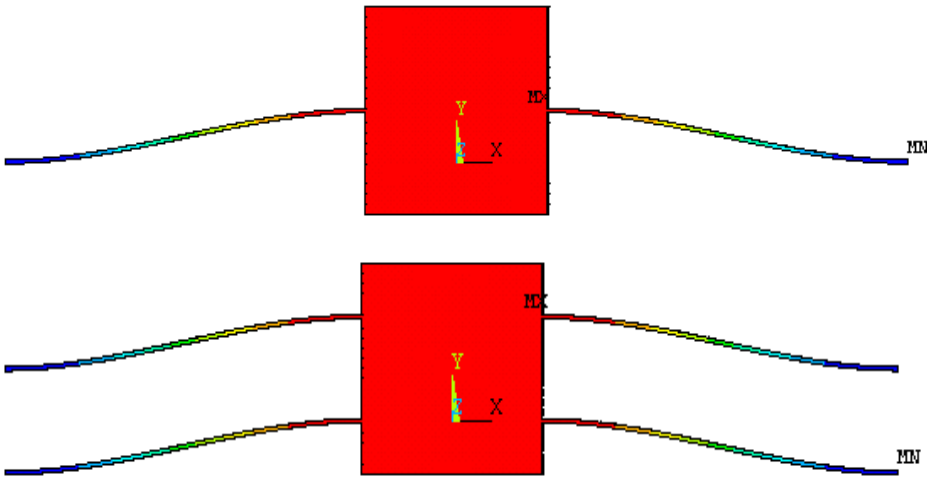

Figure 6: First vibration mode of T1 and T2.

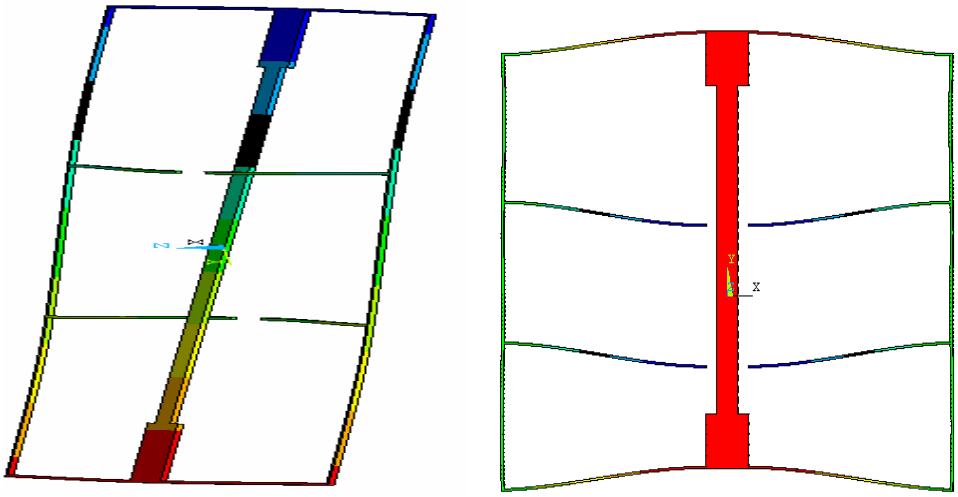

Figure 7: First (left) and third (right) modes of vibration of T3 (a).

of the structure is about 6.7% for the case of T3(a) but only 0.68% for T3(b). The notable deformation violated the assumption of rigidity masses for the analytical models and resulted in the large difference in the analytical and numerical natural frequencies.

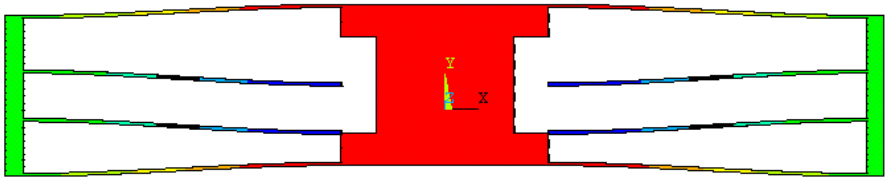

Figure 8: First vibration mode of T3 (b).

Table 4: Comparison of natural frequencies.

Typology	f_r*analítical* [Hz]	f_r *ANSYS* [Hz]	*difference* [Hz]	*relative difference* [%]
T1	16869	16843	26	0,15
T2	23532	23495	37	0,16
T3 (a)	15896	14905	991	6,23
T3 (b)	15896	15887	9	0,05

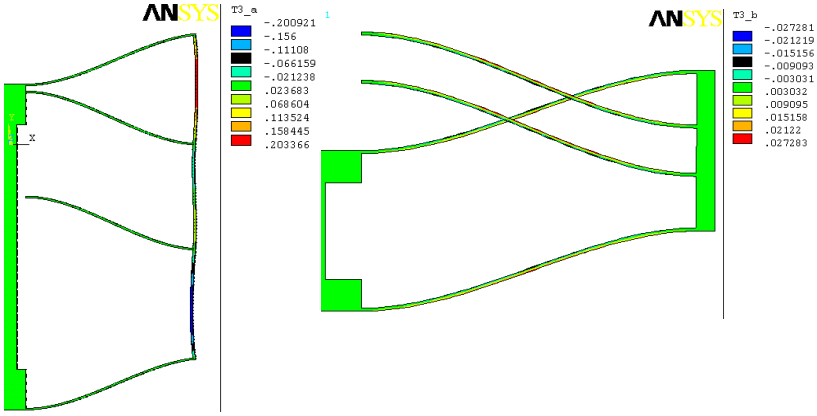

Figure 9: Displacement towards x in T3 (a), left, and shifts towards x in T3 (b), right. The scale is 16 times higher in relation to the values of the legend.

7 Conclusion

The MEMS sided resonator *comb-drive* can be modulated by such a structure consisting of elastic beams and rigid masses. The natural frequency can be obtained by equivalent mass-spring systems.

Depending on the structure typology, the equivalent stiffness can be determined from springs connected in parallel and in series. The results obtained by the software ANSYS confirm the validation of analytical formulation, deduced from equivalent systems. The analytical formulation obtained in this work can be used in the design of MEMS. The method and the concept of equivalent systems proposed can be extended to other types of MEMS. However, to achieve the desired mode of lateral vibration, the mass elements must have sufficient rigidity. This should be paid high attention in the design or manufacture of MEMS.

References

[1] Maluf, N. & Willians, K., *An Introduction to Microelectromechanical System Engineering.* Artech House, Inc.: MA, US, 2004. 282 p.
[2] Varadan, V.K., Vinoy, K.J. & Gopalakrishnan, S., *Smart Materil Systems and MEMS: Design and Development Methodologies.* John Wiley & Sons Ltd.: England, 2005.
[3] Meirovitch, L., *Elements of vibration analysis.* McGraw Hill: Singapore, 2nd edition, 1986.
[4] Tang, W.C. et al., Electrostatic-comb drive of lateral polysilicon resonators. *Sensors and Actuators,* A21-A23, pp. 328–331, 1990.

Mechanics of Solids in Brazil 2009, H.S. da Costa Mattos & Marcílio Alves (Editors)
Brazilian Society of Mechanical Sciences and Engineering, ISBN 978-85-85769-43-7

Adhesion of geopolymer bonded steel plates

Kelly Cristiane Gomes, Sandro Marden Torres, Silvio de Barros
Nucleo de Estudos e Pesquisas em Materiais NEPEM-UFPB,
Joao Pessoa/PB – Brazil

Normando Perazzo Barbosa
Laboratorio de Ensaios de Materiais e Estruturas LABEME-UFPB,
Joao Pessoa/PB – Brazil

Abstract

Known since the 70's, geopolymers are synthetic materials of acknowledged interesting chemical, mechanical and thermal performance. As far as environmental issue is concerned, the use of alkali-activated industrial by-product precursors and the near-room casting temperature (around 60°C) can be seen as an advantageous choice for many applications such as in thermo-mechanical efficient steel coatings. Whereas most epoxy resin would char at temperatures above 300°C, geopolymers can upheld good mechanical performance in temperatures as high as 1000°C. Although they have mostly been studied for coatings, the number of studies on their adhesion mechanisms is considerably less then those regarding its other properties. The main thrust of this work is to evaluate the binding potential of alkali-activated clay-based waste in steel bonded plates. The adhesion of steel plates (40x160x5mm) was evaluated using three clay-based wastes and metakaolin (MK) as precursors, provided by X-Ray fluorescence (XRF) analyses. Epoxy compound (EC) was used as a reference binder. The best result was found for the waste systems, which iron content is extremely higher then the other precursors, indicating a better adhesion performance of this system, when compared to the widely used epoxy compound.

Keywords: adhesion, geopolymer, mechanical tests.

1 Introduction

The use of adhesive bond techinology has been increasingly applied for the development of composites and laminate structures. This can be attributed to (*i*) the flexibility of the application of such materials which allows their use in several different geometries; (*ii*) better stress distribution of the bound parts when compared to rivetting and screwing and (*iii*) the inexistance of heat affected zone when compared to welding. The use of adhesives can also represent an advantageous choice when production interruption needs to be avoided. For instance, epoxic resins have been employed for reparing oil and gas pipes in the oilwell industry [1, 2]. Also, it is estimated that approximately five kilograms of

Mechanics of Solids in Brazil 2009, H.S. da Costa Mattos & Marcílio Alves (Editors)
Brazilian Society of Mechanical Sciences and Engineering, ISBN 978-85-85769-43-7

adhesive materials are used to joint some components of a popular car [3]. However, the mechanisms and durability of adhesion are very complex, therefore, demanding a broad spectrum of research [4]. Most adhesives are polymer based such as epoxy. Epoxic resins are known to have excelent mechanical properties. Nonetheless, its application is often limited to low temperature below 400°C.

Because most polymeric resins would char at temperatures above such threshold, there has been an increasing interest on other types of polymeric materials such as the geopolymers. These materials are found to upheld considerable mechanical properties in temperatures as high as 1000°C [5]. These inorganic polymers (geopolymers) were developed in France during the world oil crises of the 70s. These worldwide energy crises often help to bring up the quest for environmentally friendly engineering solutions, and the development of new materials become a paramount issue for the academics, the production sectors and governments [6]. One might consider that geopolymers can fit in the cathegory of friendly materias. Fristly, their synthesis occur at a near-room casting temperature. Secondly, they can be obtained by precursors derived from by-products of mining and industrial activities.

Most materials used to produce geopolymers are aluminosilicate such as: (*i*) kaolinite containing clays and (*ii*) steel manufacturing wastes such as ground granulated blast furnace slag and fly ash. There are several other sources of aluminosilicate containing materials that have not been yet studied as geopolymer precursors, especially in places with low steel manufacturing industrial activities such as the Brazilian northeast. Nonetheless, this region contains important sources of clay minerals and other relate by-products such as in the ceramic industry. Recent studies have aimed to evaluate the potential use of such types of wastes for the development of geopolymer. The results have shown interesting thermo-mechanical properties [7, 8].

The number of studies on the adhesion mechanisms of geopolymers are, nonetheless, considerably inferior when compared to studies on their syntheses and mechanical properties [9, 10]. The main thrust of this work is, therefore, to evaluate the binding potential of alkali-activated clay based mineral and industrial wastes as adhesive of steel bonded joints subjected to different temperatures.

2 Materials and methods

2.1 Materials

The chemical composition of the raw wastes obtained by X-Ray Fluorescence analyses is shown in Tab. 1, where:

- MK: Metakaolin was used as control, given the wide number of research in such material as geopolymer precursor.
- Waste A: Mineral waste from a local source.
- Waste B: Local industrial waste.
- Waste C: Mineral waste from a local source.

Mechanics of Solids in Brazil 2009, H.S. da Costa Mattos & Marcílio Alves (Editors)
Brazilian Society of Mechanical Sciences and Engineering, ISBN 978-85-85769-43-7

Table 1: Chemical composition of waste

	MK (%)	Waste A (%)	Waste B (%)	Waste C (%)
SiO_2	62,96	51,18	62,25	61,87
Al_2O_3	34,61	11,70	22,11	24,06
Fe_2O_3	0,63	35,97	5,99	10,87
Na_2O	0,07	0,00	1,06	0,00
K_2O	1,34	0,02	1,24	0,19
CaO	0,05	0,02	0,05	0,20

The oxide content of the activator is shown in Tab. 2.

Table 2: Chemical composition of activator

SiO_2 (%)	Na_2O (%)	H_2O
36,25	16,63	47,12

The molar ratio composition of the mixes are shown in the Tab. 3. With the exception of the silica to alumina ratio, the other parameters were kept as close as possible, although such ratio differences can be expected given the differences in both the waste composition and the texture of the powders.

Table 3: Molar ratio of geopolymer

	SiO_2/Al_2O_3	H_2O/M_2O	Al_2O_3/M_2O	M_2O/SiO_2
MK	5,43	9,73	0,96	0,19
Waste A	9,33	9,76	1,19	0,09
Waste B	7,09	9,06	0,91	0,16
Waste C	6,66	9,76	0,98	0,15

2.2 Sample preparation

The steel plates (160x40x4 mm) surfaces were lapped and polished in order to keep an uniform metal substrate. The prospective bonding faces were washed with acetone and then rinsed with ethanol prior to bonding process. The adhesive materials were poured on the treated surfaces and both plates were pressed together by a mechanical device in order to keep the adhesive thickness of 0,5mm in all samples.

2.3 Curing regimes

In order to investigate the effect of the temperature on the adhesive properties, the bonded plates were subjected to four types of curing temperature regimes, as shown in Tab. 4. In the first, the bonded steel plates were subjected to a classical curing regime, which was used as control. In the second and followings, the samples were subjected to increasing temperatures and subsequently placed in a temperature and humidity controlled environment. The highest temperature level was 400°C in order to assess the binding properties of the geopolymer in comparison with the epoxy adhesive.

Table 4: Curing regimes

Regime	22°C(day)	55°C(day)	22°C(day)	200°C(day)	400°C(day)	22°C(day)
01	01	01	05	-	-	-
02	01	01	01	01	-	05
03	01	01	01	-	01	05

2.4 Crack propagations tests

Among several classical adhesion assessment techniques, the mixed-mode flexure test (MMF) is one of the simplest to be performed. In a MMF test, both propagation modes, shear and opening, can be evaluated at the same time, in order to provide a more realistic geometry and mode of loading as in actual structures. The tests were performed using a Shimadzu Servopulser machine. The load speed applied was 0.01 mm/sec and the displacements were continuously recorded in a built-in data aquisition system.

3 Results and discussions

3.1 Near-room temperature

Figure 1 shows the crack propagation profile of the waste systems under the MMF mode at curing regime 1. It can be seen that the waste A type adhesive reached the highest crack propagation load

level, followed by the industrial waste B and mineral waste C geopolymer type adhesives, respectively.

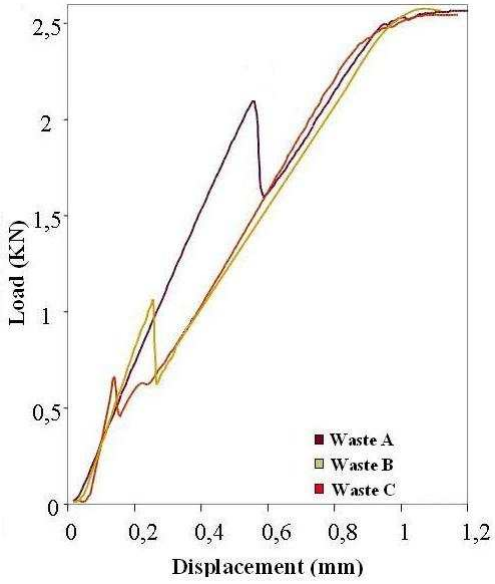

Figure 1: Crack propagation tests of curing regime 1.

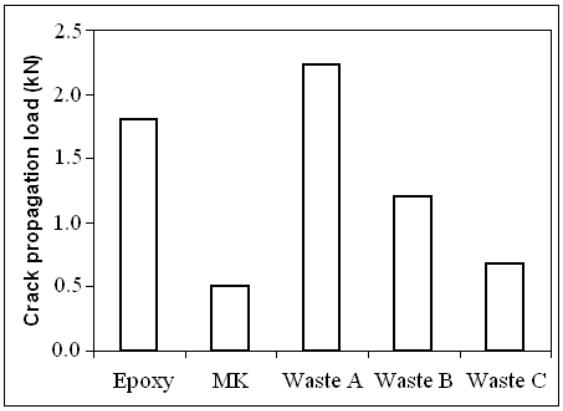

Figure 2: Crack propagation load of curing regime 1.

Figure 2 shows the crack load level of all five adhesive types tested at curing regime 1. In the epoxy system, the first propagation occurred at 1.8kN. Metakaolin system presented the lowest level, reaching around 0.5kN. When compared together, the obvious superiority of epoxy adhesive might explain the lack of studies on the adhesive properties of geopolymers at near room temperature. Indeed, metakaolin is the most widely spread precursor for this type of inorganic polymers. Also, it can be seen that all the other geopolymeric systems reached superior crack propagation load when compared to MK system alone. The mineral waste A reached the highest crack propagation load, slightly superior then the epoxy based system.

Although waste C system showed the lowest crack propagation strength, its load level can be considered equivalent to the MK one. This can be quite expected given the similar chemical composition of both MK and waste C (Tab. 1). The highest Al2O3 content was observed in MK (34.61%), followed by Waste C (24.06%). Also, the Al2O3/SiO2 ratio of both MK (5.43) and waste C (6.66) are similar, slightly higher for waste C (Tab. 3). Experimental studies have proposed that the higher this parameter, the greater the strength of the bulk material. Consequently, it appears that such parameter is also related with the adhesive properties as well. The highest value of crack propagation load observed in waste A can be associated with its highest Al2O3/SiO2 ratio (9.33). The waste B system showed a rather higher crack propagation load then system C, although their composition are quite alike in terms of aluminium and silicon oxides.

The fact that the Al2O3/SiO2 ratio of waste B (7.09) be greater than the waste C (6.66) seems to corroborate to the view that such parameter also has a role on the adhesive properties of geopolymers.

The highest load value was observed for the waste A systems in which the lowest level of alumina was observed (11.70%). Atlhouhg this level might suggest a low adhesive properties alone, this precursor presented the greatest value of Al2O3/SiO2 ratio (9.33). It is important to point out that iron content (35.97%) is extremely higher than the other precursors, nearly four times greater than the second highest (waste B). The results seem to indicate that the iron content might be another important parameter for the adhesive properties, having a positive influence on adhesion of steel systems. The greater the iron content, the higher the crack propagation load of the studied systems.

3.2 High temperature

The effect of the temperature on the crack propagation load can be observed on the Fig. 3. As expected for the epoxy based adhesive, its performance is limited to temperatures below 400°C. Although epoxy system reached the second highest crack propagation load level, this system failed without even the submission of the MMF test.

As far as the effect of temperature is concerned, it can be seen that the performance of the metakaolin geopolymer adhesive was quite constant up to 400°C. This restult is in accordance with what is reported in the literature for the thermal-mechanical properties of such material, which shows geopolymers withstanding excelent mechanical properties at much higher tempratures [8, 11]

The effect of the temperature on the performance of the waste based geopolymers followed a similar trend of load decreament as observed for the epoxy system. Although greater crack propagation loads were obtained in all the waste based geoploymeric adhesives, the crack propagatio load level decreased as the temperature increased. Nevertheless, they all retained similar load level when compared with

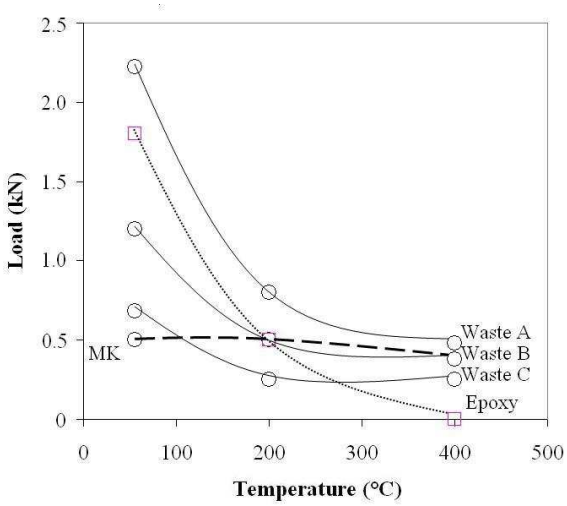

Figure 3: Crack propagation load versus increase in temperature.

the metakaolin geopolymer adhesive system. The load level decreament was more intense in Waste A, followed by Waste B and C, respectively. This decreament seems to be associated with the iron oxide content of the precursors, which decreased in the same order (see Tab. 1). This association might also explain why MK load level was kept almost constant up to the maximum tested temperature system as it had the least iron oxide content.

4 Conclusions

The results can indicate that other alkali activated aluminosilicate materials had better performance then classical geopolymer precursor (MK), as far as adhesive properties are concerned. Two different mineral and one industrial wastes based geopolymers were successfully used as adhesive in steel plates with relative thermal efficiency. Geopolymers retained load under temperature as high as 400°C, giving superior performance when compared to an epoxy based adhesive. Although the metakaolinite geopolymer system was not significantly affected by temperature increase up to 400°C, all other adhesives presented a load decreament with temperature. The role of the Si:Al ratio on the adhesive properties of geopolymers seems to follow similar trend as occur for bulk compressive strength. The greater the Si:Al ratio of the precursor, the greater the crack propagation load in all systems. Nevertheless, it seems that the greater the iron oxide content, the greater the load decreament of all systems. Hence, care must be taken concerning the presence of gas generating reactions that might occur as in the case of some hydrated iron rich phases that might be present in some mineral and industrial wastes. This reaction can be responsible to reduce the mechanical efficiency of the steel plates bond.

Responsibility notice

The author(s) is (are) the only responsible for the printed material included in this paper.

References

[1] Sampaio, R.F., Reis, J.M.L., Perrut, V.A. & Costa-Mattos, H.S., Epoxy rehabilitation of corroded steel pipelines with through-thickness damage. *Journal of Pipeline Engineering*, **7**, p. 1, 2007.
[2] Stroganov, V.F., Strakhov, D.E., Alekseev, K.P. & Stroganov, I.V., Epoxy polymers in adhesive technologies of pipeline joint. *Polymer Science, Ser C*, **49(3)**, pp. 269–271, 2004.
[3] Barquins, M. & Fadel, K., Adhesion et collage. *Decouverte*, **271**, pp. 31–46, 1999.
[4] Dillard, D.A. & Pocius, A.V., The mechanics of adhesion. *Adhesion science and engineering*, **1**, 2002.
[5] Davidovits, J., Properties of geopolymer cements. *Proceedings First International Conference on Alkaline Cements and Concretes*, Kiev, Ukraine, volume 131, 1994.
[6] Davidovits, J., Geopolymers: inorganic polymeric new materials. *Journal of Thermal Analysis*, **37**, pp. 16–33, 1991.
[7] Gomes, K.C., Nóbrega, A.F., Vieira, A.A.P., Torres, S.M., de Barros, S. & Barbosa, N.P., Ativacao alcalina de residuos de caulim. *International Conference on Non-Conventional Materials and Technologies - NOCMAT2007*, Alagoas, Brasil, 2007.
[8] Barbosa, V.F.F. & Mackenzie, K.J.D., Thermal behaviour of inorganic geopolymers and composites derived from sodium polysialate. *Materials Research Bulletin*, **38**, pp. 319–331, 2002.
[9] Latella, B.A., Perera, D.S., Escott, T.R. & Cassidy, D.J., Adhesion of glass to steel using a geopolymer. *Journal of Material Science*, **41**, pp. 1261–1264, 2006.
[10] Wang, H., Li, H. & Yan, F., Synthesis and mechanical properties of metakaolinite-based geopolymer. *Colloids and Surfaces A: Physicochem Eng Aspects*, **268**, pp. 1–6, 2005.
[11] Palomo, A., Varela, M.T.B., Granizo, M.T., Puertas, F., Varquez, T. & Grutzeck, M.W., Chemical stability of cementitious materials based on metakaolin. *Cement and Concrete Research*, **29**, pp. 997–1004, 1999.

Mechanics of Solids in Brazil 2009, H.S. da Costa Mattos & Marcílio Alves (Editors)
Brazilian Society of Mechanical Sciences and Engineering, ISBN 978-85-85769-43-7

Generalized Finite Element Method with global-local enrichments for nonlinear fracture analysis

D.-J. Kim, C.A. Duarte
Department of Civil and Environmental Engr., University of Illinois at Urbana-Champaign, Newmark Laboratory, Illinois – USA
S.P. Proença
Structural Engineering Department, School of Engineering at São Carlos - University of São Paulo, São Carlos/SP – Brazil

Abstract

The main feature of partition of unity methods such as *hp*-cloud, generalized and extended finite element methods is their ability of utilizing a priori knowledge about the solution of a problem in the form of enrichment functions. Linear combination of partition of unity shape functions can reproduce exactly the enrichment functions and thus their approximation properties are preserved. This class of shape functions enables, for example, the approximation of solutions in the neighborhood of cracks [1], inclusions, voids [2], etc. using finite element meshes that do not fit them. However, analytical derivation of enrichment functions with good approximation properties is mostly limited to two-dimensional linear problems. In this paper, we present a procedure to numerically generate enrichment functions for problems with localized nonlinearities. The procedure is based on the so-called generalized finite element method (GFEM) with global-local enrichment functions [3]. It involves the solution of boundary value problems around regions exhibiting nonlinear behavior and the enrichment of the global solution space with local solutions through the partition of unity framework used in the GFEM. This approach was originally proposed to efficiently handle crack propagation simulation [4], but it also has the potential to solve nonlinear problems accurately and with a reduced computational cost compared with the conventional finite element method. An illustrative nonlinear problem of the J_2-based plasticity theory with linear isotropic hardening is solved using the proposed procedure to demonstrate its robustness, accuracy and computational efficiency.

1 Introduction

Several technological advances attempted today require computational methods able to model complex, highly localized phenomena. A representative example is the case of mechanically short cracks. These cracks are much smaller than any dimension of a structural component, but larger than the

Mechanics of Solids in Brazil 2009, H.S. da Costa Mattos & Marcílio Alves (Editors)
Brazilian Society of Mechanical Sciences and Engineering, ISBN 978-85-85769-43-7

details of the material microstructure (polycrystalline grains in the case of metals) [5]. Non-linear process zones in these cracks, while relevant, are several orders of magnitude smaller than any structural dimension. The analysis of small cracks is critically important for structures subjected to high frequency excitations, like acoustic loads. The majority of the life of these components corresponds to the growth and incubation of small cracks. The analysis of this class of problems can not be handled simply by using available finite element methods (FEMs) and massive computer power. The mesh density required by the FEM leads to prohibitively small time steps in the case of time dependent problems. In addition, the adaptive construction of FEM discretizations may be quite costly, since it demands several adaptive cycles on very large computational models.

In this paper, we propose a novel generalized finite element method for non-linear fracture analysis of small cracks. The key ideas of the proposed method are the computation of the so-called global-local enrichment functions and the use of the partition of unity concept to build conforming approximation spaces on a *coarse* finite element mesh.

The Generalized FEM (GFEM) has had a significant impact on the solution of problems in which there is an a-priori knowledge about the behavior of the solution. By numerically constructing enrichment functions, the proposed GFEM brings the benefits of existing GFEMs to a much broader class of problems and, in particular, to non-linear fracture problems. High-order generalized finite elements and adaptivity are explored in the computation of enrichment functions able to robustly represent small scale features, like cracks, using FE meshes that are straightforward to generate. These meshes are in practice generated during the design of the component and are able to model its global response. By enriching these meshes with the proposed global-local enrichments, the resulting discretization is able to capture the interactions between the global (structural) and small scale (near crack) response. The outline of the paper is as follows. Sections 2 and 2.1 briefly review the main concepts of the GFEM and the so-called global-local enrichments, respectively. Section 2.2 presents the formulation of global-local enrichments for localized non-linearities with emphasis on fracture mechanics problems. The plasticity model used in this paper is described in Section 3. A numerical example illustrating the performance of the proposed method is presented in Section 4. The conclusions are outlined in Section 5.

2 Generalized FEM: A summary

The generalized FEM [6–9] is an instance of the partition of unity method which has its origins in the works of Babuška et al. [6, 10, 11] (under the names "special finite element methods," "generalized finite element method" and "finite element partition of unity method") and Duarte and Oden [8, 12–15] (under the names "*hp* clouds" and "cloud-based *hp* finite element method"). Several meshfree methods proposed in recent years can also be formulated as special cases of the partition of unity method. The key feature of these methods is the use of a partition of unity (POU), which is a set of functions whose values sum to the unity at each point in a domain. Additional methods based on the partition of unity concept are, for example, the extended finite element method [16], the method of finite spheres [17] and the particle partition of unity method [18], to name just a few. In these methods, discretization spaces for a Galerkin method are defined using the concept of a partition of unity and local spaces

Mechanics of Solids in Brazil 2009, H.S. da Costa Mattos & Marcílio Alves (Editors)
Brazilian Society of Mechanical Sciences and Engineering, ISBN 978-85-85769-43-7

that are built based on a-priori knowledge about the solution of a problem. A shape function, $\phi_{\alpha i}$, in the GFEM is computed from the product of a linear finite element shape function, φ_α, and an enrichment function, $L_{\alpha i}$,

$$\phi_{\alpha i}(\boldsymbol{x}) = \varphi_\alpha(\boldsymbol{x}) L_{\alpha i}(\boldsymbol{x}) \quad \text{(no summation on } \alpha) \tag{1}$$

where α is a node in the finite element mesh. Figure 1 illustrates the construction of GFEM shape functions.

The linear finite element shape functions $\varphi_\alpha,\ \alpha = 1, \ldots, N$, in a finite element mesh with N nodes constitute a partition of unity, i.e., $\sum_{\alpha=1}^{N} \varphi_\alpha(\boldsymbol{x}) = 1$ for all $\boldsymbol{x}$ in a domain Ω covered by the finite element mesh. This is a key property used in partition of unity methods. Linear combinations of the GFEM shape functions $\phi_{\alpha i},\ \alpha = 1, \ldots, N$, can represent *exactly* any enrichment function $L_{\alpha i}$ [14, 15].

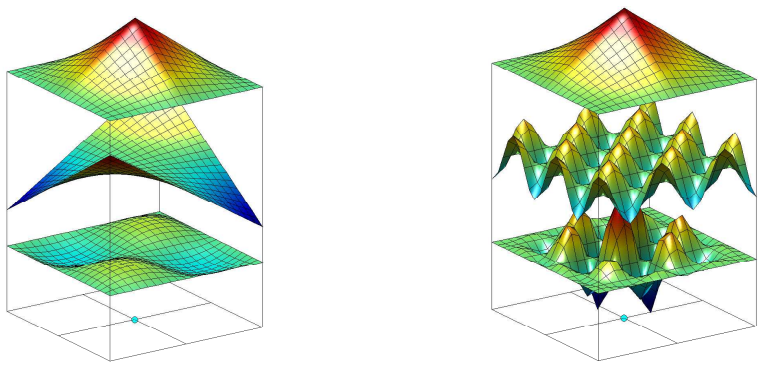

(a) (b)

Figure 1: Construction of a generalized FEM shape function using a polynomial (a) and a non-polynomial enrichment (b). Here, φ_α are the functions at the top, the enrichment functions, $L_{\alpha i}$, are the functions in the middle, and the generalized FE shape functions, $\phi_{\alpha i}$, are the resulting bottom functions.

Enrichment functions The GFEM has been successfully applied to the simulation of boundary layers [19], dynamic propagating fractures [20], line singularities [7], acoustic problems with high wave number [21, 22], polycrystalline microstructures [23], porous materials [24], etc. All these applications have relied on closed-form enrichment functions that are known to approximate well the physics of the problem. These so-called custom enrichment functions are able to provide more accurate and robust simulations than the polynomial functions traditionally used in the standard FEM, while relaxing some meshing requirements. However, for many classes of problems–like those involving material

non-linearities–enrichment functions with good approximation properties are not amenable to analytical derivation. In this paper, this limitation is removed using *global-local enrichment functions*, as described below.

2.1 Global-local enrichment functions

In this section, we present a global-local approach to numerically build enrichment functions for localized non-linearities. The approach is based on the global-local formulation presented in [3, 4, 25]. We focus on three-dimensional non-linear fracture problems. The formulation is, however, applicable to other classes of problems as well.

2.1.1 Formulation of Global Problem

Consider a domain $\bar{\Omega}_G = \Omega_G \cup \partial\Omega_G$ in $\Re^3$. The boundary is decomposed as $\partial\Omega_G = \partial\Omega_G^u \cup \partial\Omega_G^\sigma$ with $\partial\Omega_G^u \cap \partial\Omega_G^\sigma = \emptyset$.

The equilibrium equations are given by

$$\nabla \cdot \boldsymbol{\sigma} = \mathbf{0} \qquad \text{in } \Omega_G, \tag{2}$$

The constitutive relations may be given by Hooke's law, $\boldsymbol{\sigma} = \boldsymbol{C} : \boldsymbol{\varepsilon}$, where $\boldsymbol{C}$ is Hooke's tensor, or by a non-linear stress-strain relation as discussed in Section 3.

The following boundary conditions are prescribed on $\partial\Omega_G$

$$\boldsymbol{u} = \bar{\boldsymbol{u}} \text{ on } \partial\Omega_G^u \qquad \boldsymbol{\sigma} \cdot \boldsymbol{n} = \bar{\boldsymbol{t}} \text{ on } \partial\Omega_G^\sigma, \tag{3}$$

where $\boldsymbol{n}$ is the outward unit normal vector to $\partial\Omega_G^\sigma$ and $\bar{\boldsymbol{t}}$ and $\bar{\boldsymbol{u}}$ are prescribed tractions and displacements, respectively.

Let $\boldsymbol{u}_G^0$ denote the generalized FEM solution of the problem (2), (3). This is hereafter denoted as the *initial global problem*. The GFEM approximation $\boldsymbol{u}_G^0$ is the solution of the following problem:

Find $\boldsymbol{u}_G^0 \in \boldsymbol{X}_G^{hp}(\Omega_G) \subset H^1(\Omega_G)$ such that, $\forall\ \boldsymbol{v}_G^0 \in \boldsymbol{X}_G^{hp}(\Omega_G)$

$$\int_{\Omega_G} \boldsymbol{\sigma}(\boldsymbol{u}_G^0) : \boldsymbol{\varepsilon}(\boldsymbol{v}_G^0) d\boldsymbol{x} + \eta \int_{\partial\Omega_G^u} \boldsymbol{u}_G^0 \cdot \boldsymbol{v}_G^0 d\boldsymbol{s} = \int_{\partial\Omega_G^\sigma} \bar{\boldsymbol{t}} \cdot \boldsymbol{v}_G^0 d\boldsymbol{s} + \eta \int_{\partial\Omega_G^u} \bar{\boldsymbol{u}} \cdot \boldsymbol{v}_G^0 d\boldsymbol{s} \tag{4}$$

where, $\boldsymbol{X}_G^{hp}(\Omega_G)$ is a discretization of $H^1(\Omega_G)$, a Hilbert space defined on Ω_G, built with generalized or standard FEM shape functions and η is a penalty parameter. We use the penalty method due to its simplicity and generality. Detailed discussion and analysis of methods for the imposition of Dirichlet boundary conditions in generalized FEMs can be found in, e.g., [26]. Problem (4) leads to a system of linear or non-linear equations for the unknown degrees of freedom of $\boldsymbol{u}_G^0$, depending on the material model used. The mesh used to solve problem (4) is typically a coarse quasi-uniform mesh.

2.1.2 Formulation of local Problem

The proposed approach involves the solution of a local boundary value problem defined in a neighborhood Ω_{loc} of a crack or other small scale feature, and subjected to boundary conditions provided

by the global solution $\boldsymbol{u}_G^0$. The following *local problem* is solved on Ω_{loc} after the global solution $\boldsymbol{u}_G^0$ is computed as described above:

Find $\boldsymbol{u}_L \in \boldsymbol{X}_{loc}^{hp}(\Omega_{loc}) \subset H^1(\Omega_{loc})$ such that, $\forall\ \boldsymbol{v}_L \in \boldsymbol{X}_{loc}^{hp}(\Omega_{loc})$

$$\int_{\Omega_{loc}} \boldsymbol{\sigma}(\boldsymbol{u}_L) : \boldsymbol{\varepsilon}(\boldsymbol{v}_L) d\boldsymbol{x} + \eta \int_{\partial\Omega_{loc}\backslash(\partial\Omega_{loc}\cap\partial\Omega_G^{\sigma})} \boldsymbol{u}_L \cdot \boldsymbol{v}_L d\boldsymbol{s} =$$
$$\eta \int_{\partial\Omega_{loc}\backslash(\partial\Omega_{loc}\cap\partial\Omega_G)} \boldsymbol{u}_G^0 \cdot \boldsymbol{v}_L d\boldsymbol{s} + \eta \int_{\partial\Omega_{loc}\cap\partial\Omega_G^{u}} \bar{\boldsymbol{u}} \cdot \boldsymbol{v}_L d\boldsymbol{s} + \int_{\partial\Omega_{loc}\cap\partial\Omega_G^{\sigma}} \bar{\boldsymbol{t}} \cdot \boldsymbol{v}_L d\boldsymbol{s} \tag{5}$$

where, $\boldsymbol{X}_{loc}^{hp}(\Omega_{loc})$ is a discretization of $H^1(\Omega_{loc})$ using the GFEM shape functions presented in [27, 28].

A key aspect of problem (5) is the use of the generalized FEM solution of the (coarse) global problem, $\boldsymbol{u}_G^0$, as Dirichlet boundary condition on $\partial\Omega_{loc}\backslash(\partial\Omega_{loc} \cap \partial\Omega_G)$. Exact boundary conditions are prescribed on portions of $\partial\Omega_{loc}$ that intersect either $\partial\Omega_G^u$ or $\partial\Omega_G^\sigma$. Cauchy (spring) boundary conditions can also be used on $\partial\Omega_{loc}\backslash(\partial\Omega_{loc} \cap \partial\Omega_G)$.

2.2 *GFEM*$^{\text{g-l}}$ for Non-Linear Problems

The proposed *GFEM*$^{\text{g-l}}$ non-linear analysis algorithm is described with the aid of the three-dimensional model problem shown in Figure 2. In the first step of procedure, the initial global solution $\boldsymbol{u}_G^0$ is computed on a coarse global mesh as illustrated in Figure 2. The formulation of this problem is given by (4). Cracks are *not* discretized when solving this problem. *A linear elastic material law is used at this step.*

In the second step, a local problem is defined around each crack in the global domain. These local problems are automatically built using elements extracted the coarse global discretization around the cracks. Details on this procedure can be found in Section A.1 of [3]. Figure 3 illustrates the procedure. The formulation of the local problems is given by (5). In this case, a non-linear material law (cf. Section 3) is used and the local solution $\boldsymbol{u}_L$ is found with the aid of Newton's method. The *hp* GFEM presented in [27, 28] is used to discretize the local problems. Figure 4 illustrates an *hp* adapted discretization and the corresponding local solution $\boldsymbol{u}_L$ computed around a surface crack.

Global-local enrichment functions The procedure to compute the local solution $\boldsymbol{u}_L$ is based on a global-local finite element analysis, broadly used in many practical applications of the FEM [29]. The error of $\boldsymbol{u}_L$ depends not only on the discretization used in the local domain Ω_{loc}, but, it is also affected by the quality of the boundary conditions used on $\partial\Omega_{loc}\backslash(\partial\Omega_{loc}\cap\partial\Omega_G)$, i.e., the global (coarse) solution $\boldsymbol{u}_G^0$. As a result, the error of $\boldsymbol{u}_L$ may be large *even if a very fine mesh is used on* Ω_{loc}. Furthermore, the global-local FEM can *not* account for possible interactions of local (near crack, for example) and global (structural) behavior and, thus, is not suitable for problems involving multiscale phenomena. In the proposed *GFEM*$^{\text{g-l}}$, these issues are addressed by going one step further in a global-local analysis; the global problem is solved using $\boldsymbol{u}_L$ *as enrichment functions.* The local solution, $\boldsymbol{u}_L$, of the local problem defined in (5) is used to build generalized FEM shape functions for the coarse global mesh. Equation (1) is used with the partition of unity function, φ_α, provided by the global, *coarse*, FE mesh

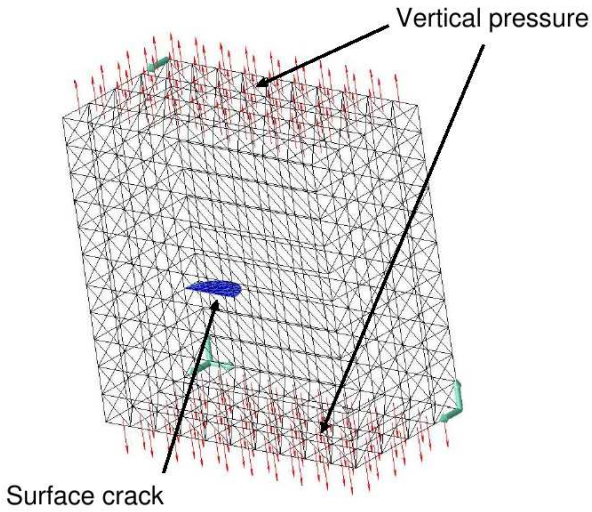

Figure 2: Model problem used to illustrate the main ideas of the $GFEM^{g\text{-}l}$. The figure shows a small surface crack in a 3-D domain. The solution computed on this coarse global mesh provides boundary conditions for the extracted local domain in a neighborhood of the crack. *The crack is shown in the global domain for illustration purposes only.* In the proposed $GFEM^{g\text{-}l}$, small scale cracks are *not* discretized in the global problem. Instead, global-local enrichment functions are used.

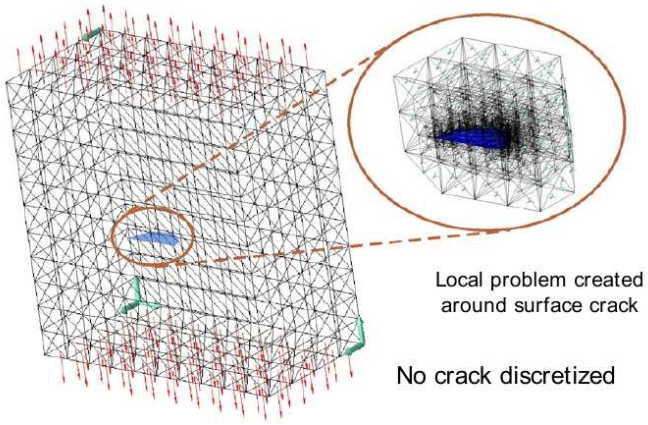

Figure 3: Definition of a local problem around a crack using elements extracted from the coarse global discretization.

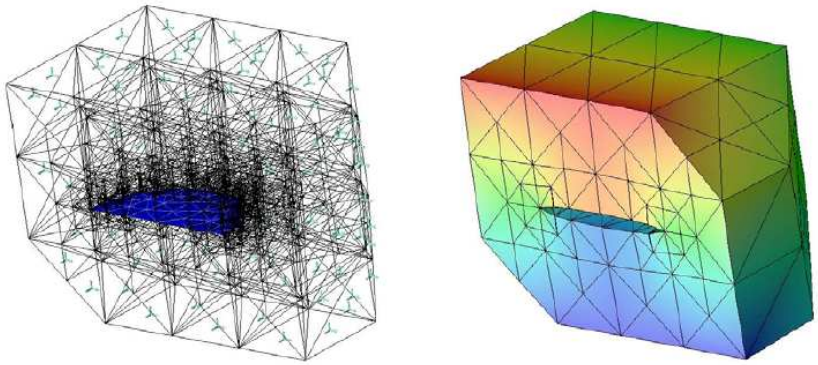

Figure 4: *Hp* adapted local discretization used for the computation of the non-linear solution $\boldsymbol{u}_L$ of a local problem.

and the enrichment function given by the solution of the local problem, i.e.,

$$\boldsymbol{\phi}_\alpha(\boldsymbol{x}) = \varphi_\alpha(\boldsymbol{x})\boldsymbol{u}_L \tag{6}$$

Hearafter, $\boldsymbol{u}_L$ is denoted a *global-local enrichment function.*

Only a few degrees of freedom are added to the global (structural scale) discretization even if the computation of the local solution requires several thousands of degrees of freedom since $\boldsymbol{u}_L$ is a known function. This is in contrast with, e.g., the S-FEM [30, 31] which adds a large number of enrichments to a global coarse mesh in order to capture small scale behavior in the global domain. The global problem is solved on the *coarse* global mesh enriched with the shape functions defined in (6). Like in the case of the local problem, a non-linear material law is used in the computation of this so-called *enriched global problem.* These shape functions (6) are hierachicaly added to the FE discretization, and thus, a few entries are added to element matrices while keeping existing ones associated with standard FE shape functions. Figure 5 illustrates the enrichment of the global coarse mesh with the solution of a local problem defined in a neighborhood of a crack.

3 Plasticity Model

In order to accounting for irreversible response and hardening effects of the medium, a classical rate-independent plasticity model suitable for three-dimensional analysis in the global-local GFEM framework was considered. A detailed description of it can be found in Simo and Hughes [32].

The main features of the adopted model are: von Mises yield function, isotropic hardening and associativity assumption assumed for both hardening law and normality rule for plastic flow.

Being $\boldsymbol{C}$ the isotropic elastic constitutive tensor, $\boldsymbol{S}$ the deviatoric part of the stress tensor, σ_t the yield stress and $\boldsymbol{K}(\alpha)$ the hardening function, the local governing equations of the model are:

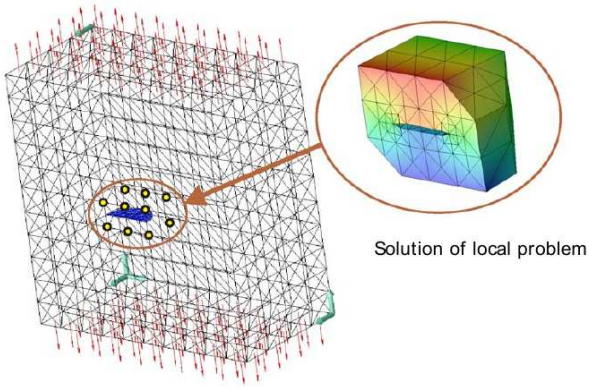

Figure 5: Enrichment of the coarse global mesh with a local solution. Only three degrees of freedom are added to nodes with yellow glyphs. The crack is shown in the global domain for illustration purposes only.

$$\sigma = C\,(\varepsilon - \varepsilon^p) \quad \text{(linear elastic stress-strain relationship)} \tag{7}$$

$$f = \|S\| - \sqrt{2/3}\,K\,(\alpha) \quad \text{(yield criterion)} \tag{8}$$

$$K\,(\alpha) = \sigma_t + h\,\alpha + (\sigma_\infty - \sigma_t)\,[1 - \exp\,(-\omega\,\alpha)] \quad \text{(nonlinear hardening function)} \tag{9}$$

$$\dot{\varepsilon}^p = \dot{\lambda}\frac{\partial f}{\partial \sigma} = \dot{\lambda}\,n; \quad n = \frac{S}{\|S\|} \quad \text{(flow rule)} \tag{10}$$

$$\dot{\alpha} = \dot{\lambda}\sqrt{\frac{2}{3}} \quad \text{(hardening rule)} \tag{11}$$

$$\dot{\lambda} \geqslant 0,\ f\,(\sigma, \alpha) \leqslant 0,\ f\,\dot{\lambda} = 0,\ \dot{f}\,\dot{\lambda} = 0 \quad \text{(Kuhn-Tucker and consistency conditions)} \tag{12}$$

It must be noted that the hardening law adopted, Düster [33], combines a linear and an exponential function, being h the linear hardening parameter, ω the hardening exponent and σ_∞ the saturation stress.

An implicit-type returning mapping algorithm (essentially, the 'trial' elastic stress vector, 'predictor', is projected onto the yield surface, 'plastic corrector') was carried out in order to integrate the incremental form of the constitutive model. Moreover, a consistent tangent elastoplastic constitutive tensor was adopted when using a Newton-Raphson iterative and incremental process aiming to compute a sequence of equilibrated and constitutive compatible responses at the solid structural analysis level.

4 Numerical Example

We perform numerical experiment to show the effectiveness of the proposed $GFEM^{g\text{-}l}$ in this section. Numerical examples are analyzed by both the GFEM and $GFEM^{g\text{-}l}$ and the result obtained by the $GFEM^{g\text{-}l}$ is compared with that obtained by the GFEM to show the accuracy of the $GFEM^{g\text{-}l}$ solution and its computational cost.

In the analysis using the $GFEM^{g\text{-}l}$, no crack is discretized in the global domain as discussed in Section 2.2. A single local problem is defined around a crack in the domain. Plastic strain is assumed to be confined to the interior of the local domain. This justifies the use of elastic material law in the initial global problem.

4.1 Small surface crack

As an example to demonstrate the effectiveness of the $GFEM^{g\text{-}l}$, we analyze a small surface crack example introduced in Section 2.2. Figure 6 shows the geometry of this model problem and applied tension at the top and bottom of the domain. This problem has a small half-circular surface breaking crack at the center of the front face. The following geometrical and loading parameters are assumed: in-plane dimensions $2b = 2.0$, $2h = 2.0$, $2r = 0.4$; domain thickness $t = 1.0$; vertical traction $t_y = 115.0$ (MPa). The domain is discretized with a uniform mesh of 6*(10x11x4) tetrahedral elements. Figure 2 shows this mesh.

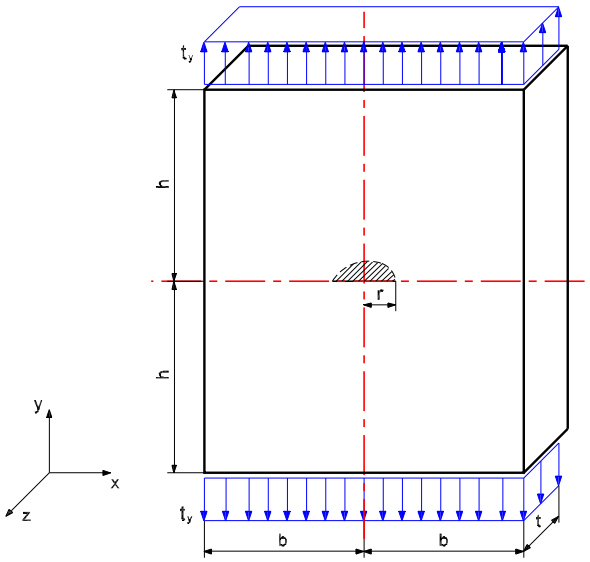

Figure 6: Domain with a small single surface crack.

Linear isotropic hardening model is used by including only a linear function from Equation (9) ($\sigma_\infty = \sigma_t$) and material properties are listed in Table 1. Newton-Rhapson method is used with load control to obtain nonlinear solutions since globally hardening behavior is expected in this analysis. We use the relative norm of residual as a tolerance criterion and the tolerance is given as 0.0001. Eight loading steps are provided for this nonlinear analysis. As a measure for accuracy of the solution, we choose the crack mouth opening displacement (CMOD), which is frequently used in fracture analysis. The CMOD is measured at the center of the surface crack boundary on the front face.

Table 1: Material data of alluminum alloy.

Young's modulus (GPa)	Poisson's ratio	σ_Y (MPa)	K (MPa)
71	0.33	135.3	576.79

Cubic shape functions are used in the global and local domains for both anayses using the GFEM and $GFEM^{\text{g-l}}$. The surface crack is discretized by Heavyside and singular Westergaard functions obtained from two-dimentional linear elastic fracture mechanics solutions. Although singular Westergaard functions do not describe nonlinear stress distribution around the crack front accurately, they can at least describe a crack opening in the element partially cut by the crack surface. In the global problem enriched with nonlinear local solutons, the surface crack is represented by the local solution.

Figure 7 shows the nonlinear load-displacement history obtained by the GFEM and $GFEM^{\text{g-l}}$. The linear elastic GFEM solution is also included in the figure for comparison purpose. Nonlinear solutions deviate from the linear elastic solution as loading increases. The solution obtained by the $GFEM^{\text{g-l}}$ exhibits a good agreement with the one by GFEM. The small differences between the nonlinear GFEM and $GFEM^{\text{g-l}}$ solutions at intermediate loading steps are expected because the nonlinear local solution enrichment is customized for the final loading step as discussed in Section 2.2. Figure 8 illustrates the deformed shape of the domain with a small surface crack obtained by the GFEM and $GFEM^{\text{g-l}}$ at the final loading step. The color in the figure represents the vertical displacement distrubution. It demonstrates that the $GFEM^{\text{g-l}}$ can achieve almost the same level of accuracy as the $GFEM^{\text{g-l}}$ even though much coarser global mesh is employed and linear elastic material law is used in the initial global problem to provide boundary conditions to local problems.

Table 2 lists the number of degrees of freedom used in the global and local problem and the number of iterations taken at each loading step. Abbreviation G and L in the table represent global and local problem, respectively. This result sheds some light on the possible cost reduction that can be achieved by using the $GFEM^{\text{g-l}}$. In the analysis by the $GFEM^{\text{g-l}}$, 19,836 and 18,744 degrees of freedom are used in the global and local problem respectively, while GFEM requires 37,104 degrees of freedom. The table indicates that the total numbers of iterations required for the two approaches are 19 and 20, which are almost the same. Thus, the $GFEM^{\text{g-l}}$ requires less amount of computational cost than GFEM and the difference in the cost between the two approaches would be more significant as more local problems are created in the domain.

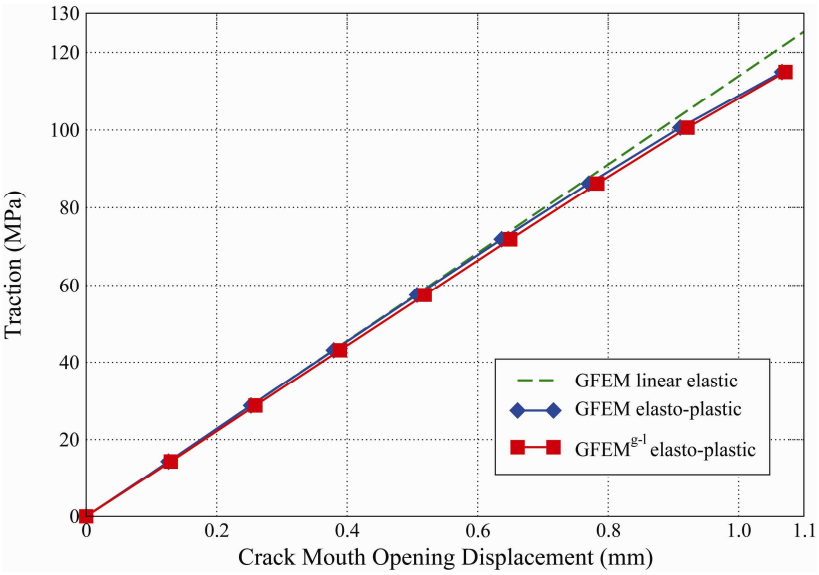

Figure 7: Nonlinear load-displacement history of the surface crack example.

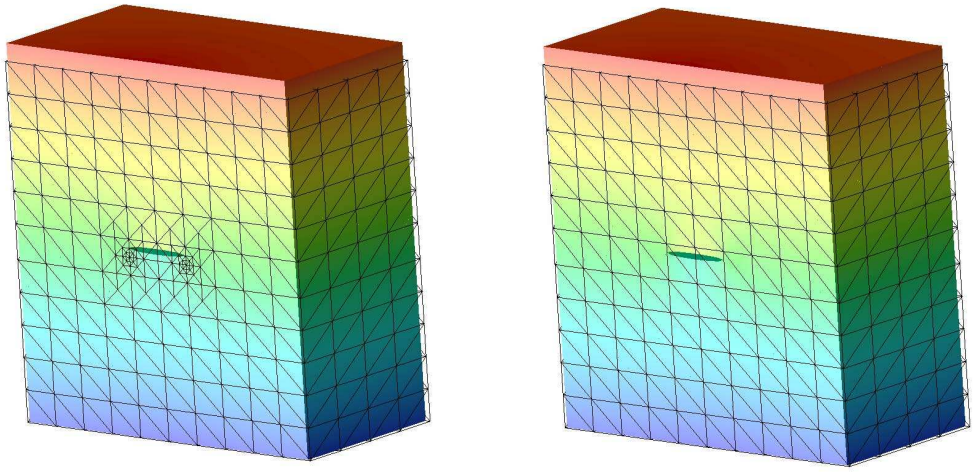

(a) Solution by the GFEM.

(b) Solution by the $GFEM^{g\text{-}l}$.

Figure 8: Deformed shape of the domain with a small surface crack.

Table 2: Number of iterations required at each loading step.

	Number of degrees of freedom			Number of iterations		
Load step	GFEM (G)	$GFEM^{g\text{-}l}$ (L)	$GFEM^{g\text{-}l}$ (G)	GFEM (G)	$GFEM^{g\text{-}l}$ (L)	$GFEM^{g\text{-}l}$ (G)
1				1		1
2				2		1
3				2		2
4	37,104	18,744	19.836	2	4	2
5				3		2
6				3		2
7				3		3
8				3		3
			Total	19	4	16

5 Conclusions

In this paper, we applied the GFEM with global-local enrichment function presented in [3, 25] to analyze nonlinear fracture mechanics problems based on J_2 plasticity theory. Our focus is on the problems where nonlinear behavior is confined to a small region of the domain and this class of problems can be very efficiently solved by the $GFEM^{g\text{-}l}$. The main conclusions of the analysis presented in this paper can be summarized as follows:

- The $GFEM^{g\text{-}l}$ allows the numerical construction of enrichment functions for problems exhibiting local nonlinear behavior where no a priori knowledge is known about their solutions, thus it brings the benefits of the existing generalized FEM to a broader class of problems.
- The $GFEM^{g\text{-}l}$ allows no crack discretization in the global domain while keeping the accuracy of solutions. A single coarse mesh can be used for any complex crack configuration.
- The numerical examples presented in Section 4 show that the $GFEM^{g\text{-}l}$ can provide nonlinear solutions almost as accurate as those obtained by the GFEM with reduced amount of computational cost.

References

[1] Oden, J.T. & Duarte, C.A.M., Chapter: Solution of singular problems using *hp* clouds. *The Mathematics of Finite Elements and Applications– Highlights 1996*, ed. J.R. Whiteman, John Wiley & Sons: New York, NY, pp. 35–54, 1997.

[2] Sukumar, N., Chopp, D., Moës, N. & Belytschko, T., Modeling holes and inclusions by level sets in the extended finite element method. *Computer Methods in Applied Mechanics and Engineering*, **190**, pp. 6183–6200, 2001.

[3] Duarte, C.A. & Kim, D.J., Analysis and applications of a generalized finite element method with global-local enrichment functions. *197*, **(6-8)**, pp. 487–504, 2008. Http://dx.doi.org/10.1016/j.cma.2007.08.017.
[4] Duarte, C.A. & Babuška, I., A global-local approach for the construction of enrichment functions for the generalized fem and its application to propagating three-dimensional cracks. *ECCOMAS Thematic Conference on Meshless Methods*, eds. V.M.A. Leitão, C.J.S. Alves & C.A. Duarte, Lisbon, Portugal, 2005. 8 pages.
[5] Tanaka, K., Mechanics and micromechanics of fatigue crack propagation. *Fracture Mechanics: Perspectives and Directions (Twentieth Symposium)*, eds. R.P. Wei & R.P. Gangloff, American Society for Testing and Materials: Philadelphia, ASTM STP 1020, pp. 151–183, 1989.
[6] Babuška, I. & Melenk, J.M., The partition of unity finite element method. *International Journal for Numerical Methods in Engineering*, **40**, pp. 727–758, 1997.
[7] Duarte, C.A., Babuška, I. & Oden, J.T., Generalized finite element methods for three dimensional structural mechanics problems. *Computers and Structures*, **77**, pp. 215–232, 2000.
[8] Oden, J.T., Duarte, C.A. & Zienkiewicz, O.C., A new cloud-based *hp* finite element method. *153*, pp. 117–126, 1998.
[9] Strouboulis, T., Copps, K. & Babuška, I., The generalized finite element method. *Computer Methods in Applied Mechanics and Engineering*, **190**, pp. 4081–4193, 2001.
[10] Babuška, I., Caloz, G. & Osborn, J.E., Special finite element methods for a class of second order elliptic problems with rough coefficients. *SIAM Journal on Numerical Analysis*, **31(4)**, pp. 745–981, 1994.
[11] Melenk, J.M. & Babuška, I., The partition of unity finite element method: Basic theory and applications. *Computer Methods in Applied Mechanics and Engineering*, **139**, pp. 289–314, 1996.
[12] Duarte, C.A.M. & Oden, J.T., Hp clouds–A meshless method to solve boundary-value problems. Technical Report 95-05, TICAM, The University of Texas at Austin, 1995.
[13] Duarte, C.A.M. & Oden, J.T., An *hp* adaptive method using clouds. *1996*, **139**, pp. 237–262.
[14] Duarte, C.A.M. & Oden, J.T., *Hp* clouds—An *hp* meshless method. *1996*, **12**, pp. 673–705.
[15] Duarte, C.A., *The hp Cloud Method*. PhD dissertation, The University of Texas at Austin, 1996. Austin, TX, USA.
[16] Moës, N., Dolbow, J. & Belytschko, T., A finite element method for crack growth without remeshing. *International Journal for Numerical Methods in Engineering*, **46**, pp. 131–150, 1999.
[17] De, S. & Bathe, K.J., The method of finite spheres. *Computational Mechanics*, **25**, pp. 329–345, 2000.
[18] Griebel, M. & Schweitzer, M.A., A particle-partition of unity method for the solution of elliptic, parabolic and hyperbolic PDEs. *SIAM Journal on Scientific Computing*, **22(3)**, pp. 853–890, 2000.
[19] Duarte, C.A. & Babuška, I., Mesh-independent directional *p*-enrichment using the generalized finite element method. *2002*, **55(12)**, pp. 1477–1492. Http://dx.doi.org/10.1002/nme.557.
[20] Duarte, C.A., Hamzeh, O.N., Liszka, T.J. & Tworzydlo, W.W., A generalized finite element method for the simulation of three-dimensional dynamic crack propagation. *2001*, **190(15-17)**, pp. 2227–2262. Http://dx.doi.org/10.1016/S0045-7825(00)00233-4.
[21] Babuška, I., Ihlenburg, F., Paik, E. & Sauter, S., A generalized finite element method for solving the Helmholtz equation in two dimensions with minimal pollution. *Computer Methods in Applied Mechanics and Engineering*, **128(3–4)**, pp. 325–360, 1995.
[22] Melenk, J.M., *On Generalized Finite Element Methods*. Ph.D. thesis, The University of Maryland, 1995.
[23] Simone, A., Duarte, C.A. & van der Giessen, E., A generalized finite element method for polycrystals with discontinuous grain boundaries. *2006*, **67(8)**, pp. 1122–1145. Http://dx.doi.org/10.1002/nme.1658.
[24] Strouboulis, T., Copps, K. & Babuška, I., The generalized finite element method: An example of its

implementation and illustration of its performance. *International Journal for Numerical Methods in Engineering*, **47(8)**, pp. 1401–1417, 2000.

[25] Duarte, C.A., Kim, D.J. & Babuška, I., Chapter: A global-local approach for the construction of enrichment functions for the generalized fem and its application to three-dimensional cracks. *Advances in Meshfree Techniques*, eds. V.M.A. Leitão, C.J.S. Alves & C.A. Duarte, Springer: The Netherlands, volume 5 of *Computational Methods in Applied Sciences*, 2007. ISBN 978-1-4020-6094-6.

[26] Babuška, I., Banerjee, U. & Osborn, J.E., Survey of meshless and generalized finite element methods: A unified approach. *Acta Numerica*, **12**, pp. 1–125, 2003.

[27] Pereira, J.P., Duarte, C.A., Guoy, D. & Jiao, X., *Hp*-Generalized FEM and crack surface representation for non-planar 3-D cracks. *2008*. Http://dx.doi.org/10.1002/nme.2419.

[28] Pereira, J.P., Duarte, C.A., Jiao, X. & Guoy, D., Generalized finite element method enrichment functions for curved singularities in 3D fracture mechanics problems. Submitted.

[29] Felippa, C.A., Introduction to finite element methods., 2004. Course Notes. Department of Aerospace Engineeing Sciences, University of Colorado at Boulder. Available at http://www.colorado.edu/engineering/Aerospace/CAS/courses.d/IFEM.d.

[30] Fish, J., The s-version of the finite element method. *Computers and Structures*, **43**, pp. 539–547, 1992.

[31] Park, J.W., Hwang, J.W. & Kim, Y.H., Efficient finite element analysis using mesh superposition technique. *Finite Elements in Analysis and Design*, **39**, pp. 619–638, 2003.

[32] Simo, C., J & Hughes, T.J., *Computational Inelasticity*. Prentice-Hall, 1998.

[33] Düster, A., *High order finite elements for three-dimensional thin walled nonlinear continua*. Ph.D. thesis, Technische Universität München, 2001.

A theoretical poro-elasto-visco-plastic model for mechanical and chemo-mechanical deformation in sedimentary basins

Samir Maghous
Universidade Federal do Rio Grande do Sul, Porto Alegre/RS – Brazil

Abstract

Intergranular pressure-solution (IPS) represents a major mechanism of deformation in sedimentary basins during diagenesis. The aim of the present contribution is to provide a comprenhensive 3D framework for modeling both mechanical and chemo-mechanica compaction is sedimentary basins. Extending concepts, previously proposed for the modeling of purely mechanical compaction in finite poroplasticity, deformation by IPS is addressed by means of additional vicoplastic terms in the state equations of the porous material. Resorting to both micromechanical reasonings and phenomenological arguments, the primary focus is on the analysis of the effects of large irreversible porosity changes on the poromechanical properties of the sediment material. The last part of the paper is intended to illustrate, through the analysis of a simplified compaction model, the main features of the proposed theoretical constitutive model.

Keywords: sedimentary basin, chemo-mechanical compaction, Intergranular Pressure-Solution, poroplasticity, poroviscoplasticity.

1 Introduction

Simulation of sedimentary basins is a complex multidisciplinary problem involving geological, chemical and mechanical aspects. Due to potential applications in the field of geoscience, which include petroleum exploration, reserve assessment and production, reconstructing the stress and deformation history of a sedimentary basin still remain a challenging and important problem in geoscience. In this context, compaction behavior of sediments material is one of the key elements controlling the sedimentary basin deformation, such as diagenetic densification, poromechanichal properties evolution over geological time and its implications on the reservoir formation to hydrocarbon production.

Actually, the mechanical response of a sedimentary basin is the consequence of complex processes involving mechanical, geochemical, geophysical and geological aspects. As far as the mechanical analysis at the macrocopic scale is concerned, two principal deformation mechanisms contribute to the compaction of sediments: (1) purely-mechanical compaction which originates mainly from rearrangement

Mechanics of Solids in Brazil 2009, H.S. da Costa Mattos & Marcílio Alves (Editors)
Brazilian Society of Mechanical Sciences and Engineering, ISBN 978-85-85769-43-7

of the solid particles during burial, and (2) chemo-mechanical compaction resulting from intergranular dissolution-precipitation mechanisms, generally induced by stress and referred to as pression-solution [1–3]. Purely mechanical phenomena prevail in the upper layers, whereas chemical compaction dominates for deeper burial as stress and temperature increase (e.g. Schmidt and McDonald [4]).

The paper deals with the theoretical modeling of both mechanical and chemo-mechanical compaction in sedimentary basins.

As regards mechanical compaction, the basic models are still based on phenomenological relationships relating porosity to effective vertical stress. At this respect, one may refer to Bernaud *et al.* [5] where a review of the state of art on this topic is given. Furthermore, a 3D constitutive model was formulated in the framework of finite poroplasticity, extending previous ideas to a more comprenhensive description of the mechanics involved in basin simulation.

Evidencies from both field and laboratory studies have confirmed that intergranular pressure-solution (IPS) represents an important mechanism of bulk deformation and porosity change. It is a key aspect of deformation in sedimentary basins during diagenesis. From a schematic point of view, IPS mechanism may be described as follows. Dissolution and diffusion occur at the grain-to-grain contacts subject to elevated stress, precipitation occurs at the free pore walls. The net result is compaction of the grains and porosity reduction, which in turn implies a decrease in permeability. Dissolution and precipitation processes are expected to produce time-dependent compaction creep and play therefore a crucial role as far as compaction of sediments over geological time periods is concerned.

Creep deformation resulting from IPS has widely been investigated since it has been identified as an important mechanism of rock deformation in the upper crust. The driving force for this deformation is the difference in effective stress between grain contacts and free pore walls. Two models have been basically proposed for IPS mechanisms in fluid saturated media, namely the "thin water film" model and the "island & channel" model (see for instance the review article by Hellmann *et al.* [6]). They both assume that the grain-to-grain contacts contain a trapped fluid which cannot be squeezed out by applied stress [7]. Both of these models are based on three material transfer processes occurring in series: dissolution of solid material at stressed grain-to-grain contacts, diffusion of dissolved material through the intergranular fluid, and precipitation on pore walls. The slowest of the three serial processes controls the overall deformation. It is primarily the physical nature of the intergranular regions that differentiates these two models. The "thin water film" is based on the presence of a continuous thin film of viscous fluid at grain-to-grain contacts [7, 8]. The "island & channel" model posits an intergranular region consisting of solid-solid contacts at islands that support the imposed stresses. These islands are surrounded by a network of interconnected channels containg fluid (e.g., Raj [9]; Lehner [10], Schutjens and Spiers [11]).

At the macroscopic scale, the intergranular pressure-solution phenomena are classically addressed in the constitutive equations by means of viscous terms. This kind of approach will be adopted in this work.

The paper is organized as follows. Section 2 describes the micromechanics-based constitutive model for the sedimentary model within the finite poro-visco-plasticity framework. Special attention is devoted to the influence of microstructure modifications on the poromechanicals properties of the sediment material. The principle of finite element implementation is then briefly presented. In section

Mechanics of Solids in Brazil 2009, H.S. da Costa Mattos & Marcílio Alves (Editors)
Brazilian Society of Mechanical Sciences and Engineering, ISBN 978-85-85769-43-7

3, the main features of the proposed constitutive equations are illustrated through the analysis of simplified compation model which is intended to represents the represents the local response of the sediment particle under oedometric conditions of compaction.

2 Theoretical aspects

During compaction process, the sediment material is subjected to large volumetric strains resulting in a significative porosity reduction, exceeding in some basins 50% as burial goes [12]. In turns, this porosity change affects the physical and mechanical properties of the sediment material. In addition to the constitutive non-linearitie, a comprenhensive modeling of the basin response should thus also take into account both the geometric non-linearities induced by large strains. In this context, a 3D constitutive model for sediment materials has been formulated within the framework of finite poroplasticity in a recent paper by Bernaud *et al.* [5]. Disregarding chemical aspects, this constitutive modeling was dedicated to purely mechanical compaction in sedimentary basins. At many aspects, this contribution represented an appreciable improvment with respect to predecessor works which are mainly formulated within a 1D setting, basically through phenomenological relationships relating porosity to effective vertical stress The purpose of this section is to provide a mechanical framework aiming to extend the model proposed in Bernaud *et al.* [5] in order to account for both mechanical and chemo-mechanical compaction.

2.1 Constitutive equations

At the macroscopic scale, the intergranular pressure-solution phenomena are classically addressed in the constitutive equations by means of viscous terms (see for example Laubsher [13], Fletcher [14], Schneider *et al.* [15, 16], Schneider and Hay [17] or Lehner and Leroy [18], to cite a few). The fundamental idea consists in relating measured strain rates resulting from dissolution-precipitation mechanisms induced by stress to porosity change. Assuming a phenomenological relationship (proportionality under certains conditions) between the latter and the vertical effective stress, a viscous law type is therefore derived for chemo-mechanical compaction.

The sedimentary rock is modelled as a fully saturated poro-elasto-visco-plastic material undergoing large strains. The anisotropy induced be compaction on the mechanical properties of the sediment material is disregarded. In addition, the elastic part of the deformation gradient of the skeleton particles is assumed to remain infinitesimal. Large strains involved during compaction process are only of irreversible nature.

The constitutive behavior formulated in Bernaud *et al.* [5] was based on the theoretical framework of finite poroplasticity proposed in Dormieux and Maghous [19, 20] and Bernaud *et al.* [21]. The above mentioned formulation is extended herein to finite poro-visco-plasticity. Denoting by $\underline{\underline{\sigma}}$ and p respectively the Cauchy stress tensor and the pore pressure, the first state equation relates the stress rate $\dot{\underline{\underline{\sigma}}}$ and pore pressure rate $\dot{p}$ to the strain rate tensor $\underline{\underline{d}}$. The proposed form for the first state equation writes

$$\frac{D_J \underline{\underline{\sigma}}'^e}{Dt} = \dot{\underline{\underline{\sigma}}}'^e + \underline{\underline{\sigma}}'^e \cdot \underline{\underline{\Omega}} - \underline{\underline{\Omega}} \cdot \underline{\underline{\sigma}}'^e = \underset{\sim}{c} : (\underline{\underline{d}} - \underline{\underline{d}}^{ir}) + \dot{\underset{\sim}{c}} : \underset{\sim}{c}^{-1} : \underline{\underline{\sigma}}'^e \tag{1}$$

Mechanics of Solids in Brazil 2009, H.S. da Costa Mattos & Marcílio Alves (Editors)
Brazilian Society of Mechanical Sciences and Engineering, ISBN 978-85-85769-43-7

where $\underline{\underline{d}}^{ir}$ stands for the irreversible strain rate

$$\underline{\underline{d}}^{ir} = \underline{\underline{d}}^{p} + \underline{\underline{d}}^{vp} \tag{2}$$

$\underline{\underline{d}}^{p}$ (resp. $\underline{\underline{d}}^{vp}$) is the plastic (resp. viscoplastic) strain rate, while $\underline{\underline{\Omega}}$ is the rotation (spin) rate tensor which aims at taking the large rotation of the elementary volume into account. This equation involves a rotational time derivative D_J/Dt of the Biot effective stress tensor $\underline{\underline{\sigma}}'^{e} = \underline{\underline{\sigma}} + b\, p\, \underline{\underline{1}}$, where b is the Biot coefficient. It also includes a term relatd to the particulate derivative $\dot{\underset{\sim}{c}}$ of the tensor of drained elastic moduli $\underset{\sim}{c}$, which aims at capturing the evolution of the elastic properties with the microstructural changes due to large irreversible strains.
Relationship (1) represents a generalization of the rate form formulation provided in Bernaud *et al.* [5].
In view of the derivation of the second state equation which relates the pore volume change to the rate $\dot{p}$ of the pore pressure and to the strain rate $\underline{\underline{d}}$, it is convenient to introduce the jacobian J of the transformation of the elementary volume, defined as the ratio between its volume in the current configuration and its initial one. Similarly, the irreversible part J^{ir} of the jacobian is defined as the jacobian in the unloaded configuration of the elementary volume. It my be split into its plastic part $\dot{J}^{p}$ and viscoplastic one $\dot{J}^{vp}$. The rates of these jacobians are given by

$$\dot{J} = J\,\mathrm{tr}\underline{\underline{d}} \quad ; \quad \dot{J}^{\alpha} = J^{\alpha}\,\mathrm{tr}\underline{\underline{d}}^{\alpha} \quad \text{with} \quad \alpha \in \{ir,\, p,\, vp\} \tag{3}$$

Let us denote by ϕ the lagrangian porosity in the current configuration of the elementary volume and by ϕ^{ir} the lagrangian porosity in the corresponding unloaded configuration. Starting from the rate form derived in finite poroplasticity by Bernaud *et al.* [21], the second state equation is generalized as

$$\dot{p} = M\left(-b\,\mathrm{tr}(\underline{\underline{d}} - \underline{\underline{d}}^{ir}) + \frac{\dot{\phi} - \dot{\phi^{ir}}}{J^{ir}}\right) + \frac{\dot{M}}{M}\,p - M\dot{b}\,\mathrm{tr}(\underset{\sim}{c}^{-1} : \underline{\underline{\sigma}}'^{e}) \tag{4}$$

M is the Biot modulus. The terms involving $\dot{M}$ and $\dot{b}$ in (4) are related to the influence of large irreversible strains on the poroelastic properties.

The complementary equations prescribe the flow rule during the irreversible transformation of the elementary volume. Within the present framework, the latter deals with the irreversible strain rate $\underline{\underline{d}}^{ir}$ and with the rate of the irreversible part of the lagrangian porosity $\dot{\phi}^{ir}$. As regards the plastic strain rate, we introduce a plastic potential $g^{p}(\underline{\underline{\sigma}}')$ depending on $\underline{\underline{\sigma}}$ and p through the so-called Terzaghi effective stress $\underline{\underline{\sigma}}' = \underline{\underline{\sigma}} + p\,\underline{\underline{1}}$:

$$\underline{\underline{d}}^{p} = \dot{\chi}\,\frac{\partial g^{p}}{\partial \underline{\underline{\sigma}}'} \tag{5}$$

where $\dot{\chi}$ is a non-negative plastic multiplier.
The time-dependent (viscoplastic) component of the strain rate is formulated adopting the following

generalized viscoplasticity model [22]:

$$\underline{\underline{d}}^{vp} = \frac{1}{\eta} \left\langle f^{vp}(\underline{\underline{\sigma}}', \zeta) \right\rangle^n \frac{\partial g^{vp}}{\partial \underline{\underline{\sigma}}'} \tag{6}$$

where η is the viscosity coefficient, n the viscosity exponent, f^{vp} the viscoplastic yield function, $g^{vp}(\underline{\underline{\sigma}}')$ the viscoplastic potential and ζ the set of hardening variables. It should be recalled that the presure-solution deformation described by the viscoplastic component $\underline{\underline{d}}^{vp}$ of the strain is generally addressed in basin engineering by means of by explicit relationships of the from (see for instance Raj [9]; de Meer and Spiers, [23, 24] or Zhang and Spiers [25])

$$\underline{\underline{d}}^{vp} = \mathcal{F}(\underline{\underline{\sigma}}') \tag{7}$$

where expression of $\mathcal{F}$ depends on the rate-limiting process during intergarnular pressure-solution and incorporate microstructural data of the sedimentary material as well as temperature and physical properties of the solute in the itergranular regions. Actually, these models attempt to account in a simplified way for available measures obtained from laboratory tests which are generally performed in a 1D setting. The ingredients of the theoretical model described by (6), should therefore be consistent with the above mentioned experiment-based models.

It should be emphazised that the theoretical descriptions of the process of intergranular pressure solution in terms of creep laws can explain features such as grain-size dependence of creep rates. However as pointed out in Lehner [26], a significant shortcoming of the creep laws proposed in the litterature is their limited applicability to macroscopically closed systems, with no solution transfer over long range transport in the pore fluid phase, as may be expected during diagenesis or metamorphism [27].

Since the irreversible part of the strain rate is given by (2), the conjunction of the plastic and viscoplastic flow rules (5) and (6) achieve the prescription of the the flow rule (direction) for $\underline{\underline{d}}^{ir}$.

To complete the formulation of the flow rule, we need to precise the flow rule for the rate of irreversible porosity $\dot{\phi}^{ir}$. A simple way to achieve this formulation relies upon the assumption of incompressibility of the solid phase during the irreversible transformation of the elementary volume. This implies that the irreversible part of the pore volume change is equal to the total volume change and yields identity $\dot{\phi}^{ir} = \dot{J}^{ir}$. Owing to (3), it is further obtained that

$$\dot{\phi}^{ir} = J^{ir} \operatorname{tr} \underline{\underline{d}}^{ir} \tag{8}$$

which indicates that the flow rule for $\dot{\phi}^{ir}$ stems directly from the flow rules (5) and (6). It is worth noting that because the irreversible strains in a sedimentry basin reduce to plastic strains in the upper layers, incompressibilty of the solid phase during the irreversible transformation of the sediment particles means either plastic or viscoplastic incompressibility.

The above model requires to specify:

• the dependence of the elastic moduli $\underset{\sim}{\dot{c}}$ as well as the poroelatic coefficients M and b on large irreversible strains;

• the influence of large irreversible strains on the plastic and viscoplastic properties of the sedimentary material.

These issues are addressed in the next section within the similar framework adopted in Bernaud *et al.* [5].

2.2 Poromechanics properties versus microstructural changes

The question of the influence of large plastic strains on the poro-elastic and plastic properties of the sediment material has been amply investigated in Dormieux and Maghous [20], Bernaud *et al.* [21] and Deudé *et al.* [28].

Since incompressiblity is assumed for the solid matrix in the irreversible range, large irreversible strain are expected to induce significant sigificant porosity and pore shape changes. A micromechanics-based reasoning is used in order to capture the influence of the plastic strains on the poroelastic properties. In the subsequent analysis, the anisotropy induced during compaction process is disregarded. This means that the pore space is entirely characterized by its volume fraction in the current configuration of the representative elementary volume, namely the eulerian or classical porosity $\varphi = \phi/J$. The Hashin-Shtrikman upper bounds which are adopted as estimates for the elastic properties of the isotropic porous media. Accordingly, the bulk K and shear μ moduli of the porous medium appear as functions of the porosity as well as of the elastic properties of the solid phase:

$$K(\varphi) = \frac{4k^s\mu^s(1-\varphi)}{3k^s\varphi + 4\mu^s} \quad ; \quad \mu(\varphi) = \frac{\mu^s(1-\varphi)(9k^s+8\mu^s)}{k^s(9+6\varphi)+\mu^s(8+12\varphi)} \tag{9}$$

where k^s and μ^s are bulk and shear moduli of the solid phase. It is recalled that the Biot coefficient and modulus are connected to K through

$$b(\varphi) = 1 - \frac{K(\varphi)}{k^s} \quad \text{and} \quad \frac{1}{M(\varphi)} = \frac{b(\varphi)-\varphi}{k^s} \tag{10}$$

In a second step, the porosity change will be connected to the irreversible strain underogone by the porous material. It can be first observed that the condition of incompressibility of the solid constituent during the irreversible transformation of the elementary volume reads

$$J^{ir} - \phi^{ir} = 1 - \varphi_o \tag{11}$$

where φ_o denotes the initial value of the porosity. In the framework of infinitesimal elastic strains, it is possible to neglect the variation of the pore volume and that of the total volume between the loaded and the unloaded configurations of the elementary volume, since these variations are reversible by definition. This justifies the following approximations

$$J^{ir} \approx J \quad ; \quad \phi^{ir} \approx \phi \tag{12}$$

Introducing (12) into (11) yields :

$$\varphi \approx 1 - \frac{1-\varphi_o}{J} \approx 1 - \frac{1-\varphi_o}{J^{ir}} \tag{13}$$

Mechanics of Solids in Brazil 2009, H.S. da Costa Mattos & Marcílio Alves (Editors)
Brazilian Society of Mechanical Sciences and Engineering, ISBN 978-85-85769-43-7

In view of (13), Eqs. (9) show that the macroscopic stiffness tensor $\underset{\sim}{c}$ is a function of the (total or irreversible) jacobian : $\underset{\sim}{c} = \underset{\sim}{c}(J^{ir})$. The same conclusion holds for the poroelastic coefficients b and M. Neglecting the induced anisotropy therefore amounts to consider that the elastic-plastic coupling is only governed by the plastic volumetric strains.

We deal now with the evolution of plastic properties of the sediment material. As regards the plastic yield surface f corresponds to the standard modified Camm-Clay (e.g., Muir Wood [29]):

$$f(\underline{\underline{\sigma}}' = \underline{\underline{\sigma}} + p\underline{\underline{1}}\,,\, p_c) = \frac{3}{2}\underline{\underline{s}} : \underline{\underline{s}} + M_{cs}^2\, p'(p' + p_c) \tag{14}$$

where $\underline{\underline{s}} = \underline{\underline{\sigma}} - \frac{1}{3}\,\mathrm{tr}\,\underline{\underline{\sigma}}\;\underline{\underline{1}}$ is the deviatoric stress tensor, $p' = \frac{1}{3}\,\mathrm{tr}\,\underline{\underline{\sigma}}'$ is the mean effective stress. p_c is the consolidation pressure and represents the hardening parameter of the model. The constant M_{cs} represents the slope of the critical state line. The plastic flow rule is associated, i.e. $g = f$.
It is assumed in the sequel that the shape of the yield locus is not affected by large irreversible strains. In contrast, the hardening law, that is the influence of large irreversible strains on the consolidation pressure, is a crucial feature of the model. In the framework of finite poroplasticity, a micromechanics-based model for the hardening law has been proposed by Deudé *et al.* [28], and implemented later by Bernaud *et al.* [5]. Unlike the classical Cam-Clay hardening law, the micromechanics-based one avoids the development of negative porosities under high isotropic compression. We adopt in the sequel the heuristic approach which consists first, in considering that only the plastic part of the irreversible strains affect the parameter p_c, and then, that the same law can reasonably model the hardening law within the present framework, which is characterized by both plastic and viscoplastic strains. Accordingly

$$p_c(J^p) = \frac{p_{co}}{\ln \varphi_o}\,\ln\left(1 - \frac{1-\varphi_o}{J^p}\right) \tag{15}$$

As regards the viscoplastic properties, the simple way to proceed is to adopt or extend the phenomenological models which are schematically described by (7). Indeed, these models already account in some extent for the morphology of the sediment microstructure through the value of porosity. Clearly enough, there is still a need for a comprehensive micromechanical approach specifically devoted to the formulation of a viscous law for deformation by pressure-solution. In this context, works had already been developed in the objective to relate, for specific microstructures, the macroscopic viscous behavior to the chemical phenomena occuring at a smaller scale (see for instance Lehner [26]; Renard *et al.* [30]; Ghoussoub and Leroy [31]).

3 A simplified compaction model

This section is intended to illustrate the main features of the theoretical model proposed in the previous sections, as well as its capabilities to simulate the stress and deformation of the sediment material during burial. A simplified framework is adopted for this purpose.

3.1 Statement of the problem and basic assumptions

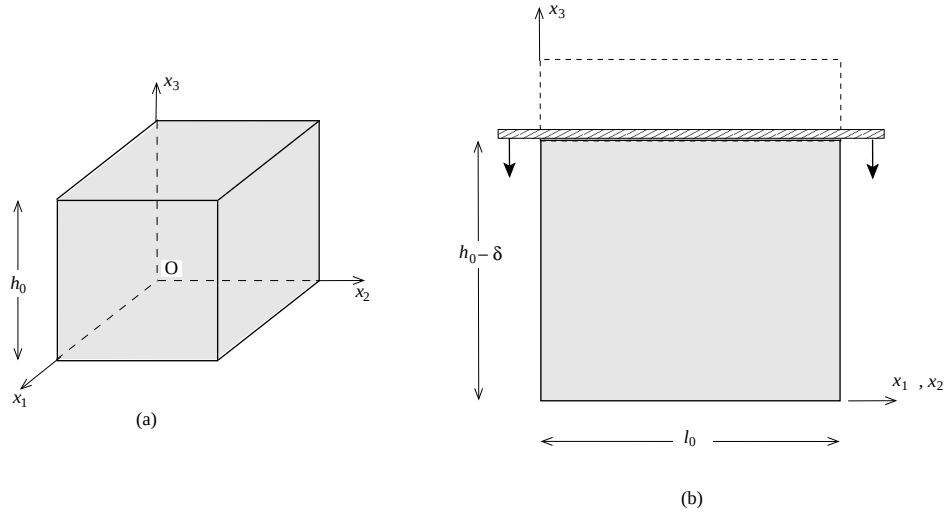

Figure 1: Geometry and loading of the simplified model

The geometry of the representative elementary volume (r.e.v) of the sedimentary material is depicted in Fig. 1a. In its initial configuration, the r.e.v is a parallelepipedic domain Ω_0 of high h_0 and horizontal sides transversal l_0. The r.e.v refers herein to the macroscopic particle of the sediment material which is undergoing compaction during burial. The loading of the r.e.v consists in one-dimensional compressive sollicitation, i.e., oedometric compression, as indicated in Fig. 1b. The vertical faces parallel to direction $\underline{e}_3$ ares kept in contact with smooth and fixed walls, while the lower and upper horizontal are placed between two rigid and smooth rams. The lower one is kept fixed whereas the upper one has a downwards vertical displacement of magnitude $\delta > 0$. In terms of displacement, the boundary conditions read as follows:

$$\begin{cases} \xi_i = 0 & \text{on the vertical faces } x_i = 0,\ l_0 \\ \xi_3 = 0 & \text{on the lower face} \\ \xi_3 = -\delta & \text{on the upper face} \end{cases} \tag{16}$$

The value of the displacement δ imposed to the r.e.v accounts in some extent for the depth level of the particle within the sedimentary basin. Indeed, the quantity $\Lambda = 1 - \delta/h_0$ represents the vertical stretch of the particle, which is obviously related to the depth within the basin. In other words, the response of the r.e.v for increasing values of δ is supposed to simulate the stress and deformation of particles located at increasing depths along the basin.

Mechanics of Solids in Brazil 2009, H.S. da Costa Mattos & Marcílio Alves (Editors)
Brazilian Society of Mechanical Sciences and Engineering, ISBN 978-85-85769-43-7

The problem is treated in drained conditions (no overpressure). The material assumptions will be decribed in the sequel. The constitutive material of the r.e.v is homogeneous with isotropic elastic, plastic and viscous mechanical properties. Besides, effects of large strains on these properties, such as stiffness increase and hardening induced by large plastic volumetric strains, are disregarded [20, 28]. Accordingly, the elastic Lamé coefficients λ and μ are in particular considered as constant.

Plasticity is modeled by a simplified cap model with associated flow rule, where the straight-line corresponding to positive hardening is defined by

$$f^p(\underline{\underline{\sigma}}, p_c) = -\frac{1}{3}\mathrm{tr}\,\underline{\underline{\sigma}} - p_c \tag{17}$$

p_c is identical to the consolidation pressure of the Cam-Clay model (e.g. Muir Wood [29]; Charlez [32]). In addition, the hardening modulus $m = -\mathrm{d}p_c/\mathrm{d}J^p$ is taken constant (i.e., linear variations of p_c with respect to the plastic volumetric strains):

$$p_c(J^p) = m\,(1 - J^p) + p_{co} \tag{18}$$

p_{co} is the initial value of p_c. If plastic yielding occurs, the plastic part of the strain rate writes

$$\underline{\underline{d}}^p = \dot{\chi}\,\frac{\partial f^p}{\partial \underline{\underline{\sigma}}} = -\frac{\dot{\chi}}{3}\,\underline{\underline{1}} \tag{19}$$

As regards the viscous behavior, which macroscopically models the effects of pressure-solution phenomena, a simplified viscoplastic criterion similar to that controlling plasticity is adopted:

$$f^{vp}(\underline{\underline{\sigma}}) = -\frac{1}{3}\mathrm{tr}\,\underline{\underline{\sigma}} - p_{vp} \tag{20}$$

Unlike p_c, the viscoplastic threshold p_{vp} is assumed as constant. In addition, its value complies with condition

$$p_{vp} > p_{co} \tag{21}$$

in order to ensure that only plastic compaction occurs for moderate values of the loading δ (i.e., in the upper layers of the sedimentary basin). The corresponding viscoplastic strain rate is derived from the "thin water film" model [33]. If diffusion is the rate-limiting process, the strain rate resulting from intergranular pressure-solution is classically taken as [25, 34]

$$\underline{\underline{d}}^{vp} = \frac{3}{\eta}\left\langle\, f^{vp}(\underline{\underline{\sigma}})\,\right\rangle \frac{\partial f^{vp}}{\partial \underline{\underline{\sigma}}} = \frac{1}{\eta}\left(\frac{1}{3}\mathrm{tr}\,\underline{\underline{\sigma}} + p_{vp}\right)\underline{\underline{1}} \quad \text{if} \quad f^{vp}(\underline{\underline{\sigma}}) \geq 0 \tag{22}$$

where $\langle\, X\,\rangle = \frac{X+|X|}{2}$ is the positive value of the scalar X, and η is the viscosity coefficient of the sediment. It incorporates the different fundamental parameters governing the creep law for pressure-solution (see for instance Rutter [7, 8]; Durney [35]), such as the characteristic grain size, the diffusitivity of the solute in the grain contact or the equlibrium concentration of the dissolved solid in the pore fluid. This macroscopic viscosity is taken as constant in the present analysis. It should however be observed that a more realistic modeling should in particular account for the effects of temprature

[1, 16] and of the microstructural changes due to large irreversible strains.

This simplified framework obviously corresponds to a highly academic situation. It should be recalled that the purpose herein is only to provide a qualitatif insight on the reltive contribution of both the mechanical and mechano-chemical compaction on the local evolution of the stresses and strains.

3.2 Stress and strain in the r.e.v: elasto-visco-plastic analysis

Starting from $\delta = 0$ at time $t = 0$, the loading process of the r.e.v consists in prscribing the continuously increasing function $t \longrightarrow \delta(t)$ (i.e., $\dot{\delta}(t) > 0$). The initial state of stress in the r.e.v is natural: $\underline{\underline{\sigma}}(t = 0) = 0$. The mechanical response of the r.e.v is determined in the sequel at any stage of the compaction level δ/h_0. Under oedometric loading, the strain rate is homogeneous in the r.e.v and reads

$$\underline{\underline{d}} = d\,\underline{e}_3 \otimes \underline{e}_3 \quad \text{with} \quad d = -\frac{\dot{\delta}/h_0}{1 - \delta/h_0} \tag{23}$$

and the jacobian of the associated transformation of the r.e.v, which characterizes the volume change of the r.e.v is $J = 1 - \delta/h_0$. The rate form of the constitutive equation reduces to

$$\dot{\underline{\underline{\sigma}}} = 2\mu\,(\underline{\underline{d}} - \underline{\underline{d}}^{ir}) + \lambda\,\mathrm{tr}\,(\underline{\underline{d}} - \underline{\underline{d}}^{ir})\,\underline{\underline{1}} \tag{24}$$

A) Infinitesimal elastic response: $0 \leq \delta \leq \delta^e$ $(0 \leq t \leq t^e)$

Because of the elastic strains are assumed to remain infinitesimal, this phase corresponds to a small range of the loading $\delta \leq \delta^e \ll h_0$, where the expression of the elastic limit δ^e will be specified below. In basin engineering practice, purely elastic compaction prevails along a very thin upper layer, and should not therefore affect the global response of the whole basin.

In the elastic range $\underline{\underline{d}}^{ir} = 0$, the stress reads

$$\underline{\underline{\sigma}} = \sigma\,\left[\,\lambda\,(\underline{e}_1 \otimes \underline{e}_1 + \underline{e}_2 \otimes \underline{e}_2) + (\lambda + 2\mu)\,\underline{e}_3 \otimes \underline{e}_3\,\right] \quad \text{with} \quad \sigma = \ln(1 - \delta/h_0) \simeq -\delta/h_0 \tag{25}$$

The conjunction of (17), (20) and condition (21) implies that plasticity occurs at the end of the elastic phase. This means that the elastic phase holds for interval $t \in [0\,,\ t^e]$ such that

$$\delta(t^e) = \delta^e \quad \text{with} \quad \frac{\delta^e}{h_0} = \left(1 - \exp\frac{-p_{co}}{K}\right) \simeq \frac{p_{co}}{K} \tag{26}$$

where $K = \lambda + 2\mu/3$ is the elastic bulk modulus. At the end of this elastic phase, the stress is

$$\underline{\underline{\sigma}}(t^e) = \underline{\underline{\sigma}}^e = -\frac{p_{co}}{K}\,\left[\,\lambda\,(\underline{e}_1 \otimes \underline{e}_1 + \underline{e}_2 \otimes \underline{e}_2) + (\lambda + 2\mu)\,\underline{e}_3 \otimes \underline{e}_3\,\right] \tag{27}$$

Time $t = t^e$ characterizes the end of the elastic phase and the activation of plasticity.

B) Elasto-plastic response: $\delta^e \leq \delta \leq \delta^p$ ($t^e \leq t \leq t^p$)

In this situation $t \geq t^e$, $\underline{\underline{d}}^{ir} = \underline{\underline{d}}^p$ is given by (19). It comes from (25) and the consistency condition $\dot{f}^p = 0$ the following expression for the plastic multiplier

$$\dot{\chi} = \frac{\dot{\delta}/h_0}{(1-\delta/h_0)(1+mJ^p/K)} \geq 0 \tag{28}$$

Owing to (28), relation $\dot{J}^p = J^p \operatorname{tr} \underline{\underline{d}}^p$ leads a differential equation governing the evolution of J^p

$$\frac{\dot{J}^p}{J^p} + \frac{m}{K}\dot{J}^p + \frac{\dot{\delta}/h_0}{1-\delta/h_0} = 0 \tag{29}$$

which solution is

$$J^p(\delta) = \frac{K}{m}\,\mathrm{W}\left(\frac{m}{K}\,\frac{1-\delta/h_0}{1-\delta^e/h_0}\,\exp\frac{m}{K}\right) = \frac{K}{m}\,\mathrm{W}\left(\frac{m}{K}\,(1-\delta/h_0)\,\exp\frac{m+p_{co}}{K}\right) \tag{30}$$

where $\mathrm{W}(x)$ is the LambertW function defined by $\mathrm{W}(x)\,\exp \mathrm{W}(x) = x$. It is recalled that this function satisfies $\mathrm{W}(x\,\exp x) = x$.

The stress field within the r.e.v results from the integration of the constitutive equation (24)

$$\underline{\underline{\sigma}} = \underline{\underline{\sigma}}^e + m\,(J^p-1)\,\underline{\underline{1}} + 2\mu\left(\ln(1-\delta/h_0) + \frac{p_{co}}{K}\right)\left[\,\underline{e}_3\otimes\underline{e}_3 - \frac{1}{3}\,\underline{\underline{1}}\right] \tag{31}$$

$J^p = J^p(\delta)$ being given by (30). This elasto-plastic phase prevails as long as $f^p(\underline{\underline{\sigma}},\, p_c) \leq f^{vp}(\underline{\underline{\sigma}})$. This condition may be expressed by

$$p_c = p_{co} - m\,(J^p-1) \leq p_{vp} \tag{32}$$

whic by virtue of (30) leads to

$$\delta(t) \;\leq\; \delta(t^p) = \delta^p \qquad \text{with} \quad \frac{\delta^p}{h_0} = 1 - \left(1 - \frac{p_{vp}-p_{co}}{m}\right)\,\exp\frac{-p_{vp}}{K} \tag{33}$$

The end of the phase is chraracterized by the following strain and stress related quantity values:

$$J^p(t^p) = J^p(\delta^p) = 1 - \frac{p_{vp}-p_{co}}{m} \quad ; \quad p_c(\delta^p) = p_{vp} \tag{34}$$

$$\underline{\underline{\sigma}}(t^p) = \underline{\underline{\sigma}}(\delta^p) = \underline{\underline{\sigma}}^e - (p_{vp}-p_{co})\,\underline{\underline{1}} + 2\mu\left(\ln(1-\frac{p_{vp}-p_{co}}{m}) - \frac{p_{vp}-p_{co}}{K}\right)\left[\,\underline{e}_3\otimes\underline{e}_3 - \frac{1}{3}\,\underline{\underline{1}}\right] \tag{35}$$

Time $t = t^p$ corresponds to characterizes the end of the elasto-plastic elastic phase and appearance of viscous strains.

C) Elasto-visco-plastic phase: $\delta^p \leq \delta \leq \delta^{vp}$ ($t^p \leq t \leq t^{vp}$)

If the loading is continued beyond δ^p, the v.e.r will *a priori* undergo viscoplastic strains due to pressure-solution phenomenon. In this case, $\underline{\underline{d}}^{ir} = \underline{\underline{d}}^{p} + \underline{\underline{d}}^{vp}$. The plastic and viscoplastic parts of the irerversible strain rate are given respectively by (19) and (22). Introducing (19), (22) and (23) into the constitutive equation (24) leads to

$$\operatorname{tr} \dot{\underline{\underline{\sigma}}}/3 = K \left(-\frac{\dot{\delta}/h_0}{1-\delta/h_0} + \dot{\chi} - \frac{3}{\eta} \left(\operatorname{tr} \underline{\underline{\sigma}}/3 + p_{vp} \right) \right) \tag{36}$$

On the other hand, the plastic condition $f^p = 0$ implies that $\operatorname{tr} \underline{\underline{\sigma}} = -3\, p_c$ while the consistency condition $\dot{f}^p = 0$ reads

$$\operatorname{tr} \dot{\underline{\underline{\sigma}}}/3 = -\dot{p}_c = m\, \dot{J}^p = m\, J^p \operatorname{tr} \underline{\underline{d}}^p = -m\, J^p\, \dot{\chi} \tag{37}$$

The combination of (36) and (37) yields

$$\dot{\chi} = \frac{1}{1 + mJ^p/K} \left(\frac{\dot{\delta}/h_0}{1-\delta/h_0} - \frac{3}{\eta} \left(p_c - p_{vp} \right) \right) \tag{38}$$

Observing that the beginning of the phase corresponds to $p_c(t^p) - p_{vp} = 0$, (38) indicates that the plastic flow rule $\dot{\chi} \geq 0$ is satisfied at $t = t^p$. Consequently, provided that the compaction rate $\dot{\delta}/h_0$ remains positive, there will exist a non-empty time interval $t^p \leq t \leq t^{vp}$ such that the plastic flow rule shall be fulfilled. Clearly enough, the quantity $p_c(t) - p_{vp}$ is an increasing function during this time interval.
Eq. (38) and the identity $\dot{\chi} = -\dot{J}^p/J^p$, which can readily be deduced from (37), lead to

$$\frac{\dot{J}^p}{J^p} + \frac{m}{K} \dot{J}^p - \frac{3}{\eta} \left(p_c - p_{vp} \right) + \frac{\dot{\delta}/h_0}{1-\delta/h_0} = 0 \tag{39}$$

By substituting expression (18) of $p_c = p_c(J^p)$ in the above equation, one obtains the differential equation governing the evolution in time of the plastic jacobian

$$\frac{\dot{J}^p}{J^p} + \frac{m}{K} \dot{J}^p + \frac{3\,m}{\eta} J^p - \frac{3}{\eta} \left(p_{co} + m - p_{vp} \right) + \frac{\dot{\delta}/h_0}{1-\delta/h_0} = 0 \tag{40}$$

It is recalled that $t \longrightarrow \delta(t)$ which defines the loading of the v.e.r is prescribed. Except for very particular situations, no closed-form solution of (40) can be derived and a numerical procedure is therefore necessary to solve this differential equation. This may be achieved by making use, for instance, of the software Maple.

Mechanics of Solids in Brazil 2009, H.S. da Costa Mattos & Marcílio Alves (Editors)
Brazilian Society of Mechanical Sciences and Engineering, ISBN 978-85-85769-43-7

Interestingly, a direct integration of (40) between $t = t^p$ (starting of the elasto-visco-plastic regime) and the current time t yields

$$\begin{aligned}\frac{3\,m}{\eta}\int_{t^p}^{t} J^p(\tau)\,\mathrm{d}\tau = \quad & \frac{3\,(p_{co}+m-p_{vp})}{\eta}\,(t-t^p) + \ln\frac{1-\delta(t)/h_0}{1-\delta(t^p)/h_0} \\ & - \ln\frac{J^p(t)}{J^p(t^p)} - \frac{m}{K}\left(J^p(t) - J^p(t^p)\right)\end{aligned} \tag{41}$$

with $J^p(t^p)$ and $\delta(t^p)$ given respectively by (33) and (34). The interest of (41) lies in fact that it provides an alternative way to compute numerically the unknown $t \longrightarrow J^p(t)$. This can simply be achieved through the discretization of interval $[t^p,\, t]$ and evaluating the term integral in (41) by means of a numerical integration. If, for instance, the trapezoidal rule is adopted together with the time discretization $t_0 = t^p$, ..., $t_i = t_{i-1} + \Delta t$ (the time increment Δt is choosen constant), it can readily be shown that

$$J^p(t_i) = \frac{1}{\frac{m}{K} + \frac{3m}{2\eta}\Delta t}\,\mathrm{W}\left(\left[\frac{m}{K} + \frac{3m}{2\eta}\Delta t\right]\,\exp(\mathcal{F}_i)\right) \tag{42}$$

where

$$\begin{aligned}\mathcal{F}_i = \quad & \frac{3\,(p_{co}+m-p_{vp})}{\eta}\,i\,\Delta t \,+\, \ln\frac{1-\delta(t_i)/h_0}{1-\delta(t_0)/h_0} \,+\, \ln J^p(t_0) \,+\, \left(\frac{m}{K} - \frac{3m}{2\eta}\Delta t\right)\,J^p(t_0) \\ & -\frac{3m}{\eta}\Delta t\,\sum_{k=1}^{i-1} J^p(t_k)\end{aligned} \tag{43}$$

Whatever the option choosen to handle with (40), $J^p(t)$ and consequently $p_c(t)$ by virtue of (18), can theoretically be considered as known at the end of the resolution procedure. The plastic multiplier $\dot\chi$ can thus be calculated from (38) as well as the plastic strain rate $\underline{\underline{d}}^p = -\dot\chi/3\,\underline{\underline{1}}$. Finally, the expression of the viscous strain rate $\underline{\underline{d}}^{vp} = \frac{1}{\eta}\left(\frac{1}{3}\mathrm{tr}\,\underline{\underline{\sigma}} + p_{vp}\right)\,\underline{\underline{1}}$ is deduced from condition $f^p = 0$ which implies that $\mathrm{tr}\,\underline{\underline{\sigma}}/3 = -p_c$.

To complete the analysis, the stress field should also be evaluatued during this regime. It comes from the constitutive equation (24) that

$$\dot{\underline{\underline{\sigma}}} = d\,\left(2\,\mu\,\underline{e}_3\otimes\underline{e}_3 + \lambda\,\underline{\underline{1}}\right) + K\,\left(\dot\chi + \frac{3}{\eta}\,(p_c - p_{vp})\right) \tag{44}$$

where (19), (22) and (23) have been used. The final expression for the stress rate is derived by combining the above equation with (37) and (38)

$$\dot{\underline{\underline{\sigma}}} = m\,\dot J^p\,\underline{\underline{1}} + 2\,\mu\,d\,\left[\underline{e}_3\otimes\underline{e}_3 - \frac{1}{3}\,\underline{\underline{1}}\right] \quad \text{with} \quad d = -\frac{\dot\delta/h_0}{1-\delta/h_0} \tag{45}$$

Integration of the above equation between t^p and the current time t yields

$$\underline{\underline{\sigma}}(t) = \underline{\underline{\sigma}}(t^p) + m\ (J^p(t) - J^p(t^p))\ \underline{\underline{1}} + 2\,\mu\,\ln\left(\frac{1-\delta(t)/h_0}{1-\delta(t^p)/h_0}\right)\left[\underline{e}_3\otimes\underline{e}_3 - \frac{1}{3}\underline{\underline{1}}\right] \tag{46}$$

in which $\delta(t^p)$ is given by (33), $J^p(t^p)$ by (34) and $\underline{\underline{\sigma}}(t^p)$ by (35).

This phase holds as long as the coexistence of plastic $\underline{\underline{d}}^p \neq 0$ and viscoplastic $\underline{\underline{d}}^{vp} \neq 0$ strain rates is compatible with the plastic flow rule, that is, with the positivity of the plastic multiplier. Consequently, the end of this regime coincides with time t^{vp} where condition $\dot{\chi} \geq 0$ ceases to be valid. Accordingly,

$$\dot{\chi}(t^{vp}) = 0 \implies p_c(t^{vp}) = p_{vp} + \frac{\eta}{3}\,\frac{\dot{\delta}(t^{vp})/h_0}{1-\delta(t^{vp})/h_0} \tag{47}$$

As $t \longrightarrow \delta(t)$ is prescribed and function $p_c(t)$ can be computed once $J^p(t)$ is determined, Eq. (47) can theoretically be solved with respect to t^{vp}. Mathematically, the existence of an effective solution t^{vp} will obviously depend on both material and loading characteristics.

At time $t = t^{vp}$, the v.e.r switches from the elaso-visco-plastic regime ($\underline{\underline{d}}^{ir} = \underline{\underline{d}}^p + \underline{\underline{d}}^{vp}$) to the elasto-viscoplastic regime ($\underline{\underline{d}}^{ir} = \underline{\underline{d}}^{vp}$). It should be observed from (18) and (47) that

$$J^p(t^{vp}) = J^p(\delta^{vp}) = 1 - \frac{p_{vp} - p_{co}}{m} - \frac{\eta}{3\,m}\,\frac{\dot{\delta}(t^{vp})/h_0}{1-\delta(t^{vp})/h_0} \tag{48}$$

where $\delta^{vp} = \delta(t^{vp})$. Clearly enough, one should check wether the following restrictions are fulfilled: $J^p(t^{vp})$ remains positive and lower than $J^p(t^p)$ characterizing the initial value of the plastic jacobian during the current phase. Owing to (34) and (48), one obtains from (46)

$$\underline{\underline{\sigma}}(t^{vp}) = \underline{\underline{\sigma}}(\delta^{vp}) = \underline{\underline{\sigma}}(t^p) - \frac{\eta}{3}\,\frac{\dot{\delta}(t^{vp})/h_0}{1-\delta(t^{vp})/h_0}\,\underline{\underline{1}} + 2\,\mu\,\ln\left(\frac{1-\delta(t^{vp})/h_0}{1-\delta(t^p)/h_0}\right)\left[\underline{e}_3\otimes\underline{e}_3 - \frac{1}{3}\underline{\underline{1}}\right] \tag{49}$$

D) Elasto-viscoplastic phase: $\delta^{vp} \leq \delta$ ($t^{vp} \leq t$)

Provided that $J^p(t^{vp}) \in]\,0,\ J^p(t^p)[$, this situation occurs if the loading δ is pursued beyond δ^{vp}. The v.e.r undergoes purely elasviscoplastic strains ($\underline{\underline{d}}^{ir} = \underline{\underline{d}}^{vp}$). In other terms, no additional plastic strain appears in the v.e.r after $t = t^{vp}$ (i.e., $\underline{\underline{d}}^p = 0$). This means in particular that $\dot{J}^p(t) = 0$ for $t^{vp} \leq t$, which in turn implies identity $\dot{p}_c(t) = 0$. In reason of the particular form (17) of the plasticity criterion, the situation of plastic unloading (i.e., $\dot{f}^p < 0$) would imply condition $\mathrm{tr}\,\dot{\underline{\underline{\sigma}}} > 0$, which is physically

irrelevant in the perspective of sedimentary basins modeling. We therefeore adopt the assumption that the v.e.r does not experience any unloading process during this phase. Consequently,

$$\dot{f}^p = -\frac{1}{3}\mathrm{tr}\,\underline{\underline{\dot{\sigma}}} - \dot{p}_c = 0 \implies \mathrm{tr}\,\underline{\underline{\dot{\sigma}}} = 0 \quad \forall\, t \geq t^{vp} \tag{50}$$

During this phase, each one of the quantities J^p, p_c and $\mathrm{tr}\,\underline{\underline{\sigma}}$ keeps a constant value, equal to that reached at $t = t^{vp}$. Hence,

$$\mathrm{tr}\,\underline{\underline{\sigma}}(t) = -3\,p_c(t^{vp}) = -3\,p_{vp} - \eta\,\frac{\dot{\delta}(t^{vp})/h_0}{1-\delta(t^{vp})/h_0} \tag{51}$$

and

$$\underline{\underline{d}}^{vp}(t) = \underbrace{-\frac{1}{3}\,\frac{\dot{\delta}(t^{vp})/h_0}{1-\delta(t^{vp})/h_0}\,\underline{\underline{1}}}_{\frac{1}{3}\,d(t^{vp})\,\underline{\underline{1}}} \tag{52}$$

The constitutive equation (24) reduces to

$$\underline{\underline{\dot{\sigma}}} = d(t)\,\left(2\,\mu\,\underline{e}_3\otimes\underline{e}_3 + \lambda\,\underline{\underline{1}}\right) - K\,d(t^{vp})\,\underline{\underline{1}} \tag{53}$$

The consistency with condition $\mathrm{tr}\,\underline{\underline{\dot{\sigma}}} = 0$ leads to the following restriction on the loading

$$d(t) = d(t^{vp}) \quad \text{or} \quad \frac{\dot{\delta}(t)/h_0}{1-\delta(t)/h_0} = \frac{\dot{\delta}(t^{vp})/h_0}{1-\delta(t^{vp})/h_0} \quad \forall\, t \geq t^{vp} \tag{54}$$

This restriction clearly emphasizes one of the shortcomings of the simplified model analyzed herein.

Integration of (53) between t^{vp} and t yields

$$\underline{\underline{\sigma}}(t) = \underline{\underline{\sigma}}(t^{vp}) - 2\,\mu\,\frac{\dot{\delta}(t^{vp})/h_0}{1-\delta(t^{vp})/h_0}\,(t-t^{vp})\,\left[\underline{e}_3\otimes\underline{e}_3 - \frac{1}{3}\,\underline{\underline{1}}\right] \tag{55}$$

3.3 Comments

The purpose herein is to summarize the previous results by analyzing a numerical example. The model parameter are taken as: Young modulus $E = 10^3$ MPa, Poisson's ratio $nu = 0.33$, $p_{c0} = 1$ MPa, hardening modulus $m = 100$ MPa, $p_{vp} = 10$ MPa, viscosity $\eta = 10$ MPa×My, where My stands for million years. The loading rate is constant and equal to $\dot{\delta} = 10$ m/My. Figure 2 displays the evolution in time of the jacobian J of the material transformation as well as its plastic part J^p. It is worth noting that the ratio J/J^p represents within the range $t \geq t^p \simeq 0.010$ My, a measure of the viscoplastic volumetric strains undergone by the material and which refers to the compaction induced by pressure-solution.

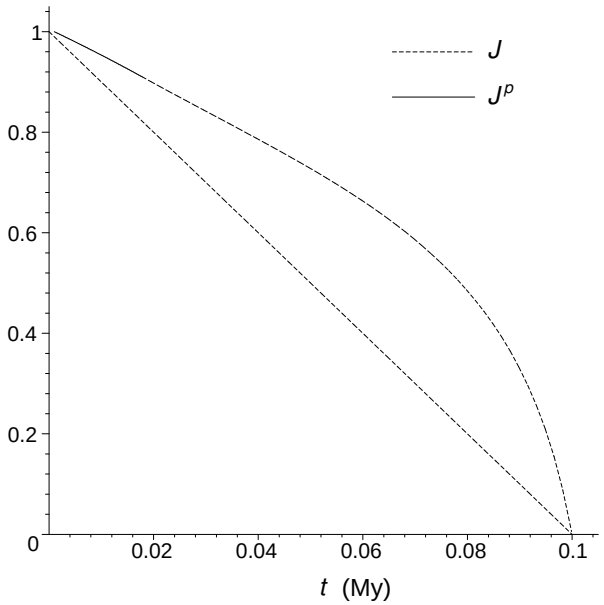

Figure 2: Transformation of the r.e.v.: time evolution of the total jacobian and its plastic part

As regards the stresses within the r.e.v, the variations of the vertical stress $\sigma_V = \sigma_{33}$ and of the horizontal stress $\sigma_H = \sigma_{11} = \sigma_{22}$ during the different phases of the macroscopic behavior are reported in Figure 3.

4 Conclusion

A 3D theoretical constitutive model has been formulated for sedimentary materials. It incorporates some of the fundamental coupled phenomena involved in the process of basin compaction by resorting to either micromechanical reasonings or phenomenological approaches. With respect to the previous work by Bernaud *et al.* [5], the main contribution lies in the fact the present model accounts for deformation by pressure-solution. Due to large porosity changes induced by compaction process, the model is formulated within the framework of large poro-visco-plasticity. Effect of large irreversible strains on the stiffness increase, on the hardening law as well as on the viscous law are accounted for through the reduction of the pore volume. The constitutive model is specifically devised for the sediment material subjected to mechanical or/and chemo-mechanical compaction.

The main features of the model have been illustrated through the analysis of a simplified compaction model. Depending on the loading level, different phases related to the response of the representative elementary volume could be predicted. The study was intended to provide a qualitative insight on

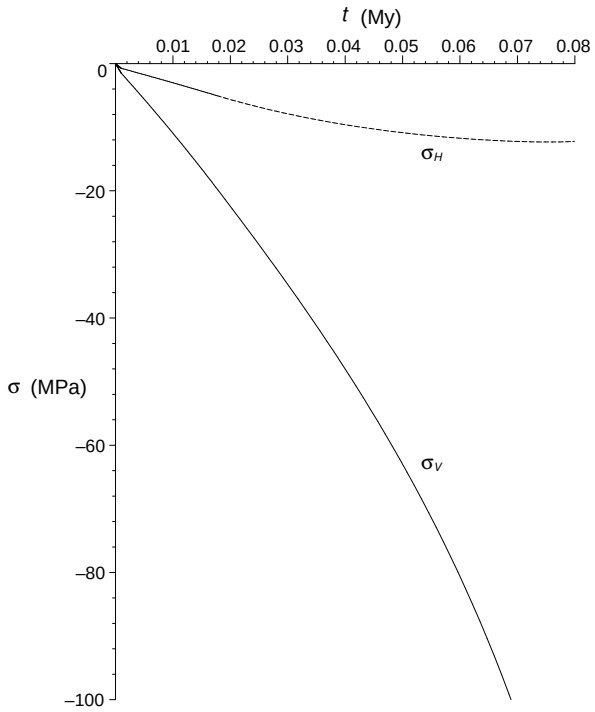

Figure 3: Evolution in time of the vertical and horizontal stresses in the r.e.v.

stress and deformation of the sediment material during burial.

The theoretical model is now being incorporated within a finite element tool dedicated to simulate sedimentary basins undergoing 2D evolutions. The extension to 3D situations such as that induced by tectonic loading is also one of the main issues to be forseen in the future.

Acknowledgements

The author is greatful for the financial support provided by CNPq (Brazil).

References

[1] Angevine, C.L. & Turcotte, D.L., Porosity reduction by model for quartz arenites pressure solution: A theoretical model for quartz arenites. *Geol Soc Am Bull*, **94**, pp. 1129–1134, 1983.

[2] Tada, R. & Siever, R., Pressure solution during diagenesis. *Ann Rev Earth Planet Sci*, **17**, pp. 89–118,

1989.
[3] Evans, B., Bernabé, Y. & Zhu, W., Evolution of pore structure and permeability of rocks in laboratory experiments. *Growth, Dissolution and Pattern Formation in Geosystems*, eds. B. Jamtveit & P. Meakin, Kluwer Academic Publishers: Dordrecht, The Netherlands, pp. 327–344, 1999.
[4] Schmidt, V. & Mc Donald, D.A., The role of secondary porosity in the course of sandstone diagenesis. *Aspects of diagenesis*, eds. P.A. Scholle & P.R. Schluger, Society of Economic paleontologists and Mineralogists Special Publication, volume 26, pp. 175–207, 1979.
[5] Bernaud, D., Dormieux, L. & Maghous, S., A constitutive and numerical model for mechanical compaction in sedimentary basins. *Computers and Geotechnics*, **33**, pp. 316–329, 2006.
[6] Hellmann, R., Renders, P.J.N., Gratier, J.P. & Guichet, R., Experimental pressure solution compaction of chalk in aqueous solutions. part 1. deformation behavior and chemistry. *Water-rock interaction, Ore Deposits, and Environmental Geochemistry*, eds. R. Hellmann & S.A. Wood, The Geochemical Society Special Publication, volume 7, pp. 129–152, 2002.
[7] Rutter, E.H., Pressure solution in nature, theory and experiment. *J Geol Soc London*, **140**, pp. 725–740, 1983.
[8] Rutter, E.H., The kinetics of rock deformation by pressure solution. *Phil Trans R Soc, London, Ser A*, **283**, pp. 203–219, 1976.
[9] Raj, R., Creep in polycrystalline aggregates by matter transport through a liquid phase. *J Geophys Res*, **87**, pp. 4731–4739, 1982.
[10] Lehner, F.K., Thermodynamics of rock deformation by pressure solution. *Deformation Process in Minerals, Ceramics and Rocks*, eds. D.J. Barber & P.G. Meredith, Unwin-Hyman: London, England, pp. 296–333, 1990.
[11] Schutjens, P.M.T.M. & Spiers, C.J., Intergranular pressure solution in NACl: grain-to-grain contact experiments under the optical microscope. *Oil & Gas Science and Technology - Revue de l'IFP*, **54**, pp. 729–750, 1999.
[12] Houseknecht, D.W., Assessing the relative importance of compaction processes and cementation to reduction of porosity in sandstones. *Am Assoc Petroleum Geologist Bull*, **71**, pp. 633–642, 1987.
[13] Laubsher, H.B., Viscous components in jura folding. *Tectonophysics*, **27**, pp. 239–254, 1975.
[14] Fletcher, R.C., Coupling of diffusional mass transport and deformation in tight rocks. *Tectonophysics*, **83**, pp. 275–292, 1982.
[15] Schneider, F., Potdevin, J.L., Wolf, S. & Faille, I., Modèle de compaction élastoplastique et viscoplastique pour simulateurs de bassins sédimentaires. *Oil & Gas Science and Technology - Revue de l'IFP*, **49**, pp. 141–148, 1994.
[16] Schneider, F., Potdevin, J.L., Wolf, S. & Faille, I., Mechanical and chemical compaction model for sedimentary basin simulators. *Tectonophysics*, **263**, pp. 307–317, 1996.
[17] Schneider, F. & Hay, S., Compaction model for quartzose sandstones application to the garn formation, haltenbanken, mid-norwegian continental shelf. *Marine Petrol Geol*, **18**, pp. 833–848, 2001.
[18] Lehner, F.K. & Leroy, Y.M., Sandstone compaction by intergranular pressure solution. *Mechanics of fluid-saturated rocks, Int. Geophys. Series*, eds. Y. Gueguen & M. Bouteca, Elsevier Academic press: London, England, pp. 115–168, 2004.
[19] Dormieux, L. & Maghous, S., Poroelasticity and poroplasticity at large strains. *Oil & Gas Science and Technology - Revue de l'IFP*, **54**, pp. 773–784, 1999.
[20] Dormieux, L. & Maghous, S., Evolution of elastic properties in finite poroplasticity. *C R Acad des Sci Paris*, **328(IIb)**, pp. 593–600, 2000.
[21] Bernaud, D., Deudé, V., Dormieux, L., Maghous, S. & Schmitt, D.P., Evolution of elastic properties in

finite poroplasticity and finite element analysis. *Int J Numer Anal Meth Geomech*, **26(9)**, pp. 845–871, 2002.
[22] Perzyna, P., Fundamental problems in viscoplasticity. *Adv Appl Mech*, **9**, pp. 243–277, 1966.
[23] De Meer, S. & Spiers, C.J., Uniaxial compaction creep of wet gypsum aggregates. *J Geophys Res*, **102**, pp. 875–891, 1997.
[24] De Meer, S. & Spiers, C.J., Mechanisms and kinetics of creep by intergranular pressure solution. *Growth, Dissolution and Pattern Formation in Geosystems*, eds. B. Jamtveit & P. Meakin, Kluwer Academic Publishers: Dordrecht, The Netherlands, pp. 345–363, 1999.
[25] Zhang, X. & Spiers, C.J., Compaction of granular calcite by pressure solution at room temperature and effects of pore fluid chemistry. *Int J Rock Mech Min Sci*, **42**, pp. 950–960, 2005.
[26] Lehner, F.K., A model for intergranular pressure solution in open systems. *Tectonophysics*, **245**, pp. 153–170, 1995.
[27] Dewers, T. & Ortoleva, P., Differentiated structures arising from mechano-chemical feedback in stressed rock. *Earth-Sci Rev*, **29**, pp. 283–298, 1990.
[28] Deudé, D., Dormieux, L., Maghous, S., Barthélémy, J.F. & Bernaud, D., Compaction process in sedimentary basins: the role of stiffness increase and hardening induced by large plastic strains. *Int J Numer Anal Meth Geomech*, **28**, pp. 1279–1303, 2004.
[29] Muir Wood, D.M., *Soil behavior and critical state soil mechanics*. Cambridge University Press: Cambridge, England, 1990.
[30] Renard, F., Park, A., Ortoleva, P. & Gratier, J.P., An integrated model for transitional pressure solution in sandstones. *Tectonophysics*, **312**, pp. 97–115, 1999.
[31] Ghoussoub, J. & Leroy, Y.M., Solid-fluid phase transformation within grain boundaries during compaction by pressure solution. *J Mech Phys Solids*, **49**, pp. 2385–2430, 2001.
[32] Charlez, P.A., *Rock Mechanics, vol. 2: Petroleum applications*. Technip: Paris, France, 1997.
[33] Tada, R., Maliva, R. & Siever, R., A new mechanism for pressure solution in porous quartzose sandstone. *Geochim Cosmochim Acta*, **51**, pp. 2295–2301, 1987.
[34] Shimizu, T., Kinetics of pressure solution creep in quartz: theoretical considerations. *Tectonophysics*, **245**, pp. 121–134, 1995.
[35] Durney, D.W., Early theories and hypotheses on pressure-solution-redeposition. *Geology*, **9**, pp. 419–424, 1978.

Shear bands: formulation, analysis and numerical simulations

Rosa María García Márquez
Departamento de Matemática. FFP-UERJ, Universidade Estadual do Rio de Janeiro, RJ – Brazil

Fernando Pereira Duda
Programa de Engenharia Mecânica. COPPE-UFRJ. Universidade Federal do Rio de Janeiro, RJ – Brazil

Ângela Cristina Cardoso de Souza
Departamento de Engenharia Mecânica. PGMEC-UFF, Universidade Federal Fluminense, RJ – Brazil

Abstract

This work deals with the formulation, analysis and computational simulation of non-local and rate dependent plasticity models in one dimensional set. In the formulation, described within the continuum mechanics scheme, the plastic deformation is viewed as an additional degree of freedom. The basic laws are: the principle of virtual power and inequality of dissipation. A thermodynamically consistent theory is developed, in which non-local and rate effects are accounted for by allowing constitutive dependence on the gradient and rate of plastic deformation. The governing equations are obtained after combining the basic balances with the constitutive theory. In particular, theories of plasticity with and without elastic region are obtained. A simplified version of the theory with elastic region is subject to a linear stability analysis in order to obtain instability criterion, a qualitative analysis showing that shear bands are associated with homoclinic (heteroclinic) orbit. A computational simulation based on the finite element method and an Euler implicit scheme and staggered algorithm is presented. The numerical results illustrate the accumulation of plastic deformation in narrow bands.

Keywords: non-local plasticity, shear bands, rate dependent plasticity, continuum mechanics.

1 Introduction

Nowadays there is a renewed interest in the study of the phenomenon of plasticity. This occurs because plastic deformation is a high dissipative problem and still remains not fully understood, and moreover, because of its importance in the study of the mechanical behavior of structural components.

Mechanics of Solids in Brazil 2009, H.S. da Costa Mattos & Marcílio Alves (Editors)
Brazilian Society of Mechanical Sciences and Engineering, ISBN 978-85-85769-43-7

There are an increasing interest in models which take into account effects not considered by the conventional theories, such as microstructure, non-local effects and rate dependence. These important issues are essential in the development of capable theories to represent the most diverse kinds of plastic instability, a phenomenon with a rich phenomenology classified as transients (momentary) or permanent (persistent), stationary or propagative. The most well known phenomena of instability are the shear bands, Lüders' bands and the effect of Portevin-Le Chatelier (PLC effect). The shear bands occur after a certain increase of flow plastic, the material exhibits a softening and may occur strain concentration in narrows bands, and once they take place they persist in the initial positions, and hence it is classified as stationary instability permanent [1, 2]. The Lüders' bands occur at a level of constant stress and are classified as propagative and transient instabilities [3, 4]. The PLC effect is associated with a negative strain rate, when a strain plastic is concentrated in narrow bands which propagate through the sample in pico-second or few hours. This phenomenon refers to instability in a form of repeated stress drops followed by periods of reloading, observed when tensile specimens are deformed in a certain range of strain rates and temperatures. It is classified as propagative and permanent instability [5–7]. There is an extensive literature about the diversity aspect of plasticity see for example Aifantis [8, 9], Gurtin [10], Anand et al. [11], Borst [4], Sikora et al. [12], Wang [1], Estrin [13], Kubin and Estrin [6].

To study the phenomenon of plastic instability in accordance with the formalism of modern continuum mechanics [14], we elaborate the framework by introducing the basic balances, the free energy imbalance and a theory constitutive. The plastic deformation is considered as an additional degree of freedom, and by introducing the plastic gradient deformation, we take into account non-local effects. We deduce the governing equations by considering microstructure processes and scale effect, within the scheme given by Duda and Souza [15]. In addition the forces pattern, micro forces were introduced with the assumptions of additive decomposition of the deformation into its elastic and plastic parts.

We consider as basic laws the principle of virtual work and the dissipation inequality, and combined with thermodynamic consistent constitutive theory, we obtain the equations which govern the plasticity theory. The balance of micro forces has resulted in two groups of kinetic laws and, with appropriate choice, some classical theories and different phenomenon of plasticity could be boarded. In the second part we carry out a qualitative analysis of the stationary problem to obtain an instability criterion, the size of localization zones and the propagation velocity of plastic waves. We look for special solutions, such as orbits which bound the points of saddle (homoclinic, heteroclinic), because they represent the localization zones of deformation connecting two constant states of different deformations. Finally we present the numerical results and illustrate the accumulations of plastic deformation in narrows bands.

2 Theoretical framework

2.1 Preliminaries

Let be B a one-dimensional body identified with the fixed interval $[0, L]$. We denote x an element or particle of B, and t a time instant. We denote $D := [x_1, x_2]$ one typical part of B. A generic quantity

of interest f is a regular function of x and t, with spatial and temporal derivates denoted by $f_x = \frac{\partial f}{\partial x}$ and $\dot{f} = \frac{\partial f}{\partial t}$ respectively.

The notation is showed in Table 1.

Table 1: Notation

t	time	ε	deformation	σ_{ext}	external stress
x	position	ε_e	elastic deformation	s_{int}	micro internal force
u	displacement	ε_p	plastic deformation	s_{ext}	micro external force
y	placement	σ	stress	σ_c	stress contact
v	macroscopic velocity	ξ	micro stress	ρ	the mass density per unit length

The longitudinal motion of B is described by a mapping:

$$y(x,t) := x + u(x,t) \tag{1}$$

In the micro processes, the micro kinematics is described by the elastic and plastic deformation with additive decomposition:

$$\varepsilon(x,t) = \varepsilon_e(x,t) + \varepsilon_p(x,t) \tag{2}$$

In the rate form: $\dot{\varepsilon}(x,t) = \dot{\varepsilon}_e(x,t) + \dot{\varepsilon}_p(x,t)$, where: $\dot{\varepsilon}(x,t) = \frac{\partial v(x,t)}{\partial x}$

By considering Eqs. (1) and (2) we conclude that two of the three fields y,ε_e and ε_p are independents. We consider y and ε_p as independent kinetically descriptor. We define $V := (v, v_p)$ the velocity field, $\mathbf{V}$ the virtual velocity space and $\bar{V} := (\bar{v}, \bar{v}_p)$ a generic element of $\mathbf{V}$, where $\bar{v}$ and $\bar{v}_p$ are the virtual velocities associated to display and plastic deformation respectively.

2.2 Basic laws

The principle of virtual power is used to generate the field equations and the boundary conditions, corresponding to the basic force balances. For any part $D \subset B$ and within a first-gradient theory, we adopt the following prescriptions for the virtual power of the external and internal forces expended on an arbitrary virtual velocity $\bar{v}$:

- Virtual power of the external forces:

$$P_{ext}(D, \bar{V}) := \int_{x_1}^{x_2} (\sigma_{ext}\bar{v} + s_{ext}\bar{v}_p)dx + \sum_{i=1}^{2} (\sigma_c(x_i)\bar{v}(x_i) + q(x_i)\bar{v}_p(x_i)) \tag{3}$$

where the smooth field σ_c and σ_{ext} describe contact and external forces; s_{ext} and q describe the external and contact micro force.

- Virtual power of the internal forces:

$$P_{\text{int}}(D,\bar{V}) := -\int_{x_1}^{x_2}\left(\sigma\frac{\partial\bar{v}}{\partial x}+\xi\frac{\partial\bar{v}_p}{\partial x}+s_{\text{int}}\bar{v}_p\right)dx \tag{4}$$

where the smooth field σ, ξ and s_{int} describe internal interactions.

In Eqs. (3) and (4) we introduce the system for macroscopic and microscopic forces. The macro force system, associated with y, is formed by the stress σ and contact force σ_c. The micro force system, associated with the microstructure (plastic deformation), is formed by the micro-stress ξ, internal and external micro forces (s_{ext} and s_{int}), and the contact micro force q.

The principle of virtual power [16] considers that for the each fixed time and part D:

$$P_{ext}(D,\bar{V})+P_{\text{int}}(D,\bar{V})=0 \tag{5}$$

By considering Eq. (3), (4) and (5), we have:

$$\int_{x_1}^{x_2}\left(-\sigma\frac{\partial\bar{v}}{\partial x}-\xi\frac{\partial\bar{v}_p}{\partial x}-s_{\text{int}}\bar{v}_p+\sigma_{ext}\bar{v}+s_{ext}\bar{v}_p\right)dx+\sum_{i=1}^{2}\left(\sigma_c\left(x_i\right)\bar{v}\left(x_i\right)+q\left(x_i\right)\bar{v}_p\left(x_i\right)\right)=0 \tag{6}$$

In the local form:

$$\begin{cases}\dfrac{\partial\sigma}{\partial x}+\sigma_{ext}=0\\[2ex] \dfrac{\partial\xi}{\partial x}+s_{ext}-s_{\text{int}}=0\end{cases}\qquad\qquad\begin{cases}\sigma(x_2)=\sigma_c(x_2), & \sigma(x_1)=-\sigma_c(x_1)\\ \xi(x_2)=q(x_2), & \xi(x_1)=-q(x_1)\end{cases} \tag{7}$$

We also consider as basic a mechanical version of the second law thermodynamics. Namely ψ the free energy per unit of length, we have:

$$\frac{d}{dt}\int_D\psi dx\leqslant P_{ext}(D,V) \tag{8}$$

for each part $D\subset B$. After using the principle virtual power, this version localizes into the dissipation inequality:

$$\dot{\psi}\leqslant\sigma\dot{\varepsilon}+\boldsymbol{s}_{\text{int}}\dot{\varepsilon}_p+\xi\dot{\boldsymbol{p}}=\sigma\dot{\varepsilon}_e+\pi\dot{\varepsilon}_p+\xi\dot{\boldsymbol{p}} \tag{9}$$

where $\boldsymbol{p}:=\frac{\partial\varepsilon_p}{\partial x}$ and $\pi:=\boldsymbol{s}_{\text{int}}+\sigma$

2.3 Constitutive theory

In the absence of internal links, the inequality of dissipation Eq. (9) suggests that constitutive prescriptions should be given for ψ, σ, ξ and π. We consider the list $(\varepsilon_e,\varepsilon_p,\dot{\varepsilon}_p,\boldsymbol{p})$ as the independent variables, i.e.:

$$\psi = \hat{\psi}(\mathbf{e}, \dot{\varepsilon}_p), \quad \sigma = \hat{\sigma}(\boldsymbol{e}, \dot{\varepsilon}_p), \quad \xi = \hat{\xi}(\boldsymbol{e}, \dot{\varepsilon}_p), \quad \pi = \hat{\pi}(\boldsymbol{e}, \dot{\varepsilon}_p) \tag{10}$$

where $\boldsymbol{e} := (\varepsilon_e, \varepsilon_p, \boldsymbol{p})$. These response functions are considered smooth, excepting $\hat{\pi}$. In the following case 1, $\hat{\pi}$ is smooth for parts (discontinuous in $\dot{\varepsilon}_p = 0$), and in the case 2, $\hat{\pi}$ is smooth everywhere (continuous on $\dot{\varepsilon}_p = 0$), and then, π is not constitutively determined when $\dot{\varepsilon}_p = 0$.

Using the procedure of Coleman-Noll [17] in the inequality (9), we get the following restrictions:

$$\frac{\partial \hat{\psi}}{\partial \dot{\varepsilon}_p} = 0, \quad \hat{\sigma} = \frac{\partial \hat{\psi}}{\partial \varepsilon_e}, \quad \hat{\xi} = \frac{\partial \hat{\psi}}{\partial p} \tag{11}$$

And, the response function $\hat{\pi}$ satisfies the reduced inequality:

$$\left(\hat{\pi} - \frac{\partial \hat{\psi}}{\partial \varepsilon_p} \right) \dot{\varepsilon}_p \geqslant 0 \tag{12}$$

Therefore, from Eq. (11), we have: $\psi = \hat{\psi}(\mathbf{e}), \sigma = \hat{\sigma}(\mathbf{e}), \xi = \hat{\xi}(\mathbf{e})$

By denoting $\hat{\pi}_d := \hat{\pi} - \frac{\partial \hat{\psi}}{\partial \varepsilon_p}$ in Eq. (12), the reduced inequality can be written as:

$$\hat{\pi}_d(\mathbf{e}, \dot{\varepsilon}_p).\dot{\varepsilon}_p \geqslant 0 \rightarrow \begin{cases} \hat{\pi}_d(\mathbf{e}, \dot{\varepsilon}_p) \geqslant 0 & \text{if} \quad \dot{\varepsilon}_p > 0 \\ \hat{\pi}_d(\mathbf{e}, \dot{\varepsilon}_p) \leqslant 0 & \text{if} \quad \dot{\varepsilon}_p < 0 \end{cases} \tag{13}$$

By considering the micro forces balance and the constitutive equations, we obtain the kinetic equation for the plastic deformation. In general we have:

$$\hat{\pi}_d(\mathbf{e}, \dot{\varepsilon}_p) = \hat{\boldsymbol{a}}(\mathbf{e}, \dot{\varepsilon}_p) + \hat{\boldsymbol{b}}(\mathbf{e}, \dot{\varepsilon}_p) \tag{14}$$

where:

$$\hat{\boldsymbol{a}}(\mathbf{e}, \dot{\varepsilon}_p) = \begin{cases} \boldsymbol{a}^+(\mathbf{e}) & \text{if} \quad \dot{\varepsilon}_p > 0 \\ \boldsymbol{a}^-(\mathbf{e}) & \text{if} \quad \dot{\varepsilon}_p < 0 \end{cases} \quad \hat{\boldsymbol{b}}(\mathbf{e}, \dot{\varepsilon}_p) = \begin{cases} \boldsymbol{b}^+(\mathbf{e}, \dot{\varepsilon}_p) & \text{if} \quad \dot{\varepsilon}_p > 0 \\ \boldsymbol{b}^-(\mathbf{e}, \dot{\varepsilon}_p) & \text{if} \quad \dot{\varepsilon}_p < 0 \end{cases} \tag{15}$$

The signals $(\pm)$ are dependent of the $\dot{\varepsilon}_p$ signal. We consider two cases: the case 1, with elastic region, and the case 2 without.

Case 1: With elastic region ($\hat{\boldsymbol{a}} \neq 0$).

This case is separated in two sub-cases:

Sub-case 1a: We consider a theory of plasticity rate independent, and then the kinetic equation is given by:

$$\hat{\sigma}(\mathbf{e}) - \left(\hat{\boldsymbol{a}}(\mathbf{e}, \dot{\varepsilon}_p) - \frac{\partial^2 \hat{\psi}}{\partial \boldsymbol{x} \partial \mathrm{p}} + \frac{\partial \hat{\psi}}{\partial \varepsilon_p} \right) = 0 \tag{16}$$

Sub-case 1b: We consider a theory of plasticity rate dependent, and then the kinetic equation is given by:

$$\hat{\boldsymbol{b}}(\mathbf{e},\dot{\varepsilon}_p) := \hat{\sigma}(\mathbf{e}) - \left(\hat{\boldsymbol{a}}(\mathbf{e},\dot{\varepsilon}_p) - \frac{\partial^2\hat{\psi}}{\partial \boldsymbol{x}\partial\mathbf{p}} + \frac{\partial\hat{\psi}}{\partial\varepsilon_p}\right), \quad \text{if } \dot{\varepsilon}_p \neq 0 \tag{17}$$

Case 2: Rate dependent, without elastic region ($\hat{\boldsymbol{a}} = 0$).

In this case the dissipative response function is smooth and thermodynamically ensures that $\hat{\pi}_d$ is zero when $\dot{\varepsilon}_p = 0$. In this case the micro forces balance provides directly the equation that governs the plastic deformation, without additional constitutive assumptions, thus:

$$\hat{\boldsymbol{b}}(\mathbf{e},\dot{\varepsilon}_p) := \sigma(\mathbf{e}) - \left(\frac{\partial\hat{\psi}}{\partial\varepsilon_p} - \frac{\partial^2\hat{\psi}}{\partial \boldsymbol{x}\partial\mathbf{p}}\right), \quad \text{if } \dot{\varepsilon}_p \neq 0 \tag{18}$$

Observation: By choosing adequately, the response functions $\hat{a}$ and $\hat{b}$ can represent some of the classic theories of plasticity, as for instance, different behavior in traction and compression, rate independence, perfectly plastic material, isotropic hardening, Perzynas' model, viscous-plastic regularization, effect of Baushinger, shear bands, effect of PLC and others.

2.4 Simplified model

In this simplified model we are interested in the **sub-case 1b**, when there is plastic deformation by traction, i.e., $\dot{\varepsilon}_p > 0$. Let us consider a bar, fixed at one end and tensioned at the other.

We consider the following free energy:

$$\psi(\mathbf{e}) = \frac{\boldsymbol{E}\varepsilon_e^2}{2} + \frac{\boldsymbol{c}}{2}\mathbf{p}^2 \tag{19}$$

where E is the Young module, and $\boldsymbol{c}$ is the diffusion coefficient related with the micro-scale displacement. The first term represents the strain energy, and the second term is the interface energy. In Eq. (17) we define $\hat{\boldsymbol{a}}(\mathbf{e}) = \boldsymbol{g}_o(\varepsilon_p), \hat{\boldsymbol{b}}(\mathbf{e},\dot{\varepsilon}_p) = \boldsymbol{g}_1(\dot{\varepsilon}_p), \boldsymbol{g}_1(0) = 0$, where $\boldsymbol{g}_o$ and $\boldsymbol{g}_1$ are smooth functions and differentiable in almost everywhere.

With these assumptions we have:

$$\begin{cases} \sigma = \boldsymbol{E}\varepsilon_e \\ \xi = \boldsymbol{c}\frac{\partial\varepsilon_p}{\partial\boldsymbol{x}} \end{cases} \tag{20}$$

Therefore the micro force balance is:

$$\boldsymbol{c}\frac{\partial^2\varepsilon_p}{\partial\boldsymbol{x}^2} + \sigma - \boldsymbol{g}_o(\varepsilon_p) - \boldsymbol{g}_1(\dot{\varepsilon}_p) = 0 \tag{21}$$

By considering the body force as inertial, the external force takes the form $\sigma_{ext} = -\rho\ddot{\boldsymbol{u}}$, with $\rho \geqslant 0$. From the balance laws and the above assumptions we have the following relations:

$$\begin{cases} \sigma = \boldsymbol{E}\varepsilon_e = \boldsymbol{E}(\varepsilon - \varepsilon_p) \\ \varepsilon = \varepsilon_e + \varepsilon_p \\ \dfrac{\partial \sigma}{\partial \boldsymbol{x}} = \rho \ddot{\boldsymbol{u}} \\ \boldsymbol{c}\dfrac{\partial^2 \varepsilon_p}{\partial x^2} - \boldsymbol{g}_o(\varepsilon_p) - \boldsymbol{g}_1(\dot{\varepsilon}_p) + \sigma = 0 \end{cases} \tag{22}$$

By taking the derivative of Eq. (22) $_1$, we have the following equations system:

$$\begin{cases} \boldsymbol{E}\left(\dfrac{\partial^2 \boldsymbol{u}}{\partial \boldsymbol{x}^2} - \dfrac{\partial \varepsilon_p}{\partial \boldsymbol{x}}\right) = \rho \ddot{\boldsymbol{u}} \\ \boldsymbol{c}\dfrac{\partial^2 \varepsilon_p}{\partial \boldsymbol{x}^2} - \boldsymbol{g}_o(\varepsilon_p) - \boldsymbol{g}_1(\dot{\varepsilon}_p) + \boldsymbol{E}\left(\dfrac{\partial \boldsymbol{u}}{\partial \boldsymbol{x}} - \varepsilon_p\right) = 0 \end{cases} \tag{23}$$

2.4.1 Qualitative analysis of the traction problem

Motivated by the work of Kubin et al. [6], Estrin [13], Brechet et al. [7], Coleman et al. [2] and Anand et al. [11], we consider a qualitative analysis of Eq. (23) in the quasi-static case. We start finding some trivial solutions. In this case, Eq. (23) is reduced to the nonlinear differential equation:

$$c\frac{\partial^2 \varepsilon_p}{\partial x^2} - g_o(\varepsilon_p) - g_1(\dot{\varepsilon}_p) + \sigma(t) = 0 \tag{24}$$

Trivial solutions

(a) There is a stationary uniform solution [2, 7, 14] of Eq. (24). Thus, the solution satisfies:

$$\boldsymbol{c}\frac{d^2 \varepsilon_{p_s}(\boldsymbol{x})}{d\boldsymbol{x}^2} - \boldsymbol{g}_o(\varepsilon_{p_s}(\boldsymbol{x})) + \sigma_0 = 0 \tag{25}$$

where σ_o is a constant prescribed stress.

(b) There is a steady state homogeneous solution [1, 6, 18] of Eq. (24). Thus, the solution satisfies:

$$\boldsymbol{g}_o(\varepsilon_{p_s}(\boldsymbol{t})) + \boldsymbol{g}_1(\dot{\varepsilon}_{p_s}(\boldsymbol{t})) - \sigma(\boldsymbol{t}) = 0 \tag{26}$$

(c) There is a stationary homogenous and uniform solution [1, 12] of Eq. (24) satisfying the relationship:

$$\boldsymbol{g}_o(\varepsilon_{p_s}) - \sigma_0 = 0 \tag{27}$$

2.4.2 Stability analysis

We analyze the plastic instability by linearizing Eq. (24) around a homogeneous state $\varepsilon_{p_s}(\boldsymbol{t})$. We consider solutions of the form: $\varepsilon_p(\boldsymbol{x}, \boldsymbol{t}) = \varepsilon_{p_s}(\boldsymbol{t}) + \delta\varepsilon_p$, where $\delta\varepsilon_p(\boldsymbol{x}, \boldsymbol{t}) = \delta\varepsilon_o e^{\boldsymbol{ikx}+\boldsymbol{\omega t}}$ is a small

perturbation, $\delta\varepsilon_o$ is the initial perturbation, $\boldsymbol{k}$ is the wave number and ω is the amplification rate or attenuation, that determines the growth or decline of the disturbance. By substituting this solution in Eq. (24), we have:

$$\left(\boldsymbol{s}\omega + \boldsymbol{h} + \boldsymbol{c}\boldsymbol{k}^2\right)\delta\varepsilon_p = 0, \quad \text{then } \omega = -\frac{\boldsymbol{h} + \boldsymbol{c}\boldsymbol{k}^2}{\boldsymbol{s}} \tag{28}$$

where: $\boldsymbol{h} := \frac{\partial \boldsymbol{g}_o(\varepsilon_{ps})}{\partial \varepsilon_p}$ and $\boldsymbol{s} := \frac{\partial \boldsymbol{g}_1(\dot{\varepsilon}_{ps})}{\partial \dot{\varepsilon}_p}$.

The linear stability is guaranteed when $\omega < 0$, otherwise we have instability, which occurs when:

$$\begin{cases} \boldsymbol{s} < 0 \quad \text{and} \quad \boldsymbol{h} + \boldsymbol{c}\boldsymbol{k}^2 \geq 0 \\ \boldsymbol{s} > 0 \quad \text{and} \quad \boldsymbol{h} + \boldsymbol{c}\boldsymbol{k}^2 \leq 0 \end{cases} \tag{29}$$

We get the following types of instability:

- **Type H**: $\boldsymbol{s} < 0, \boldsymbol{h} < 0, \boldsymbol{c} > 0, \boldsymbol{h} + \boldsymbol{c}\boldsymbol{k}^2 \leq 0$
- **Type S**: $\boldsymbol{s} < 0, \boldsymbol{h} > 0, \boldsymbol{c} < 0, \boldsymbol{h} + \boldsymbol{c}\boldsymbol{k}^2 \geq 0$ or just when $\boldsymbol{s} < 0$.

Observations:

(a) The value of $\boldsymbol{h}$ is not necessarily positive in the inequality (29).

(b) It is possible to determine the length of the critical wave $\boldsymbol{L}_c = \frac{2\pi}{\boldsymbol{k}_c}$ when $\boldsymbol{c}$ and $\boldsymbol{h}$ have opposite signs. The parameter $\boldsymbol{k}_c := \sqrt{\frac{-\boldsymbol{h}}{\boldsymbol{c}}}$ is called critical wave number because can occur a bifurcation or the deformation can become heterogeneous. The length $\boldsymbol{L}_c$, called *internal characteristic length scale*, appears in different studies of wave dispersion and traveling waves.

2.5 Shear bands

After a certain increase of plastic flow, the material exhibits deformation by softening and may occur a concentration of strain in narrow bands [7, 9]. In Eq. (23) we consider $\boldsymbol{g}_1(\dot{\varepsilon}_p) = \boldsymbol{s}\dot{\varepsilon}_p$ and $\boldsymbol{g}_o$ a continuous function, differentiable and not monotonous, so that $\boldsymbol{g}_o(0) = \sigma_y$, (σ_y is yield stress), and $\boldsymbol{s}$ a positive parameter. Therefore we get the shear bands model:

$$\boldsymbol{c}\frac{\partial^2 \varepsilon_p}{\partial \boldsymbol{x}^2} - \boldsymbol{g}_o(\varepsilon_p) - \boldsymbol{s}\dot{\varepsilon}_p + \boldsymbol{E}\left(\frac{\partial \boldsymbol{u}}{\partial \boldsymbol{x}} - \varepsilon_p\right) = 0 \tag{30}$$

The evolution of the bands occurs when $\boldsymbol{g}'_o(\varepsilon_p) < 0$ [12]. This type of deformation can be seen in soft steel, polymers and various metals, such as: $\boldsymbol{Cu}$ 4% $\boldsymbol{Si}$, $\boldsymbol{Al}$ 0.7% $\boldsymbol{Li}$, etc.

Motivated by the work of Coleman et al. [2], Anand et al. [11] and Sikora et al. [12], we are interested in the stationary uniform solution of Eq. (30), assuming that the diffusion coefficient $\boldsymbol{c} > 0$. The Eq. (30) is equivalent to the first order system:

$$\begin{cases} \dfrac{d\varepsilon_p}{d\boldsymbol{x}} = \boldsymbol{w} \\ \dfrac{d\boldsymbol{w}}{d\boldsymbol{x}} = \dfrac{1}{\boldsymbol{c}}\left(\boldsymbol{g}_o(\varepsilon_p) - \sigma_o\right) \end{cases} \tag{31}$$

We say that an equilibrium point is *homogenous* if it is constant related with x, i.e., when $\boldsymbol{w} = 0, \boldsymbol{g}_o(\varepsilon_p) = \sigma_o$. Therefore, the equilibrium points are $(\varepsilon_{p_s}, 0)$. The first integral of the system is given by:

$$\boldsymbol{K} = \frac{\boldsymbol{w}^2}{2} + \boldsymbol{V}(\varepsilon_p) \tag{32}$$

where $\boldsymbol{K} = \boldsymbol{K}(\varepsilon_p, w)$ is constant through any solution, and the function $\boldsymbol{V}$ is obtained through the integral:

$$\boldsymbol{V}(\varepsilon_p) := \frac{1}{\boldsymbol{c}} \int_{\varepsilon_{p_o}}^{\varepsilon_p} (\sigma_o - \boldsymbol{g}_o(\varsigma_p))\, \boldsymbol{d}\varsigma_p \tag{33}$$

The system (31) is the Hamiltonian type. The first integral corresponds to *total energy function*, where the *kinetic energy* is given by $\boldsymbol{E}_c := \frac{\boldsymbol{w}^2}{2}$, and the *potential energy* is given by $\boldsymbol{V}$. From Eqs. (32) and (33) we get:

$$\frac{\boldsymbol{d}\varepsilon_p}{\boldsymbol{dx}} = \boldsymbol{w} = \pm\sqrt{2(\boldsymbol{K} - \boldsymbol{V}(\varepsilon_p))} \tag{34}$$

Then:

$$\boldsymbol{x} = \int_{\varepsilon_p(0)}^{\varepsilon_p(x)} \frac{\boldsymbol{d}\zeta_p}{\sqrt{2(\boldsymbol{K} - \boldsymbol{V}(\zeta_p))}} \tag{35}$$

As the kinetic energy is not negative $\boldsymbol{K} > \boldsymbol{V}(\varepsilon_p)$, for different values of $\boldsymbol{K}$ is possible to draw the trajectories in the phase-plane (level curves).

Comments: The point $(\varepsilon_{p_s}, 0)$ is an equilibrium point if and only if $\boldsymbol{g}(\varepsilon_{p_s}) = \sigma_o$ (or $\boldsymbol{V}'(\varepsilon_p) = 0$). These points represent the equilibrium homogeneous stationary solutions, where the system stops moving in the phase-space.

- If $\boldsymbol{K} = \min \boldsymbol{V}(\varepsilon_p)$, the solution of Eq. (31) corresponds to an equilibrium point.
- If $\min \boldsymbol{V}(\varepsilon_p) < \boldsymbol{K} < \max \boldsymbol{V}(\varepsilon_p)$, the system (31) admits periodic orbits with characteristic length $\boldsymbol{L}_c = 2\pi\sqrt{\frac{\boldsymbol{c}}{-\boldsymbol{h}}}$.
- If $\boldsymbol{K} = \max \boldsymbol{V}(\varepsilon_p)$, the solution of Eq. (31) is an invariant manifold that corresponds to homoclinic (heteroclinic) orbits. Each homoclinic orbit represents a homoclinic shear band that starts and ends at the some value to slip. And each heteroclinic orbit represents a shear band connecting two homogeneous stationary states and uniforms for different deformations.

2.6 Numerical results

In this section we describe some numerical simulations of the shear bands Eq. (30). We consider a bar of 100 mm. length, with cross section 1.00 mm^2, fixed at one end. We simulate the softening by

prescribing a monotonous displacement at free end ($\boldsymbol{u}_L(\boldsymbol{t}) = \boldsymbol{a}$) and plastic deformation in both ends ($\varepsilon_p(0, \boldsymbol{t}) = \varepsilon_p(\boldsymbol{L}, \boldsymbol{t}) = 0$). We consider the initial conditions: $\boldsymbol{u}(\boldsymbol{x}, 0) = 0, \dot{\boldsymbol{u}}(\boldsymbol{x}, 0) > 0, \varepsilon_p(\boldsymbol{x}, 0) = 0$.

The used parameters are showed in Table 2.

Table 2: Parameters

Elasticity modulus (Pa)	$\boldsymbol{E} = 20 \cdot 10^9$	Yield stress (Pa)	$\sigma_y = 2 \cdot 10^6$
Softening modulus (Pa)	$\boldsymbol{h} = -2 \cdot 10^9$	Kinematic modulus (1/s)	$\boldsymbol{s} = 2.10^3$
Diffusion coefficient (N)	$\boldsymbol{c} = 5 \cdot 10^4$	Loading parameter (mm)	$\boldsymbol{a} = 0.125$

Figures 1-6 display the results for different values of diffusion coefficient $\boldsymbol{c}$. The Figures 1 and 2 show the plastic deformation field and the stress strain diagram, respectively, for the boundary conditions described previously. In the Figure 1 we can observe a concentration of plastic deformation at the middle of bar, and then the Figure 2 exhibits the stress strain diagram at this point, where we can see the softening effect. Figures 3 and 4 show the stress evolution at the middle of the bar and the displacement field, respectively. It is interesting to observe that the diffusion coefficient affects basically the localization of plastic deformation.

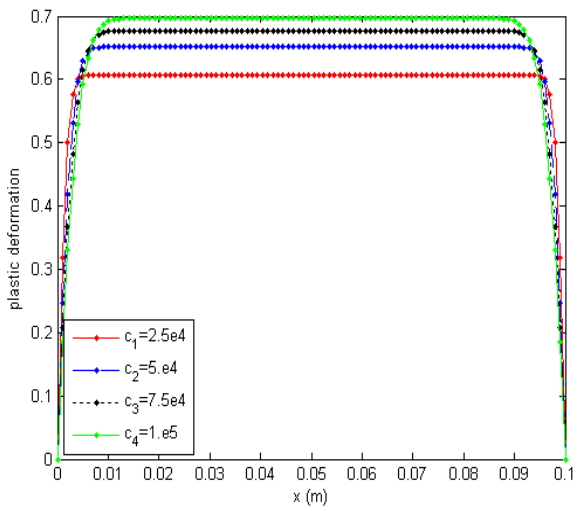

Figure 1: Plastic deformation field.

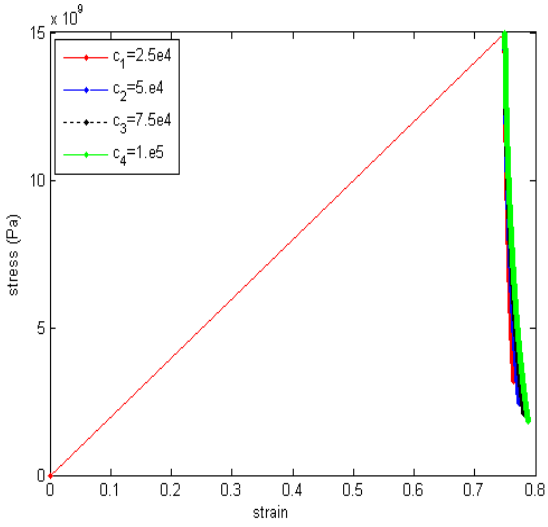

Figure 2: Stress strain diagram at the middle of the bar.

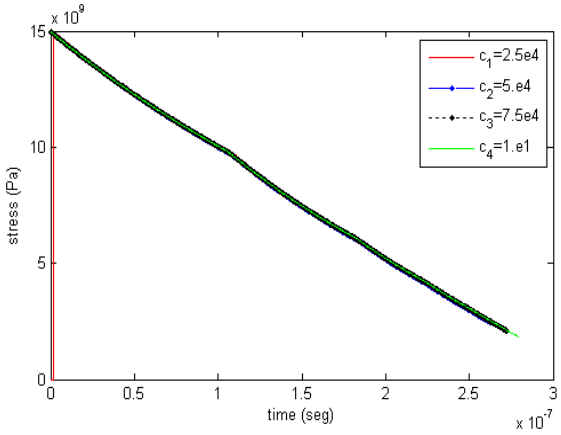

Figure 3: Stress evolution at the middle of the bar.

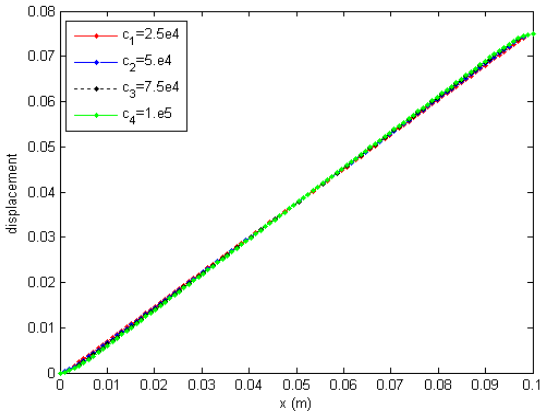

Figure 4: Displacement field.

We consider in Figures 5 and 6 as initial condition a plastic deformation of 0.09 prescribed in the middle bar. Figure 5 shows the plastic deformation field with this initial prescribed value, whereas the Figure 6 show the stress strain diagram at the middle of the bar.

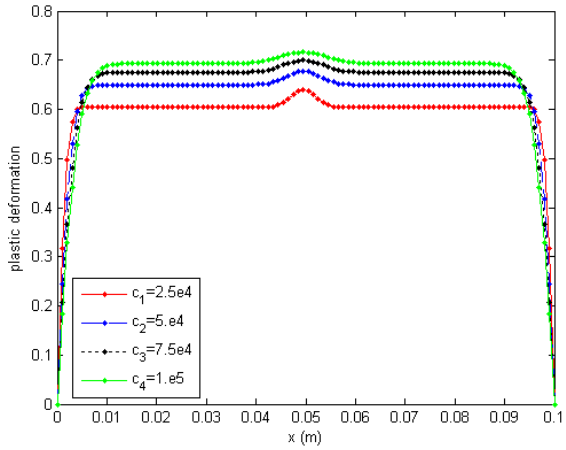

Figure 5: Plastic deformation field.

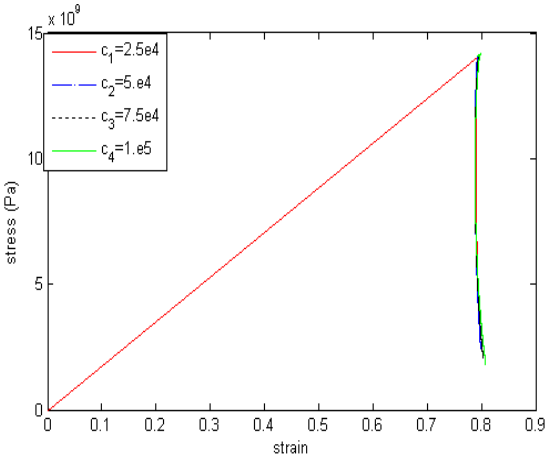

Figure 6: Stress strain diagram at the middle of the bar.

The Figures 7 and 8 display different curves related with different values of prescribed displacement at the free end $\boldsymbol{a}$. As the latter case, a plastic deformation of 0.09 was prescribed in the middle

bar as initial condition. Since the diffusion coefficient is the same for all curves, we do not observe different effects in the localization of plastic deformation in Figure 7, only the effect of the prescribed displacement. However, in contrast with the Figure 6, Figure 8 displays distinct curves in consequence of different prescribed displacements.

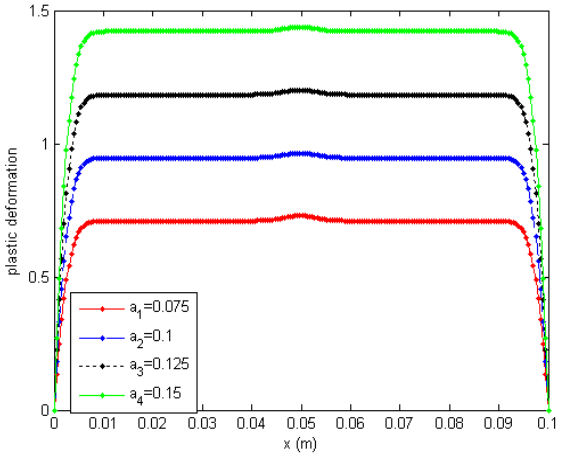

Figure 7: Plastic deformation field.

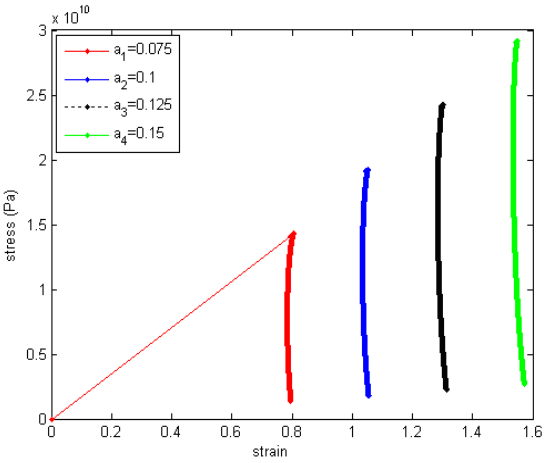

Figure 8: Stress strain diagram at the middle of the bar.

References

[1] Wang, W.M., *Stationary and Propagative Instabilities in Metals, Doctoral Thesis*. Delft University of Technology, 1997.

[2] Coleman, B.D. & Hodgdon, M.L., On shear bands in ductile materials. *Arch Rational Mech Analysis*, **90(3)**, pp. 219–247, 1985.

[3] Wang, W.M., Sluys, L.J. & Borst, R.D., Interaction between material length scale and imperfection size for localization phenomena in viscoplastic media. *European Journal of Mechanics, A/Solids*, **15(3)**, pp. 447–464, 1996.

[4] Borst, R.D. & Giessen, E., *Material Instabilities in Solids*. John Wiley and Sons Ltd, 1998. Hardcover.

[5] Penning, P., Mathematics of the portevin-le le chatelier effect. *Acta Metallurgica*, **20(10)**, pp. 1169–1175, 1972.

[6] Kubin, L.P. & Estrin, Y., The portevin-le chatelier effect in deformation with constant stress rate. *Acta Metall*, **3**, pp. 397–407, 1985.

[7] Brechet, Y. & Louchet, F., Localization of plastic deformation. *Solid State Phenomena*, **3(4)**, pp. 347–356, 1988.

[8] Aifantis, E.C., On the problem of dislocation pattering and persistent slip bands. *Solid State Phenomen*, **39(4)**, pp. 397–406, 1988.

[9] Aifantis, E.C., Pattern formation in plasticity. *International Journal of Engineering Science*, **33(15)**, pp. 2161–2178, 1995.
[10] Gurtin, M.E., On the plasticity of single crystals: free energy, micro forces, plastic-strain gradients. *Journal of the Mechanics and Physics of Solids*, **48(5)**, pp. 989–1036, 2000.
[11] Anand, L., Gurtin, M.E., Lele, P., S. & Gething, C., An one-dimensional theory of strain-gradient plasticity: Formulation, analysis, numerical results. *Journal of the Mechanics and Physics of Solids*, **53(8)**, pp. 1789–1826, 2005.
[12] Sikora, J., Cusumano, J. & William, J., Spatial periodic solutions in a 1D model of phase transitions with order parameter. *Physica D*, **121**, pp. 275–294, 1998.
[13] Estrin, Y., Classification of plastic instabilities by linear analysis. *Solid State Phenomena*, **3(4)**, pp. 417–428, 1988.
[14] Gurtin, M.E., *An Introduction to Continuum Mechanics*. Academic Press: New York, 1981.
[15] Duda, F.P. & Souza, A.C., Continuum mechanics, inelastic behavior and multiscale modeling in mechanics of materials. *Computational and Applied Mathematics*, **21(2)**, pp. 445–498, 2002.
[16] Germain, P., The method of virtual power in continuum mechanics. *J Applied Math*, **25(3)**, pp. 556–575, 1973.
[17] Coleman, B.D. & Noll, W., The thermodynamics of elastic materials with heat conduction and viscosity. *Archive for Rational Mechanical and Analysis*, **13**, pp. 163–178, 1963.
[18] Estrin, Y. & Kubin, L.P., Plastic instabilities: Classification and physical mechanics. *Research Mechanica*, **23**, pp. 197–221, 1988.

Mechanics of Solids in Brazil 2009, H.S. da Costa Mattos & Marcílio Alves (Editors)
Brazilian Society of Mechanical Sciences and Engineering, ISBN 978-85-85769-43-7

Evaluation of multiaxial stress-strain models and fatigue life prediction methods under proportional loading

Marco Antonio Meggiolaro, Jaime Tupiassú Pinho de Castro
Department of Mechanical Engineering, Pontifical Catholic University of Rio de Janeiro, Rio de Janeiro/RJ – Brazil
Antonio Carlos de Oliveira Miranda
Tecgraf, Pontifical Catholic University of Rio de Janeiro, Rio de Janeiro/RJ – Brazil

Abstract

Multiaxial fatigue damage occurs when the principal stress directions vary during the loading induced by several independent forces, such as out-of-phase bending and torsion. Uniaxial damage models cannot be reliably applied in this case. Besides the need for multiaxial damage models, another key issue to reliably model such problems is how to calculate the elastic-plastic stresses from the multiaxial strains. Hooke's law cannot be used to correlate stresses and strains for short lives due to plasticity effects. Ramberg-Osgood cannot be used either to directly correlate principal stresses and strains under multiaxial loading, because this model has been developed for the uniaxial case. The purpose of this work is to critically review and compare the main fatigue crack initiation models under multiaxial loading. The studied models include stress-based ones such as Sines, Findley and Dang Van, and strain-based ones such as the γN curve, Brown-Miller, Fatemi-Socie and Smith-Watson-Topper models. Modified formulations of the strain-based models are presented to incorporate Findley's idea of using critical planes that maximize damage. To incorporate plasticity effects, four models are studied and compared to correlate stresses and strains under proportional loading: the method of the highest K_t, the constant ratio model, Hoffmann-Seeger's and Dowling's models.

Keywords: multiaxial fatigue, crack initiation, life prediction models, stress-strain models.

1 Introduction

Real loads can induce combined bending, torsional, axial and shear stresses, which can generate bi- or tri-axial variable stress/strain histories at the critical point (in general a notch root), causing the so-called multiaxial fatigue problems. The load history is said to be proportional when it generates stresses with principal axes which maintain a fixed orientation, while non-proportional loading is associated with principal directions which change in time during the loading history.

Mechanics of Solids in Brazil 2009, H.S. da Costa Mattos & Marcílio Alves (Editors)
Brazilian Society of Mechanical Sciences and Engineering, ISBN 978-85-85769-43-7

For periodic loads with same frequency, one can also define the concept of in-phase and out-of-phase loading. In-phase loading always leads to proportional histories, however the opposite is not true: e.g., the stresses $\sigma_x = \sigma_I$ and $\sigma_y = \sigma_{II}$ induced on a plate by perpendicular ($\perp$) forces F_x and F_y are always proportional, because the principal axes maintain a fixed direction even if F_x and F_y are out-of-phase.

On the other hand, out-of-phase axial and torsional stresses always generate non-proportional (NP) loading [1]. The non-proportionality factor F_{np} of the applied loads can be obtained from the shape of the ellipsis that encloses the history of normal and shear strains induced by them, ε and γ. Considering a and b ($b \leq a$) as the semi-axes of the ellipsis which encloses the strain path in the Mises diagram $\varepsilon \times \gamma/\sqrt{3}$, then the non-proportionality factor F_{np} is defined as b/a ($0 \leq F_{np} \leq 1$), see Fig. 1. A further discussion on enclosing ellipses, and hyper-ellipsoids, can be found in [2].

All proportional loadings have shear strains γ proportional to the normal strains ε, with $F_{np} = 0$ and a straight-line trajectory in the $\varepsilon \times \gamma/\sqrt{3}$ diagram. Any loading history with $F_{np} > 0$ is NP. Note e.g. that the loading $(\sigma_a \sin\omega t + \tau_a \cos\omega t)$ with $\tau_a = \sigma_a\sqrt{3/2}(1+\nu)$, caused by a traction and a properly scaled torsion 90º out of phase, has $F_{np} = 1$, therefore the maximum possible non-proportionality.

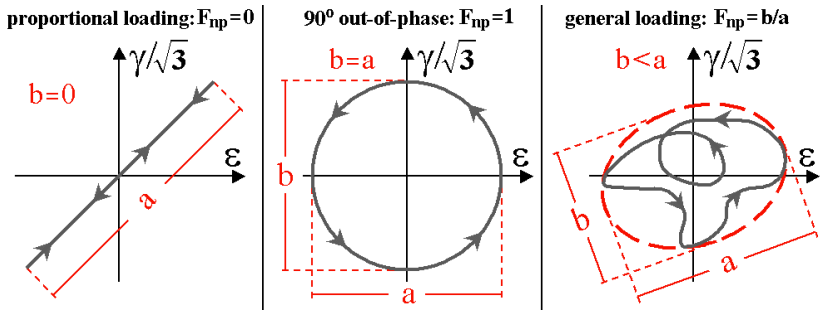

Figure 1: Diagram $\varepsilon \times \gamma/\sqrt{3}$, and associated non-proportionality factors (Socie and Marquis, 1999).

Predictions with NP histories can be very complex, because they involve at least three potential problems:

1. NP hardening: the cyclic hardening coefficient H_c and the ratio $\Delta\sigma/\Delta\varepsilon$ of a few materials increase under NP loading, which significantly decreases the fatigue life of parts subject to a constant $\Delta\varepsilon$;
2. Damage calculation: the SN and εN curves, measured under proportional loading, cannot be directly used when principal directions vary, because in this case the crack propagation plane in general does not match the one from the tests; and
3. Cycle counting: the traditional rain-flow counting techniques cannot be applied to variable amplitude NP loading, because the peaks and valleys of ε in general do not match with the ones of γ, becoming impossible to decide *a priori* which points should be accounted for.

The first two problems will be addressed in this work. A NP hardening model will be presented, to allow for the correct calculation of the equivalent stresses, and multiaxial models based on stress

or strain measurements will be used to calculate the damage generated both by proportional and NP loadings.

A few classical models that correlate stresses or strains with multiaxial fatigue life are studied below. Stress-based models (which can be applied for long life predictions) proposed by Sines, Findley and Dang Van are presented, as well as strain-based models proposed by Brown-Miller, Fatemi-Socie and Smith-Watson-Topper (SWT), which must be used for short lives.

One problem with the application of the Fatemi-Socie or SWT models is the need to calculate the elastic-plastic stresses from the multiaxial strains, because Ramberg-Osgood is only valid for uniaxial stresses. Another challenge in multiaxial fatigue life calculations is the modeling of the notch effect. The elastic stress concentration factor K_σ and strain concentration factor K_ε are the same for uniaxial loading, but in general in the multiaxial case K_σ is different from K_ε even under elastic stresses.

Therefore, even in the elastic case, it is not trivial to study the notch effect under multiaxial loading. The problem is worse in the elastic-plastic case, where even uniaxial loadings can generate NP multiaxial stress and strain histories, due to the tri-axial stress state at the notch root and to the difference between the elastic and plastic Poisson coefficients. Typically, metallic alloys have $1/4 \leq \nu_{el} \leq 1/3$ and $\nu_{pl} = 0.5$. In the following sections the multiaxial stress-strain models are presented and compared, including notch effects.

2 Non-proportional loading

A few materials under NP cyclic loading can harden much more than it would be predicted from the traditional cyclic $\sigma\varepsilon$ curve. This phenomenon, called NP hardening, depends on the load history (through the NP factor F_{np}) and on the material (through a constant α_{np} of NP hardening, where $0 \leq \alpha_{np} \leq 1$). The NP hardening can be modeled in general using the same Ramberg-Osgood plastic exponent h_c from the uniaxial cyclic σ-ε curve, and using a new coefficient $H_{cnp} = H_c \cdot (1 + \alpha_{np} \cdot F_{np})$, where H_c is the uniaxial Ramberg-Osgood plastic coefficient, see Fig. 2. Note that the NP hardening can multiply the uniaxial strain hardening coefficient H_c by a value as high as 2.

The largest NP hardening occurs when $F_{np} = 1$, e.g. under a properly scaled traction-torsion loading 90^o out of phase which generates a circle in the $\varepsilon \times \gamma/\sqrt{3}$ Mises diagram.

Typically, the NP hardening effect is high in austenitic stainless steels at room temperature ($\alpha_{np} \cong 1$ in the stainless steel 316), medium in carbon steels ($\alpha_{np} \cong 0.3$ in the 1045 steel) and low in aluminum alloys ($\alpha_{np} \cong 0$ for Al 7075). Note that proportional histories do not lead to NP hardening.

The NP hardening happens in materials with low fault stacking energy (which in austenitic stainless steels is only 23mJ/m^2) and well spaced dislocations, where the slip bands generated by proportional loading are always planar. In these materials, the NP loads activate crossed slip bands in several directions (due to the rotation of the maximum shear planes), therefore increasing the hardening effect ($\alpha_{np} \gg 0$) with respect to the proportional loadings. But in materials with high fault stacking energy (such as aluminum alloys, with a typical value of 250mJ/m^2) and with close dislocations, the crossed slip bands already happen naturally even under proportional loading, therefore the NP histories do not cause any significant difference in hardening ($\alpha_{np} \cong 0$).

But the Coffin-Manson or the Morrow crack initiation equations cannot account for the influence of

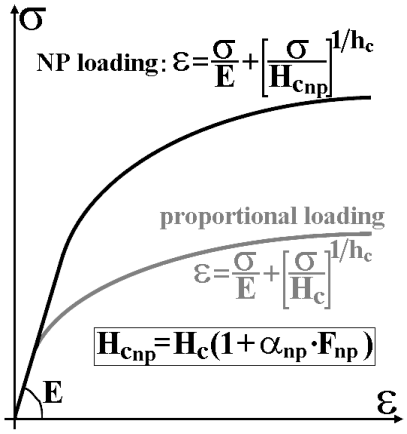

Figure 2: Effect of cyclic NP loadings on the NP hardening.

NP hardening. This implies that the use of traditional εN equations, which were developed to model uniaxial fatigue problems, can be non-conservative when the loading histories are NP.

However, it must be noted that the NP hardening reduces fatigue life only in strain-controlled problems (such as in εN specimen tests or very sharp notches, e.g.), because the stresses $\Delta\sigma$ caused by a given $\Delta\varepsilon$ are higher than in the proportional case. But in stress-controlled problems (the most common case in practice), the $\Delta\varepsilon$ generated by a given $\Delta\sigma$ is lower under NP loading, therefore the fatigue life is higher than in the proportional case (the uniaxial εN equations can lead to conservative predictions in this case). In the following sections, the multiaxial models to predict NP damage are studied.

3 Stress-based multiaxial fatigue damage models

It is well known that Tresca or Mises equivalent stresses must be used to predict crack initiation lives, which depend on the cyclic movement of dislocations. However, crack initiation can and should be divided into:

- formation of microcracks, which is almost insensitive to mean stresses and hydrostatic pressure in metals, because it only depends on dislocation movement; followed by
- propagation of the dominant microcrack, which also depends on the crack face opening and the friction between the faces, becoming increasingly sensitive to the applied mean stress σ_m as the microcrack grows.

Microcracks are cracks with sizes up to the order of the metal grain sizes. Their modeling using classical fracture mechanics is questionable, as opposed to long cracks (typically larger than 1 or 2mm), which have crack propagation rates controlled by ΔK.

However, SN and εN tests bring test specimens (TS) to fracture, or to the generation of a small, finite crack, therefore they include both microcrack initiation and propagation phases. Thus, since the shear stress $\Delta\tau$ controls the initiation of a microcrack, while the normal stress $\sigma_\perp$ perpendicular to its plane (or the hydrostatic stress σ_h, invariant defined as the mean of the normal stresses) controls its opening, both are important to predict the fatigue lives of SN and εN specimens.

In fact, a component under uniaxial traction $\sigma_x = \sigma$ and another under torsion $\tau_{xy} = \sigma/2$ work under the same Tresca equivalent stress, but the microcracks on the plane of τ_{max} in the first component are subject to a normal stress $\sigma_\perp$ perpendicular to that plane that tends to keep their mouth open, exposing the crack tips and decreasing the crack face friction, see Fig. 3. Therefore, the fatigue damage generated by $\Delta\sigma$ can be greater than the one caused by the pure torsion $\Delta\tau = \Delta\sigma/2$.

The Mises equivalent stress is able to, at least in part, consider such effect, because the component under torsion would have $\sigma_{Mises} = \tau_{xy}\sqrt{3} = 0.866 \cdot \sigma_x < \sigma$, however σ_{Mises} is insensitive to the hydrostatic stress σ_h. The Mises shear strain τ_{Mises}, which acts on the octahedric planes, does not consider as well the effects of σ_h, relating with σ_{Mises} through:

$$\begin{aligned}\sigma_{Mises} &= \frac{3}{\sqrt{2}}\tau_{Mises} = \frac{1}{\sqrt{2}}\sqrt{(\sigma_1-\sigma_2)^2+(\sigma_1-\sigma_3)^2+(\sigma_2-\sigma_3)^2} = \\ &= \frac{1}{\sqrt{2}}\sqrt{(\sigma_x-\sigma_y)^2+(\sigma_y-\sigma_z)^2+(\sigma_x-\sigma_z)^2+6(\tau_{xy}^2+\tau_{yz}^2+\tau_{xz}^2)}\end{aligned} \tag{1}$$

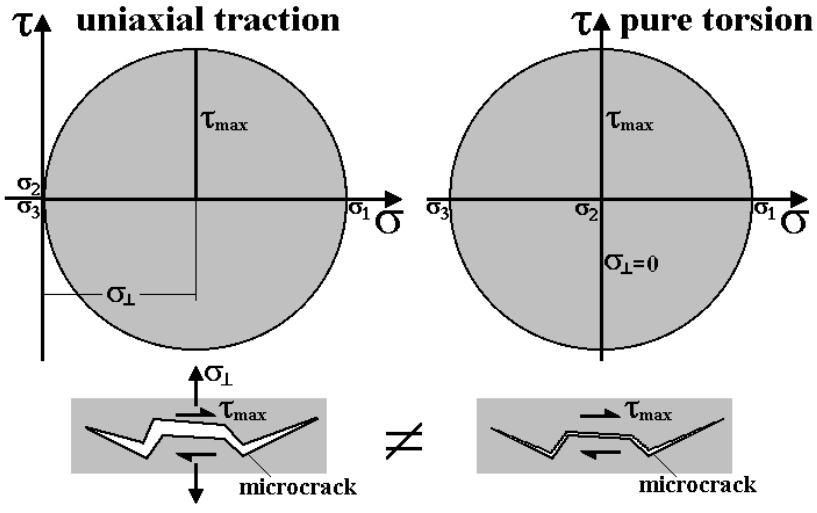

Figure 3: Mohr circles showing why under the same $\Delta\sigma_{Tresca}$ equivalent loading the component under pure torsion can have a higher fatigue life than the one under pure traction.

Sines [3] has proposed a fatigue failure criterion under proportional multiaxial stresses, based on $\Delta\tau_{Mises}$ and on $\sigma_{hm} = (\sigma_{xm} + \sigma_{ym} + \sigma_{zm})/3$, the hydrostatic component of the mean stresses (insensitive to the shear stresses):

$$\frac{\Delta\tau_{Mises}}{2} + \alpha_S \cdot (3 \cdot \sigma_{h_m}) = \beta_S \tag{2}$$

where α_S and β_S are adjustable constants for each material, and

$$\Delta\tau_{Mises} = \frac{1}{3}\sqrt{(\Delta\sigma_1 - \Delta\sigma_2)^2 + (\Delta\sigma_1 - \Delta\sigma_3)^2 + (\Delta\sigma_2 - \Delta\sigma_3)^2} \tag{3}$$

In this way, according to the Sines criterion, a component will have infinite fatigue life under proportional loading if

$$\Delta\tau_{Mises}/2 + \alpha_S \cdot (3 \cdot \sigma_{hm}) < \beta_S \tag{4}$$

On the other hand, the Findley [4] criterion, which is also applicable to NP multiaxial loadings, assumes that the crack initiates at the critical plane of the critical point. This idea is interesting, because it is on this plane that the damage caused by the combination $\Delta\tau/2 + \alpha_F \cdot \sigma_\perp$ is maximum, where $\Delta\tau/2$ is the shear stress amplitude on that plane and $\sigma_\perp$ is the normal stress perpendicular to it. Thus, according to Findley the fatigue failure criterion at the critical plane of the critical point is

$$\left(\frac{\Delta\tau}{2} + \alpha_F \cdot \sigma_\perp\right)_{\max} = \beta_F \tag{5}$$

where α_F and β_F are constants which must be fitted by measurements in at least two types of fatigue tests, e.g., under rotating bending and under pure torsion, or in push-pull tests under two different R ratios.

The critical plane can vary at each i-th event of the NP loads, even when the critical point remains the same, but Findley predicts fatigue failure based on the plane where the sum of the damages associated with $[\Delta\tau_i(\theta)/2 + \alpha_F \cdot \sigma_{\perp i}(\theta)]$ is maximum, where θ is the angle of such plane with respect to a reference direction.

Under pure torsion, Eq. (5) can be written as

$$\sqrt{1 + \alpha_F^2} \cdot \frac{\Delta\tau}{2} = \beta_F \tag{6}$$

And under cyclic uniaxial traction with alternate component σ_a and maximum component σ_{max}, it can be shown that Findley's criterion can be written as

$$0.5\sigma_a \left[\sqrt{1 + \left(\frac{2\alpha_F}{1-R}\right)^2} + \frac{2\alpha_F}{1-R}\right] = \beta_F \tag{7}$$

where $R = \sigma_{min}/\sigma_{max}$ is the stress ratio, which quantifies the mean stress effects.

Therefore, from Findley it is possible to estimate the fatigue limit $S_L(R)$ under any ratio R from α_F and the fatigue limit S_L (obtained under zero mean loads, i.e., with $R = -1$, see Fig. 4) through

$$\frac{S_L(R)}{S_L} = \frac{\sigma_a(R)}{\sigma_a} = \frac{\sqrt{1+\alpha_F^2}+\alpha_F}{\sqrt{1+\left(\frac{2\alpha_F}{1-R}\right)^2}+\frac{2\alpha_F}{1-R}} \tag{8}$$

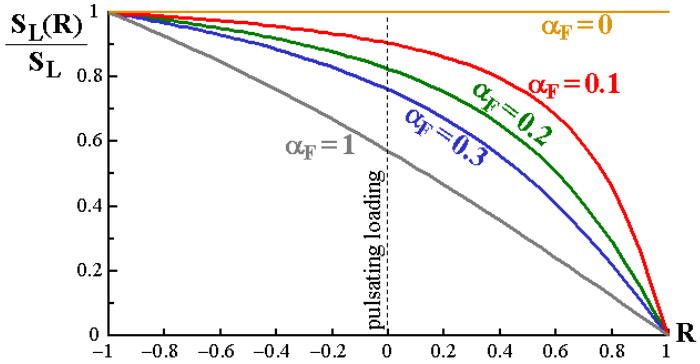

Figure 4: Fatigue limit $S_L(R)$ as a function of R, according to Findley.

From the principle that the damage associated with the initiation of fatigue microcracks cannot be detected from macroscopic measurements, Dang Van [5] proposed a model that considers the variable micro stresses that act inside a characteristic volume element (VE) of the material, where the macroscopic stresses and strains are supposedly constant. The VE is the unit used in structural analysis to represent the material properties, such as its Young modulus and its several strengths. Thus the VE must be small compared to the component's dimensions, but large compared to the parameter that characterizes the intrinsic anisotropy of the material. For instance, a VE of only 1mm^3 is sufficient for most structural metal alloys, which have a grain size g typically between 10 and 100μm (the grain itself, being a monocrystal, is intrinsically anisotropic).

Inside a VE, the local micro stresses $[\sigma_{ij}]_\mu = \sigma_\mu$ and strains $[\varepsilon_{ij}]_\mu = \varepsilon_\mu$ acting between grains, or between them and small imperfections such as inclusions, e.g., can significantly differ from the macro stresses $[\sigma_{ij}]_M = \sigma_M$ and strains $[\varepsilon_{ij}]_M = \varepsilon_M$, assumed constant in the macroscopic analysis normally used in mechanical design. Therefore, these micro quantities can significantly influence crack initiation. Note that if the term "microscopic" is reserved to the scale associated with interatomic stresses, domain of solid state physics, then its is recommended to use the term "mesoscopic" to describe the intra or intergranular stresses. Thus, the macroscopic stresses reflect the average of the mesoscopic stresses in a VE: $\sigma_M = \int \sigma_\mu dV/V$, where V is the volume of the VE. Similarly, $\varepsilon_M = \int \varepsilon_\mu dV/V$.

In other words, the macroscopic stresses and strains are assumed constant at the characteristic volume element VE of the material, however the mesoscopic intergranular stresses can vary a lot, influencing crack initiation.

Since the microcracks initiate at persistent slip bands, Dang Van assumed that fatigue damage was caused by the mesoscopic shear strain history τ_μ(t) and influenced by the mesoscopic hydrostatic stress history $\sigma_{\mu h}$(t). The simplest failure criterion involving these components is the linear combination given by:

$$\tau_\mu(t) + \alpha_{DV} \cdot \sigma_{\mu_h}(t) = \beta_{DV} \tag{9}$$

Note that the Sines, Findley and Dang Van criteria can be included in the general class of Mohr models against material failure, which use combinations of the shear stress τ that acts on a certain plane with the normal or hydrostatic stresses σ on this plane:

$$\tau + \alpha \cdot \sigma = \beta \tag{10}$$

The Sines criterion uses the Mises or octahedric plane and the hydrostatic stresses, therefore $\tau \equiv \Delta\tau_{Mises}/2$, $\sigma \equiv 3 \cdot \sigma_{hm}$, $\alpha \equiv \alpha_S$, $\beta \equiv \beta_S$; Findley uses the shear stress on the critical plane and the normal stress perpendicular to it, thus $\tau \equiv \Delta\tau/2$, $\sigma \equiv \sigma_\perp$, $\alpha \equiv \alpha_F$, $\beta \equiv \beta_F$; and Dang Van can be obtained from $\tau \equiv \tau_\mu(t)$, $\sigma \equiv \sigma_{\mu h}(t)$, $\alpha \equiv \alpha_{DV}$, $\beta \equiv \beta_{DV}$. Other similar criteria can be found in [1] and [6].

Finally, it is important to remember that the SN and εN tests involve both microcrack initiation (sensitive to τ) and propagation (more sensitive to σ) phases, and therefore fatigue damage can be more influenced by τ or σ, depending on the percentage of the life spent at each phase. Therefore, materials with large values of α are more sensitive to σ (normal stresses are more important to them), probably spending more cycles to propagate than to initiate the microcrack.

4 Strain-based multiaxial fatigue damage models

The three multiaxial failure criteria presented above are based on macroscopic stresses that are supposedly elastic, therefore they are only applicable when σ_{Mises} is much smaller than the cyclic yielding strength S_{yc}. Thus, as in the case of the SN method, they should only be used to predict long fatigue lives. Otherwise, it is imperative to use fatigue damage criteria based on applied strains instead of stresses [1], using the principles studied in the so-called εN method.

One of the simplest models is the one based on the γN curve, similar to Coffin-Manson's equation, which uses the largest shear strain range $\Delta\gamma_{max}$ acting on the specimen (γ_{ij} ($2\varepsilon_{ij}$, $i \neq j$) to predict fatigue life

$$\frac{\Delta\gamma_{\max}}{2} = \frac{\tau_c}{G}(2N)^{b_\gamma} + \gamma_c(2N)^{c_\gamma} \tag{11}$$

where τ_c, b_γ, γ_c and c_γ are parameters similar to the ones used in Coffin-Manson's equation. In this way, since the shear modulus $G = E/\left[2(1+\nu)\right]$, ν being Poisson's coefficient, if no experimental data is available, then the γN curve can be estimated assuming $\tau_c \cong \sigma_c/\sqrt{3}$, $b_\gamma \cong b$, $\gamma_c \cong \varepsilon_c\sqrt{3}$ and $c_\gamma \cong c$, resulting in

$$\frac{\Delta\gamma_{\max}}{2} \cong \frac{\sigma_c}{E}\frac{2(1+\nu)}{\sqrt{3}}(2N)^b + \varepsilon_c\sqrt{3}(2N)^c \tag{12}$$

The γN curve is only recommended to model fatigue damage in materials that are more sensitive to shear strains (which have small α in the Mohr models), and if the mean loads are zero. It would be expected that such materials would have a shorter torsional fatigue life than similar materials more sensitive to normal stresses.

The Brown-Miller [7] model can consider the mean stress effects, combining the maximum range of the shear strain $\Delta\gamma_{max}$ to the range of normal strain $\Delta\varepsilon_\perp$ (through the term $\Delta\gamma_{max}/2 + \alpha_{BM}\cdot\Delta\varepsilon_\perp$) and the mean normal stress $\sigma_{\perp m}$ perpendicular to the plane of maximum shear strain, to obtain the fatigue life N:

$$\frac{\Delta\gamma_{\max}}{2} + \alpha_{BM}\cdot\Delta\varepsilon_\perp = \beta_1\frac{\sigma_c - 2\sigma_{\perp m}}{E}(2N)^b + \beta_2\varepsilon_c(2N)^c \tag{13}$$

where α_{BM} is a fitting parameter ($\alpha_{BM} \cong 0.3$ for ductile metals in lives near the fatigue limit), $\beta_1 = (1+\nu+(1-\nu)\cdot\alpha_{BM}$, and $\beta_2 = 1.5 + 0.5\cdot\alpha_{BM}$.

This equation was adapted from Morrow to fit uniaxial traction test data, where the mean stress σ_m is equal to $2\sigma_{\perp m}$ (because $\sigma_{\perp m}$ acts perpendicularly to the plane of γ_{max}, therefore it is worth half of σ_m).

The values of β_1 and β_2 are obtained assuming uniaxial traction, see Fig. 5:

$$\left.\begin{aligned}\Delta\gamma_{\max} &= (1+\nu)\Delta\varepsilon\\ \Delta\varepsilon_\perp &= (1-\nu)\Delta\varepsilon/2\end{aligned}\right\} \Rightarrow \frac{\Delta\gamma_{\max}}{2} + \alpha_{BM}\Delta\varepsilon_\perp = \frac{\Delta\varepsilon}{2}\left[(1+\nu) + \alpha_{BM}(1-\nu)\right] \tag{14}$$

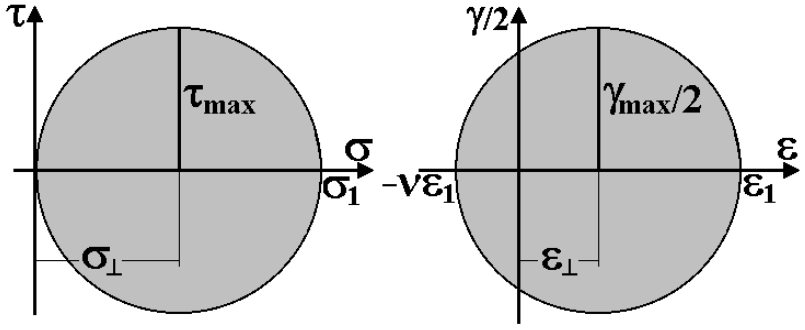

Figure 5: Mohr circles for stresses and strains under uniaxial traction.

From Eq. (14), the coefficients $\beta_1 = (1+\nu) + (1-\nu)\cdot\alpha_{BM}$ and $\beta_2 = 1.5 + 0.5\cdot\alpha_{BM}$ are obtained, because $\nu = 0.5$ for plastic strains, which preserve volume. The original Brown-Miller model assumes that the elastic strains have $\nu = 0.3$, therefore $\beta_1 \cong (1+0.3) + (1-0.3)\cdot\alpha_{BM} = 1.3 + 0.7\cdot\alpha_{BM}$.

The Brown-Miller model is frequently used in multiaxial fatigue, even though it is not reasonable to assume that $\Delta\varepsilon_\perp$ can control the opening and closure of microcracks, because the range $\Delta\varepsilon$ does not include information about maximum stresses or strains. E.g., two microcracks with the same $\Delta\gamma_{max}$ and $\Delta\varepsilon_\perp$ can have very different fatigue lives if one is opened (under traction) and the other closed (under compression) due to the mean load effect. The use of $\sigma_{\perp m}$ compensates in part for this model flaw, however the mean stress effect is only considered in the elastic part.

Fatemi and Socie [8] suggested replacing $\Delta\varepsilon_\perp$ by the maximum normal stress $\sigma_{\perp max}$ perpendicular to the plane of maximum shear strain, applying it to the γN curve:

$$\frac{\Delta\gamma_{\max}}{2}\left(1+\alpha_{FS}\frac{\sigma_{\perp\max}}{S_{yc}}\right) = \frac{\tau_c}{G}(2N)^{b_\gamma} + \gamma_c(2N)^{c_\gamma} \tag{15}$$

Note that the value of α_{BM} and α_{FS} indicates whether the material is more sensitive to τ (α_{BM} or $\alpha_{FS} \ll 1$) or to σ (α_{BM} or $\alpha_{FS} \gg 1$).

If the propagation phase of the microcracks (more sensitive to σ) is dominant over initiation, the Smith-Watson-Topper (SWT) multiaxial model can be used [9]:

$$\frac{\Delta\varepsilon_1}{2}\cdot\sigma_{\perp 1\,\max} = \frac{\sigma_c^2}{E}(2N)^{2b} + \sigma_c\varepsilon_c(2N)^{b+c} \tag{16}$$

where $\Delta\varepsilon_1$ is the range of the maximum principal strain and $\sigma_{(1max}$ is the stress peak in the direction perpendicular to ε_1.

Figure 6 summarizes the parameters used in the above strain-based models. In addition, there are several other models based on the plastic energy dissipated by the hysteresis loops, and other combining energy with critical planes, see [1].

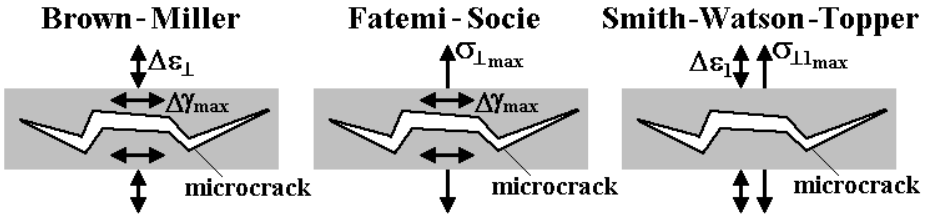

Figure 6: Parameters which affect the strain-based multiaxial models.

It is important to note that the plane of maximum shear strain amplitude $\Delta\gamma_{max}/2$ (used in Brown-Miller's and Fatemi-Socie's models) is in general different from the planes that would maximize the respective damage parameters ($\Delta\gamma/2 + \alpha_{BM}(\Delta\varepsilon_\perp$ for Brown-Miller, and $\Delta\gamma((1 + \alpha_{FS}(\sigma_{\perp max}/S_{yc})/2$

for Fatemi-Socie). But if these are the parameters that cause damage, it is reasonable to argue that fatigue life should be calculated on the critical plane that maximizes them (in a similar way as done in Findley's model), and not on the plane of $\Delta\gamma_{max}$. In this way, it is a good idea to modify the Brown-Miller and Fatemi-Socie models introducing a subtle but important change:

$$\frac{\Delta\gamma_{\max}}{2} + \alpha_{BM} \cdot \Delta\varepsilon_{\perp} \Rightarrow \left(\frac{\Delta\gamma}{2} + \alpha_{BM} \cdot \Delta\varepsilon_{\perp} \right)_{\max} \tag{17}$$

$$\frac{\Delta\gamma_{\max}}{2} \left(1 + \alpha_{FS} \frac{\sigma_{\perp \max}}{S_{yc}} \right) \Rightarrow \left(\frac{\Delta\gamma}{2} + \alpha_{FS} \frac{\Delta\gamma}{2} \frac{\sigma_{\perp\gamma}}{S_{yc}} \right)_{\max} \tag{18}$$

The use of critical planes that maximize the damage parameters in each model has the advantage of predicting not only the fatigue life but also the dominant planes where the crack will initiate. However, these calculations are not simple and require the use of sophisticated numerical methods.

This idea can also be applied to the SWT model, calculating the critical plane where the product between the normal strain range $\Delta\varepsilon_{\perp}$ and the normal stress peak $\sigma_{\perp max}$ is maximized, adopting the modification

$$\frac{\Delta\varepsilon_1}{2} \cdot \sigma_{\perp 1\,\max} \Rightarrow \left(\frac{\Delta\varepsilon_{\perp}}{2} \cdot \sigma_{\perp \max} \right)_{\max} \tag{19}$$

A great advantage of the Fatemi-Socie (or SWT) model is to be able to consider the effect of NP hardening from the peak of normal stress $\sigma_{\perp max}$ (or $\sigma_{\perp 1max}$). In stainless steels, e.g., a NP history leads to a much higher damage than a proportional one with the same $\Delta\gamma_{max}$ and $\Delta\varepsilon_{\perp}$, because the NP hardening increases the value of $\sigma_{\perp max}$ (or $\sigma_{\perp 1max}$). Note that Brown-Miller would wrongfully predict the same damage in both histories (because $\Delta\gamma_{max}$ and $\Delta\varepsilon_{\perp}$ would be the same), and only the Fatemi-Socie and SWT models would be able to correctly account for the greater damage of the NP loading (assuming that H_{cnp} would be used to obtain $\sigma_{\perp max}$ and $\sigma_{\perp 1max}$).

5 Multiaxial stress-strain relations

Hooke's law cannot be used to correlate stresses and strains for short multiaxial fatigue life predictions, due to plasticity effects. The hookean stresses and strains, $\tilde{\sigma}$ and $\tilde{\varepsilon}$, defined as the values of σ and ε obtained assuming that the material would be linear elastic (using Hooke's law and, at the notches, considering elastic K_{σ} and K_{ε}), can only be applied for long life predictions.

In addition, Ramberg-Osgood cannot be used either to directly correlate principal stresses and strains σ_i and ε_i (i = 1, 2, 3) of a multiaxial history, because this model has been developed for the uniaxial case.

However, if the elastic nominal stress range $\Delta\sigma_n$ is caused by in-phase loading, then it is trivial to calculate the elastic-plastic stresses and strains at the notch root using the "highest K_t method". In this approximate method, the equivalent nominal stress range $\Delta\sigma_n$ calculated from Tresca or Mises is used to obtain $\Delta\sigma$ and $\Delta\varepsilon$ at the notch root using Ramberg-Osgood and (for safety, because the method is conservative) the highest K_t in Neuber's rule. Remember that the multiaxial loadings can result, at

the same notch root, in different values of K_t for traction, bending, torsion and shear loadings, but only the maximum one is used. To generate more accurate predictions for notches under combined stresses, it is recommended to use multiaxial σ-ε relations.

Several models have been proposed to correlate σ_i and ε_i in proportional histories, e.g.: the constant ratio model [1], Hoffmann-Seeger's model ([10], and Dowling's model [11]. To present these three models, it is necessary to define a few variables involved in their formulation:

- $\tilde{\sigma}_1$, $\tilde{\sigma}_2$, $\tilde{\sigma}_3$, $\tilde{\varepsilon}_1$, $\tilde{\varepsilon}_2$, $\tilde{\varepsilon}_3$: hookean principal stresses and strains at the notch root (elastically calculated using Hooke's law and elastic K_σ and K_ε);
- $\tilde{\sigma}_{Mises}$, $\tilde{\varepsilon}_{Mises}$: hookean Mises stress and strain (at the notch root), calculated using the above variables;
- σ_1, σ_2, σ_3, ε_1, ε_2, ε_3: elastic-plastic principal stresses and strains (notch root);
- σ_{Mises}, ε_{Mises}: Mises stress and strain (notch root);
- λ_2, λ_3: ratios between pairs of principal stresses, where $\lambda_2 = \sigma_2/\sigma_1$ and $\lambda_3 = \sigma_3/\sigma_1$, both between -1 and 1;
- φ_2, φ_3: ratios between pairs of principal strains, where $\varphi_2 = \varepsilon_2/\varepsilon_1$, $\varphi_3 = \varepsilon_3/\varepsilon_1$, both between -1 and 1; and
- λ_{Mises}, φ_{Mises}: Mises ratios $\lambda_{Mises} = \sigma_{Mises}/\sigma_1$ and $\varphi_{Mises} = \varepsilon_{Mises}/\varepsilon_1$.

From the above definitions, it is possible to obtain

$$\lambda_{Mises} = \frac{\sigma_{Mises}}{\sigma_1} = \frac{1}{\sqrt{2}}\sqrt{(1-\lambda_2)^2 + (1-\lambda_3)^2 + (\lambda_2-\lambda_3)^2} \tag{20}$$

$$\phi_{Mises} = \frac{\varepsilon_{Mises}}{\varepsilon_1} = \frac{1}{\sqrt{2}(1+\nu)}\sqrt{(1-\phi_2)^2 + (1-\phi_3)^2 + (\phi_2-\phi_3)^2} \tag{21}$$

The three models are described next.

5.1 Constant ratio model

The *constant ratio model* [1] assumes that, under a proportional history, the bi-axial ratios λ_2, λ_3, φ_2 and φ_3 remain constant even after yielding has occurred. Since the elastic Poisson coefficient ν_{el} is typically between $1/4$ and $1/3$ in most metal alloys, significantly different than the plastic $\nu_{pl} = 0.5$, these ratios are in fact not constant, but for small plastic strains this is a good approximation.

Thus, these ratios can be estimated from the elastic (hookean) stresses and strains, obtained from Hooke's law using elastic K_σ and K_ε:

$$\lambda_2 \cong \frac{\tilde{\sigma}_2}{\tilde{\sigma}_1},\ \lambda_3 \cong \frac{\tilde{\sigma}_3}{\tilde{\sigma}_1},\ \phi_2 \cong \frac{\tilde{\varepsilon}_2}{\tilde{\varepsilon}_1},\ \phi_3 \cong \frac{\tilde{\varepsilon}_3}{\tilde{\varepsilon}_1} \tag{22}$$

Therefore, λ_{Mises} is also a constant, leading to

$$\lambda_{Mises} \cong \frac{\tilde{\sigma}_{Mises}}{\tilde{\sigma}_1} \Rightarrow \tilde{\sigma}_{Mises} \cong \frac{\tilde{\sigma}_1}{\sqrt{2}}\sqrt{(1-\lambda_2)^2 + (1-\lambda_3)^2 + (\lambda_2-\lambda_3)^2} \tag{23}$$

and, similarly, φ_{Mises} can be calculated from φ_2 and φ_3. The cyclic σ-ε relation is then defined using Mises and the Ramberg-Osgood uniaxial parameters

$$\varepsilon_{Mises} = \frac{\sigma_{Mises}}{E} + \left(\frac{\sigma_{Mises}}{H_c}\right)^{1/h_c} \tag{24}$$

If no notches are present, then the above equation is used together with the estimates for λ_{Mises}, φ_{Mises}, λ_2, λ_3, φ_2 and φ_3 to obtain σ_i from ε_i (i = 1, 2, 3), or vice-versa. In notched components, $\tilde{\sigma}_{Mises}$ (elastically calculated including the K_ts) is applied to a variation of the Neuber's rule to calculate the Mises elastic-plastic stress σ_{Mises} and, finally, ε_{Mises}, σ_i and ε_i (i = 1, 2, 3):

$$\frac{\left(\tilde{\sigma}_{Mises}\right)^2}{E} = \sigma_{Mises} \cdot \varepsilon_{Mises} = \frac{\left(\sigma_{Mises}\right)^2}{E} + \sigma_{Mises} \cdot \left(\frac{\sigma_{Mises}}{H_c}\right)^{1/h_c} \tag{25}$$

After calculating σ_{Mises} and ε_{Mises}, the constant ratio model obtains the principal stress and strain using:

$$\begin{cases} \sigma_1 = \sigma_{Mises}/\lambda_{Mises},\ \sigma_2 = \lambda_2\sigma_1,\ \sigma_3 = \lambda_3\sigma_1 \\ \varepsilon_1 = \varepsilon_{Mises}/\phi_{Mises},\ \varepsilon_2 = \phi_2\varepsilon_1,\ \varepsilon_3 = \phi_3\varepsilon_1 \end{cases} \tag{26}$$

5.2 Hoffmann-Seeger's model

Hoffmann-Seeger's model [10] uses the same cyclic σ-ε relation and the same variation of Neuber's rule presented above to calculate σ_{Mises} and ε_{Mises}, but it assumes that:

- the critical point happens at the surface, with principal stresses σ_1 and σ_2;
- σ_3 is defined normal to the surface, therefore $\sigma_3 = 0$ (and then $\lambda_3 = 0$); and
- only the ratio $\phi_2 = \tilde{\varepsilon}_2/\tilde{\varepsilon}_1$ is estimated using the linear elastic (hookean) values.

After calculating σ_{Mises} and ε_{Mises}, σ_i and ε_i are estimated from:

$$\begin{cases} \sigma_1 = \sigma_{Mises}/\bar{\lambda}_{Mises},\ \sigma_2 = \bar{\lambda}_2\sigma_1,\ \sigma_3 = 0 \\ \varepsilon_1 = \frac{(1-\bar{\lambda}_2\bar{\nu})\varepsilon_{Mises}}{\bar{\lambda}_{Mises}},\ \varepsilon_2 = \phi_2\varepsilon_1,\ \varepsilon_3 = -\bar{\nu}\varepsilon_1\frac{1+\bar{\lambda}_2}{1-\bar{\lambda}_2\bar{\nu}} \end{cases} \tag{27}$$

$$\bar{\nu} = \frac{1}{2} - \frac{(1/2 - \nu_{el})\sigma_{Mises}}{E \cdot \varepsilon_{Mises}},\ \bar{\lambda}_2 = \frac{\phi_2 + \bar{\nu}}{1 + \phi_2\bar{\nu}},\ \bar{\lambda}_{Mises} = \sqrt{1 - \bar{\lambda}_2 + \bar{\lambda}_2^2} \tag{28}$$

5.3 Dowling's model

The model proposed in [11] also assumes that the principal stresses σ_1 and σ_2 act on the surface of the critical point (therefore σ_3 is zero), and it considers λ_2 and φ_2 constant, estimating them from their hookean values

$$\lambda_2 = \frac{\sigma_2}{\sigma_1} \cong \frac{\tilde{\sigma}_2}{\tilde{\sigma}_1} \cong \frac{\phi_2 + \nu}{1 + \phi_2\nu},\ \phi_2 = \frac{\varepsilon_2}{\varepsilon_1} \cong \frac{\tilde{\varepsilon}_2}{\tilde{\varepsilon}_1} \cong \frac{\lambda_2 - \nu}{1 - \lambda_2\nu} \tag{29}$$

Exceptionally, σ_2 is defined here as the lowest principal stress at the surface, even if σ_2 is smaller than σ_3 (i.e. the convention $\sigma_3 \leq \sigma_2 \leq \sigma_1$ is violated if $\lambda_2 < 0$).

The greatest difference between the previous two models and Dowling's is that the latter correlates σ_1 and ε_1 directly using effective Ramberg-Osgood parameters E^* and H_c^*

$$E^* = \left(\frac{1+\phi_2\nu}{1-\nu^2}\right)\cdot E,\ H_c^* = H_c\cdot\left(\frac{2}{2-\lambda_2}\right)^{h_c}(1-\lambda_2+{\lambda_2}^2)^{0.5(h_c-1)} \tag{30}$$

and the effective relation between σ_1 and ε_1 is [11]

$$\varepsilon_1 = \frac{\sigma_1}{E^*} + \left(\frac{\sigma_1}{{H_c}^*}\right)^{1/h_c} \tag{31}$$

Figure 7 presents the principal stress-strain relation for the 1020 steel, according to Dowling's model.

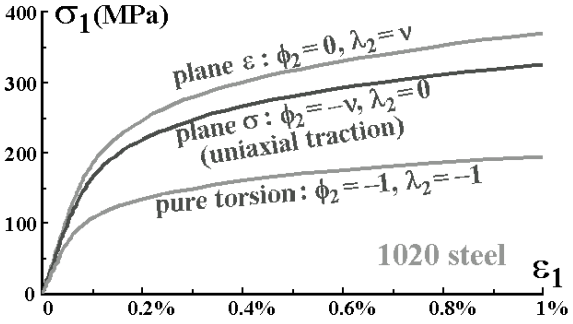

Figure 7: Principal stress-strain relations under plane strain, plane stress and pure torsion, according to Dowling.

In notched components, another variation of Neuber's rule must be used to calculate σ_1 (and then ε_1) from $\tilde{\sigma}_{Mises}$:

$$\frac{\left(\tilde{\sigma}_{Mises}\right)^2}{E} = \sigma_1\cdot\varepsilon_1 = \frac{\sigma_1^2}{E^*} + \sigma_1\cdot\left(\frac{\sigma_1}{H_c^*}\right)^{1/h_c} \tag{32}$$

The other principal stresses and strains are obtained from σ_1 and ε_1:

$$\begin{gathered}\sigma_2 = \lambda_2\sigma_1,\ \sigma_3 = 0 \\ \varepsilon_2 = \phi_2\varepsilon_1,\ \varepsilon_3 = -\bar{\nu}\varepsilon_1\tfrac{1+\lambda_2}{1-\lambda_2\bar{\nu}},\ \bar{\nu} = \tfrac{1}{2} - (\tfrac{1}{2}-\nu)\tfrac{\sigma_1}{E^*\varepsilon_1}\end{gathered} \tag{33}$$

The largest shear strain γ_{max} can then be calculated from the maximum difference between the principal strains ε_i (i = 1, 2, 3), obtaining not only its magnitude but also the plane where this maximum occurs.

It is important to note that the three presented models (formulated using the cyclic σ-ε curve) can also be applied to the hysteresis loops equations, by replacing in each equation ε with $\Delta\varepsilon/2$ and also σ with $\Delta\sigma/2$. The presented models are compared next.

6 Comparison among the multiaxial models

The presented multiaxial models are compared considering a notched 1020 steel shaft with diameter d equal to 60mm under alternate bending moment M_a of 2kNm and torsion T_a of 3kNm, in phase, with stress concentration factors in bending K_{tM} equal to 3.4 and in torsion K_{tT} equal to 2.4.

Assuming the alternate nominal stress σ_{na} as elastic,

$$\sigma_{n_a} = \frac{\sqrt{(32M_a)^2 + 3(16T_a)^2}}{\pi d^3} \tag{34}$$

then σ_{na} = 155MPa. This stress is lower than the cyclic yielding strength S_{yc}= 241MPa, therefore the hypothesis of σ_{na} elastic is valid.

Using the "highest K_t method" through the highest $K_t = 3.4$, σ_a and ε_a are calculated using Mises and Neuber

$$(K_t\sigma_{n_a})^2 = (3.4 \cdot 155)^2 = \sigma_a\varepsilon_a E = {\sigma_a}^2 + 203000 \cdot \sigma_a\left(\frac{\sigma_a}{772}\right)^{1/0.18} \Rightarrow \begin{cases} \sigma_a = 279MPa \\ \varepsilon_a = 0.49\% \end{cases} \tag{35}$$

and then the life N estimated for the shaft is

$$\frac{\Delta\varepsilon}{2} = \varepsilon_a = \frac{896}{203000}(2N)^{-0.12} + 0.41(2N)^{-0.51} \Rightarrow N = 5871\ cycles \tag{36}$$

To use the multiaxial stress-strain models, the hookean stresses at the notch root are calculated considering $K_{tM} = 3.4$ and $K_{tT} = 2.4$ as purely elastic:

$$\tilde{\sigma}_{a_{Mises}} = \sqrt{(K_{tM}\sigma_M)^2 + 3(K_{tT}\tau_T)^2} = \frac{\sqrt{(3.4 \cdot 32 \cdot M_a)^2 + 3(2.4 \cdot 16 \cdot T_a)^2}}{\pi(0.060)^3} \tag{37}$$

$$\tilde{\sigma}_{a_{1,2}} = \frac{K_{tM}\sigma_M}{2} \pm \sqrt{\left(\frac{K_{tM}\sigma_M}{2}\right)^2 + (K_{tT}\tau_T)^2} = 160 \pm 234MPa \tag{38}$$

Thus, the hookean stresses are $\tilde{\sigma}_{a_{Mises}}$ = 435MPa, $\tilde{\sigma}_{a_1}$ = 394MPa, $\tilde{\sigma}_{a_2}$ = -73MPa and $\tilde{\sigma}_{a_3}$ = 0, which can be correlated to the principal hookean strains from Hooke's law (considering $\nu = 0.3$):

$$\begin{aligned} \tilde{\varepsilon}_{a_1} &= [394 - 0.3(-73 + 0)]/203000 = 0.205\% \\ \tilde{\varepsilon}_{a_2} &= [-73 - 0.3(394 + 0)]/203000 = -0.094\% \\ \tilde{\varepsilon}_{a_3} &= [0 - 0.3(-73 + 394)]/203000 = -0.047\% \end{aligned} \tag{39}$$

$$\tilde{\varepsilon}_{a_{Mises}} = \frac{1}{\sqrt{2}(1+\nu)}\sqrt{(\tilde{\varepsilon}_{a_1} - \tilde{\varepsilon}_{a_2})^2 + (\tilde{\varepsilon}_{a_1} - \tilde{\varepsilon}_{a_3})^2 + (\tilde{\varepsilon}_{a_2} - \tilde{\varepsilon}_{a_3})^2} = 0.214\% \tag{40}$$

From the constant ratio and Hoffmann-Seeger models,

$$\frac{\tilde{\sigma}^2_{a_{Mises}}}{E} == 0.93 = \frac{{\sigma_{aMises}}^2}{E} + \sigma_{a_{Mises}} \cdot \left(\frac{\sigma_{a_{Mises}}}{772}\right)^{1/0.18} \Rightarrow \sigma_{a_{Mises}} = 259MPa \tag{41}$$

$$\varepsilon_{a_{Mises}} = \frac{\sigma_{aMises}}{203000} + \left(\frac{\sigma_{aMises}}{772}\right)^{1/0.18} \Rightarrow \varepsilon_{a_{Mises}} = 0.360\% \tag{42}$$

Note, as expected, that $\sigma_{a_{Mises}} < \tilde{\sigma}_{a_{Mises}}$ and $\varepsilon_{a_{Mises}} > \tilde{\varepsilon}_{a_{Mises}}$.

From the constant ratio model, the hookean stresses and strains can be used to estimate λ_{Mises} = 1.105, λ_2 = -0.185, λ_3 = 0, φ_{Mises} = 1.046, φ_2 = -0.460 and φ_3 = -0.231, so the alternate principal stresses and strains are

$$\begin{aligned} &\sigma_{a_1} = 259/1.1 = 235MPa,\ \sigma_{a2} = \lambda_2\sigma_{a_1} = -44MPa,\ \sigma_{a3} = 0 \\ &\varepsilon_{a_1} = 0.359\%/1.046 = 0.344\%,\ \varepsilon_{a_2} = \phi_2\varepsilon_{a1} = -0.158\%,\ \varepsilon_{a_3} = \phi_3\varepsilon_{a_1} = -0.080\% \end{aligned} \tag{43}$$

On the other hand, Hoffmann-Seeger's model predicts

$$\begin{aligned} &\bar{\nu} = \frac{1}{2} - \left(\frac{1}{2} - \nu\right)\frac{\sigma_{a_{Mises}}}{E \cdot \varepsilon_{a_{Mises}}} = 0.5 - 0.2\frac{259}{203000 \cdot 0.00359} = 0.429 \\ &\bar{\lambda}_2 = \frac{\phi_2 + \bar{\nu}}{1 + \phi_2\bar{\nu}} = \frac{-0.46 + \bar{\nu}}{1 - 0.46\bar{\nu}} = -0.0387,\ \bar{\lambda}_{Mises} = \sqrt{1 - \bar{\lambda}_2 + \bar{\lambda}_2^2} = 1.02 \end{aligned} \tag{44}$$

resulting in alternate principal stresses and strains

$$\begin{cases} \sigma_{a_1} = 259/1.02 = 254MPa,\ \sigma_{a_2} = -0.0387 \cdot \sigma_{a_1} = -10MPa,\ \sigma_{a_3} = 0 \\ \varepsilon_{a_1} = (1 - \bar{\lambda}_2\bar{\nu})0.360\%/1.02 = 0.359\%,\ \varepsilon_{a_2} = \phi_2\varepsilon_{a1} = -0.165\% \\ \varepsilon_{a_3} = -\bar{\nu}\varepsilon_{a_1}(1 + \bar{\lambda}_2)/(1 - \bar{\lambda}_2\bar{\nu}) = -0.146\% \end{cases} \tag{45}$$

Dowling's model uses the elastic ratios λ_2 = -0.185 and φ_2 = -0.460 to calculate the effective parameters of the hardening curve

$$E^* = \left(\frac{1 + \phi_2\nu}{1 - \nu^2}\right) \cdot E = \left(\frac{1 - 0.46 \cdot 0.3}{1 - 0.3^2}\right) \cdot 203GPa = 192GPa \tag{46}$$

$$H_c^* = 772MPa \cdot \left(\frac{2}{2 - \lambda_2}\right)^{0.18} (1 - \lambda_2 + {\lambda_2}^2)^{0.5(0.18-1)} = 700MPa \tag{47}$$

$$\frac{\left(\tilde{\sigma}_{a_{Mises}}\right)^2}{E} = 0.93 = \sigma_{a1} \cdot \varepsilon_{a_1} = \frac{\sigma_{a_1}^2}{E^*} + \sigma_{a1} \cdot (\frac{\sigma_{a_1}}{H_c^*})^{1/h_c} \Rightarrow \begin{cases} \sigma_{a_1} = 240MPa \\ \varepsilon_{a_1} = 0.388\% \end{cases} \tag{48}$$

$$\begin{cases} \sigma_{a_2} = \lambda_2\sigma_{a_1} = -45MPa,\ \sigma_{a_3} = 0 \\ \varepsilon_{a_2} = \phi_2\varepsilon_{a_1} = -0.179\%,\ \varepsilon_{a3} = -\bar{\nu}\varepsilon_{a1}\frac{1+\lambda_2}{1-\lambda_2\bar{\nu}} = -0.127\%\ (\bar{\nu} = 0.436) \end{cases} \tag{49}$$

For all considered models, the maximum shear strain amplitude is calculated from $\gamma_{amax} = \varepsilon_{a1} - \varepsilon_{a2}$, assuming that the directions 1 and 2 are respectively the ones with maximum and minimum principal strains. The maximum normal strains and stresses in the plane of γ_{amax} are

$$\varepsilon_{a\perp} = (\varepsilon_{a1} + \varepsilon_{a_2})/2 \text{ and } \sigma_{a\perp} = (\sigma_{a_1} + \sigma_{a_2})/2 \tag{50}$$

Since in this problem the mean stresses and strains are zero, the values used by the Brown-Miller, Fatemi-Socie and SWT strain-life models are respectively $\Delta\varepsilon_\perp = 2\varepsilon_{a\perp}$, $\sigma_{\perp max} = \sigma_{a\perp}$ and $\sigma_{\perp 1max} = \sigma_{a_1}$.

Table 1 summarizes the stresses and strains obtained from the hookean values (obtained assuming elastic stresses, which must not be used in life predictions in the presence of significant plasticity), from the "highest K_t method", and from the three presented multiaxial stress-strain models: the constant ratio, Hoffmann-Seeger's and Dowling's.

Table 1: Stresses (in MPa) and strains predicted from the studied models.

	hookean values	highest K_t method	constant ratio	Hoffman-Seeger	Dowling
$\sigma_{a_{Mises}}$	435	279	259	259	265
$\varepsilon_{a_{Mises}}$	0.214%	0.488%	0.360%	0.360%	0.418%
σ_{a_1}	394	253	235	254	240
σ_{a_2}	-73	-47	-44	-10	-45
σ_{a_3}	0	0	0	0	0
ε_{a_1}	0.205%	0.466%	0.344%	0.359%	0.388%
ε_{a_2}	-0.094%	-0.215%	-0.158%	-0.165%	-0.179%
ε_{a_3}	-0.047%	-0.108%	-0.080%	-0.146%	-0.127%
$\gamma_{a_{max}}$	0.299%	0.681%	0.502%	0.524%	0.567%
$\Delta\varepsilon_\perp$	0.111%	0.251%	0.186%	0.194%	0.209%
$\sigma_{\perp max}$	160	103	95	122	98

Note from Table 1 that the "highest K_t method" is conservative, especially for the calculated strains, but not too much, therefore it could be used in practice. The three multiaxial models are in theory more accurate, predicting approximately the same values.

Now, using e.g. Dowling's model, the fatigue life N can be obtained from the several damage models. Considering the εN curve and using the Mises strain $\varepsilon_{a_{Mises}} = 0.418\%$, then it is found that $N = 8765$ cycles.

If, instead of the εN curve, the γN curve is considered, estimating its coefficients from $\tau_c \cong \sigma_c/\sqrt{3}$, $b_\gamma \cong b$, $\gamma_c \cong \varepsilon_c\sqrt{3}$ and $c_\gamma \cong c$, and using $\gamma_{a_{max}} = 0.567\%$, then it is found that $N = 14693$ cycles.

Considering the Brown-Miller's model, with its constants estimated from $\alpha_{BM} \cong 0.3$, $\beta_1 = 1.3 + 0.7\cdot\alpha_{BM} = 1.51$ and $\beta_2 = 1.5 + 0.5\cdot\alpha_{BM} = 1.65$, with $\Delta\varepsilon_\perp = 0.209\%$, then it is found that $N = 10290$ cycles.

Fatemi-Socie's model, using $\alpha_{FS} \cong S_{yc}/\sigma_c = 241\text{MPa}/896\text{MPa} \cong 0.27$ and the γN curve estimated as above, where $\sigma_{\perp max} = 98\text{MPa}$, results in $N = 11201$ cycles.

And finally, considering the SWT's model, which is appropriate for materials more sensitive to normal stresses, with $\Delta\varepsilon_1/2 = \varepsilon_{a_1} = 0.388\%$ and, since the mean loads are zero, $\sigma_{\perp 1max} = \sigma_{a_1} = 240\text{MPa}$, then $N = 13577$ cycles.

The above results, based on stresses and strains from Dowling's model, are recalculated considering hookean values, the "highest K_t method", the constant ratio and Hoffmann-Seeger models, using the ViDa fatigue design software [12, 13]. The results are shown in Table 2.

Table 2: Fatigue lives (in cycles) predicted from the studied multiaxial models.

	Mises + εN curve	γN curve	Brown-Miller	Fatemi-Socie	SWT
hookean values	59500	94300	63000	56200	18300
highest K_t method	5900	9120	6440	6940	8470
constant ratio	13000	20300	14100	15500	18300
Hoffmann-Seeger	13000	18100	12600	12900	14200
Dowling	8770	14700	10300	11200	13600

Except from the results obtained from the hookean values (which are significantly non-conservative), all combinations of multiaxial damage models with multiaxial stress-strain relations resulted in predicted lives not too different, varying between 5900 and 20300 cycles. Therefore, it is reasonable to consider in proportional histories the use of simplifications such as the "highest K_t method" and the εN curve applied to $\Delta\varepsilon_{Mises}/2$, despite the conservative predictions.

The hookean values result in poor estimates, overestimating σ_{a_1} and underestimating ε_{a_1}, but it interestingly estimates quite well the product $\sigma_{a_1}\varepsilon_{a1}$ (because, according to Neuber, $\tilde{\sigma}_{a_1}\tilde{\varepsilon}_{a_1} \cong \sigma_{a_1}\varepsilon_{a_1}$), therefore they resulted in good predictions when combined with SWT's model, which is based on this product.

But in NP histories, the NP hardening can have a significant effect in the fatigue life. In addition, none of the presented σ-ε models is valid in the NP case (because all of them assumed φ_2 constant). In the NP case, incremental plasticity models must be used [1].

7 Conclusions

In this work, the multiaxial damage models of Sines, Findley and Dang Van, applicable to long fatigue lives, and Brown-Miller, Fatemi-Socie and Smith-Watson-Topper (SWT), which consider plasticity, were reviewed. The Sines model is easy to compute, it considers the effect of the second principal stress σ_2 (because it uses the Mises plane), but it is only valid for proportional histories. On the other

hand, Findley's model is hard to compute, because it requires the search for a critical plane, but for long lives it is valid for any load history, proportional or NP. Dang Van's model is able to consider the damage in a mesoscopic scale, but it has the limitations of the stress-based models.

The strain-based models are valid for any life, short or long. Among them, the Brown-Miller and Fatemi-Socie models give more value to the shear strains γ, while SWT does it for normal strains ε. Brown-Miller and Fatemi-Socie combine $\Delta\gamma_{max}$ to $\Delta\varepsilon_{\perp}$ or to $\sigma_{\perp max}$ normal to the direction of γ_{max}, being applicable to proportional or NP histories. SWT uses the principal strain ε_1. The most versatile models among the studied ones are the Fatemi-Socie and SWT, because they can include the NP hardening effect. But in order to generate a more realistic model, it is important to modify these criteria to calculate the fatigue life in the critical plane where the damage parameters of each model are maximized.

The main multiaxial stress-strain models were also reviewed and compared. It can be concluded that multiaxial stress-strain relations must be used instead of uniaxial ones, even though a few simplifications are adequate, such as the "highest K_t method" for notched components. Since the critical point of a structure is usually in its surface, in general a 2D analysis (under plane stress) is enough for multiaxial fatigue design. Except for the results from the hookean values, which are significantly non-conservative, all combinations of strain-based multiaxial damage models with multiaxial stress-strain relations resulted in not too different lives (within a factor of 2) for the considered example, which has significant plastic strains (but they were not much higher than the elastic ones). The best predictions should be the ones from multiaxial models that use the critical plane idea, where the damage parameters are maximized. However, none of the studied stress-strain models is valid for NP hardening, which can have a significant influence in the fatigue lives of e.g. stainless steels.

References

[1] Socie, D.F. & Marquis, G.B., Multiaxial fatigue. *SAE International*, 1999.
[2] Zouain, N., Mamiya, E.N. & Comes, F., Using enclosing ellipsoids in multiaxial fatigue strength criteria. *European Journal of Mechanics - A, Solids*, **25**, pp. 51–71, 2006.
[3] Sines, G., Behavior of metals under complex static and alternating stresses. *Metal Fatigue*, McGraw-Hill, pp. 145–169, 1959.
[4] Findley, W.N., A theory for the effect of mean stress on fatigue of metals under combined torsion and axial load or bending. *Journal of Engineering for Industry*, pp. 301–306, 1959.
[5] Dang Van, K. & Papadopoulos, I.V., *High-Cycle Metal Fatigue*. Springer, 1999.
[6] Gonçalves, C.A., Araújo, J.A. & Mamiya, E.N., Multiaxial fatigue: a stress based criterion for hard metals. *International Journal of Fatigue*, **27**, pp. 177–187, 2005.
[7] Brown, M. & Miller, K.J., A theory for fatigue under multiaxial stress-strain conditions. *Institute of Mech Engineers*, **187**, pp. 745–756, 1973.
[8] Fatemi, A. & Socie, D.F., A critical plane approach to multiaxial damage including out-of-phase loading. *Fatigue and Fracture of Eng Materials and Structures*, **11(3)**, pp. 149–166, 1988.
[9] Smith, R.N., Watson, P. & Topper, T.H., A stress-strain parameter for the fatigue of metals. *J of Materials*, **5(4)**, pp. 767–778, 1970.
[10] Hoffmann, M. & Seeger, T., A generalized method for estimating multiaxial elastic-plastic notch stresses

and strains, Part 1: Theory. *J Eng Materials & Technology*, **107**, pp. 250–254, 1985.
[11] Dowling, N.E., Brose, W.R. & Wilson, W.K., Notched member fatigue life predictions by the local strain approach. *Fatigue Under Complex Loading: Analysis and Experiments, AE-6, SAE*, 1977.
[12] Meggiolaro, M.A. & Castro, J.T.P., Vida 98 - danômetro visual para automatizar o projeto à fadiga sob carregamentos complexos. *Journal of the Brazilian Society of Mechanical Sciences*, **20(4)**, pp. 666–685, 1998.
[13] Miranda, A.C.O., Meggiolaro, M.A., Castro, J.T.P., Martha, L.F. & Bittencourt, T.N., Fatigue life and crack path prediction in generic 2D structural components. *Engineering Fracture Mechanics*, **70**, pp. 1259–1279, 2003.

Mechanics of Solids in Brazil 2009, H.S. da Costa Mattos & Marcílio Alves (Editors)
Brazilian Society of Mechanical Sciences and Engineering, ISBN 978-85-85769-43-7

Composite tube behavior under low velocity impact

Giangiacomo Minak, Daniele Ghelli, Riccardo Panciroli, Andrea Zucchelli

Alma Mater Studiorum – Università di Bologna, Mechanical Engineering Department DIEM, Bologna – Italy

Abstract

Advanced applications of tubes made of carbon-epoxy composites in which the main external load is torque, have been recently developed in the industrial and sports fields.
In order to use these high specific performance material components, a fundamental problem for the designer is the low energy and velocity impact behavior. In fact such load events are very common during normal service life and their real effects on in-service component behavior are not well understood.
In the present work the results of an experimental test campaign performed with the aim of evaluating the mechanical behavior of tubular structures under impact, with and without torsional pre-load, are presented. In particular, the aspects on which the research was focused are the stacking sequence and the pre-load level, that proved to be a key factor for the impact response of the material. A numerical model based on the Ansys software was developed to describe the material behavior up to the first load drop.

Keywords: composites, carbon fiber, epoxy matrix, tubes, impact.

1 Introduction

Laminated composite materials, consisting of a polymer matrix reinforced by long carbon fiber, possess excellent mechanical properties (specific stiffness and strength, for example) when loaded in their plane but can be easily damaged by impact loads, such as those caused by accidental collisions during the production, operation or maintenance phases [1]. By virtue of their mechanical properties and despite their high cost, these materials have recently been used to produce components in the form of tubes such as high speed shafts for power transmission in paper industry machines or in high-performance applications and sports (masts and winches in sailboats, fishing rods, etc.).

While the international research on the impact on composite laminated plates includes many different contributions, including some by the authors of this paper [2–4], the phenomenon of side impact on tubes was studied only to a limited extent in recent years in the scientific literature, by analytical models [5, 6], numerical models [7–9] or experimentally [10].

Mechanics of Solids in Brazil 2009, H.S. da Costa Mattos & Marcílio Alves (Editors)
Brazilian Society of Mechanical Sciences and Engineering, ISBN 978-85-85769-43-7

In particular, the studies by Christoforou *et al.* [5] and Christoforou and Swanson [6] are focused on the dynamic response of the pipe, which takes account of the damage with simple analytical models. An exhaustive investigation conducted by means of a parametric finite element model was carried out by Krishnamurthy *et al* [7]. The parameters considered in this work are impactor mass and velocity, stacking sequence and boundary conditions, and their effect on the damage of the matrix and the magnitude of delaminated area, assessed with appropriate criteria from the calculated stresses, are determined. Using methods similar to those of the previous work, Kim *et al* [8] and Her and Liang [9] numerically investigated the effect of the stacking sequence and of the curvature on the dynamic response and damage in sequences comparable with those used in this memory. Finally, Doyum and Altay [10] focused on damage caused in glass-epoxy tubes by non-instrumented impacts of energy comparable to the energy of the present study, but on markedly different stacking sequences.

The final aim of this research is the determination of residual resistance to twisting of tubular composite structures subjected to lateral low velocity impacts. In this part, the results of impact tests performed considering different lay-ups and different conditions of pre-loading in torsion are discussed. The interpretation of the experimental results was assisted by a suitable non linear FEM model.

2 Materials and methods

The tubes considered, 200 mm long, 50 mm inside diameter and thickness 2.55 mm, were produced in an autoclave by overlapping 16 unidirectional plies of epoxy matrix reinforced with 60% in volume of T300 carbon fiber. Different lay-ups were utilized, two cross-ply listed as CP and two quasi-isotropic mentioned as QI (see Table 1 where the direction of 0º was cylinder generatrix one). As can be seen, there are two symmetrical lay-ups (CPS and QIS) and two non-symmetrical ones (CPNS and QINS).

Table 1: Stacking sequences.

label	lay-up
CPS	$[45/\text{-}45]_{4s}$
CPNS	$[45/\text{-}45]_{8}$
QIS	$[0_2/45/\text{-}45/45/\text{-}45/90_2]_s$
QINS	$[0_2/45/\text{-}45/45/\text{-}45/90_4/45/\text{-}45/45/\text{-}45/0_2]$

2.1 Experimental set-up

The low velocity impact was produced by an instrumented pendulum equipped with a piezoelectric load cell (PCB Piezotronics, Model 208A35) with semi-spherical head 12.7 mm in diameter which hit the middle of the tube in the orthogonal direction. The estimated impact energy was 7J, corresponding

to that of a small tool falling from about a meter, whereas the velocity was 3.5 m/s. Each tube was also instrumented by means of a couple of strain gauges (HBM LY41-6/350, 350 Ω, grid 6 mm), each connected in half bridge configuration with a heat compensator, in order to further investigate the evolution of the damage and its influence on mechanical properties.

The strain gauges were located at a distance of about 15 mm from the impact point, except in cases of impact on specimens with high torsional pre-load where they were positioned on the opposite side. The orientation of the grid was at ± 45º relative to the tube generatrix in order to acquire the deformation caused both by impact and torque.

The acquisition of the high speed signals (load and deformation) was made by a National Instruments board with a sampling frequency of 100 kHz. The tubes during the impact were blocked by a pair of grips to a torsional testing machine because the ultimate purpose was to measure the residual resistance to twisting after impact or to impose a torsional pre-load during impact.

Figure 1 shows the grasping system, consisting of four semi-cylindrical steel shells glued to the tube by a high resistance bi-component epoxy glue (Scotch-Weld 9323B / A 3M). The grips were appropriately shaped to transmit the torque and to reduce the stress concentration on the glue [11].

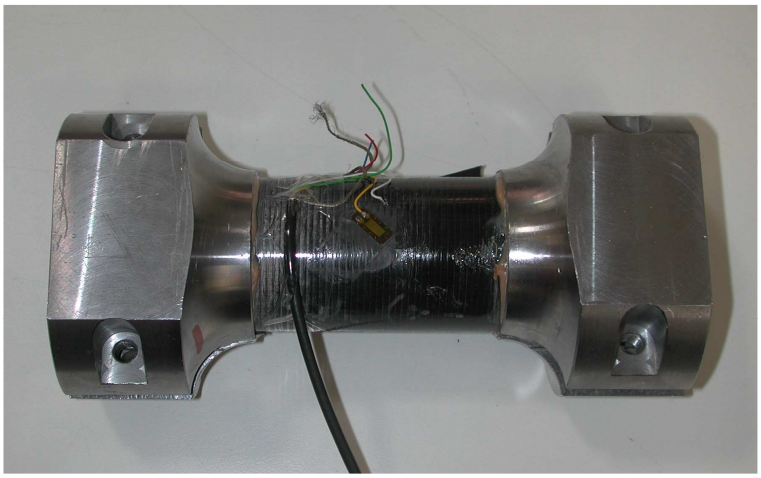

Figure 1: Tubular specimen with the grasping system.

Figure 2 shows the full experimental set-up, including: the Italsigma torsional testing machine, the instrumented pendulum and the signal acquisition system (torque, rotation, deformation of strain gauges, impact force and finally Acoustic Emission, whose details are not discussed in this paper).

The lateral impact tests were performed on specimens simply bound to the machine and on specimens pre-loaded in torsion (by controlling the displacement) with a torque equal to 65% or 130% of the torsional residual resistance (RRT) of not pre-loaded specimens.

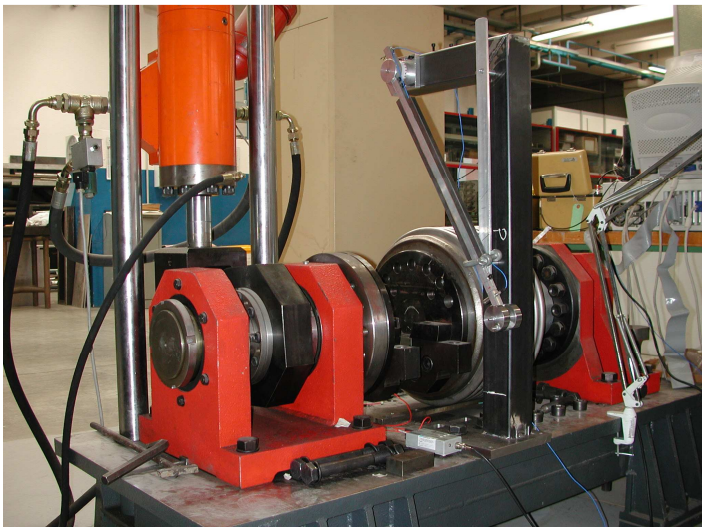

Figure 2: Experimental set-up.

2.2 Numerical model

The numerical modelling of CPS and QIS lamination sequences was performed using the finite element code ANSYS.

Solid185 Layered 8-node elements with three displacement degrees of freedom were used. Thus, by using the Layered option it was possible to define layer thickness and layer material direction angles as well as the orthotropic material properties shown in table 2. The load cell head was modeled as a rigid body and contact elements were placed close to the impacted area as shown in fig. 3. Sixteen elements 0.16mm thick were placed along the tube thickness (one for each lamina). A pure torque and a static lateral force, equal to the first peak load measured in the experimental test, were applied by placing them directly on pilot nodes. Furthermore, the analysis was performed in the condition of non-linear geometric behavior.

Table 2: Carbon/Epoxy elastic properties.

E_1	$E_2 = E_3$	$G_{12} = G_{13}$	G_{23}	$\nu_{12} = \nu_{13}$	ν_{23}
105 GPa	6.5 GPa	5.5 GPa	2.0 GPa	0.28	0.0256

As a failure criteria the 3-D Hashin-type [12] used in [2] was adopted and the values of matrix and fiber resistance, reported in table 3, were derived from the results of AE monitored torsion tests.

Table 3: Fiber and matrix resistance in tension,compression and shear.

σ_{FT}	σ_{FC}	σ_{MT}	σ_{MC}	τ_M
2390 MPa	-1670 MPa	25 MPa	-150 MPa	60 MPa

Since the static approximation was presumed to be valid and dynamic effects were ignored, fixed displacements and rotation of the free section of the tube were imposed as boundary conditions.

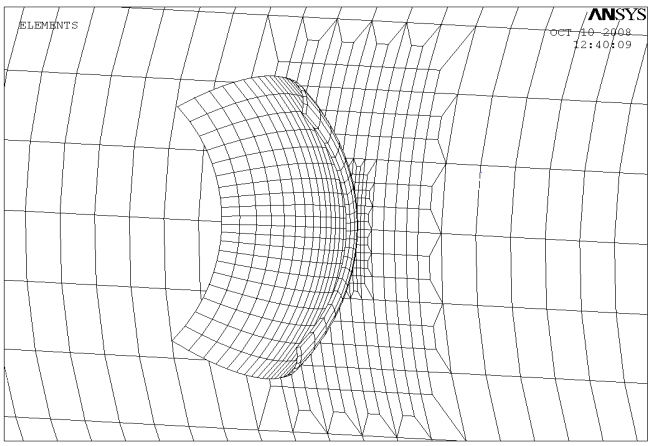

Figure 3: Model discretization.

3 Results

In Figure 4, the impact behaviors of the different lay-ups can be observed. The two quasi-isotropic sequences, QIS and QINS, had the same behavior, so only one trend was reported. In all three cases, a strongly accentuated initial peak followed by a fall, more pronounced for the cross ply specimens, can be noted.

A slowly growing load phase then follows, before the rebound of the impactor and the unloading of the specimen. The initial ascent phase represents the response of the undamaged material until the first failure, located at the beginning of the fall. The subsequent recovery of load was due to the global behavior of the structure that began to react when an greater impactor area came into contact with the material surface.

The impact damage was analogous in QI and CPS specimens while due to slightly greater damage the CPNS specimens reached lower load levels and longer impact duration.

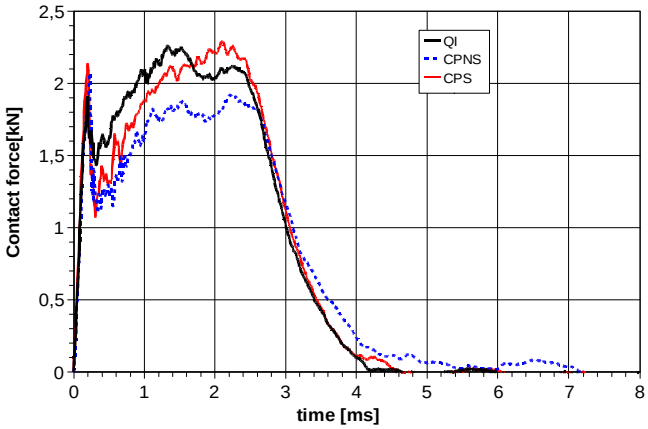

Figure 4: Effect of the lay-up on the impact load evolution.

Ignoring the difference in response due to the symmetry of the stacking sequences (only detectable in CP samples), Figures 5 and 6 report the contact force evolution versus time for the two configurations (QI and CP) having different torsional pre-load levels.

In the case of QI specimens it is possible to observe that the pre-load did not substantially change the response to impact, while the highest pre-load caused an elongation of the load fall phase with an increase of the overall duration of impact.

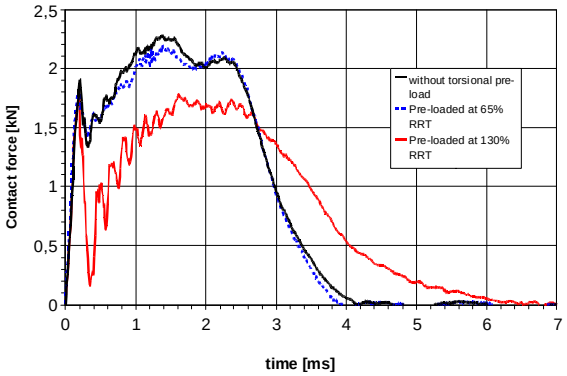

Figure 5: Effect of the pre-load on QI specimens.

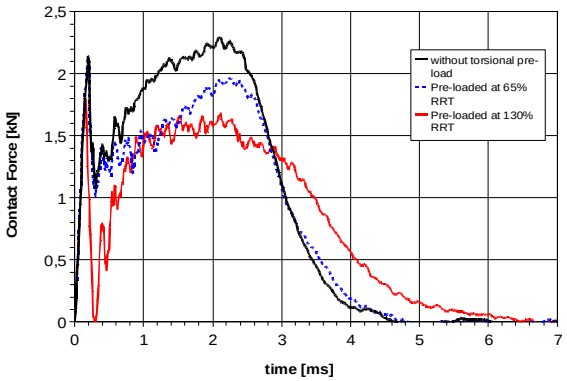

Figure 6: Effect of the pre-load on CP specimens.

The behavior of CP tubes was different. In fact, the pre-load of 65% of RRT significantly changed the response; the load recovery after the first failure did not exceed the level reached by the first peak

as observed in the case of non pre-loaded specimens.

The impact on the pre-loaded tube at the highest level of torque provoked huge damage that led the first load to drop to zero. As in the case of QI specimens, the second load peak was significantly lower and the impact had a longer duration.

The strain gauge data made it possible to understand the mechanism of damage in more detail, albeit within the limits of local approach. Figures 7 to 9 show three representative examples of acquisition of strain trend during impacts. In the cases of high torsional pre-load when the gauges were glued near the point of impact, the gauge or the electrical connection braking always occurred in the earliest test phases. It was therefore decided to glue the gauge on the opposite side of the specimen.

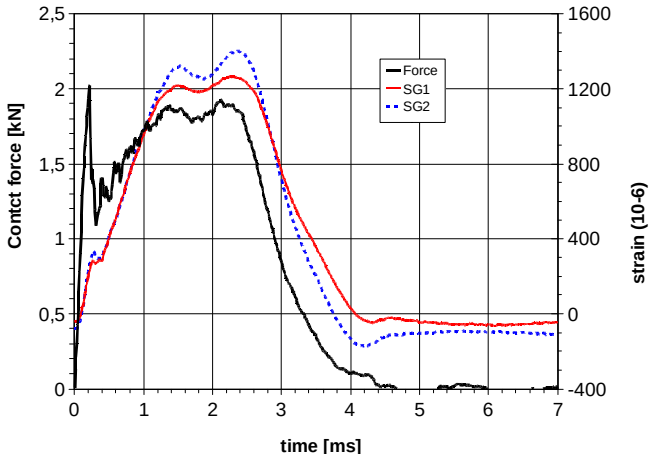

Figure 7: Strain in the presence of localized damage (CP not pre-loaded).

The key feature of all the readings is that the first peak load was detected barely or not at all.

On the contrary, in the subsequent phase of load recovery, in some cases, as in Figure 7, the deformation proportionally followed the trends of force, while in other cases, like that of Figure 8, the deformation followed the load up to a certain point, and then deviated significantly .

This behavior can certainly be related to the progression of delamination; in fact, when the strain ceases to be proportional to the load it can be reasonably due to the delamination front passing under the strain gauges.

In Figure 9 it is possible to see the overall effect in a highly pre-loaded specimen. In this case, the gauges, placed at 45° relative to the cylinder generatrix, and perpendicular to each other, due to the impact and with a slight delay of 200 microseconds, are downloaded near to zero, showing the relaxation of the pre-load.

The visual inspection of the damaged zones showed clear differences both in stacking sequence (between QI and CP, while there were no noticeable differences due to the presence or absence of symmetry) and as regards the effect of pre-load.

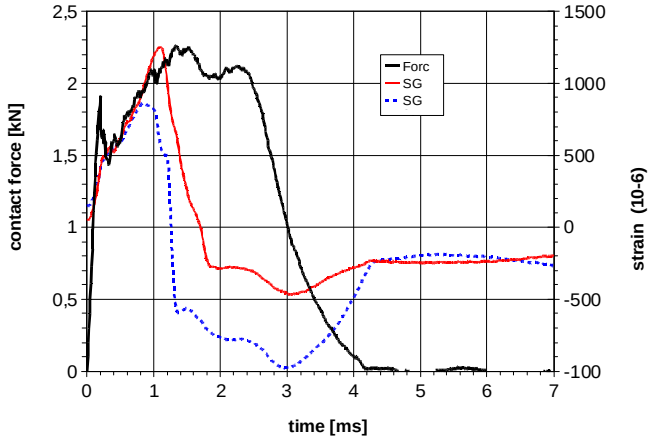

Figure 8: Strain in the presence of delamination (QI not pre-loaded).

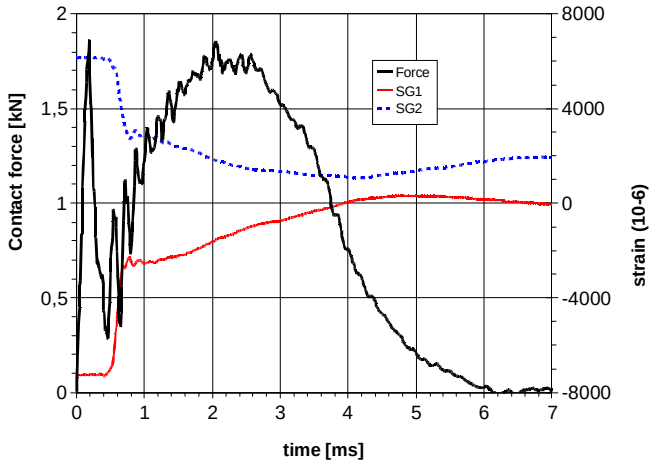

Figure 9: Strain in highly damaged specimen (QI pre-loaded at 130% RRT, strain gages far from the impact point).

Figure 10 shows the macroscopic effects of impact on not pre-loaded specimens on the outer surface and on the correspondent inner surface. In QI specimens, the damage produced is barely visible outside (Figure 10A) with a slight dent, small matrix cracks and some fiber cracking. Inside (Figure 10B), we see instead a small swelling due to delamination, sometimes accompanied by a slight splitting. In the CP samples signs of splitting are visible on the external lamina (Figure 10C) around the impact mark (Figure 10D) and on the external ply just below the impact point.

The effects of the pre-load on test are shown in Figure 11. In this case we have only the image of the exterior of the tube after the collision because the samples were immediately broken in torsion without releasing the pre-load and this made it impossible to document the damage on the inner face.

The QI tubes pre-loaded to 65% of RRT (Figure 11A) showed a marked imprint, clearly visible, and the detachment of the 0º external lamina, fractured in the direction perpendicular to the fibers.

The QI specimens pre-loaded at 130% of the RRT (Figure 11B) experienced a marked breakdown of the internal plies that led to the detachment of the external lamina in several places (without breaking the fibers placed at 0º).

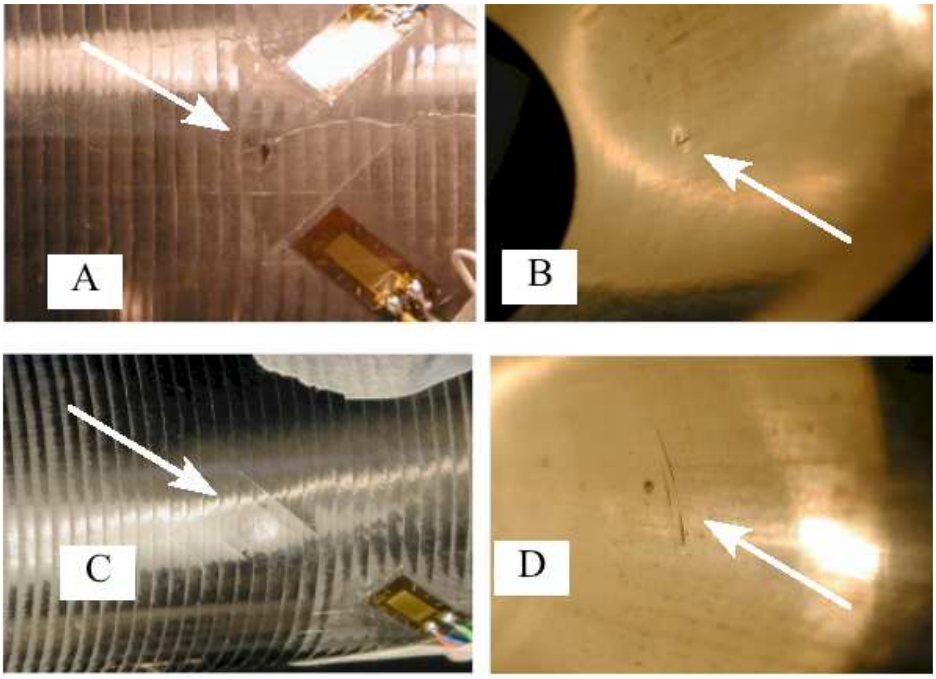

Figure 10: Damage of not pre-loaded specimens QI ((A) inner surface, (B) outer s.) and CP ((C) outer s., (D) inner s.).

In CP samples at the lowest level of pre-load (Figure 11C), a hollow centered at the point of impact and oriented to 45º was produced. Finally, in the tubes pre-loaded at the highest level of torque (Figure 11D) the hollow became a twisted fracture that affected the entire length of the tube as far as the grips and, as seen by rotating in the opposite direction to the one that caused the initial pre-load, crossed the whole thickness.

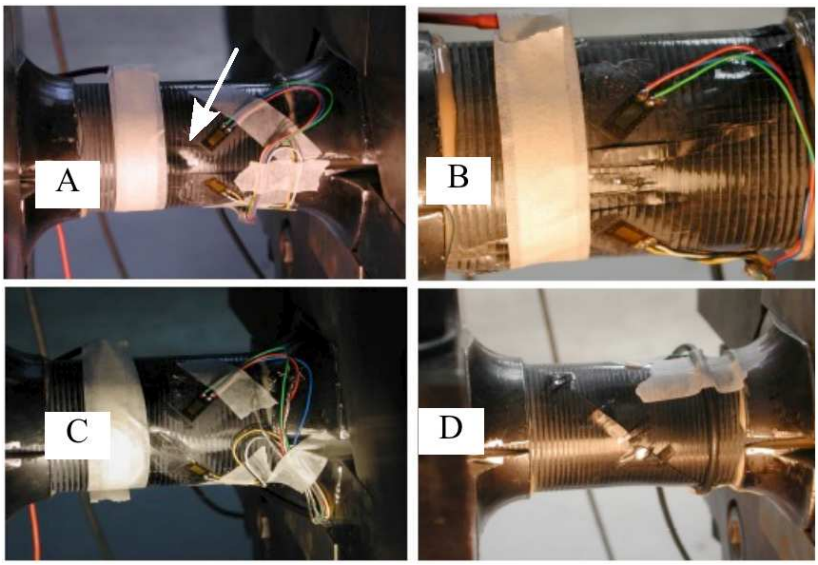

Figure 11: Damage of pre-loaded specimens (A) QI 65% RRT, (B) QI 130% RRT, (C) CP 65% RRT, (D) CP 130%RRT.

The following four figures show results of numerical simulations in terms of contour plots of the Hashin criterion for fiber and matrix failure. In particular, two different layups for the outermost ply and for the internal one are considered.

The square area represented in the figures has a dimension of $15\times15\text{mm}^2$ and is centered in the contact point. The plots relative to the three levels of pre-load are shown.

In figures 12 and 13 fiber failure is considered respectively for QI and CP specimens. The damage index value and the dimension of the damaged area are independent of (for QI) or slightly dependent (for CP) on the torsional preload. In both cases, the fiber failure condition is obtained in the outermost lamina.

The matrix damage index contours are shown in Figure 13 for QI and in Figure 14 for CP specimens.

From these index contour maps it is possible to see that the inner lamina had a larger matrix damaged area than the external one and it increased for higher pre-loads, while in the case of CP tubes the damaged area of the external ply was independent of the pre-load.

In all cases, the matrix damage index indicated the presence of matrix cracking that is the origin of delamination in the case of components with high flexural stiffness, like the tubes [13].

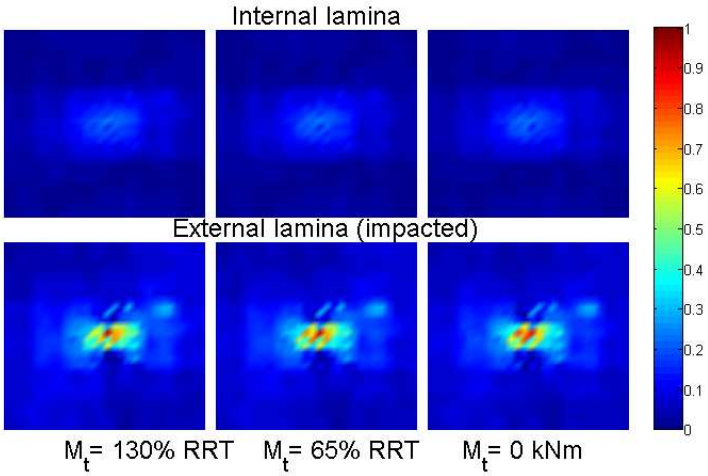

Figure 12: Hashin Criterion for fiber failure in QI lay-up.

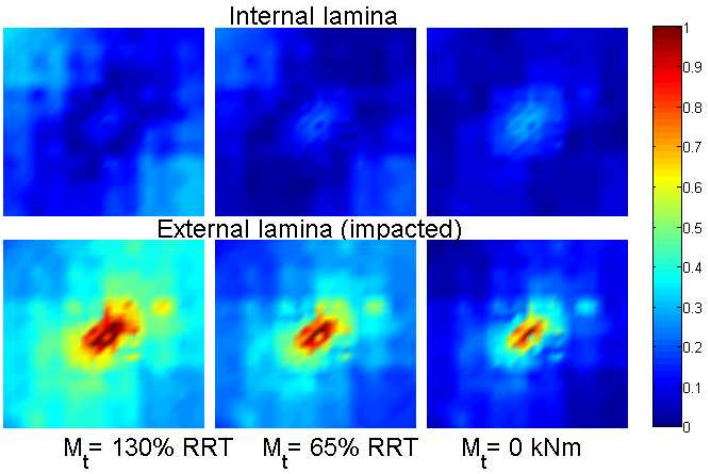

Figure 13: Hashin Criterion for fiber failure in CP lay-up.

4 Discussion

The measures of contact force and deformation during the impact, together with the observation of the specimens after testing and with the numerical simulations, suggest some considerations about the effects of the lay-up and of the level of torsional pre-load on the impact behavior and in particular on the mechanisms of fracture.

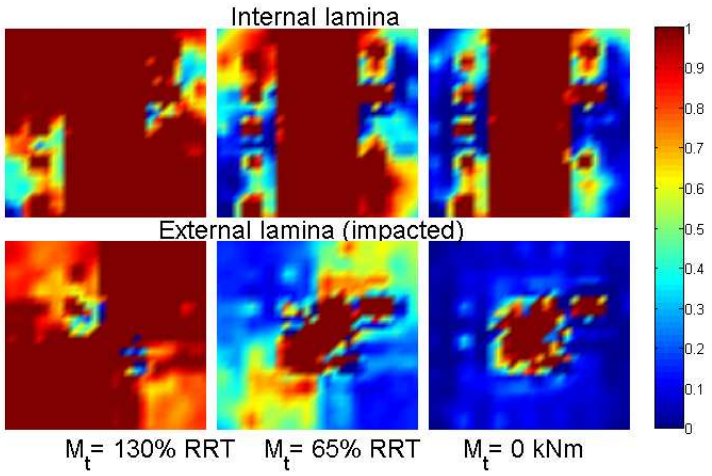

Figure 14: Hashin Criterion for matrix failure in QI lay-up.

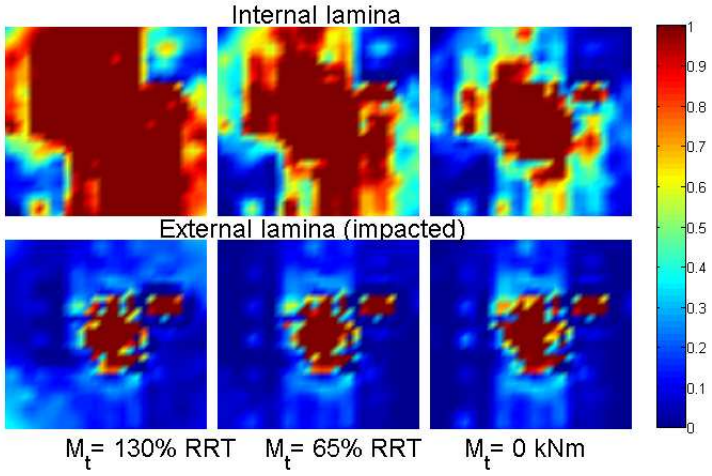

Figure 15: Hashin Criterion for matrix failure in CP lay-up.

As regards the QI tubes, no difference in impact behavior between QIS and QINS was noted, and this is not surprising since this is a flexural problem in which the external 0º fiber stiffness tends to prevail [8]. On the contrary, in the CP specimens it was possible to note the effect of the succession of the different interfaces present in the CPNS tubes compared with the CPS ones (Fig. 4).

In general, the torsional pre-load role was to provide a certain amount of strain energy available for the propagation of the initial damage provoked by the impact. The response in the early moments

did not change compared to the case without pre-load and the maximum load reached was the same; from that point onwards, the trends were different because of the different evolution of damage. From the value of force measured in the second peak and from the visual inspection it can be deduced that the QI specimens were less damaged than the CP ones in this particular loading condition (Figs. 5 and 6).

Turning to the mechanisms of fracture, without doubt the matrix fracture and delamination were present and in some cases it was possible to see failure of the fibers on the outer ply with the naked eye. The peak of force (and the next fall) highlighted in the very first moments of all the impact tests did not match a similar trend of the deformation acquired by the strain gauges, which at most showed only slight discontinuity or change of slope. Only in the following phases were the readings of the gauges consistent with the reading of the load cell. This means that the initial material damage caused by the first peak load occurred in the early stages in a small area adjacent to the point of impact, at a shorter distance than the one between the point of impact and the strain gauges (which was about 15 mm).

This interpretation is confirmed by the numerical model; in fact, for both lay-ups, the fibers and the matrix of the external ply, on which the strain gauges were glued, were considered broken in a small area around the contact point, according to the Hashin criterion (see Figs 12-15).

Due to this localized failure the amplitude of the elastic wave that reached the gauges was significantly lower than what could be expected considering the value of the peak load. In the following few instants the impactor came into contact with larger parts of the laminate so the extent of deformation increased due to the global flexural behavior.

It is likely that the first load drop was provoked by delamination, induced by the first matrix failure visible on the outer surface [13] and foreseen also by the numerical model (see Figs. 14,15).

The delamination continued to spread even further, as shown by some of the measures of the strain gauges (Fig.8) where a rapid change of the strain trend can be noted. This strain trend variation can be explained as a consequence of delaminations between the external ply, over which the sensor is placed, and the rest of the laminate

Among other things, this observation confirms that, as usually happens in CFRP laminates, the inner impact damage is much more extensive than visual inspection may show.

Summarizing, the failure mechanism started with the matrix breakage in the contact area; this originated the delamination onset and growth at least under the outer lamina. The inner lamina also showed delamination and it was probably spread all through the thickness. In the pre-loaded specimens delamination induced the buckling of the laminas in compression and finally also the laminas in tension failed due to overstress.

5 Conclusion

The effects of the lay-up and of the level of torsional pre-load on the response of composite tubes under impact were studied.

The experimental testing and the numerical modelling showed that:

1. in all cases the impact damage is highly localized as regards fiber failure, while delamination and matrix cracking are spread through the thickness;
2. the QI specimens were less damaged than the CP ones and among these the CPS specimens have a slightly better behavior than CPNS samples while there is no difference between QIS and QINS specimens.
3. the presence of the torsional pre-load significantly changed the elastic response and increased the amount of damage, especially in the case of CP samples, in some cases up to complete breakage of the specimen.

Acknowledgements

The authors thank Dario Comand and the company REGLASS H.T. S.r.l for supporting the research.

References

[1] Abrate, S., *Impact on composite structures*. Cambridge University Press: New York, 1998.
[2] Cesari, F., Dal Re, V., Minak, G. & Zucchelli, A., Damage and residual strength of laminated carbon-epoxy composite circular plates loaded at the centre. *Composites Part A: Applied Science and Manufacturing*, **38(4)**, pp. 1163–1173, 2006.
[3] Minak, G., Morelli, P. & Zucchelli, A., Fatigue residual strength of laminated graphite-epoxy composite circular plates damaged by transversal loads. *Composite Science and Technology*, 2008. In Press 10.1016/j.compscitech.2008.05.025.
[4] Minak, G. & Ghelli, D., Influence of diameter and boundary conditions on low velocity impact response of CFRP circular laminated plates. *Composites Part B: Engineering*, **39**, pp. 962–972, 2008.
[5] Christoforou, A.P., Swanson, S.R. & Beckwith, S.W., Lateral impact of composite cylinders. *Composite Materials: Fatigue and Fracture*, **2(ASTM STP 1012)**, pp. 373–386, 1989.
[6] Christoforou, A.P. & Swanson, S.R., Analysis of simply-supported orthotropic cylindrical shells subject to lateral impact loads. *Transactions of the ASME*, **57**, p. 376, 1990.
[7] Krishnamurthy, K.S., Mahajan, P. & Mittal, R.K., A parametric study of the impact response and damage of laminated cylindrical composite shells. *Composites Science and Technology*, **61**, pp. 1655–1669, 2001.
[8] Kim, S.J., Goo, N.S. & Kim, T.W., The effect of curvature on the dynamic response and impact-induced damage in composite laminates. *Composites Science and Technology*, **51**, pp. 763–773, 1997.
[9] Her, S.C. & Liang, Y.C., The finite element analysis of composite laminates and shell structures subjected to low velocity impact. *Composite Structures*, **66**, pp. 277–285, 2004.
[10] Doyum, A.B. & Altay, U.B., Low-velocity impact damage in glass fibre/epoxy cylindrical tubes. *Materials & Design*, **18(3)**, pp. 131–135, 1997.
[11] Minak, G., Ghelli, D. & Zucchelli, A., Torsion testing of cfrp laminate tubes. *5th ESIS TC4 International Conference on Fracture of Polymers, Composites and Adhesives*, Les Diablerets, 2008.
[12] Hashin, Z., Failure criteria for unidirectional composites. *J Appl Mech*, **47**, pp. 329–334, 1980.
[13] Abrate, S., Impact on laminated composite materials. *Appl Mech Rev*, **44(4)**, pp. 155–190, 1991.

Analysis of asymmetric radial deformation in pipe with local wall thinning under internal pressure using strain energy method

V.M.F. Nascimento
Departameto de Engenharia Mecânica TEM, UFF, Rio de Janeiro – Brazil
L.C.S. Nunes
Programa de Engenharia Mecânica TEM/PGMEC, Universidade Federal Fluminense - UFF, Rio de Janeiro – Brazil

Abstract

Structural integrity of pipe has been an interesting area for many researchers in last years. To avoid the problems and the routine procedure of inspection and maintenance several works have been proposed. Metals like Carbon steel are used extensively in pipeline industries due to simplicity and economy. However, flaws like as cracks, pitting, local wall thinning can be generated by corrosion, erosion, and environmental exposure to various substances. It is very important to evaluate the strength of flaw to maintain the integrity of the pipeline systems. Many woks on local wall thinning have been developed focusing the mechanical behavior of pipe under combined loading. In this paper, an analysis of asymmetric radial deformation in pipe with local wall thinning under internal pressure is presented. The asymmetric radial displacements are estimated using strain energy method based on the Castigliano's theorem. Finally, the results are compared and valided using a commercially available finite element code.

Keywords: structural integrity, energy method, local wall thinning.

1 Introduction

Recently, there has been growing interest in structural integrity of pipe. A large number of the pipes are made of metals, like carbon steel, and they are used extensively in the petrochemical, refinery, and pipeline industries [1]. The reason for this is simply economic. It is widely available, inexpensive, and maintainable. However, this type of material is susceptible to flaws like as cracks, pitting, local wall thinning, which can be generate by corrosion, erosion, and environmental exposure to various substances [2–4]. Therefore, it is very important to evaluate the strength of pipe with local wall thinning to maintain the integrity of the pipeline systems. Many woks [5–7] on local wall thinning have been

Mechanics of Solids in Brazil 2009, H.S. da Costa Mattos & Marcílio Alves (Editors)
Brazilian Society of Mechanical Sciences and Engineering, ISBN 978-85-85769-43-7

developed focusing the mechanical behavior of pipe under combined loading. Some literatures [2, 4, 8] using finite element method to investigate the mechanical behavior of pipe with defect. Nevertheless, in many cases the analyses expend a lot of computing time. The purpose of this paper is to analyze the asymmetric radial deformations in pipe with local wall thinning under internal pressure. The analytical radial displacements are estimated using the classical theorem of Castigliano [9–11], and the results are compared and valided with finite element (FE) analyses.

2 Circular pipe with local wall thinning subject to internal pressure

Considerer a pipe like a thin-walled cylinder of mean radius r and thickness t, as shown in Fig. 1(a). The pipe with internal defect (local wall thinning) is submitted to the action of uniformly distributed internal pressure of intensity p. The defect is represented by an angle of 2θ and a depth of d. In this work, for simplicity, the defect is assumed to be symmetric along the circumferential axis and it is extend throughout the entire length of the cylinder. The problem can geometrically be interpreted as shown in Fig. 1 (b). In order to solve this statically indeterminate the problem the Castigliano's theorem is used.

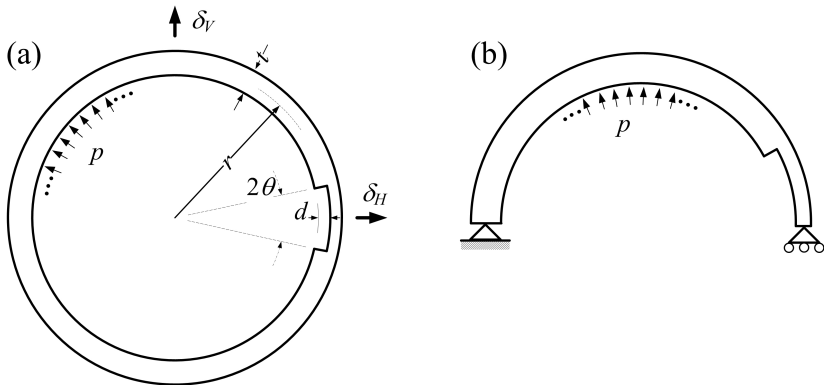

Figure 1: Geometry of pipe with local wall thinning.

In the present analysis, it will be considered that the radial displacements, δ_H and δ_V, which are associated the strain energy, are only due to bending moment and longitudinal force acting on the cross section. This hypothesis is reasonable because the strain energy due to shearing force is smaller when compared with others, thus it can be neglected.

2.1 Bending moments and reaction forces

In the first, the magnitude of the bending moments, M_2 and M_1, and reaction forces, V_1 and V_2, will be determinate by means of Castigliano theorem. Let us consider the bending moment of curved bar at any cross section, as illustrated in Fig 2., it can be given by

$$M(\xi,\phi) \equiv \begin{cases} M_\rho = M(\rho,\phi), & 0 \leqslant \phi < \theta \\ M_r = M(r,\phi), & \theta \leqslant \phi \leqslant \pi \end{cases} \tag{1}$$

where the mean radiuses in non-defect and defect region are $\rho = r_i + (d+t)/2$, $r = r_i + t/2$, respectively. The bending moments in two regions can be written as

$$M_\rho = M_2 - \left(V_2\rho - p\rho^2\right)(1-\cos\phi) \tag{2}$$

$$M_r = M_2 - V_2(\rho - r\cos\phi) - pr\rho\cos\phi + \frac{p}{2}\left(r^2+\rho^2\right) \tag{3}$$

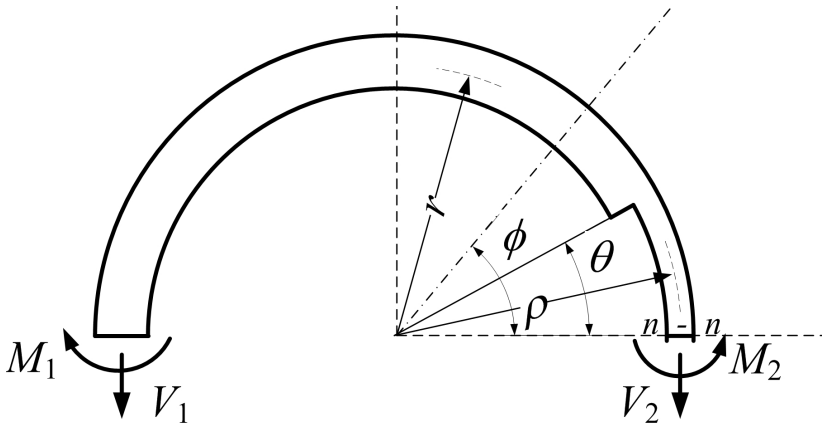

Figure 2: Scheme representative of half pipe.

In order to determinate V_2 and M_2, it can be assumed two hypotheses: (i) due the symmetry, the cross section $n-n$ does not rotate during the bending of the pipe and (ii) the displacement in the direction of V_2 at cross section $n-n$ is zero. Then, from the first hypothesis we have

$$\frac{dU}{dM_2} = 0 \tag{4}$$

in which U is the strain energy of half pipe which we are considering. Substituting the eqs. (2) and (3) into (4), we find the following expression

$$\frac{\rho}{I_\rho}\int_0^\theta \frac{\partial M_\rho}{\partial M_2} M_\rho d\phi + \frac{r}{I_r}\int_\theta^\pi \frac{\partial M_r}{\partial M_2} M_r d\phi = 0 \tag{5}$$

where, $\frac{\partial M_\rho}{\partial M_2} = \frac{\partial M_r}{\partial M_2} = 1$, and the moments of inertia are $I_\rho = \frac{(t-d)^3}{12}$ and $I_r = \frac{t^3}{12}$ then,

$$\frac{\rho}{I_\rho}\int_0^\theta M_\rho d\phi + \frac{r}{I_r}\int_\theta^\pi M_r d\phi = 0 \tag{6}$$

by the second hypothesis, following the same idea

$$\frac{dU}{dV_2} = 0 \tag{7}$$

where, $\frac{\partial M_\rho}{\partial V_2} = -\rho\,(1-\cos\phi)$, $\frac{\partial M_r}{\partial V_2} = -\,(\rho - r\cos\phi)$ then,

$$\frac{\rho}{I_\rho}\int_0^\theta M_\rho \rho\,(1-\cos\phi)\,d\phi + \frac{r}{I_r}\int_\theta^\pi M_r\,(\rho - r\cos\phi)\,d\phi = 0 \tag{8}$$

From (5) and (8), it is possible to obtain the reaction V_2 and M_2. In addition, the bending moment M_1 here are determined substituting $\phi = \pi$ into eq. (3), then

$$M_1 = M_r^{\phi=\pi} = M_2 - V_2\,(\rho + r) + \frac{p}{2}(\rho + r)^2 \tag{9}$$

and using the equilibrium equation, is ease to find the reaction force V_1 given by

$$V_1 = p\,(\rho + r) - V_2 \tag{10}$$

2.2 Stress distribution analysis

In this work, it is assumed that the thickness of the wall is small in comparison with the radii, i.e., a case of thin-walled tube. Thus, the stress state can be expressed in circumferential and longitudinal components. The circumferential stress distribution can be divided in two parts, one associate with bending moment and other with normal tension,

$$\sigma_\varphi\,(\xi,\varphi) = \begin{cases} \sigma_\varphi^\rho\,(\rho,\varphi) = -\frac{M_\rho}{I_\rho}\,(\rho' - \rho) + \frac{p\rho_i}{t-d}, & \rho_i < \rho' < \rho_o \;\; and \;\; 0 < \varphi < \theta \\ \sigma_\varphi^r\,(r,\varphi) = -\frac{M_r}{I_r}\,(r' - r) + \frac{pr_i}{t}, & r_i < r' < r_o \;\; and \;\; \theta < \varphi < \pi \end{cases} \tag{11}$$

In order to determine the longitudinal component let us assume that the cylinder is subject to a plane strain distribution. Hence, using generalized Hooke's law, we have

$$\varepsilon_r = \frac{\sigma_\varphi}{E}\left[-\nu\left(1+\nu\right)\right]$$
$$\varepsilon_\varphi = \frac{\sigma_\varphi}{E}\left[1-\nu^2\right] \tag{12}$$
$$\sigma_z = \nu\sigma_\varphi$$

Figure 3 shows the circumferential and longitudinal components of stress distribution as a function of the angle φ. In this analysis were considered the following parameters: Young's modulus, E, equal to 200 GPa; Poisson's coefficient, ν, equal to 0.3; inner pressure, p, equal to 1 Mpa; inner radius, r_i, equal to 50 mm; wall thickness, t, equal to 2 mm; half angle of total defect, θ, equal to 60 degree; depth of local wall thinning, d, equal to 1 mm.

As illustrated in Fig. 3, there is a significant discontinuity in stress distribution due to defect. The maximum external stress occur when the angle φ is equal to zero, on the other hand, the maximum internal stress is observed in the discontinuity, when the angle of defect is assumed at limit value, i.e., θ equal to 60 degree. It can also be observed the good agreement between analytical results and numerical using finite element method

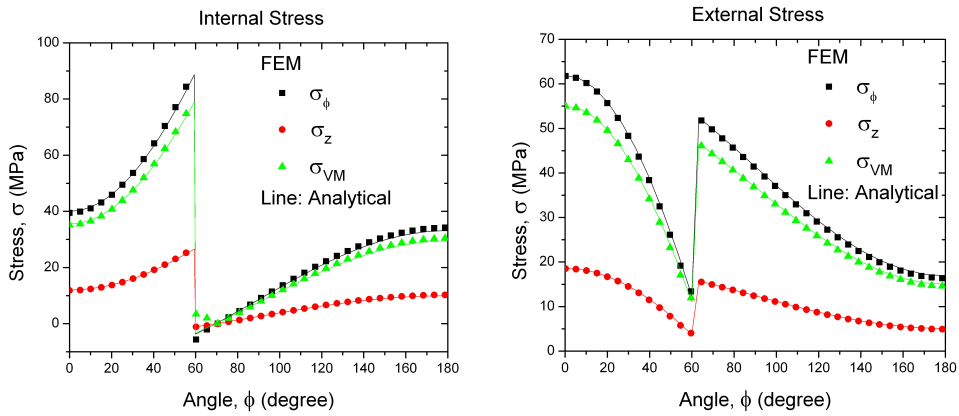

Figure 3: Internal and external stress distribution in pipe with local wall thinning: defect angle of 60 degree and depth of 1 mm.

In the present analyses, it is taken into account the linearly elastic behavior of materials, thus it is necessary to impose a criteria for initial yielding in pipe with local wall thinning to validate the results. The equivalent stress criterion based on Von Mises is considered and the equivalent stress can be defined as

$$\sigma_{VM} = \sqrt{\frac{1}{2}\left[\left(\sigma_\phi - \sigma_z\right)^2 + {\sigma_\phi}^2 + {\sigma_z}^2\right]} = \sigma_\phi\sqrt{\left(1+\nu^2-\nu\right)} \leqslant SMYS \tag{13}$$

As can be seen in Fig. 3, the equivalent stress is also plotted and it is observed the good agreement between the results. In order to guarantees the best performance of the analytical results, the stress value is taken less than the specified minimum yield strength of the material (*SMYS*).

A carbon steel pipe with the specified minimum yield strength of the material (*SMYS*) equal to 250 MPa is assumed in the present analysis. This type of pipe is commonly used in the piping system. Fig. 4 illustrate the maximum value of equivalent stress as a function of the depth of defect for different angle of defect. These results were obtained considering the same parameters introduced before.

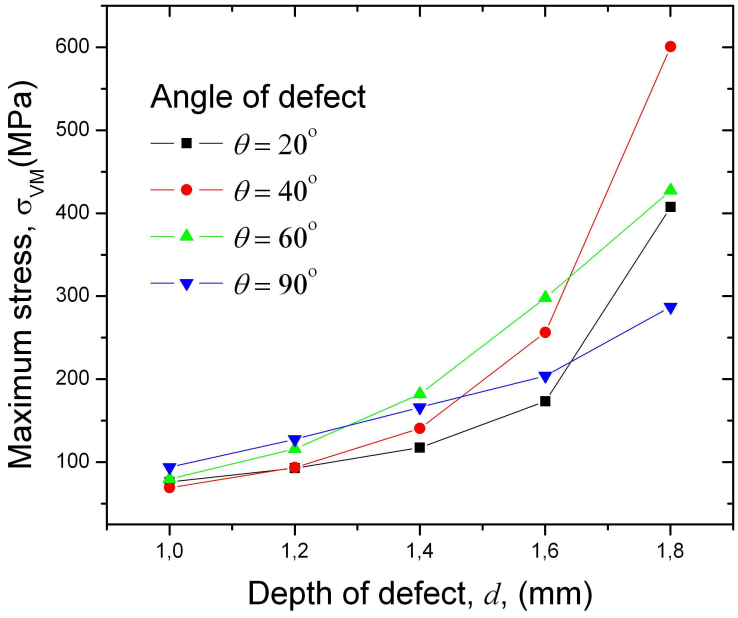

Figure 4: Maximum stress associated with Mises yield criterion.

The results presented in Fig. 4, show that for a depth of defect smaller than 1.5 mm, for all angle of defect, the maximum value of equivalent stress is linear elastic behavior of material.

2.3 Asymmetric displacement analyses

In the following discussion it is assumed that the pipe is a curved bar as shown in Figs. 1 and 2. In order to calculate the deflections of the curved bar, will be used strain energy method, in particular the Castigliano theorem. Hence, the total strain energy stored in the an elastic solid occupying a region Ω is then given by the integral over the domain

$$U = \int_{\Omega} U_0 d\Omega \tag{14}$$

where, considering the linearly elastic behavior of isotropic materials, the strain energy density is defined by

$$U_0 = \frac{1+\nu}{E}\left(\sigma_\phi^2 + \sigma_z^2\right) - \frac{\nu}{2E}(\sigma_\phi + \sigma_z)^2 \tag{15}$$

To determine the horizontal and vertical displacements, the half pipe, represented by the curved bar, can be divided in two quadrants to simplify the problem. The solution of this problem is developed in the following item.

2.3.1 Horizontal displacements analyses of the pipe with local wall thinning

The total horizontal displacement is composed by the two components associated to each quadrant. To determine them, each horizontal displacement is calculated separately, and to make this, it is necessary introduction imaginary forces, H_1 and H_2, as illustrated in Fig. 5 and 6. The total displacement can be given by

$$\delta_H = \delta_{H1} + \delta_{H2} \tag{16}$$

using the eqs. (14) and (15), we have

$$\delta_{H_1} = \left.\frac{\partial U}{\partial H_1}\right|_{H_1=0} = \frac{1-\nu^2}{E}\left[\int_{r_i}^{r_o}\int_{\pi/2}^{\pi}\left[\sigma_\varphi^r \frac{\partial \sigma_\varphi^r}{\partial H_1}\right]_{H_1=0} r'\, d\varphi\, dr'\right] \tag{17}$$

where the circumferential stress, presented in eq. (11), can be rewritten adding the term of imaginary force H_1, that it is ease to take from Fig. 5. Then,

$$\sigma_\varphi^r = \sigma_\varphi^r - \frac{(r'-r)}{2I_r} H_1 r \sin\varphi|_{H_1=0} \tag{18}$$

following the same idea, considering the quadrant with local wall thinning,

$$\delta_{H_2} = \left.\frac{\partial U}{\partial H_2}\right|_{H_2=0} = \frac{1-\nu^2}{E}\left[\int_{\rho_i}^{\rho_o}\int_{0}^{\theta}\left[\sigma_\varphi^\rho \frac{\partial \sigma_\varphi^\rho}{\partial H_2}\right]_{H_2=0} \rho'\, d\varphi\, d\rho' + \int_{r_i}^{r_o}\int_{\theta}^{\pi/2}\left[\sigma_\varphi^r \frac{\partial \sigma_\varphi^r}{\partial H_2}\right]_{H_2=0} r'\, d\varphi\, dr'\right] \tag{19}$$

$$\sigma_\varphi^r = \sigma_\varphi^r - \frac{(r'-r)}{2I_r} H_2 r \sin\varphi|_{H_2=0} \tag{20}$$

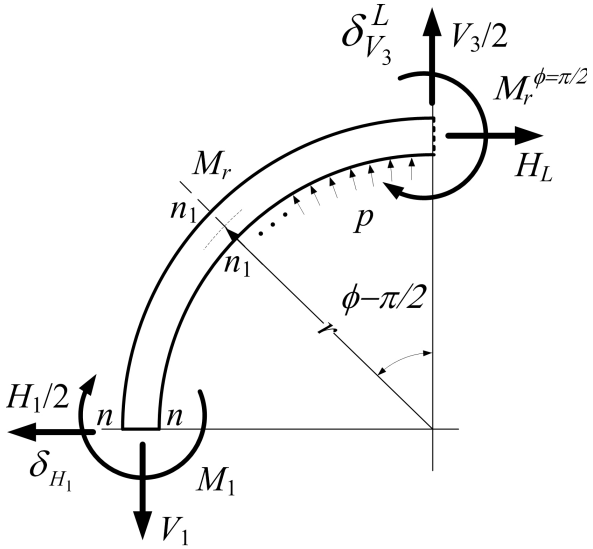

Figure 5: Geometry considering one quadrant of the pipe.

2.3.2 Vertical displacements analyses of the pipe with local wall thinning

For the total vertical displacement, defined by

$$\delta_V = \delta^L_{V_3} + \delta^R_{V_3} \tag{21}$$

we have, following the same idea,

$$\delta^L_{V_3} = \left.\frac{\partial U}{\partial V_3}\right|_{V_3=0} = \frac{1-\nu^2}{E}\left[\int_{r_i}^{r_o}\int_{\pi/2}^{\pi}\left[\sigma^r_\varphi \frac{\partial \sigma^r_\varphi}{\partial V_3}\right]_{V_3=0} r'\,d\varphi\,dr'\right] \tag{22}$$

$$\sigma^r_\varphi = \sigma^r_\varphi + \frac{(r'-r)}{2I_r}\,V_3 r\cos\varphi|_{V_3=0} \tag{23}$$

$$\delta^R_{V_3} = \left.\frac{\partial U}{\partial V_3}\right|_{V_3=0} = \frac{1-\nu^2}{E}\left[\int_{\rho_i}^{\rho_o}\int_{0}^{\theta}\left[\sigma^\rho_\varphi \frac{\partial \sigma^\rho_\varphi}{\partial V_3}\right]_{V_3=0}\rho'\,d\varphi\,d\rho' + \int_{r_i}^{r_o}\int_{\theta}^{\pi/2}\left[\sigma^r_\varphi \frac{\partial \sigma^r_\varphi}{\partial V_3}\right]_{V_3=0} r'\,d\varphi\,dr'\right] \tag{24}$$

$$\sigma^r_\varphi = \sigma^r_\varphi - \frac{(r'-r)}{2I_r}\,V_3 r\cos\varphi|_{V_3=0} \tag{25}$$

In order to evaluate the asymmetric radial displacements in pipe with local wall thinning, the analyses are initially conducted by assuming an inner pressure p equal to 1MPa, diameter-thickness

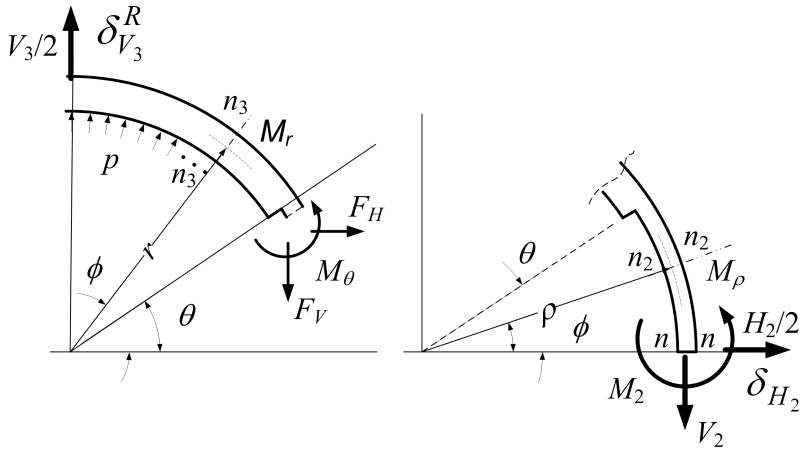

Figure 6: Geometry considering the local wall thinning.

radio D/t > 20 and different defect forms. In Figure 7, the horizontal and vertical displacements are obtained taken into account a pipe with inner radius equal to 50 mm, a pipe wall thickness equal to 2 mm, and for each half angle of total defect, 20, 40, 60 and 90 degree, the depth of local wall thinning is assumed of 0 to 1.8 mm.

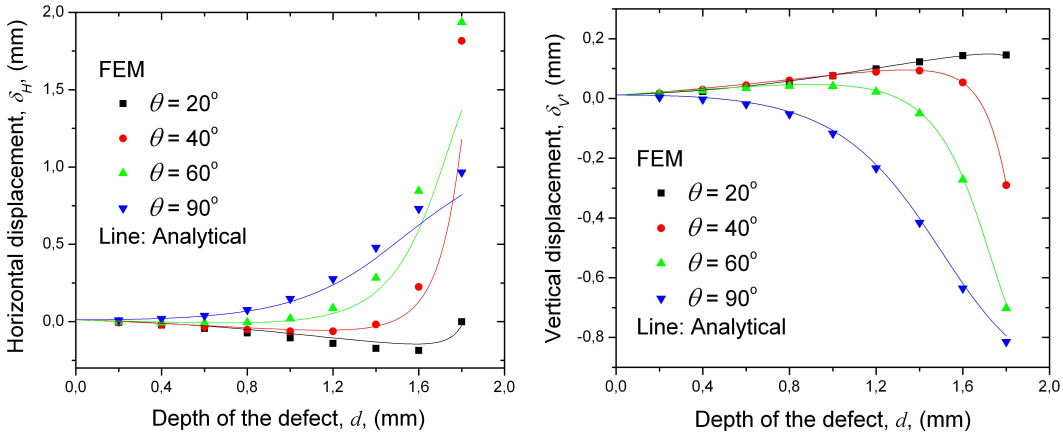

Figure 7: Horizontal and vertical displacement in pipe with internal defect subject a internal pressure.

It can be observed from Fig. 7, that the analytical results obtained using the analyses developed

here is in agreement with simulated results using finite elements method. It is important to observe that, these results are valid for depth of the defect value smaller than 1.5 mm due to elastic limit.

3 Conclutions and comments

This study was designed to analyze the asymmetric radial deformation generated by local wall thinning in pipe under internal pressure. The idea of these preliminary results is to provide an alternative means of estimating the internal defect in pipe by means measurement of diameter variations. To solve this, a simple and inexpensive method to obtain asymmetric radial deformation was suggested based on classical Castigliano theorem. Taking into account the approximations, it can be considered a very good agreement between the analytical results and numerical results using finite element method. If the radial displacements are well known it is possible to estimate the defect dimension and consequently to predict failure in pipe. The authors expected that by mean of radial measurements, associate with present analysis, it will be possible to replace or add inspection like pig scan. It is important to emphasize that pig scan is only used in pipeline, does not being used in tub system. For future work the authors aim to approach the problem using experimental results.

Acknowledgements

The authors would like to express their gratitude to the Ministry of Science and Technology. The present work received financial support from Brazilian agencies CNPq and FAPERJ.

References

[1] Escoe, A.K., *Piping and pipeline assessment guide*. Elsevier Inc., 2006.
[2] Kim, Y.J. & Son, B.G., Finite element based stress concentration factors for pipes with local wall thinning. *International Journal of Pressure Vessels and Piping*, **81**, pp. 897–906, 2004.
[3] Kim, Y.J., Kim, J., Ahn, J., Hong, S.P. & Park, C.Y., Effects of local wall thinning on plastic limit loads of elbows using geometrically linear fe limit analyses. *Engineering Fracture Mechanics*, **75**, pp. 2225–2245, 2008.
[4] Staat, M., Local and global collapse pressure of longitudinally flawed pipes and cylindrical vessels. *International Journal of Pressure Vessels and Piping*, **82**, pp. 217–225, 2005.
[5] Guarracino, F., On the analysis of cylindrical tubes under flexure: theoretical formulations, experimental data and finite element analyses. *Thin-Walled Structures*, **41**, pp. 127–147, 2003.
[6] Fatt, M.S.H., Elastic-plastic collapse of non-uniform cylindrical shells subjected to uniform external pessure. *Thin-Walled Structures*, **35**, pp. 117–137, 1999.
[7] Heitzer, M., Plastic limit loads of defective pipes under combined internal pressure and axial tension. *International Journal of Mechanical Sciences*, **44**, pp. 1219–1224, 2002.
[8] Netto, T.A., Ferraz, U.S. & Botto, A., On the effect of corrosion defects on the collapse pressure of pipeline. *International Journal of Solids and Structures*, **44**, pp. 7597–7614, 2007.
[9] Timoshenko, S.P. & Goodier, J.N., *Theory of Elasticity*. McGRAW-HILL, 1970.

[10] Timoshenko, S.P., *Strength of Materials*. D. Van Nostrand Company Inc.: New York, 3rd edition, 1936.
[11] Langhaar, H.L., *Energy Methods in Applied Mechanics*. John Wiley and Sons, Inc.: New York, 1962.

Mechanics of Solids in Brazil 2009, H.S. da Costa Mattos & Marcílio Alves (Editors)
Brazilian Society of Mechanical Sciences and Engineering, ISBN 978-85-85769-43-7

FEMSYS – An explicit finite element code for non-linear dynamic structural analysis: a time integration strategy

Carlos Alberto Nunes Dias, Larissa Driemeier
Group of Solid Mechanics and Structural Impact,
University of São Paulo, São Paulo/SP – Brazil
Marco Lucio Bittencourt
Department of Machine Design, University of Campinas, Campinas/SP – Brazil
Marcílio Alves
Group of Solid Mechanics and Structural Impact,
University of São Paulo, São Paulo/SP – Brazil

Abstract

This article describes the general strategy adopted in an explicit finite element code for time integration. It is introduced some details of the code and implementation strategies to handle non-linear response of 3D structures. Next, an integration algorithm within the framework of control theory is outlined, with some examples indicating the merits of the method. A discussion is presented in the context of the development of an open Brazilian finite element programme for use in the development of material models and finite elements.

1 Introduction

The analysis of structures subjected to loads of high intensity and short duration is one of the most challenges areas in Solid Mechanics. Phenomena like material visco-plastic behaviour, inertia effects, contact, large rotations and deformation and inertia effects add to other complex issues such as complex boundary conditions and initial conditions difficult to be known. No wonder that analytical methods cannot take all this effect into account, so a detailed analysis can only be performed using numerical methods.

There are a few numerical techniques capable of handling, albeit in different ways, the aspects listed above. The simulation in Figure 1, for instance, of a plate impacted by a soft cylinder, was performed using the so called SPH method, Smooth Particle Hydrodynamics.

But no doubt that, chiefly among the numerical techniques, it is the Finite Element Method, FEM, the most mature technique for structural analysis. This technique acquired a technological impulse with the continuous demand of the industry for user-friendly software. Nowadays, a dozen of packages

Mechanics of Solids in Brazil 2009, H.S. da Costa Mattos & Marcílio Alves (Editors)
Brazilian Society of Mechanical Sciences and Engineering, ISBN 978-85-85769-43-7

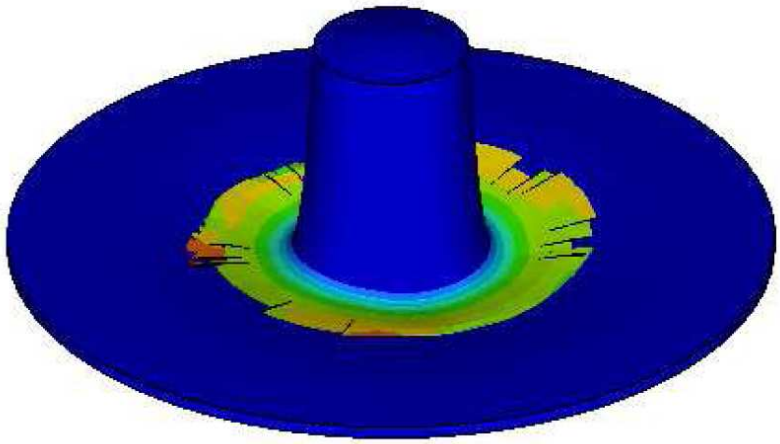

Figure 1: A composite plate impacted by a soft cylinder analysed using the SPH method.

are available capable of handling the issues raised above.

The finite element market is worldwide dominated by powerful software such as ABAQUS, ANSYS, DYTRAN, NASTRAN , LS-DYNA, RADIUS. It is interesting to note that Brazil is more and more a product developer, with important design activities in the automotive and aircraft industries, naval architecture and related products in general, to name a few. Many of these branches use intensively the FEM. It seems that, in Brazil, there is no systematic effort to bring out, if not to the market but at least to the academic community, a finite element package capable of handling large scale non-linear dynamic problems. Such is the objective of the authors, as far as they are developing a code which will allow other researchers to incorporate new finite elements and constitutive laws.

In this article, we outline an Explicit FEM code starting by giving an overall idea of its basic structure. We then show that the integration algorithm should be robust and efficient, so section 3 describes an explicit algorithm, with section 4 presenting some basic examples. Section 5 discusses some aspects of the programme, of pre and post model handling, of high order finite elements, of contact and of failure criteria, with section 6 closing the article.

2 Basic code

The FEMSYS code is built around functions. At the moment, there are two versions, one written in Matlab code and the other in Fortran. Matlab was chosen for developing the routines and testing them, while Fortran, being more robust, handles larger problems more efficiently. However, a new Matlab Tool Box allows parallel processing, which greatly simplifies parallel computing. Hence, it is likely that the final version 0 of the code will be available as a Matlab compiled version. The fact that

a Matlab platform is being used reduces further developing time and programming resources, allows more expeditiously documentation and facilitates the use of the programme as a teaching tool.

In cases of dynamic beam response or general structural impact, the structure response is obtained by time integration of the equilibrium equations. In this case, it is meaningful to talk about implicit and explicit time integration.

For quasi-static problems, the finite element problem seeks to find the structure configuration, u, via

$$u(x) = K^{-1}(x)F(x)$$

We see that the approach requires to find the inverse of the stiffness matrix, K, for each displacement of force, F, increment. This is in frank contrast with dynamic problems, whose general equation to be solved is

$$M(x)\ddot{x} + C(x,t)\dot{x} + K(x,t)x = F(x,t)$$

Here, M and C are the mass and damping matrices. Observe that it is possible to obtain the displacement, velocity and acceleration of the structure by marching forward in time with no inversion of the stiffness matrix. Hence, explicit methods can be of advantage in dynamic problems whose overall time duration is much less than the first natural period of the structure under analysis. Also, to allow uncoupling of the system above, the mass matrix should be diagonal. It is clear from above that, crucial to the efficiency of the process is the time integration algorithm. This lead the authors to develop an integration algorithm meant to be efficient, robust and with little user interference.

3 An explicit integration algorithm

Explicit algorithms are unstable in the sense that the time integration of the equilibrium equation governing the behaviour of a structure may not converge to a physical solution as time progresses. In fact, there is no guarantee that even implicit methods are stable in the context of nonlinear structural analysis [1]. It is a common practice to define the minimum time step in explicit algorithms based on the highest natural frequency of the finite element model, leading to time steps of the order of micro-seconds.

Explicit integration has the chief advantage of solving an uncoupled algebraic system. This leads to smaller processing time at each iteration. Also, it is not necessary to work with the stiffness matrix directly; instead, one can use the internal forces.

Clearly, it is interesting to have different time steps in the time integration of the equilibrium equations. Hence, if no stability is detected in the procedure, one could increase the time step so decreasing the overall processing time when bearing in mind that a normal dynamic non-linear transient analysis comprises thousands of iterations.

In our FE programme, we adapted a Proportional, Integral, Derivative, PID, control [2] as a basic tool to change the time step as the simulation progresses, whose analogy with the level of a water tank, as in Figure 3, amounts to its understanding. The main tank is fed by a continuous flux of

inputs and feeds the secondary tank. The aim is to fill in the secondary tank in the least possible time, which requires a high main tank level. However, due to the road and driver manoeuvres, the fluid can spill out of the main tank, which can be avoided by setting a maximum reference level. But this level should change continuously to take advantage of the stability of the driving solution process, should it occur. With the PID control, it is possible to fine tune the time step by defining only three equations which, based on the difference between integration error and tolerance, define the actions of the PID control, so establishing a more suitable time step.

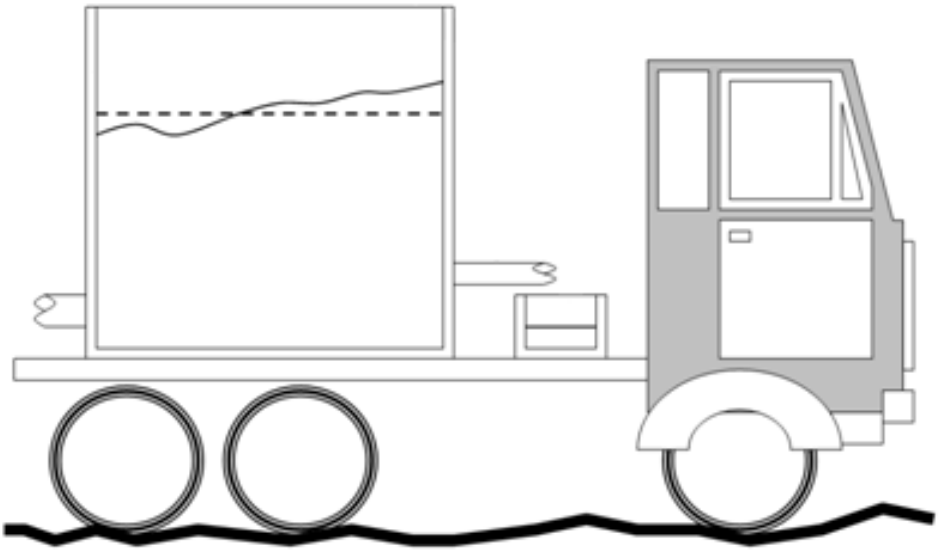

Figure 2: Understanding the PID control used in FEMSYS.

3.1 Linear acceleration (supply) method

A major difference between the central difference method, not detailed here, and the Linear Acceleration Method, LAM [3] is that, in the later, equilibrium is imposed at the end of the interval. In this case, the kinematic parameters of the system are yet to be known, so it is necessary to adjust the equilibrium via an interactive process. This increases a little the processing time but improves dramatically the quality of the results.

In order to describe the LAM, let us consider a single degree of freedom model, with the acceleration varying linearly in the interval $[t;\, t+dt]$. For $0 \leqslant \tau \leqslant dt$ one can write

$$\ddot{\bar{x}}(\tau) = A\tau + \ddot{x}_n \tag{1}$$

$$\dot{\bar{x}}(\tau) = A\tau^2/2 + \ddot{x}_n\tau + \dot{x}_n \tag{2}$$

$$\bar{x}(\tau) = A\tau^3/6 + \ddot{x}_n\tau^2/2 + \dot{x}_n\tau + x_n \tag{3}$$

with x_n, $\dot{x}_n$and $\ddot{x}_n$ being the displacement, velocity and acceleration, respectively, already known in the beginning of the interval. A is a constant, which can be determined by enforcing equilibrium at $t + dt \Leftrightarrow \tau = dt$, and represents the gradient of the acceleration. Equilibrium and kinematic relations lead to

$$x^i_{n+1} = x_n + dt\dot{x}_n + (dt^2/2)\ddot{x}_n + (dt^3/6)A^{i-1}_n \tag{4}$$

$$\dot{x}^i_{n+1} = \dot{x}_n + dt\ddot{x}_n + (dt^2/2)A^{i-1}_n \tag{5}$$

$$\ddot{x}^i_{n+1} = m^{-1}(F^{ext}_{n+1} - c\dot{x}^i_{n+1} - P^i_{n+1}) \tag{6}$$

$$A^i_n = (\ddot{x}^i_{n+1} - \ddot{x}_n)/dt \tag{7}$$

with i standing for current iteration, F^{ext}_{n+1} external loads and P^i_{n+1} internal elastic forces in position x^i_{n+1} , both at $t = \tau$. The iterative process starts with $A^{i-1}_n = A^I_{n-1}$ and finishes when the acceleration rate, $\left\|A^i_n - A^{i-1}_n\right\| / \left\|A^i_n\right\| \leqslant tolA$, attains a value lower than a pre-defined tolerance, *tolA*. Once this tolerance is attained, after I iterations, the kinematic parameters are given by

$$x_{n+1} = A^I_n dt^3/6 + \ddot{x}_n dt^2/2 + \dot{x}_n dt + x_n \tag{8}$$

$$\dot{x}_{n+1} = A^I_n dt^2/2 + \ddot{x}_n dt + \dot{x}_n \tag{9}$$

$$\ddot{x}_{n+1} = A^I_n dt + \ddot{x}_n \tag{10}$$

This method equally applies to a system of several degrees of freedom, with the remark that the mass matrix is diagonal so that equation (6) is uncoupled, which justifies the adjective *explicit* to the method.

3.2 PID control

For linear problems, the critical time step in explicit time integration procedures can be written as

$$dt \leqslant dt_{cr} = \frac{2}{\omega_{n_{\max}}} \tag{11}$$

with $\omega_{n_{max}}$being the maximum natural frequency of the discrete model. Equation (11) implies that, contrary to the common sense, finer meshes leads to smaller time integration teps. A remark is that the maximum natural frequency, although an eigen value of the mathematical problem, has no physical meaning.

Noels et al. [4] present a complicate strategy for the establishment of the time step. Here, this task is greatly simplified by using the adaptative control, which can even be used for low velocity problems, i.e. quasi-static problems.

The time step, dta, in our strategy is calculated according to

$$dta = (2^{a_T})dtb \tag{12}$$

with a_T a control parameter which increases ($a_T > 0$) , decreases ($a_T < 0$) or maintains ($a_T = 0$) the time step, i.e. a_T scales the time step.

The initial time step is set as the critical time step, the later based on the maximum natural frequency of the initial structure configuration.

The control action a_T can be split by the sum of the proportional a_P, integral a_I and derivative a_D actions [2], i.e.

$$a_T = a_P + a_I + a_D \tag{13}$$

with

$$a_P^{n+1} = g_P(V_n - R_n) \tag{14}$$

$$a_I^{n+1} = a_I^n + f_{aI}(V_n - R_n) \tag{15}$$

$$f_{aI} = g_P T_S / T_I \tag{16}$$

$$a_D^{n+1} = f_{aD} a_D^n - f_{cD}(V_n - V_{n-1}) \tag{17}$$

$$f_{aD} = T_D/(T_D + NT_S) \tag{18}$$

$$f_{cD} = g_P N f_{aD} \tag{19}$$

Here, $V_n$is the variable to be controlled and kept close to the reference R_n, with a gain g_P. T is the time, with indexes I, D and S standing for integral, derivative and sampling, N ($3 \leqslant N \leqslant 20$), limits the high frequency filter. It follows that the new time step is given by

$$dt^{n+1} = 2(a_P^{n+1} + a_I^{n+1} + a_D^{n+1})dtb \tag{20}$$

These three gains are adjusted in the present approach just once. This strategy removes from the analyst the burden of choosing, or guessing, the best values. The disadvantage is that, for each time step, the optimum control parameters should vary.

Of course there is an integration error, which we evaluate via

$$e(t) = dt^2(\Delta\ddot{Q})_{\max}/Q_{est} \tag{21}$$

with dt being the time step value, $(\Delta\ddot{Q})_{\max}$ the maximum acceleration variation among all the degrees of freedom of the structure and Q_{est} the maximum structure displacement under a quasi-static load. This measure of error varies with time but it was found that its change is more dramatic when the time step changes, hence it is an interesting measure to work with.

To obtain the amplitude and frequency of $e(t)$ we work with its last four values, e_n , e_{n-1}, e_{n-2} and e_{n-3} at time t_n, t_{n-1}, t_{n-2} and t_{n-3}. The error frequency comes from

$$\omega^2(t) = \left| D \left\langle \frac{\ddot{e}(t)}{e(t)}; \frac{\dddot{e}(t)}{\dot{e}(t)} \right\rangle \right| \tag{22}$$

with $D\langle \bullet; \bullet \rangle$ representing the minimum value between $\ddot{e}/e$ and $\dddot{e}/\dot{e}$. The amplitude of the error is given by

$$A_n = \sqrt{e_n^2 + \dot{e}_n^2 / w_n^2} \tag{23}$$

which is filtered according to

$$\bar{A}_n = \left(\sum_{i=n-nf+1}^{n} A_i \right) / nf \tag{24}$$

$$E_I^n = \bar{\bar{A}}_n = (\bar{A}_n + p_A \bar{\bar{A}}_{n-1})/(1 + p_A) \tag{25}$$

being E_I^n the final integration error to be used in the time step control algorithm. Here, p_A is a factor which aims to limit sudden changes in the error amplitude.

For the LAM, the current error is penalised, i being the number of iterations, by

$$\bar{e}_n = [1 + (i/10)^4] e_n \tag{26}$$

so that, for $i << 10$, $\bar{e}_n \cong e_n$. For $i \approx 10$ the error is penalised by 100% and increases for $i > 10$. Hence, when the number of iterations grows, the time step decreases, and vice versa.

It is useful to note that the integration error exhibits an oscillation related to instability. Accordingly, when the integration is stable, the integration error oscillates with a period much longer than the time step, i.e. closer to the first natural periods of the structure. Conversely, close to instability, the period of error oscillation decreases substantially, getting closer to time integration step. Hence, it is possible to obtain some hints about the stability of the solution by observing the integration error behaviour. This, in turn, assists one to alter the integration time step, which in the present programme is performed automatically.

There are other issues to be considered, like the initial time step to be used and the strategy to be adopted for the change in the error tolerance as instability approaches, but they are not considered here.

4 Examples

The integration method LAM is explored in this section together with the automatic time step control based on PID. We start by analyzing a linear single degree of freedom system excited by a harmonic function. Tables 1 and 2 show the results when using the Central Difference, CDM, and LAM methods, with Table 3 summarizing the CPU time.

In order to explore different numerical integration difficulties, we adopt three damping factors of 1, 10 e 50 %, and three dynamic configurations of high velocity (impact), medium velocity (resonance)

and low velocity (quasi-static equilibrium) via the adoption of the three excitation to natural frequency ratios of 10, 1 and 0.1, respectively.

Table 1: Response of one degree of freedom system calculated according to the Central Difference methods. $m = 1$, $k = 1$, integration time $4\pi/\omega$, load amplitude 1, initial time step 10ms, sampling time $T_s = 10$ms, zero initial conditions, proportional gain $1/R_i$, integral time $100T_s$, derivative time $5T_s$.

ω/ω_n	ζ	Time step				Integration error				Error (%) Analyt.
		Initial E-2(s)	% of initial time step			Initial toler. E-6 (s)	% of initial toler.			
			min	med	max		min	med	max	
10	0.01	1.5708	40.25	51.69	99.02	3.5076	92.50	151.83	206.24	0.71
	0.1	=	41.64	51.89	99.01	3.4948	92.47	151.47	202.12	0.68
	0.5	=	36.19	51.18	99.00	3.4450	92.39	153.13	207.14	0.53
1	0.01	2.0000	48.78	71.75	100.00	6.3400	80.94	108.86	133.93	5.50
	0.1	=	53.19	77.30	100.00	6.1950	75.37	107.16	143.14	4.32
	0.5	=	81.09	96.80	112.77	6.1182	75.10	100.92	119.15	2.00
0.1	0.01	2.0000	66.06	111.84	137.84	0.6372	72.41	99.33	145.87	8.63
	0.1	=	91.76	265.17	532.17	0.6273	68.35	90.97	134.09	1.13
	0.5	=	93.08	434.10	769.73	0.6410	21.08	81.19	164.5	1.28

From the tables, the Central Difference method is less accurate and not recommended for medium and low velocities. On the other hand, the Supply method is adequate for all the three situations explored in these examples. This is so because the Supply method is capable of adjusting itself to these rather different situations, although to the expense of CPU time, as seen in Table 3. Figures 4, 5 and 6 present the time variation of various solution parameters for the cases of high, medium and low velocity loading, respectively.

Next, we apply both integration methods to a non-linear single degree of freedom problem. The system displaces backwards with greater amplitude than when moving forwards with high velocity. This causes sudden changes in the system behavior, which should be handled by the integration algorithm.

Figure 7 and 8 depict the behavior of the system with time, as calculated using the central difference and the linear acceleration methods, respectively. The various parameters of the system used in the computation are given in the caption.

Table 2: As in Table 1 but for the LAM method.

ω/ω_n	ζ	Time step				Integration error				Error (%) Analyt.
		Initial E-2(s)	% of initial time step			Initial toler. E-6 (s)	% of initial toler.			
			min	med	max		min	med	max	
10	0.01	1.5708	42.13	53,34	99.50	3.8265	95.47	149.54	191.83	0.090
	0.1	=	32.86	50.98	99.52	3.8760	95.19	154.81	216.92	0.100
	0.5	=	1.391	19.81	99.51	0.5279	60.72	156.31	610.45	0.144
1	0.01	2.000	43.37	74.83	100	6.8970	79.01	108.34	150.84	0.007
	0.1	=	60.32	81.00	100	7.0771	79.03	106.06	126.34	0.006
	0.5	=	100.00	120.24	132.23	13.452	78.31	94.48	105.35	0.005
0.1	0.01	2.000	73.26	145.32	222.17	0.6871	72.59	97.40	136.80	0.014
	0.1	=	93.02	323.27	732.31	0.7204	52.10	86.39	115.62	0.0009
	0.5	=	98.49	474.96	705.39	0.9750	21.50	79.86	130.84	0.0002

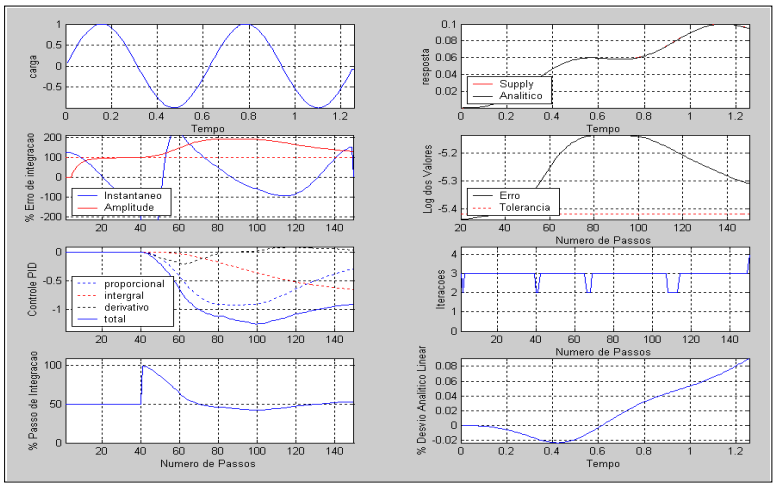

Figure 3: Various parameters of the response of the one degree of freedom system: high velocity (impact).

Table 3: Comparison of processing time (s) for Central Difference, CDM, and Linear Acceleration, LAM, methods. Pentium IV 2533MHz, MatLab, Windows 2000.

ω/ω_n	ζ	LAM	CDM
10	0.01	0.438	0.172
	0,1	0.218	0.156
	0.5	0.515	0.172
1	0.01	0.984	0.687
	0,1	0.937	0.641
	0.5	0.672	0.531
0.1	0.01	7.453	7.484
	0,1	2.578	2.031
	0.5	1.812	1.157
TOTAL		15.61	13.03

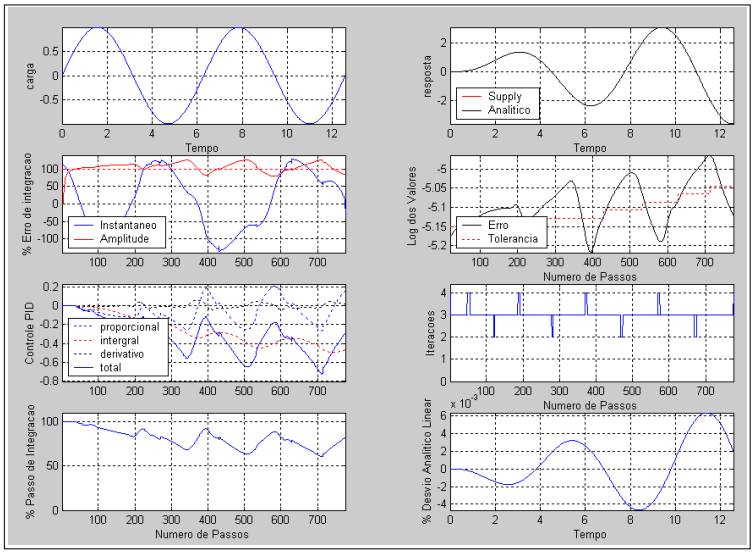

Figure 4: Various parameters of the response of the one degree of freedom system: medium velocity (resonance).

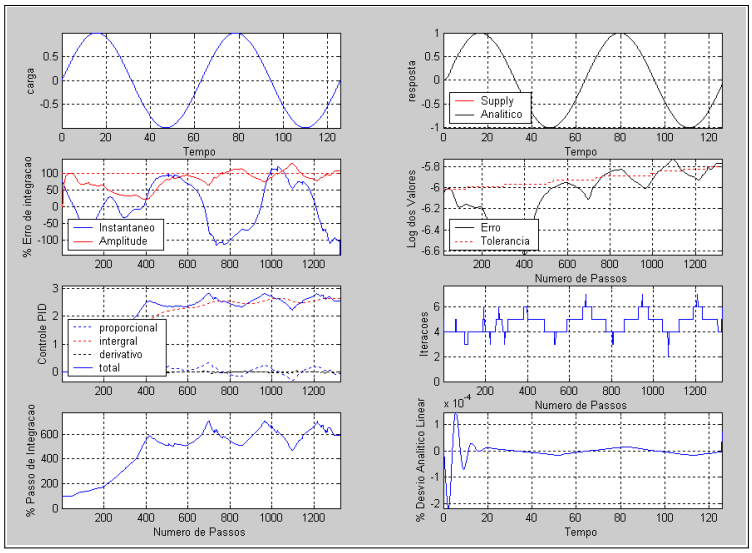

Figure 5: Various parameters of the response of the one degree of freedom system: low velocity (quasi-static).

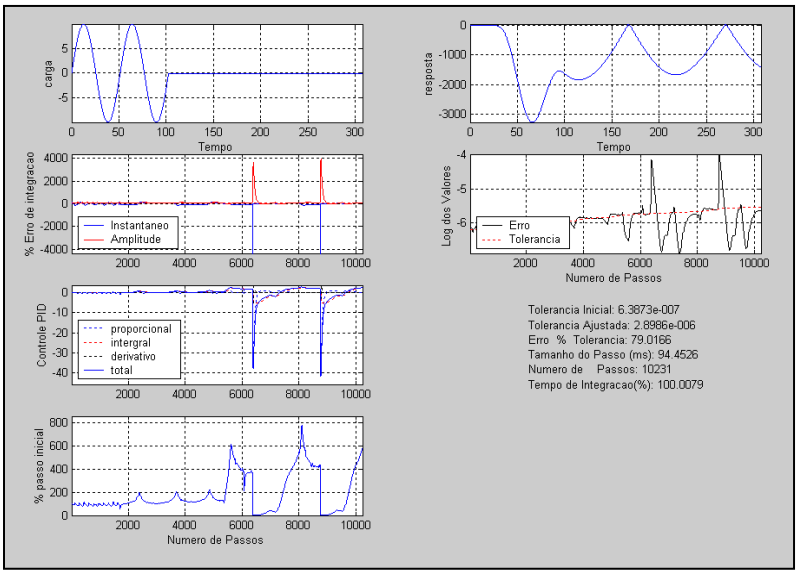

Figure 6: Non-linear system response according to the central difference method. m=1, $k_{forward} = 1.5$, $k_{backward} = 0.001$, $\xi = 0.1\%$, load amplitude = 10, load frequency = 0.1225, load duration = 102.60, initial conditions zero.

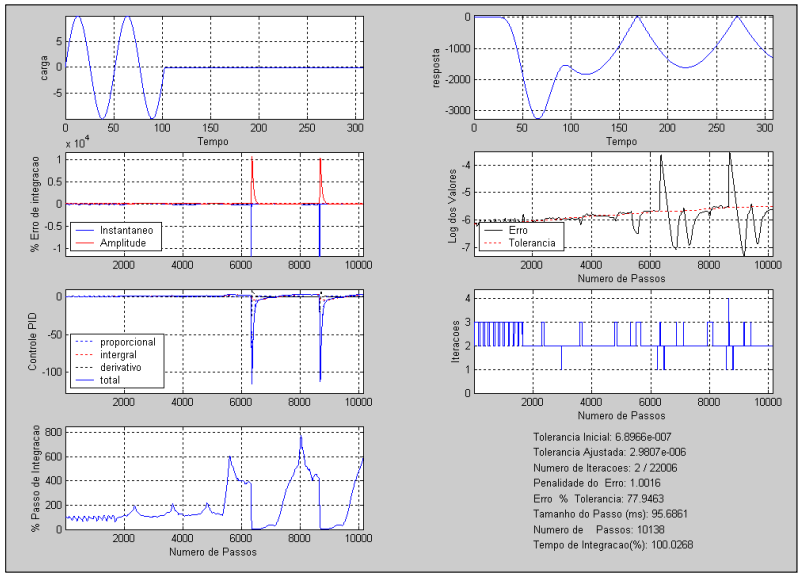

Figure 7: Non-linear system response according to the linear acceleration method. System parameters as in Figure 7 plus dtb = 1.633e-2, Ri = 6.8966e-7; Ts = dtb, proportional gain = 1/Ri, integral time = 100Ts, derivative time = 5Ts.

5 Closure

An explicit finite element code is introduced in the hope that can serve for other researchers to use for implementing new material models and finite elements. This will lead to further development of the code, equipping the academia with a useful tool for analysis, research and teaching.

The explicit code is underpinned by time integration of the equilibrium equations. This point to an efficient algorithm, here described. When comparing with the classical Central Difference Method, the Linear Acceleration Method outlined here is a more robust tool to deal with the time integration. As a novelty, we offer an automatic time step control, which sets longer or shorter time steps as the solution progresses.

There are other aspects of an explicit code, not addressed here, which requires the user input, such as hour-glass parameters. But, at least for the integration algorithm, the method frees the user of input figures whose precise effect is not well known. Such a strategy has been tested for more complex models, comprising hundreds of finite elements, and the results are all promising.

References

[1] Bath, K.J., *Finite Element Procedures*. Prentice Hall: New Jersey, 1996.
[2] Caon, J.R., *Controladores PID Industriais com Sintonia Automática por Realimentação a Relê*. Master's thesis, USP/São Carlos, 1999.
[3] Francisco, C.A. & Nunes Dias, C.A., Introdução ao estudo de vibrações sub-harmônicas em embarcações amarradas. *Revista Brasileira de Engenharia Caderno de Engenharia Naval*, **5(1)**, 1988. ISSN 0102-2679.
[4] Noels, L., Stainer, L. & Ponthot, J.P., Self-adapting time integration management in crash-worthiness and sheet metal forming computation. *Int J of Vehicle Design*, **30(1/2)**, 2002.

Changes in the characterization of the human scalp due to the process of successive skin expansion

Djenane Cordeiro Pamplona, Claudio R. Carvalho
Civil Engineering Department, Catholic University, PUC-Rio, Rio de Janeiro – Brazil
Henrique Radwasnki, Ivo Pitanguy
38th Enfermaria da Santa Casa da Misericórdia, Rio de Janeiro – Brazil

Abstract

This research investigates the large deformations of the extended human skin of the scalp due to the surgical process of skin expansion. A detailed in vivo analysis is carried out involving two different patients. For each patient the data of at least four expansions were monitored obtaining no less than five measurements relating the volume inserted and pressure inside the skin expander for each expansion. To obtain a constitutive equation that could describe the human scalp, several well known constitutive relations were analyzed and Delfino's constitutive equation was selected. To obtain the parameters for the several steps of the expansion a numerical procedure was carried out. The skin of the scalp was considered for numerical purpose as a isotropic, homogeneous, incompressible and hiperelastic membrane. The comparison between the in vivo and numerical results for the membrane under expansion is used to identify the material elastic parameters of the model. The numerical analysis of the membrane was done using finite element by the software ABAQUS and the Newton Raphson Method by means of MATLAB. To our knowledge this is a pioneer work in this field and the results obtained in this research we can improve considerably the understanding of the human skin and the skin under successive expansions.

Keywords: human skin, skin expanders, finite elements.

1 Introduction

Skin expansion is a physiological process, defined as the ability of human skin to increase its superficial area responding to stress or a given deformation. Since the skin presents creep or relaxation, after a certain time of the imposed deformation the resulting stress decreases. The physiology of the skin expansion is not stretching the skin only, but using the relaxation process, to obtain an extra flap of the skin with the characteristics needed. Skin expansions are used to reconstruct burned areas, hiding scars, breasts after mastectomy, among many others. Skin expansion done near the places were

Mechanics of Solids in Brazil 2009, H.S. da Costa Mattos & Marcílio Alves (Editors)
Brazilian Society of Mechanical Sciences and Engineering, ISBN 978-85-85769-43-7

the skin is needed provides skin of the same color, texture, sensibility and structure of the one to be removed, in cases of scars, burns and etc.

To model numerically reconstructive plastic surgeries and achieve a better understanding of them, it is crucial to determine the mechanical properties of the skin in vivo. Lately, several studies have been performed with this goal. Overviews were given by Piërard and co-workers and Rodrigues. The most frequently used techniques are tensile, indentation, torsion and suction experiments on the skin. Diridollou already mentioned that the data obtained is mainly descriptive. Occasionally, a model exhibiting (linear) Hookean material behavior is applied to obtain a Young's modulus. However, the value of the Young's modulus obtained is affected by various factors such as the amount of deformation (due to the non-linear stress-strain behavior), hydration, and length scale of the experiment (for example, indenter diameter or aperture size). It also varies considerably for different experimental techniques. Bader and Bowker, obtained for the Young's Modulus, E = 1.1-2.0 kPa measuring indentation using a 20 mm indenter. Agache obtained E = 0.42-0.85 MPa from torsion experiments using a disc of 25 mm diameter and guard ring of 35 mm diameter. Manschot in his work obtained E = 4.6-20 MPa for tensile tests using load pads of 10 × 10mm. Suction tests performed by Barel resulted in E = 0.13-0.26 MPa. Suction experiments performed by Diridollou using 100 mbar suction and an aperture size of 6 mm resulted in E = 153 kPa. In the above mentioned papers different techniques and models were used. What all these papers have in common is the use of simplified geometric models and boundary conditions, because all authors wanted to use closed form solutions for the numerical analysis. This might explain the different outcome of different types of experiments. In fact this means that the models only describe successfully the mechanical behavior of the skin for the particular loading case used in that experiment. In the literature, only few studies investigated the biomechanics of the tissue expansion. Socci L. and co-workers [1], studied the stresses and strains of the skin due to the inflation of an expander, only considering an axially-symmetric configuration, in which a flat circular flap of a thin membrane (i.e. the skin) is expanded by a spherical balloon. A phenomenological approach was adopted for the modeling of the growth after expander implantation. The following tasks were carried out developing a finite element model able to simulate the skin expansion procedure and validate this model using an experimental setup. It was implement an analytical growth law and a time-stepping algorithm in order to determine the skin growth within a discrete framework simulating a clinical skin expansion.

Our aim, in the present research is to develop a method to characterize the non-linear mechanical skin behavior for the skin under expansion using a numerical-*in vivo* technique. A consistent constitutive equation for the skin will allow the understanding of the skin under expansion permitting a better plan of the surgery, number and size of expanders, as well as in the numerical analysis of sutures, scars and a wide range of surgeries.

The present study is pioneer in its goal to model the human skin in successive skin expansions, obtaining different parameters to characterize the skin as the expansions go on. A detailed *in vivo* analysis is carried out. For each patient the data of at least four expansions were monitored obtaining at least five measurements relating the volume inserted and pressure inside the skin expander for each expansion. To obtain a constitutive equation that could describe the human skin, several well known constitutive relations were analyzed and Delfino's constitutive equation was chosen.

Skin expanders are silicone bags with several shapes and volumes. The first step to expand the skin is the surgery to implant the skin expander under the skin. The surgeon draws on the skin, with ink, the shape and size of the skin expander. The choice for expanders is the biggest for that region and also it has to be big enough to provide pressures that can make the skin expand. Through an incision done on one side of the drawing, the surgeon separates the skin of the muscles, obeying the drawing, and in this way it is delimited the flap of skin to be expanded. Also through this incision the surgeon inserts the skin expander under the skin. The valve that is connected to the expander is also implanted under the skin. After the incision closed a saline solution, that should be equivalent to 10% of the nominal volume of the skin expander, is inserted inside the skin expander using a needle in the implanted valve. Only 15 days after the surgery, the process of expansion begins, in this way the process of cicatrisation is guaranteed. During the skin expansion procedure, weekly a certain volume of saline solution is inserted inside the expander. The volume depends on the size of the expander and mostly on the discomfort of the patient. As the solution is inserted the skin expands due to the increase of pressure inside of the expander producing pain in the patient. Due to the visco-elastic properties of the skin, after some time the skin relaxes diminishing the pressure inside the expander. After a week there is no measurable pressure inside the expander. The major disadvantage of the process is the need of two surgeries, one to implant the expander, the other to remove the expander and repair the problem.

2 *In vivo* analisys

To identify the behavior of the scalp due to successive skin expansions it is necessary to measure the pressure inside the skin expander previously, during and after the infiltration of the saline solution inside the expander. For this purpose an apparatus was developed, providing a pressure sensor coupled to a needle, Fig. 1.

2.1 Results

Two patients were analyzed, patient 1: with light dark skin; female, 33 years old, brunette, weighing 530 N and 1.60 m height, with a rectangular expander (400 ml) and patient 2: with white skin, female, 12 years old, weighing 350 N and 1.50 m height, with a semi-lunar croissant expander (300 ml). To measure the pressure inside the expander in each step, figure 2, the apparatus described in Figure 1 was coupled to a plastic Y tube. One upper side of the Y tube was attached to the syringe with the saline solution to be inserted, the other upper side of the tube was coupled to the apparatus developed to measure the pressure, and on the lower side of the Y tube was attached the needle used to insert the saline solution in the expander's valve. At each 5 or 10 ml of liquid inserted, after a small interval, the pressure inside of the expander was measured, providing a curve relating the volume inserted and the pressure measured at this volume, as seen in each curve. Figure 3 shows the results of the six weekly successive expansions done in patient 1. Six days after each expansion, due to the visco-elastic properties of the skin, the pressure inside of the expander reaches zero, Fig. 4.

Mechanics of Solids in Brazil 2009, H.S. da Costa Mattos & Marcílio Alves (Editors)
Brazilian Society of Mechanical Sciences and Engineering, ISBN 978-85-85769-43-7

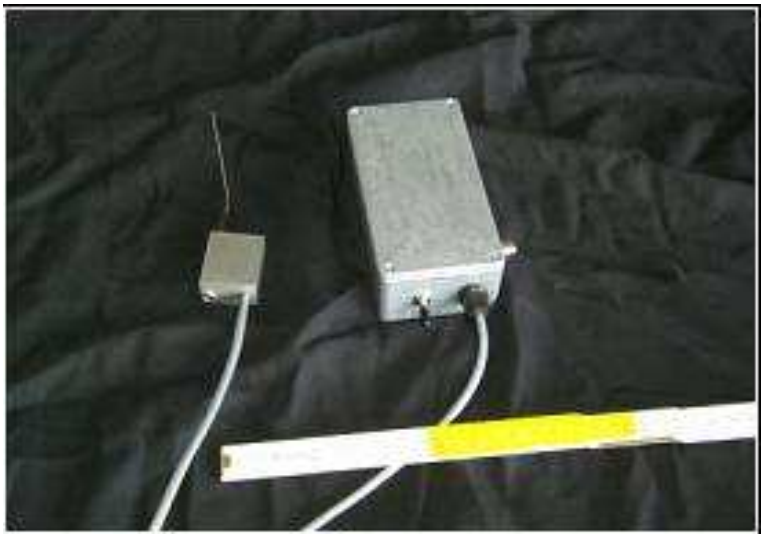

Figure 1: Apparatus to measure the pressure inside the skin expander.

Figure 2: Measuring the skin expansion in patient 1, (a) needle, (b) syringe, (c) apparatus.

Mechanics of Solids in Brazil 2009, H.S. da Costa Mattos & Marcílio Alves (Editors)
Brazilian Society of Mechanical Sciences and Engineering, ISBN 978-85-85769-43-7

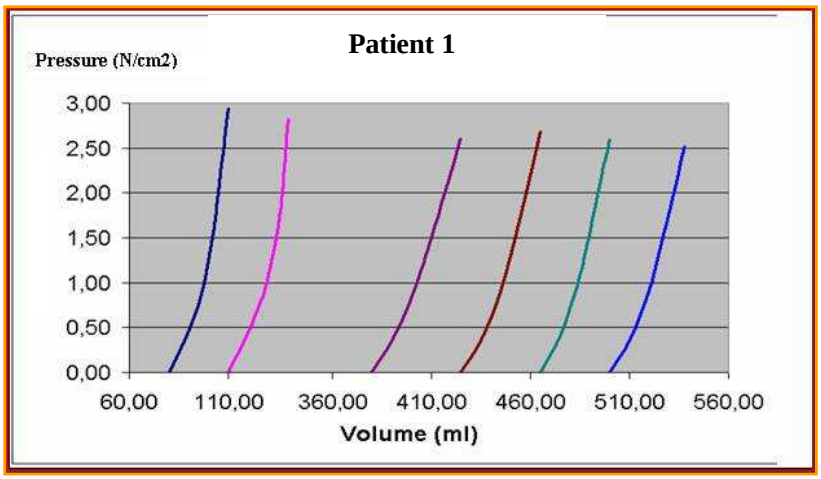

Figure 3: Measured pressures in six weekly successive expansions done in patient 1.

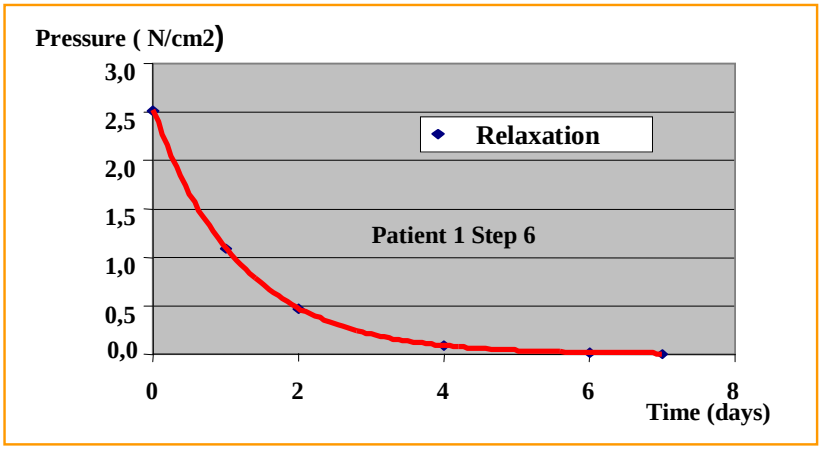

Figure 4: Relaxation of the skin measured in days after the sixth expansion of patient 1.

Tables 1 and 2 contain the results of maximum pressure reached in each weekly expansion, some expansions could not be measured for different reasons and they are pointed in the tables with empty rows. The letter A means the insertion of fluid done during the surgery.

Table 1: Patient 1 rectangular expander (Vexp=400ml), scalp; initial thickness 0.5 mm.

Step (i)	Initial Volume (V_{i-1} – ml)	Final Volume (V_{i-}- ml)	V_i-V_{i-1}(ml)	V*=V_i/Vexp	V**=$\frac{V_i - V_{i-1}}{V_{i-1}}$	Pressure (kPa)
A	00	80	80	x	x	x
1	80	110	30	0.28	0.38	29.50
2	110	140	30	0.35	0.27	28.20
3	140	380	240			
4	380	425	45	1.06	0.12	26.10
5	425	465	40	1.16	0.09	26.80
6	465	500	35	1.25	0.08	26.00
7	500	538	38	1.35	0.08	25.20

Table 2: Patient 2 croissant expander (Vexp=300ml), scalp; initial thickness 0.5 mm.

Step (i)	Initial Volume (V_{i-1} - ml)	Final Volume (V_{i-}- ml)	V_i-V_{i-1}(ml)	V*=V_i/Vexp	V**=$\frac{V_i - V_{i-1}}{V_{i-1}}$	Pressure (kPa)
A	00	214	214	x	x	xx
1	214	254	40	0.85	0.19	26.00
2	254	298	44	0.99	0.17	25.10
3	298	338	40	1.13	0.13	23.90
4	338	376	38	1.25	0.11	21.90

3 Numerical analisys

Although the number of patients studied is small, this works obtains one elastic constitutive equation that can characterize the skin of the scalp. To characterize the skin during expansion was necessary

to model numerically the procedure and this was done using the finite elements method with the commercial program ABAQUS, coupled with the Newton Raphson method using the commercial program MATLAB.

3.1 Finite element formulation

Membrane structures are load adaptive, as they change their geometry to accommodate external loads with the minimum variation in stress levels. To do the numerical finite element analysis a mesh of linear hybrid membrane elements, (M3D4 e M3D3) was used, the thickness was provided by the surgeon. The choice for membrane elements was made after trying several type of elements even shell elements, since the deformation is very large, some elements could not be used. Given that the control of the volume inserted inside the skin expander was essential to model the medical procedure, it was made necessary to use fluid finite elements under the membrane. In those elements the pressure is applied on one unique node, called reference of cavity node; this pressure simulates the filling of the skin expander done with fluid. For both membrane and fluid elements the middle surface is the reference, the nodes in the boundary were considered simply supported, free to rotate. This boundary condition was chosen after criterions observation of the expanded skin, being sure that the skin in the boundaries to not presented peeling.

The skin was considered homogenous, hiperelastic, presenting visco-elastic behavior. The elastic behavior of this material is characterized through the Strain Energy Density, W, written as function of the strain invariants I_1, I_2 and I_3, For incompressible materials, as biological tissues, and consequently the skin, the third invariant I_3=*1*. There are several strain energies densities with those characteristics, and they are used to describe each material, the most known are Mooney-Rivlin, Neo-Hookean, Ogden, Polynomial, Fung's and Delfino's Exponential functions. After trying those equations to describe numerically the results of the performed expansions done in patients, Delfino's Exponential function was selected. Delfino [2] proposed it to describe the human artery under several loads; this function is represented by the following expression:

$$W = \frac{a}{b}\{\exp[\frac{b}{2}(I_1 - 3)] - 1\} \tag{1}$$

where W is the strain energy density; a e b are parameters of the material and I_1 is the first strain invariant defined by the principal stretches, λ_i .

$$I_1 = \lambda_1^2 + \lambda_2^2 + \lambda_3^2. \tag{2}$$

The numerical model was done based on the *in vivo*, successive expansions, the final geometry of one expansion, is used as the initial geometry for the next expansion, with zero stress, since the pressure inside goes to zero in a week. Because the expansions are successive, at the end of every expansion done numerically the thickness of the modeled skin changes, but not uniformly. Since the final geometry of the previous expansion is used to begin the next expansion, to model different thickness for every membrane element was made impossible; thus the mean thickness of all elements obtained in the previous expansion was used in the successive one along with the previous geometry.

The ABAQUS code has a command to obtain the thickness of each finite element after deformed, in the end of each expansion. To identify the parameters that best describe the skin in each patient, as said before, the skin expansion in each step was modeled creating a inserted volume x pressure reached for each step of the successive expansions. To fit the numerical curve to the curves obtained during the expansions performed on the patients, and in this way finding the parameters for the skin in that specific expansion, the Newton Raphson method was used. To choose iteratively the parameter that would present smaller difference between the results obtained during the expansion *in vivo* and numerically, the Finite Element code was used with the MATLAB code.

3.2 Results

To obtain the elastic parameters of Delfino's constitutive equation for the scalp the following procedure was pursued. Since the skin expanders for the two patients had different total volumes, given by the factory, and shapes, the ratio, V*, between the total volume inside of the expander at the end of each expansion and the nominal volume of the expander given by the factory, is used as the variable to be related with the final pressure.

3.2.1 Patient 1

The dimensions of the rectangular skin expander of this patient are 13,6cm x 5,5cm x 5,6cm, and a mesh of 126 quadrilateral finite elements was used. Table 3 shows the results, for all the steps of this patient. For each expansion parameters a and b for Delfinos's function were obtained, showing that as the skin expands the parameters change. Parameter a changes from 0.213 MPa to 1.787 MPa, and parameter b changes from 31.5 to 120.5. The initial thickness of 0.5cm reaches a final thickness of 0.13cm, and as we said before, this value should be even smaller because we used the mean value for the thickness as the expansions went on. The maximum stretch, $\lambda\, max$, achieved is 3.65 and the maximum stress 67.96 N/cm^2. With the maximum stretch of the skin it is possible to know the amount of skin provided by the skin expansion. The maximum stress reached in each expansion is an important data, since this is what measures the discomfort or pain of the patient during the expansion.

3.2.2 Patient 2

The dimensions of the rectangular skin expander of this patient are 10.1cm x 5.6cm x 5.8cm, and a mesh of 161 triangular finite elements was used. Table 4 shows the results, for all the steps of this patient. For each expansion parameters a and b for Delfinos's function were obtained, showing that as the skin expands the parameters change. Parameter a changes from 0.636 MPa to 1.500 MPa, and parameter b changes from 42.65 to 65.6. The initial thickness of 0.5cm reaches a final thickness of 0.07cm, and as we said before, this value should be even smaller because we used the mean value for the thickness as the expansions went on. The maximum stretch, $\lambda\, max$, achieved is 4.72 and the maximum stress 106.1 N/cm^2. With the maximum stretch of the skin it is possible to know the amount of skin provided by the skin expansion. The maximum stress reached in each expansion is an important data, since this is what measures the discomfort or pain of the patient during the expansion.

Table 3: Results for Patient 1.

Step (i)	Initial Volume (V_i) ml	Final Volume V_f (ml)	$V_f - V_i$ (ml)	V_f/V_{mx} V *	Pressure (KPa)	λmáx (step)	λmáx (added)	σ máx(t) (N/cm^2)	Parameters	
									a (Mpa)	b
A	0	80	80	x	x	1,35	1,35	x	x	x
1	80	110	30	0,28	29,50	1,11	1,50	7,97	0,213	31,5
2	110	140	30	0,35	28,20	1,11	1,66	7,48	0,222	33,4
B	140	380	x	x	x	1,77	2,94	x	x	x
3	380	425	45	1,06	26,10	1,07	3,15	8,03	0,986	51,3
4	425	465	40	1,16	26,80	1,06	3,34	9,07	1,298	75,2
5	465	500	35	1,25	26,00	1,05	3,51	8,99	1,463	134,5
6	500	538	38	1,35	25,20	1,04	3,65	8,83	1,787	120,5

Table 4: Results for Patient 2.

Step (i)	Initial Volume (V_i) ml	Final Volume V_f (ml)	$V_f - V_i$ (ml)	V_f/V_{mx} V *	Pressure (KPa)	λmáx (step)	λmáx (added)	σ máx(t) (N/cm^2)	Parameters	
									a (Mpa)	b
A	0	214	x	x	x	3,60	3,60	x	x	x
1	214	254	40	x	26,00	1,09	3,92	11,65	0,636	42,6
2	254	298	44	0,85	25,10	1,08	4,24	11,22	0,491	48,2
3	298	338	40	0,99	23,90	1,06	4,49	8,60	1,007	49,8
4	338	376	38	1,13	21,90	1,05	4,72	7,43	1,500	65,6

3.2.3 Analysis of the results for the scalp

The goal is to obtain a curve that shows the change of the parameters as the skin is expanded. To obtain this change of the elastic parameters, a and b of Delfino's constitutive equation for the scalp the following procedure was pursued. The results obtained for the relation V* and the parameter a, from table 3 and 4, for each skin expansion were put together in Figure 5, permitting to obtain a mean curve to describe the behavior of the parameter a. Table 5 shows the variance and standard deviation representing the mean value and the obtained fitted values for parameters a.

The same practice was done for parameter b in Figure 6. Table 6 shows the variance and standard deviation representing the mean value and the obtained fitted values for parameters b.

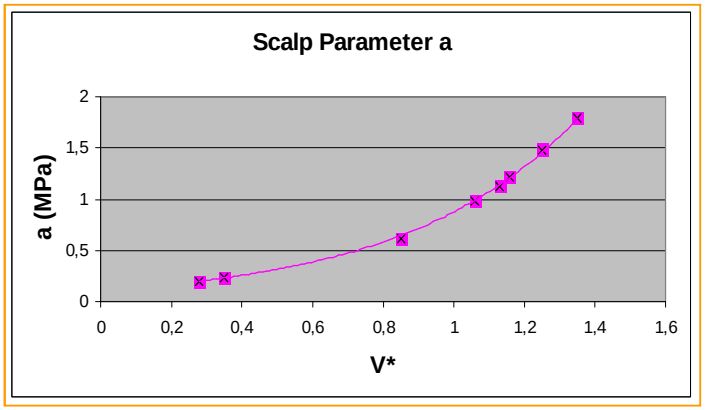

Figure 5: Curve describing the change in parameter a with the variable V^*.

Table 5: Results for the variance and standard deviation of the mean value and the obtained value for parameter a, the grey cells are the results of patient 2.

a MPa (ABAQUS)	V*	a MPa (curve)	Differences	Variance	Standard deviation
0,213	0,28	0,199	-0,0140	0,00005	0,010
0,222	0,35	0,241	0,0190	0,00009	0,013
0,636	0,85	0,616	-0,0200	0,00010	0,014
0,986	1,06	0,976	-0,0100	0,00002	0,007
1,007	1,13	1,123	0,1160	0,00338	0,082
1,298	1,16	1,215	-0,0830	0,00174	0,059
1,463	1,25	1,486	0,0230	0,00001	0,003
1,500	1,25	1,478	-0,0220	0,00012	0,015
1,787	1,35	1,796	0,0090	0,00002	0,006

The same practice was done for parameter b in Figure 6. Tables 5 and 6 shows the variance and standard deviation representing the mean value and the obtained fitted values for parameters a and b respectively.

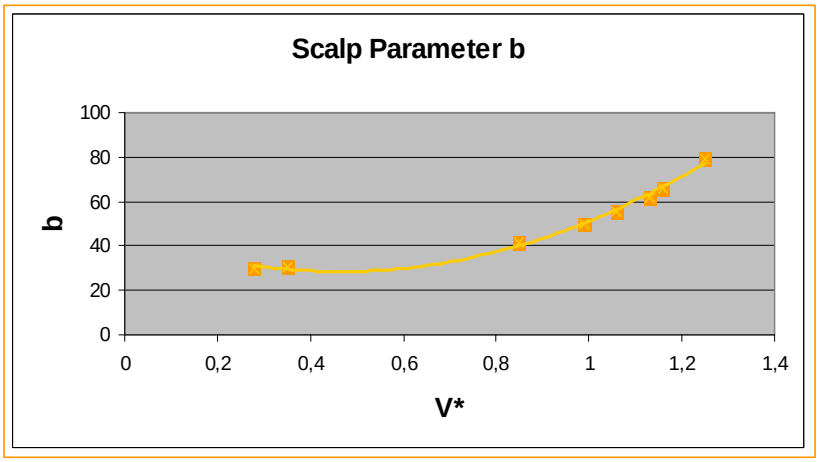

Figure 6: Curve describing the change in parameter b and the variable V^*.

Table 6: Results for the variance and standard deviation of the mean value and the obtained value for parameter b, the dashed cells are the results of patient 2.

b (ABAQUS)	V*	b (curve)	Differences	Variance	Standard deviation
31,5	0,28	30,09	-1,41	0,50	1,00
33,4	0,35	30,68	-2,72	1,84	1,92
42,6	0,85	41,72	-0,88	0,20	0,63
48,2	0,99	49,84	1,64	0,67	1,16
51,3	1,06	55,62	4,32	4,66	3,05
49,8	1,13	61,99	12,19	37,16	8,62
75,2	1,16	66,17	-9,03	20,39	6,39
65,6	1,25	79,20	13,60	46,23	9,62

4 Conclusions

The maximum difference between the curve obtained numerically using the fitted parameter a and b and the curve obtained *in vivo,* is of 1%, which is very encouraging. The pressures measured *in vivo* in the beginning of each expansion were very small and it was difficult and almost impossible to measure. We consider the results obtained for the parameters a and b quite reliable, taking in account

the differences between the patients, age and race, although it is advisable to have more patients to obtain a more confinable result for the parameters to describe the scalp under expansion. The following is the curve that describes the behavior of constant a during expansion.

$$a = 1.187V^{*3} - 1.395V^{*2} + 1.075V^{*} - 0,015. \tag{3}$$

For parameter b the curve is in Equation 4,

$$b = 27.9 + 0.9e^{(V^{*}/0.31)}. \tag{4}$$

With the results obtained here we can have a better knowledge of the human skin under expansion. It is reasonable to understand that as the skin is extended, process done by the use of expanders, the collagen fibers are extended and in this way the resistance to expansion will increase, this can be seen by the increase of parameters a and b, of Delfinos's constitutive equation, as the expansion goes on. The present study is pioneer in its goal to model the human skin under successive expansions, obtaining different parameters to characterize the skin as the expansions go on.

The results, although the number of patients analyzed were small, only two, were quite encouraging, and we believe they can be used as an initial guess for the problem. Each patient had, between four and six expansion measured, obtaining at least five measurement for each expansion. The total data for this research contained more then 60 volumexpressure items. A further research can provide the type, number and volume of skin expanders necessary to obtain an extra amount of skin to repair a certain medical problem. Based in the results we can warn the surgeons against to expansion of the skin in regions over elastic foundation, as abdomen or over fatty tissue as on the upper leg.

Acknowledgements

We are especially grateful to Professor Ivo Pitanguy and his staff who has supported our projects over the years. To Dr. Henrique Radiwansky for his assistance during the *in vivo* measurements, in Santa Casa da Misericórdia RJ, (38th Enfermar. - Serviço do Professor I. Pitanguy) and Institute Ivo Pitanguy. Special thanks to CNPq and FAPERJ for the support with the research projects. Last but not least for the support and enthusiasm of the patients without whom this work was made possible.

References

[1] Socci, L. et al., An axisymmetric computational model of skin expansion and growth. *Biomechanics and Modeling in Mechanobiology*, **6(3)**, 2007.

[2] Delfino, A., Stergiopulos, N., Moore, J.E. & Meister, J., Residual strain effects on the stress field in a thick wall finite element model of the human carotid bifurcation. *Journal of Biomechanical*, **30(8)**, pp. 777–786, 1997.

A comparative assessment of polymer concrete strength after degradation cycles

J.M.L. Reis

Universidade federal Fluminense - UFF, Programa de Pós-graduação em Engenharia Mecânica - PGMEC, Laboratório de Mecânica Teórica e Aplicada - LMTA, Niterói/RJ – Brazil

Abstract

A comparative study of the influence of chemical degradation effects on flexural and compressive strength of polymer concrete was performed. For this purpose, specimens of epoxy polymer mortars were exposed to four different degradation agents represent those that often account for corrosive processes in industrial environments. Some compositions in the study showed evidence of physical surface changes and weight loss. A decrease in the flexural and compressive strength of the samples exposed to corrosive agents was observed. However, even in those samples, the remaining strength values remained far higher than those found in mortars prepared with Portland cement, an inorganic binder.

Keywords: composite materials, polymer concrete, chemical degradation.

1 Introduction

Significant efforts and resources have been devoted to condition assessment, rehabilitation and repair of deteriorating infrastructure. In the last few decades, polymers have been used in the production of a unique composite material with improved mechanical strength and durability [1, 2]. This concrete like composite material has a polymeric resin as binder instead of Portland cement and water. Polymer Concrete (PC) displays high flexural and compressive strength, as well as improved chemical resistance to degradation environments, especially when compared to ordinary Portland cement concrete [3].

Portland cement concrete hydration products are alkaline and when submitted to acid environments they react. When exposed to a certain period of time those concretes will show sign of wear [4]. However, due to polymeric binder, polyester, epoxy, vinyl, methylmetacrylate resins, PC shows good chemical resistance to degradation environments and composite materials manufactured with thermoset resins as binder tends to reproduce their inherent characteristics of the unreinforced matrix [3].

For Rebeiz and Fowler [5] PC is the material of choice for coatings because of its strong bonding with Portland cement concrete, its resistance to abrasion and weathering, its impermeability and the

Mechanics of Solids in Brazil 2009, H.S. da Costa Mattos & Marcílio Alves (Editors)
Brazilian Society of Mechanical Sciences and Engineering, ISBN 978-85-85769-43-7

low weight resulting from the small layer thicknesses used. PC also shows good sound and thermal insulation properties because of its low thermal conductivity and good dampening characteristics. In hydraulic structures such as dams, dikes, reservoirs and piers, PC creates a highly abrasion-resistant surface [6].

Fowler [1] observed that in the United States, the most common applications of PC are found in highway surfaces and bridge decks as well as in the petrochemical industry. In Canada and Japan, PC is often used in underground constructions and road surfaces, mainly because of severe weather conditions. In Europe, however, a large share of the applications is represented by precast materials for the civil construction sector, in the metal-mechanical industry as a replacement for cast metals and in the construction of reservoirs and coating materials in the chemical and food industry.

Most polymeric materials undergo degradation on exposure to UV radiation and aggressive chemicals. Vipulanandan and Paul [7] have investigated degradation of polymer concrete without fiber reinforcement. They found that polymer concrete specimens immersed in alkaline solutions lost considerable strength after even short exposures. Water is also known to cause degradation of polymer concrete. In this study, the effect on strength of exposure to seawater, sulfuric acid, distilled water and soft drink in detail. Since the motivation for the research was to determine the durability of polymer concrete, it was considered important to simulate the types of aggressive environments that could conceivably be brought into contact with the material.

2 Materials and experimental procedure

To perform this research, PC formulations were prepared by mixing aggregates with thermosetting resins. The aggregate used was foundry sand, which consists in quartz sand, designed by 40/50, with a uniform granulometry.

The epoxy resin system used is based on a diglycidyl ether bisphenol A and an aliphatic amine hardener with low viscosity (500-700 MPa.s), which cluster the sand. Epoxy resin produces a high performance polymer concrete, which results in durability, low permeability and fast cure. Resin content used was 12% by weight. Previous studied performed by the author showed the lowest binder concentration that would deliver an optimal cost/performance ratio [8, 9].

With these binder formulations and mix proportions, polymer concrete were mixed and molded. For flexural tests prismatic (40x40x160 mm^3) specimens were manufactured, as illustrated in Fig. 1, and cylindrical specimens (φ 50x100 mm) were produced for compression tests, see figure 2, according to the RILEM standard CPT PC-2 [10]. All specimens were allowed to cure for 7 days at room temperature and then postured at 60°C for 4h, before being submitted to corrosive environment.

The test method for degradation followed the procedure presented by Camps *et al.* [11]. After specimens production a 14-day exposure cycles were started. Each exposure cycle consisted of immersing the samples for 7 days in a chemical solution and then allowing them to dry for 7 days. The specimens were weighed before the beginning of each test cycle. After the immersion cycle, the specimens were washed with pressurized water in order to simulate the effect of mechanical abrasion and to remove any corrosion products from their surface. The specimens were then allowed to dry in a controlled laboratory atmosphere for 7 days. At the end of the drying cycle, the specimens were again weighed

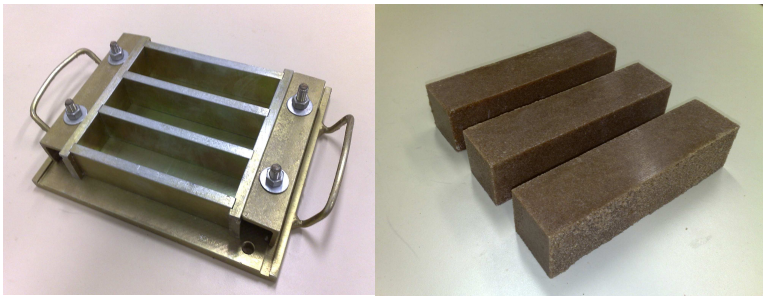

Figure 1: Flexural test specimens.

Figure 2: Compression test specimens.

thus completing the 14-day cycle. After each new cycle, the aggressive agent solution was replaced with fresh solution. The pH of the solutions was measured before immersing the specimens and after they were removed. The aggressive agents used were lactic acid, sulfuric acid, cola soft drink and distilled water. Lactic and sulfuric acid were diluted to 5%. The ph solutions are presented in table 1.

Table 1: pH from all aggressive solutions.

Solution	pH
Distilled Water	5.1
Sulfuric Acid	1.1
Lactic Acid	1.9
Seawater	8.2

Five exposure cycles were scheduled. The volume of aggressive solutions amounted to 4 times the specimen's volume. After the final exposure cycle measurements of polymer concrete under different loading conditions quasi-static tests were performed in flexural and compression to evaluate how each degradation solution affect polymer concrete mechanical strength. Prismatic polymer concrete beams were tested in three-point bending up to failure at the loading rate of 1 mm min-1, with the span of length of 100 mm, according to RILEM CPT PCM-8 standard test method [12]. The specifications of this standard, in terms of specimen geometry a span length, are similar to those specified in ASTM C348-02, standard test method for flexural strength of hydraulic cement mortars [13]. In both mentioned standards, shear effect is not taken into account on calculation procedure of flexural strength. Despite the very short span compared to the thickness, shear effect is disregarded. Polymer concrete is considered an isotropic material and the theory of plane cross-section was used. Flexural strength, considered as the strength under normal stress, was determined applying the following equation:

$$\sigma_f = \frac{3Pl}{2bh^2} \tag{1}$$

where σf is the flexural strength; P is the maximum load recorded, l is the span length; b and h are respectively, the width and height of the prismatic specimens.

Cylinder polymer concrete specimens were tested in compression at the loading rate of 1.25 mm/min according to ASTM C39-05 standard [14].

Compressive strength were calculated according the following equation:

$$\sigma_c = \frac{F}{A} \tag{2}$$

where σc is the compressive strength; F is the maximum load recorded; and A is the cross-sectional area of cylinder specimens.

Both flexural and compressive testing set-up, are presented in figure 3.

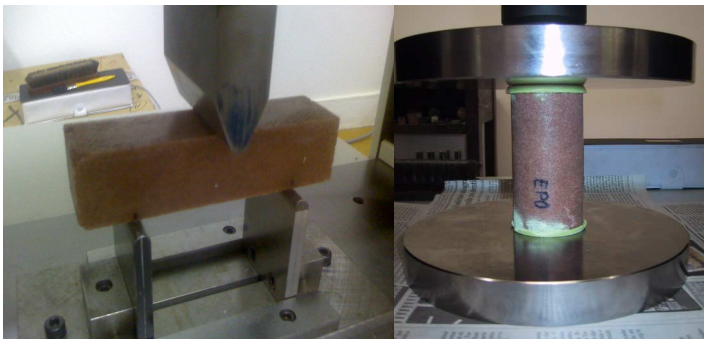

Figure 3: Flexural and compression test set-up.

3 Test results and discussion

Flexural and compressive test results in order to obtain polymer concrete mechanical strength are discussed in this section. Table 2 represents the flexural strength test results of polymer concrete subjected to degradation environments compared to reference (no degradation) results.

Table 2: Flexural strength of polymer concrete after degradation cycles.

Solution Type	Mean Strength (MPa)	% Flexural Strength Loss	% Weight Gain
Reference	24.734	-	
Distilled Water	23.364	5.54	0.3
Sulfuric Acid	22.158	10.41	0.6
Lactic Acid	-	-	0.7
Seawater	23.035	6.87	0.3

After three-point bending tests, when compared to reference values, polymer concrete displayed a decrease in the flexural strength. Specimens submitted to sulfuric acid degradation solution decreased 10.41% and a loss of 6.87% and 5.54% were obtained for seawater and distilled water degradation solutions respectively. A severe damage was observed to specimens subjected to lactic acid solution and tests could not be performed.

Table 3 displays the compressive test results of polymer concrete after degradation exposure.

Table 3: Compressive strength of polymer concrete after degradation cycles.

Solution Type	Mean Strength (MPa)	% Compressive Strength Loss	% Weight Gain
Reference	52.845	-	
Distilled Water	51.937	1.7	0.2
Sulfuric Acid	51.723	2.1	1.1
Lactic Acid	-	-	1.7
Seawater	49.145	7.0	0.4

When specimens submitted to seawater degradation solution a reduction of 7.0% in polymer concrete compressive strength were measured. A decrease of 2.1% was obtained by specimens submitted to sulfuric acid solution and for specimens degraded in distilled water a 1.7% loss was observed when compared to reference polymer concrete specimens. Again a severe damage was observed to compressive specimens and tests could not be perfomed.

For flexural test specimens low percentages of weight variation were observed, lower than 1% and for compressive blocks a higher gain in weight were recorded. For sulfuric and lactic acid solutions specimens increased its weight by 1.1 and 1.7% respectively.

Polymer concrete surface changes after 5 degradation cycles when exposed to sulfuric and lactic acid. Figure 4 displays polymer concrete specimens after lactic acid degradation cycles. A severe damage was observed in the specimens and flexural and compressive test could not be performed.

Figure 4: Specimens after lactic acid degradation.

A higher loss of strength was observed on flexural strength compared to compressive strength of polymer concrete. The solution which most affected polymer concrete was lactic acid and the less aggressive was distilled water, for both types of specimens tested, in flexure and in compression.

When the loss of strength of polymer concrete is compared to ordinary cement concrete, it becomes clear that large percentages losses are observed [3]. The remaining strength level after degradation cycles is higher than the values observed in cement concrete with no chemical attack.

It is reasonable to believe that the polymer matrix used in the polymer concrete production did not suffer significant losses. The loss of strength can be attributed to an increase of porosity in PC samples with increased capillary diffusion of solutions, which weakens the bond between the aggregate and the matrix.

4 Conclusions

The present study aimed to investigate the degradation of polymer concrete when submitted to different aggressive agents.

The values of both flexural and compressive strength after exposure were quite high when compared to typical values of high strength cement concrete. Unlike what is observed in ordinary Portland cement concrete compounds [15].

No significant weight loss but visual changes were observed, especially when specimens were exposed to sulfuric and lactic acid.

Lactic acid produces a severe damage to polymer concrete structure. Sulfuric acid with low pH did not degraded polymer concrete like lactic acid with higher pH proving that lower ph does not affect directly epoxy binder nor the mixture.

This study produces information for epoxy polymer concrete users in industrial or commercial environments. The results reveal the weakness of the material and provide important information for design and applications of polymer concrete.

Acknowledgements

The financial support of FAPERJ under the JOVEM CIENTISTA DO ESTADO program is gratefully acknowledged.

References

[1] Fowler, D.W., Polymers in concrete – where have we been and where are we going? *Proceedings of the 10th International Congress on Polymers in Concrete*, Hawaii, USA, 2001.
[2] Fowler, D.W., Polymers in concrete: a vision for the 21st century. *Cement Concrete Composites*, **21(5-6)**, pp. 449–52, 1999.
[3] Gorninski, J.P., Dal Molin, D.C. & Kazmierczak, C.S., Strength degradation of polymer concrete in acidic environments. *Cement and Concrete Composites*, **29**, pp. 637–645, 2007.
[4] Steinberg, M., Concrete polymer materials and its worldwide development. *Proceedings of International symposium on polymers in concrete*, Detroit, American Concrete Institute, pp. 123–137, 1973. (ACI.SP40).
[5] Rebeiz, K.S. & Fowler, D.W., Recycling plastics in polymer concrete systems for engineering applications. *Polymer Plastics Technol Eng*, **30**, pp. 809–825, 1991.
[6] Fowler, D.W., State of the art in concrete-polymer materials in the u.s. *Proceedings of the 11th international congress on polymer in concrete*, ed. M. Maultzsch, Berlin, pp. 597–603, 2004.
[7] Vipulanandan, C. & Paul, E., Performance of epoxy and polyester polymer concrete. *ACI Materials Journal*, pp. 241–251, 1991.
[8] Reis, J.M.L., Mechanical properties of textile waste reinforced polymer concrete. *Proceedings of the 19th International Congress of Mechanical Engineering*, Brasília, 2007.
[9] Reis, J.M.L., The influence textile fibers in the mechanical properties of polymer concrete. *Proceedings of the V National Congress of Mechanical Engineering*, Salvador, 2008.
[10] TC 113, UK, *RILEM-CPT PC-2: Method of making polymer concrete and mortar specimens*, 1995.

[11] Camps, J.P., Laplanche, A. & Al Rim, K., Corrosion of concrete by sequestrating agents of detergents. *Proceedings of Protection of concrete Dundee*, Dundee, Scotland, volume 1, pp. 63–73, 1990.
[12] TC 113, UK, *RILEM-CPT PC-8: Method of test for flexural strength and deflection of polymer-modified mortar*, 1995.
[13] ASTM, USA, *ASTM C 348-02: Standard Test Method for flexural strength and modulus of hydraulic cement mortars*, 2002.
[14] ASTM, USA, *ASTM C39 / C39M - 05e1: Standard Test Method for Compressive Strength of Cylindrical Concrete Specimens*, 2005.
[15] Kulakowski, M.P., Vieira, F.P. & Dal Molin, D.C., Relatório convênio camargo corrêa industrial. Technical report, NORIE/CPGEC/UFRGS, Porto Alegre, 1997.

Mechanics of Solids in Brazil 2009, H.S. da Costa Mattos & Marcílio Alves (Editors)
Brazilian Society of Mechanical Sciences and Engineering, ISBN 978-85-85769-43-7

Semi-analytical solution of dam-resevoir interaction in the fundamental mode shape

Paulo Marcelo Vieira Ribeiro, Carlos Augusto Elias Melo
and Lineu José Pedroso
Department of Civil and Evironmental Engineering - ENC/UnB
Brasília/DF – Brazil

Abstract

This paper describes a semi-analytical procedure for solution of dam-reservoir interaction in the fundamental mode shape. The fundamental frequency is solved using a generalized coordinate approach mixed with a wave equation analytical solution for a flexible boundary, resulting in a coupled system equilibrium frequency equation. Pressure field in the fluid domain and fluid added mass are obtained upon the solution of this equation. A full development of the theory will be presented, along with application examples. Results indicate good agreement between finite element solution for the coupled system and the resulting fluid added mass solution. This methodology provides a useful resource for solution of the coupled system and can be readily applied in dam engineering problems.

Keywords: dams, reservoir, fluid-structure interaction, analytical, solution.

1 Introduction

The aim of this work is to evaluate the influence of hydrodynamics pressures in systems with fluid-structure coupling. Two approaches may be used: solutions involving both solid and fluid domain, and representation of fluid effects through added masses along the structure. The added mass technique consists in substituting the hydrodynamic pressures exerted on the structure's face by a set of masses, which are proportionally accelerated as the structure vibrates. This provides an equivalent system which is able to represent the coupling effects for a given mass configuration. The major advantage of this sort of representation is the elimination of an additional step in the solution of the coupled problem, which is the consideration of fluid domain.

The fluid-structure interaction problem involves the determination of structure and fluid responses. However, it is important to emphasize that these responses are not independent. Fluid domain pressure field depends on the structural displacement, which in turn depends on the forces exerted by the fluid on the structure's face. A very efficient solution for this problem consists in determining, for

Mechanics of Solids in Brazil 2009, H.S. da Costa Mattos & Marcílio Alves (Editors)
Brazilian Society of Mechanical Sciences and Engineering, ISBN 978-85-85769-43-7

an imposed structural displacement, the fluid produced pressure field. This provides a possible way to develop analytical solutions for the fluid domain. Numerous solutions that consider compressible and incompressible fluids are available in literature, either for rigid boundaries or flexible boundaries (with an imposed deformed shape along fluid-structure interface). The pressure field produced by these solutions along the fluid-structure interface represents exactly the loads that must be added to the structure, providing the coupling effects between these two systems. The combination between analytical solution for pressure in fluid domain and analytical solution for structural response allows the development of a global solution that provides the effects of fluid produced actions in the structure.

The studies presented below involve the analysis of dynamic systems in generalized coordinates, considering only the structure's fundamental mode shape. The results involving coupled and uncoupled systems with effects of added mass will be compared in order to validate the proposed procedure. The effects produced by the fluid added mass presence will be studied, including its application in practical dam engineering analysis.

2 Literature review

The problem of dam-reservoir interaction has been widely studied in the last decades. The first attempt to solve this problem was made by Westergaard [1]. He considered a dam accelerated at its base as a perfect rigid body with a continuum infinite length reservoir. Because of the perfect rigidity of the dam, its acceleration along the structure was considered constant and equal to the foundation's acceleration. For these conditions, Westergaard found out a solution for the pressure field, which acts on the dam's face when it is under a seismic excitation. These studies demonstrated that fluid pressure had a parabolic shape, being proportional to earthquake acceleration. This is the simplest form of treating the dam-reservoir problem. However this solution has the limitations of not being valid for flexible structures and not considering the fluid compressibility.

Many other researchers determined the hydrodynamics pressure exerted on the dam's face as a result of earthquake ground motions for an incompressible fluid. To determine it using the Finite Element Formulation, a problem in modeling arises for unbounded domains of reservoir. To solve this problem, the unbounded domain should be truncated at a certain distance away from the structure. Zienkiewicz & Newton [2] used the Sommerfeld's radiation boundary condition for the truncating surface; Sharan [3] and Küçükarslan [4] determined numerically other boundary conditions for truncating surface of unbounded fluid domain; Silva & Pedroso [5] determined a solution for this problem using separation of variables technique for the same boundary conditions used for Zienkiewicz & Newton and Sharan & Küçükarslan, and proposed a new boundary condition.

Chopra [6] found out that water compressibility plays an important role in dam-reservoir interaction problems. According to his studies, fluid compressibility can significantly modify the seismic response. Chopra [7] investigated the response of a concrete gravity dam under horizontal earthquake excitation considering interactions effects and water compressibility, and concluded that commonly used simplified analysis, which neglect the interaction between dam and reservoir, and water compressibility, can result in significant errors. Chopra (1978) proposed a methodology in which the above-mentioned considerations were included.

Mechanics of Solids in Brazil 2009, H.S. da Costa Mattos & Marcílio Alves (Editors)
Brazilian Society of Mechanical Sciences and Engineering, ISBN 978-85-85769-43-7

Chopra & Fenves [8, 9] studied a system compound of a concrete gravity dam including the effects of water-foundation-rock interaction and the alluvium, and other sediments that deposit at the bottom of reservoirs. The interaction between the water and the reservoir bottom materials is approximately modeled by a boundary condition that permits partial absorption of hydrodynamic pressure waves at the reservoir bottom. In brief, it was show that the earthquake response of concrete gravity dam is increased by dam-water interaction, but decreased by reservoir bottom absorption with the magnitude of these effects dependent on the flexibility of the foundation rock, and dam-water interaction and reservoir bottom absorption both have a profound effect on the response of dams to vertical ground motion, but relatively less effect on the response to horizontal ground motion if foundation-rock flexibility is considered.

Many researches, for instance, Saini et al. [10], Chopra & Chakrabarti [11], Hall & Chopra [12], Fenves & Chopra [13], Fok & Chopra [14], and Lotfi et al. [15] studied dam-reservoir interaction problem in the frequency domain considering water compressibility using the Finite Element Method.

Ribeiro [16] proposed a methodology which provides an analytical solution of stress field in concrete gravity dams during earthquakes. This solution was developed taking the Gravity Method as a basis. This method, proposed by the United States Bureau of Reclamation – USBR [17], is designed for static and pseudo-static analysis (dam as a perfect rigid body and fluid incompressible) of concrete gravity dams. Ribeiro combined this solution with the methodology proposed by Chopra [18]. This combination allowed consideration of water compressibility and structural flexibility in the Gravity Method. The achieved results with this methodology are slightly conservative when compared to Chopra's procedure. It was shown that structural flexibility and water compressibility increases the earthquake response of concrete dams.

Silva [19] proposed an analytical formulation using separation of variables technique for the hydrodynamic pressure exerted on the dam's face under seismic excitation, considering structural flexibility and water compressibility. His results indicated a good agreement with the Finite Element Method.

3 Fluid domain analytical solution

Consider the following domain which is governed by the wave equation in two dimensions and represented in Fig. 1, where $S1$, $S2$, $S3$ and $S4$ represent the following boundary conditions:

$$S1 = \left.\frac{\partial p(x,y,t)}{\partial x}\right|_{x=0} = -\rho\phi\ddot{U}_g \tag{1}$$

$$S2 = \left.\frac{\partial p(x,y,t)}{\partial y}\right|_{y=0} = 0 \tag{2}$$

$$S3 = \left. p(x,y,t)\right|_{x\to 8} = 0 \tag{3}$$

$$S4 = \left. p(x,y,t)\right|_{y=H} = 0 \tag{4}$$

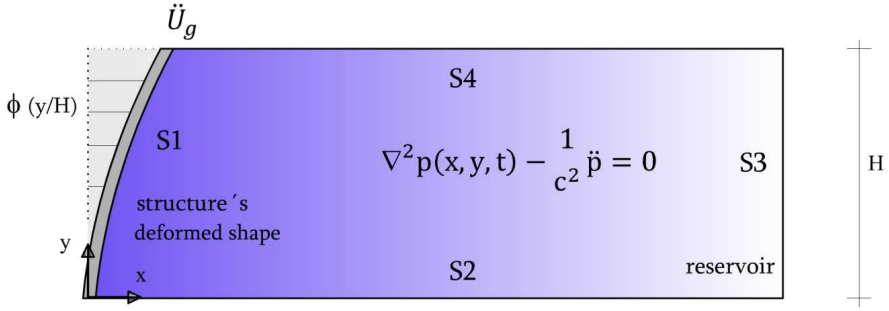

Figure 1: Fluid domain representation with boundary conditions.

and $\ddot{U}_g$ represents the acceleration at the structure's free edge ($y = H$). Silva [19] proposed a solution for this problem where the shape function $\phi(y)$ can be defined as an arbitrary function. This solution considers the fluid compressibility and depends on the frequency of the coupled system (ω).

$$p(x,y) = 2\rho\ddot{U}_g \sum_{n=1}^{\infty} \frac{I_n}{\sqrt{\mu_n^2 - \left(\frac{\omega H}{c}\right)^2}}\, e^{-\sqrt{\mu_n^2 - \left(\frac{\omega H}{c}\right)^2}\,\frac{x}{H}}\, cos\left(\mu_n \frac{y}{H}\right) \tag{5}$$

$$I_n = \int_0^H \phi\left(\frac{y}{H}\right) \cos\left(\mu_n \frac{y}{H}\right) dy \tag{6}$$

$$\mu_n = \frac{(2n-1)\,\pi}{2} \tag{7}$$

In the case of analysis that will be developed in this study, the function adopted corresponds to the fundamental deformed shape. Therefore, an analytical solution for the pressure field produced by the structural displacement in the fundamental vibration mode is achieved. The pressure field exerted on the fluid-structure interface can be obtained by setting up $x = 0$ in the above equations. Doing so, we get:

$$p(0,y) = 2\rho\ddot{U}_g \sum_{n=1}^{\infty} \frac{I_n}{\sqrt{\mu_n^2 - \left(\frac{\omega H}{c}\right)^2}} \cos\left(\mu_n \frac{y}{H}\right) \tag{8}$$

which represents the pressure field developed along the fluid-structure interface for a boundary with acceleration proportional to the adopted shape function $\phi(y)$. The latter expression is the starting point for the inclusion of the fluid participation in the dynamic response of the structure. It is important to remember that the parameter $\omega H/c$, called compressibility parameter, is an important indicator in this type of solution (the pressure field suffers important modifications when this parameter varies, as shown in Fig. 2).

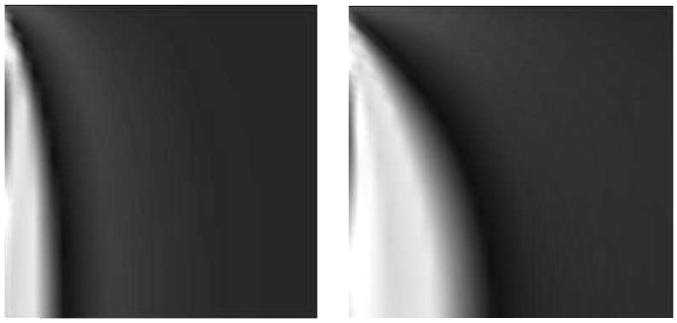

(a) (b)

Figure 2: Hidrodynamic pressure field variation along the reservoir for $\omega H/c = 0$ (a) and $\omega H/c = 1$ (b).

The characteristics of the hydrodynamic pressure approaches the behavior of an incompressible fluid as this parameter tends to zero (Fig. 3), resulting in a solution of a flexible boundary in an incompressible fluid. This indicates that the above solution is a general, valid for both compressible and incompressible fluid behavior.

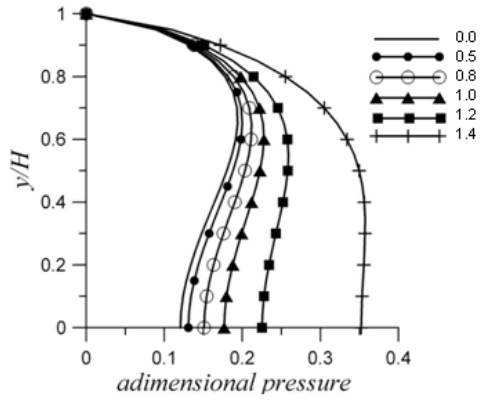

Figure 3: Pressure along fluid-structure interface for $\omega H/c$ parameter variation (fundamental mode).

4 Analytical solution for the structural system

The structural problem is represented by a clamped-free beam, where the generalized properties of the system (mass, stiffness and excitation) for an arbitrary vibration function were derived. Thus, it will

be possible to represent the dynamic response of the model through a single coordinate $X(t)$. This kind of solution will be very useful for the introduction of fluid effects since the analytical solution for this domain was obtained for an imposed frequency (ω) and shape function $\phi(y)$.

Consider the structure below with the arbitrary following parameters: mass per unit length $\mu(y)$, flexural stiffness $EI(y)$ and under a transverse loading $P(y,t)$.

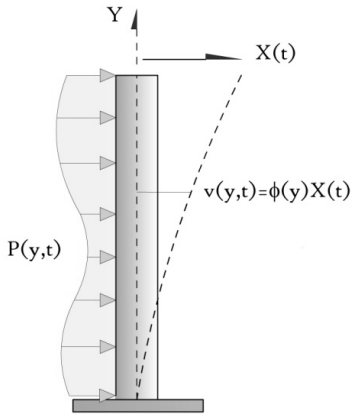

Figure 4: Structural model representation.

where the transverse-displacement response is represented by $v(y,t)$ and is related to the deformation at the top of the beam $X(t)$ by means of an arbitrary shape function $\phi(\mathrm{y})$. Doing so, we get:

$$v(y,t) = \phi(y)\, X(t) \tag{9}$$

The resistant forces in this system during the structure displacement are given by Inertial Force (Eq. 10) and Internal Bending Moment (Eq. 11):

$$f_i(y,\ t) = \mu(y)\, \ddot{v}(y,t) = \mu(y)\left[\ddot{X}\phi(y)\right] \tag{10}$$

$$m(y,\ t) = EI(y)\, \frac{\partial^2 v}{\partial y^2} = EI(y)\left[X \frac{d^2\phi(y)}{dy^2}\right] \tag{11}$$

Thus, it is assumed that only bending deformations will occur and the elastic moments developed will be proportional to curvature $\partial^2 v/\partial y^2$. The system's equation of motion can be obtained through the application of the principle of virtual work, equaling the work of internal forces to the work of external forces. The virtual displacement (δv) consistent with structural deformation ϕ is given by:

$$\delta v = \phi\,(\mathrm{y})\,\delta X \tag{12}$$

where δX corresponds to an arbitrary virtual displacement in the free edge of the structure. The work of external forces during this virtual displacement is given by:

$$W_e = \int_0^H P\,(y,t)\;\delta v\;dy = \delta X \int_0^H P\,(y,t)\,\phi\,(\mathrm{y})dy \tag{13}$$

The work of the internal forces (inertia and bending moment) is given by:

$$W_i = \int_0^H f_i\,(y,t)\delta v\;dy \quad + \quad \int_0^H m\,(y,t)\delta\frac{\partial^2 v}{\partial y^2}\;dy \tag{14}$$

Substituting the expressions of inertia force (Eq. 10) and internal bending moment (Eq. 11) in the expression above, and remembering that:

$$\delta v = \phi\,(\mathrm{y})\,\delta X \tag{15}$$

$$\delta\frac{\partial^2 v}{\partial y^2} = \;\delta X\frac{d^2\phi\,(y)}{dy^2} \tag{16}$$

provides:

$$W_i = \int_0^H \mu\,(y)\left[\ddot{X}\;\phi\,(y)\right]\phi\,(y)\,\delta X\;dy + \int_0^H EI\,(y)\left[X\frac{d^2\phi\,(y)}{dy^2}\right]\delta X\frac{d^2\phi\,(y)}{dy^2}dy \tag{17}$$

When simplified, the expression above results in:

$$W_i = \ddot{X}\delta X\int_0^H \mu\,(y)\left[\phi\,(y)\right]^2\;dy + X\delta X\int_0^H EI\,(y)\left[\frac{d^2\phi\,(y)}{dy^2}\right]^2 dy \tag{18}$$

Equaling external work with internal work and dividing the resultant expression by the arbitrary virtual displacement δX, gives:

$$\int_0^H P\,(y,t)\,\phi\,(\mathrm{y})dy = \ddot{X}\int_0^H \mu\,(y)\left[\phi\,(y)\right]^2 dy + X\int_0^H EI\,(y)\left[\frac{d^2\phi\,(y)}{dy^2}\right]^2 dy \tag{19}$$

Finally, introducing the following notations, we get the Generalized Mass $\tilde{M}$ (Eq. 20), the Generalized stiffness $\tilde{K}$ (Eq. 21), and the Generalized Force $\tilde{P}$ (Eq. 22):

$$\tilde{M} = \int_0^H \mu\,(y)\,[\phi\,(y)]^2\,dy \tag{20}$$

$$\tilde{K} = \int_0^H EI\,(y)\left[\frac{d^2\phi\,(y)}{dy^2}\right]^2 dy \tag{21}$$

$$\tilde{P} = \int_0^H P\,(y,t)\,\phi\,(\mathrm{y})dy \tag{22}$$

And substituting these notations in Eq. 19, results in:

$$\tilde{M}\ddot{X} + \tilde{K}X = \tilde{P}\,(t) \tag{23}$$

This is the system's dynamic equilibrium equation which has a vibration frequency equal to:

$$\omega = \sqrt{\tilde{K}/\tilde{M}} \tag{24}$$

It should be emphasized that the generalized stiffness obtained for this system includes only the effects of bending deformation. Additional effects can be introduced through the modification of this generalized parameter. Damping could also be added to this structure, and in this case it would be more appropriate to express it by damping ratio (ξ). Thus, we have:

$$\tilde{C} = 2\xi\tilde{M}\omega \tag{25}$$

5 Coupled problem analytical solution

The solutions presented above are valid for each isolated domain, both solid and fluid. However, a problem of great interest arises when it is necessary to verify the interaction effects produced between these two systems. In the case of the solution presented for the fluid domain, it is known the pressure field for a particular shape function. This pressure field can be properly added to the structural solution, since it is known the external forces produced by the hydrodynamic interaction. So, we have:

$$P\,(y,t) = p\,(0,y) = 2\rho\ddot{X}\sum_{n=1}^{\infty}\frac{I_n}{\sqrt{\mu_n^2 - \left(\frac{\omega H}{c}\right)^2}}\cos\left(\mu_n\frac{y}{H}\right) \tag{26}$$

Where the external forces are associated to the coupled frequency (ω) of the system and depend on the coupled shape function $\phi\,(y)$ of the structure. It is important to remember that the term $\ddot{U}_g$ was properly substituted by $\ddot{X}$, since in the coupled system accelerations of the free edge of the structure and of the flexible boundary are equal. Substituting the last equation (Eq. 26) in the generalized force equation (Eq. 22), results in:

$$\tilde{P}(t) = \ddot{X} \int_0^H \left[2\rho \sum_{n=1}^{\infty} \frac{I_n}{\sqrt{\mu_n^2 - \left(\frac{\omega H}{c}\right)^2}} \cos\left(\mu_n \frac{y}{H}\right) \right] \phi(\mathrm{y})\, dy = \ddot{X} \int_0^H \left[\frac{\beta}{\phi(\mathrm{y})}\right] [\phi(\mathrm{y})]^2 dy \tag{27}$$

It is interesting to note the similarity between the simplified result of this expression and the generalized mass equation in the structural model. We can rewrite the dynamic equilibrium equation of the structure to check the influence of this parameter. Thus:

$$\tilde{M}\ddot{X} + \tilde{K}X + \ddot{X} \int_0^H \left[\frac{\beta}{\phi(\mathrm{y})}\right] [\phi(\mathrm{y})]^2 dy = 0 \tag{28}$$

In this equation, the generalized force expression was placed on its left side, since the hydrodynamic pressures acts in the same direction of the inertia and elastic forces. We can rewrite Eq. (28), noticing that there are two terms along with $\ddot{X}$. This results in:

$$\left(\tilde{M} + \int_0^H \left[\frac{\beta}{\phi(\mathrm{y})}\right] [\phi(\mathrm{y})]^2 dy \right) \ddot{X} + \tilde{K}X = 0 \tag{29}$$

This equation represents the free-vibration of the structural model with a generalized mass produced by the interaction between fluid and solid domain. Physically, this means that the structure in contact with the fluid presents an additional vibrating mass which is distributed per unit length because the expression for generalized mass can be rewritten as follows:

$$\tilde{M}_{total} = \int_0^H \left\{ \mu(y) + \left[\frac{\beta}{\phi(\mathrm{y})}\right] \right\} [\phi(\mathrm{y})]^2 dy \tag{30}$$

where $\frac{\beta}{\phi(y)}$ represents the added mass per unit length caused by fluid presence.

The new dynamic equilibrium equation of the system is given by:

$$\tilde{M}_{total}\ddot{X} + \tilde{K}X = 0 \tag{31}$$

where it should be remembered that the generalized stiffness parameter is still defined by:

$$\tilde{K} = \int_0^H EI(y) \left[\frac{d^2\phi(y)}{dy^2}\right]^2 dy \tag{32}$$

It is important to remember that the shape function $\phi(y)$ now refers to the coupled system. Therefore, it should be taken great care not to confuse the shape function of the coupled system with the one for the uncoupled system. Similarly, the vibration frequency ω also refers to the coupled system and is given by:

$$\omega = \sqrt{\frac{\tilde{K}}{\tilde{M}_{total}}} \tag{33}$$

This frequency equation, although presented in a simple manner, is not an easy problem to be solved. It should be noted that the frequency is a function of the generalized stiffness, which is a function of the coupled system shape function $\phi(y)$. Also, the system's total mass is a function not only of $\phi(y)$, but also a function of the coupled frequency *(ω)* of the system. Therefore, this problem defines only one equation and two unknown parameters.

6 Application example 1 – incompressible fluid

In this example a cantilever beam of uniform cross section will be analyzed. By this way, it is intended to validate the afore-mentioned procedure and verify the effects produced by fluid-structure coupling in the fundamental mode. Figure 5 and Table 1 illustrates the structure that will be analyzed and its material and geometrical properties:

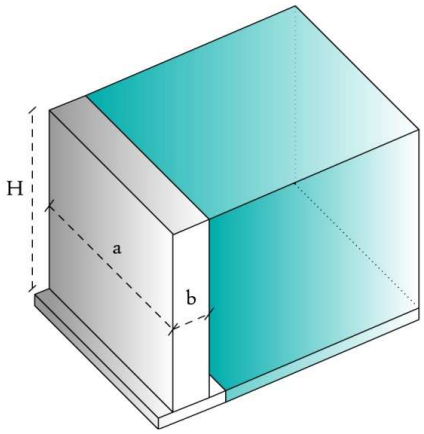

Figure 5: System representation.

Table 1: Geometrical and material properties.

a	1.00 m
b	0.10 m
H	1.00 m
Transverse Young's Modulus (E)	2.10 x 10^4 MPa
Structural mass density (ρ_e)	2000 kg/m^3
Fluid mass density (ρ_f)	1000 kg/m^3
Fluid sonic velocity (c)	1500 m/s

6.1 Uncoupled solution

For the uncoupled solution, the generalized mass and stiffness defined for the structural domain can be used. The exact fundamental mode shape function for a cantilever beam is given by:

$$\phi(y) = \frac{1}{2}\cosh\left(1.8751\frac{y}{H}\right) - \frac{1}{2}\cos\left(1.8751\frac{y}{H}\right) - 0.3670\sinh\left(1.8751\frac{y}{H}\right) + 0.3670\sin\left(1.8751\frac{y}{H}\right) \quad (34)$$

Substituting the above equation along with system's material and geometrical properties in the generalized parameters gives:

$$\tilde{M} = \int_0^H \mu(y)\left[\phi(y)\right]^2 dy = \mu\int_0^H \left[\phi(y)\right]^2 dy \cong 0.25\mu H = 5.00\times 10\ \frac{Ns^2}{m} \quad (35)$$

$$\tilde{K} = \int_0^H EI(y)\left[\frac{d^2\phi(y)}{dy^2}\right]^2 dy = EI\int_0^1 \left[\frac{d^2\phi(y)}{dy^2}\right]^2 dy \cong 3.09\frac{EI}{H^3} = 5.41\times 10^6\ \frac{N}{m} \quad (36)$$

$$\omega = \sqrt{\tilde{K}/\tilde{M}} = 328.94\ \frac{rad}{s} \quad (37)$$

The last equation represents the fundamental frequency for uncoupled system.

6.2 Coupled solution

For calculation of generalized parameters including coupling effects, a previous knowledge of the shape function $\phi(y)$ of the system is needed. The exact solution for the uncoupled fundamental mode shape is known. Therefore, we will assume that in the coupled system the fundamental mode shape function does not suffer influence due to fluid presence. So, it is assumed that the deformed shape function is identical in both coupled and uncoupled systems (although this kind of behavior does not always happens, as it will be verified later). The same problem occurs in respect to the coupled frequency. This parameter is also needed for calculation of the generalized added mass. However, this frequency is also an unknown parameter of the problem. But, as mentioned before, it is possible to find the system's frequency solution with an imposed shape function. To simplify the mathematical operations involved in calculating the generalized added mass, which leads to a great computational effort, a polynomial approximation to the fundamental exact mode shape is adopted. This leads to:

$$\phi_{approx.}\ (y) = -0.6457\left(\frac{y}{H}\right)^3 + 1.6082\left(\frac{y}{H}\right)^2 + 0.037\left(\frac{y}{H}\right) - 0.0016 \quad (38)$$

For $\tilde{M}$ and $\tilde{K}$, the exact deformed shape defined previously will be adopted. Special attention should be given to use of polynomial approximations in parameter $\tilde{K}$, which involves second order derivatives of $\phi(y)$ in its formulation. It should be noted that curves of polynomial approximation can produce unsatisfactory results for higher order derivatives of a particular function. Figure 6 compares the results obtained for the exact shape function and the polynomial approximation.

The equation for fundamental frequency solution is given by:

$$\omega = \sqrt{\tilde{K}/\tilde{M}_{total}} = \sqrt{\frac{5.41\times 10^6}{5.00\times 10 + \int_0^H \left[\frac{\beta}{\phi_{aprox.}(y)}\right]\left[\phi_{aprox.}(y)\right]^2 dy}} \quad (39)$$

This equation can be rewritten as:

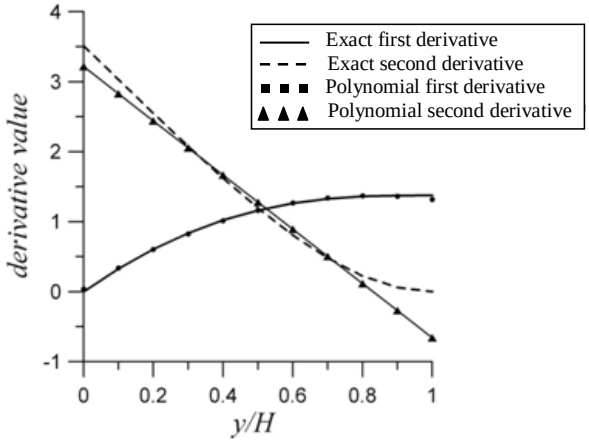

Figure 6: Comparison between exact and polynomial approximation derivatives.

$$5.41 \times 10^6 - \left(5.00 \times 10 + \int_0^H \left[\frac{\beta}{\phi_{aprox.}(y)}\right] [\phi_{aprox.}(y)]^2 dy\right) \omega^2 = 0 \tag{40}$$

where:

$$\beta = 2\rho \sum_{n=1}^{\infty} \frac{I_n}{\sqrt{\mu_n^2 - \left(\frac{\omega H}{c}\right)^2}} \cos\left(\mu_n \frac{y}{H}\right) \tag{41}$$

The solution of the fundamental frequency equation is related to calculation of β parameter, which depends on the number of terms used in summation. The results obtained using Maple 12 software for evaluation of Eq. (40) are listed in Table 2. These results are compared to a reference value obtained using the Finite Element Method (FEM) for a coupled system.

Table 2: Frequency, number of terms used in summation and processing time.

Number of terms in summation	**3**	**5**	**10**	**20**	**100**	**FEM (reference)**
Frequency (rad/s)	225.5931	223.2586	222.2825	222.0393	221.9615	222.2111
Processing time (s)	2.13	2.54	8.00	63.56	23913.88	-

It can be observed that the number of terms in summation exerts little influence on results, which achieves fast convergence to 222 rad/s. However, processing time is heavily influenced by this parameter. When compared to the reference value, the relative error is close to 0.1%. This frequency represents a decrease of 32.5% when compared to the uncoupled case. The coupled frequency, once established, allows the calculation of the added mass. Thus:

$$\tilde{M}_{fluid} = \int_0^H \left[\frac{\beta}{\phi\,(\mathrm{y})}\right][\phi\,(\mathrm{y})]^2 dy = 5.98 \times 10 \frac{Ns^2}{m} \tag{42}$$

This corresponds to a value greater than the generalized structural mass. Thus, we have the following parameters for the generalized coupled case:

$$\tilde{M} = 5.00 \times 10 + 5.98 \times 10 = 10.98 \times 10\ \frac{Ns^2}{m} \tag{43}$$

$$\tilde{K} = 5.41 \times 10^6 \frac{N}{m} \tag{44}$$

It is important to check the value of the compressibility parameter of this problem, which is given by:

$$\frac{\omega H}{c} = \frac{222.00 \frac{1}{s} \times 1m}{1500 \frac{m}{s}} \cong 0.15 \tag{45}$$

This value indicates a close to an incompressible fluid behavior. Thus, it is concluded that satisfactory results would be obtained if the hypothesis of an incompressible fluid was used. In fact, considering this behavior, the achieved frequency would be close to 222.20 rad/s. This value is almost identical to the value obtained for the compressible analysis with a great advantage: that is the elimination of ω in the β parameter.

6.3 Comparative studies between analytical and numerical results (forced vibration)

The equation of motion in free vibration for the structural coupled system can be built after the establishment of generalized parameters. We have:

$$[5.00 \times 10]\,\ddot{X} + \left[5.41 \times 10^6\right] X = 0 \quad (uncoupled) \tag{46}$$

$$[10.98 \times 10]\,\ddot{X} + \left[5.41 \times 10^6\right] X = 0 \quad (coupled) \tag{47}$$

For this analysis it will be defined a sine wave excitation applied at the structure's free edge, given by:

$$\tilde{P}\,(t) = 10^6 \times sin\,(50t) \tag{48}$$

Substitution of Eq. (48) in (46) and (47), gives:

$$[5.00 \times 10]\,\ddot{X} + \left[5.41 \times 10^6\right] X = 10^6 \times sin\,(50t) \quad (uncoupled) \tag{49}$$

$$[10.98 \times 10]\,\ddot{X} + \left[5.41 \times 10^6\right] X = 10^6 \times sin\,(50t) \quad (coupled) \tag{50}$$

Solution of the above equation results in:

$$X\,(t) = -0.028769 \times \sin\,(328.8931t) + 0.189239 \times \sin\,(50t) \quad (uncoupled) \tag{51}$$

$$X\,(t) = -0.043870 \times \sin\,(221.9586t) + 0.194748 \times \sin\,(50t) \quad (coupled) \tag{52}$$

Velocity and acceleration solutions are given, respectively, by first and second derivatives of Eq. (51) and Eq. (52). Comparison of these functions with coupled and uncoupled finite element solutions is shown on the Fig. 7.

7 Application example 2 – compressible fluid

In this analysis the previous example will be studied with the same geometrical and material properties, except for the Young's modulus, that will be taken as 2.10 x 10^{12} MPa.

7.1 Uncoupled solution

For the uncoupled solution the following generalized parameter are readily obtained:

$$\tilde{M} = \int_0^H \mu\,(y)\,[\phi\,(y)]^2\,dy = \mu \int_0^H [\phi\,(y)]^2\,dy \cong 0.25\mu H = 5.00 \times 10\,\frac{Ns^2}{m} \tag{53}$$

$$\tilde{K} = \int_0^H EI\,(y)\left[\frac{d^2\phi\,(y)}{dy^2}\right]^2 dy = EI\int_0^1 \left[\frac{d^2\phi\,(y)}{dy^2}\right]^2 dy \cong 3.09\frac{EI}{H^3} = 5.41 \times 10^8\frac{N}{m} \tag{54}$$

$$\omega = \sqrt{\tilde{K}/\tilde{M}} = 3289.34\,\frac{rad}{s} \tag{55}$$

7.2 Coupled solution

The fundamental frequency equation is given by:

$$5.41 \times 10^8 - \left(5.00 \times 10 + \int_0^H \left[\frac{\beta}{\phi_{aprox.}\ (y)}\right][\phi_{aprox.}\ (y)]^2 dy\right)\omega^2 = 0 \tag{56}$$

The results obtained using Maple 12 software for evaluation of Eq. (56) are listed in Table 3. These results are compared to a reference value obtained using the Finite Element Method (FEM) for a coupled system.

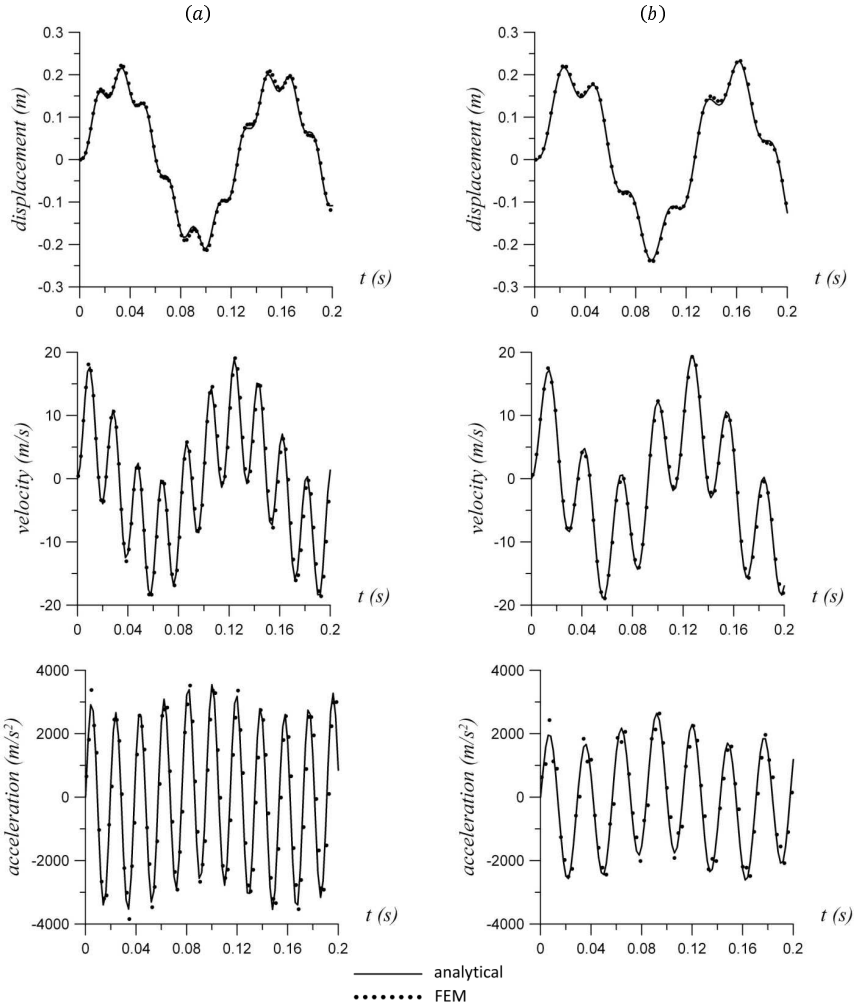

Figure 7: Comparison between FEM response (including all modes) and analytical results. Uncoupled (a) and coupled systems (b).

The above result reaches a fast convergence to values near 1990 rad/s. When compared to the reference value this result indicates a less than 0.2% relative error.

With the fundamental frequency the following generalized parameter is readily obtained:

$$\tilde{M}_{fluid} = \int_0^H \left[\frac{\beta}{\phi\,(\mathrm{y})}\right][\phi\,(\mathrm{y})]^2 dy = 8.67 \times 10 \frac{Ns^2}{m} \tag{57}$$

Table 3: Frequency, number of terms used in summation and processing time.

Number of terms in summation	3	5	10	20	FEM (reference)
Frequency (rad/s)	2006.1886	1995.4492	1990.8595	1989.7070	1986.0520
Processing time (s)	2.10	2.84	7.69	60.15	-

As in the previous analysis, this value is higher than the structural's generalized mass. It should be noted that this fluid added mass is greater than the one obtained in the incompressible case, indicating the effect of a higher compressibility parameter. The added mass produced a 39.5% reduction of the fundamental frequency. In the incompressible analysis this reduction was of 32.5%. These results indicate that fluid compressibility must not be neglected, and that higher fluid added masses are expected with the increase of this parameter, given by:

$$\frac{\omega H}{c} = \frac{1990.00\frac{1}{s} \times 1m}{1500\frac{m}{s}} \cong 1.33 \tag{58}$$

Equation (58) indicates a compressible fluid behavior. Treating this problem with an incompressible hypothesis could lead to considerable errors. In fact, the fundamental frequency obtained using an incompressible fluid model would result in 2221.00 rad/s (11.6% higher than the one obtained using a compressible fluid model).

7.3 Comparative studies between analytical and numerical results (forced vibration)

The following structural responses results from a sine wave $\tilde{P}(t) = 10^6 \times sin(450t)$ excitation:

$$X(t) = -0.000258 \times \sin(3288.9312t) + 0.001884 \times \sin(450t) \quad (uncoupled) \tag{59}$$

$$X(t) = -0.000441 \times \sin(1988.9737t) + 0.001948 \times \sin(450t) \quad (coupled) \tag{60}$$

Comparison of these functions and its derivatives with finite element solutions is shown on Fig. 8.

8 Application example 3 – concrete gravity dam

In this example a concrete gravity dam with geometrical and material properties given by Fig. 9 and Table 4 will be analyzed (FERC, 2002). However, the analytical generalized procedure will not be used in this analysis. Analytical treatment of these parameters is a complex task, since this structure's geometry is irregular and the fundamental mode shape occurs in both directions (varying both in x and y). Instead it will be used a semi-analytical procedure, where the uncoupled generalized parameters

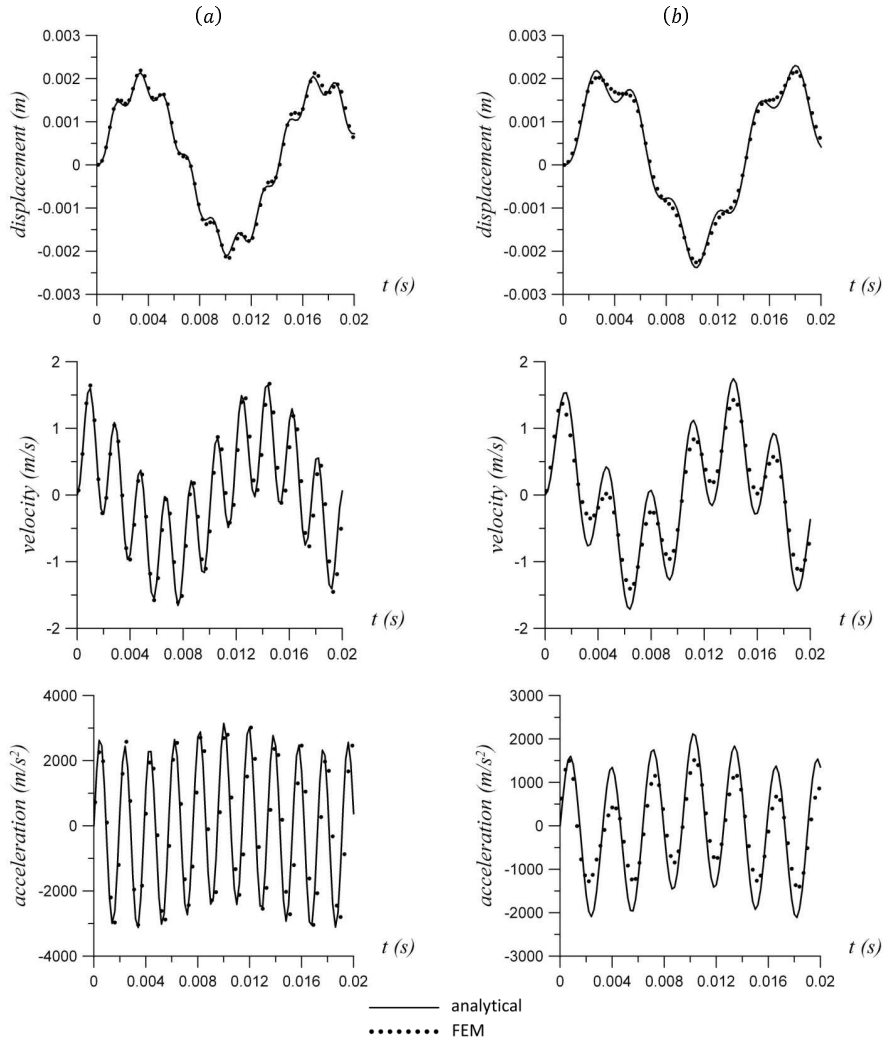

Figure 8: Comparison between FEM response (including all modes) and analytical results. Uncoupled (a) and coupled systems (b).

are going to be obtained from an uncoupled finite element analysis. These results will be introduced in the frequency equilibrium equation, for evaluation of the fundamental coupled frequency.

The generalized parameters obtained in the uncoupled finite element analysis are listed on Table 5. Additionally Eq. (61) indicates a polynomial approximation to the uncoupled fundamental mode shape function. These parameters along with this function are used in the frequency equation, for solution

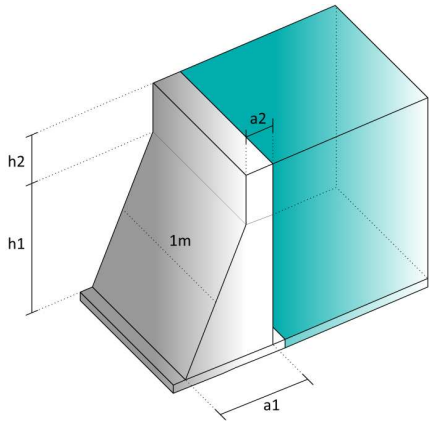

Figure 9: System representation.

Table 4: Geometrical and material properties.

a1	30.48 m
a2	4.57 m
h1	41.45 m
h2	7.32 m
Transverse Young's Modulus (E)	2.10 x 104 MPa
Structural mass density (ρ_e)	2000 kg/m^3
Fluid mass density (ρ_f)	1000 kg/m^3
Fluid sonic velocity (c)	1500 m/s

of the coupled system fundamental frequency.

Table 5: Generalized parameters – fundamental mode uncoupled analysis.

Generalized Mass $\left(\frac{Ns^2}{m}\right)$ $\widetilde{M}$	**Generalized Stiffness** $\left(\frac{N}{m}\right)$ $\widetilde{K}$	**Earthquake Participation Factor** $\left(\frac{Ns^2}{m}\right)$ $\widetilde{L}$
$\mathbf{1.0164\times10^5}$	2.1085×10^8	2.4086×10^5

$$\phi_{approx.}\ (y) = 0.10851\left(\frac{y}{H}\right)^4 + 0.61270\left(\frac{y}{H}\right)^3 + 0.07918\left(\frac{y}{H}\right)^2 + 0.20411\left(\frac{y}{H}\right) + 0.00105 \qquad (61)$$

The uncoupled fundamental frequency of this system is given by: $\omega = \sqrt{\tilde{K}/\tilde{M}} \cong 45.55\ \frac{rad}{s}$.

These parameters can be readily substituted in the frequency equation. Results are shown on Table 6.

From Table 6 it can be observed that the coupled frequency converges to a value near 32.90 rad/s. Comparison with the reference value indicates a 1% relative error. This added mass produced a 27.8% reduction of the fundamental frequency. This generalized parameter is given by:

$$\tilde{M}_{fluid} = \int_0^H \left[\frac{\beta}{\phi\,(\mathrm{y})}\right][\phi\,(\mathrm{y})]^2 dy = 0.9339 \times 10^5 \frac{Ns^2}{m} \qquad (62)$$

Verification of the compressibility parameter indicates a compressive behavior for this analysis:

Table 6: Frequency, number of terms used in summation and processing time.

Number of terms in summation	3	5	10	20	FEM (reference)
Frequency (rad/s)	33.4910	33.0988	32.9259	32.8822	33.2462
Processing time (s)	1.23	1.88	6.80	46.81	-

$$\frac{\omega H}{c} = \frac{32.90\frac{1}{s} \times 48.77m}{1500\frac{m}{s}} \cong 1.07 \tag{63}$$

The fluid added mass corresponds to approximately 92% of the structural mass. If this mass is included in the finite element model, representation of the coupled effects in the fundamental mode could be produced without the need of the reservoir. It should be noticed the different behavior between the structural and the fluid added mass. The first one is related to displacements in both directions (x and y). However, the fluid mass is related only to horizontal displacements given by $\phi\,(\mathrm{y})$, since it is assumed that hydrodynamic pressures develop only due to horizontal accelerations. When the model participation in the y direction is minimal and there is no variation of the mode shape in the transverse direction, then the entire model could be approximated by a single function for all generalized parameters, including the fluid added mass. This is exactly what happened in the previous examples.

For determination of the additional masses that will be inserted in the model, it will be necessary to calculate the β parameter. However calculation is needed only on the exact node locations where these masses are going to be inserted. Consider, as an example, the finite element model illustrated on Fig. 10. Added masses will be placed in 24 nodes along the dam's upstream face. The main objective is to replace the integral given in Eq. (62) by a discrete product of masses and related displacements. Table 7 indicates the calculation procedure.

After the inclusion of the added masses a fundamental modal analysis is required. This will provide the coupled frequency as well as the new deformed shape of the system. It should be noticed that these masses are related only to the fundamental mode of vibration. Figure 11 indicates a comparison between deformed shape results. One of the curves is a representation of transversal displacements x along the dam's height (in this problem defined as U_x). The other one indicates the total displacement, including both directions (x and y, in this problem defined as U_{sum}). We are assuming that fluid added masses should participate only in the transverse direction, but in the first approach the vertical displacements on the dam's upstream face are being neglected (Table 7). From Fig. 11 it can be noticed that this first approach might lead to poor results, since in the finite element model these masses will participate in both directions. Another option, that will provide much better results, is to introduce a modification in column (c), given by:

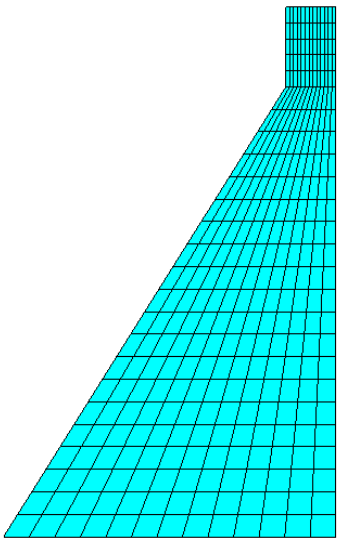

Figure 10: Finite element model.

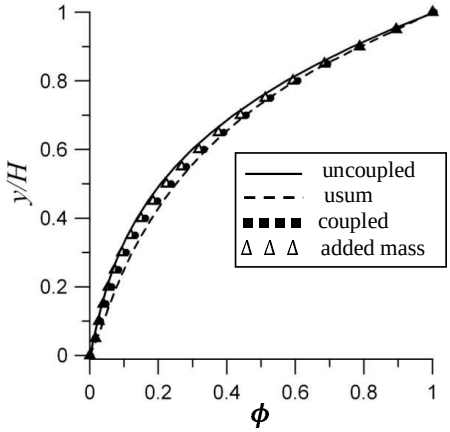

Figure 11: Deformed shape results.

Table 7: Added mass calculation procedure – first procedure (neglecting vertical displacements).

(a)	(b)	(c)	(d)	(e)	(f)
Node	**Elevation** $(\mathbf{m})$	$\phi(\mathbf{y})$	**Pressure**[1] **(normalized)** $\mathbf{p_{norm}}$	**Nodal tributary area** $\left(\mathbf{m^2}\right)$ $\mathbf{A_{node}}$	**Nodal mass**[2] $\left(\mathbf{10^6 Ns^2/m}\right)$ $\mathbf{M_{node}}$
48	2.0726	0.0099	0.1347	2.0726	1.3735
49	4.1453	0.0194	0.1358	2.0726	0.7093
50	6.2179	0.0297	0.1373	2.0726	0.4679
51	8.2906	0.0411	0.1392	2.0726	0.3420
.	.	.	.	.	.
.	.	.	.	.	.
.	.	.	.	.	.

[1] *normalized pressure* = $p/\left(\rho_f \ddot{X} H\right) = \beta/\left(\rho_f H\right)$
[2] *nodal mass* = $(d)/(c) \times A_{node} \times \rho_f H$

$$\phi(y) \longrightarrow \alpha(y) = \frac{\left[U_{sum}(y)\right]^2}{U_x(y)} \tag{64}$$

This proposed modification takes in account displacements in both directions, and will result exactly

on a product of nodal masses with transverse displacements U_x. Table 8 indicates some sample results for this second procedure.

Table 8: Added mass calculation procedure – second procedure (including vertical displacements).

(a)	(b)	(c)	(d)	(e)	(f)
Node	**Elevation** $(\mathbf{m})$	$\phi(\mathbf{y})$	**Pressure**[1] **(normalized)** $\mathbf{p_{norm}}$	**Nodal tributary area** $\left(\mathbf{m^2}\right)$ $\mathbf{A_{node}}$	**Nodal mass**[2] $\left(10^6\mathbf{Ns^2/m}\right)$ $\mathbf{M_{node}}$
48	2.0726	0.0313	0.1347	2.0726	0.4350
49	4.1453	0.0606	0.1358	2.0726	0.2264
50	6.2179	0.0868	0.1373	2.0726	0.1598
51	8.2906	0.1107	0.1392	2.0726	0.1271
.	.	.	.	.	.
.	.	.	.	.	.
.	.	.	.	.	.

[1] *normalized pressure* = $p/\left(\rho_f \ddot{X} H\right) = \beta/\left(\rho_f H\right)$
[2] *nodal mass* = $(d)/(c) \times A_{node} \times \rho_f H$

Frequencies obtained in both procedures are given in Table 9. It should be noticed that results obtained from the second approach converges to the previously determined coupled frequency. This is exactly what one should expect, since the added masses act as a replacement of Eq. (62).

Table 9: Results comparison between proposed procedures and reference value.

Procedure	**first**	**second**	**FEM (reference)**
Frequency (rad/s)	30.67	32.78	33.25
Relative error (%)	7.76	1.41	-

It can be noticed that the second approach provides much better results when compared to the first procedure. In this analysis vertical displacements can highly influence the fundamental frequency of the system. The differences between the uncoupled and usum curves in Fig. 11 clarify the effect of the vertical component of displacement. This figure also indicates that the fluid added mass approximates the deformed shape to the coupled solution result. If no further refinement is required, then the analysis

could be concluded in this step, with the second procedure added mass solution acting as the coupled system.

8.1 Comparative studies between analytical and numerical results (forced vibration)

In this analysis results from a coupled and uncoupled finite element models are compared to the proposed procedure. The main objective is to verify the dynamic response and the stress field in both approaches during a seismic excitation produced by the north-south component of El Centro earthquake - 1940 (Fig. 12). An excitation time windows of one second is used to simulate this horizontal ground displacement.

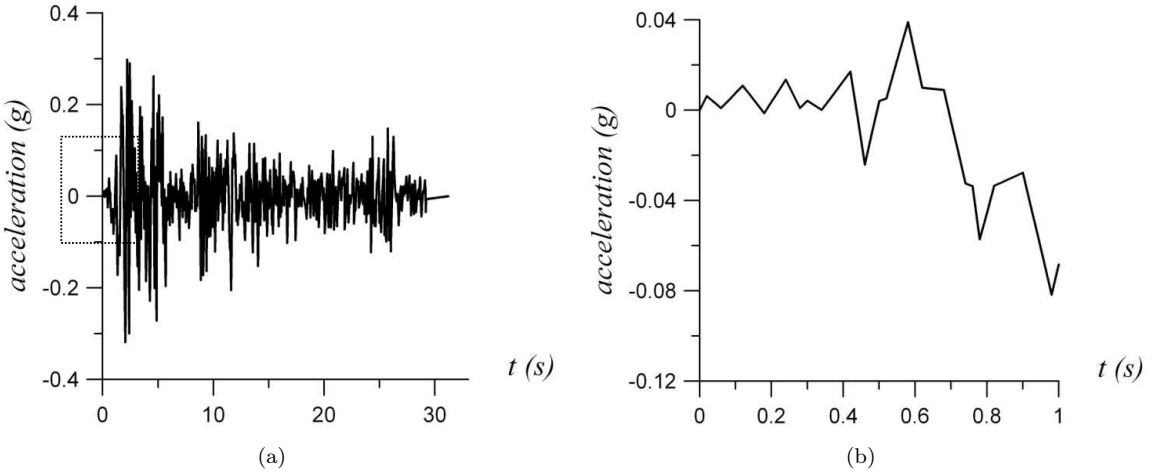

Figure 12: Full record (a) and analysis time window (b) of the north south component of El Centro Earthquake.

The uncoupled equation of motion for this problem is readily obtained with the use of Table 5 parameters. Thus:

$$\left[1.0164 \times 10^5\right] \ddot{X} + \left[2.1085 \times 10^8\right] X = -\ddot{u}_g\left(t\right) \times 2.4086 \times 10^5 \quad (uncoupled) \tag{65}$$

where $\ddot{u}_g\left(t\right)$ indicates the horizontal component of ground motion produced by the earthquake. Equation (65) assumes that only translational contributions are involved in the equilibrium equation. However, it should be noticed that this assumption is not entirely right. This equation is solved for the earthquake input using a fourth order Runge-Kutta numerical integration routine. Figure 13a illustrates the dynamic response for the uncoupled solution. Results indicate that this solution leads

to slightly higher displacements when compared to a finite element model response on the fundamental mode shape. Additionally it can be observed on Fig. 13b a comparison between the fundamental solution with a dynamic response including all mode shapes.

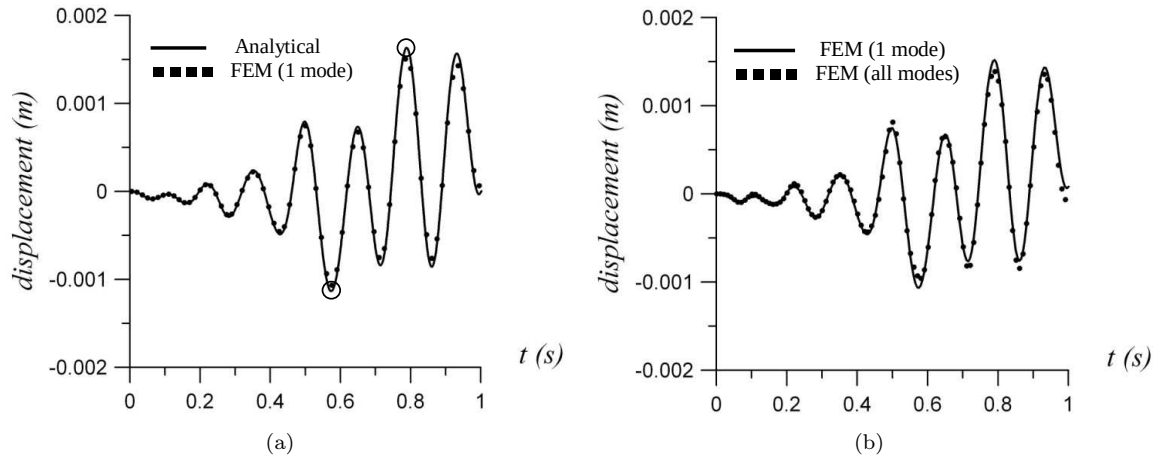

Figure 13: Comparison between analytical and finite element response for the uncoupled system. Analytical and finite element fundamental response (a). Finite element fundamental response and finite element solution including all modes (b).

The above figure indicates that seismic response suffers a significant influence from the fundamental mode shape. Thus, using a fundamental mode analytical approach, with generalized parameters obtained from a finite element analysis provides satisfactory results for the uncoupled case. Equation (65) can be evaluated for other seismic excitations using a numerical integration procedure. This will provide faster results and will allow the prediction of maximum structural responses.

Effective earthquake forces and stress distribution can be readily evaluated once the displacements are known. But there is no need for a time-history evaluation, since peak displacements can be noticed clearly on Fig. 13a. The minimum response value occurs at $t = 0.579s$. And the maximum response occurs at $t = 0.789s$. Figures 14 through 16 illustrate the stress distribution for those peak responses, including the fundamental and the full mode solutions.

The coupled equation of motion for this problem is readily obtained with the use of Table 5 parameters together with the generalized fluid added mass, given by Eq. (62). Thus:

$$\left[1.9503 \times 10^5\right] \ddot{X} + \left[2.1085 \times 10^8\right] X = -\ddot{u}_g\,(t) \times 4.2187 \times 10^5 \qquad (coupled) \tag{66}$$

where it should be noticed that both the generalized added mass and the generalized excitation now have additional terms that represent the coupling effects. The new generalized added mass is given by

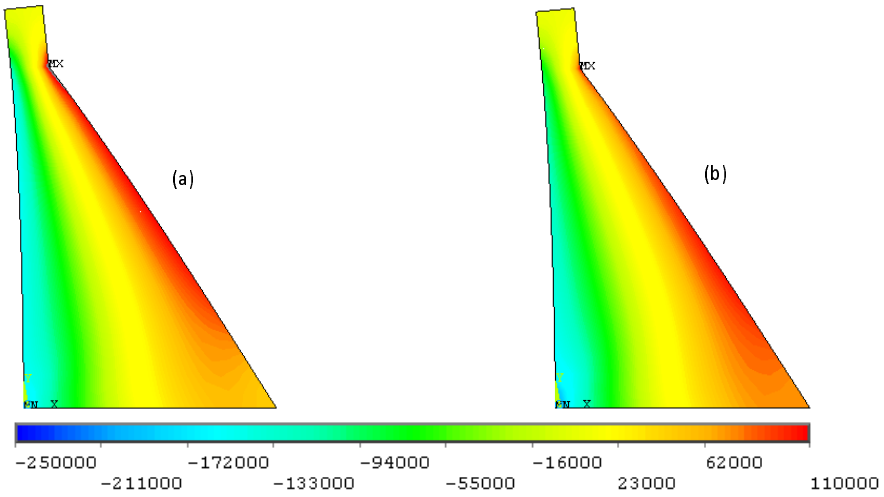

Figure 14: Vertical normal stress distribution for finite element fundamental (a) and full mode solution (b) at $t = 0.579s$. Uncoupled analysis. Stresses in Pa.

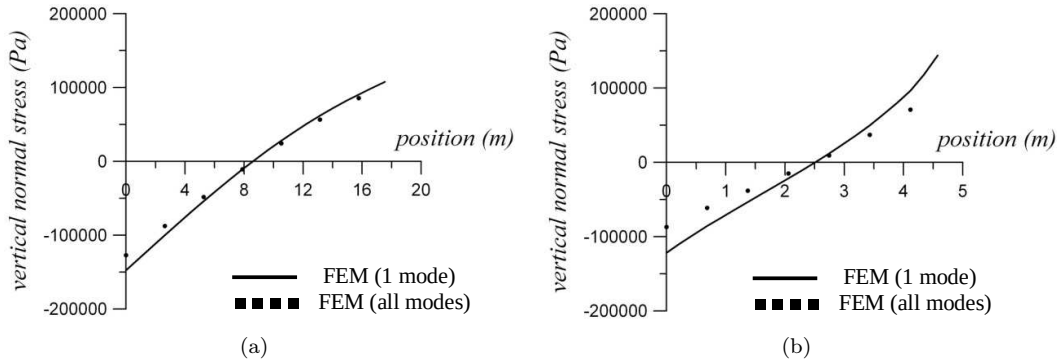

Figure 15: Vertical normal stress distribution at elevations: 20.7264m (a) and 41.4528m (b) at $t = 0.579s$.

the sum of the structural mass with the fluid added mass. And the generalized excitation is given by the sum of the previous parameter with the following term:

$$\tilde{L}_{fluid} = \sum M_{node} \times U_x\,(y) = 1.8101 \times 10^5 \frac{Ns^2}{m} \tag{67}$$

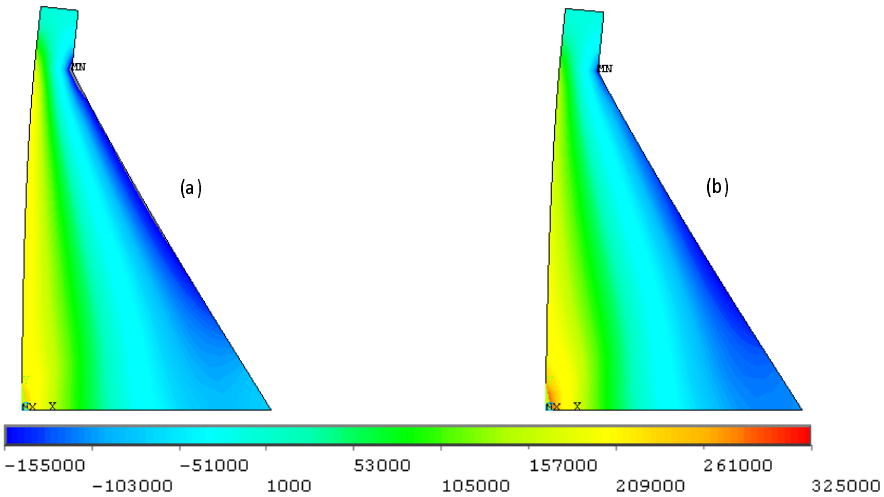

Figure 16: Vertical normal stress distribution for finite element fundamental (a) and full mode solution (b) at $t = 0.789s$. Uncoupled analysis. Stresses in Pa.

which represents the additional mass that participates on the horizontal excitation. Figure 17 illustrates the dynamic response for the coupled solution.

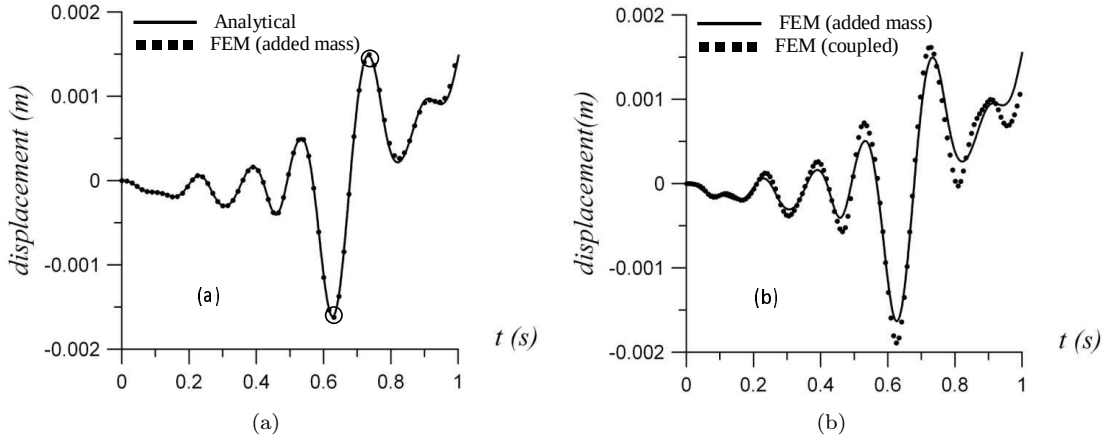

Figure 17: Comparison between analytical and finite element response for the coupled system. Analytical and finite element added mass model fundamental response (a). Finite element added mass model fundamental response and coupled solution including all modes (b).

Figure 17 indicates that seismic response suffers a significant influence from the fundamental mode shape. Thus, using a fundamental mode analytical approach, with generalized parameters obtained from a finite element analysis provides satisfactory results for the coupled case as well. However, it should be noticed that these results have an inferior quality when compared to the uncoupled analysis results.

Effective earthquake forces and stress distribution can be readily evaluated once the displacements are known. But there is no need for a time-history evaluation, since peak displacements can be noticed clearly on Fig. 17a. The minimum response value occurs at $t = 0.627s$. And the maximum response occurs at $t = 0.732s$. Figures 18 and 19 illustrate the stress distribution for those peak responses, including the added mass fundamental and the full mode solutions.

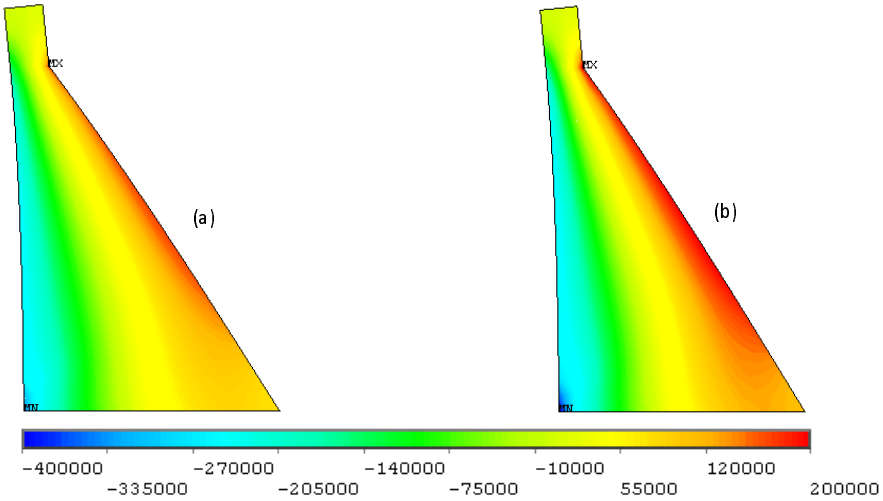

Figure 18: Vertical normal stress distribution for finite element added mass fundamental (a) and full mode solution (b) at $t = 0.627s$. Coupled analysis. Stresses in Pa.

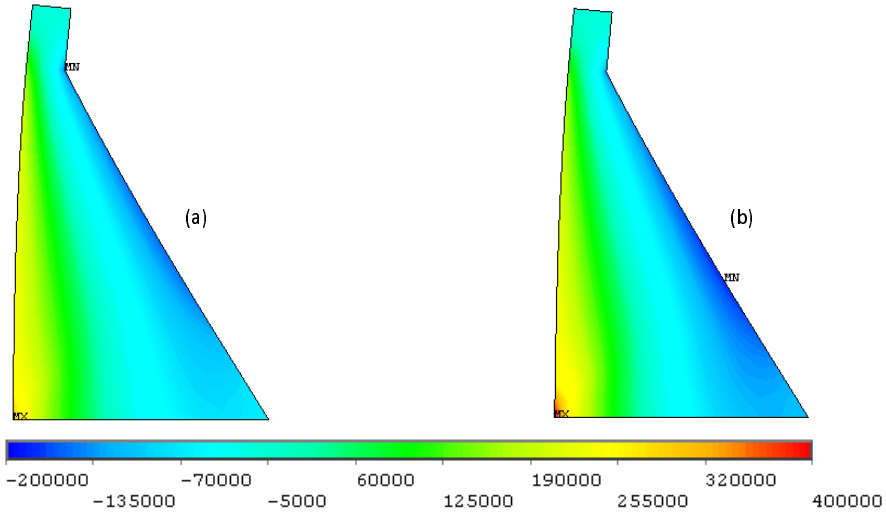

Figure 19: Vertical normal stress distribution for finite element added mass fundamental (a) and full mode solution (b) at $t = 0.732s$. Coupled analysis. Stresses in Pa.

9 Conclusions

A semi-analytical procedure for solution of coupled problems in which a flexible boundary moves into an acoustic fluid domain was presented. On the mathematical development it was proven that hydrodynamic pressures acting on the fluid-structure interface are proportional to the boundary acceleration. This observation provided a link between the structural and fluid systems. A frequency equation was established, being dependent on both the frequency and mode shape of the coupled system. This equation leads to a problem with two unknowns and therefore a solution cannot be found without the previous assumption of one of these parameters. For the mode shape it was adopted the fundamental deformation, leading to problems where frequencies and responses of the first mode were solved. This technique was first introduced to simple problems, where generalized parameters could be easily developed. Complete analytical solutions were found, with results indicating an excellent agreement with coupled results, which considered all modes of vibration. Coupled frequencies had inferior values when compared to uncoupled system results. This provided a conclusion that additional fluid masses were coupled to the structural system. It was also verified that fluid compressibility cannot be neglected on certain analysis, since this parameter provides an additional fluid mass when compared to an incompressible fluid behavior. Therefore, treating a compressible fluid as incompressible will lead to higher coupled frequency values and consequently reduced fluid added masses.

On the second part of this paper the procedure was extended to a more complex geometry. The analysis was developed on a concrete gravity dam, subjected to a seismic excitation. For this analysis

the full analytical solution was replaced by a semi-analytical procedure, in which the generalized parameters for the uncoupled analysis were obtained from a finite element model of this geometry. These parameters were readily substituted in the frequency equation, which provided the coupled frequency, the added mass and an analytical equation of motion. Results indicated a good agreement between the semi-analytical frequency and the coupled value. Later these added fluid masses were introduced on a finite element model and a dynamic analysis considering only the first mode was performed. Stress distribution on this model was compared to a coupled system including all modes. It was shown that the first model provides an approximate solution to the dynamic response, which is highly influenced by the fundamental mode. The great advantage of the added mass procedure is that there is no need to model the reservoir system. Thus this provides a useful resource for finite element computer codes without fluid-structure analysis capabilities. However it should also be noticed that coupled models are more time consuming when compared to uncoupled models. Another great advantage of this procedure is that it provides an analytical equation of motion once the generalized parameters are known. This provides a very efficient tool for estimating maximum structural responses under all sorts of excitations. For simple geometries a full analytical solution can be established, providing coupled frequencies and responses for a given mode shape. So this procedure could also be extended to account for participation of higher modes in the structural response.

Acknowledgements

The authors are grateful for the financial support provided by CAPES and CNPq scholarships.

References

[1] Westergaard, H.M., Water pressures on dams during earthquakes. *Transactions ASCE*, **98**, pp. 418–472, 1933.
[2] Zienkiewicz, O.C. & Newton, R.E., Coupled vibrations of a structure submerged in a compressible fluid. *International Symposium on Finite Element Techniques*, Stuttgart, Germany, 1969.
[3] Sharan, S.K., Finite Element analysis of unbounded and incompressible fluid domains. *International Journal for Numerical Methods in Engineering*, **21**, pp. 1659–1669, 1985.
[4] Küçükarslan, S., Dam-reservoir interaction for incompressible-unbounded fluid domains using an exact truncation boundary condition. *16th ASCE Engineering Mechanics Conference*, University of Washington: Seattle, p. 9, 2003.
[5] Silva, S.F. & Pedroso, L.J., Estudo analítico-numérico do campo de pressões e da massa adicional em barragens durante terremotos. Technical Report RTP-SFS2, UnB-FT/ENC, Brasília, 2005.
[6] Chopra, A.K., Earthquake behavior of dam-reservoir systems. *Journal of Engineering Mechanics, ASCE*, **94**, pp. 1475–1499, 1968.
[7] Chopra, A.K., *Earthquake Response of Concrete Gravity Dams*. UCB/EERC-70/01, Earthquake Engineering Research Center, University of California: Berkeley, p. 20, 1970.
[8] Fenves, G.L. & Chopra, A.K., *EAGD-84: A Computer Program for Earthquake Analysis of Concrete Gravity Dam*. UCB/EERC-84/11, Earthquake Engineering Research Center, University of California: Berkeley, p. 92, 1984.

[9] Fenves, G.L. & Chopra, A.K., *Earthquake Analysis and Response of Concrete Gravity Dams*. UCB/EERC-84/10, Earthquake Engineering Research Center, University of California: Berkeley, p. 228, 1984.
[10] Saini, S., Bettess, P. & Zienkiewicz, O.C., Coupled hydrodynamic response of concrete dams using Finite and Infinite Elements. *Earthquake Engineering and Structural Dynamics*, **6**, pp. 363–374, 1978.
[11] Chopra, A.K. & Chakrabarti, P., Earthquake analysis of concrete gravity dams including dam-fluid-foundation rock interaction. *Earthquake Engineering and Structural Dynamics*, **9**, pp. 363–383, 1981.
[12] Hall, J.F. & Chopra, A.K., Two dimensional dynamic analysis of concrete gravity and embankment dams including hydrodynamic effects. *Earthquake Engineering and Structural Dynamics*, **10**, pp. 305–332, 1982.
[13] Fenves, G. & Chopra, A.K., Effects of reservoir bottom absorption and dam-water-foundation rock interaction on frequency response functions for concrete gravity dams. *Earthquake Engineering and Structural Dynamics*, **13**, pp. 13–31, 1985.
[14] Fok, K.L. & Chopra, A.K., *Earthquake Analysis and Response of Concrete Arch Dams*. UBC/EERC-85/07, Earthquake Engineering Research Center, University of California: Berkeley, p. 207, 1985.
[15] Lotfi, V., Roesset, J.M. & Tassoulas, J.L., A technique for the analysis of the response of dams to earthquakes. *Earthquake Engineering and Structural Dynamics*, **15**, pp. 463–490, 1987.
[16] Ribeiro, P.M.V., *Uma Metodologia Analítica para Avaliação do Campo de Tensões em Barragens de Concreto Durante Terremotos, Dissertação de Mestrado em Estruturas e Construção Civil, Publicação E.DM-003A/06*. Departamento de Engenharia Civil e Ambiental, Universidade de Brasília: Brasília, DF, p. 162, 2006.
[17] USBR (United States Bureau of Reclamation), *Design of gravity dams*. United States Department of the Interior - Bureau of Reclamation, 1976.
[18] Chopra, A.K., Earthquake resistant design of concrete gravity dams. *Journal of the Structural Division, ASCE*, **104(ST6)**, pp. 953–971, 1978.
[19] Silva, S.F., *Interação Dinâmica Barragem-Reservatório: Modelos Analíticos e Numéricos, Tese de Doutorado em Estruturas e Construção Civil, Publicação E.TD-05A/07*. Departamento de Engenharia Civil e Ambiental, Universidade de Brasília: Brasília, DF, p. 220, 2007.

Mechanics of Solids in Brazil 2009, H.S. da Costa Mattos & Marcílio Alves (Editors)
Brazilian Society of Mechanical Sciences and Engineering, ISBN 978-85-85769-43-7

Improved estimations of the plastic zones ahead of crack tips using linear elastic fracture mechanics concepts

Habib Zambrano Rodríguez
Department of Engineering Design and Materials, Norwegian University of Science and Technology, Trondheim – Norway
Jaime Tupiassú Pinho de Castro, Marco Antonio Meggiolaro
Department of Mechanical Engineering, Pontifical Catholic University of Rio de Janeiro, Rio de Janeiro/RJ – Brazil

Abstract

Crack tip plastic zones can be and usually are severely underestimated at the high load levels associated with the yield safety factors $1.2 < \varphi_Y < 3$ typically used in the design of tough metallic structures. This happens because the stress field around the tip is supposed to be solely controlled by the stress intensity factor, neglecting the significant effect of the nominal stress to the yield strength ratio, σ_n/S_Y. Since most Fracture Mechanics design methods use plastic zone size estimates and stress intensity similitude assumptions, this fact is more than an academic issue, it is a matter of great practical interest. This problem is demonstrated by using Inglis or Westergaard stress functions to generate the complete stress field around the crack tip in an infinite plate considering in an appropriate way the important σ_n/S_Y effects.

Keywords: Fracture Mechanics, plastic zone estimates, nominal stress effects.

1 Introduction

For both academic and design purposes, the plastic zones size and shape $pz(\theta)$ ahead of a crack tip are traditionally estimated from simplified linear elastic (LE) stress analysis, assuming that the stress field depends only on the stress intensity factor (SIF) K_I (or K_{II} or K_{III}). For example, assuming that $\sigma_{ij} = [K_I] \cdot [1/\sqrt{(2\pi r)}] \cdot [f_{ij}(\theta)] = f(K_I)$, where r is the distance from the crack tip, θ is the angle measured from the crack plane and $f_{ij}(\theta)$ are the mode I Williams θ-functions, and equating the resulting Mises stress to S_Y, the yielding strength, the simplest elastic-plastic frontiers in plane stress and in plane strain are estimated by [1].

Mechanics of Solids in Brazil 2009, H.S. da Costa Mattos & Marcílio Alves (Editors)
Brazilian Society of Mechanical Sciences and Engineering, ISBN 978-85-85769-43-7

$$pz(\theta)_{pl-\sigma} = (K_I^2/2\pi S_Y^2) \cdot \cos^2(\theta/2) \cdot [1 + 3\sin^2(\theta/2)]$$
$$pz(\theta)_{pl-\varepsilon} = (K_I^2/2\pi S_Y^2) \cdot \cos^2(\theta/2) \cdot [(1-2\nu)^2 + 3\sin^2(\theta/2)] \quad (1)$$

where ν is Poisson's coefficient. Thus, according to this simplified estimate, the plastic zone size directly ahead of a crack tip in plane stress should be $pz(0)_{pl-\sigma} = pz_0 = (1/2\pi)(K_I/S_Y)^2$. This value is the reference used to normalize all the plastic zone plots presented below.

However, the classical $\sigma_{ij} = f(K_I)$ hypothesis almost universally used in LEFM analysis is only valid very close to the crack tip, more specifically if $r \to 0$, exactly where the assumed elastic behavior breaks down. In particular, this approximation predicts that the normal stress perpendicular to the crack plane in a Griffith plate is $\sigma_y(x \to \infty, y = 0) = 0$, instead of $\sigma_y(x \to \infty, y = 0) = \sigma_n$, as it should. Therefore, the classical $\sigma_{ij} = f(K_I)$ hypothesis does ***not*** obey all the plate boundary conditions (this same problem, by the way, also happens with the more elaborated HRR elastic-plastic field.) Therefore, as the plastic zone borders are not necessarily (neither are usually) too close to the crack tip, it is worth to at least estimate the effect of the nominal stress to the yield strength ratio σ_n/S_Y on $pz(\theta)$, instead of simply neglecting it.

A quite simple, but certainly not unreasonable first estimate of the σ_n/S_Y effect on the plastic zones frontiers around the crack tips can be made by forcing $\sigma_y(x \to \infty, y = 0) = \sigma_n$, adding up a constant $\sigma_y = \sigma_n$ stress to the Williams (or Irwin) stress LE field to obtain

$$\sigma(\theta)^{Williams+\sigma_n}_{Mises,pl-\sigma} = \sigma(\theta)^{Wil+\sigma_n}_{M,pl-\sigma} = [(\kappa f_x)^2 + (\kappa f_y + \sigma_n)^2 - (\kappa f_x)(\kappa f_y + \sigma_n) + 3(\kappa f_{xy})^2]^{1/2} \quad (2)$$

where $\sigma(\theta)^{Wil+\sigma_n}_{M,pl-\sigma}$ is the resulting LE Mises stress distribution around the crack tip in plane stress (considering the σ_n/S_Y effect), $\kappa = K_I/\sqrt{(2\pi r)}$, and f_x, f_y and f_{xy} are the θ-functions associated with the σ_x, σ_y and τ_{xy} Williams (or Irwin) stresses in mode I. Equating $\sigma(\theta)^{Wil+\sigma_n}_{M,pl-\sigma} = S_Y$ and repeating the process for plane strain, $pz(\theta)^{Wil+\sigma_n}_{M,pl-\sigma} \big/ pz_0$ and $pz(\theta)^{Wil+\sigma_n}_{M,pl-\varepsilon} \big/ pz_0$ plots can be generated to enhance the searched σ_n/S_Y effect, as shown in Figure 1.

Figure 1 indicates that the estimated σ_n/S_Y influence on the size and the shape of the plastic zones that surround the crack tips under real normal loading conditions, which can reach ratios $\sigma_n/S_Y > 0.8$ in structures designed for minimum weight, is clearly not negligible. However, it cannot be prove that the σ_n/S_Y effects are really that important, since the hypothesis used to generate its plots is not mathematically sound. But this simple estimate nevertheless points out that the plastic zone dependence on σ_n/S_Y should be studied in a more careful way, as done in the following sections.

2 Plastic zones estimated using the Inglis stresses

A much better estimate for the σ_n/S_Y influence on the size and shape of the plastic zones $pz(\theta)$ can be generated by using the classical Inglis stress field in an infinite plate with a crack-like very sharp elliptical notch, with its major semi-axis a perpendicular to the tensile nominal stress σ_n, and with its minor semi-axis $b << a$.

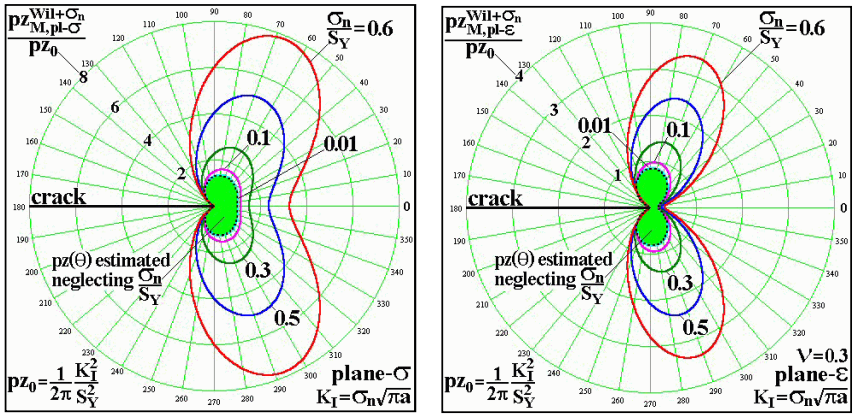

Figure 1: Mode I plastic zones estimated for the infinite cracked plate, which has $K_I = \sigma_n\sqrt{(\pi a)}$, by summing σ_n to the Williams $\sigma_y(K_I)$ stress, to force σ_y (σ_n far from the crack tips.

Therefore, making $x = c{\cdot}\cosh\alpha{\cdot}\cos\beta$ and $y = c{\cdot}\sinh\alpha{\cdot}\sin\beta$, such a crack-like sharp notch is quite simply described in elliptical coordinates (α,β) by $\alpha = \alpha_0$, where $a = c{\cdot}\cosh\alpha_0$, $b = c{\cdot}\sinh\alpha_0$, and $c = a/\cos\alpha_0$. The linear elastic stresses in the Inglis plate loaded by a general bi-axial nominal stress field are given by the following infinite series [2, 3]

$$\begin{aligned}\sigma_\alpha = \gamma\sum_n A_n\{&(n+1)e^{(1-n)\alpha}\cos(n+3)\beta + (n-1)e^{-(n+1)\alpha}\cos(n-3)\beta -\\ &-[4e^{-(n+1)\alpha} + (n+3)e^{(3-n)\alpha}]\cos(n+1)\beta + [4e^{(1-n)\alpha} + (3-n)e^{-(n+3)\alpha}]\cos(n-1)\beta\} +\\ &+B_n\{e^{-(n+1)\alpha}[n\cos(n+3)\beta + (n+2)\cos(n-1)\beta] - [(n+2)e^{(1-n)\alpha} + ne^{-(n+3)\alpha}]\cos(n+1)\beta\}\end{aligned} \tag{3}$$

$$\begin{aligned}\sigma_\beta = \gamma\sum_n A_n\{&(3-n)e^{(1-n)\alpha}\cos(n+3)\beta - (n+3)e^{-(n+1)\alpha}\cos(n-3)\beta -\\ &-[4e^{-(n+1)\alpha} - (n-1)e^{(3-n)\alpha}]\cos(n+1)\beta + [4e^{(1-n)\alpha} + (n+1)e^{-(n+3)\alpha}]\cos(n-1)\beta\} -\\ &-B_n\{e^{-(n+1)\alpha}[n\cos(n+3)\beta + (n+2)\cos(n-1)\beta] - [(n+2)e^{(1-n)\alpha} + ne^{-(n+3)\alpha}]\cos(n+1)\beta\}\end{aligned} \tag{4}$$

$$\begin{aligned}\tau_{\alpha\beta} = \gamma\sum_n A_n\{&(n-1)e^{(1-n)\alpha}\sin(n+3)\beta + (n+1)e^{-(n+1)\alpha}\sin(n-3)\beta - (n+1)e^{(3-n)\alpha}]\sin(n+1)\beta -\\ &-(n-1)e^{-(n+3)\alpha}]\sin(n-1)\beta\} -\\ &-B_n\{e^{-(n+1)\alpha}[n\sin(n+3)\beta + (n+2)\sin(n-1)\beta] - [(n+2)e^{(1-n)\alpha} + ne^{-(n+3)\alpha}]\sin(n+1)\beta\}\end{aligned} \tag{5}$$

where $\gamma = (\cosh 2\alpha - \cos 2\beta)^{-2}$ and n is an integer.

Fortunately, only 5 of these infinite series constants are non-zero when the Inglis plate is loaded by a simpler uni-axial tensile stress σ_n perpendicular to the elliptical hole major axis, namely

$$\begin{cases} \mathbf{A_1} = -\sigma_\mathbf{n}[\mathbf{1} + \mathbf{2exp}(\mathbf{2}\alpha_\mathbf{0})] \\ \mathbf{A_{-1}} = \sigma_\mathbf{n}/16 \\ \mathbf{B_1} = \sigma_\mathbf{n}\mathbf{exp}(\mathbf{4}\alpha_\mathbf{0}) \\ \mathbf{B_{-1}} = \sigma_\mathbf{n}(\mathbf{1} + \mathbf{cosh2}\alpha_\mathbf{0}) \\ B_{-3} = \sigma_n/8 \end{cases} \tag{6}$$

Modeling the crack as a very sharp elliptical notch, with a tiny but nevertheless finite tip radius estimated as half the crack tip opening displacement, $\rho = b^2/a = CTOD/2 = 2K_I{}^2/\pi S_Y E'$, where $E' = E$ in plane stress and $E' = E/(1 - \nu^2)$ in plane strain, and knowing that whereas the cracked infinite plate has a SIF $K_I = \sigma_n\sqrt{(\pi a)}$, the notched one has a corresponding stress concentration factor $K_t = 1 + 2a/b$, then

$$K_t = 1 + 2 \cdot \frac{a}{b} = 1 + 2\sqrt{\frac{a}{\rho}} = 1 + 2 \cdot \sqrt{\frac{a\pi E' S_Y}{2 \cdot \sigma_n^2 \pi a}} \Rightarrow \frac{a}{b} = \sqrt{\frac{E'}{2 \cdot \sigma_n} \cdot \frac{S_Y}{\sigma_n}} = \sqrt{\frac{E'\phi_Y}{2 \cdot \sigma_n}} \tag{7}$$

where $\varphi_Y = S_Y/\sigma_n$ is its nominal safety factor against yielding. Using this a/b ratio to obtain the notch shape that simulates the crack by $\alpha_0 = tanh^{-1}(b/a)$, then the LE stresses in the cracked plate can be calculated substituting the 5 constants specified above in (3-5), a tedious but certainly not a difficult task. Finally, the Mises stress resulting from σ_α, σ_β, $\tau_{\alpha\beta}$, and (in the plane strain case) $\sigma_z = \nu(\sigma_\alpha + \sigma_\beta)$ can be used to estimate the Inglis plastic zones by numerically solving equations (8-9) for $|\theta| \leq \pi$:

$$\sigma^{Ing}_{M,pl-\sigma} = \sqrt{\sigma_\alpha^2 + \sigma_\beta^2 - \sigma_\alpha\sigma_\beta + 3\tau_{\alpha\beta}^2} = S_Y \tag{8}$$

$$\sigma^{Ing}_{M,pl-\varepsilon} = \sqrt{0.5[(\sigma_\alpha - \sigma_\beta)^2 + (\sigma_\alpha - \sigma_z)^2 + (\sigma_z - \sigma_\beta)^2] + 3\tau_{\alpha\beta}^2} = S_Y \tag{9}$$

Some resulting $pz(\theta)^{Ing}_{M,pl-\sigma}\big/pz_0$ and $pz(\theta)^{Ing}_{M,pl-\varepsilon}\big/pz_0$ frontiers, obtained from the numerical solution of equations (8) and (9), are shown in Figure 2.

Therefore, the influence of the nominal stress to the yield strength ratio on the plastic zones, although a little less than estimated by the simple approximation presented in Figure 1, is indeed significant and should not be neglected in practical applications. This is a strong assertion, but it is supported by the exact LE stress field solution for the infinite cracked plate in mode I, when the crack is modeled as an elliptical sharp notch of tip radius $\rho = CTOD/2$, a quite reasonable hypothesis. Nevertheless, it is worth to use an alternative approach to confirm it, as follows.

3 Plastic zones estimated using the Westergaard stress function

The appropriate use of an adequate Westergaard $Z(z)$ stress function provides an alternative way to rigorously estimate the size and the shape of the plastic zones ahead of crack tips departing from the LE stress field. However, since the elastic-plastic frontier is not adjacent to the crack tip, the full

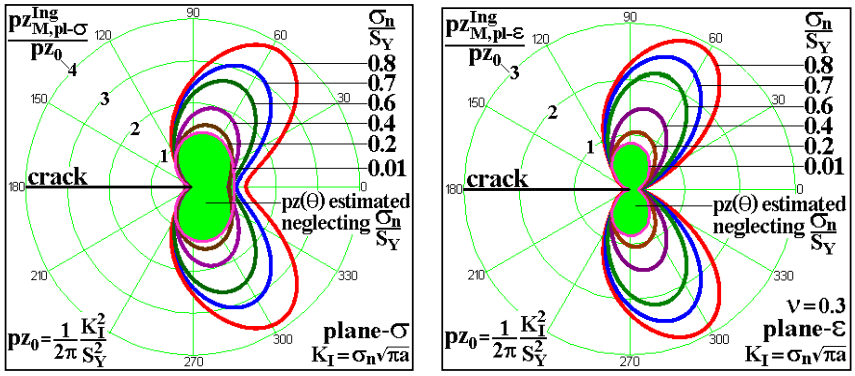

Figure 2: Mises plastic zones in plane stress and in plane strain, calculated using the Inglis linear elastic stress field in an infinite cracked plate loaded in mode I, modeling the crack as a very sharp elliptical notch of tip radius ρ = *CTOD/2* (avoiding in this way the physically unrealistic singularity at the crack tip).

stresses generated from $Z(z)$ must be used in such a calculation. This can be easily demonstrated by revisiting the classical Irwin solution for the cracked infinite plate loaded in mode I.

Thus, if (x, y) and *(r, θ)* are the Cartesian and the polar coordinates centered at the crack tip, $i = \sqrt{-1}$ is the complex unity and $z = x + iy$ is a complex variable, the Irwin solution is obtained from the Westergaard stress function [4–6]

$$Z(z) = z\sigma_n/\sqrt{(z^2 - a^2)} \Rightarrow Z'(z) = dZ/dz = -a^2\sigma_n/(z^2 - a^2)^{3/2} \tag{10}$$

The linear elastic stresses around the crack tip can be calculated from the stress function $Z(z)$ and from its derivative *Z'(z)* by

$$\begin{cases} \sigma_x = \mathrm{Re}(Z) - y\,\mathrm{Im}(Z') - \sigma_n \\ \sigma_y = \mathrm{Re}(Z) + y\,\mathrm{Im}(Z') \\ \tau_{xy} = -y\,\mathrm{Re}(Z') \end{cases} \tag{11}$$

Note that to solve the mode I problem from $Z(z)$, a constant term $-\sigma_n$ has to be summed to the σ_x = *Re(Z) - yIm(Z')* formula to force $\sigma_x(\infty)$ = *0* in the plate, an adequate mathematical trick since a constant stress in the x direction does not affect the stress field near the crack tip. However, the σ_y = *Re(Z) - y·Im(Z')* stress is usually approximated to generate a stress intensity factor (generally a highly desirable feature but not for estimating *pz(θ)*, since it neglects the σ_n/S_Y influence far from the crack tip) by writing

$$\sigma_y(\theta = 0) = \sigma_n(x + a)/[(x + a)^2 - a^2]^{1/2} \cong \sigma_n a/\sqrt{(2ax)} = K_I/\sqrt{(2\pi r)} \quad (\text{if } x << a) \tag{12}$$

where *2a* is the crack size perpendicular to the nominal tensile stress σ_n.

Note that equation (12) yields $\sigma_y(\theta = 0) = K_I/\sqrt{(2\pi r)} = 0$ if $r \to \infty$, thus it does ***not*** generate the stress far from the crack tip. Thus this classical approximation cannot be used to study the σ_n/S_Y influence on $pz(\theta)$, which is not too close to the crack tip. But this task can be fulfilled by first rewriting Z and Z' in polar coordinates centered at the crack tip

$$Z = \frac{[a + (r \cdot \cos\theta) + i\,(r \cdot \sin\theta)] \cdot \sigma_n}{\sqrt{[a + (r \cdot \cos\theta) + i\,(r \cdot \sin\theta)]^2 - a^2}} \Rightarrow Z' = \frac{-a^2 \cdot \sigma_n}{\left\{[a + (r \cdot \cos\theta) + i\,(r \cdot \sin\theta)]^2 - a^2\right\}^{3/2}} \tag{13}$$

and then by using the ***complete*** stress field generated from Z and Z' to calculate the resulting Mises (or Tresca, for that matter) stress. This equivalent stress is then equated to the yielding strength to obtain the required $pz(\theta)$ elastic-plastic frontiers considering the σ_n/S_Y effect. For example, in plane stress this procedure generates equation (14). The same process can be easily applied for plane strain case. The numerical solution of equation (14) generates the required Westergaard elastic-plastic frontier $pz(\theta)^{Wtg}_{M,pl-\sigma}\big/pz_0$, see Figure 3. And the corresponding equation for the plane strain case can also be numerically solved to generate $pz(\theta)^{Wtg}_{M,pl-\sigma}\big/pz_0$, as also shown in Figure 3.

Note that these estimates for the elastic-plastic frontiers based on the Westergaard stress function, like the estimates based on the Inglis stresses obtained above, are mathematically sound, indicating that the claimed σ_n/S_Y effect on $pz(\theta)$ is indeed significant, and should not be neglected.

$$\begin{aligned}
&\left\{\left[\mathrm{Re}\left(\frac{(a+r\cdot\cos\theta+i\cdot rsin\theta)\cdot\sigma_n}{\sqrt{(a+r\cdot\cos\theta+i\cdot rsin\theta)^2-a^2}}\right) - y\,\mathrm{Im}\left(\frac{-a^2\cdot\sigma_n}{\left[(a+r\cdot\cos\theta+i\cdot rsin\theta)^2-a^2\right]^{3/2}}\right) - \sigma_n\right]^2 + \right.\\
&\quad + \left[\mathrm{Re}\left(\frac{(a+r\cdot\cos\theta+i\cdot rsin\theta)\cdot\sigma_n}{\sqrt{(a+r\cdot\cos\theta+i\cdot rsin\theta)^2-a^2}}\right) + y\,\mathrm{Im}\left(\frac{-a^2\cdot\sigma_n}{\left[(a+r\cdot\cos\theta+i\cdot rsin\theta)^2-a^2\right]^{3/2}}\right)\right]^2 - \\
&\quad - \left[\mathrm{Re}\left(\frac{(a+r\cdot\cos\theta+i\cdot rsin\theta)\cdot\sigma_n}{\sqrt{(a+r\cdot\cos\theta+i\cdot rsin\theta)^2-a^2}}\right) - y\,\mathrm{Im}\left(\frac{-a^2\cdot\sigma_n}{\left[(a+r\cdot\cos\theta+i\cdot rsin\theta)^2-a^2\right]^{3/2}}\right) - \sigma_n\right]\cdot \\
&\quad \cdot \left[\mathrm{Re}\left(\frac{(a+r\cdot\cos\theta+i\cdot rsin\theta)\cdot\sigma_n}{\sqrt{(a+r\cdot\cos\theta+i\cdot rsin\theta)^2-a^2}}\right) + y\,\mathrm{Im}\left(\frac{-a^2\cdot\sigma_n}{\left[(a+r\cdot\cos\theta+i\cdot rsin\theta)^2-a^2\right]^{3/2}}\right)\right] + \\
&\quad \left. +3\cdot\left[-y\,\mathrm{Re}\left(\frac{-a^2\cdot\sigma_n}{\left[(a+r\cdot\cos\theta+i\cdot rsin\theta)^2-a^2\right]^{3/2}}\right)\right]^2\right\}^{1/2} = S_Y
\end{aligned} \tag{14}$$

4 Comparing the plastic zones estimated from Inglis and from Westergaard

Figure 4 compares the Mises plastic zones calculated using the Inglis stresses assuming that the crack is a very sharp elliptical notch of tip radius $\rho = CTOD/2$, and the complete stresses generated by the Westergaard stress function, without the simplification required to obtain the classical $K_I = \sigma\sqrt{(\pi a)}$ formula.

As $pz_{Ing}(\theta)$ and $pz_{Wtg}(\theta)$ are obtained from completely different equations, their near coincidence is certainly not fortuitous. Therefore, the large σ_n/S_Y effect predicted by these rigorous solutions really should not be neglected in practice. This point must be emphasized, since it is the plastic zone size that ***validates*** most LEFM predictions. Moreover, the Inglis and Westergaard plastic zones virtually

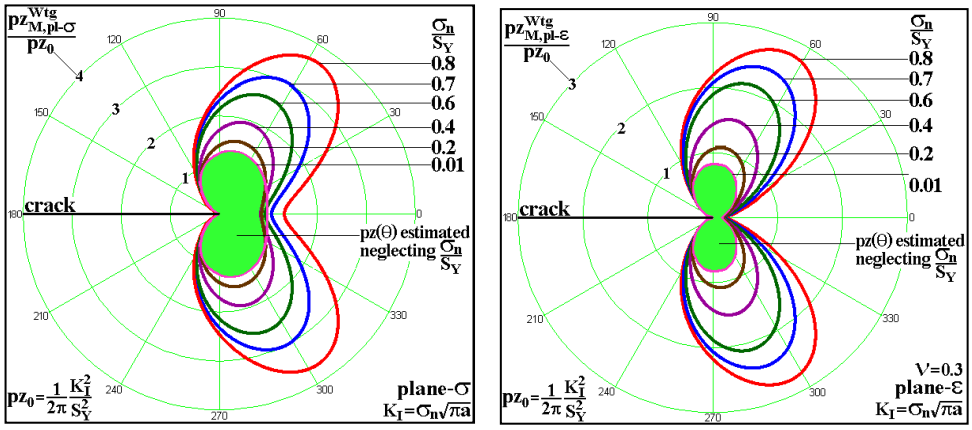

Figure 3: Mises plastic zones in plane stress and in plane strain in an infinite cracked plate in mode I, calculated using the complete stresses generated by the Westergaard stress function.

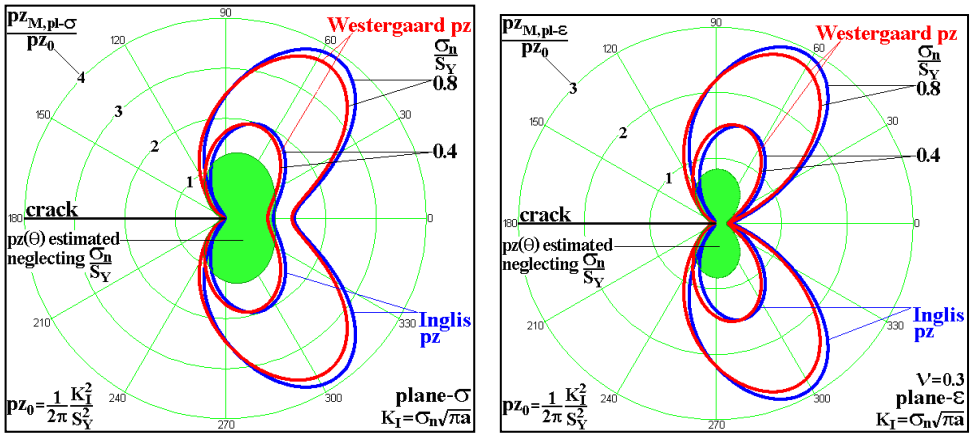

Figure 4: Comparison of the Mises plastic zones estimated from Inglis (using $\rho = CTOD/2$) and from Westergaard under plane stress and plane strain.

coincide when the sharp ellipsis used to model the crack has its minor semi-axis (instead of its tip radius) assumed as half the classical crack opening displacement estimated by Irwin, $b = CTOD/2 = 2K_I^2/\pi S_Y E'$, see Figure 5.

It is interesting to note that assuming the Inglis and the Westergaard-based $pz(\theta)$ must coincide, a quite reasonable hypothesis since they describe the same linear elastic problem, then a new estimate for the *CTOD* can be proposed, since if $b = 2K_I^2/\pi S_Y E'$ and $\rho = b^2/a$, then

$$CTOD = 2\rho = 2\frac{4K_I^4}{\left(\pi S_Y E'\right)^2 \cdot a} = \frac{8}{\pi}\left(\frac{K_I \sigma_n}{E' S_Y}\right)^2 = \frac{8}{\pi}\left(\frac{K_I}{E'}\phi_Y\right)^2 \cong 2.55\left(\frac{K_I}{E'}\phi_Y\right)^2 \tag{15}$$

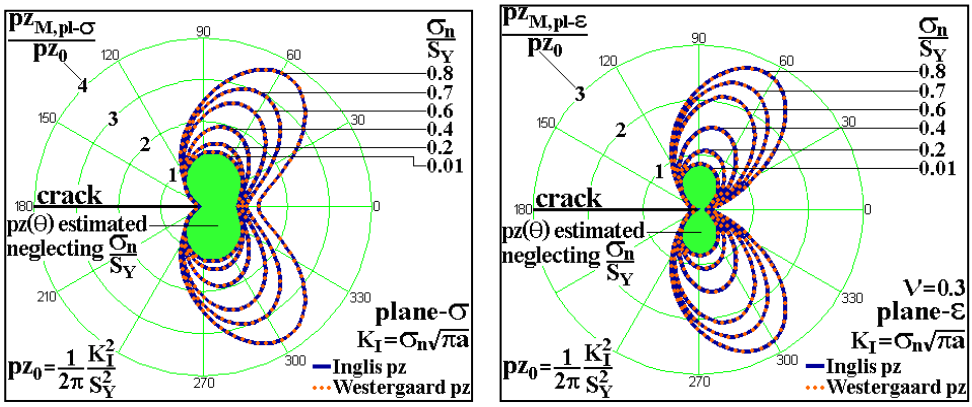

Figure 5: The plastic zones estimated using the complete linear elastic stresses induced by the Westergaard stress function are visually undistinguishable from the plastic zones estimated from the Inglis stresses when a sharp elliptical notch with $b = CTOD/2 = 2K_I^2/\pi S_Y E'$ instead of $\rho = CTOD/2$ is used to model the crack.

5 Corrected plastic zone estimates including equilibrium considerations

The so-called Inglis and Westergaard plastic zones are already an improvement over the traditional $pz(\theta)$ estimates based solely on K_I, such as those expressed in equations (1). They take into account the σ_n/S_Y effect which, as demonstrated above, is indeed quite important under real loading conditions, where yielding safety factors in the range $1.2 < S_Y/\sigma_n = \varphi_Y < 3$ are common practice when designing and using tough metallic structures. But they can be further enhanced because, in spite of obeying all contour conditions, they intrinsically suppose that the stresses remain LE in the whole studied plate, neglecting the yielding near the crack tip. In other words, they do not consider the force loss caused by the yielding-induced stress limitation inside the plastic zone and, in consequence, they violate the equilibrium equation.

This problem can, of course, be corrected following Irwin's classical idea, assuming that:

1. the material does not strain harden, thus the Mises (or Tresca) stress remains fixed inside the plastic zone, where $\sigma_M = S_Y$; and
2. the original LE stress distribution can be simply displaced by a value $r^*(\theta)$ to balance the force originally associated with $\sigma_M(r, \theta) > S_Y$ or, in other words, the LE stresses outside the plastic zone can be expressed by $\sigma_{ij}(r - r^*(\theta), \theta)$.

The Irwin plastic zone $pz_{Irw}(\theta)$, which is corrected following his two assumptions to balance the force generated bythe K_I-induced σ_y stress, is generally calculated only at the crack plane, where $pz_{Irw}(\theta = 0) = K_I{}^2/\pi S_Y{}^2 = 2pz_0$. But his idea can be easily extended to generate the whole $pz_{Irw}(\theta)$ elastic-plastic frontier by solving $\sigma_M(r = pz_{Irw}(\theta), \theta) = S_Y$, a task that can be accomplished by first calculating the σ_y linear elastic stress at the classical $pz(\theta)$ frontier described by equation (1):

$$\sigma_y[pz(\theta), \theta] = \frac{K_I}{\sqrt{2\pi \cdot pz(\theta)}} \cos\frac{\theta}{2}\left[1 + sin\frac{\theta}{2} sin\frac{3\theta}{2}\right] \tag{16}$$

This $\sigma_y(\theta)$ stress at the $pz(\theta)$ frontier must remain constant inside $pz_{Irw}(\theta)$, since Irwin assumed that the material does not strain-harden, but it must also generate the same force caused by the singular LE $\sigma_y(\theta)$ original stress to maintain the plate under equilibrium (neglecting the σ_n/S_Y ratio contribution), thus

$$\sigma_y(r = pz(\theta), \theta) \cdot zp_{Irw}(r, \theta) = \int_0^{pz(\theta)} \left[\frac{K_I}{\sqrt{2\pi r}} \cos\frac{\theta}{2}\left(1 + \sin\frac{\theta}{2}\sin\frac{3\theta}{2}\right)\right] dr \tag{17}$$

Therefore, the classical $pz_{Irw}(\theta)$ in plane stress can be expressed by an unique analytical expression:

$$pz_{Irw}(\theta) = \frac{2K_I\sqrt{pz(\theta)}}{\sqrt{2\pi} \cdot \sigma_y[pz(\theta), \theta]} \cos\frac{\theta}{2}\left[1 + sin\frac{\theta}{2} sin\frac{3\theta}{2}\right] \tag{18}$$

It is relatively simple to reproduce this analysis to treat the plane strain case, see Figure 6. As expected, the $pz_{Irw}(\theta)$ are just σ_n/S_Y-independent hypertrophied versions of the traditionally estimated K_I-induced $pz(\theta)$ plastic zones.

Now Irwin's idea can be finally adapted to estimate the Mises plastic zones around a crack tip using the complete stresses generated by the Westergaard stress function, obeying at the same time the contour condition $\sigma_y(x \to \infty) = \sigma_n$ and the equilibrium of the applied force on the Irwin plate, as any decent estimate should always do. It is interesting to note that it is not necessary to repeat this exercise departing from the Inglis stresses, since the plastic zones generated from them are almost identical to the Westergaard plastic zones, $pz_{Ing}(\theta) \cong pz_{Wtg}(\theta)$ if $b = 2K_I{}^2/\pi S_Y E'$, as demonstrated above.

A procedure very similar to the one used for generating equation (18), based on the assumption that the $\sigma_y(\theta)$ stress remain fixed inside the plastic zone because the material does not strain-harden, can be applied to accomplish this purpose:

$$\begin{gathered} \sigma_y[pz_{Wtg}(\theta), \theta] \cdot pz_{eql}(\theta) = \int_0^{pz_{Wtg}(\theta)} \sigma_y(r, \theta) dr \Rightarrow \\ pz_{eql}(\theta) = \frac{1}{\sigma_y[zp_{Wtg}(\theta), \theta]} \int_0^{pz_{Wtg}(\theta)} \left\{\mathrm{Re}[Z(r, \theta)] + y\,\mathrm{Im}'[Z'(r, \theta)]\right\} dr \end{gathered} \tag{19}$$

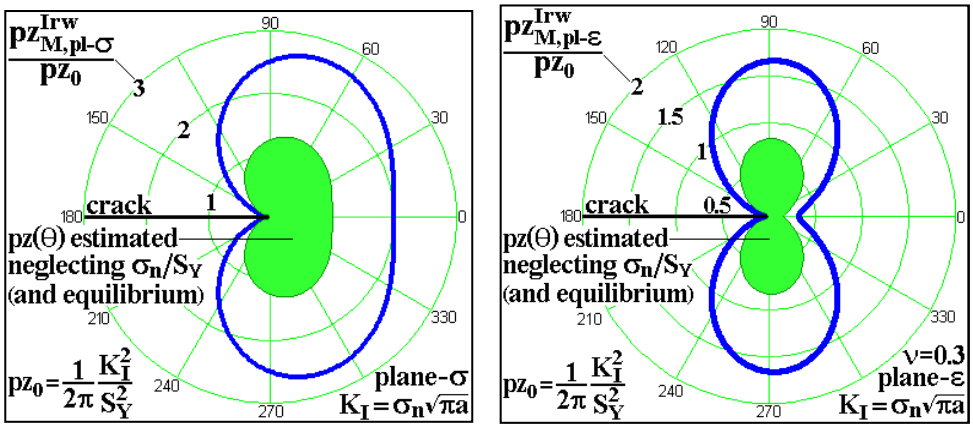

Figure 6: Irwin plastic zones $pz_{Irw}(\theta)$ in plane stress and plane strain, generated to balance the force generated by the K_I-induced σ_y stress, without taking into account the σ_n/S_Y effects.

The resulting plastic zone estimates, $pz_{eql}(\theta)$, for the cracked infinite plate loaded in mode I in plane stress and in plane strain considering both the σ_n/S_Y ratio ***and*** the equilibrium influence, can then be finally obtained by numerically integrating equation (19), see Figure 7.

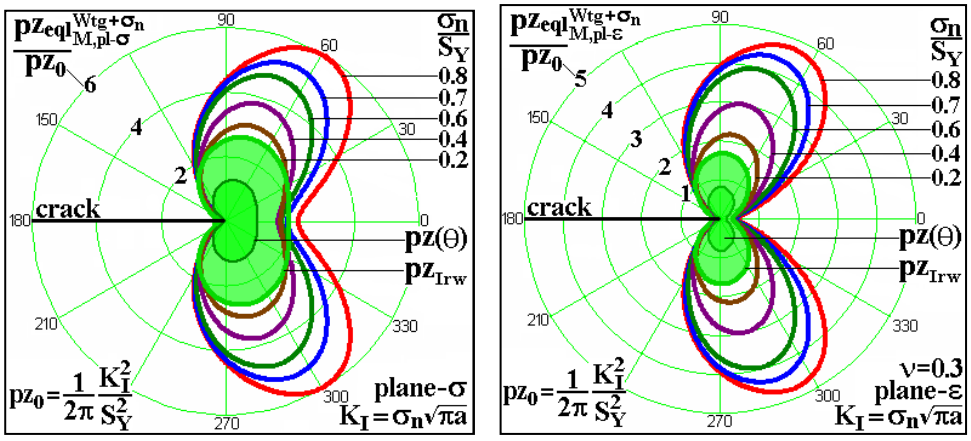

Figure 7: Mises $pz(\theta)$ estimated using the complete stresses induced by the Westergaard stress function for the Griffith plate, considering both the σ_n/S_Y ratio ***and*** the equilibrium effects.

Figure 7 presents the best plastic zones that can be estimated from the linear elastic stress field in a cracked Irwin plate, neglecting strain-hardening but considering both the nominal stress to the yield

strength ratio σ_n/S_Y and the force equilibrium effects, based on relatively simple but sound analytical procedures. It is important to note that at $\sigma_n/S_Y = 0.8$ the maximum dimension of this $pz_{eql}(\theta)$ in plane stress is about 6 (six) times bigger than the frequently used classical $pz_0 = K_I^2/2\pi S_Y^2$ estimate, whereas in plane strain it is almost 5 times bigger, values that certainly are not negligible.

And it is worth mentioning that these simple estimates do reproduce the familiar butterfly shape of the plastic zone around the crack tip, well known by anyone who ever made a fatigue crack propagation or a toughness measurement using a polished specimen.

6 Fitting the equilibrated plastic zone estimates

It is interesting to propose empirical equations to fit the obtained numerical solutions of the analytically proposed plastic zone frontiers which consider both the σ_n/S_Y and the equilibrium effects. The plastic zone size at an angle $\theta = 0$ can be expressed for $0 \leq \sigma_n/S_Y \leq 0.8$ within 1% by (see Figure 8)

$$\begin{aligned} pz_{eql}(\theta=0)_{pl-\sigma} &= 2pz_0\left[1 - 0.63\frac{\sigma_n}{S_Y} - 0.1\left(\frac{\sigma_n}{S_Y}\right)^2 + 1.35\left(\frac{\sigma_n}{S_Y}\right)^3\right] \\ pz_{eql}(\theta=0)_{pl-\varepsilon} &= 2pz_0(1-2\nu)^2\left[1 - 0.17\frac{\sigma_n}{S_Y} - 0.3\left(\frac{\sigma_n}{S_Y}\right)^2 + 1.4\left(\frac{\sigma_n}{S_Y}\right)^3\right] \end{aligned} \tag{20}$$

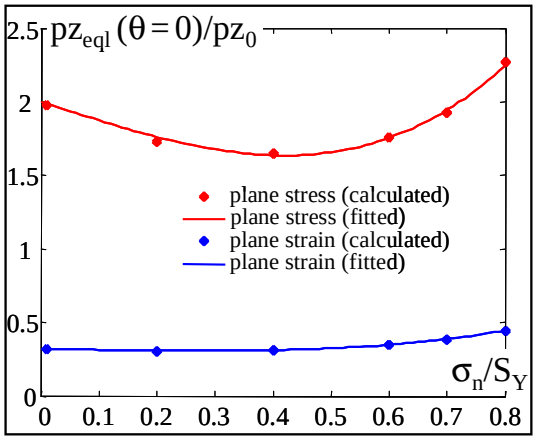

Figure 8: Calculated and fitted values of the equilibrated plastic zone size at the crack plane divided by the reference plastic zone size, $pz_{eql}(\theta = 0)/pz_0$, as a function of the ratio σ_n/S_Y, for the Griffith infinite cracked plate loaded in mode I, for plane stress and plane strain ($\nu = 0.3$).

The above results agree with Finite Element calculations from Newman et al. [7] for elastic-perfectly plastic middle-crack tension specimens M(T), which had thicknesses in the range $1.25 < t < 20mm$,

Poisson's ratio $\nu = 0.3$, and a flow stress $\sigma_0 = (S_Y + S_U)/2 = 500MPa$, where S_Y and S_U are the yield and the (tensile) ultimate strength, resulting in the empirical equations

$$pz_{Newman}(\theta = 0) = pz_0 \cdot \frac{\pi^2}{4 \cdot \alpha_g^2} \tag{21}$$

In the plane stress case, associated with a thickness t tending towards zero, the constraint factor α_g clearly tends to 1.15, resulting in $pz_{Newman,pl-\sigma} \cong 1.87 \cdot pz_0$. And under plane strain, assuming a very large t, the above expression tends to $\alpha_g = 2.40$ for the M(T) specimen, therefore $pz_{Newman,pl-\epsilon} \cong 0.43 \cdot pz_0$. For a σ_n/S_Y ratio of 0.7 used in the calculations, equations (20) would result in $pz_{eql,pl-\sigma} = 1.95 \cdot pz_0$ and $pz_{eql,pl-\epsilon} = 0.39 \cdot pz_0$, a quite reasonable agreement.

The maximum size of the plastic zone, pz_{max}, and its associated direction $\theta = \theta_{max}$ can also be fitted with similar expressions for $0 \leq \sigma_n/S_Y \leq 0.8$, resulting in (see Figure 9)

$$\begin{aligned} pz_{eql}(\theta = \theta_{\max})_{pl-\sigma} &= 2pz_0 \left[1.33 + 0.7\left(\frac{\sigma_n}{S_Y}\right) + 1.7 \cdot \left(\frac{\sigma_n}{S_Y}\right)^2\right] \\ pz_{eql}(\theta = \theta_{\max},\ \nu = 0.3)_{pl-\varepsilon} &= 2pz_0 \left[0.8 + 1.5\left(\frac{\sigma_n}{S_Y}\right) + 0.62\left(\frac{\sigma_n}{S_Y}\right)^2\right] \end{aligned} \tag{22}$$

$$\begin{aligned} \theta_{\max pl-\sigma} &= \pm\cos^{-1}\left[0.33 - 0.07\left(\frac{\sigma_n}{S_Y}\right) - 0.25\left(\frac{\sigma_n}{S_Y}\right)^2 + 0.76\left(\frac{\sigma_n}{S_Y}\right)^3\right] \\ \theta_{\max pl-\varepsilon}(\nu = 0.3) &= \pm\cos^{-1}\left[0.053 + 0.84\left(\frac{\sigma_n}{S_Y}\right) - 1.57\left(\frac{\sigma_n}{S_Y}\right)^2 + 1.36\left(\frac{\sigma_n}{S_Y}\right)^3\right] \end{aligned} \tag{23}$$

Note that the above expressions for the maximum angles agree with the expected values for low nominal stresses, i.e., if σ_n/S_Y tends to zero then

$$\begin{aligned} \theta_{\max pl-\sigma} &= \pm\cos^{-1}0.33 \cong \pm 70.5^o \\ \theta_{\max pl-\varepsilon}(\nu = 0.3) &= \pm\cos^{-1}0.053 = \pm\cos^{-1}[(1-2\nu)^2/3] \cong \pm 86.9^o \end{aligned} \tag{24}$$

Note also from Figure 9 that the angle θ_{max} under plane strain decreases in absolute value (because its cosine increases) when the ratio σ_n/S_Y gets higher, a clear indication of the "butterfly effect" on the plastic zone shape. This also happens under plane stress, however only for $\sigma_n/S_Y > 0.3$. Finally, expressions are proposed to fit the shape of the calculated plastic zones:

$$\begin{aligned} pz_{eql}(\theta) &= pz_{eql}(\theta_{\max}) - [pz_{eql}(\theta_{\max}) - pz_{eql}(0)]\left[\frac{\cos\theta - \cos\theta_{\max}}{1 - \cos\theta_{\max}}\right]^2, \quad |\theta| \leqslant \theta_{\max} \\ pz_{eql}(\theta) &= pz_{eql}(\theta_{\max}) \cdot \left[\frac{\cos\theta + 1}{\cos\theta_{\max} + 1}\right]^{1+0.8\frac{\sigma_n}{S_Y}} \cdot \left[\frac{\cos\theta - \gamma}{\cos\theta_{\max} - \gamma}\right]^{1-0.8\frac{\sigma_n}{S_Y}}, \quad \theta_{\max} < |\theta| \leqslant \pi \end{aligned} \tag{25}$$

where the auxiliary variable γ is defined as

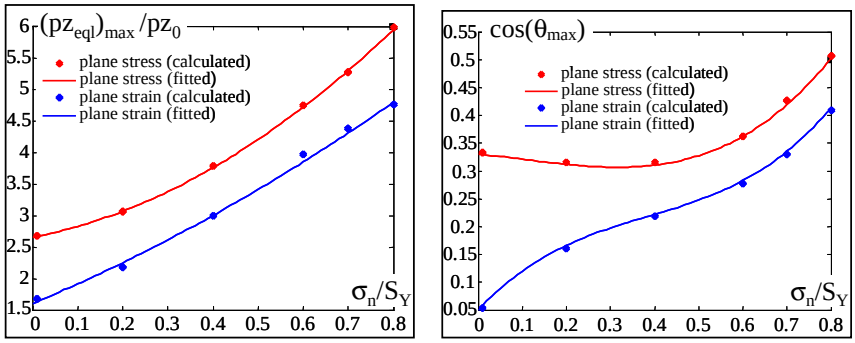

Figure 9: Calculated and fitted values of the maximum normalized plastic zone size $(pz_{eql})_{max}/pz_0$ (left) and associated angle θ_{max} (right), as a function of σ_n/S_Y, for plane stress and plane strain ($\nu = 0.3$).

$$\gamma \equiv \frac{1 - 0.8 \cdot \sigma_n/S_Y + 2 \cdot \cos\theta_{\max}}{1 + 0.8 \cdot \sigma_n/S_Y} \tag{26}$$

Finally note that the above expressions are valid for either plane stress or plane strain, as long as the appropriate values of $pz_{eql}(0)$, $pz_{eql}(\theta_{max})$ and θ_{max} presented above are used. The quality of the fitting can be seen in Figure 10 for plane stress and plane strain.

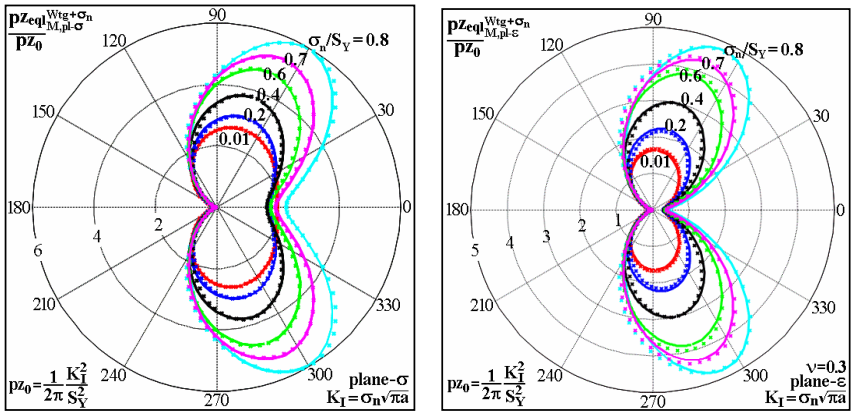

Figure 10: Fitted curves to the Mises plastic zones under plane stress (left) and plane strain (right) considering both the σ_n/S_Y and the equilibrium effects.

However, these $pz_{eql}(\theta)$ are specific for the Irwin plate, but the same procedure can be applied to estimate the plastic zones of any other geometry for which an appropriate Westergaard stress function is available. Moreover, these estimates can be used for calibrating finite-element plastic zone calculations, which can be quite tricky.

7 Conclusions

The nominal stress to the yield strength ratio, σ_n/S_Y, significantly affects the size and the shape of the plastic zones ahead of crack tips, as demonstrated by the rigorous solution of the Irwin crack problem. Therefore, contrary to what is usually accepted and taught in the traditional LEFM literature, the plastic zones do ***not*** depend only on the magnitude of the stress intensity factor K_I. This fact has important consequences, as it can be used to seriously question the similitude principle, one milestone in the practice of mechanical design against fracture. Thus, it should be better explored and understood.

Acknowledgements

The authors have been partially supported by research scholarships provided by the Brazilian National Research Council, CNPq.

References

[1] Unger, D.J., *Analytical Fracture Mechanics*. Dover, 2001.
[2] Inglis, C.E., Stress in a plate due to the presence of cracks and sharp corners. *Philosophical Transactions of the Royal Society series A*, **215**, pp. 119–233, 1913.
[3] Tay, T.E., Yap, C.N. & Tay, C.G., Crack tip and notch tip plastic zone size measurement by the laser speckle technique. *Eng Fract Mech*, **52(5)**, pp. 879–893, 1995.
[4] Sanford, R.J., *Principles of Fracture Mechanics*. Pearson Education, 2003.
[5] Tada, H., Paris, P.C. & Irwin, G.R., *The Stress Analysis of Cracks Handbook*. ASM, 3rd edition, 2000.
[6] Anderson, T.L., *Fracture Mechanics*. CRC, 3rd edition, 2005.
[7] Newman, J.C., Crews, J.H., Bigelow, C.A. & Dawicke, D.S., Variations of a global constraint factor in cracked bodies under tension and bending loads. *ASTM STP 1244*, pp. 21–42, 1995.

Residual life predictions of repaired fatigue cracks

Hao Wu
Mechanics Laboratory of Lille, Ecole Polytech'Lille, University of Lille1 – France
Jaime Tupiassú Pinho de Castro
Department of Mechanical Engineering, Pontifical Catholic University of Rio de Janeiro, Rio de Janeiro/RJ – Brazil
Abdelatif Imad
Mechanics Laboratory of Lille, Ecole Polytech'Lille, University of Lille1 – France
Marco Antonio Meggiolaro
Department of Mechanical Engineering, Pontifical Catholic University of Rio de Janeiro, Rio de Janeiro/RJ – Brazil
Benseddiq Nourredine
Mechanics Laboratory of Lille, Ecole Polytech'Lille, University of Lille1 – France

Abstract

The stop-hole method is a simple and economic repair technique widely used to retard or even to stop the propagation of a fatigue crack in structural components that cannot be replaced immediately after the detection of the crack. Its principle is to drill a hole at or close to the crack tip to transform the crack into a notch, reducing in this way its stress concentration effect. The fatigue life increment that can be achieved with this technique can be modeled by assuming that it is equal to the number of cycles required to re-initiate the crack at the resulting notch root, which depends at least on the crack size and on the hole diameter. To study the effectiveness of this repair method, classical ϵN techniques are adapted to explain the results of several experiments carried out on aluminum plates, taking into account short crack concepts. The comparison among the experimental and the calculation results show that the life increment caused by the stop-holes can be effectively predicted in this way.

Keywords: Stop-hole, crack repair, ϵN method, short cracks, notch sensitivity.

1 Introduction

The so-called stop-hole method is a traditional and popular emergency repair technique that has been employed for a long time to extend the fatigue life of cracked structural components that cannot be

Mechanics of Solids in Brazil 2009, H.S. da Costa Mattos & Marcílio Alves (Editors)
Brazilian Society of Mechanical Sciences and Engineering, ISBN 978-85-85769-43-7

replaced as soon as the crack is discovered, a situation that is not uncommon when dealing with huge components which cannot be stocked nor are shelf available [1–5]. This classical resource is used by many maintenance crews all over the world, since it is relatively inexpensive, simple and fast to apply. Moreover, particularly on remote field conditions, it is frequently the last resort or the only practical option available. In its simplest form, this method consists of drilling a hole in the vicinity of, or centred at the crack tip, to transform the crack into a notch. The stop-hole can in this way increase the residual fatigue life of the cracked structure in comparison to the life it would have if not repaired.

However, in most practical cases the size and the location of the stop-hole are decided in a completely empirical or arbitrary way, totally dependent on the crew experience, beliefs and skill. In consequence, sometimes the stop-hole works very well, producing significant life increments and effectively extending the cracked component service campaign, delaying its replacement time. But in other cases, their results can be disappointing, or even harmful. Therefore, a simple and reliable calculation method to predict beforehand the results of this handy emergency repair technique can be quite useful in real-life situations.

But the appropriate modelling of this apparently trivial problem is not that simple. Several parameters can influence the fatigue life increment caused by the stop-hole. Among them, it is important to mention at least the radius, the position and the surface finish of the hole; the type and the size of the crack; the geometry and the mechanical properties of the component; the history, the type and the magnitude of the load; and the residual stresses around the stop-hole border, since they can all influence the effectiveness of the repair. The purpose of this work is to study a particular case of this complex set, the effect of the stop-hole size. As it turns out to be, even this relatively simple problem presents some quite interesting modelling challenges.

As a general rule, the increase of the stop-hole diameter contributes to decrease the value of the stress concentration factor K_t of the resulting notch, but it also increases the nominal stresses in the residual ligament of the repaired component. Indeed, the originally cracked component is transformed into a notched one after the repair, but it loses material in this process. If the stop-hole is too big, the nominal stress increase can overcome the K_t decrease, compromising its utility. On the other hand, if the stop-hole diameter is too small, the K_t reduction may not be effective. Moreover, it also may not remove the residual stresses associated with the plastic zones which always follow a fatigue crack tip. But this balance is even more delicate, since small stop-hole diameters are associated with smaller notch sensitivities q, which decrease the resulting K_t effect in the fatigue crack (re)initiation life. This effect is quantified by the so-called fatigue stress concentration factor K_f, classically defined by [6–10]

$$K_f = 1 + q \cdot (K_t - 1) \tag{1}$$

However, when a long crack is repaired by a relatively small stop-hole, it forms an elongated notch with a high K_t, which is associated with a steep stress/strain gradient around its root. Consequently, its notch sensitivity q cannot be well predicted by the classical Peterson recipe [11]. Therefore, the model for predicting the residual fatigue life of repaired cracked structures must take this fact into account, as shown below.

Mechanics of Solids in Brazil 2009, H.S. da Costa Mattos & Marcílio Alves (Editors)
Brazilian Society of Mechanical Sciences and Engineering, ISBN 978-85-85769-43-7

2 Experimental program

A set of fatigue tests was carried out on modified SE(T) specimens of thickness $B = 8$ mm and width $W = 80$ mm, see Fig. 1, to measure the number of cycles required to re-initiate the crack after repairing it by drilling a stop-hole of diameter 2ρ centred at the tip of the original crack, when it reached a pre-established length a. This process causes a local delay on the crack propagation rate, and effectively increases its fatigue life. The tested material was an Al alloy 6082 T6, with yielding strength $S_Y = 280MPa$, ultimate tensile strength $S_U = 327MPa$, Young's modulus $E = 68GPa$, and area reduction $RA = 12\%$. The specimens were cut on the LT direction, and the fatigue tests were carried out under constant load range ΔP at $R = P_{min}/P_{max} = 0.57$. This high R-ratio was chosen to avoid any crack closure interference on the crack propagation behavior. The test frequency was set at 30Hz.

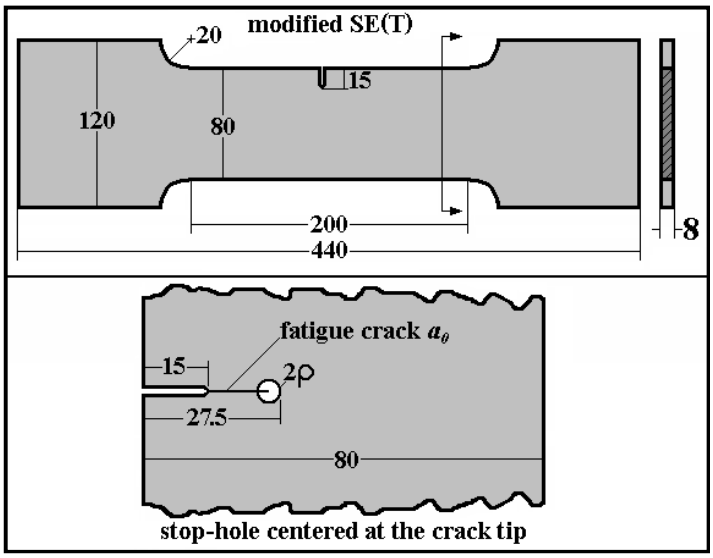

Figure 1: The tested specimens.

After propagating the crack until it achieved the correct length, the specimen was carefully removed from the testing machine, and then fixed and positioned on a milling machine, to machine the 2, 5 or 6 mm diameter stop-holes. Great care was taken to precisely center the drill at the fatigue crack tips. The drilling operation was made at low feedings with plenty refrigeration, and after that the stop-hole was reamed to achieve a 1.5μm diameter accuracy. The specimen was then re-mounted on the test machine, and finally the fatigue test was restarted at the same previous conditions, meaning that the load range ΔP was always maintained constant, before and after the drilling of the stop-holes. All necessary precautions were followed to avoid introducing residual stresses by any means during this

crack repair process, designed to generate notches with the same length $a_n = a_0 + \rho = 27.5$ mm $\Rightarrow$ $a_n/W = 27.5/80 = 0.344$, see Table 1.

Table 1: Loads and nominal stresses $\sigma = P/B(W - a_n)$ associated with the pseudo stress intensity range applied on the notch, $\Delta K^* = 0.838 \cdot \Delta P$ (in MPa$\sqrt{\text{m}}$, calculated using $a_n/W = 0.344$ and ΔP in kN in the standard E-647 SE(T) stress intensity factor formula [12]) after introducing the stop-hole.

ΔK^* (MPa$\sqrt{\text{m}}$)	6	7.4	7.5	8	8.1	9	10.1	13.5	14
ΔP (kN)	7.163	8.835	8.954	9.551	9.671	10.75	12.06	16.12	16.71
P_{min} (kN)	16.66	20.55	20.82	22.21	22.49	24.99	28.04	37.48	38.87
P_{max} (kN)	9.496	11.71	11.87	12.66	12.82	14.24	15.98	21.37	22.16
$\Delta\sigma$ (MPa)	17.06	21.04	21.32	22.74	23.03	25.58	28.71	38.38	39.80
σ_m (MPa)	31.14	38.40	38.92	41.52	42.03	46.70	52.41	70.06	72.65

Twenty-three specimens were tested, and in all of them a number of (delay) cycles N_d had to be spent until a new crack was able to reinitiate from the stop-hole edge. Fig. 2 shows some typical crack propagation curves measured in 3 specimens with different stop-hole radii, all tested under the same loading conditions: the beneficial influence of the stop-holes and the effect of their diameter is clearly identified in this figure. Table 2 summarizes the number of delay cycles N_d caused by the stop-holes under the several testing conditions studied in this program. Note that $N_d > 2 \cdot 10^6$ cycles means that the tests were interrupted if a fatigue crack was not detected at the stop-hole root after this life.

Table 2: Number of measured delay cycles N_d after introducing the stop-hole.

$\rho = 1$ mm		$\rho = 2.5$ mm		$\rho = 3$ mm	
ΔK^* MPa$\sqrt{\text{m}}$	N_d $\times 10^3$ cycles	ΔK^* MPa$\sqrt{\text{m}}$	N_d $\times 10^3$ cycles	ΔK^* MPa$\sqrt{\text{m}}$	N_d $\times 10^3$ cycles
6.0	*> 2000*	7.5	*> 2000*	8.5	*> 2000*
7.4	*980, 724, 580*	8.1	1800	9.0	1150, 960
8.0	*600, 560, 510*	10.1	355, 270	10.1	611, 580
10.1	119, 84	13.5	*65, 58, 37*	14.0	60, 32

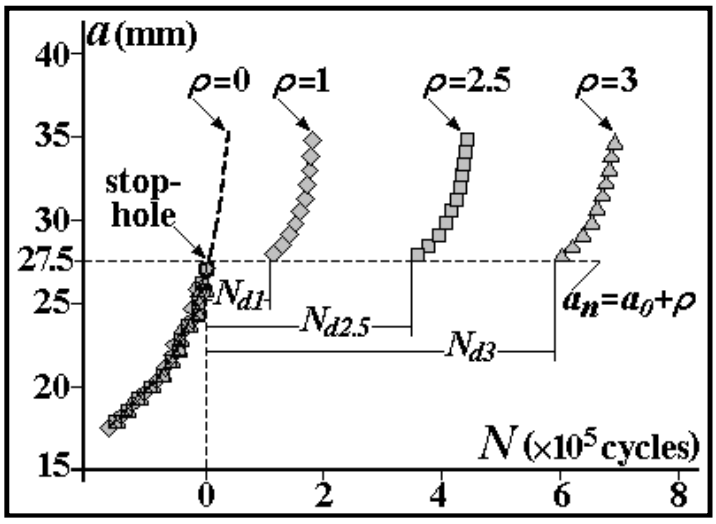

Figure 2: Typical effect of the stop-hole on the subsequent fatigue crack propagation.

3 The basic stop-hole model

The fatigue crack re-initiation lives at the stop-hole roots can be modeled by ϵN local strain procedures, using (i) the cyclic properties of the 6082 T6 Al alloy, namely the four Coffin-Manson parameters σ'_f, b, ϵ'_f and c, σ'_f = *485* MPa, *b= -0.0695*, ϵ'_f = *0.733*, *c = -0.827*, and the coefficient and exponent of the cyclic Ramberg-Osgood stress-strain curve, *H' = 443* MPa, *h' = 0.064* [13]; (ii) the nominal stress history (see table 3); and (iii) the stress concentration factor K_t of the notches generated by repairing the cracks drilling a stop-hole at their tips. Such factors can be estimated by Inglis, giving for hole radii ρ =*1*, 2.5 or 3 mm, respectively

$$K_t \cong 1 + 2\sqrt{(a/\rho)} = 11.49, 7.63 \text{ or } 7.06 \tag{2}$$

The classical ϵN models neglect hardening transients, supposing that the fatigue behavior can be described by an unique Ramberg-Osgood cyclic stress/strain $\sigma\epsilon$ curve, whose parameters *H'* and *h'* can also be used to describe the elastic-plastic hysteresis loop $\Delta\sigma\Delta\epsilon$ curves. These equations should model both the nominal and the notch root cyclic stress/strain behavior, to avoid the logical inconsistency of using two different models for describing the same material (Hookean for the nominal and Ramberg-Osgood for the notch root stresses), and also the significant prediction errors that can be introduced at higher nominal loads by such a regrettably widespread practice [14]. Moreover, as all the studied stop-hole radii were much bigger than the cyclic plastic zones which followed the original fatigue crack tips, it is also reasonable to suppose that they did remove all the damaged material ahead of the cracks and that the material at the resulting notch root can be treated as virgin.

The stop-hole can be modeled by first calculating the stresses and strains maxima and ranges at the notches roots according to a proper stress/strain concentration rule, which should then be used to calculate the crack re-initiation lives by some $\Delta\epsilon \times N$ rule, considering the influence of the static or mean load component. Neglecting this effect could lead to severely non-conservative predictions, as the R-ratio used in the tests was quite high. All the required fatigue life calculations were made using the ViDa software, as summarized in figures 3-5, which show that the lives predicted by Morrow El, Morrow EP and SWT are similar in this case (but it must be emphasized that such a similarity cannot be assumed beforehand, since in many other cases these rules can predict very different fatigue lives!), whereas the Coffin-Manson predictions are highly non-conservative, thus absolutely useless.

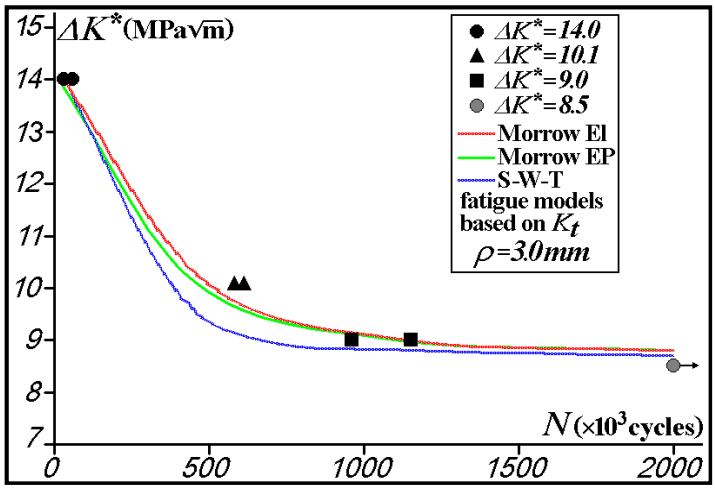

Figure 3: Predicted and measured crack re-initiation lives at the stop-holes roots of radius ρ = *3.0mm*, using the K_t of the repaired crack.

For the two bigger stop-holes (with radii ρ = *3.0* and ρ = *2.5mm*) the predictions reproduce quite well the measured fatigue crack re-initiation lives. In fact, so well that it is worth to point out that the curves in those plots result from calculated life predictions, not from data fitting. But the predictions obtained by the same calculation procedures for the smaller stop-hole with ρ = *1.0mm* are much more conservative. This behavior is a little bit surprising, but since for design purposes this performance is not really that bad, the relatively simple procedure used above could probably be recommended as a useful design tool, at least based on the limited but representative data measured,.

There are few mechanical reasons which can explain the better than expected fatigue lives obtained from the specimens with the ρ = *1mm* stop-holes. Significant compressive residual stresses could be one of them. But all the holes were drilled and reamed following identical procedures, and the bigger stop-hole lives were well predicted supposing σ_{res} = *0*. Therefore, it is difficult to justify why high compressive residual stresses would be present only at the smaller stop-holes roots. The same can

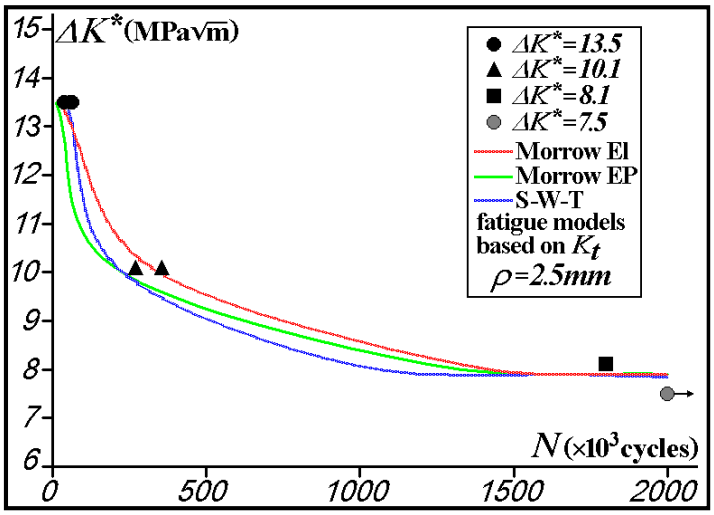

Figure 4: Predicted and measured crack re-initiation lives at the stop-holes roots of radius $\rho = 2.5mm$, using K_t of the repaired crack.

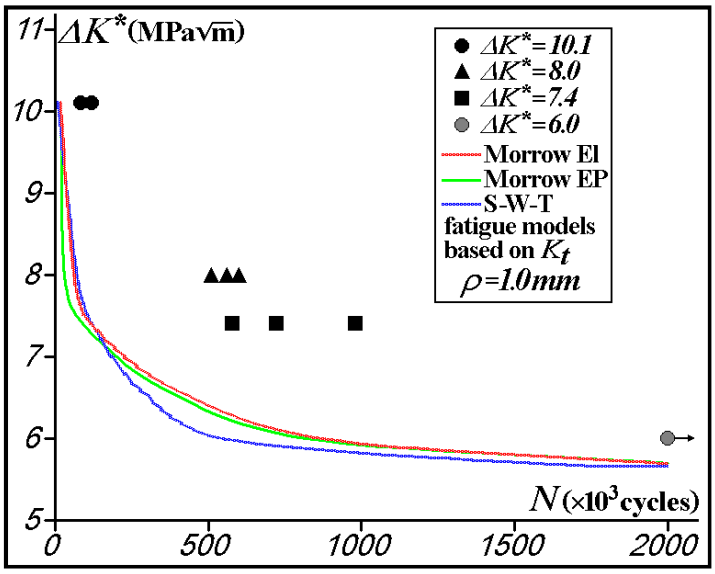

Figure 5: Predicted and measured crack re-initiation lives at the stop-holes roots of radius $\rho = 1.0mm$, using the K_t of the repaired crack.

be said about the surface finish of the stop-holes. However, the smaller stop-holes generate a notch with a bigger K_t and with a much steeper stress gradient near their roots. This effect can significantly affect the growth of short cracks and, consequently, the fatigue notch sensitivity [11], mechanically explaining the measured behavior, as follows.

4 Analytical prediction of the notch sensitivity

Long cracks grow under a given $\Delta\sigma$ and R set when $\Delta K = \Delta\sigma\sqrt{(\pi a)}\cdot f(a/w) > \Delta K_{th}(R)$, where $\Delta K_{th}(R)$ is the propagation threshold at that R-ratio. Therefore, short cracks (which have $a \cong 0$) must propagate in an intrinsically different way, as otherwise $\Delta K(a \to 0, R) > \Delta K_{th}(R) \Rightarrow \Delta\sigma \to \infty$, which is a non-sense, as a stress range $\Delta\sigma > 2S_L(R)$ can generate and propagate a fatigue crack, where $S_L(R)$ is the fatigue limit of the material at R. To conciliate the fatigue limit (e.g.) at R = 0, $\Delta S_0 = 2S_L(0)$, with the propagation threshold under pulsating loads $\Delta K_0 = \Delta K_{th}(0)$, a small "short crack characteristic size" a_0 [15] can be summed to the actual crack size a to obtain

$$\Delta K_{\mathrm{I}} = \Delta\sigma\sqrt{\pi(a + a_0)} \tag{3}$$

These equations correctly predict that the biggest stress range which does not propagate a micro-crack is the fatigue limit: if $a << a_0$, $\Delta K_I = \Delta K_0 \Rightarrow \Delta\sigma \to \Delta S_0$. However, when the crack departs from a notch, as usual, its driving force is the stress range at the notch root $\Delta\sigma$, not the nominal stress range $\Delta\sigma_n$, which is generally used on the ΔK expressions. As in these cases the factor $f(a/w)$ includes the stress concentration effect of the notch, it is better to define $f(a/w)$ separating it in two parts: $f(a/w) = \eta\cdot\phi(a)$, where $\phi(a)$ quantifies the stress gradient effect near the notch, with $\phi(a \to 0) \to K_t$, while the constant η quantifies the free surface effect, to obtain

$$\Delta K_{\mathrm{I}} = \eta \cdot \varphi(a) \cdot \Delta\sigma_n\sqrt{\pi(a + a_0)} \tag{4}$$

Using the traditional definition $\Delta K = f(a/w)\cdot\Delta\sigma\sqrt{(\pi a)}$, an alternate way to model the short crack effect is to suppose that the fatigue crack propagation threshold depends on the crack size, $\Delta K_{th}(a, R = 0) = \Delta K_{th}(a)$, through a function given by

$$\frac{\Delta K_{th}(a)}{\Delta K_0} = \frac{\Delta\sigma\sqrt{\pi a}\cdot f(a/w)}{\Delta\sigma\sqrt{\pi(a + a_0)}\cdot f(a/w)} = \sqrt{\frac{a}{a + a_0}} \Rightarrow \Delta K_{th}(a) = \frac{\Delta K_0}{\sqrt{1 + (a_0/a)}} \tag{5}$$

However, an additional adjustable parameter γ in the $\Delta K_{th}(a)$ expression allows a better fitting of the experimental data [16]

$$\Delta K_{th}(a) = \Delta K_0\left[1 + (a_0/a)^{\gamma/2}\right]^{-1/\gamma} \tag{6}$$

If S'_L and $S_L = S'_L/K_f$ are the fatigue limits measured in standard (non-notched, polished) and in similar but notched SN specimens, $K_t \geq K_f = 1 + q\cdot(K_t - 1)$, where q is the notch sensitivity factor, which can be modeled using the short crack behavior, since it can be associated to tiny cracks which can initiate at the notch root but do not propagate if $2S'_L/K_t < \Delta\sigma < 2S'_L/K_f$ [17]. For example,

the stress intensity factor of a crack that departs from a circular hole of radius ρ in a Kirsh (infinite) plate loaded in mode I is given by [17]

$$\Delta K_{\mathrm{I}} = \eta \cdot \varphi\,(a/\rho) \cdot \Delta\sigma\sqrt{\pi a} = 1.1215 \cdot \varphi\,(a/\rho) \cdot \Delta\sigma\sqrt{\pi a} \tag{7}$$

where $\phi(a/\rho) \equiv \phi(x)$ is given by:

$$\varphi(x) = \left(1 + \frac{0.2}{(1+x)} + \frac{0.3}{(1+x)^6}\right) \cdot \left(2 - 2.354\frac{x}{1+x} + 1.206\left(\frac{x}{1+x}\right)^2 - 0.221\left(\frac{x}{1+x}\right)^3\right) \tag{8}$$

Note that this equation (8) yields $\lim_{a\to 0} \Delta K_{\mathrm{I}} = 1.1215 \cdot 3 \cdot \Delta\sigma\sqrt{\pi a}$ and $\lim_{a\to\infty} \Delta K_{\mathrm{I}} = \Delta\sigma\sqrt{\pi a/2}$, exactly as expected. Thus, if $a_0 = (\Delta K_0/\eta \cdot \Delta S_0\sqrt{\pi})^2$, any crack departing from a Kirsh hole will propagate when

$$\Delta K_I = \eta \cdot \varphi\,(a/\rho) \cdot \Delta\sigma\sqrt{\pi a} > \Delta K_{th} = \Delta K_0 \cdot \left[1 + (a_0/a)^{\gamma/2}\right]^{-1/\gamma} \tag{9}$$

The propagation criterion for these fatigue cracks can then be rewritten as [11]

$$\varphi\left(\frac{a}{\rho}\right) > \frac{\left(\frac{\Delta K_0}{\Delta S_0\sqrt{\rho}}\right) \cdot \left(\frac{\Delta S_0}{\Delta\sigma}\right)}{\left[\left(\eta\sqrt{\frac{\pi a}{\rho}}\right)^{\gamma} + \left(\frac{\Delta K_0}{\Delta S_0\sqrt{\rho}}\right)^{\gamma}\right]^{1/\gamma}} \equiv g\left(\frac{a}{\rho}, \frac{\Delta S_0}{\Delta\sigma}, \frac{\Delta K_0}{\Delta S_0\sqrt{\rho}}, \gamma\right) \tag{10}$$

Therefore, $K_f = \Delta S_0/\Delta\sigma$ can be calculated from the material fatigue limit ΔS_0 and crack propagation threshold ΔK_0, and from the geometry of the cracked piece by

$$\begin{cases} \varphi(a/\rho) = g(a/\rho, \Delta S_0/\Delta\sigma, \Delta K_0/\Delta S_0\sqrt{\rho}, \gamma) \\ \frac{\partial}{\partial a}\varphi(a/\rho) = \frac{\partial}{\partial a} g(a/\rho, \Delta S_0/\Delta\sigma, \Delta K_0/\Delta S_0\sqrt{\rho}, \gamma) \end{cases} \tag{11}$$

This system can be solved for several combinations of materials and hole radii, given by $\Delta K_0/\Delta S_0\sqrt{\rho}$ and γ, to obtain the Kirsh plate notch sensitivity as a function of the hole radius ρ and material fatigue properties. Figure 6 compares the q values calculated in this way with the traditional Peterson curves.

This analytical approach includes the Bazant's exponent γ which allows a better fitting of the short crack propagation data, and it can be generalized to deal with other notch geometries, an important step here, since the stop-hole repaired cracks are similar to an elongated semi-elliptical notch, not to a Kirsh hole. The stress intensity factor of a crack a which departs from such a notch with semi-axes b and c, with a and b in the same direction perpendicular to the (nominal) stress $\Delta\sigma$, is given by

$$\Delta K_{\mathrm{I}} = \eta \cdot F\,(a/b, c/b) \cdot \Delta\sigma\sqrt{\pi a} \tag{12}$$

where $\eta = 1.1215$ is the free surface correction factor and $F(a/b, c/b)$ is the geometric factor associated to the notch stress concentration, which can be calculated as a function of the non-dimensional parameter $s = a/(a + b)$ and of K_t, given by [11]

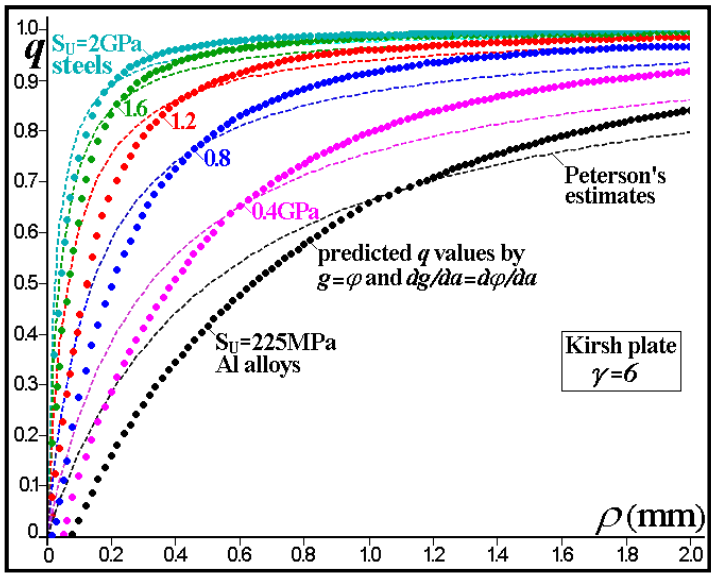

Figure 6: Notch sensitivity q as a function of the Kirsh hole diameter ρ, estimated using mean ΔK_0, ΔS_0 and S_U from 450 steels and aluminium alloys for $\gamma = 6$.

$$K_t = \left(1 + 2\frac{b}{c}\right) \cdot \left[1 + \frac{0.1215}{(1 + c/b)^{2.5}}\right] \tag{13}$$

An analytical expression for the *F(a/b, c/b)* of deep semi-elliptical notches with $c \leq b$ was fitted to a series of finite element numerical calculations

$$F(\frac{a}{b}, \frac{c}{b}) \equiv f\,(K_t, s) = K_t \sqrt{\frac{1 - \exp(-K_t^2 \cdot s)}{K_t^2 \cdot s}} \tag{14}$$

Making $g = \phi$ and $\partial \mathrm{g}/\partial \mathrm{a} = \partial\phi/\partial \mathrm{a}$ in (11), one can calculate the smallest stress range $\Delta\sigma$ required to initiate and propagate a fatigue crack from the notch root at a given combination of γ and $\Delta K_0/\Delta S_0\sqrt{\rho}$, which can be used to calculate $K_f = \Delta S_0/\Delta\sigma$ and q. Indeed, in the lack of compressive residual stresses at the notch border, the mechanical reason for stopping a crack initiated at that border (when it reaches a size a_{st}) is the stress gradient near the notch root: to stop the crack it is necessary that the stress range decrease due to the gradient near the border overcomes the effect of increasing the crack size: a short crack $a < a_{st}$ departing from the notch boundary stops when it reaches

$$\Delta K_I = \eta \cdot \varphi(a_{st}) \cdot \Delta\sigma\sqrt{\pi a_{st}} = \Delta K_0 \cdot \left[1 + (a_0/a_{st})^{\gamma/2}\right]^{-1/\gamma} \tag{15}$$

Traditional notch sensitivity estimates suppose that the sensitivity q depends only on the notch root ρ and the material ultimate strength S_U. However, as shown in Fig. 7, the sensitivity of semi-elliptical notches, besides depending on ρ, ΔS_0, ΔK_0 and γ, is also strongly dependent on the c/b ratio. Moreover, there are reasonable relationships between ΔS_0 and S_U, but not between ΔK_0 and S_U. This means that (e.g.) two steels with same S_U but different ΔK_0 can behave in a way not predictable by the traditional estimates. The curves in figure 8 are calculated for typical Al alloys with mean ultimate strength $S_U = 225MPa$, fatigue limit $S_L = 90MPa \Rightarrow \Delta S_0 = 2S_L S_R/(S_L + S_R) = 129MPa$, propagation threshold $\Delta K_0 = 2.9MPa\sqrt{m}$, and $\gamma = 6$. Note that the corresponding Peterson's curve is well approximated by the semi-circular $c/b = 1$ notch.

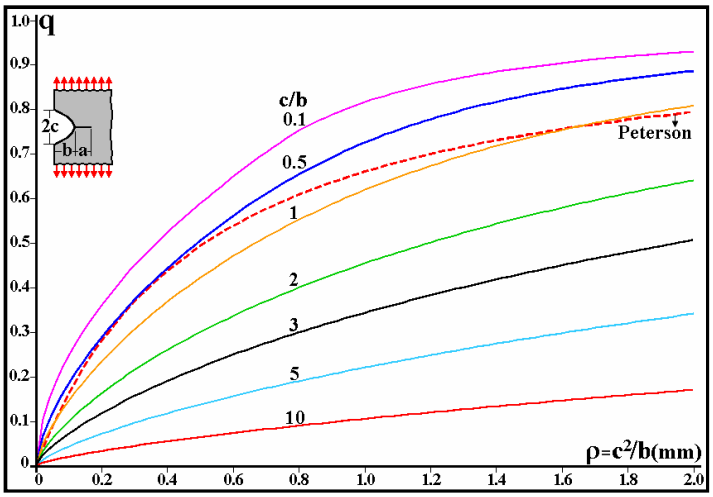

Figure 7: Notch sensitivity q versus the semi-elliptical notch tip radius ρ for plates of typical Al alloys ($\Delta S_0 = 129MPa$, $\Delta K_0 = 2.9MPa\sqrt{m}$, $\gamma = 6$) loaded in mode I.

5 The improved stop-hole model

An improved model for predicting the effect of the stop holes on the crack re-initiation fatigue lives can be generated by using: (i) a semi-elliptical notch with $b = 27.5mm$ and $\rho = c^2/b = 1$, 2.5 or $3mm$ to simulate the stop-hole repaired specimens; (ii) the mechanical properties of the 6082 T6 Al alloy studied in this work; (iii) equation (11) to calculate the notch sensitivity and equation (15) for the stress intensity factor of the repaired specimens; and finally (iv) K_f instead of K_t in the ϵN model.

The predictions generated by such an improved model are presented in Fig. 8, 9 and 10. Since $q \cong 1$ for the $\rho = 3.0$ and $\rho = 2.5mm$ stop-holes, the predictions obtained using their calculated $K_f = 7.0$ and $K_f = 7.2$, respectively, are as good as those obtained using their estimated K_t. However,

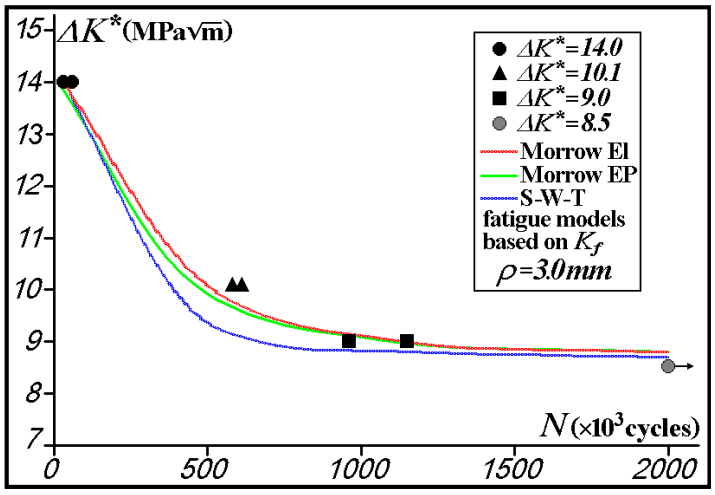

Figure 8: Predicted and measured crack re-initiation lives at the stop-holes roots of radius $\rho = 3.0mm$, using the K_f (instead of K_t) of the repaired crack.

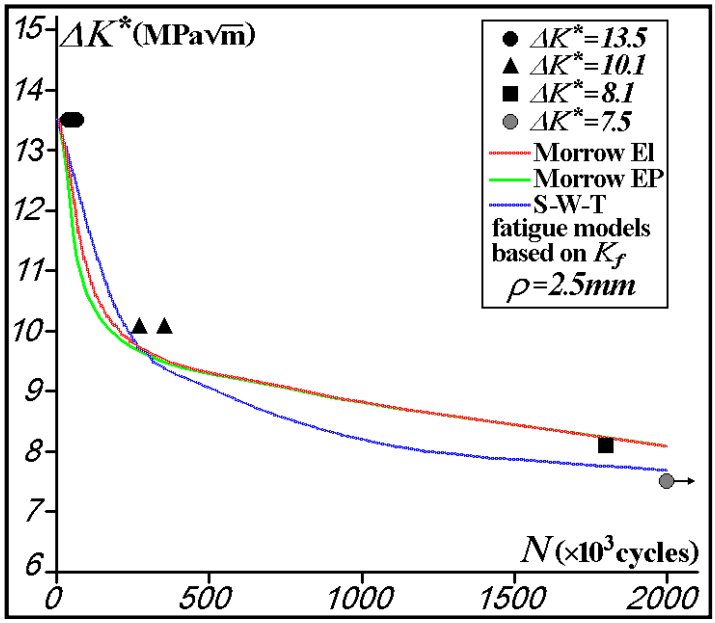

Figure 9: Predicted and measured crack re-initiation lives at the stop-holes roots of radius $\rho = 2.5mm$, using the K_f (instead of K_t) of the repaired crack.

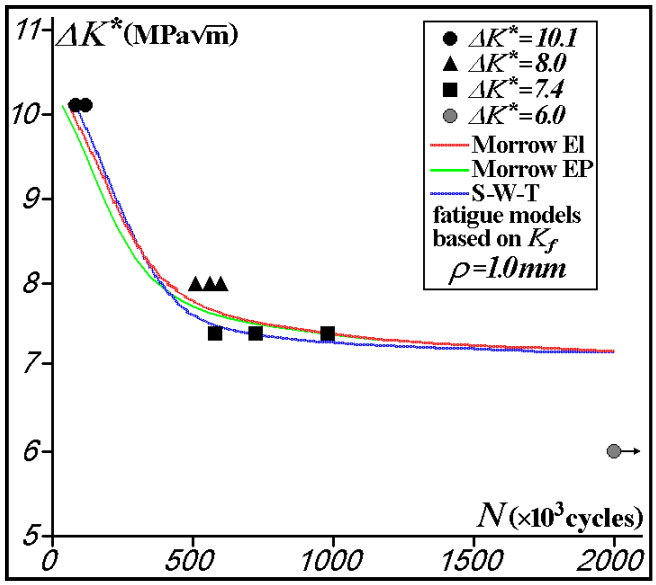

Figure 10: Predicted and measured crack re-initiation lives at the stop-holes roots of radius $\rho = 1.0mm$, using the K_f (instead of K_t) of the repaired crack.

the overly conservative initial predictions formerly obtained for the smaller $\rho = 1mm$ stop-hole, which were generated using its estimated $K_t \cong 11.5$, are much improved when the notch sensitivity effect quantified by its properly calculated $K_f = 8.3$ (considering the important influence of the elongated involving notch geometry) is used in the fatigue crack re-initiation calculations.

The Al 6082 T6 fatigue limit and fatigue crack propagation threshold under pulsating loads required to calculate K_f are estimated as $\Delta K_0 = 4.8\,MPa\sqrt{m}$ and $\Delta S_0 = 110MPa$, following traditional structural design practices [7-10, 22-24], and the Bazant's exponent was chosen, as recommended by Meggiolaro et al. [11], as $\gamma = 6$.

6 Conclusion

Classical ϵN techniques were used with properly estimated properties to reproduce the measured fatigue crack re-initiation lives after stop-hole repairing several modified SEN(T) specimens. The predicted lives were not too dependent on the mean load ϵN model, and the larger stop-hole measured lives could be well reproduced using the stress concentration factor K_t in the Neuber/Ramberg-Osgood system. But such an approach yielded grossly conservative prediction for the smaller stop-hole life improvements. This problem was solved using the fatigue stress concentration factor K_f of the resulting notch instead of K_t in that system. However, the notch sensitivity q required to estimate K_f must be

calculated in a proper way, considering the very important effect of the elongated notch geometry, since classical q estimates are only valid for approximately semi-circular notches.

Acknowledgments

CNPq has provided research scholarships for Castro,JTP and Meggiolaro,MA.

References

[1] Zeljko, D., Comparison of fatigue crack retardation methods. *Eng Failure Analysis*, **3(2)**, pp. 137–147, 1996.
[2] Naned, V., Stjepan, J. & Vatroslav, G., Validation of crack arrest technique by numerical modeling. *Int J Fatigue*, **19(4)**, pp. 283–291, 1997.
[3] Ghfiri, R., Amrouche, A., Imad, A. & Mesmacque, G., Fatigue life estimation after crack repair in 6005 AT-6 aluminium alloy using the cold expansion hole technique. *Fatigue Fract Eng Mater Struct*, **23**, p. 911, 2000.
[4] Song, P.S. & Shieh, Y.L., Stop drilling procedure for fatigue life improvement. *Int J Fatigue*, **26(12)**, pp. 1333–1339, 2004.
[5] Anggit, M., Chobin, M., Akihide, S. & K., R., A crack-growth arresting technique in aluminum alloy. *Eng Failure Analysis*, **15(4)**, pp. 302–310, 2008.
[6] Peterson, R.E., *Stress Concentration Factors*. Wiley, 1974.
[7] Dowling, N.E., *Mechanical behavior of materials*. Prentice-Hall: New Jersey, 1999.
[8] Shigley, J.E., Mischke, C.R. & Budynas, R.G., *Mechanical Engineering Design*. McGraw-Hill, 7th edition, 2004.
[9] Juvinall, R.C. & Marshek, K.M., *Fundamentals of Machine Component Design*. Wiley, 4th edition, 2005.
[10] Norton, R.L., *Machine Design, An Integrated Approach*. Prentice-Hall, 3rd edition, 2005.
[11] Meggiolaro, M.A., Miranda, A.C.O. & Castro, J.T.P., Short crack threshold estimates to predict notch sensitivity factors in fatigue. *Int J Fatigue*, **29(9-11)**, pp. 2022–2031, 2007.
[12] ASTM E647, *Standard test method for measurement of fatigue crack growth rates, ASTM Standards*. ASTM Standards v. 03.01, 2007.
[13] Borrego, L.P., Ferreira, J.M., Pinho da Cruz, J.M. & Costa, J.M., Evaluation of overload effects on fatigue crack growth and closure. *Eng Fract Mech*, **70(11)**, pp. 1379–1397, 2003.
[14] Meggiolaro, M.A. & Castro, J.T.P., Evaluation of the errors induced by high nominal stresses in the classical ϵn method. *Fatigue 2002*, ed. A.F. Blom, 2, pp. 1451–1458, 2002. EMAS 2002.
[15] El Haddad, M.H., Topper, T.H. & Smith, K.N., Prediction of non-propagating cracks. *Eng Fract Mech*, **11**, pp. 573–584, 1979.
[16] Bazant & P., Z., Scaling of quasibrittle fracture: asymptotic analysis. *Int J Fract*, **83(1)**, pp. 19–40, 1997.
[17] Frost, N.E., Marsh, K.J. & Pook, L.P., *Metal fatigue*. Dover, 1999.

Some variational formulations for non-associated hardening plasticity

Nestor Zouain
Mechanical Engineering Department, COPPE, EE - Federal University of Rio de Janeiro, Rio de Janeiro/RJ – Brazil

Abstract

The aim of this paper is to present some generalized variational formulations that find application in incremental or limit analysis of an elastic-plastic continuum including hardening effects and non-associated plastic flow laws.

The class of variational principles focused here are obtained with the aid of a generalized potential function, named bipotential by [1]. This pseudo-potential is used to derive, in a non-standard form, the constitutive relation describing the particular elastic-plastic behavior considered. The device is applicable, for instance, to represent non-associated hardening behaviors. This is the case of the Modified Cam-clay model, widely used in soil mechanics and other areas dealing with frictional materials.

The main result in the paper is a criterion, for this class of generalized material models, that is able to determine whether the phenomenon of plastic collapse will occur or not when the loading is proportionally increased. This criterion is based on a mixed minimum principle.

Keywords: plastic collapse, non-associated plasticity, hardening.

1 Introduction

This paper is focused on some variational formulations that find application in a class of elastoplastic materials that includes hardening behavior and nonassociated flow rules, such as frictional materials. This class is characterized by mathematical models whose flow laws are derived, by means of partial subdifferentiation, of a generalized potential, called bipotential. The arguments of the bipotential are generalized stresses and plastic strain rates, so that partial subdifferentiation ends up with implicit equations for the fluxes; this justifies the name Implicit Standard Materials (ISM) given by G. de Saxcé and coworkers [1–3]. The class of implicit standard materials includes the generalized standard materials (GSM) introduced by [4], which only consider associated flow laws.

The main result in the paper is a criterion for this class of generalized material models, based on a minimum principle and aimed to determine whether the phenomenon of plastic collapse will occur or

Mechanics of Solids in Brazil 2009, H.S. da Costa Mattos & Marcílio Alves (Editors)
Brazilian Society of Mechanical Sciences and Engineering, ISBN 978-85-85769-43-7

not when the loading is proportionally increased.

The scope of the paper includes a brief presentation of: (i) the constitutive equations of plasticity with internal variables allowing for non-associated evolution equations, (ii) the GSM approach and the bipotential generalization, (iii) a minimum principle characterizing the flow law of GSM materials, and (iv) plastic collapse for non-associated elastic-plastic materials and a related minimum principle, first obtained by [5]. New theoretical results, concerning the principles introduced in the aforementioned reference, are developed in this work.

We use the notation: $\boldsymbol{\sigma}$ for stress tensors, $\boldsymbol{\varepsilon}$ for strain tensors and $\boldsymbol{d}$ for strain rate tensors. Mean and deviatoric parts of the stress are denoted by

$$\sigma_m := \frac{1}{3}\mathrm{tr}\,\boldsymbol{\sigma} \qquad \boldsymbol{S} := \boldsymbol{\sigma} - \sigma_m \boldsymbol{1} \tag{1}$$

where $\boldsymbol{1}$ is the identity, tr is the trace operator and dev denotes the deviatoric part of a tensor. Then, the volumetric components of the strain and strain rate are defined as

$$\varepsilon_v := \mathrm{tr}\,\boldsymbol{\varepsilon} \qquad \varepsilon_v := \mathrm{tr}\,\boldsymbol{d} \tag{2}$$

Superscripts e and p identify elastic and plastic parts of strain or strain rates.

2 Generalized Standard Materials (GSM)

In this section we consider associated elastic-plastic materials with internal variables, representing hardening, included in the framework of generalized standard materials [6, 7].

Let the plastic admissibility domain be denoted by

$$P = \{(\boldsymbol{\sigma}, \boldsymbol{A}) \;\mid\; f(\boldsymbol{\sigma}, \boldsymbol{A}) \leqslant 0\} \tag{3}$$

where $\boldsymbol{A}$ is a list of thermodynamic forces associated to hardening mechanisms of the material. This domain is convex and contains the origin $(\boldsymbol{\sigma}, \boldsymbol{A}) = (0, 0)$. The yield function f is assumed regular here for the sake of simplicity. Accordingly, the dissipation potential is defined as

$$D(\boldsymbol{d}^p, \dot{\boldsymbol{\beta}}) := \sup_{(\boldsymbol{\sigma}^*, \boldsymbol{A}^*) \in P} \left(\boldsymbol{\sigma}^* \cdot \boldsymbol{d}^p + \boldsymbol{A}^* \cdot \dot{\boldsymbol{\beta}} \right) \tag{4}$$

where $\dot{\boldsymbol{\beta}}$ denotes the list of internal fluxes corresponding by duality to the internal forces $\boldsymbol{A}$. Then, the associative constitutive equations relating inelastic fluxes and internal forces are equivalently stated as one of the following equations

$$(\boldsymbol{d}^p, \dot{\boldsymbol{\beta}}) \in \partial \mathcal{I}_P(\boldsymbol{\sigma}, \boldsymbol{A}) \tag{5}$$

$$(\boldsymbol{\sigma}, \boldsymbol{A}) \in \partial D(\boldsymbol{d}^p, \dot{\boldsymbol{\beta}}) \tag{6}$$

$$D(\boldsymbol{d}^p, \dot{\boldsymbol{\beta}}) + \mathcal{I}_P(\boldsymbol{\sigma}, \boldsymbol{A}) = \boldsymbol{\sigma} \cdot \boldsymbol{d}^p + \boldsymbol{A} \cdot \dot{\boldsymbol{\beta}} \tag{7}$$

where the symbol ∂ denotes subdifferential and the indicator function $\mathcal{I}_P(\boldsymbol{\sigma}, \boldsymbol{A})$ equals 0 if $(\boldsymbol{\sigma}, \boldsymbol{A}) \in P$, or $+\infty$ otherwise. The subdifferential set $\partial \mathcal{I}_P(\boldsymbol{\sigma}, \boldsymbol{A})$ contains all the outward normals to the boundary of P at $(\boldsymbol{\sigma}, \boldsymbol{A})$ (see for instance: [8, p. 285]; [6, p. 48]; [2, p. 397]; [9]; [10]).

Mechanics of Solids in Brazil 2009, H.S. da Costa Mattos & Marcílio Alves (Editors)
Brazilian Society of Mechanical Sciences and Engineering, ISBN 978-85-85769-43-7

In terms of the plastic function, this flow law is more often expressed by the system

$$(\boldsymbol{d}^p, \dot{\boldsymbol{\beta}}) = \dot{\lambda} \nabla f(\boldsymbol{\sigma}, \boldsymbol{A}) \tag{8}$$

$$\dot{\lambda} f(\boldsymbol{\sigma}, \boldsymbol{A}) = 0 \qquad f(\boldsymbol{\sigma}, \boldsymbol{A}) \leqslant 0 \qquad \dot{\lambda} \geqslant 0 \tag{9}$$

where ∇f is the gradient of f. Notice that (8) may also be written as $\boldsymbol{d}^p = \dot{\lambda} \nabla_{\boldsymbol{\sigma}} f(\boldsymbol{\sigma}, \boldsymbol{A})$ and $\dot{\boldsymbol{\beta}} = \dot{\lambda} \nabla_{\boldsymbol{A}} f(\boldsymbol{\sigma}, \boldsymbol{A})$, where $\nabla_{\boldsymbol{\sigma}} f(\boldsymbol{\sigma}, \boldsymbol{A})$ denotes partial differentiation.

The plastic admissibility of generalized stresses is enforced by (7) when it is taken into account that the right hand side is always finite. Hence, this equation reduces to $D(\boldsymbol{d}^p, \dot{\boldsymbol{\beta}}) = \boldsymbol{\sigma} \cdot \boldsymbol{d}^p + \boldsymbol{A} \cdot \dot{\boldsymbol{\beta}}$ together with $(\boldsymbol{\sigma}, \boldsymbol{A}) \in P$. Moreover, by the definition of the dissipation function it follows that

$$D(\boldsymbol{d}^p, \dot{\boldsymbol{\beta}}) + \mathcal{I}_P(\boldsymbol{\sigma}, \boldsymbol{A}) \geqslant \boldsymbol{\sigma} \cdot \boldsymbol{d}^p + \boldsymbol{A} \cdot \dot{\boldsymbol{\beta}} \qquad \forall \, \{(\boldsymbol{\sigma}, \boldsymbol{A}), (\boldsymbol{d}^p, \dot{\boldsymbol{\beta}})\} \tag{10}$$

and the equality holds if and only if the generalized stress and strain are related by the flow law that is been described in this section.

3 Implicit Standard Materials (ISM)

The variational inequality given by (10) is the starting formulation to introduce the concept of bipotentials, which is intended to enhance the field of application of pseudo-potentials formulations for constitutive relations.

For convenience, we define generalized stress and strain rate as follows

$$\boldsymbol{\Sigma} := (\boldsymbol{\sigma}, \boldsymbol{A}) \qquad \boldsymbol{D}^p := (\boldsymbol{d}^p, \dot{\boldsymbol{\beta}}) \tag{11}$$

with scalar product

$$\boldsymbol{\Sigma} \cdot \boldsymbol{D}^p = \boldsymbol{\sigma} \cdot \boldsymbol{d}^p + \boldsymbol{A} \cdot \dot{\boldsymbol{\beta}} \tag{12}$$

meaning dissipated power.

A function $b(\boldsymbol{\Sigma}, \boldsymbol{D}^p)$, with values in $[-\infty, \infty]$, is said to be a bipotential if it is separately convex with respect to $\boldsymbol{\Sigma}$ and $\boldsymbol{D}^p$, not identically $+\infty$, and satisfies the following condition

$$b(\boldsymbol{\Sigma}, \boldsymbol{D}^p) \geqslant \boldsymbol{\Sigma} \cdot \boldsymbol{D}^p \qquad \forall \, (\boldsymbol{\Sigma}, \boldsymbol{D}^p) \tag{13}$$

For a function $b(\boldsymbol{\Sigma}, \boldsymbol{D}^p)$ complying with the above definition, it is proven that any pair $(\boldsymbol{\Sigma}, \boldsymbol{D}^p)$ satisfying one of the three conditions below will also satisfy the remaining two conditions:

$$\boldsymbol{D}^p \in \partial_{\boldsymbol{\Sigma}} b(\boldsymbol{\Sigma}, \boldsymbol{D}^p) \tag{14}$$

$$\boldsymbol{\Sigma} \in \partial_{\boldsymbol{D}^p} b(\boldsymbol{\Sigma}, \boldsymbol{D}^p) \tag{15}$$

$$b(\boldsymbol{\Sigma}, \boldsymbol{D}^p) = \boldsymbol{\Sigma} \cdot \boldsymbol{D}^p \tag{16}$$

For a proof of the above equivalence see, for instance, Appendix A in [5].

We are using in (14) the notation $\partial_{\boldsymbol{\Sigma}} b(\boldsymbol{\Sigma}, \boldsymbol{D}^p)$ for the partial subdifferential of b with respect to $\boldsymbol{\Sigma}$. This is, by definition, the set of all $\boldsymbol{D}^p$ such that

$$b(\boldsymbol{\Sigma}^*, \boldsymbol{D}^p) - b(\boldsymbol{\Sigma}, \boldsymbol{D}^p) \geqslant (\boldsymbol{\Sigma}^* - \boldsymbol{\Sigma}) \cdot \boldsymbol{D}^p \qquad \forall \boldsymbol{\Sigma}^* \tag{17}$$

Likewise, (15) is equivalent, by definition, to

$$b(\boldsymbol{\Sigma}, \boldsymbol{D}^{p*}) - b(\boldsymbol{\Sigma}, \boldsymbol{D}^p) \geqslant \boldsymbol{\Sigma} \cdot (\boldsymbol{D}^{p*} - \boldsymbol{D}^p) \qquad \forall \boldsymbol{D}^{p*} \tag{18}$$

Moreover, the above conditions are also equivalent to the following

$$\boldsymbol{\Sigma} \in \arg\inf_{\boldsymbol{\Sigma}^*} \{b(\boldsymbol{\Sigma}^*, \boldsymbol{D}^p) - \boldsymbol{\Sigma}^* \cdot \boldsymbol{D}^p\} \tag{19}$$

$$\boldsymbol{D}^p \in \arg\inf_{\boldsymbol{D}^{p*}} \{b(\boldsymbol{\Sigma}, \boldsymbol{D}^{p*}) - \boldsymbol{\Sigma} \cdot \boldsymbol{D}^{p*}\} \tag{20}$$

with $\arg\inf$ denoting the set of solutions of the minimization problem.

Then, we use the bipotential to characterize a particular flow law in the following manner: a generalized stress $\boldsymbol{\Sigma}$ and a generalized plastic strain rate $\boldsymbol{D}^p$ are related by the flow law, and we denote this by

$$(\boldsymbol{\Sigma}, \boldsymbol{D}^p) \in \mathsf{FlowLaw} \tag{21}$$

if and only if this pair is extremal for the bipotential, i.e. this pair satisfies one of the equivalent conditions (16) to (20). Implicit standard materials (ISM) are characterized by evolution equations of this particular kind.

We introduce now a key concept for the present paper. The gap function $\psi(\boldsymbol{\Sigma}, \boldsymbol{D}^p)$, associated to the flow law emanating from the bipotential, is defined as follows

$$\psi(\boldsymbol{\Sigma}, \boldsymbol{D}^p) := b(\boldsymbol{\Sigma}, \boldsymbol{D}^p) - \boldsymbol{\Sigma} \cdot \boldsymbol{D}^p \tag{22}$$

For an arbitrary choice of $(\boldsymbol{\Sigma}, \boldsymbol{D}^p)$ the gap function gives the difference between the available power of dissipation to the actual dissipated power of the arguments.

The following proposition gives the relation of this gap function to the flow law.

Proposition 1. Let ψ be given by (22) and FlowLaw defined in (21), then

$$\psi_0 := \inf_{\boldsymbol{\Sigma}, \boldsymbol{D}^p} \psi(\boldsymbol{\Sigma}, \boldsymbol{D}^p) \tag{23}$$

is finite and nonnegative. Further

1. If $\psi_0 = 0$ then

$$(\boldsymbol{\Sigma}, \boldsymbol{D}^p) \in \mathsf{FlowLaw} \qquad \Leftrightarrow \qquad (\boldsymbol{\Sigma}, \boldsymbol{D}^p) \in \arg\inf_{\boldsymbol{\Sigma}, \boldsymbol{D}^p} \psi(\boldsymbol{\Sigma}, \boldsymbol{D}^p) \tag{24}$$

2. If $\psi_0 > 0$ then FlowLaw is empty.

Proof. The gap function $\psi(\boldsymbol{\Sigma}^*, \boldsymbol{D}^{p*})$ is proper [10] and nonnegative for all $(\boldsymbol{\Sigma}^*, \boldsymbol{D}^{p*})$, as a consequence of the definition of the bipotential. Further, if $(\boldsymbol{\Sigma}, \boldsymbol{D}^p) \in \mathsf{FlowLaw}$ then, using (16), it follows that $\psi(\boldsymbol{\Sigma}, \boldsymbol{D}^p) = 0$, which leads directly to the thesis. □

We assume from now on that the constitutive model is such that FlowLaw is not empty. However, we will show that, even under this hypothesis for the material behavior, a proposition analogous to the one stated above describes the situation of an ISM body with respect to the occurrence of plastic collapse.

3.1 An ISM model for frictional materials

As an example of a material that can be cast in the framework of implicit standard materials, i.e. with an evolution equation derived froma a bipotential, we give in this subsection a very brief description of the Modified Cam-clay model (MCC) widely used in soil mechanics [9, 11, 12]. A bipotential for this type of material was given in [1] (see also [13, p. 65]) and it is considered in the following.

Plastic admissibility of generalized stresses is represented by the following constraint

$$f(\boldsymbol{\sigma},\rho) := \sqrt{\frac{3}{2M^2}\|\boldsymbol{S}\|^2 + (\sigma_m+\rho)^2} - \rho \leqslant 0 \tag{25}$$

where the scalar hardening variable ρ is the only stress-like internal variable of the model. That is, with reference to our general notation, we have in this particular case $\boldsymbol{A} \equiv \rho$ and $\boldsymbol{\sigma} \equiv (\boldsymbol{S}, \sigma_m)$.

The usual flow law for MCC is written

$$\boldsymbol{d}^{p\,\mathrm{dev}} = \dot{\lambda}\nabla_{\boldsymbol{S}} f = \frac{3\dot{\lambda}}{2M^2 R(\boldsymbol{\sigma},\rho)}\boldsymbol{S} \tag{26}$$

$$d_v^p = \dot{\lambda}\nabla_{\sigma_m} f = \frac{\dot{\lambda}(\sigma_m+\rho)}{R(\boldsymbol{\sigma},\rho)} \tag{27}$$

$$\dot{\beta} = \frac{\dot{\lambda}(\sigma_m+\rho)}{R(\boldsymbol{\sigma},\rho)} \tag{28}$$

with the notation

$$R(\boldsymbol{\sigma},\rho) := \sqrt{\frac{3}{2M^2}\|\boldsymbol{S}\|^2 + (\sigma_m+\rho)^2} \tag{29}$$

The Cam-clay model described here is not a generalized standard material in the sense of [6] since this model adopts the non-associated hardening evolution equation (28). The hardening part (28) of the flow law is justified by experimental observation on these materials indicating that hardening is dependent on the volumetric plastic strain. Accordingly, (28) produces the appropriate link between the hardening internal variable and the volumetric plastic strain.

The hardening flux $\dot{\beta}$ is maintained, for convenience, formally distinct to the volumetric plastic strain rate $\boldsymbol{d}^p$, although both are identical in any actual evolution process. This equality is enforced by defining a set K such that $(\boldsymbol{d}^p, \dot{\beta}) \in K$ if and only if $d_v^p = \dot{\beta}$. The indicator of K is the function $\mathcal{I}_K(\boldsymbol{d}^p, \dot{\beta})$ that equals 0 if $d_v^p = \dot{\beta}$ and $+\infty$ otherwise.

With the notation introduced above the bipotential is written as follows

$$b(\boldsymbol{\sigma},\rho,\boldsymbol{d}^p,\dot{\beta}) = M\rho\sqrt{\frac{2}{3}\|\boldsymbol{d}^{p\ \mathrm{dev}}\|^2+\frac{1}{M^2}(d_v^p)^2}+\mathcal{I}_P(\boldsymbol{\sigma},\rho)+\mathcal{I}_K(\boldsymbol{d}^p,\dot{\beta}) \tag{30}$$

that is

$$b(\boldsymbol{\sigma},\rho,\boldsymbol{d}^p,\dot{\beta}) = \begin{cases} M\rho\sqrt{\frac{2}{3}\|\boldsymbol{d}^{p\ \mathrm{dev}}\|^2+\frac{1}{M^2}(d_v^p)^2} & \text{if} \quad d_v^p=\dot{\beta} \quad \text{and} \quad f(\boldsymbol{\sigma},\rho)\leqslant 0 \\ +\infty & \text{otherwise} \end{cases} \tag{31}$$

4 Plastic collapse of solids obeying the ISM model

Elastic-plastic bodies or structures may collapse under a constant system of loads in a process where the stress distribution remains constant while the body undergoes unbounded purely plastic deformation. This phenomenon is eventually experienced by solids made of materials with associated flow rules or even with non-associated laws.

In classical associative plasticity it is proven that the load producing plastic collapse is the maximum load that the body can sustain in equilibrium. It is well known that for non-associated plastic behavior these two concepts, namely: plastic collapse and limit load, are not necessarily linked.

Accordingly, the first concern in this section is to give a precise mathematical formulation characterizing plastic collapse for materials with hardening and represented by means of bipotentials. Afterwards, we propose a variational problem and prove a proposition relating, in a non-standard manner, the solution of this minimization problem with the existence of collapse solutions.

Some additional notation is introduced now: The symbol $\mathcal{D}$ denotes the linear deformation operator mapping velocities (displacements) into compatible strain rates (respectively strains). The internal power associated with a stress field $\boldsymbol{\sigma}$ and a velocity distribution w is denoted

$$\langle\boldsymbol{\sigma},\mathcal{D}\boldsymbol{w}\rangle := \int_{\mathcal{B}}\boldsymbol{\sigma}\cdot\mathcal{D}\boldsymbol{w}\,d\mathcal{B} \tag{32}$$

Likewise, the external power associated with a load system $\boldsymbol{F}$ is

$$\langle\boldsymbol{F},\boldsymbol{w}\rangle := \int_{\mathcal{B}}\boldsymbol{b}\cdot\boldsymbol{w}\,d\mathcal{B}+\int_{\Gamma_u}\boldsymbol{\tau}\cdot\boldsymbol{w}\,d\Gamma \tag{33}$$

where $\boldsymbol{b}$ and $\boldsymbol{\tau}$ are volume and surface load densities, Γ denotes area and Γ_u is part of the boundary where null displacements are prescribed. Accordingly, the set of stress fields in equilibrium with a given load system $\boldsymbol{F}$ is defined as

$$\mathcal{S}(\boldsymbol{F}) := \{\boldsymbol{\sigma} \mid \langle\boldsymbol{\sigma},\mathcal{D}\boldsymbol{w}\rangle = \langle\boldsymbol{F},\boldsymbol{w}\rangle\ \forall\ \boldsymbol{w}\} \tag{34}$$

where the virtual velocity $\boldsymbol{w}$ varies in the linear space of admissible velocities.

4.1 The equations of plastic collapse

When the body undergoes plastic collapse the stress and the internal thermodynamical forces remain constant. In view of the elastic state equations, a constant stress field induces an elastic deformation distribution that is also constant in time. This, in turn, means that the strain rate field is at the same time compatible and purely plastic.

Likewise, according to the state equation relative to internal variables, internal hardening forces being constant during plastic collapse implies that the kinematical internal variables are also constant, that is, $\dot{\boldsymbol{\beta}} = 0$ at all points in the body.

This description of plastic collapse is implemented in the sequel. The computation of the critical factor α that amplifies a prescribed load system $\boldsymbol{F}$ so as to produce unbounded purely plastic deformation, when superposed to a fixed (non-amplified) load $\boldsymbol{F}^0$, can be formulated as follows:

PC - *The plastic collapse problem.* Find $(\alpha, \boldsymbol{\sigma}, \boldsymbol{A}, v)$ such that

$$\boldsymbol{\sigma} \in \mathcal{S}(\boldsymbol{F}^0 + \alpha \boldsymbol{F}) \tag{35}$$

$$\langle \boldsymbol{F}, \boldsymbol{v} \rangle = 1 \tag{36}$$

$$b(\boldsymbol{\sigma}, \boldsymbol{A}, \mathcal{D}\boldsymbol{v}, 0) = \boldsymbol{\sigma} \cdot \mathcal{D}\boldsymbol{v} \quad \text{in } \mathcal{B} \tag{37}$$

$$\alpha \geqslant 0 \tag{38}$$

Notice that (36) has only been included to select one normalized velocity distribution, so discarding all its multiples by a scalar, which would also be solutions otherwise.

4.2 Variational plastic collapse analysis for ISM

We propose in this subsection a minimization problem and then explain how it can be used for the purpose of determining the existence of collapse solutions to PC, i.e. $(\alpha, \boldsymbol{\sigma}, \boldsymbol{A}, v)$ satisfying (35-38).

In order to obtain the desired variational formulation, given below, we impose (37) in the form of a minimum principle as given in (22), but now we adjoin (35), (36) and (38) as constraints.

MP - *A minimum principle*

$$\Upsilon = \inf_{\alpha, \boldsymbol{\sigma}, \boldsymbol{A}, \boldsymbol{v}} \left\{ \Psi(\boldsymbol{\sigma}, \boldsymbol{A}, \mathcal{D}\boldsymbol{v}, 0) \quad | \quad \boldsymbol{\sigma} \in \mathcal{S}(\boldsymbol{F}^0 + \alpha \boldsymbol{F});\ \langle \boldsymbol{F}, \boldsymbol{v} \rangle = 1;\ \alpha \geqslant 0 \right\} \tag{39}$$

where $\Psi := \int_{\mathcal{B}} \psi d\mathcal{B}$.

A first remark on the use of this variational formulation is the following lemma, whose proof is straightforward.

Lemma. The infimum Υ of the minimum principle MP is finite and nonnegative if the feasible set is nonempty, otherwise it is $+\infty$.

Using the constraints in (39) we get

$$\Psi(\boldsymbol{\sigma}, \boldsymbol{A}, \mathcal{D}\boldsymbol{v}, 0) = \mathtt{b}(\boldsymbol{\sigma}, \boldsymbol{A}, \mathcal{D}\boldsymbol{v}, 0) - \langle \boldsymbol{\sigma}, \mathcal{D}\boldsymbol{v} \rangle = \mathtt{b}(\boldsymbol{\sigma}, \boldsymbol{A}, \mathcal{D}\boldsymbol{v}, 0) - \langle \boldsymbol{F}^0, \boldsymbol{v} \rangle - \alpha \tag{40}$$

where $\mathtt{b} := \int_{\mathcal{B}} b d\mathcal{B}$.

Thus, the minimum principle (39) can be rewritten as

$$\Upsilon = \inf_{\alpha,\boldsymbol{\sigma},\boldsymbol{A},\boldsymbol{v}} \Big\{ \mathfrak{b}(\boldsymbol{\sigma},\boldsymbol{A},\mathcal{D}\boldsymbol{v},0) - \langle \boldsymbol{F}^0,\boldsymbol{v}\rangle - \alpha \quad | \quad \boldsymbol{\sigma} \in \mathcal{S}(\boldsymbol{F}^0+\alpha\boldsymbol{F});\ \langle \boldsymbol{F},\boldsymbol{v}\rangle = 1;\ \alpha \geqslant 0 \Big\} \tag{41}$$

Now, the main remarks and results: (i) MP has always a solution for Υ, and (ii) finding this solution can give the answer to the question about existence of solutions to PC. More precisely:

Proposition 2. The plastic collapse problem PC and the minimum principle MP are related by the following implications:

1. If there exists a solution $(\alpha,\boldsymbol{\sigma},\boldsymbol{A},\boldsymbol{v})$ of PC, then this set is a minimizer for MP and corresponds to $\Upsilon = 0$.
2. If MP has a minimizer $(\alpha,\boldsymbol{\sigma},\boldsymbol{A},\boldsymbol{v})$ such that $\Upsilon = 0$, then this set is a solution for PC.

Proof.

1. Collapse solutions satisfy all constraints in MP and give $\Upsilon = 0$ since $\psi = 0$ on $\mathcal{B}$.
2. $\Upsilon = 0$ implies $\psi = 0$ on $\mathcal{B}$ and this completes the set of equations in PC. □

In other words, if we solve the minimization problem MP, analytically or numerically, we can conclude that:

1. If $\Upsilon = 0$ then the computed minimal solution describes the plastic collapse for the obtained amplifcation factor α.
2. If $\Upsilon > 0$ then the body does not collapse for any loading of the form $\boldsymbol{F}^0 + \alpha\boldsymbol{F}$.

4.3 Back to generalized standard materials

In this section we analyze the particular form of the principle MP for the case of associated plasticity with hardening. In this case it holds that

$$\mathfrak{b}(\boldsymbol{\sigma},\boldsymbol{A},\boldsymbol{d}^p,\dot{\boldsymbol{\beta}}) = D(\boldsymbol{d}^p,\dot{\boldsymbol{\beta}}) + \mathcal{I}_P(\boldsymbol{\sigma},\boldsymbol{A}) \tag{42}$$

Then the formulation MP becomes

$$\Upsilon = \inf_{\alpha,\boldsymbol{\sigma},\boldsymbol{A},\boldsymbol{v}} \Big\{ D(\mathcal{D}\boldsymbol{v},0) - \langle \boldsymbol{F}^0,\boldsymbol{v}\rangle - \alpha \quad | \quad \boldsymbol{\sigma} \in \mathcal{S}(\boldsymbol{F}^0+\alpha\boldsymbol{F});\ (\boldsymbol{\sigma},\boldsymbol{A}) \in \mathsf{P};\ \langle \boldsymbol{F},\boldsymbol{v}\rangle = 1;\ \alpha \geqslant 0 \Big\} \tag{43}$$

where $(\boldsymbol{\sigma},\boldsymbol{A}) \in \mathsf{P}$ means that $(\boldsymbol{\sigma}(\mathbf{x}),\boldsymbol{A}(\mathbf{x})) \in P$ for all $\mathbf{x} \in \mathcal{B}$.

The optimization problem above can be separated as follows

$$\Upsilon = \mathsf{U} - \mathsf{L} \tag{44}$$

with

$$\mathsf{U} := \inf_{v} \Big\{ D(\mathcal{D}\boldsymbol{v},0) - \langle \boldsymbol{F}^0,\boldsymbol{v}\rangle \ \mid\ \langle \boldsymbol{F},\boldsymbol{v}\rangle = 1 \Big\} \tag{45}$$

$$\mathsf{L} := \sup_{\alpha,\boldsymbol{\sigma},\boldsymbol{A}} \Big\{ \alpha \ \mid\ \boldsymbol{\sigma} \in \mathcal{S}(\boldsymbol{F}^0+\alpha\boldsymbol{F});\ (\boldsymbol{\sigma},\boldsymbol{A}) \in \mathsf{P};\ \alpha \geqslant 0 \Big\} \tag{46}$$

The optimization principles (45) and (46) are the kinematical and statical formulations of limit analysis. These are dual optimization principles representing the limit analysis problem, which in

this case coincides with the plastic collapse problem under some conditions on the functional spaces describing the mechanical system. Dual optimization problems are the subject of minimax theory in convex analysis (see e.g. [14, p. 327]) where two basic results are called the weak and the strong duality theorems. The weak duality theorem, proven under mild hypotheses, when applied to the present situation, ensures that $\mathsf{U} \geqslant \mathsf{L}$. Strong duality demands more stringent conditions so as to prove that there exists $\mathsf{U} = \mathsf{L}$ and also that this number is a saddle value of the Lagrangian.

5 Conclusions

We analyzed two variational formulations, given in (23) and (41), restricted to a special class of materials, denoted ISM, whose evolution equations are derived from a bipotential by partial subdifferentiation.

The first minimization principle, (23), constitutes a variational formulation of the flow law that is used to obtain the second one.

The main result in the paper is precisely described in Proposition 2. It is a criterion, based on the minimum principle (41), aimed to determine whether the phenomenon of plastic collapse will occur or not when the loading is proportionally increased. This minimization principle (41), that is a mixed one in the sense that involves both kinematical and statical variables, is different to the statical and kinematical variational formulations proposed by [2]. The derivation of the minimization principle MP shown in the present paper is different, and more clearly motivated, compared to the presentation in [5].

Responsibility notice

The author is the only responsible for the printed material included in this paper

References

[1] de Saxcé, G., The bipotential method, a new variational and numerical treatment of the disssipative laws of materials. *10th Int. Conf. on Mathematical and Computer Modelling and Scientific Computing*, pp. 1–6, 1995.

[2] de Saxcé, G. & Bousshine, L., Limit analysis for implicit standard materials: Application to the unilateral contact with dry friction and the non-associated flow rules in soils and rocks. *International Journal of Mechanical Sciences*, **40(4)**, pp. 387–398, 1998.

[3] Bodovillé, G. & de Saxcé, G., Plasticity with non-linear kinematic hardening: modelling and shakedown analysis by the bipotential approach. *European Journal of Mechanics A/Solids*, **20**, pp. 99–112, 2001.

[4] Halphen, B. & Nguyen, Q.S., Sur les matériaux standard généralisés. *Journal de Mécanique Théorique et Appliquée*, **14**, pp. 1–37, 1975.

[5] Zouain, N., Pontes, I., Borges, L. & Costa, L., Plastic collapse in non-associated hardening materials with application to Cam-clay. *International Journal of Solids and Structures*, **44(13)**, pp. 4382–4398, 2007.

[6] Nguyen, Q.S., *Stability and Nonlinear Solid Mechanics*. Wiley, 2000.

[7] Lemaitre, J., *Mechanics of Solid Materials*. Cambridge University Press, 1990.
[8] Maugin, G.A., *The Thermomechanics of Plasticity and Fracture*. Cambridge University Press: UK, 1992.
[9] Houlsby, G.T. & Puzrin, A.M., *Principles of Hyperplasticity: An approach to plasticity theory based on thermodynamic principles*. Springer-Verlag: London, 2006.
[10] Rockafellar, R.T., *Convex Analysis*. Princeton University Press, 1970.
[11] Roscoe, K.H. & Burland, J.B., On the generalized behaviour of "wet" clay. *Engineering Plasticity*, **48**, pp. 535–609, 1968.
[12] Ulm, F.J. & Coussy, O., *Mechanics and Durability of Solids, Volume I*. MIT, Prentice Hall: New Jersey, 2003.
[13] Hjiaj, M., *Sur la classe des matériaux standard implicites: Concept, aspects discrétisés et estimation de l'erreur* a posteriori. Ph.D. thesis, Faculté Polytechnique de Mons, 1999. Docteur en Sciences Appliquées.
[14] Hiriart-Urruty, J.B. & Lemaréchal, C., *Convex Analysis and Minimization Algorithms I*. Springer-Verlag: Berlin, 1993.

Mechanics of Solids in Brazil 2009, H.S. da Costa Mattos & Marcílio Alves (Editors)
Brazilian Society of Mechanical Sciences and Engineering, ISBN 978-85-85769-43-7

Author Index

Mechanics of Solids in Brazil 2009, H.S. da Costa Mattos & Marcílio Alves (Editors)
Brazilian Society of Mechanical Sciences and Engineering, ISBN 978-85-85769-43-7

Mechanics of Solids in Brazil 2009, H.S. da Costa Mattos & Marcílio Alves (Editors)
Brazilian Society of Mechanical Sciences and Engineering, ISBN 978-85-85769-43-7